AMME

Advances in Mechanical and Materials Engineering

Advances in Mechanical and Materials Engineering

41

2024

SPIS TREŚCI

Original Research

The Influence of Plasma Nitriding Process Conditions on the Microstructure of Coatings Obtained on the Substrate of Selected Tool Steels

Magdalena Mokrzycka [1] , **Adrianna Przybyło [2]** , **Marek Góral [1],*** , **Barbara Kościelniak [1]** , **Marcin Drajewicz [1]** , **Tadeusz Kubaszek [1]** , **Kamil Gancarczyk [1]** , **Andrzej Gradzik [1]** , **Kamil Dychtoń [1]** , **Marek Poręba [1]** , **Jakub Jopek [1]** , **Maciej Pytel [1]**

[1] Rzeszow University of Technology, Research and Development Laboratory for Aerospace Materials, Zwirki i Wigury 4, 35-959 Rzeszow, Poland; magdamok007@wp.pl (M. Mokrzycka), b.koscielnia@prz.edu.pl (B. Kościelniak), drajewic@prz.edu.pl (M. Drajewicz), tkubaszek@prz.edu.pl (T. Kubaszek), Kamil-Gancarczyk@prz.edu.pl (K. Gancarczyk), andrzej_gradzik@prz.edu.pl (A. Gradzik), kdychton@prz.edu.pl (K. Dychtoń), poreba@prz.edu.pl (M. Poręba), jakub.jopek01@gmail.com (J. Jopek), mpytel@prz.edu.pl (M. Pytel)

[2] Doctoral School of Engineering and Technical Sciences at the Rzeszow University of Technology, Rzeszow University of Technology, Powstancow Warszawy 12, Rzeszow, 35-959, Poland; przybylo.ada@gmail.com

* Correspondence: mgoral@prz.edu.pl

Abstract

This study presents the results of research into the influence of the time of the plasma nitriding process on the microstructure of the coatings obtained. Cold-work tool steels (60WCrV8, 90MnCrV8, 145Cr6), hot-work tool steel (X37CrMoV5-1) and high-speed tool steel (HS6-5-2) were selected as substrate material. The processes were carried out under industrial conditions using an Ionit device from Oerlikon Metaplas with variable process times of 2, 4 and 6 hours. According to literature data, a nitriding mixture consisting of 5% nitrogen and 95% hydrogen was chosen, which allowed the expected diffusion layer to be obtained without a white layer (composed of iron nitrides). Analysis of elemental mapping indicates that the presence and content of nitride-forming elements influences the formation of alloy additive nitrides in the microstructure of the diffusion layer. It was also found that an increase in the duration of plasma nitriding, results in an increase in the depth of the nitrided layers formed on the substrate of high-alloy steels: X37CrMoV5-1 and HS6-5-2. Nitrides of alloying additives, present in the diffusion layer, are formed in the high-alloyed the hot-work steel X37CrMoV5-1, indicating that these steels are the most suitable for plasma nitriding of the entire tool steels analysed.

Keywords: plasma nitriding, tool steel, heat treatment, kinetic of nitriding

1. Introduction

Thermochemical treatment processes are performed to improve tribological and mechanical properties and increase corrosion resistance. They are implemented by combining thermal treatments with a targeted change in the chemical composition of the surface layer (Skrzypek & Przybyłowicz, 2020). At a specific temperature and time, the near-surface zone is diffusely saturated with an element or elements in solid (Ucar et al., 2020; Xie et al., 2012), liquid (Ghelloudj et al., 2018; Kul et al., 2020; Sen et al., 2005), gaseous (Barnaby et al., 1975; Liu et al., 2020; Torchane, 2021) and plasma (Drajewicz et al., 2021) media. One such process is plasma nitriding, which aims to improve the anti-corrosive properties (Kusmič & Hrubý, 2015; Kusmič et al., 2021), fatigue resistance (Kovacı et al., 2016a) and abrasive wear (Karaoğlu, 2002; Kovacı et al., 2019) of steels, titanium alloys and iron matrix sinters (Çelik et al., 2000; Rakowski et al., 2006).
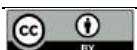
The plasma nitriding process is carried out under vacuum. After the charge is gradually heated to the required temperature by cathodic screens or resistance heating in the furnace retort, gas is delivered to the retort at a fixed pressure of 10-2÷1 Pa. The nitrided elements are at negative potential with respect to the furnace walls, the anode is the furnace retort. The applied voltage induces a glow discharge. In an electric field, ionisation of the gas takes place, whose positive ions and high-energy neutral particles bombard the surfaces of the workpieces. This results in the release of heat necessary for the thermal activation of the nitrogen and its diffusion, as well as the occurrence of cathodic sputtering, which removes a layer of passive oxides from the surface. The surface of the objects is developed by making grain boundaries and other defects in the crystal structure visible. The described process favours the activation of the surface so that the adsorption and nucleation of new phases is facilitated, thus eliminating the problem of overcoming the surface passivity barrier. Nitrogen atoms form FeN nitrides with the precipitated iron atoms, which are adsorbed onto the surface of the product and then decompose. Iron and alloying element atoms combine with diffusing nitrogen atoms to form nitrides (Aghajani & Behranghi, 2017; Blicharski, 2012; Burakowski & Wierzchoń, 1995; Chattopadhyay, 2004; Dobrzański, 2006; Kula, 2000; Przybyłowicz, 1999; Świć & Gola, 2017).

The surface layers formed during the nitriding process are characterised by a zonal structure. They may include phases from the iron-nitride system such as γ', ε and solid solution α (Głowacki et al. 2005a; Wang et al., 2013). The compound layer, otherwise known as the white zone, is formed by $Fe_{2-3}N$ and Fe_4N nitrides, often also $Fe_2(C_xN_y)$ carbide nitrides. The dominant phase near the surface is the ε-phase, the content of which decreases moving deeper into the material, while the content of the γ' phase increases until it dominates in front of the diffusion zone (Głowacki et al., 2005b). It is not only the presence of the ε phase that is responsible for the porosity of the white zone, as demonstrated by (Michalski et al., 2005) during a controlled gas nitriding process. They observed that porosity is formed in layers of compounds consisting of ε and γ' phase as well as in layers with γ' phase only. The $Fe_{2-3}N$ nitride layer is characterized by greater hardness and brittleness than the Fe_4N layer. It is also more resistant to wear and corrosion. The Fe_4N nitride layer tolerates overload more favorably and has a higher resistance to fracture. The values of the thermal expansion coefficients of the γ' and ε phases are different, making the compound layer prone to cracking and falling off at the interface (Spies & Dalke, 2014). Given the properties of the ε and γ' phases that make up the white zone, it is described as hard and resistant to abrasive and adhesive wear. It is also brittle, which, if thicker, can result in spelling in service (Lan & Wen, 2012; Yang et al., 2017). The compound layer is often removed from the component before use by grinding, polishing or chemical etching in solutions of cyan compounds (Czerwiński, 2012). The microstructure of the core matrix of the nitrided component coincides with the microstructure of the diffusion zone matrix. When the limiting solubility of nitrogen in the zone is exceeded, fine nitrides of the alloying elements aluminium, chromium, molybdenum, vanadium and tungsten are released. Their presence causes an increase in hardness by distorting the crystal structure of the matrix (Blicharski, 2012; Czerwiński, 2012; Wang & Chung, 2013). The diffusion zone is characterised by higher impact strength than the white zone (Zhang & Bell, 1985). It also determines the strength of the nitrided layer; due to its high resistance to thermal fatigue and abrasive wear (Lan & Wen, 2012; Yang et al., 2017). Furthermore, the resulting coating increases resistance to seizure, corrosion and the tempering effect of heat.

The main advantage of plasma nitriding is that it is possible to form a layer of compounds with only the ε or γ' phase, or to produce a nitrided layer consisting only of the diffusion zone. Plasma nitriding allows diffusion of nitrogen across grain boundaries and lattice diffusion (Blicharski, 2012). The advantage of this process is a surface with much less roughness than gas nitriding and minimal distortion of the feedstock. Therefore, products after the process do not require additional machining (Aghajani & Behrangi, 2017; Spies & Dalke, 2014).

In order to make the best use of the nitriding potential, special steels with a specific chemical composition have been developed containing, among others, aluminium, chromium, molybdenum and vanadium, which have a high affinity for nitrogen (Blicharski, 2012; Spies & Dalke, 2014) The carbon content should not exceed 0.5 % because chromium, molybdenum and vanadium form stable carbides, hindering the formation of nitrides (Aghajani & Behrangi, 2017). Due to the low solubility of nitrogen, the alloying elements separate almost entirely in the form of finely dispersed nitrides. The resulting volume difference causes local distortion of the crystal lattice, resulting in a strengthening effect and increased solubility of nitrogen in the iron matrix (Spies & Dalke, 2014). The presence of alloying additives in the surface layer increases hardness, provides high hardenability and resistance to temper-

ing embrittlement (Blicharski, 2017; Burzyńska-Szyszko, 2011; Chattopadhyay, 2004). With increasing nitriding time and temperature, coagulation of the precipitated nitrides can occur, as indicated by a decrease in hardness. Under constant nitriding process conditions, an increase in the content of alloying additives results in a decrease in the depth of the compound layer. In the case of alloyed steels, an increase in the content of nitride-forming elements leads to a decrease in the thickness of the diffusion layer and an increase in hardness at its surface (Spies & Dalke, 2014). Also the process atmosphere influences the microstructure of the nitrided layers. A small addition of oxidising compounds to the nitriding mixture during plasma or gas nitriding has a beneficial effect on the nitrided layer - the presence of oxygen stabilises the ε -phase and increases the growth rate of the layer (Czerwiński, 2012).

Appropriate selection of the process parameters makes it possible to obtain surface layers with a variety of structures, which is much more difficult in the case of conventional nitriding methods (Çelik et al., 2000; Karaoğlu, 2003; Rakowski et al., 2006). An analysis of the literature (Albarran et al., 1992; Berkowski, 2005; Blicharski, 2012; Borgolli et al., 2002; Głowacki et al., 2005a, 2005b; Höck et al., 1996; Karamiş et al., 2019; Kovacı et al., 2016b; Krbaťa et al., 2019; Kusmič et al., 2021; Ozbaysal et al., 1986; Podgornik & Vižintin, 1999, 2001; Skonieski et al., 2013; Zhao et al., 2021) allows us to conclude that it is preferable to produce nitrided layers consisting of a compound zone and a diffusion zone. However, for some applications, a more favourable set of properties is offered by the diffusion layer alone - good resistance to abrasive wear, thermal fatigue and impact strength. Hot working dies are subjected to harsh working conditions such as repeated impacts and heating and cooling cycles. Plasma nitriding of hot work dies made from AISI H13 steel allowed only a diffusion zone to be obtained, resulting in a 10-fold increase in the service life of the machined tools (Peng et al., 2020). In order to create a nitrided layer with only a diffusion layer, it is necessary to limit the nitrogen content of the nitriding mixture.

Literature data (Blicharski, 2012) indicate the following chemical composition of the nitriding gas mixture: 1-5% nitrogen, the rest carrier gas. Podgornik and Vižintin (1999), wishing to form a nitrided layer without a compound zone on 42CrMo4 heat-treatable steel, proposed the following parameters for the plasma nitriding process: gas mixture composition $0.6\%N_2$ and $99.4\%H_2$, temperature 540^oC and time 17 h. When observing the microstructure, a forming layer of compounds was noticed in addition to the diffusion layer. In the work (Skonieski et al., 2013), the tempering steel 42CrMo4 was subjected to plasma nitriding. The process took place at 500^oC and the variables were time and composition of the gas mixture. No white zone was observed during microscopic examination although the results of the analysis of the glow discharge optical emission spectroscopy (GDOES) profiles suggested its presence (depths of less than 1 μm). Kovaci et al. (2016a), for 42CrMo4 steel, obtained a white zone depth of 1-2 μm and a diffusion zone of 120-130 μm, during the process at 400^oC with a gas mixture of $50\%N_2$ and $50\%H_2$. Głowacki et al. (2005a) investigated the effect of the nitrogen content of the H_2-N_2 mixture on the plasma nitriding process of 38HMJ nitridable steel and WCL hot work tool steel. The treatment was carried out for 2 h at 550^oC. From the diffractograms, it was found that the structure of the layers formed on 38HMJ and WCL steels consisted of: solution α - at 3% N_2, solution α and phase γ' - at 5% N_2, solution α, phase γ' and ε - at 9% N_2 and solution α and phase γ' at 26% N_2. A thin layer of iron nitrides (9% N_2) and a solid film of iron nitrides and alloying additives (26% N_2) were also observed. In (Da Silva Rocha et al., 1999), AISI M_2 tool steel was plasma nitrided at 350, 400, 450 and 500^oC with a gas mixture of 5% N_2 and 95% H_2 for 30 min. A nitrided layer consisting of a diffusion zone alone was obtained, the depth of which increased with increasing nitriding time.

The aim of this study was to determine the influence of the plasma nitriding process parameters and the chemical composition of the substrate material on the microstructure of the nitride layers formed, on the substrates of selected tool steels, and to determine the growth kinetics of the diffusion layer below. The influence of chemical composition of tool steels from each group (cold work, hot work and HSS) on nitriding process was investigated. The plasma nitriding time was selected as a main factor of coatings formation. The all processes were conducted in semi-industrial conditions.

2. Experimental

According to experimental plan plasma nitriding, at 550ºC and times of 2, 4 and 6 hours, was carried out on five selected tool steels, the chemical composition of which is shown in Table 1. Process was conducted using industrial system (Ionit, Sulzer-Metaplas, Germany).

Table 1. Chemical composition of steel according to EN ISO 4957 (2004) and PN-H-85023 (1986) standards.

Steel designation	Chemical composition [wt.%]								
	C	Si	Mn	P	S	Cr	Mo	V	W
60WCrV8	0.55-0.65	0.70-1.00	0.15-0.45	-	-	0.90-1.20	-	0.10-0.20	1.70-2.20
90MnCrV8	0.85-0.95	0.10-0.40	1.80-2.20	-	-	0.20-0.50	-	0.05-0.20	-
145Cr6	1.30-1.45	0.15-0.40	0.40-0.70	≤ 0.030	≤ 0.030	1.30-1.65	-	0.10-0.25	-
X37CrMoV5-1	0.33-0.41	0.80-1.20	0.25-0.50	-	-	4.80-5.50	1.10-1.50	0.30-0.50	-
HS6-5-2	0.80-0.88	≤0.45	-	-	-	3.80-4.50	4.70-5.20	1.70-2.10	5.90-6.70

The samples, measuring Ø30 mm × 30 mm, were supplied in tempered condition from one batch of steels. The surfaces to be tested were sandblasted with electrocorundum and then ground on an ATM GmbH Saphir 330 grinder with SiC grit sandpaper with a gradation of 80 to 500. 90 specimens were prepared - 2 specimens for each steel grade at three time variants: 2 h, 4 h and 6 h. The time variants were chosen for optimisation of nitriding time and selection of shortest time for diffusion layer formation. Before the processes, the samples were cleaned in an ultrasonic cleaner. The invariant process parameters are shown in Table 2. The process was controlled and monitored using built-in software in nitriding system. The composition of plasma gasses was selected for formation only of diffusion layer without outer nitride layers.

Table 2. Plasma nitriding process parameters.

Composition of nitrided mixture, l/h	Temperature, °C	Frequency, kHz	Voltage, V	Intensity, A	Pressure, mbar	Pulse
$5N_2 + 95H_2$	550	10	400	15	3.6	20/80

After the plasma nitriding processes, metallographic samples were taken. The microstructure of the nitrided layers was studied on a Phenom XL scanning electron microscope from PIK Instruments, using a back-scattered electron detector - BSE. The coating thickness was measured in 10 places on the cross-section of sample and average thickness value was calculated. The chemical composition was analysed using a secondary X-ray energy dispersive spectrometer - EDS, integrated with the Phenom XL microscope. Maps showing the relative content of chemical elements from the analysed areas were obtained. All samples were etched with Nital 4% to measure the depth of the layers formed. The phase composition was analysed using X-ray diffraction (XRD) method and ARL X'TRa diffractometer.

3. Results and discussion

3.1. Cold-work tool steel 60WCrV8

The microstructure of the 60WCrV8 steel, after each of the three nitriding processes (Fig. 1a-c), consists of a dark matrix and bright irregularly shaped precipitates, occurring mainly on the grain boundaries. The increased concentration of tungsten in the chemical composition analysis maps (Fig. 1) indicates that these are tungsten carbides. This is also indicated by the carbon content (0.55-0.65 wt.%), which may have increased the ability of the alloying additives to form carbides and decreased the ability to form nitrides (Aghajani & Behrangi, 2017). The near-surface layers of 60WCrV8 steel after plasma nitriding at 2, 4 and 6 h show areas of increased nitrogen concentration, the amount of which decreases with increasing distance from the surface of the samples. During the plasma nitriding process at 2 h, a diffusion layer with an average depth of 0.79 μm, was obtained. After 4 h of the process, a layer with an average depth of 2.14 μm was obtained, and after 6 h: 2.12 μm. The XRD phase analysis from the surface of sample showed presence of Fe_4N (γ') and Fe_3N (ε) nitrides (Fig. 2). It confirms the formation of thin nitrides layer on the surface of samples. The presence of FeO oxides was also confirmed by XRD phase analysis.
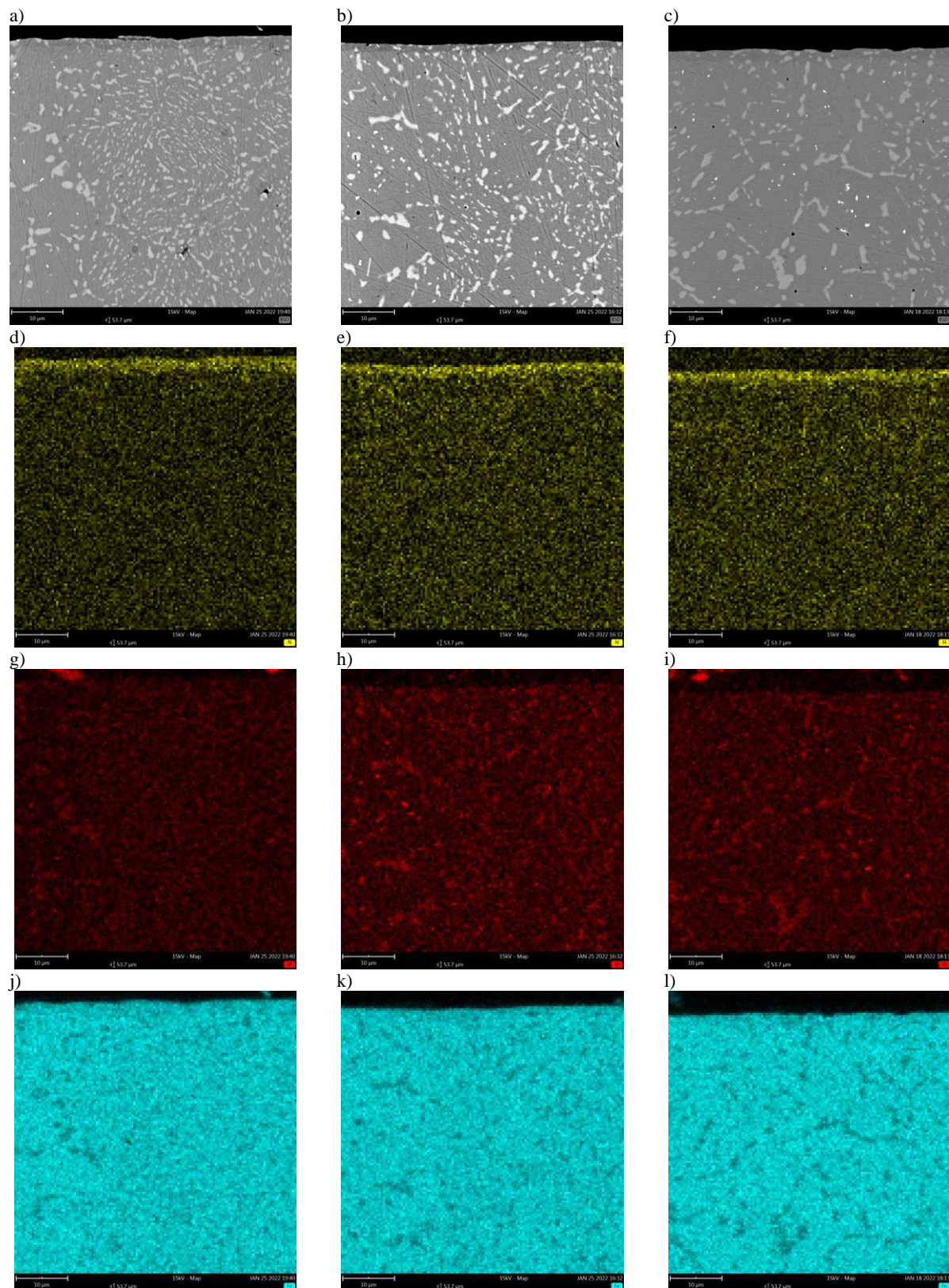
Fig. 1. a)-l) Microstructure of the layer after 2, 4 and 6 h of the nitriding process carried out on a tool steel grade 60WCrV8 substrate and the result of the relative concentrations of nitrogen, tungsten and iron.
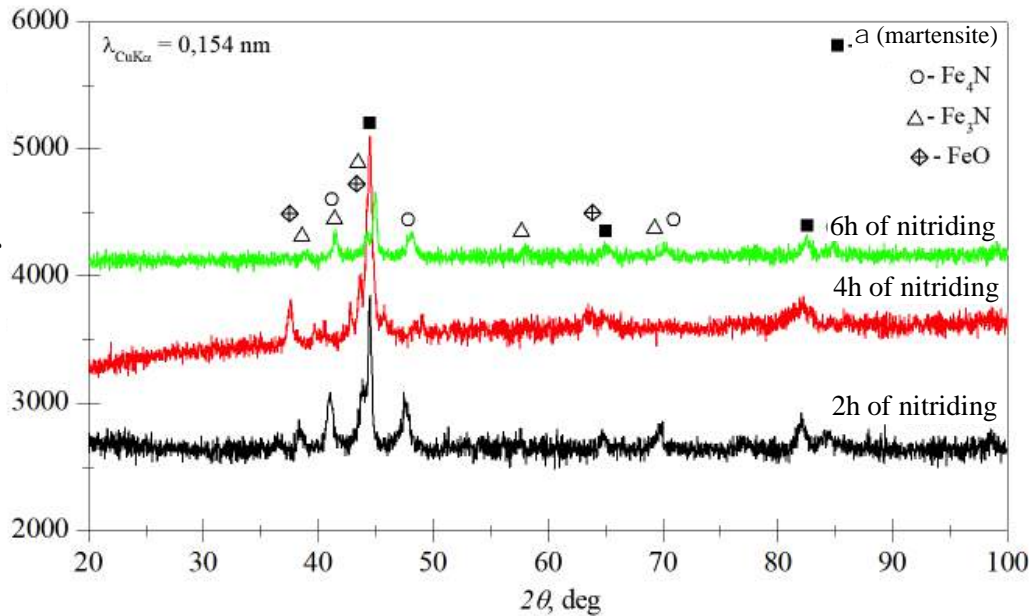
Fig. 2. The results of XRD phase analysis from samples of 60WCrV8 cold wor steel after 2, 4 and 6h of plasma nitriding process.

3.2. Cold-work tool steel 90MnCrV8

The results of XRD phase analysis confirmed the formation of Fe_4N (γ') nitride as well as FeO on the surface of 90MnCrV8 steel samples after plasma nitriding process (Fig. 3). The microstructure of samples after plasma nitriding at 2, 4 and 6 h (Fig. 4a-c) consists of a light matrix and dark globular precipitates. They are uniformly distributed in the microstructure, mainly in the grains, but also at the grain boundaries (Fig. 4a-c). Identification of the precipitates requires further study. The near-surface layer of the samples shows areas of slightly increased nitrogen concentration, the amount of which decreases with increasing distance from the surface of the samples (Fig. 4d-f). This indicates the formation of a diffusion layer on the substrate of the 90MnCrV8 steel, plasma nitrided at 2, 4 and 6 h. No nitrides were observed in the microstructure of the steel, as confirmed by the chemical composition analysis. No changes in iron and chromium concentrations were observed (Fig. 4g-l). The high carbon content (0.85-0.95 wt.%) and the low content of nitride-forming elements (0.20-0.50 wt.% chromium and 0.05-0.20 wt.% vanadium) hinder the possibility of alloy additive nitride formation (Aghajani & Behrangi, 2017; Blicharski, 2012). The average layer depth is 1.17 μm, for treatment after 2 h. After the nitriding process at 4 h, the average layer depth is 0.66 μm, and after 6 h: 0.57 μm.
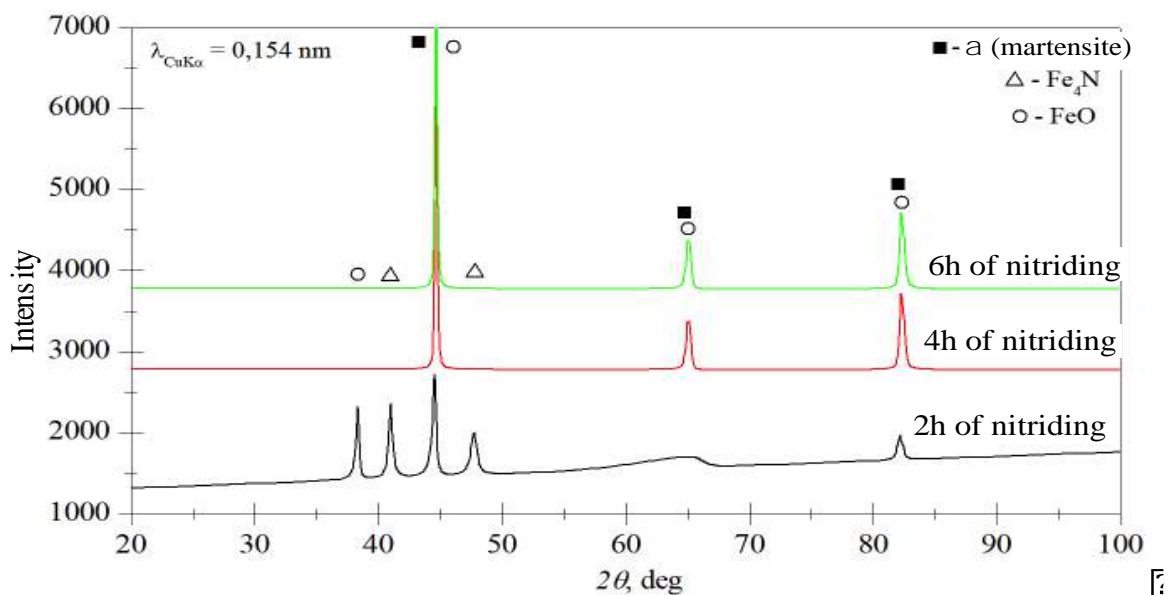
Fig. 3. The results of XRD phase analysis from samples of 60WCrV8 cold wor steel after 2, 4 and 6h of plasma nitriding process.
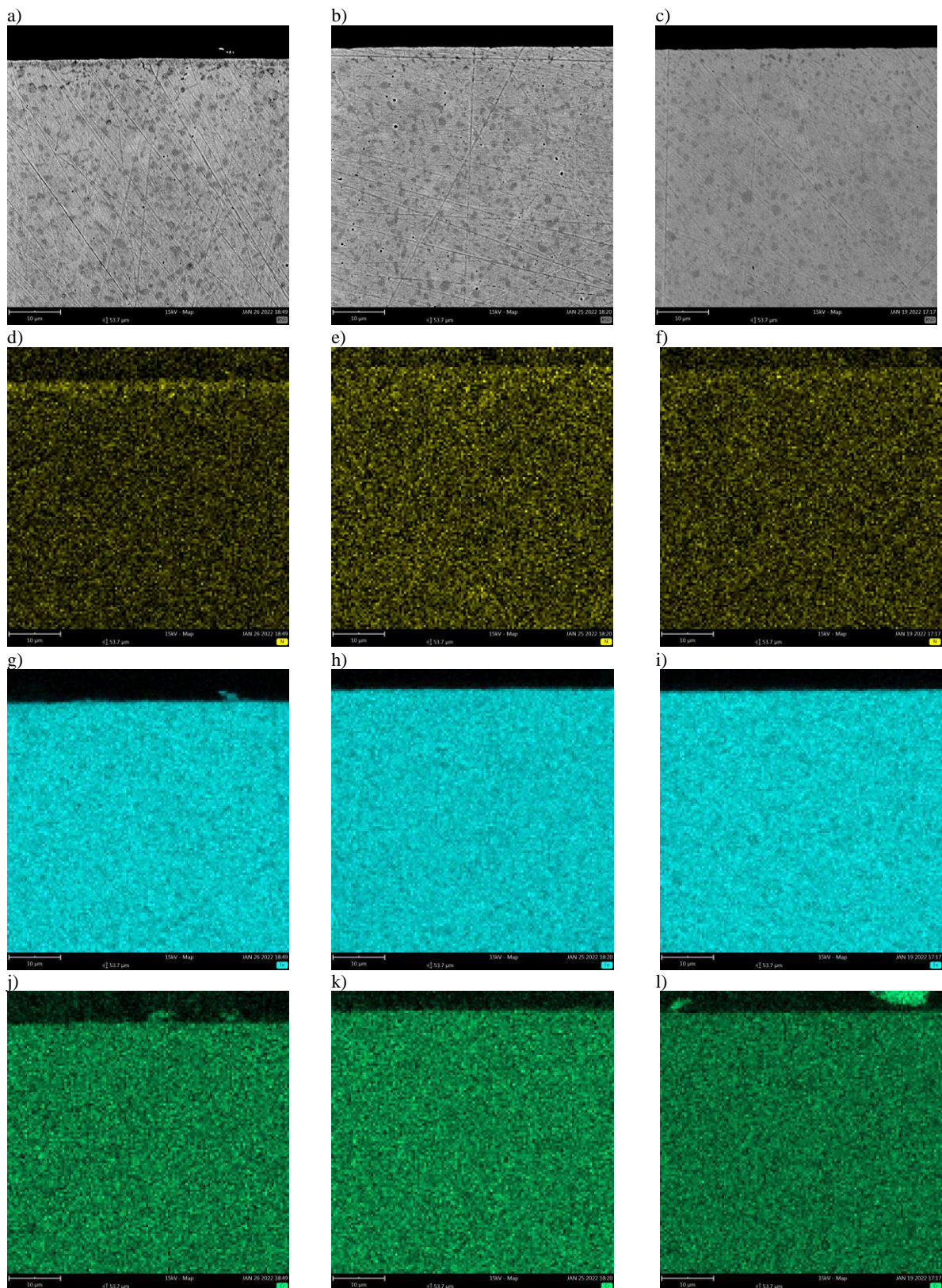
Fig. 4. a)-l) Microstructure of the layer after 2, 4 and 6 h of the nitriding process carried out on a tool steel grade 90MnCrV8 substrate and the result of the relative concentrations of nitrogen, iron and chromium.

3.3. Cold-work tool steel 145Cr6

The XRD phase analysis showed the presence of F_4N (γ') phase on the surface of 145Cr6 samples after each plasma nidriding process conditions (Fig. 5). The microstructure of 145Cr6 steel, after each of the three plasma nitriding processes (Fig. 6a-c), consists of a light matrix and irregularly shaped

dark precipitates arranged in bands perpendicular to the surface. Plasma nitriding of 145Cr6 steel for 2 h leads to the formation of a diffusion layer, as evidenced by the increased nitrogen intensity near the surface (Fig. 6d). The layer formed is porous (Fig. 6a). Its depth is approximately 1.65 μm. The change in iron and chromium content is negligible, as evidenced by the surface analysis of these elements shown in Fig. 6g, j. The result of plasma nitriding for 4 h is a diffusion layer with an average depth of 11.72 μm, as confirmed by the chemical composition analysis performed (Fig. 6e). The nitrogen content decreases from the surface into the depth of the material. In Fig. 6b, no dark precipitates are observed in the diffusion layer, the presence of which was identified in the layers formed during the plasma nitriding process at 2 and 6 h. A small number of pores are also visible. Plasma nitriding of 145Cr6 steel at 6 h leads to the formation of a nitrided layer consisting of a white zone and a diffusion zone, as evidenced by the increased nitrogen intensity near the surface, which decreases deep into the substrate (Fig. 6c,f). The resulting white layer is neither continuous nor adherent, as can be seen in Fig. 6c. In the region of about 10 μm from the white layer-diffusion layer boundary, large longitudinal and globular-shaped separations are no longer visible. The average depth of the white layer is 1.50 μm, while that of the entire nitrided layer is 14.32 μm.
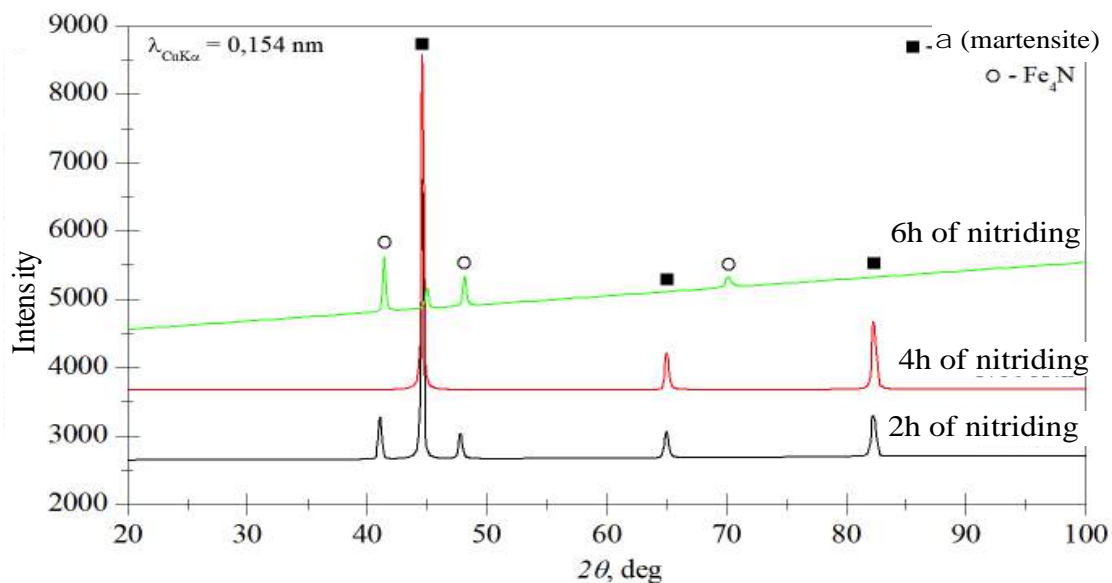
Fig. 5. The results of XRD phase analysis from samples of 145Cr6 cold work steel after 2, 4 and 6h of plasma nitriding process.

4. Summary

On the basis of microstructure photographs, relative elemental concentration analysis, it was shown that plasma nitriding of selected tool steels, carried out for 2, 4 and 6 h, in a nitriding mixture of 5% N_2 and 95% H_2 and at 550°C, leads for most of the analysed steels to the formation of diffusion/nitrided layers on their substrate. The time of the plasma nitriding process has an ambiguous effect on the depth of the nitrided layers formed on the substrate of the selected steels. The parabolic-like growth pattern of the nitrided layer was found to be characteristic of steels with high alloying element content: HS6-5-2.

The formation of a diffusion layer was observed on the substrate of each steel flux-nitrided in a mixture consisting of 5% N_2 and 95% H_2. The formation of a white layer was also observed during the nitriding of 145Cr6 steel at 6 h. Chromium nitrides were formed in the diffusion layer of the hot-work steel X37CrMoV5-1. In high-speed steel HS6-5-2, no nitrides were observed despite the high content of nitride-forming additives. Literature data (Doan et al., 2016) report that for high-speed steels, vanadium-rich primary MC carbides are converted to nitrides very slowly. Inside these types of carbides and nitrides, the diffusion coefficient of nitrogen is very low. According to Lachtin and Kogan (1982), the diffusion coefficient of vanadium nitride at 550°C is 1016 lower compared to ferrite. The formation of very thin layer s and the absence of nitrides in the 60WCr5 and 90MnCrV8 steels is attributed to the low content of nitride-forming elements (Table 1). Literature data indicate that the reduction in the possibility of nitride formation is also influenced by the higher carbon content (compared to nitridable steels - above 0.4 wt.%).
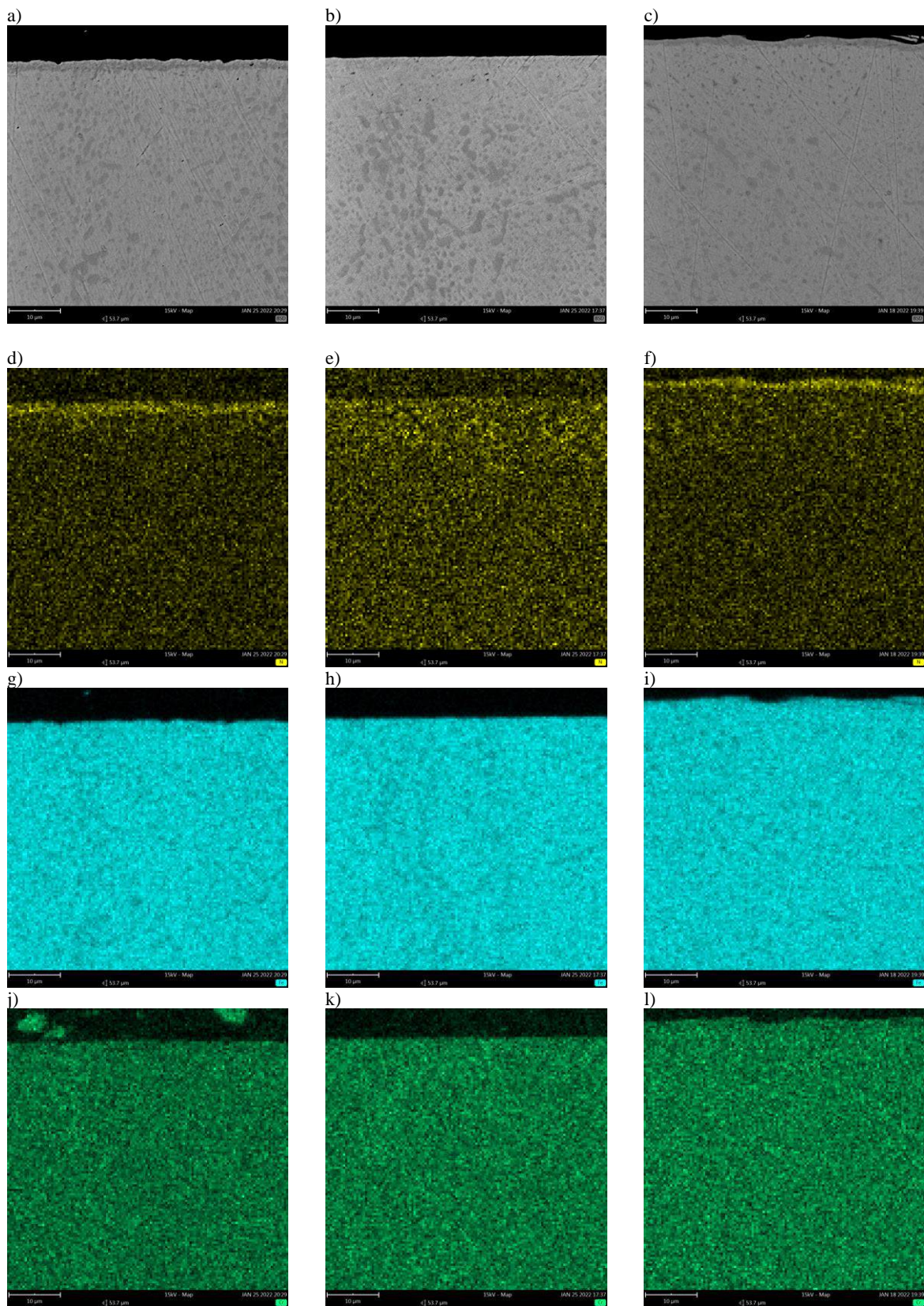
Fig. 6. a)-l) Microstructure of the layer after 2, 4 and 6 h of the nitriding process carried out on a substrate of 145Cr6 tool steel and results of the analysis of the relative concentrations of nitrogen, iron and chromium.

5. Conclusions

1) The presence and morphology of the resulting nitrided layer, formed on the substrate of 60WCr5, 90MnCrV8, 145Cr6, X37CrMoV5-1 and HS6-5-2 steels, during plasma nitriding at

550ºC in a mixture of 5% N_2 and 95% H_2, depends on the duration of the process and the chemical composition of the nitrided steel.

2) An increase in the duration of plasma nitriding, results in an increase in the depth of the nitrided layer formed on the substrate of high-alloy steels X37CrMoV5-1 and HS6-5-2.

3) Nitriding in a mixture of 5% nitrogen and 95% hydrogen produces a nitrided layer without a compound zone.

4) The presence and mass content of nitride-forming elements influences the formation of alloying additive nitrides in the microstructure of the diffusion layer.

5) Nitrides of alloying additives, present in the diffusion layer, are formed in the hot-work steel X37CrMoV5-1.

6) The results obtained indicate that X37CrMoV5-1 steel due to their alloying element content and carbon content - are the most suitable for the plasma nitriding process among the analysed steels.

Acknowledgement

References

Aghajani, H., & Behrangi, S. (2017). *Plasma nitriding of steels*. Springer International Publishing.

Albarran, J. L., Juárez-Islas, J. A., & Martinez, L. (1992). Nitride width and microstructure in H-12 ion nitrided steel. *Materials Letters*, *15*, 68-72.

Barnaby, J. T.; Haq, M. I., & Smith, C. G. (1975). Toughness of carburized steels. *Metals Technology*, *2*(1), 535-537. https://doi.org/10.1179/030716975803276871

Berkowski, L. (2005). Wpływ struktury na skutki azotowania chromowych stali ledeburytycznych. Część 1: Informacje o materiale do badań. *Obróbka Plastyczna*, *5*, 5-15.

Blicharski, M. (2012). *Inżynieria powierzchni*. Wydawnictwa Naukowo-Techniczne.

Blicharski, M. (2017). *Inżynieria materiałowa stali*. Wydawnictwo Naukowe PWN.

Borgoili, F., Galvanetto, E., Fossati, A., & Bacci, T. (2002). Glow-discharge nitriding and post-oxidising treatments of AISI H11. *Surface and Coatings Technology*, *162*(1), 61-66. https://doi.org/10.1016/S0257-8972(02)00574-1

Burakowski, T., & Wierzchoń, T. (1995). *Inżynieria powierzchni metali*. Wydawnictwa Naukowo-Techniczne.

Burzyńska-Szyszko, M. (2011). *Materiały konstrukcyjne*. Politechnika Warszawska.

Chattopadhyay, R. (2004). *Advanced thermally assisted surface engineering process*. Springer. https://doi.org/10.1007/b105271

Czerwinski, F. (2012). *Thermochemical treatment of metals. heat treatment – conventional and novel applications*. IntechOpen.

Çelik, A., Efeoğlu, I., & Sakar, G. (2000). Microstructure and structural behavior of ion-nitrided AISI 8620 steel. *Materials Characterization*, *46*(1), 39-44. https://doi.org/10.1016/S1044-5803(00)00091-7

da Silva Rocha, A, Strohaecker, T., Tomala, V., & Hirsch, T. (1999). Microstructure and residual stresses of plasma-nitrided M2 tool steel. *Surface Coatings Technology*, *115* (1), 24-31. https://doi.org/10.1016/S0257-8972(99)00063-8

Doan, T. V., Dobrocký, D., Pokorny, Z., Kusmic, D., & Nguyen, V. T. (2016). Effect of plasma nitriding on mechanical and tribological properties of 42CrMo4. *ECS Transcations*, *74*(1), 231-238. https://doi.org/10.1149/07401.0231ecst

Dobrzański, L. A. (2006). *Podstawy nauki o materiałach i metaloznawstwo. Materiały inżynierskie i projektowanie materiałowe*. Wydawnictwa Naukowo-Techniczne.

Drajewicz, M., Góral, M., Pytel, M., Kościelniak, B., Kubaszek, T., Wierzba, P., & Cichosz, P. (2021). The duplex coating formation using plasma nitriding and CrN PVD deposition on X39CrMo17-1 stainless steel. *Solid State Phenomena 320*, 43-48. https://doi.org/10.4028/www.scientific.net/SSP.320.43

EN ISO 4957. (2004). European Committee for Standardization. Stale narzędziowe.

Ghelloudj, E., Hannachi, M. T., & Djebaili, H. (2018). Effect of time of the compound layer formed during salt bath ntinitriding of AISI 4140 steel. *Acta Metallurgica Slovaca 24*(4), 280-286. https://doi.org/10.12776/ams.v24i4.1111

Głowacki, S., Majchrzak, A., & Majchrzak, W. (2005a). Wpływ proporcji składników atmosfery azotującej na strukturę warstwy azotowanej jonowo. *Obróbka Plastyczna Metali*, *2*, 15-22.

Głowacki, S., Majchrzak, A., & Majchrzak, W. (2005b). Zależność grubości warstwy azotowanej jonowo od proporcji składników atmosfery azotującej. *Obróbka Plastyczna*, *1*, 37-46.

Höck, K., Soies, H-J., Larisch, B., Leonhardt, G., Buecken, B. (1996). Wear resistance of prenitrided hardcoates steels for tools and machine components. *Surface and Coatings Technology*, *88*(1-3), 44-49. https://doi.org/10.1016/S0257-8972(96)02914-3

Karamiş, M. B., Yıldızlı, K., & Aydın, G. C. (2019). Sliding/rolling wear performance of plasma nitrided H11 hot working steel. *Tribology International*, *51*, 18-24. https://doi.org/10.1016/j.triboint.2012.02.005

Karaoğlu, S. (2002). Structural characterization and wear behaviour of plasma-nitried AISI 5140 low-alloy steel. *Materials Characterization*, *49*(4), 349-357. https://doi.org/10.1016/S1044-5803(03)00031-7

Kovacı, H., Hacısalihoğlub, İ., Yetim, A. F., & Çelik, A. (2019). Effects of shot peening pre-treatment and plasma nitriding parameters on the structural, mechanical and tribological properties of AISI 4140 low-alloy steel. *Surface & Coatings Technology*, *358*, 256-265. https://doi.org/10.1016/j.surfcoat.2018.11.043

Kovacı, H., Yetim, A. F., Baran, O., & Celik, A. (2016a). Fatigue crack growth analysis of plasma nitrided AISI 4140 low-alloy steel: Part 1-constant ampitude loading. *Materials Science & Engineering: A, 627*, 257-264. https://doi.org/10.1016/j.msea.2016.07.002

Kovacı, H., Yetim, A. F., Baran, Ö., & Çelik, A. (2016b). Fatigue crack growth analysis of plasma nitrided AISI 4140 low-alloy steel: Part 2-Variable amplitude loading and load interactions. *Materials Science & Engineering: A*, *627*, 265-275. https://doi.org/10.1016/j.msea.2016.07.003

Krbaťa, M., Majerik, J., Barényi, I., Mikušová, I., & Kusmič D. (2019). Mechanical and tribological features of the 90MnCrV8 steel after plasma nitriding. *Manufacturing Technology*, *19*(2), 238-242. https://doi.org/10.21062/ujep/276.2019/a/1213-2489/MT/19/2/238

Kul, M., Danacai, I., Gezer, Ş., & Kacara, B. (2020). Effect of boronizing composition on hardness of boronized AISI 1045 steel. *Materials Letters*, *279*, Article 128510. https://doi.org/10.1016/j.matlet.2020.128510

Kula, P. (2000). *Inżynieria warstwy wierzchniej*. Wydawnictwo Politechniki Łódzkiej.

Kusmič, D., & Hrubý, V. (2015). Corrosion resistance of plasma nitrided strutural steels. *Manufacturing Technology*, *15*(1), 64-69. http://dx.doi.org/10.21062/ujep/x.2015/a/1213-2489/MT/15/1/64

Kusmič, D., Čech, O., & Klakurková, L. (2021). Corrosion resistance of ferritic stainless steel X12Cr13 after application of low-temperature and high-temeprature plasma nitriding. *Manufacturing Technology*, *21*(1), 98-104. https://doi.org/10.21062/mft.2021.013

Lachtin, J. M., & Kogan, J. D. (1982). *Structure and strength of nitrided alloys*. Metallurgia.

Lan, H-Y., & Wen, D-C. (2012). Improving the erosion and erocsion-corrosion properties of precipitation hardening mold steel by plasma nitriding. *Materials Transactions*, *53*(8), 1443-1448. https://doi.org/10.2320/matertrans.M2012083

Liu, Z., Peng, Y., Chen, C., Gong, J., & Jiang, Y. (2020). Effect of surface nanocrystallization on low temperaturę gas carburization for AISI 316L austenitic stainless steel. *International Journal of Pressure Vessels and Piping*, *182*, Article 104053. https://doi.org/10.1016/j.ijpvp.2020.104053

Luty, W. (1977). *Poradnik inżyniera. Obróbka cieplna stopów żelaza*. Wydawnictwo Naukowo-Techniczne.

Michalski, J., Tacikowski, J., Wach, P., Lunarska, E., & Baum, H. (2005). Formation of single-phase layer of γ'-nitride in controlled gas nitriding. *Metal Science and Heat Treatment*, *47*(11), 516-519. https://doi.org/10.1007/s11041-006-0023-0

Ozbaysal, K., Inal, O. T., & Romig Jr., A. D. (1986). Ion-nitriding behavior of several tool steels. *Materials Science & Engineering*, *78* (2), 179-191. https://doi.org/10.1016/0025-5416(86)90322-8

Peng, T., Zhao, X., Chen, Y., Tang, L., Wei K. & Hu, J. (2020). Improvement of stamping performance of H13 steel by compound-layer free plasma nitriding. *Surface Engineering*, *36*(5), 492-497. https://doi.org/10.1080/02670844.2019.1609172

Pessin, M.A., Tier, M.D., Strohaecker, T.R., Bloyce, A., Sun, Y., & Bell, T. (2000). The effects of plasma nitriding process parameters on the wear characteristics of AISI M2 tool steel. *Tribology Letters*, *8*, 223-228. https://doi.org/10.1023/A:1019199604963

PN-H-85023. (1986). Polski Komitet Normalizacyjny. Stal narzędziowa stopowa do pracy na zimno – Gatunki.

Podgornik, B., & Vižintin, J. (1999). Wear properties of plasma nitrided steel in dry sliding conditions. *Journal of Tribology*, *121*(4), 802-807. https://doi.org/10.1115/1.2834138

Podgornik, B., & Vižintin, J. (2001). Wear resistance of pulse plasma nitrided AISI 4140 and A355 steels. *Materials Science and Engineering: A*, 315(1-2), 28-34. https://doi.org/10.1016/S0921-5093(01)01202-3

Przybyłowicz, K. (1999). *Metaloznawstwo*. Wydawnictwa Naukowo-Techniczne.

Rakowski, W. A., Kot, M., Zimowski, S., & Wierzchoń, T. (2006). Właściwości warstw azotowanych jarzeniowo, wytworzonych na stali 316L. *Problemy Eksploatacji*, *3*, 107-116.

Sen, S., Sen, U., & Bindal, C. (2005). The growth kinetics of borides formed on boronized AISI 4140 steel. *Vacuum*, *77*(2), 195-202. https://doi.org/10.1016/j.vacuum.2004.09.005

Skonieski, A. F. O., dos Santos, G. R., Hirsch, T. K., & da Silva Rocha, A. (2013). Metallurgical responce of an AISI 4140 steel to different plasma nitriding gas mixtures. *Materials Research*, *16*(4), 884-890. https://doi.org/10.1590/S1516-14392013005000073

Skrzypek, S. J., Przybyłowicz, K. (2020). *Inżynieria metali i technologie materiałowe*. Wydawnictwo Naukowe PWN.

Spies, H-J., Dalke, A. (2014). Case structure and properties of nitrided steel. *Comprehensive Materials Processing*, *12*, 438-488. https://doi.org/10.1016/B978-0-08-096532-1.01216-4

Staub, F., Haas, J., Malkiewicz, T., Orzechowski, S., Przegaliński, S. (1964). *Stal. Atlas metalograficzny struktur*. Wydawnictwa Naukowo-Techniczne.

Świć, A., & Gola, A. (2017). *Współczesne technologie w inżynierii produkcji*. Politechnika Lubelska.

Torchane, L. (2021). Influence of rare earths on the gas nitriding inetics of 32CrMoNiV5 steel at low temperature. *Surfaces and Interaces*, *23*, 101016. https://doi.org/10.1016/j.surfin.2021.101016

Ucar, N., Yigit, M., & Calik, A. (2020). Metallurgical characterization and kinetics of borodied 34CrNiMo6 steel. *Advanced in Materials Science*, *20*(4(66)), 38-48. https://doi.org/10.2478/adms-2020-0021

Wang, Q. J., & Chung, Y-W. (2013). *Encyclopedia of tribology*. Springer https://doi.org/10.1007/978-0-387-92897-5

Xie, F., Sun, L., & Pan, J. (2012). Characteristics and mechanisms of accelerating pack boriding by direct current field at low and moderate temperatures. *Surface & Coatings Technology*, *206*(11-12), 2839-2844. https://doi.org/10.1016/j.surfcoat.2011.12.003

Yang, R., Wu, G. L., Zhang, X., Fu, W. T., & Huang, X. (2017). Gradient microstructure and microhardness in nitried 18CrNiMo7-6 gear steel. *IOP Conference Series: Materials Science & Engineering*, *219*(1), 012047. https://doi.org/10.1088/1757-899X/219/1/012047

Zhang, Z. L., & Bell, T. (1985). Strucutre and corrosion resistance of plasma nitrided stainless steel. *Surface Engineering*, *1*(2), 131-136. https://doi.org/10.1179/sur.1985.1.2.131

Zhao, F. S., Zhang, Z. H., Shao, M. H., Bi, Y. J., Wang, Z. W., Li, Y., Li, H. H., Xu, X. G., He, Y. Y. (2021). Mechanical and wear properties of 42CrMo Steel by plasma nitriding assisted hollow cathode ion source. *Materials Research*, *24*(4), 1-10. https://doi.org/10.1590/1980-5373-MR-2021-0137

Wpływ Warunków Azotowania Plazmowego na Mikrostrukturę Powłok Uzyskanych na Podłożu Wybranych Stali Narzędziowych

Streszczenie

W pracy przedstawiono wyniki badań wpływu czasu procesu azotowania plazmowego na mikrostrukturę otrzymanych powłok. Jako materiał podłoża wybrano stale narzędziowe do pracy na zimno (60WCrV8, 90MnCrV8, 145Cr6), stale narzędziowe do pracy na gorąco (X37CrMoV5-1) oraz szybkotnące (HS6-5-2). Procesy prowadzono w warunkach przemysłowych z wykorzystaniem urządzenia Ionit firmy Oerlikon Metaplas ze zmiennymi czasami procesu 2, 4 i 6 godzin. Zgodnie z danymi literaturowymi wybrano mieszaninę azotującą składającą się z 5% azotu i 95% wodoru, co pozwoliło na uzyskanie oczekiwanej warstwy dyfuzyjnej bez warstwy białej (złożonej z azotków żelaza). Analiza mapowania pierwiastkowego wskazuje, że obecność i zawartość pierwiastków azototwórczych wpływa na powstawanie azotków dodatku stopowego w mikrostrukturze warstwy dyfuzyjnej. Stwierdzono również, że wydłużenie czasu azotowania plazmowego powoduje zwiększenie głębokości warstw azotowanych powstających na podłożu ze stali wysokostopowych: X37CrMoV5-1 i HS6-5-2. Azotki dodatków stopowych, obecne w warstwie dyfuzyjnej, powstają w wysokostopowej stali do pracy na gorąco X37CrMoV5-1, co wskazuje, że stale te są najbardziej odpowiednie do azotowania plazmowego spośród wszystkich analizowanych stali narzędziowych.

Słowa kluczowe: azotowanie plazmowe, stal narzędziowa, obróbka cieplna, kinetyka azotowania

Original Research

Analysis of the Thermal Expansion Coefficient of Glass- and Carbon-Fibre-Reinforced Composites

Romuald Fejkiel [1],* [iD], Krystian Skwara [2] [iD]

[1] Department of Mechanics and Machine Building, The University College of Applied Sciences in Krosno, ul. Wyspiańskiego 20, 38-400 Krosno, Poland

[2] P.H.U. Wypożyczalnia Maszyn Krystian Skwara, ul. Jasielska 30, 38-230 Nowy Żmigród, Poland; kskwara20@gmail.com

* Correspondence: romuald.fejkiel@pans.krosno.pl

Abstract

With the development of manufacturing processes, an increase in the importance of metal-fibre composites in mechanical engineering is observed. These are materials consisting of appropriately arranged layers of metal and various types of fibres. The very wide use of composite materials in the construction of machine and equipment components means they are often exposed to work in variable temperature conditions. The aim of this article was analysis of the thermal expansion of typical composites: carbon fibre-reinforced polymer, glass fibre-reinforced polymer, glass-reinforced aluminium laminate and carbon-fibre reinforced aluminium laminate. EN AW-6060 aluminium alloy was used as the reference material. The aim of the dilatometric tests was to determine the coefficient of thermal expansion and the dimensional stability of composite materials at elevated temperatures up to 100 °C. The EN AW-6060 aluminium alloy was characterized by the highest linear expansion coefficient (20.27×10^{-6} 1/K). Composites containing glass fibres were characterized by the lowest positive linear thermal expansion coefficient. Among the composite materials tested, CARALLs exhibit the lowest thermal expansion coefficient.

Keywords: coefficient of thermal expansion, composites, dilatometric analysis, temperature, thermal expansion

1. Introduction

Composite materials play an increasingly important role in many fields of engineering. A composite is a hybrid material consisting of at least two materials with different properties (Ashrith et al., 2023). Such a material combination makes it possible to obtain elements that cannot be produced using conventional methods (Wang et al., 2007). Composites play a significant role in many areas of the aerospace (Bielawski et al., 2015), space (Samuel et al., 2021), shipbuilding (Barsotti et al., 2020), defence (Siengchin, 2023), sports and recreation (Ribeiro et al., 2019) and automotive (Garofano et al., 2023) industries. Carbon fibres used in carbon-fibre-reinforced polymers (CFRPs) allow for a significant reduction in vehicle weight while increasing safety (Ahmad et al., 2020). The unique properties of fibre metal laminates (FMLs) (Jakubczak et al., 2016) and composites with anti-wear properties (Walczak et al., 2017) means they are increasingly used in the automotive industry.

Each material has different physical, chemical and mechanical properties and not all materials can work together. This is due, among other things, to different electrical potentials or different values of the thermal expansion coefficients. If the potential difference between the components of the composite is large, a galvanic cell phenomenon occurs and corrosion may occur inside the composite (Hamill et al., 2017; Song et al., 2021). In the case of different thermal expansion, delamination may occur. In particular, this concerns FMLs consisting of alternating layers of metal and a polymer matrix laminate reinforced with continuous fibres (Costa et al., 2023). In composite materials subjected to long-term thermomechanical loads, there is a phenomenon of gradual changes in mechanical properties as a re-

sult of the gradual development of microcracks. Fibre breakage is a characteristic feature in carbon- and glass-fibre-reinforced polymers. In this context, the directionality of the reinforcing phase compared to the loading direction of the composite is important. In flat composite elements compressed in the plane, the primary damage is delamination (Trębacki & Królicka, 2017).

The basic goal of thermomechanical research is to understand how specific materials behave under particular temperature conditions. Based on the results of thermal and thermomechanical tests, it is possible to obtain characteristic properties such as the melting point, phase transformations and thermal expansion (James, 2017). When the thermal expansion of the matrix material and the reinforcing particle differ significantly, there is a risk of delamination at the interface and dimensional instability of the products (Fu et al., 2019; Ray, 2005). Knowledge of the relationship between rheological behaviour of materials and their behaviour under load is particularly important in the case of non-uniform members such as stepped, tapered columns (De Macêdo Wahrhaftig et al., 2023). There are many ways for measuring the mechanical characteristics of the macroscale samples, i.e. indentation tests, tensile and compression tests, three-point bending tests etc. (Al-Abboodi et al., 2023). However, methods for determining thermal properties of materials are limited. Due to the research method, thermomechanical analysis (TMA) (Saba & Jawaid, 2018), dynamic-load TMA (DLTMA) (Shaikh et al., 2023), and dilatometry (DIL) (Dergal et al., 2022) can be distinguished. The DLTMA method is based on periodic monitoring of a sample subjected to force. The tested element can be cyclically bent, stretched, compressed or sheared. The result of such a study is the measurement of the change in the sample's Young's modulus depending on temperature. In TMA analysis, the pressure exerted on the sample does not change over time. As a result of the applied force, the element changes its dimensions. In this method, pressure is applied through variously shaped measuring probes, which may be flat or semicircular. Dilatometric tests enable the registration of changes in the length of a sample of the tested material caused by temperature changes. Due to the measurement method, the following thermal expansion coefficients are distinguished: linear, surface and volume.

The study of thermomechanical properties has been the subject of many works over recent years. Łągiewka et al. (2009) investigated the thermal expansion of metal composites based on the AlMg9 alloy reinforced with chopped carbon fibres and composites containing graphite particles. It was found that the coefficient of thermal expansion in the tested composites is higher than for the matrix alloy. This may indicate the lack of adhesive connections at the phase interface. Dilatometric tests of composites based on the AK9 alloy with various ceramic fibre contents (10, 15, 20 vol.%) show the dependence of the thermal expansion coefficients on the fibre content in the composite. The mismatch in the coefficient of thermal expansion between fibre-reinforced polymers (FRPs) and metal is the main cause of residual stresses in FRP/metal composites (Tinkloh et al., 2020), which can lead to delamination in the absence of any external loads (Prussak et al., 2018). Large thermal residual stresses induce low static strength and low fatigue strengths of carbon-fibre-reinforced aluminium laminates (CARALLs) (Hu et al., 2022). Xue et al. (2011) used thermal expansion of the clamp during the curing process to apply tensile stress to CFRP layers. Dul (2013) presented an overview of the possibilities of thermal expansion analysis for composites with high thermal conductivity. Based on the literature analysis, it can be concluded that most authors focused on examining limited number of materials or they investigated thermal expansion of group of similar materials, which makes it difficult to compare the results. Moreover, research on the thermal expansion of hybrid materials is quite limited. Inspired by the results of other researchers, the authors of this work decided to test and compare the behaviour of various construction materials with different structures, including fibre-metal laminates.

This article compares the thermal expansion coefficients of five materials: EN AW-6060 aluminium alloy, CFRP, GFRP and two aluminium-based laminates. In the experimental studies, dilatometric analysis was used.

2. Material and methods

2.1. Materials

An aluminium alloy EN AW-6060 (EN 573-3+A1, 2022), GFRP, CFRP, Glass-Reinforced Aluminium Laminate (GLARE) and Carbon-Reinforced Aluminium Laminate (CARALL) in the form of rods with a diameter of $8_{-0.1}$ mm were used as the test materials (Fig. 1). The length of all samples for dilatometric tests was 30±0.1 mm. Selected physical and mechanical properties of EN AW-6060 aluminium alloy are listed in Table 1. Carbon fabric weighing 160 g/m^2, with a thickness of 0.25 mm and

twill weave, and glass fabric weighing 80 g/m^2, a thickness of 0.4 mm, and twill weave were used as reinforcement.

Using the lamination operation, samples of a circular cross-section with a diameter of 8 mm were made with a core of aluminium alloy EN AW-6060. Aluminium alloy rods with a diameter of 6 mm were used as a semi-finished product to produce the GLARE and CARALL.

Schematic diagram of the dilatometric test is presented in Fig. 2. To laminate two different materials with different characteristics, special brass sleeves were prepared as shown in Fig. 3.
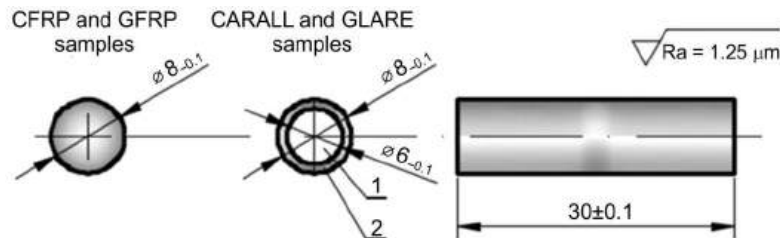
Fig. 1. Dimensions of the samples for dilatometric (dimensions in mm): 1 – metal core, 2 – continuous fibre-reinforced laminate.

Table 1. Physical properties of the EN AW-6060 aluminium alloy, prepared on the basis of (PA38, 2023).

Parameter	Value
Flow temperature	655 °C
Freezing point	610 °C
Thermal conductivity	209 W/mK
Electric conductivity	54 %
Specific heat	898 J/kgK
Rigidity modules (G)	26 100 MPa
Young's modulus (E)	69 000 MPa
Poisson's ratio	0.33
Density	2.7 g/cm^3
Thermal expansion coefficient	23.4×10^{-6} 1/K
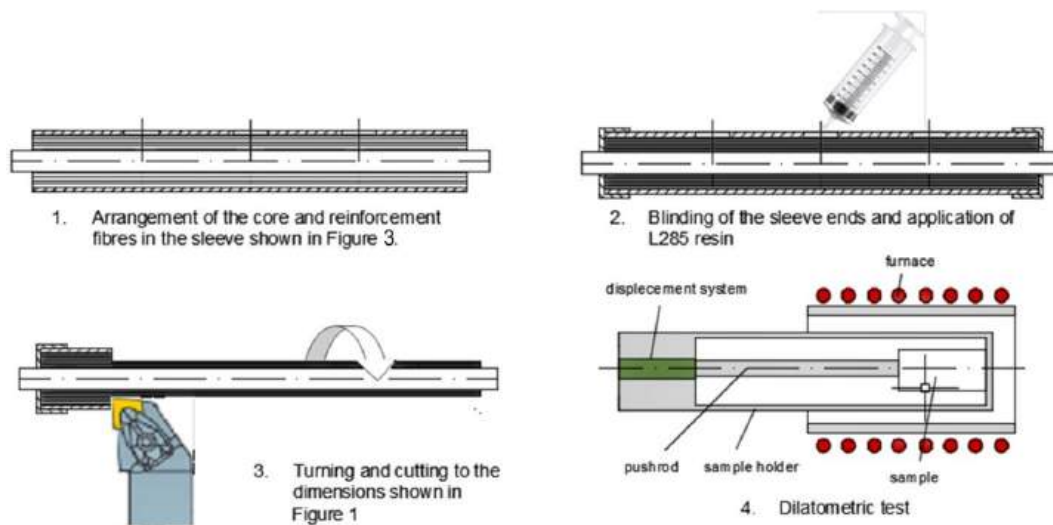
Fig. 2. Schematic diagram of dilatometric test.
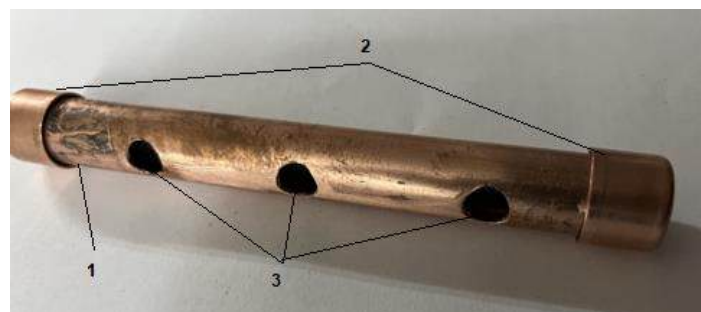
Fig. 3. Brass sleeve: 1 – sleeve, 2 – blinds, 3 – holes for resin application.

The purpose of using the sleeves was to fix the bonded elements in an appropriately symmetrical, stationary position. Holes with a diameter of 8 mm were drilled in three symmetrically placed points, through which a binder (liquid epoxy resin L285) was applied. Strips about 20 mm wide, cut from carbon or glass fibre fabric, were wound onto the rod. The prepared samples were subjected to the lamination process.

2.2. Experimental procedure

Dilatometric tests were carried out using the DIL 402 PC (Erich NETZSCH GmbH & Co. Holding KG, Selb, Germany) dilatometer, which is shown in Fig. 4. The DIL 402 PC dilatometer combines easy operation and high adaptability to various applications. The optimized design of the measurement system with an inductive transducer ensures a high degree of reproducibility even without external cooling. The dilatometer was turned on two hours before the measurements began.

Fig. 4. DIL 402 PC dilatometer.

The samples were installed in a sample carrier. Using an adjustment screw, the sample was initially pressed to the measuring tip. The correct pressure is indicated by the diode on the base unit. After ensuring the thermocouple was close to the workpiece under test (without touching it), the furnace was closed. The ambient temperature and heating rate were $T_0 = 31.3$ °C and 5 °C/min, respectively. The increase in length during the test was measured using an inductive transducer, which monitors the pushrod displacement resulting from the expansion of the sample.

Measurements with a dilatometer involves observing the change in the length of the tested sample depending on the increase in temperature ΔT (Fig. 5). As a result, a dilatometric curve is obtained, which is helpful in determining one of the most important values characterizing the tested material – the coefficient of linear thermal expansion. In this method, no external force acts on the sample (Sierpiński, 2023). The value of the thermal expansion coefficient is determined based on the Eq. (1):

$$\alpha = \frac{\Delta L}{L(T_1) \times \Delta T} \tag{1}$$

where α is the coefficient of thermal expansion, ΔL is the increase in length, $L(T_1)$ is body length at the reference temperature (31.3 °C), ΔT is the temperature increase.
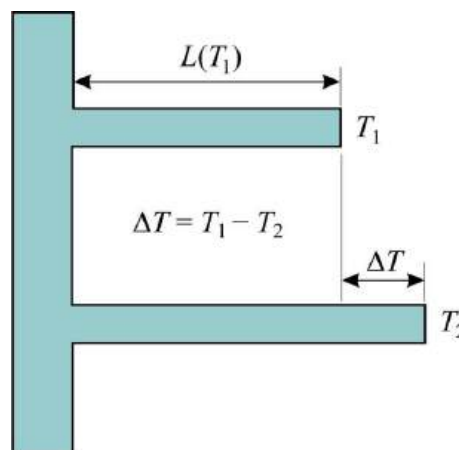
Fig. 5. The linear change in sample dimension due to temperature change.

3. Results and discussion

Based on the results obtained, the value of the linear expansion coefficient and the value of the stresses occurring in the individual samples were determined. According to Hooke's law (Eq. (2)), the dependence of the stresses σ on the thermal expansion coefficient α was derived (Eqs. (3)-(5)). The adopted values of Young's modulus E and the obtained results are presented in Table 2.

$$\sigma = E \cdot \varepsilon \tag{2}$$

$$\varepsilon = \frac{\Delta L}{L} \tag{3}$$

$$\alpha = \frac{\varepsilon}{\Delta T} \tag{4}$$

$$\sigma = \alpha \cdot E \cdot \Delta T \tag{5}$$

where σ is stress, E is the Young's modulus, $\mathcal{E}$ is strain, ΔL is the increase in sample length, L is the initial length, ΔT is the temperature increase.

As a result of the measurements, diagrams of the changes in sample length and temperature during the tests were obtained (Figs. 6-10). The diagrams clearly show that the highest coefficient of linear expansion is characterized by the EN AW-6060 aluminium alloy (Fig. 6). The value of the thermal expansion coefficient of this alloy is $20.27 \cdot 10^{-6}$ 1/K (Table 2) and is close to the requirements of manufacturers of metallurgical materials (Aluminium 6060, 2023; EN AW-6060, 2023). The change in the dimensions of the tested sample is regular – as the temperature increases, the elongation value gradually increases and reaches an extreme when the temperature is above 100 °C (Fig. 6).

Table 2. Values of Young's modulus E, stresses σ and coefficient of thermal expansion α for specific materials.

Material	E, MPa	α, 1/K	σ, MPa
EN AW-6060	69 000	$20.27 \cdot 10^{-6}$	106.24
GLARE	49 000 (Bieniaś et al., 2020)	$5.73 \cdot 10^{-6}$	21.53
CARALL	100 000	$14.5 \cdot 10^{-6}$	111.21
GFRP	69 000	$4.74 \cdot 10^{-6}$	24.75
CFRP	160 000	$-24.17 \cdot 10^{-6}$	−292.75

A sample of the glass-reinforced aluminium laminate behaves similarly to an aluminium alloy sample at temperatures up to approximately 50 °C (Fig. 7). Both samples achieve an elongation value of 0.0004 mm. Then, the composite sample quickly obtains a negative increase in length, and in the final stage of the measurement it stabilizes. During the entire duration of the tests, the elongation value changes with a very large amplitude.

The carbon-fibre-reinforced aluminium laminate showed an equally large amplitude of changes in the elongation value (Fig. 8). When the temperature reaches 70 °C, a local extreme occurs and the material shows a high elongation value. In the next stage, the elongation begins to decrease rapidly, down to negative values (approximately $\Delta L/L_0 = -0.0004$). In the final part of the test, the sample reaches the minimum elongation value, approaching zero.

The glass-fibre-reinforced polymer has the lowest positive coefficient of thermal expansion (Fig. 9). This value is more than five times lower compared to the EN AW-6060 aluminium alloy. This confirms the commonly known feature of glass fibres, that is, it is a material that is insensitive to temperature changes. The GFRP composite sample achieved the greatest elongation at a temperature of approximately 100 °C, but the elongation curve is uneven. In the initial phase of the test, the material showed a negative growth value (Fig. 9).

The elongation curve of the carbon fibre-reinforced polymer sample has an unusual shape (Fig. 10). In the first phase, until the material reaches a temperature of approximately 60 °C, the material shows almost no reaction to the temperature change. However, at higher temperatures the results mean that the CFRP exhibits a negative thermal expansion coefficient. In terms of absolute value, the greatest value of length change is achieved at a maximum temperature of approximately 105 °C. Then, as the temperature slowly decreases, the elongation value remains almost unchanged (Fig. 10).
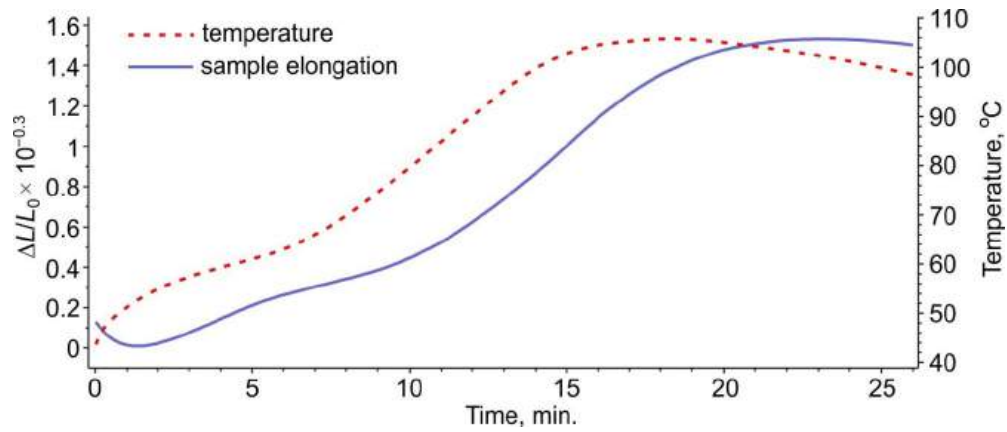
Fig. 6. Dilatometric analysis of the EN AW-6060 sample.
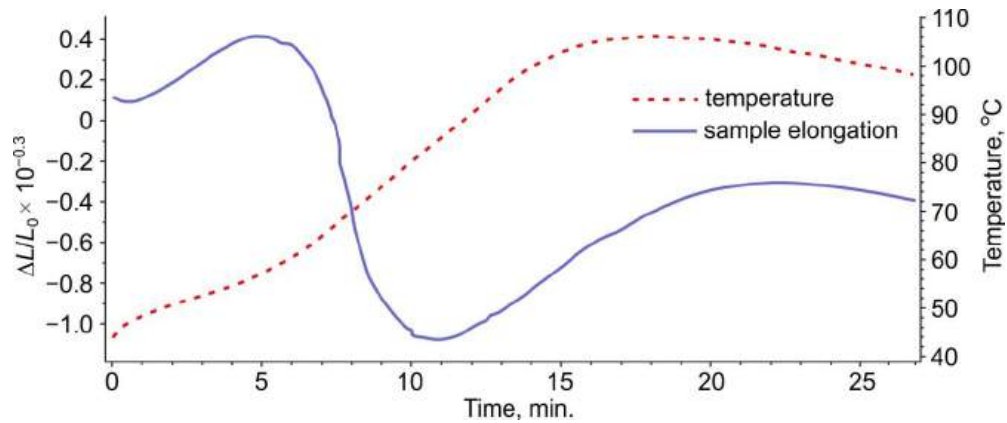
Fig. 7. Dilatometric analysis of the GLARE sample.
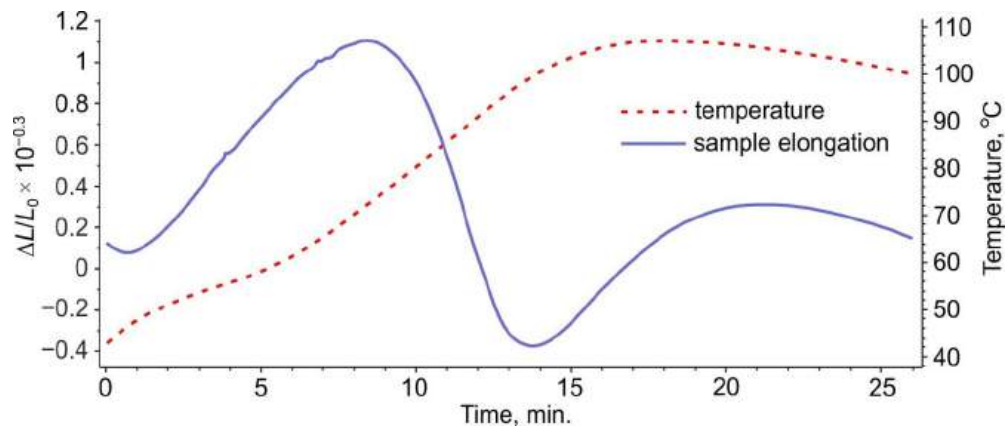
Fig. 8. Dilatometric analysis of the CARALL sample.
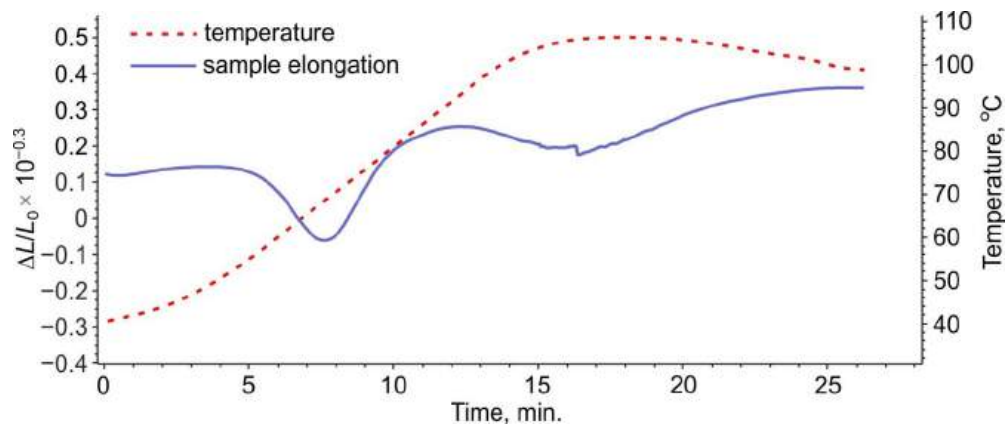
Fig. 9. Dilatometric analysis of the GFRP sample.
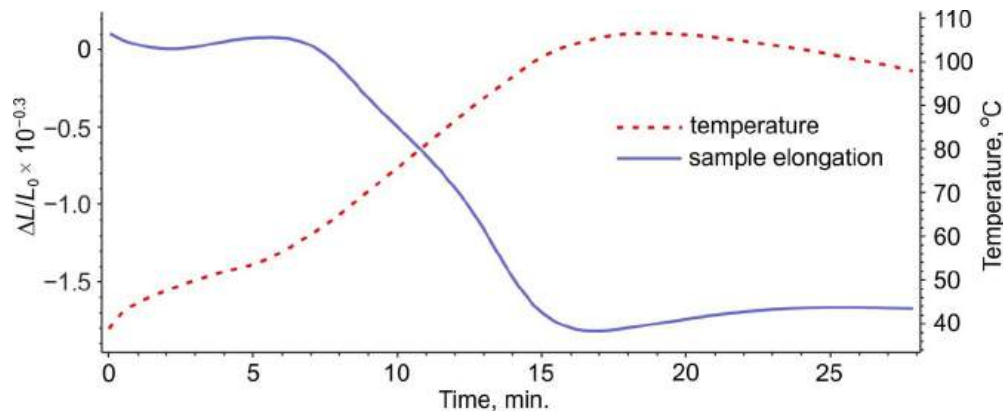
Fig. 10. Dilatometric analysis of the CFRP sample.

The values of the maximum elongations of the samples and the corresponding temperature increases are presented in Table 3. The value of relative elongation was automatically determined by the software, while the temperature increase was determined based on Eq. (6).

Table 3. Sample length and temperature increases.

Material	$\Delta L/L_0$	ΔT, °C
EN AW-6060	0.0154	75.96
GLARE	0.00044	76.7
CARALL	0.00111	76.7
GFRP	0.000359	75.7
CFRP	−0.00183	75.7

$$\Delta T = T_k - T_0 \tag{6}$$

where ΔT is temperature increase, T_k is final temperature and T_0 is initial temperature.

Samples containing glass fibres have the lowest positive linear thermal expansion coefficient. Therefore, when testing these materials, the lowest stresses occurred, which are closely related to the value of the thermal expansion coefficient. In the case of the absolute value, the highest stress value occurred in the CFRP sample (Table 3). These are compressive stresses resulting from the negative coefficient of thermal expansion.

The difference in the internal structure of the fibres and the aluminium alloy causes an uneven increase in the length of the composite samples during heating. The aluminium alloy has a positive coefficient of thermal expansion, while the carbon fibre sample shows a negative coefficient of thermal expansion, similar to glass fibres over a certain temperature range. Carbon fibre fabric shrinks in size under the influence of increased temperature, in contrast to the aluminium alloy. Moreover, fibre-reinforced composites, as anisotropic materials, have different properties depending on the arrangement of the fibres. These are important factors in the production of hybrid composites. There is a risk of an inappropriate combination of materials, which will result in stresses causing cracks and delamination in the composite.

However, it should be assumed that fibre-reinforced composites are characterized by greater durability than popular metal-fibre composites. Therefore, the use of CARALL and GLARE composites at elevated temperatures cannot be completely disqualified. However, one must make sure that such materials will not be operated at too high temperatures.

4. Conclusions

Determining the value of the thermal expansion coefficient makes it possible to determine changes in body dimensions under the influence of increased or decreased temperature. This property is particularly important for materials operating in rapidly changing atmospheric conditions. Changing the dimensions of materials causes the occurrence of internal stresses of variable values, which intensifies material fatigue. Based on the research results contained in this article, the following conclusions can be drawn:

- During dilatometric tests, the elongation value of the GLARE composite changes with a very large amplitude. This is the result of a large difference in the thermo-mechanical properties of the component materials of this composite.
- The elongation value of the CARALL composite is subjected to strong changes from positive values in the temperature range of 45–90 °C to negative elongation values in the temperature range of 90–105 °C.
- The glass-fibre-reinforced composite exhibits the lowest positive coefficient of thermal expansion. This value is more than five times lower compared to the EN AW-6060 aluminium alloy.
- The composite reinforced with carbon fibres does not undergo significant deformation until the temperature reaches approximately 50 °C. However, at higher temperatures it turns out that the carbon-fibre-reinforced polymer exhibits a negative thermal expansion coefficient.

In future research, it would be desirable to perform thorough tests of these types of composites at reduced temperatures and under thermal shock conditions. It would also be advisable to carry out strength tests of materials at elevated and reduced temperatures.

References

Ahmad, H., Markina, A. A., Porotnikov, M. V., & Ahmad, F. (2020). A review of carbon fibre materials in automotive industry. *IOP Conference Series: Materials Science and Engineering*, 971, Article 032011. https://doi.org/10.1088/1757-899X/971/3/032011

Al-Abboodi, H., Fan, H., Al-Bahrani, M., Abdelhussien, A., & Mohamad, B. (2023). Mechanical characteristics of nano-crystalline material in metallic glass formers. *Facta Universitatis-Series Mechanical Engineering*. https://doi.org/10.22190/FUME230128016A

Aluminium 6060 (2023, November 22). Aluminium 6060 / 3.3206 / Al-MgSi. https://xometry.eu/wp-content/uploads/2021/02/Aluminium-3.3206.pdf

Ashrith, H. S., Jeevan, T. P., & Xu, J. (2023). A review on the fabrication and mechanical characterization of fibrous composites for engineering applications. *Journal of Composites Science*, 7(6), Article 252. https://doi.org/10.3390/jcs7060252

Barsotti, B., Gaiotti, M., & Rizzo. C. M. (2020). Recent industrial developments of marine composites limit states and design approaches on strength. *Journal of Marine Science and Application*, 19, 553–566. https://doi.org/10.1007/s11804-020-00171-1

Bielawski, R., Rządkowski, W., Augustyn, S., & Pyrzanowski, P. (2015). Nowoczesne materiały stosowane w konstrukcjach lotniczych - wybrane problemy oraz kierunki rozwoju [Modern materials used in aircraft constructions selected problems and directions for development]. *Zeszyty Naukowe Politechniki Rzeszowskiej – Mechanika*, 32(291), 203-216. http://dx.doi.org/10.7862/rm.2015.20

Bieniaś, J., Jakubczak, P., Droździel, M., & Surowska, B. (2020). Interlaminar shear strength and failure analysis of aluminium-carbon laminates with a glass fiber interlayer after moisture absorption. *Materials*, 13, Article 2999. https://doi.org/10.3390/ma13132999

Costa, R. D. F. S., Sales-Contini, R. C. M., Silva, F. J. G., Sebbe, N., & Jesus, A. M. P. A. (2023). Critical review on fibre metal laminates (FML): From manufacturing to sustainable processing. *Metals*, 13(4), Article 638. https://doi.org/10.3390/met13040638

De Macêdo Wahrhaftig, A., Plevris, V., Mohamad, B. A., & Pereira, D. L. (2023). Minimum design bending moment for systems of equivalent stiffness. *Structures*, 57, Article 105224. https://doi.org/10.1016/j.istruc.2023.105224

Dergal, E., Kudrevatykh, O., & Quinn, N. (2022). A dilatometer for the carbon fibre composite tubes. *System Design and Analysis of Aerospace Technique Characteristics*, 27(2), 15–26. https://doi.org/10.15421/471919

Dul, Ł. (2013). Analiza możliwości pomiarów rozszerzalności liniowej kompozytów o dużej przewodności cieplnej z wykorzystaniem metod analitycznych [Analysis of possibility of lineat expansion measurements on composites of high thermal conductivity using analytical methods]. *Zeszyty Naukowe Ostrołęckiego Towarzystwa Naukowego, 27*, 244–259.

EN 573-3+A1. (2022). Aluminium and aluminium alloys - Chemical composition and form of wrought products - Part 3: Chemical composition and form of products. European Committee for Standardization.

EN AW-6060. (2023, November 22). Material Data Sheet. EN AW-6060. https://ucpcdn.thyssenkrupp.com/_legacy/UCPthyssenkruppBAMXUK/assets.files/material-data-sheets/aluminium/aluminium-6060.pdf

Fu, Q., Wang, L., Tian, X., & Shen, Q. (2019). Effects of thermal shock on the microstructures, mechanical and thermophysical properties of SiCnws-C/C composites. *Composites Part B: Engineering*, 164, 620–628. https://doi.org/10.1016/j.compositesb.2019.01.079

Garofano, A., Acanfora, V., & Fittipaldi, F. (2023). On the use of a hybrid metallic-composite design to increase mechanical performance of an automotive chassis. *Journal of Materials Engineering and Performance 32*, 3853–3870. https://doi.org/10.1007/s11665-023-08206-8

Hamill, L., Hofmann, D. C., & Nutt, S. (2017). Galvanic corrosion and mechanical behavior of fibre metal laminates of metallic glass and carbon fibre composites. *Advanced Engineering Materials*, *20*(2), Article 1700711. https://doi.org/10.1002/adem.201700711

Hu, H., Wei, Q., Liu, B., Liu, Y., Hu, N., Ma, Q., & Wang, C. (2022). Progressive damage behaviour analysis and comparison with 2d/3d Hashin failure models on carbon fibre–reinforced aluminium laminates. *Polymers*, *14*, 2946. https://doi.org/10.3390/polym14142946

Jakubczak, P., Surowska, B., Bieniaś, J. (2016). Evaluation of force-time changes during impact of hybrid laminates made of titanium and fibrous composite. *Archives of Metallurgy and Materials*, *61*(2), 689–694. https://doi.org/10.1515/amm-2016-0117

James, J. (2017). *Chapter 7 - Thermomechanical Analysis and Its Applications*. In S. Thomas, R. Thomas, A. K., Zachariah, R. K. Mishra (Eds.), Thermal and rheological measurement techniques for nanomaterials characterization (2nd ed., pp. 159–171). Elsevier Inc.

Łagiewka, M., Komopka, Z., Zyska, A., & Nadolski, M. (2009). Wpływ rodzaju zbrojenia na rozszerzalność cieplną metalowych materiałów kompozytowych [The influence of the reinforcement type on thermal expansion of metal matrix composites]. *Kompozyty*, *9*(4), 380–383.

PA38. (2023, November 22). PA38 (AW-6060). https://www.kronosedm.pl/aluminium-pa38-aw-6060/

Prussak, R., Stefaniak, D., Hühne, C., & Sinapius, M. (2018). Evaluation of residual stress development in FRP-metal hybrids using fibre Bragg grating sensors. *Production Engineering Research and Development*, *12*, 259–267. https://doi.org/10.1007/s11740-018-0793-4

Ray, B. C. (2005). Thermal shock and thermal fatigue on delamination of glass-fibre-reinforced polymeric composites. *Journal of Reinforced Plastics and Composites*, *24*(1), 111–116. https://doi.org/10.1177/0731684405042953

Ribeiro, I., Kaufmann, J., Götze, U., Peças, P., & Henriques, E. (2019). Fibre reinforced polymers in the sports industry – Life Cycle Engineering methodology applied to a snowboard using anisotropic layer design. *International Journal of Sustainable Engineering*, *12*(3), 201–211. https://doi.org/10.1080/19397038.2018.1508318

Saba, N., & Jawaid, M. (2018). A review on thermomechanical properties of polymers and fibres reinforced polymer composites. *Journal of Industrial and Engineering Chemistry*, *67*, 1–11. https://doi.org/10.1016/j.jiec.2018.06.018

Samuel, R., Ramadoss, K. N., Gunasekaran, K., Logesh, S., Gnanaraj, S. J. P., & Abdul, M. (2021). Studies on mechanical properties and characterization of carbon fibre reinforced hybrid composite for aero space application. *Materials Today Proceedings*, *47*, 4438–4443. https://doi.org/10.1016/j.matpr.2021.05.304

Shaikh, H., Alothman, O. Y., Alshammari, B. A., & Jawaid, M. (2023). Dynamic and thermo-mechanical properties of polypropylene reinforced with date palm nano filler. *Journal of King Saud University - Science*, *35*(3), Article 102561. https://doi.org/10.1016/j.jksus.2023.102561

Siengchin, S. (2023). A review on lightweight materials for defence applications: Present and future developments. *Defence Technology*, *24*, 1-17. https://doi.org/10.1016/j.dt.2023.02.025

Sierpiński, Z. (2023, November 22). Analiza termiczna w metaloznawstwie - mozliwości i zastosowania. Cz. 1. Skaningowa kalorymetria różnicowa [Thermal analysis in materials science - possibilities and applications. Vol. 1. Differential scanning calorimetry]. https://home.agh.edu.pl/~blaz/wyklady/pliki/analiza.pdf

Song, G. L., Zhang, C., Chen, X., & Zheng, D. (2021). Galvanic activity of carbon fibre reinforced polymers and electrochemical behavior of carbon fibre. *Corrosion Communications*, *1*, 26–39. https://doi.org/10.1016/j.corcom.2021.05.003

Tinkloh, S., Wu, T., Tröster, T., & Niendorf, T. (2020). A micromechanical-based finite element simulation of process-induced residual stresses in metal-CFRP-hybrid structures. *Composite Structures*, *238*, Article 111926. https://doi.org/10.1016/j.compstruct.2020.111926

Trębacki, K., & Królicka, A. (2017). Wpływ struktury materiałów kompozytowych na własności mechaniczne [The influence a structure of composite materials on mechanical property]. *Autobusy*, *9*, 129–131.

Walczak, M., Zwierzchowski, M., Bieniaś, J., & Caban, J. (2017). The tribological characteristics of Al-Si/graphite composite. *Tribologia*, *1*, 97–104.

Wang, W. X., Takao, Y., & Matsubara, T. (2007, July 8-13). Galvanic corrosion-resistant carbon fibre metal laminates. Proceedings of the 16th International Conference on Composite Materials, pp. 1–10. Japan Society for Composite Materials and Japan Aerospace Exploration Agency.

Xue, J., Wang, W. X., Takao, Y., & Matsubara, T. (2011). Reduction of thermal residual stress in carbon fibre aluminum laminates using a thermal expansion clamp. *Composites Part A*: *Applied Science and Manufacturing*, *42*(8), 986–992. https://doi.org/10.1016/j.compositesa.2011.04.001

Analiza Współczynnika Rozszerzalności Cieplnej Kompozytów Wzmocnionych Włóknami Szklanymi i Węglowymi

Streszczenie

Wraz z rozwojem techniki, możemy zaobserwować wzrost znaczenia kompozytów metalowo-włóknistych w inżynierii mechanicznej. Są to materiały składające się z odpowiednio ułożonych warstw metalu oraz różnego rodzaju włókien. Bardzo szerokie zastosowanie materiałów kompozytowych w budowie elementów maszyn i urządzeń powoduje, że niejednokrotnie są one narażone na pracę w warunkach zmiennych temperatur. Celem tego artykułu była analiza rozszerzalności cieplnej typowych materiałów kompozytowych wzmocnionych włóknami węglowymi i szklanymi oraz laminatów typu GLARE i CARALL. Jako materiał referencyjny wykorzystano stop aluminium EN AW-6060. Celem badań dylatometrycznych było określenie rozszerzalności cieplnej i stabilności wymiarowej materiałów kompozytowych w podwyższonych temperaturach do 100°C z szybkością nagrzewania 5°C/min. Największym współczynnikiem rozszerzalności liniowej (20,27 × 10^{-6} 1/K) charakteryzował się stop aluminium EN AW-6060. Najmniejszym dodatnim liniowym współczynnikiem rozszerzalności cieplnej charakteryzowały się kompozyty zawierające włókna szklane. Spośród materiałów kompozytowych, najmniejszym współczynnikiem rozszerzalności cieplnej charakteryzował się kompozyt typu CARALL.

Słowa kluczowe: współczynnik rozszerzalności cieplnej, kompozyty, analiza dylatometryczna, temperatura, rozszerzalność cieplna

Original Research

Effect of Floating-Plug Drawing Process Parameters on Surface Finish of Inner and Outer Surfaces of AISI 321 Stainless Steel Thin-Walled Tubes

Krzysztof Żaba [1],* iD, Marcin Szpunar [2] iD

[1] Department of Metal Working and Physical Metallurgy of Non-Ferrous Metals, AGH—University of Science and Technology, al. Adama Mickiewcza 30, 30-059 Cracow, Poland

[2] Doctoral School of the Rzeszow University of Technology, Rzeszow University of Technology, al. Powstańców Warszawy 12, 35-959 Rzeszów, Poland; d547@stud.prz.edu.pl

* Correspondence: krzyzaba@agh.edu.pl

Abstract

This article presents the results of the analysis of changes in the surface topography of AISI 321 (1.4541) thin-walled stainless steel tubes in single-pass Floating-Plug Drawing (FPD) process. Experimental tests were carried out with variable drawing speed (1, 2, 3, 4, 6, and 10 m/min) and different angles of floating plug (11.3°, 13° and 14°). Wisura DSO7010 (Fuchs Oil) lubricant was used in the experiments. Mean roughness Ra and ten point height of irregularities Rz were adopted as surface quality indicators. Roughness parameters were measured independently on the inner and outer surfaces of thin-walled tubes. Analysis of variance was used to analyse the relationship between process parameters (drawing speed and angle of floating plug) and surface roughness of tubes. A decrease in the values of both analyzed roughness parameters was observed as a result of the drawing process. The FPD process significantly improves the inner surface quality of AISI 321 thin-walled stainless steel tubes. The mean roughness value tends to increase with increasing drawing speed, while the angle of the floating-plug has no significant effect on the mean roughness Ra.

Keywords: analysis of variance, floating plug, stainless steel, surface roughness, tube drawing

1. Introduction

Floating-plug drawing (FPD) process has become the most advanced technology in the manufacture of thin-walled seamless tubes. The main advantages of FPD process are high wall thickness reduction ratio, high productivity and thin walls (Pernis & Kasala, 2013). A floating plug does not limit the length of a manufactured tube (Pernis, 2001). The undoubted limitations of drawing technology are the small production possibilities related to the characteristics of the process in terms of the shape of the manufactured products. In the tube drawing process, unlike rod drawing, the external and internal surfaces of the pipe are formed simultaneously. Thick-walled tubes can be drawn using floating-plug drawing process only under the condition that plug head diameter is smaller than diameter of the die (Pernis & Kasala, 2013). Moreover, through appropriate heat treatment of metal before the drawing process, it is possible to obtain high-strength products while maintaining good plastic properties (Bartnicki & Pater, 2005; Łuksza, 2001).

Drawing technology includes the processes of preparing material for drawing and the finishing processes of drawn products. If the surface of the workpiece is covered with a layer of oxides, it should be removed by etching in acid solutions. The phenomenon of friction in drawing processes is unfavorable and causes uneven deformation and increases the drawing force (Necpal et al., 2018). It is estimated that approximately 30-50% of the total drawing force is used to overcome friction forces (Skoblik & Wilczewski, 2006). Uneven deformations cause local residual stresses and create material defects (Martínez et al., 2022). Excessive friction causes rapid wear of dies and makes it difficult to obtain the appropriate smoothness of the surface of the finished products (Patil et al., 2020; 2021). To reduce friction,

metallic, phosphate or lubricant coatings can be applied to the surface of the workpiece immediately before processing. Reducing friction is achieved by using appropriate liquid lubricants which are a composition of various oils or solid lubricants (de Castro Maciel et al., 2016; Larsson et al., 2019). In drawing components from high-strength steels and alloys, the so-called self-lubricating coatings facilitating the forming process. To ensure liquid friction conditions, hydrostatic and hydrodynamic lubricant feeding methods are used (Byon et al., 2011).

Optimisation of the floating-plug drawing process of difficult-to-form materials was presented by Pasierb et al. (2000). The developed computer program allowed for the determination of optimal technological parameters of the drawing process of materials that are difficult to deform. In another article, Żaba and Pasierb (2004) investigated the influence of the geometry of dies and plugs as well as the drawing speed on the properties of 1H18N10T steel tubes drawn using floating plug. The investigations were focused on the analysis of microhardness on the cross-section of tubes before and after drawing. Pernis and Kasala (2013) investigated the conditions under which tube drawing of thick-wall tubes is possible. They also provided equation that enables to calculate the difference of die and plug angles to achieve stable drawing conditions. Campos and Cetlin (1998) investigated the effect of the coefficient of friction (CoF) on the decrease of uniform tensile elongation of copper bars. They found that CoF has no influence on the elongation. Świątkowski and Hatalak (2001) proposed a floating plug to stabilise of the tube drawing process. The proposed tool increases the wall-thickness reduction ratio and provides the minimization of the zone of tube sinking. Smith and Bramley (1973) for the first time used the upper-bound technique to establish the relative importance of the various parameters of the FPD proces.

The tube drawing process has been analyzed using various numerical methods e.g. finite element method (Kwan, 2002; Yoshida et al., 2001) and upper bound method (Pouyafar et al., 2022). Danckert and Endelt (2009) conducted FE-based numerical modelling of FPD and proposed a new plug design with "self-catching plug" principle, where the cylindrical plug land is replaced with a circular profiled plug land (conventionally the plug land is cylindrical). The self-catching plug reduces the risk for failure during start up of the FPD process. Wang and Wang (2008) modified conventional slab model (CSM) to analysed FPD process of hollow copper tubes. They concluded that proposed model was more accurate than the CSM. Um and Lee (1997) found that the drawing stress in the tube drawing with a fixed plug is related to the increase in the CoF. Rubio et al. (2006) modelled the plastic deformation zone using triangular rigid zones which allowed to calculate the dimensional overall energy involved in FPD process. Shen et al. (2009) investigated the effect of equivalent strain, equivalent stress and temperature on the stability of the FPD process of copper tubes with pores. The analyses were carried out using finite element software Msc.Marc. It was found that the floating-plug axial movement affect the surface finish of the tube with pores. Rubio et al. (2017) provided the guidelines for selecting plugs used in the FPD of thin-walled tubes. The theoretical considerations on the floating plug positions in the deformation zone are given by Sadok and Pietrzyk (1981).

As shown by the review of literature, research works on designing of tube drawing process are focused on optimization of the plug shape, lubrication conditions and mechanical properties of the components. However, analysis of the surface finish of stainless steel thin-walled tubes has not attracted much attention. Therefore, this article presents the results of the analysis of surface topography changes of thin-walled AISI 321 stainless steel tubes in FPD process. Analysis of variance was used to analyse the relationships between process parameters (drawing speed and angle of floating plug) and tube surface roughness parameters.

2. Material and methods

2.1. Test material

Experimental tests using the FPD process were carried out on austenitic chromium-nickel-stainless AISI 321 (EN symbol X6CrNiTi18-10) steel pipes. The outer diameter of the pipes was 19 mm and the wall thickness was 1.2 mm. In order to facilitate the drawing process, the outer surface of the tubes was grinded and etched. Grinding was intended to create oil pockets on the surface of workpiece, which ensures that the appropriate amount of oil is supplied to the contact zone. Proper lubrication is crucial in the FPD process. It reduces the non-uniformity of deformation and limits the generation of heat caused by friction.

2.2. Experimental procedure

Thin-walled tubes were drawn on a floating plug (Fig. 1) using a drawing machine with a maximum capacity of 70 kN. Floating plugs were made with a half angle of the angle of inclination of the conical part of the plug $\beta = 11.3°$ ($L = 22.8$ mm), 13° ($L = 22$ mm), and 14° ($L = 21.7$ mm). A die was used with the following geometry $D_k = 16$, mm, $\alpha = 16°$ (Fig. 2). Both die and floating plug were made of a tungsten carbide G10. The tubes were drawn at speeds of 1, 2, 3, 4, 6, and 10 m/min. Wisura DSO7010 (Fuchs Oil) lubricant was used in the experiments. The geometric parameters of the tubes before and after drawing are listed in Table 1.
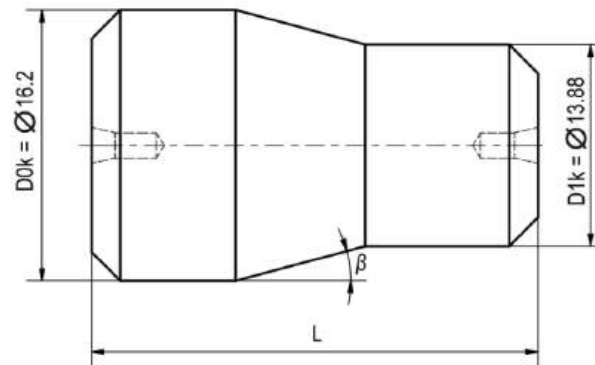
Fig. 1. Geometry of floating plug (dimensions in mm).
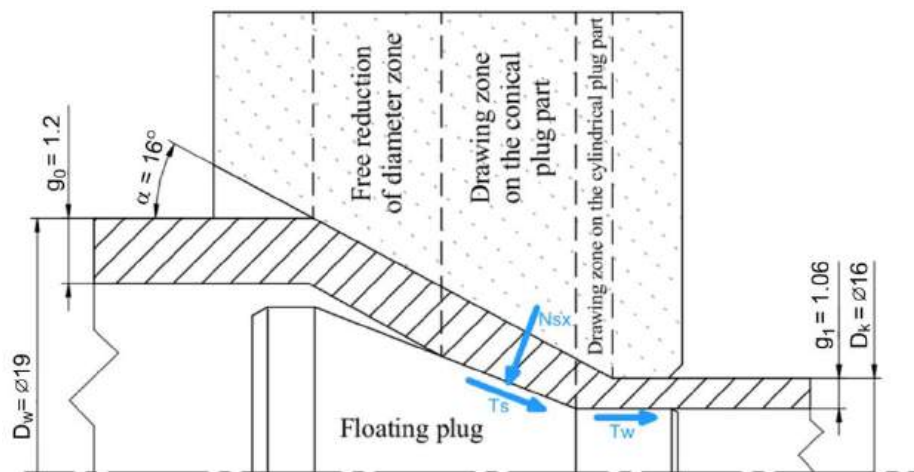
Fig. 2. Schematic diagram of the FPD process (dimensions in mm).

Table 1. The geometric parameters of the tubes before and after drawing.

Parameter	Value	
	before drawing	after drawing
Outer diameter	19 mm	16 mm
Wall thickness	1.2 mm	1.06 mm

The essence of the floating-plug drawing process is shown in Fig. 2, which shows a cross-section through the deformation zone. A floating plug is inserted into the pipe in front of the die, then the pipe is crimped. After inserting the workpiece into the die, the drawing process begins. The shape and dimensions of the plug are selected so that the frictional forces of drawing are equal to the pushing forces coming from the contact force N_{sx}. The pulling forces have two components: T_s – the friction force in the conical part of the plug, T_w – the friction force in the cylindrical part of the plug (Fig. 2). The balance condition of plug can therefore be written as (Nowosielski et al., 2014):

$$N_{sx} = T_s + T_w \tag{1}$$

The surface roughness of the inner and outer surfaces of the tubes were measured using LEXT OLS4100 confocal laser microscope with 405 nm UV laser light (Leica Microsystems). Surface roughness results are presented by the two most commonly used parameters, i.e., Ra – arithmetic average of the absolute values of the profile heights over the evaluation length and Rz – the average value of the

absolute values of the heights of five highest-profile peaks and the depths of five deepest valleys within the evaluation length. The ground surface of the batch material and the surfaces of the tubes after drawing were analysed.

2.3. Analysis of variance

The experiment was designed to investigate the effects of three input factors: Drawing speed, angle of floating plug β and two surface roughness parameters (Ra and Rz) responses. The factor levels were coded to facilitate the analysis. The significance of the model and the model terms were determined using the F-value and the p-value. Model terms with p-values less than 0.05 were considered significant. Model terms with p-values greater than 0.05 were considered not significant. The models were evaluated based on the following parameters. Sequential p-value was used to determine the significance of the model. A smaller p-value generally indicates that the model is significant. Lack of fit p-value was used to check the goodness of fit of the model. A larger p-value is desirable as it indicates a satisfying fit. Adjusted R^2 is the coefficient of determination, adjusted based on the number of predictors in the model. It indicates the proportion of the variance in the dependent variable that is predictable from the independent variables. A higher adjusted R^2 indicates a better fit of the model. Predicted R^2 is an estimate of the population coefficient of determination. It provides an indication of how well the model will predict responses for new observations. A higher predicted R^2 indicates a better predictive ability of the model. The integrity of fit of the models was evaluated using several fit statistics including standard deviation, mean value, coefficient of variation, R^2, adjusted R^2, predicted R^2 and adequate precision. A predicted R^2 in reasonable agreement with the adjusted R^2 (i.e., the difference is less than 0.2) and an adequate precision ratio greater than 4 were considered desirable for navigating the design space.

Table 2 presents the data used in the analysis of variance. The angle of floating plug and drawing speed were used as input (explanatory) variables. Two independent analyzes of variance were performed. In the first analysis, the Ra parameter measured on the inner and outer surfaces of the tubes was used as the output (explained) variables. In the second model, the parameter Rz measured on the inner and outer surfaces of the tubes were used as output variables.

Table 2. Roughness parameters Ra and Rz of inner and outer surfaces of tubes.

Angle of floating plug β, °	Drawing speed v_c, m/min	Ra, μm		Rz, μm	
		Outer surface	Inner surface	Outer surface	Inner surface
11.5	1	-	-	-	-
	2	0.49	0.13	4.79	1.39
	3	0.47	0.18	5.38	2.06
	4	0.63	0.23	6.14	2.76
	6	0.73	0.26	6.47	2.9
	10	0.76	0.3	6.45	3.34
13	1	0.45	0.11	4.69	1.58
	2	0.46	0.26	4.63	2.67
	4	0.47	0.35	4.57	2.71
14	1	0.43	0.23	4.77	2.1
	2	0.61	0.24	5.73	2.13
	4	0.53	0.25	5.27	2.74

3. Results and discussion

Fig. 3a shows the change of the Ra parameter on both sides of tubes for different values of angles of floating plug β and drawing speeds. The greatest reduction in mean roughness occurs on the inner surface of the tube. There is also a tendency for the mean roughness value to increase with increasing drawing speed. There is no clear influence of the floating plug on the change of the Ra parameter value. The largest change in the initial mean roughness, for all angles of the floating plug, occurs on the inner surface of the thin-walled tube. Similar qualitative conclusions can be made regarding the influence of drawing speed and angle of floating plug on the ten point height of irregularities Rz (Fig. 3b). The larger the angle of floating plug β at a constant die angle α, the smaller the gap between the outer surface of the plug and the inner surface of the tube. It causes less lubricant to enter the deformation zone. At the same time, the contact area between the floating plug and the tube surface increases. This increases the friction between the contact surfaces and reduces the surface roughness of the inner surface of the tube.
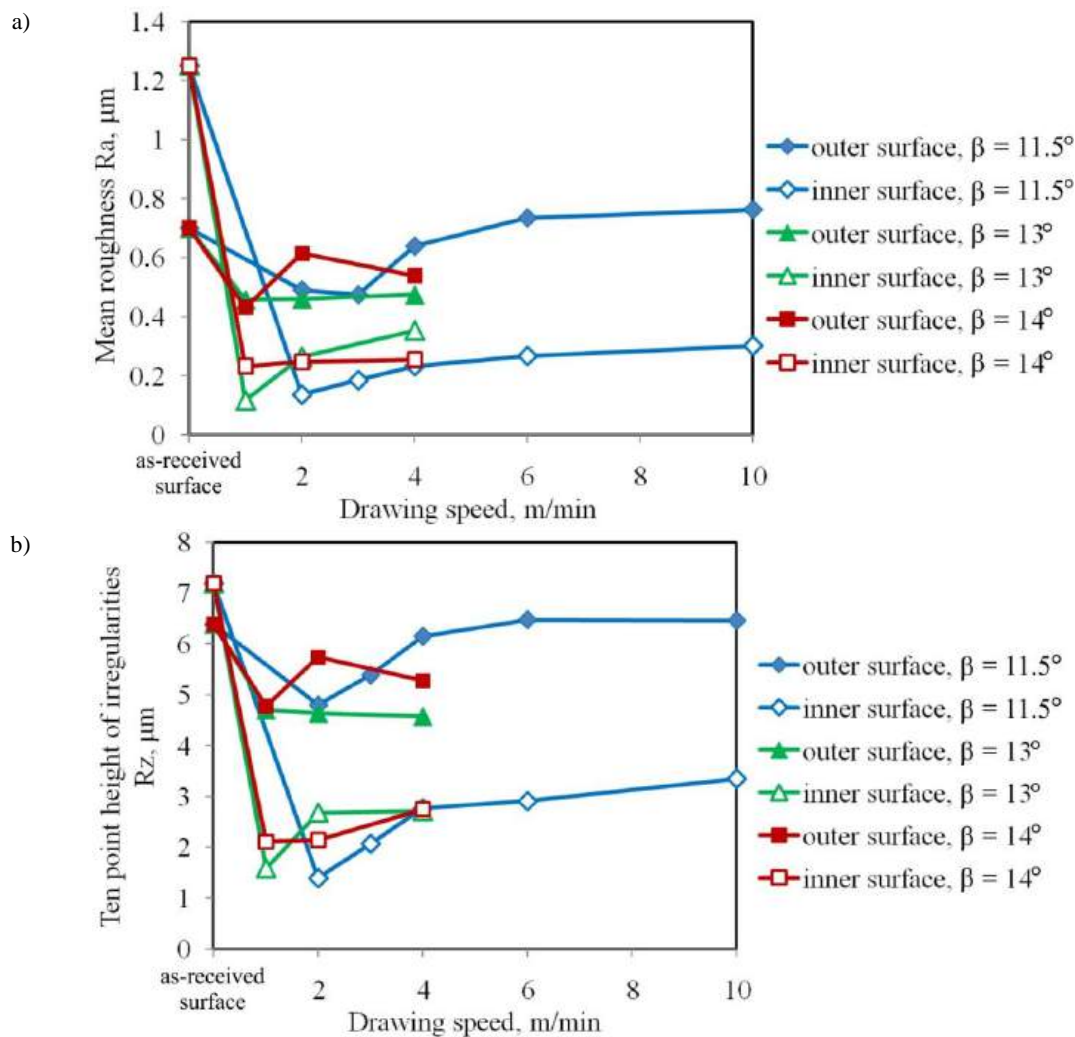
Fig. 3. Effect of drawing speed on the value of a) Ra and b) Rz parameters.

3.1. Mean roughness Ra

The Fisher test is a statistical test used to compare the variances of two population samples. The test is based on the F distribution, which is a probability distribution comparing the ratio of two variances. The F test was used to test the homogeneity of variance between multiple groups. It was used to determine whether the variances of two groups are equal or not.

The F-value of 66.04 determined using ANOVA implies the model is significant. Moreover, the p-value less that 0.0001 indicate model terms are significant. Angle of the floating plug ($p = 0.0004$) and location of mean roughness measurement on the tube surface ($p < 0.0001$) are also significant model terms. The difference between adjusted R^2 (0.861) and predicted R^2 (0.817) is less than 0.2. So, it can be concluded that these parameters are in statistically reasonable agreement.

The scatter plots presented in the Fig. 4 provide valuable insights into the dataset's characteristics. Fig 4a shows a positive correlation between the externally studentized residuals and the normal probability. This is evidenced by the data points closely aligning with the line of best fit. Fig. 4b illustrates the spread of externally studentized residuals against predicted values. Interestingly, the data points do not form any clear pattern or trend, indicating a random distribution of residuals. Fig 4c presents a strong positive correlation between actual and predicted values. The data points align closely with a diagonal line, indicating an effective model performance. This suggests that the model is accurately predicting the outcomes, which is a desirable attribute in predictive modeling.
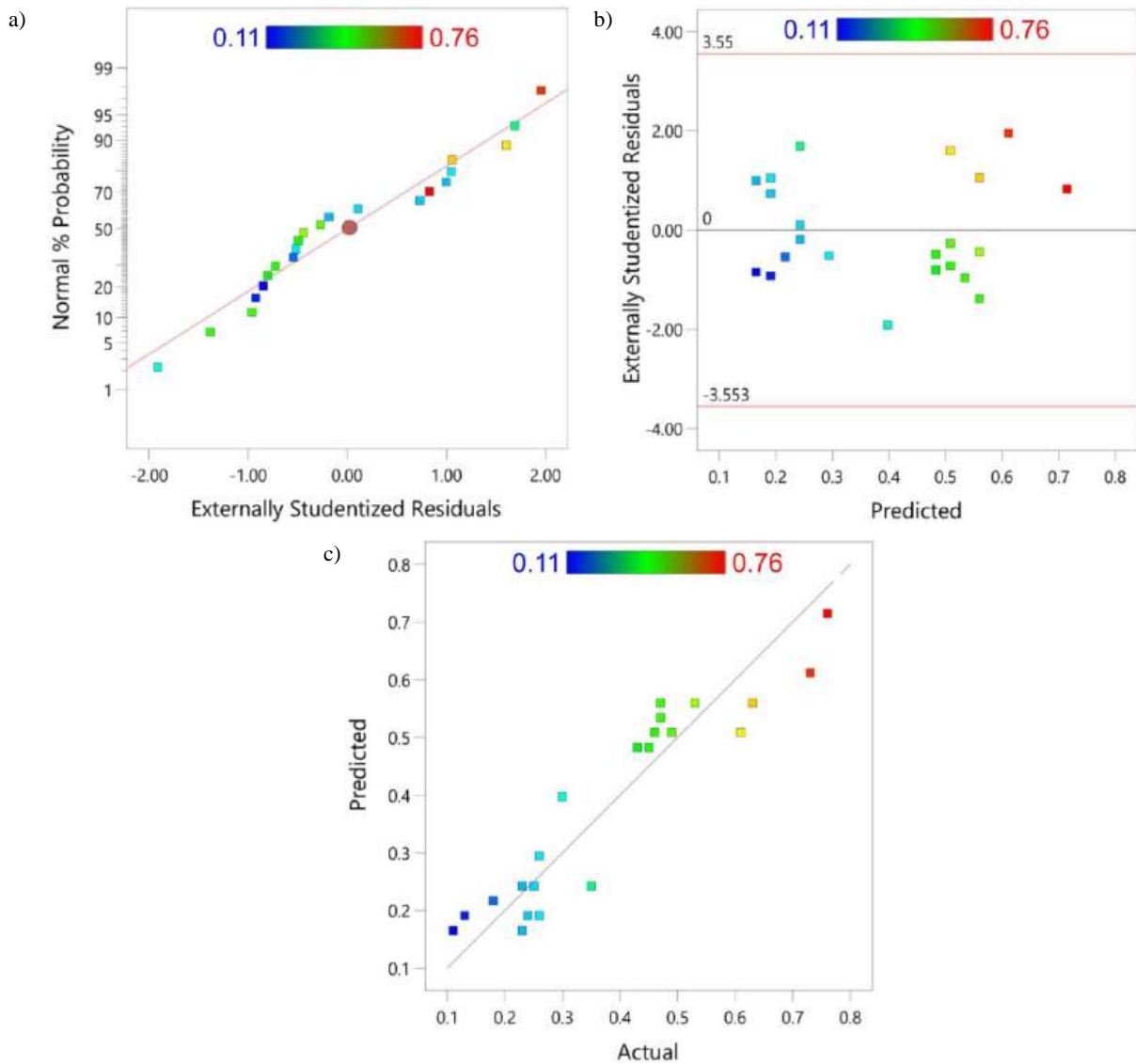
Fig. 4. a) normal probability plot, b) residuals with reference to predicted value of Ra parameter and c) predicted versus actual response for mean roughness Ra.

Based on the results of the ANOVA model, it can be concluded that the angle of floating plug in the range of $\beta = 11.5\text{-}14°$ has no effect on the value of mean roughness Ra (Figs. 5, 6). Increasing the drawing speed increases the value of roughness parameter Ra. This character is almost the same for the Ra parameter measured at inner side (Fig. 5) and outer side (Fig. 6) of the tube. Increasing the drawing speed causes an increase in temperature in the contact zone and a change in the mechanical properties of the workpiece. Moreover, the temperature rise on the contact surface causes a thermal decomposition of the lubricant. Effect of sliding speed on the mean drawing force and the maximum temperature in the contact zone is shown in Fig. 7. At a drawing speed of 10 m/min, the temperature was reduced compared to the drawing speeds of 4 and 6 mm/min due to the fact that the tube did not reach a high temperature during drawing. Probably with a longer feed tube, at a speed of 10 m/min, the temperature would reach a higher value than for lower drawing speeds. The reduced amount of lubricant is the main factor for deterioration of surface roughness. Suliga (2014) found that the heat-affected surface layer becomes thicker with a decreased drawing speed. The FPD process greatly improved the inner surface quality of tube, which is in agreement with results by Yan et al. (2022).
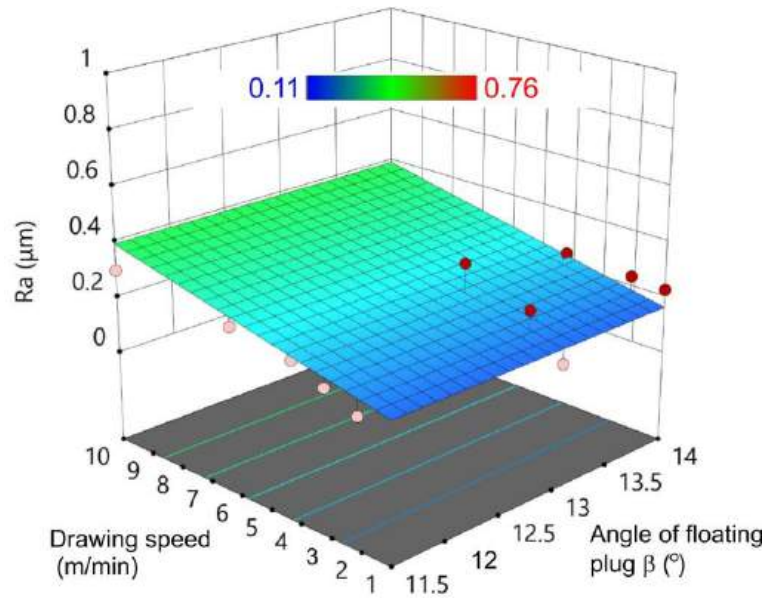
Fig. 5. Effect of angle of floating plug and drawing speed on the mean roughness Ra measured at inner side of the tube.
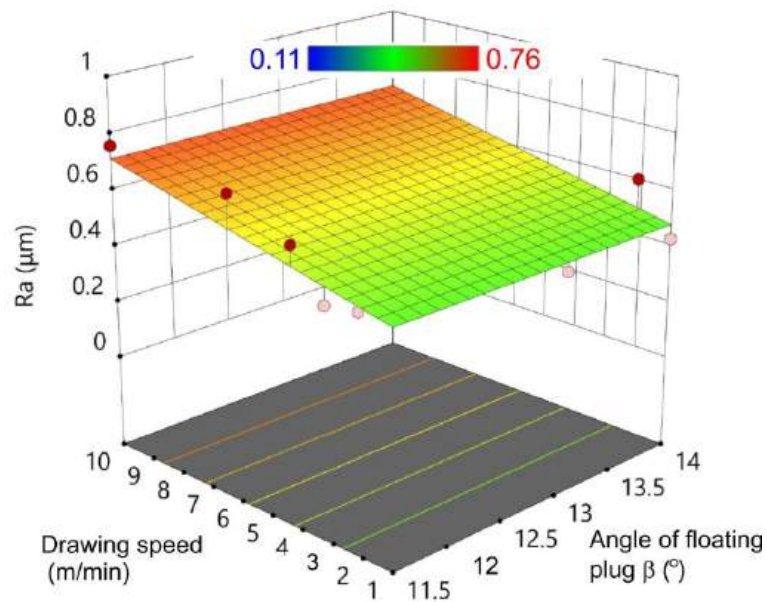
Fig. 6. Effect of angle of floating plug and drawing speed on the mean roughness Ra measured at outer side of the tube.
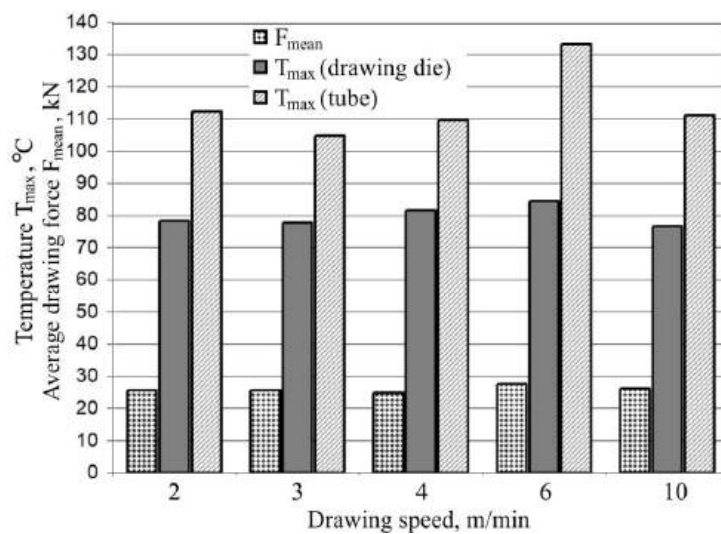
Fig. 7. Effect of drawing speed on the mean drawing force and the maximum temperature in the contact zone.

3.2. Ten point height of irregularities Rz

The F-value of 69.94 determined using ANOVA implies the model is significant. Moreover, the p-value less that 0.0001 indicate model terms are significant. Angle of the floating plug ($p = 0.7063$), location of measurement of ten point height of irregularities Rz on the tube surface ($p < 0.0001$) and product of drawing speed and angle of the floating plug ($p = 0.0254$) are also significant model terms. The difference between adjusted R^2 (0.942) and predicted R^2 (0.927) is less than 0.2. So, it can be concluded that these parameters are in statistically reasonable agreement.

Diagnostic plots in Fig. 8 presents perspective on the dataset's properties. Fig. 8a demonstrates a positive correlation between the externally studentized residuals and the normal probability. This is evidenced by the data points that closely follow the line of best fit. Fig. 8b plot showcases the distribution of externally studentized residuals against predicted values. The data points are scattered randomly, indicating a lack of any discernible pattern or trend. This randomness is a positive sign as it suggests that the model's assumptions are likely being met. Fig. 8c plot reveals a strong positive correlation between actual and predicted values. The data points closely align with a diagonal line, indicating that the model is performing well in its predictions. This is a desirable characteristic in predictive modeling.
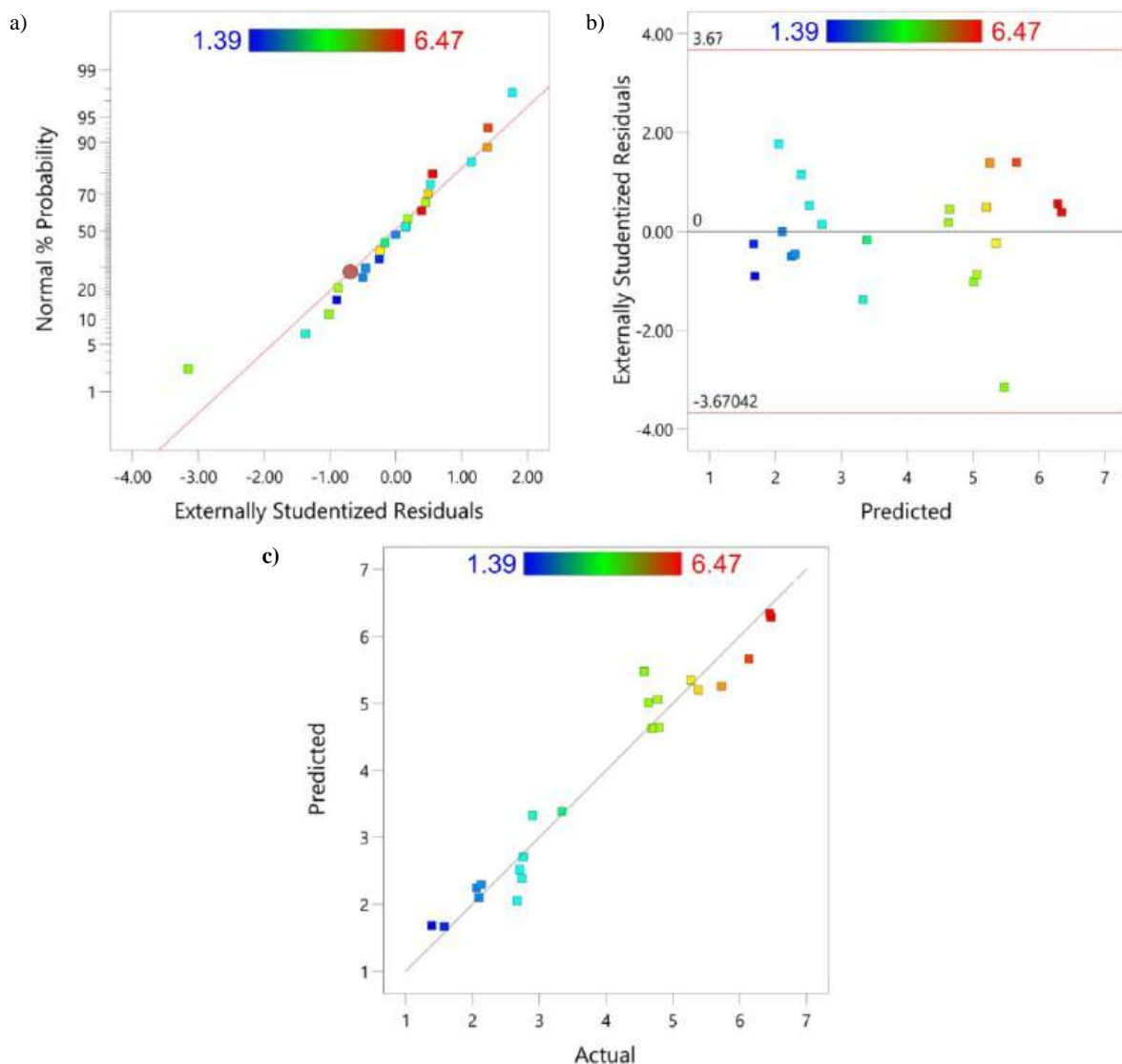
Fig. 8. a) normal probability plot, b) residuals with reference to predicted value of Rz parameter and c) predicted versus actual response for ten point height of irregularities Rz.

The influence of the angle of floating plug on the point height of irregularities Rz depends on the drawing speed (Figs. 9, 10). At low drawing speeds, the value of the Rz parameter increases as the angle of floating plug increases. At the highest sliding speed (10 m/min), increasing the angle of floating plug reduces the Rz parameter. The mentioned conclusions refer to the inner (Fig. 9) and outer (Fig. 10) surface of the tube. For the tool with the lowest value of the angle of floating plug, the value of the Rz

parameter increases over the entire range of analyzed drawing speeds. At the angle of floating $\beta = 14°$, starting from a speed of approximately 4 m/min, the value of the ten point height of irregularities Rz decreases.
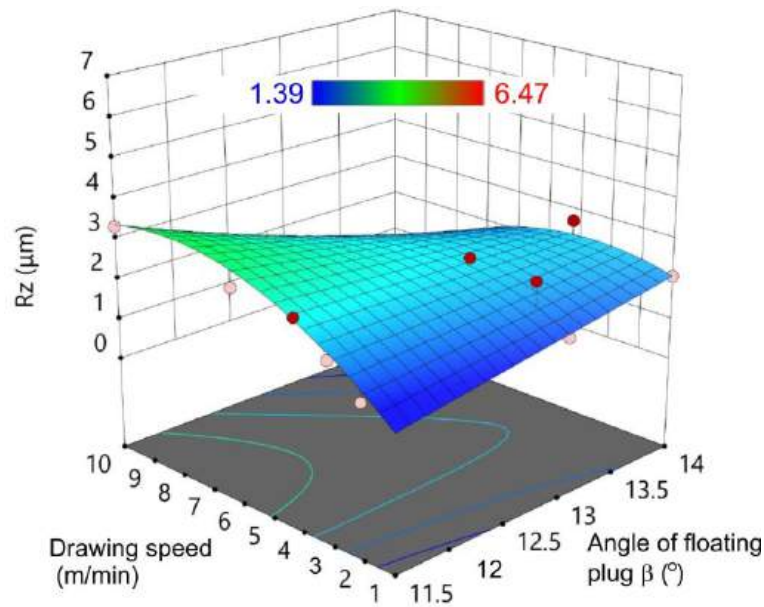
Fig. 9. Effect of angle of floating plug and drawing speed on the ten point height of irregularities Rz measured at inner side of the tube.
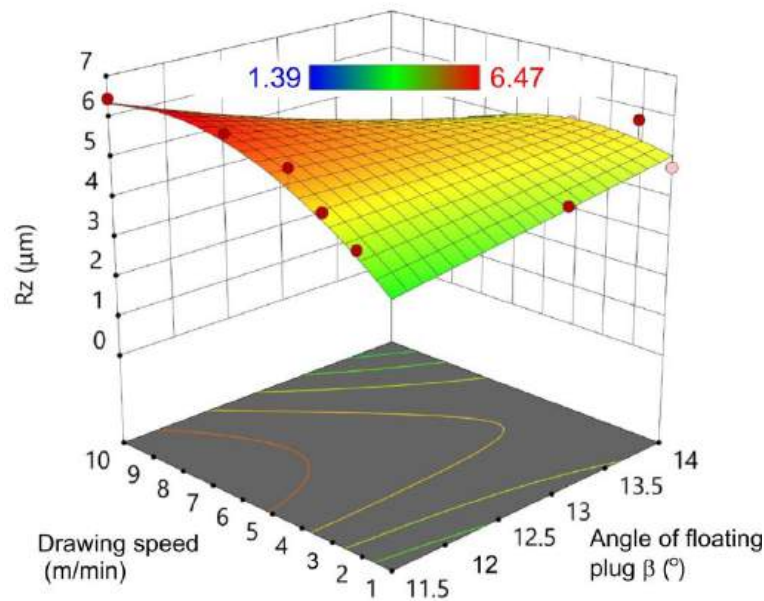
Fig. 10. Effect of angle of floating plug and drawing speed on the ten point height of irregularities Rz measured at outer side of the tube.

4. Conclusions

This article presents the results of the analysis of changes in the surface topography of AISI 321 thin-walled stainless steel tubes in floating-plug drawing process. Based on the analysis of variance presented in this article, the following conclusions can be drawn:

- The greatest reduction in mean roughness occurs on the inner surface of the tube. This suggests that the FPD process significantly improves the inner surface quality of the tube.
- There is a tendency for the mean roughness value to increase with increasing drawing speed. This is due to the increase in temperature in the contact zone and a change in the mechanical properties of the workpiece, which leads to a thermal decomposition of the lubricant.

- The angle of the floating plug β in the range of 11.5-14° has no effect on the value of mean roughness Ra. This indicates that the floating plug's angle does not significantly influence the roughness of the tube surface.
- The influence of the angle of the floating plug on the point height of irregularities Rz depends on the drawing speed. At low drawing speeds, the value of the Rz parameter increases as the angle of the floating plug increases, while at the highest sliding speed, increasing the angle of the floating plug reduces the Rz parameter.

References

Bartnicki, J., & Pater, Z. (2005). *Walcowanie poprzeczno – klinowe wyrobów drążonych* [*Cross-wedge rolling of hollow products*]. Wydawnictwo Politechniki Lubelskiej.

Byon, S. M., Lee, S. J., Lee, D. W., Lee, Y. H., & Lee, Y. (2011). Effect of coating material and lubricant on forming force and surface defects in wire drawing process. *Transactions of Nonferrous Metals Society of China*, *21*, 104–110. https://doi.org/10.1016/S1003-6326(11)61071-6

Campos, H. B., & Cetlin, P. R. (1998). The influence of die semi-angle and of the coefficient of friction on the uniform tensile elongation of drawn copper bars. *Journal of Materials Processing Technology*, *80–81*, 388–391. https://doi.org/10.1016/S0924-0136(98)00117-4

Danckert, J., & Endelt, B. (2009). LS-Dyna(R) used to analyse the drawing of precision tubes. *Proceedings of the 7th European LS_DYNA Conference*, Salzburg, Austria, 14-15 May 2009, pp. 1–14.

de Castro Maciel, D., Martins, N., Corradi, D. R., Gomes, D. J. C., Dutra, J. M. S., & da Silva, G. C. (2016). Lubrication influence in the drawing process of aluminum, steel and copper alloys. *Proceedings of the 5th International Conference on Integrity-Reliability-Failure*, 24-28 July 2016, Porto, Portugal, pp. 145–156.

Kwan, C. T. (2002). A generalized velocity field for axisymmetric tube drawing through an arbitrarily curved die with an arbitrarily curved plug. *Journal of Materials Processing Technology*, *122*(2-3), 213–219. https://doi.org/10.1016/S0924-0136(02)00013-4

Larsson, J., Jansson, A., & Karlssomn, P. (2019). Monitoring and evaluation of the wire drawing process using thermal imaging. *International Journal of Advanced Manufacturing Technology*, *101*, 2121–2134. https://doi.org/10.1007/s00170-018-3021-7

Łuksza, J. (2001). *Elementy ciągarstwa* [*Fundamentals of drawing*]. Wydawnictwo AGH.

Martínez, G. A. S., Rodriguez-Alabanda, O., Prosco, U., Tintelecan, M., & Kabayama, L. K. (2022). The influences of the variable speed and internal die geometry on the performance of two commercial soluble oils in the drawing process of pure copper fine wire. *International Journal of Advanced Manufacturing Technology*, *118*, 3749–3760. https://doi.org/10.1007/s00170-021-08172-2

Necpal, M., Martinkovič, M., & Vaclav, Š. (2018). Determination of the coefficient of friction under cold tube drawing using FEM simulation and drawing force measurement. *Research Papers Faculty of Materials Science and Technology Slovak University of Technology*, *26*(42), 29–34. https://doi.org/10.2478/rput-2018-0003

Nowosielski, M., Żaba, K., Nowak, S., & Świątek, B. (2016, May 23-25). Projektowanie procesu ciągnienia rur z brązu na trzpieniu swobodnym [Design of the floating-plug drawing of bronze tubes]. *Proceedings of the 4th Conference "Doskonalenie Jakości Procesów Technologicznych"*. Sromowce Niżne, Poland, pp. 95–111.

Pasierb, A., Osika, J., & Żaba, K. (2000). Optymalizacja procesu ciągnienia rur na korku swobodnym z materiałów trudno odkształcalnych [Optimum conditions for drawing of pipes, from hard-deformable materials, on free plug]. *Rudy i Metale Nieżelazne*, *45*(10–11), 520–527.

Patil, M., Singh, V., Gupta, A. K., Regalla, S. P., Bera, T. C., Simhachalam, B., & Srinivas, K. (2021). Tin layer as a solid lubricant for cold tube drawing processes. *International Journal of Precision Engineering and Manufacturing-Green Technology, 9*, 459–472. https://doi.org/10.1007/s40684-020-00301-8

Patil, M., Singh, V., Simhachalam, B., & Srinivas, K. (2020). Effect of lubrication technique in tube drawing. *Materials Today: Proceedings*, *28*, 426–431. https://doi.org/10.1016/j.matpr.2019.10.027

Pernis, R. (2001). Ciągnienie rur na trzpieniu swobodnym [Floating-plug drawing of tubes]. *Rudy i Metale Nieżelazne*, *46*(7), 305–311.

Pernis, R., & Kasala, J. (2013). The influence of the die and floating plug geometry on the drawing process of tubing. *International Journal of Advanced Manufacturing Technology*, *65*, 1081–1089. https://doi.org/10.1007/s00170-012-4241-x

Pouyafar, V., Bolandi, H., & Meshkabadi, R. (2022). Tube drawing analysis using upper bound and energy methods and validation by Cockcroft-Latham failure criteria. *Journal of the Brazilian Society of Mechanical Sciences and Engineering*, *44*, Article 9. https://doi.org/10.1007/s40430-021-03302-z

Rubio, E. M., Camacho, A. M., Pérez, R., & Marín, M. M. (2017). Guidelines for selecting plugs used in thin-walled tube drawing processes of metallic alloys. *Metals*, *7*, Article 572. https://doi.org/10.3390/met7120572

Rubio, E. M., González, C., Marcos, M., & Sebastián, M. A. (2006). Energetic analysis of tube drawing processes with fixed plug by upper bound method. *Journal of Materials Processing Technology*, *177*, 175–178. https://doi.org/10.1016/j.jmatprotec.2006.03.193

Sadok, L., & Pietrzyk, M. (1981). Analiza pracy korka swobodnego w obszarze odkształcenia [Analysis of the work of a free plug in the deformation area]. *Hutnik*, *2*, 62–65.

Shen, W. H., Li, Z. G., Zhang, S. H., & Liu H. M. (2009). Numerical simulation of floating-plug drawing of copper tubes with pores. *International Journal of Product Development*, *7*(3-4), 301–310. https://doi.org/10.1504/IJPD.2009.023324

Skoblik, R., & Wilczewski, L. (2006). *Technologia Metali. Laboratorium* [*Metal Technology. Laboratory*]. Politechnika Gdańska.

Smith, D. J., Bramley, A. N. (1973). A theoretical study of tube drawing with a floating plug. In: Tobias, S.A., Koenigsberger, F. (eds) *Proceedings of the Thirteenth International Machine Tool Design and Research Conference*. Palgrave, London. https://doi.org/10.1007/978-1-349-01857-4_70

Suliga, M. (2014). Analysis of the heating of steel wires during high speed multipass drawing process. *Archives of Metallurgy and Materials*, *59*(4), 1475–1480. https://doi.org/10.2478/amm-2014-0251

Świątkowski, K., & Hatalak, R. (2001). Study of the new floating-plug drawing process of thin-walled tubes. *Journal of Materials Processing Technology*, *151*(1–3), 105–114. https://doi.org/10.1016/j.jmatprotec.2004.04.024

Um, K. K., & Lec, D. N. (1997). An upper bound solution of tube drawing. *Journal of Materials Processing Technology*, *63*(1-3), 43-48. https://doi.org/10.1016/S0924-0136(96)02597-6

Wang, C. S., & Wang, Y. C. (2008). The theoretical and experimental of tube drawing with floating plug for micro heat-pipes. *Journal of Mechanics*, *24*(2), 111–117. https://doi.org/10.1017/S1727719100002136

Yan, J. P., Zhao, R., Meng, B., Wan, M., & Wang, Z. X. Analysis of the properties and microstructure of ultra-thin tube. *IOP Conference Series: Materials Science and Engineering*, *1270*, Article 012023. https://doi.org/10.1088/1757-899X/1270/1/012

Yoshida, K., Watanabe, M., & Ishikawa, H. (2001). Drawing of Ni–Ti shape-memory-alloy fine tubes used in medical tests. *Journal of Materials Processing Technology*, *118*, 251–255. https://doi.org/10.1016/S0924-0136(01)00930-X

Żaba, K., & Pasierb, A. (2004). Analiza parametrów procesu ciągnienia rur na korku swobodnym ze stali 1H18N10T pod kątem stanu i własności otrzymanych wyrobów [Analysis of floating-plug drawing process of 1H18N10T steel tubes with consideration of condition and properties of the obtained products]. *Rudy i Metale Nieżelazne*, *48*(10-11), 524–517.

Wpływ Procesu Ciągnienia na Korku Swobodnym na Wykończenie Powierzchni Wewnętrznej i Zewnętrznej Rur Cienkościennych Wykonanych ze Stali Nierdzewnej AISI 321

Streszczenie

W artykule przedstawiono wyniki analizy zmian topografii powierzchni rur cienkościennych ze stali nierdzewnej AISI 321 po procesie ciągnienia na korku swobodnym. Badania eksperymentalne przeprowadzono w jednym przejściu, ze zmienną prędkością ciągnienia (1, 2, 3, 4, 6, and 10 m/min) oraz różnymi kątami β korka swobodnego (11.3°, 13° and 14°). W badaniach eksperymentalnych wykorzystano smar Wisura DSO7010 (Fuchs Oil). Jako wskaźniki jakości powierzchni przyjęto średnie arytmetyczne odchylenie rzędnych profilu Ra oraz wysokość chropowatości według 10 punktów Rz. Parametry chropowatości mierzono niezależnie na wewnętrznej i zewnętrznej powierzchni rur cienkościennych. Do analizy związków pomiędzy parametrami procesu ciągnienia (prędkość ciągnienia i kąt korka swobodnego) wykorzystano analizę wariancji. Zaobserwowano zmniejszenie wartości obydwu analizowanych parametrów chropowatości w wyniku procesu ciągnienia. Proces ciągnienia na korku swobodnym znacznie poprawia jakość wewnętrznej powierzchni cienkościennych rur ze stali nierdzewnej AISI 321. Zaobserwowano tendencję do zwiększania się parametru Ra wraz ze wzrostem prędkości ciągnienia, podczas gdy kąt β korka swobodnego nie miał znaczącego wpływu na średnią chropowatość Ra.

Słowa kluczowe: analiza wariancji, korek swobodny, stal nierdzewna, chropowatość powierzchni, ciągnienie rur

Review

The Impact of Particle Size in Fluidized Bed on Heat Transfer Behavior: A Review

Ahmed Hammood Darweesh * (iD)**, Musa Mustafa Weis** (iD)

Northern Technical University/Technical College of Engineering, 36001 Kirkuk, Iraq; musa.weis@ntu.edu.iq (M. M. Weis)

* Correspondence: ahmed.derweesh87@gmail.com

Abstract

This review paper explores the significance of fluidized bed heat exchangers in various industrial applications. By delving into the operation of fluidized beds as multiphase flow systems, the aim is to enhance their capabilities and efficiency. Key parameters such as minimum fluidization velocity and local gas holdup are crucial for characterizing the hydrodynamic behavior of materials within fluidized beds. Fluidization, achieved by passing atmospheric air through particulate solids, imparts fluid-like properties to the bed. Fluidized beds serve as reactors where this phenomenon takes place, offering several advantages in industrial processes, including high rates of heat and mass transfer, low pressure drops, and uniform temperature distribution. In future work, a focus on understanding and optimizing the fluidization process will contribute to further advancements in the performance of fluidized bed heat exchangers.

Keywords: fluidized bed, heat transfer, heat exchanger, thermal conductivity, siliceous sand, particle size

Nomenclature

c_e	heat capacity for emulsion phase [kJ/kgK]
c_g	heat capacity for gas phase [kJ/kgK]
c_s	specific heat capacity for solid phase [kJ/kgK]
d^*	dimensionless particle diameter [-]
d_p	mean bed particle diameter [mm]
d_t	cylinder/tube diameter [mm]
e_b	bed emissivity [-]
e_p	particle emissivity [-]
g	acceleration due to gravity [m^2/s]
k_e	emulsion thermal conductivity [W/m°C]
k_g	thermal conductivity of gas phase [W/mK]
k_s	thermal conductivity of solid phase [W/m°C]
ε_e	voidage of emulsion phase [-]
ε_{mf}	voidage of main fluid [-]
φ_b	bed porosity [-]
ρ_e	density of emulsion phase [kg/m^3]
ρ_s	density of solid phase [kg/m^3]

1. Introduction

Fluidized bed heat exchangers play a crucial role in numerous industrial applications. Enhancing our understanding of the operations of a fluidized bed as a multiphase flow system can significantly improve its capabilities and overall efficiency. The minimum fluidization velocity and local gas holdup are key parameters used to characterize the hydrodynamic behavior of materials within the fluidized bed. Fluidization, defined as the process of conferring fluid-like properties to a bed of particulate solids

by passing atmospheric air through the material, is a fundamental phenomenon. Fluidized beds function as reactors where the fluidization of particulate solids occurs, serving as essential assets in various industrial processes. These beds offer several advantages, including high rates of heat and mass transfer, low pressure drops, and uniform temperature distribution (Rasouli et al., 2005). Hou et al. (2016) research investigates the impact of material properties and tube array settings on gas-solid flow and heat transfer in fluidized beds with tubes, using a combination of computational fluid dynamics (CFD), discrete element method (DEM), and heat transfer models. The study revealed significant differences in gas-solid flow between cohesive and non-cohesive powders, emphasizing the dominance of conductive heat transfer for small cohesive particles and convective heat transfer for large non-cohesive particles. The research also explored the complex effects of material properties and gas velocity on the uniformity of particle velocity and temperature fields. Additionally, the study examined the influence of tube array settings, uncovering intricate gas-solid flow and heat transfer characteristics. The findings aim to provide insights for optimizing the operation and design of fluidized systems with tubes.

In response to these challenges, there is a growing interest in the adsorption process utilizing solid sorbents as an alternative to the energy-intensive aqueous amine scrubbing technologies (Samanta et al., 2012). A continuous temperature swing adsorption process (Pröll et al., 2016; Schöny et al., 2016) for CO_2 separation emerges as a promising alternative. Gas-solid fluidized bed reactors, known for their excellent mixing properties, create practically isothermal conditions, ensuring high rates of heat and mass transfer between gas and solids. Their suitability for large-scale plants, efficient heat transfer rates between immersed objects and the fluidized bed, and the capability for continuous, automatically controlled operation make them an attractive option (Kunii & Levenspiel, 1991).

Moreover, the unique characteristics of gas-solid fluidized bed reactors, including a liquid-like solids flow, enable their versatile application in various physical and chemical processes such as combustion (Cui et al., 2020), gasification (Arena, 2013; Blaszczuk et al., 2018), heat recovery (Cai et al., 2019; Li et al., 2020), coating (Sjösten et al., 2004; Foroughi-Dahr et al., 2017), drying (Das et al., 2020), and temperature swing adsorption (Wormsbecker et al., 2009). Extensive studies continue to be conducted on gas-solid fluidized bed reactors to enhance our understanding of their operation (Wormsbecker et al., 2009) and applications (Dietrich et al., 2018; Zerobin & Pröll, 2020).

Kim et al. (2003) conducted a study on heat transfer and bubble characteristics within a fluidized bed featuring an immersed horizontal tube bundle. Their findings demonstrated that the average heat transfer coefficient exhibits an initial increase with ascending gas velocity, reaching a peak value before subsequently decreasing. In a related investigation, Al-Busoul and Abu-Ein (2003) explored the heat transfer characteristics around a horizontally heated tube immersed in a fluidized bed. Their results indicated an inverse proportionality between the local heat transfer coefficient and the solid particle diameter within the range of 108–856 μm.

Chen and Pei (1985) proposed a heat transfer model for the interaction between fluidized beds and immersed surfaces. The model, developed on the basis of the two-phase boundary layer and surface renewal theory, yielded a correlation for predicting the maximum heat transfer coefficient.

Devaru and Kolar (1995) reported that the performance of a tube bundle in a fluidized bed heat exchanger is contingent upon various factors. These factors include fluidization parameters such as fluidizing gas velocity, bed particle diameter, and static bed height; bundle characteristics like tube orientation, size, pitch, and location; and tube surface characteristics encompassing smooth or finned surfaces, fin height, fin pitch, fin thickness, material, and fin type.

Nag and Moral (1990) delved into the impact of rectangular fins on heat transfer within circulating fluidized beds. Their findings indicated that the utilization of fins led to a decrease in the heat transfer coefficient. Subsequently, Nag et al. (1995) formulated a mathematical model to predict heat transfer from finned surfaces in a circulating fluidized bed. Their summarization of results revealed several key trends: an augmentation in suspension density correlated with an increase in bed-to-wall heat transfer, the incorporation of fins resulted in a decrease in the heat transfer coefficient, and an escalation in the number of fins was associated with a reduction in the heat transfer coefficient.

2. Experimental procedures

The experimental setup includes a range of apparatuses essential for studying the impact of sand particle size on a fluidized bed heat exchanger. These comprise the fluidized bed heat exchanger itself, sand particles with varying sizes, temperature sensors, pressure gauges, flow meters, and the heat transfer fluid.

The experimental procedure used by Rasouli et al. (2005) involves several key steps to ensure a systematic and reliable study. Firstly, the fluidized bed is prepared by filling it with sand particles of the chosen size. Subsequently, the system is initialized, stabilizing it with the heat transfer fluid at a specified temperature and flow rate. Data collection is then initiated, systematically varying the particle size during the experiment. To ensure consistency, experiments are repeated for each particle size. The literature data available in Table 1. Safety measures are implemented throughout the experiment, and thorough documentation of all relevant parameters and observations is conducted.

Continuous monitoring of temperature, pressure, and flow rate is crucial throughout each experiment to gather comprehensive data. Post-experiment, data analysis is performed using appropriate software tools such as Excel. Regular calibration of instruments is emphasized to maintain the accuracy and reliability of the collected data.

It is important to note that this methodology and experimental setup can be tailored based on specific requirements and available resources. Ethical considerations and adherence to safety protocols remain paramount throughout the experimental process as shown in Fig. 1.
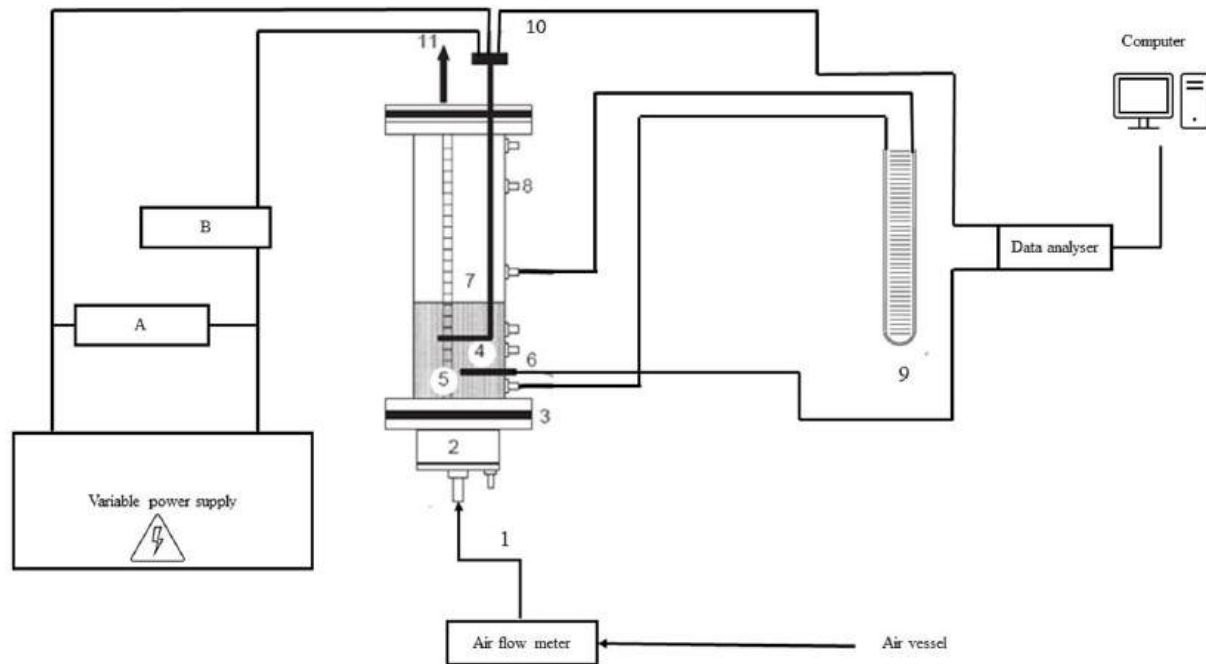
Fig. 1. Schematic diagram of the experimental set-up: (1) air inlet, (2) air distribution chamber, (3) distributor plate, (4) horizontal tube, (5) scaling for bed height measurement, (6) thermocouple for bed temperature, (7) hollow tube, (8) pressure taps, (9) pressure difference measurement device, (10) test probe thermocouple and (11) exhaust air openings, prepared on the basis of (Rasouli et al., 2005).

Table 1. Experimental conditions.

Equipment type	Particle diameter, mm	Reference
vertical	136	Ozkaynak and Chen (1980)
horizontal	256, 340, 568	Pence et al. (1994)
horizontal	240	Kim et al. (2003)
horizontal	219, 232, 246, 365, 444	Blaszczuk et al. (2018)
vertical	120, 320, 650	Baskakov et al. (1973)

Blaszczuk and Jagodzik (2021) scrutinized the energy exchange process between a dense fluidized bed and a submerged horizontal tube bundle within a commercial external heat exchanger (EHE). Conducting eight performance tests in a fluidized bed heat exchange chamber with specific dimensions, the authors developed a mechanistic model to predict the average heat transfer coefficient. This model factors in the geometric structure of the tube bundle and the location of the heat transfer surface, revealing that superficial gas velocity and suspension density significantly impact the average heat transfer coefficient, with bed particle size playing a comparatively minor role. Empirical correlations were proposed to predict heat transfer data due to the insufficiency of existing literature data for industrial fluidized bed heat exchangers, the details in Table 2. The research identified optimal conditions for heat transfer based on evaluated operating conditions, and the developed mechanistic heat transfer model was validated against experimental data obtained in the study.

Table 2. The correlations used to determine physical properties of emulsion.

Item	Equation	Reference
Emulsion heat capacity, c_e	$c_e = c_s(1 - \varepsilon_e) + \varepsilon_e c_g$	Yusuf et al. (2005)
Emulsion thermal conductivity, k_e	$k_e = \varepsilon_e k_g + (1 - \varepsilon_e)k_s \left[\dfrac{1}{\varphi_b \left(\dfrac{k_s}{k_g} \right) + \dfrac{2}{3}} \right]$	Kunii and Levenspiel (1991)
Emulsion (packet) density, ρ_e	$\rho_e = \rho_s(1 - \varepsilon_e)$	Ozkaynak and Chen (1980)
Voidage of emulsion phase, ε_e	$\varepsilon_e = 1 - \dfrac{(1 - \varepsilon_{mf})\left[0.7293 + 0.5139 \dfrac{dp}{dt} \right]}{1 + \dfrac{dp}{dt}}$	Saxena (1989)

Andersson's (1996) study involved measuring local heat transfer values to membrane walls in a circulating fluidized bed (CFB) boiler, utilizing silica sand of three different sizes with mean diameters of 0.22, 0.34, and 0.44 mm. Altering the sand size from 0.44 to 0.22 mm under constant fluidization velocity resulted in a substantial increase in particle concentration and, consequently, enhanced heat transfer. Despite variations in bed particle size, the average heat transfer coefficient across the membrane wall remained insensitive at a given cross-sectional average bulk density. The lateral distribution of heat flow to the crest, side of the tube, and fin was found to be independent of particle size under similar bulk densities, achieved by maintaining a constant ratio of fluidization velocity to the terminal velocity of a single average size particle. The study demonstrated the feasibility of estimating the vertical distribution of the heat transfer coefficient in the CFB furnace with an accuracy of +20% using a straightforward semi-empirical method. Papadikis et al. (2010) research was focused on modeling the fluid-particle interaction and examining the influence of varying heat transfer conditions on biomass pyrolysis within a 150 g/h fluidized bed reactor. Two distinct biomass particle sizes (350 μm and 550 μm in diameter) are introduced into the fluidized bed, leading to different heat transfer conditions. The 350 μm particle, smaller than the sand particles in the reactor (440 μm), experiences conductive heat transfer, while biomass-sand contacts for the larger 550 μm particle are deemed significant. The study utilizes the Eulerian approach to model the sand's bubbling behavior as a continuum. Biomass reaction kinetics are represented by a two-stage, semi-global model accounting for secondary reactions. Particle motion within the reactor is computed using drag laws dependent on the local volume fraction of each phase. The simulations employ FLUENT 6.2 as the modeling framework, with the entire pyrolysis model integrated as a User Defined Function (UDF). Ngoh and Lim (2016) investigated the fluidization and heat transfer behaviors in a bubbling fluidized bed using Computational Fluid Dynamics (CFD). Their simulations explored various operating conditions with different particle sizes and inlet gas superficial velocities. Analysis of solid volume fraction, solid temperature, air temperature, solid velocity vectors, and air velocity vectors revealed symmetrical and non-uniform solid volume fraction profiles during the initial phase of fluidization. Bubbles generated in this phase increased with higher inlet air superficial velocities and smaller particle sizes. The coupled analysis of solid volume fraction and temperature profiles highlighted the significance of both conductive and convective heat transfer between phases. The results indicated that the heat transfer rate from air to particles depended on interfacial surface area, influenced by voidage within the bed. Optimal operating conditions for efficient heat transfer were suggested, while over-fluidization led to poor heat transfer due to channeling, and under-fluidization resulted in suboptimal convective heat transfer compensated by increased conductive particle-to-particle heat transfer. In experimental study by Błaszczuk et al. (2018), a supercritical circulating fluidized bed combustor was employed to investigate the impact of bed particle size on the bed-to-wall heat transfer coefficient. The bed comprised particles with Sauter mean diameters of 0.219, 0.246, and 0.411 mm. Operating parameters, such as superficial gas velocity, circulation rate of solids, secondary air fraction, and pressure drop, were varied within the ranges of 3.13 to 5.11 m/s, 23.7 to 26.2 kg/m²s, 0.33, and 7500 to 8440 Pa, respectively. Experimental variables included bed temperature, suspension density, and parameters of the cluster renewal approach along the furnace height. The study utilized the cluster renewal approach to predict the bed-to-wall heat transfer coefficient, and a simple semi-empirical method was introduced to estimate the overall heat transfer coefficient based on particle size and suspension density. Computational results were compared with experimental data, providing valuable insights.

3. Heat transfer characteristics

Berkache et al. (2022) investigated the behavior of a boundary layer type viscous flow with thermal effects. The study involves experimental and numerical analyses of the flow in a three-dimensional field with uniform infinite velocity, focusing on an adiabatic wall with heat input. The experiments took place in the Thermal Laboratory (LET) of the Prime Institute of Poitiers in France. The experimental work utilized a wind tunnel to create a turbulent boundary layer on the surface of a flat plate covered with epoxy resin. The flat plate was heated to 80°C using an HP 6012A power supply system that provided circulating heat flux through the Joule effect.

The numerical results highlight a distinct variation in the evolution of the thermal boundary layer at three different wall temperatures. This suggests that temperature plays a significant role in influencing the behavior of the boundary layer in viscous flow. The findings contribute to a better understanding of the thermal effects on turbulent boundary layers in three-dimensional fields, providing valuable insights for related applications or further research in fluid dynamics.

The study conducted by Qader et al. (2023) investigated forced convection heat transfer in a horizontally heated circular pipe with constant heat flux. The researchers created a porous medium within the pipe using stainless-steel balls of 1 and 3 mm diameters, resulting in porosities of 0.3690 and 0.3912, respectively. The Reynolds numbers ranged from 3,200 to 6,500 based on the pipe diameter, and the heat flux rates were set at 6,250 and 12,500 W m^{-2}. The simulation was performed using ANSYS Fluent on a stainless-steel pipe with a diameter of 51.4 mm, thickness of 5 mm, and length of 304 mm. The results indicated an increase in turbulence and the formation of eddies within the system. The analysis revealed higher convective heat transfer coefficients, pressure drops, and Nusselt numbers with an increase in Reynolds number. Additionally, the Nusselt number increased with the diameter of the stainless-steel balls (1–3 mm). An increase in porosity by 6% led to an 84.4% reduction in pressure drop. The Nusselt number increased by 46.7% (Reynolds 3,200–6,500) and 4.36% (heat flux 6,250^{-12}, 500 W m^{-2}). These findings provide insights into the impact of porous media and various parameters on heat transfer characteristics in horizontally heated pipes. Miri et al. (2023) focused on the magnetohydrodynamic laminar forced convection of nanoliquid within a rectangular channel featuring an extended surface, a moving top wall, and three cylindrical blocks. The study utilized the Lattice Boltzmann method to numerically analyze the governing equations. The researchers validated their numerical code using published results, demonstrating good agreement.

The investigation explores the effects of several parameters, including Reynolds number ($50 \leq Re \leq 200$), Hartmann number ($0 \leq Ha \leq 50$), nanoparticles volume fraction ($0 \leq \varphi \leq 4\%$), and Eckert number ($0.25 \leq Ec \leq 1$). The numerical solution reveals that both local and average Nusselt numbers improve with increasing Reynolds number, Eckert number, and nanoparticles volume fraction. However, the Nusselt numbers decrease as the Hartmann number is increased. Notably, the study finds that viscous dissipation has a more pronounced impact on heat transfer rate and entropy generation in the presence of a magnetic field.

An interesting observation is that the addition of 4% nanoparticles enhances the local Nusselt number by approximately 7%. These findings contribute valuable insights into the complex interplay of various parameters in the magnetohydrodynamic forced convection of nanoliquids, offering potential applications in optimizing heat transfer processes. Mohammed et al. (2023) focused on the utilization of flat-plate solar collectors (FPSCs), considered as effective and environmentally friendly heating systems. FPSCs are commonly employed to convert solar radiation into usable heat for various thermal applications. The study emphasizes the use of nano-fluids in FPSCs as a beneficial technique to enhance their performance.

Nano-fluids, defined as colloidal suspensions containing nano-sized particles with diameters smaller than 100 nm, are explored for their potential to improve the thermo-physical features of FPSCs. These nanoparticles contribute to enhancing the thermal conductivity and convective heat transfer of liquids when mixed with the base fluid.

The article provides a comprehensive review of scientific advancements in the field of nano-fluids applied to flat-plate solar collectors. Previous research is discussed, highlighting successful applications of nano-fluids to enhance the efficiency of FPSCs. However, the study acknowledges that nano-fluids may have higher pressure drops compared to conventional liquids, and their pressure drops, along with pumping power, increase as the volume flow rate rises. Key aspects covered in the article include the concept of nano-fluids, various forms of nanoparticles, methods for preparing nano-fluids, and their thermo-physical properties. The conclusion offers observations and suggestions regarding the usage of nano-fluids in flat-plate solar collectors. Overall, the article serves as a valuable summary of research

studies in this area, providing insights that may prove beneficial for future experimental studies in the field of improving solar collector efficiency using nano-fluids.

Mu et al. (2020) conducted a numerical simulation study to investigate the combined thermal behavior and hydrodynamics of a pseudo-2D fluidized bed using computational fluid dynamics–discrete element method (CFD-DEM). The simulation incorporated a constant heat source to mimic the effects of heterogeneous exothermic reactions. The research analyzed the impacts of superficial gas velocity, bed height, and heat source distribution by examining averaged volume fraction, temperature distributions, and velocity profiles. The findings highlighted significant influences of both gas superficial velocity and bed aspect ratio on fluidization behavior and temperature distributions.

Park et al. (2020) investigated the thermal performance of a directly-irradiated fluidized bed gas heater for solar thermal heating. Focusing on the impact of SiC particle size on heat transfer characteristics, experiments were conducted in a 50 mm-ID by 100 mm high solar fluidized bed gas heater. The outlet gas temperatures exhibited a maximum value with increasing gas velocity, influenced by particle motion due to bubble behavior. Heat absorption from the receiver increased with gas velocity, reaching maximum values of 18 W for fine SiC and 23 W for coarse SiC. The thermal efficiency of the receiver improved with higher gas velocity but was affected by the content of finer particles. The maximum thermal efficiency was 14% for fine SiC and 20% for coarse SiC within the experimental range. Design considerations were proposed for enhancing the system's thermal efficiency.

4. Conclusions

In conclusion, the collection of research articles discussed here presents a comprehensive exploration of heat transfer characteristics in fluidized beds, particularly emphasizing the influence of bed particle size on heat transfer coefficients. Silica sand, recognized for its favorable fluidizing properties, plays a crucial role in fluidized bed systems. The study emphasizes that the overall heat transfer coefficient exhibits an upward trend with increasing velocity. Conversely, larger particle sizes demonstrate a decrease in the heat transfer coefficient. Furthermore, the impact of varying particle sizes on pressure drop reveals a significant correlation: as particle size increases, the pressure drop also increases. Notably, smaller particle sizes result in lower pressure drop values, leading to enhanced particle collection in the fluidized bed compared to larger particles. These findings underscore the intricate relationship between particle size, heat transfer, and pressure drop in fluidized beds, offering valuable insights for optimizing the performance of fluidized bed heat exchangers. Future work may involve refining fluidization processes and exploring particle size distributions to further enhance the efficiency of fluidized bed systems.

References

Al-Busoul, M., & Abu-Ein, S. (2003). Local heat transfer coefficients around a horizontal heated tube immersed in a gas fluidized bed. *Heat and Mass Transfer Journal*, *39*, 355–358. https://doi.org/10.1007/s00231-002-0330-y

Andersson, B. Å. (1996). Effects of bed particle size on heat transfer in circulating fluidized bed boilers. *Powder Technology*, *87*(3), 239–248. https://doi.org/10.1016/0032-5910(96)03092-6

Arena, U. (2013). 17 - Fluidized bed gasification. In F. Scala (Ed.). *Fluidized bed gasification. fluidized bed technologies for near-zero emission combustion and gasification* (pp. 765–812). Woodhead Publishing Limited.

Baskakov, P., Berg, B. V., Vitt, O. K., Filippovsky, N. F., Kirakosyan, V. A., Goldobin, J. M., & Maskaev, V. K. (1973). Heat transfer to objects immersed in fluidized beds. *Powder Technology*, *8*(5–6), 273–282. https://doi.org/10.1016/0032-5910(73)80092-0

Berkache, A., Amroune, S., Golbaf, A., & Mohamad, B. (2022). Experimental and numerical investigations of a turbulent boundary layer under variable temperature gradients. *Journal of the Serbian Society for Computational Mechanics, 16*(1), 1–15. https://doi.org/10.24874/jsscm.2022.16.01.01

Blaszczuk, A., & Jagodzik, S. (2021). Investigation of heat transfer in a large-scale external heat exchanger with horizontal smooth tube bundle. *Energies*, *14*(17), Article 5553. https://doi.org/10.3390/en14175553

Blaszczuk, A., Pogorzelec, M., & Shimizu, T. (2018). Heat transfer characteristics in a large-scale bubbling fluidized bed with immersed horizontal tube bundles. *Energy*, *162*, 10−19. https://doi.org/10.1016/j.energy.2018.08.008

Cai, R., Zhang, M., Ge, R., Zhang, X., Cai, J., Zhang, Y., Huang, Y., Yang, H., & Lyu, J. (2019). Experimental study on local heat transfer and hydrodynamics with single tube and tube bundles in an external heat exchanger. *Applied Thermal Engineering*, *149*, 924−938. https://doi.org/10.1016/j.applthermaleng.2018.12.040

Chen, P., & Pei, D. C. T. (1985). A model of heat transfer between fluidized beds and immersed surfaces. *International Journal of Heat and Mass Transfer*, 28(3), 675–682. https://doi.org/10.1016/0017-9310(85)90189-9

Cui, Y., Liu, X., & Zhong, W. (2020). Simulations of coal combustion in a pressurized supercritical CO_2 circulating fluidized bed. *Energy & Fuels*, 34(4), 4977−4992. https://doi.org/10.1021/acs.energyfuels.0c00418

Das, H. J., Mahanta, P., Saikia, R., & Aamir, M. S. (2020). Performance evaluation of drying characteristics in conical bubbling fluidized bed dryer. *Powder Technology*, 374, 534−543. https://doi.org/10.1016/j.powtec.2020.06.051

Devaru, C. B., & Kolar, A. K. (1995, May 7-10). *Heat transfer from a horizontal finned tube bundle in bubbling fluidized beds of small and large particles*. Proceedings of the 13th International Conference on Fluidized-Bed Combustion, Orlando, FL, USA.

Dietrich, F., Schöny, G., Fuchs, J., & Hofbauer, H. (2018). Experimental study of the adsorber performance in a multi-stage fluidized bed system for continuous CO_2 capture by means of temperature swing adsorption. *Fuel Processing Technology*, 173, 103−111. https://doi.org/10.1016/j.fuproc.2018.01.013

Foroughi-Dahr, M., Mostoufi, N., Sotudeh-Gharebagh, R., & Chaouki, J. (2017). Particle coating in fluidized beds. In *Reference Module in Chemistry, Molecular Sciences and Chemical Engineering*. Elsevier. https://doi.org/10.1016/B978-0-12-409547-2.12206-1

Hou, Q. F., Zhou, Z. Y., & Yu, A. B. (2016). Gas–solid flow and heat transfer in fluidized beds with tubes: Effects of material properties and tube array settings. *Powder Technology*, 296, 59−71. https://doi.org/10.1016/j.powtec.2015.03.028

Kim, S. W., Ahn, J. Y., Kim, S. D., & Lee, D. H. (2003). Heat transfer and bubble characteristics in a fluidized bed with immersed horizontal tube bundle. *International Journal of Heat and Mass Transfer*, 46(3), 399–409. https://doi.org/10.1016/S0017-9310(02)00296-X

Kunii, D., & Levenspiel, O. (1991). *Fluidization engineering* (2nd ed.). Butterworth-Heinemann. https://doi.org/10.1016/C2009-0-24190-0

Li, D., Cai, R., Zhang, M., Yang, H., Choi, K., Ahn, S., & Jeon, C. H. (2020). Operation characteristics of a bubbling fluidized bed heat exchanger with internal solid circulation for a 550-MWe ultrasupercritical CFB boiler. *Energy*, 192, Article 116503. https://doi.org/10.1016/j.energy.2019.116503

Miri, R., Mliki, B., Mohamad, B. A., Abbassi, M. A., Oreijah, M., Guedri, K., & Abderafi, S. (2023). Entropy generation and heat transfer rate for MHD forced convection of nanoliquid in the presence of the viscous dissipation term. *CFD Letters, 15*(12), 77–106. https://doi.org/10.37934/cfdl.15.12.77106

Mohammed, F. Z., Hussein, A. M., Danook, S. H., & Mohamad, B. (2023). Characterization of a flat plate solar water heating system using different nano-fluids. *AIP Conference Proceedings, 2901*(1), Article 100018. https://doi.org/10.1063/5.0178901

Mu, L., Buist, K. A., Kuipers, J. A. M., & Deen, N. G. (2020). Hydrodynamic and heat transfer study of a fluidized bed by discrete particle simulations. *Processes*, 8(4), Article 463. https://doi.org/10.3390/pr8040463

Nag, P. K., Ali, M. N., Basu, P. (1995). A mathematical model for the prediction of heat transfer from finned surfaces in a circulating fluidized bed. *International Journal of Heat and Mass Transfer*, 38(9), 1675–1681. https://doi.org/10.1016/0017-9310(94)00284-3

Nag, P. K., & Moral, M. (1990). The influence of rectangular fins on heat transfer in circulating fluidized bed boilers. *Journal of the Institute of Energy*, 143–147.

Ngoh, J., & Lim, E. W. C. (2016). Effects of particle size and bubbling behavior on heat transfer in gas fluidized beds. *Applied Thermal Engineering*, 105, 225–242. https://doi.org/10.1016/j.applthermaleng.2016.05.165

Ozkaynak, T. F., & Chen, J. C. (1980). Emulsion phase residence time and its use in heat transfer models in fluidized beds. *AIChE Journal*, 26(4), 544–550. https://doi.org/10.1002/aic.690260404

Papadikis, K., Gu, S., & Bridgwater, A. V. (2010). Computational modelling of the impact of particle size to the heat transfer coefficient between biomass particles and a fluidised bed. *Fuel Processing Technology*, 91(1), 68–79. https://doi.org/10.1016/j.fuproc.2009.08.016

Park, S. H., Yeo, C. E., Lee, M. J., & Kim, S. W. (2020). Effect of bed particle size on thermal performance of a directly-irradiated fluidized bed gas heater. *Processes*, 8(8), Article 967. https://doi.org/10.3390/pr8080967

Pence, D. V., Beasley, D. E., & Figliola, R. S. (1994). Heat transfer and surface renewal dynamics in gas-fluidized beds. *ASME Journal of Heat and Mass Transfer*, 116(4), 929–937. https://doi.org/10.1115/1.2911468

Pröll, T., Schöny, G., Sprachmann, G., & Hofbauer, H. (2016). Introduction and evaluation of a double loop staged fluidized bed system for post-combustion CO_2 capture using solid sorbents in a continuous temperature swing adsorption process. *Chemical Engineering Science*, 141, 166−174. https://doi.org/10.1016/j.ces.2015.11.005

Qader, F. F., Mohamad, B., Hussein, A. M., & Danook, S. H. (2023). Numerical study of heat transfer in a circular pipe filled with porous medium. *Pollack Periodica*. Online first: https://doi.org/10.1556/606.2023.00869

Rasouli, S., Golriz, M. R., & Hamidi, A. A. (2005). Effect of annular fins on heat transfer of horizontal immersed tube in bubbling fluidized beds. *Powder Technology*, 154(1), 9–13. https://doi.org/10.1016/j.powtec.2005.02.008

Samanta, A., Zhao, A., Shimizu, G. K. H., Sarkar, P., & Gupta, R. (2012). Post-combustion CO_2 capture using solid sorbents: A review. *Industrial & Engineering Chemistry Research*, 51(4), 1438−1463. https://doi.org/10.1021/ie200686q

Saxena, S. C. (1989). Heat transfer between immersed surfaces and gas-fluidized beds. *Advances in Heat Transfer*, *19*, 97–190. https://doi.org/10.1016/S0065-2717(08)70212-0

Schöny, G., Zehetner, E., Fuchs, J., Pröll, T., Sprachmann, G., & Hofbauer, H. (2016). Design of a bench scale unit for continuous CO_2 capture via temperature swing adsorption—Fluid-dynamic feasibility study. *Chemical Engineering Research and Design*, *106*, 155−167. https://doi.org/10.1016/j.cherd.2015.12.018

Sjösten, J., Golriz, M. R., Nordin, A., & Grace, J. R. (2004). Effect of particle coating on fluidized-bed heat transfer. *Industrial & Engineering Chemistry Research*, *43*(18), 5763−5769. https://doi.org/10.1021/ie034317u

Wormsbecker, M., Pugsley, T., & Tanfara, H. (2009). Interpretation of the hydrodynamic behaviour in a conical fluidized bed dryer. *Chemical Engineering Science*, *64*(8), 1739−1746. https://doi.org/10.1016/j.ces.2008.11.025

Yusuf, R., Melaaen, M. C., & Mathiesen, V. (2005). Convective heat and mass transfer modeling in gas-fluidized beds. *Chemical Engineering Technol*ogy, *28*(1), 13–24. https://doi.org/10.1002/ceat.200407014

Zerobin, F., & Pröll, T. (2020). Concentrated carbon dioxide (CO_2) from diluted sources through continuous temperature swing adsorption (TSA). *Industrial & Engineering Chemistry Research*, *59*(19), 9207−9214. https://doi.org/10.1021/acs.iecr.9b06177

Wpływ Wielkości Cząstek w Złożu Fluidalnym na Przenoszenia Ciepła: Przegląd

Streszczenie

W artykule przedstawiono przegląd literatury dotyczący znaczenia wymienników ciepła ze złożem fluidalnym w różnych zastosowaniach przemysłowych. Zwiększenie możliwości i wydajności złóż fluidalnych jest celem badań tych wielofazowych systemów przepływowych. Kluczowe parametry, takie jak minimalna prędkość fluidyzacji i lokalne zatrzymywanie gazu, mają kluczowe znaczenie dla scharakteryzowania zachowania hydrodynamicznego materiałów w złożach fluidalnych. Fluidyzacja, osiągnięta poprzez przepuszczanie powietrza atmosferycznego przez cząstki stałe, nadaje złożu właściwości zbliżone do płynu. Złoża fluidalne służą jako reaktory, w których zachodzi zjawisko fluidyzacji, oferując szereg korzyści w procesach przemysłowych, w tym wysokie szybkości wymiany ciepła i masy, niskie spadki ciśnienia i równomierny rozkład temperatury. W przyszłych pracach skupienie się na zrozumieniu i optymalizacji procesu fluidyzacji przyczyni się do dalszego postępu w wydajności wymienników ciepła ze złożem fluidalnym.

Słowa kluczowe: złoże fluidalne, wymiana ciepła, wymiennik ciepła, przewodność cieplna, piasek krzemionkowy, wielkość cząstek

Original Research

Assessment of the Depth of the Plastically Deformed Top Layer in Burnishing Process of Shaft Using a Ceramic Tool

Piotr Paszta [1]* [iD] **, Leszek Chałko [2]** [iD] **, Rafał Kowalik [3]** [iD]

[1] Faculty of Mechanical Engineering and Computer Science, Czestochowa University of Technology, al. Armii Krajowej 21, 42-201 Częstochowa, Poland

[2] Faculty of Mechanical Engineering, Casimir Pulaski Radom University, ul. Stasieckiego 54, 26-600 Radom, Poland; leszek.chalko@uthrad.pl

[3] Institute of Technical Sciences and Aeronautics, The University College of Applied Sciences in Chełm, ul. Pocztowa 54, 22-100 Chełm, Poland; rk16410@nauka.panschelm.edu.pl

* Correspondence: piotr.paszta@pcz.pl, tel.: +48 34 3250559

Abstract

Burnishing is one of the most effective methods of improving the strength of the surface layer of shafts as a result of strain strengthening of the material. This article presents an analytical approach to determining the the depth of the plastically deformed top layer of shaft based on Belyaev's theory. Contact of two bodies with an asymmetric stress state was assumed. A classic (symmetrical) solution was also considered. The aim of the research was to compare the calculated values of the depth of the plastically deformed top layer determined using these two methods. The calculations considered burnishing of shafts with a diameter of 48 mm made of steel with a yield stress of $R_e = 450$ MPa and $R_e = 900$ MPa. A burnishing tool with a Si_3N_4 ceramic tip was used for burnishing. It was found that in the range of low contact forces, the calculated values of the depth of the plastically deformed top layer using the asymmetric solution and the classical method are similar. It was also found that the relationship between the depth of the plastically deformed top layer and the contact force can be explained by a power equation with an accuracy of $R^2 > 0.999$.

Keywords: burnishing, plastically deformed layer, Belyaev's theory, shafts

1. Introduction

Burnishing involves applying pressure to the surface of the workpiece with a smooth and hard burnishing element (Zaleski, 2018). Burnishing using mechanical methods uses the pressure of a tool (pressure burnishing) or the kinetic energy of the tool or free particles (impact burnishing) (Czechowski and Kalisz, 2015; Skoczylas & Zaleski, 2022). This process is characterized by high efficiency in smoothing the surface of the workpiece and processing without the need to cool the burnished zone (Dobrzyński et al., 2019; Przybylski, 2016). Burnishing treatment is a technologically and economically effective method of producing the surface layers of machine parts (Kaldunski et al, 2019). In some cases, burnishing can replace the need for heat treatment of large elements (Kułakowska et al., 2014). Smooth burnishing is used to reduce the average surface roughness to approximately Ra = 0.05–0.10 µm (Czechowski & Toboła, 2017). The strengthening treatment is intended to ensure the required properties of the surface layer. Surface burnishing can produce a specific texture (up to a depth of several millimetres) and introduce compressive stresses up to approximately – 1200 MPa (Przybylski, 1987). The beneficial effects of burnishing treatment include: increasing the hardness of the material, improving fatigue life, increasing resistance to abrasion and surface corrosion (Sachin et al., 2021; Zaleski & Skoczylas, 2019). Burnishing can be used to process internal and external surfaces, e.g. holes, cylinders, cones, shafts, as well as flat surfaces (Chodor & Kukielka, 2014; Dyl, 2011). Some burnishing methods can be used to create lubricating microgrooves on the mating

surfaces of bearing journals and bearing sleeves in order to increase the wear resistance of the mating elements (Patyk et al., 2017).

An analysis of contemporary work related to burnishing process shows that this technology is constantly being developed. Patyk et al. (2017) investigated the influence of burnishing depth on the surface roughness of shafts made of C45 steel. It was found that there is a burnishing depth value beyond which the surface roughness parameters will begin to increase, which is associated with the formation of flashes on the surface or the occurrence of local damage to the surface layer in the so-called Belyaev's points. Studies on burnishing of C45 steel shafts have shown that the greatest strengthening effect can be obtained after burnishing and subsequent hardening (Dyl, 2010). The opportunity of using SiC ceramic as a burnishing tool was investigated by Gałda and Pająk (2022). Dzierwa et al. (2020) analysed the effect of slide burnishing process on friction and wear of steel elements. The results of experiments proved the beneficial effect of the slide burnishing process on the reduction of volumetric wear.

In the exploitation of machines and devices, the issue of contact between two bodies occurs both when the tool comes into contact with the workpiece and when two cooperating parts come into contact. In both cases, surface pressures occur, which influence the value of elastic and plastic deformations. To determine the depth of the plastically deformed top layer in the process of surface burnishing with a ceramic tool, the description of the state of elastic stresses in contact between two bodies according to the Huber's hypothesis (Huber, 1904) can be used. Jezierski and Mazur (2002) developed the model of plasticised zone in the surface burnishing process based on the Huber's hypothesis of plastic deformation. Determining the depth of a plastically deformed layer using analytical methods is difficult. This article presents an analytical model for determining the depth of the plastically deformed top layer in the burnishing process.

2. Analytical analysis

2.1. Assumptions

The analysis of the burnishing process, the aim of which was to determine the thickness of the plastically deformed layer, was carried out using a Nklh2525 ball burnisher with a hydraulic presser (Fig. 1). The burnishing element was a bearing ball made of Si_3N_4 technical ceramics with a diameter of 6.25 mm. Ceramics as a tool material is used in machine technology in both machining and sliding burnishing. Steel shafts with the following material yield strengths of $R_e = 450$ MPa and $R_e = 900$ MPa were burnished. The hardness of the shaft material was 23 and 56 HRC. The diameter of the shafts was 48 mm. In all analyses, the tool pressure force was 200 N.
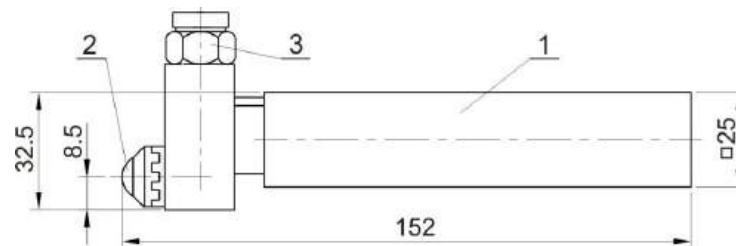
Fig. 1. The Nklh2525 ball burnisher with hydraulic presser: 1 – shank, 2 – ceramic ball, 3 – oil supply (Przybylski, 2004).

2.2. State of stress in contact between two bodies

The general formulas for describing the state of elastic stresses in contact between two bodies (Fig. 2) along the line of action of the contact force according to Belyaev's theory have the form (1)-(3) (Belyaev, 1957).
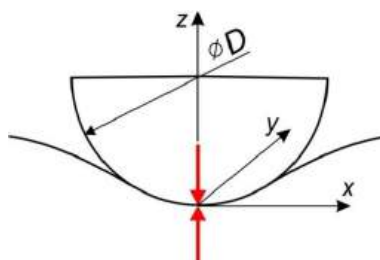
Fig. 2. Contact between two bodies in the x, y, z coordinate system.

$$\sigma_x = \frac{3F}{4\pi}2z(1-v)\int_{z^2}^{\infty}\frac{ds}{(a^2+s)\sqrt{s(a^2+s)(b^2+s)}} - \frac{3F}{4\pi}2zv\int_{z^2}^{\infty}\frac{ds}{s\sqrt{s(a^2+s)(b^2+s)}}$$
$$- \frac{3F}{4\pi}(1-2v)\int_{z^2}^{\infty}\frac{ds}{(a^2+s)\sqrt{(a^2+s)(b^2+s)}} \tag{1}$$

$$\sigma_y = \frac{3F}{4\pi}2z(1-v)\int_{z^2}^{\infty}\frac{ds}{(b^2+s)\sqrt{s(a^2+s)(b^2+s)}} - \frac{3F}{4\pi}2zv\int_{z^2}^{\infty}\frac{ds}{s\sqrt{s(a^2+s)(b^2+s)}}$$
$$+ \frac{3F}{4\pi}(1-2v)\int_{z^2}^{\infty}\frac{ds}{(b^2+s)\sqrt{(a^2+s)(b^2+s)}} \tag{2}$$

$$\sigma_z = \frac{3F}{2\pi}\frac{1}{\sqrt{(a^2+z^2)(b^2+z^2)}} \tag{3}$$

where F is feed force of the tool to the workpiece; s is contact surface area of the tool and the workpiece; a and b are the minor and major semi-axis of the contact ellipse of the tool and the workpiece along the x and y axes, respectively; v is Poisson's ratio; z is coordinate determining the depth of occurrence elastic stresses σ_x, σ_y and σ_z on the line of action of the feed force.

After solving the integrals in Eqs. (1) and (2) for $b > a$ (Ryzyk & Gradsztejn, 1964), the relationships (1)-(3) take the form:

$$\sigma_x = \frac{3F}{4\pi}2z(1-v)\left[\frac{2b}{(b^2-a^2)}E(\varphi,k) - \frac{2}{b(b^2-a^2)}F(\varphi,k) - \frac{2z}{a^2}\frac{1}{\sqrt{(b^2+z^2)(a^2+z^2)}}\right]$$
$$+ \frac{3F}{4\pi}2zv\left[\frac{2}{a^2z}\sqrt{\frac{a^2+z^2}{b^2+z^2}} - \frac{2}{a^2b}E(\varphi,k)\right]$$
$$- \frac{3F}{4\pi}(1-2v)\frac{2}{a^2-b^2}\left(1 - \sqrt{\frac{b^2+z^2}{a^2+z^2}}\right) \tag{4}$$

$$\sigma_y = \frac{3F}{4\pi}2z(1-v)\frac{2}{b(b^2-a^2)}[F(\varphi,k) - E(\varphi,k)]$$
$$- \frac{3F}{4\pi}2zv\left[\frac{2}{a^2z}\sqrt{\frac{a^2+z^2}{b^2+z^2}} - \frac{2}{a^2b}E(\varphi,k)\right]$$
$$+ \frac{3F}{4\pi}(1-2v)\frac{2}{b^2-a^2}\left(1 - \sqrt{\frac{a^2+z^2}{b^2+z^2}}\right) \tag{5}$$

$$\sigma_z = -\frac{3F}{2\pi}\frac{1}{\sqrt{(a^2+z^2)(b^2+z^2)}} \tag{6}$$

$$\varphi = arcsin\sqrt{\frac{b^2}{b^2+z^2}} = arcctg\frac{z}{g} \tag{7}$$

$$k = \sqrt{\frac{b^2-a^2}{b^2}} \text{ for } b > a \tag{8}$$

where $E(\varphi, k)$ is an elliptic integral of the second order:

$$E(\varphi, k) = \int_0^{\varphi} \sqrt{1 - k^2 \sin^2 \varphi} \, d\varphi \tag{9}$$

and $F(\varphi, k)$ is an elliptic integral of the first order:

$$F(\varphi, k) = \int_0^{\varphi} \frac{d\varphi}{\sqrt{1 - k^2 \sin^2 \varphi}} \tag{10}$$

To solve the problem of the thickness of the plastically deformed layer, the Huber-Mises-Hencky yield criterion according to Eq. (11) and integral tables (Ryzyk & Gradsztejn, 1964) should be used.

$$\sigma_{red} = \sqrt{\frac{1}{2}(\sigma_x - \sigma_v)^2 + (\sigma_v - \sigma_z)^2 + (\sigma_z - \sigma_x)^2} \tag{11}$$

where σ_{red} is equivalent stress; σ_1, σ_2 and σ_3 are principal stresses.

3.2. Thickness of plastically deformed layer

Based on the work by Mazur (2003), a short description of the theoretical solution for the thickness of a plastically deformed layer in contact between two bodies is presented. In equations (4)–(6) given in the section 3.1, the elliptic functions $E(\varphi, k)$ and $F(\varphi, k)$ can be expanded in series for calculations. Finishing their expansion with the second term, we get:

$$E(\varphi, k) = arcctg \frac{z}{b}\left(1 - \frac{1}{4}k^2 - \frac{3}{64}k^4\right) + \frac{z}{b}\frac{1}{1 + \left(\frac{z}{b}\right)^2}\left[\frac{1}{4}k^2 + \frac{3}{64}k^4 + \frac{1}{32}k^4 \frac{1}{1 + \left(\frac{z}{b}\right)^2}\right] \tag{12}$$

$$F(\varphi, k) = arcctg \frac{z}{b}\left(1 + \frac{1}{4}k^2 + \frac{9}{64}k^4\right) + \frac{z}{b}\frac{1}{1 + \left(\frac{z}{b}\right)^2}\left[\frac{1}{4}k^2 + \frac{9}{64}k^4 + \frac{3}{32}k^4 \frac{1}{1 + \left(\frac{z}{b}\right)^2}\right] \tag{13}$$

By grouping the appropriate expressions in the equations (4)–(6) and also introducing an auxiliary variable $w = \frac{a^2}{b^2} < 1$ and making appropriate transformations, we can obtain the final relationships for the stress components in the elastic zone at the contact of two bodies, which will be used to determine the feed force.

$$\sigma_x = \frac{3F}{\pi}\frac{1}{b^2(1-w)}\left[\frac{z}{b}\left(\frac{1-wv}{w}E(\varphi, k) - (1-v)F(\varphi, k)\right) + \frac{1-2v}{2}\left(1 - \sqrt{\frac{b^2 + z^2}{b^2 w + z^2}}\right)\right.$$
$$\left. - \frac{1-w}{w}\frac{b^2 wv + z^2}{\sqrt{(b^2 w + z^2)(b^2 + z^2)}}\right] \tag{14}$$

$$\sigma_y = \frac{3F}{\pi}\frac{1}{b^2(1-w)}\left[\frac{z}{b}\left(\frac{v-w}{w}E(\varphi, k) + (1-v)F(\varphi, k)\right) - \frac{2v-w}{2w}\sqrt{\frac{b^2 w + z^2}{b^2 + z^2}} - \frac{1-2v}{2}\right] \tag{15}$$

$$\sigma_z = \frac{3F}{\pi}\frac{1}{b^2(1-w)}\left[-\frac{b^2(1-w)}{2}\frac{1}{\sqrt{(b^2 w + z^2)(b^2 + z^2)}}\right] \tag{16}$$

where the functions $E(\varphi, k)$ and $F(\varphi, k)$ modify to the form:

$$E(\varphi,k) = arcctg\frac{z}{b}\left[1 - \frac{1}{4}(1-w) - \frac{3}{64}(1-w)^2\right]$$
$$+ \frac{z}{b}\frac{1}{1+\left(\frac{z}{b}\right)^2}\left[\frac{1}{4}(1-w) + \frac{3}{64}(1-w)^2 + \frac{1}{32}(1-w)^2\frac{1}{1+\left(\frac{z}{b}\right)^2}\right] \tag{17}$$

$$F(\varphi,k) = arcctg\frac{z}{b}\left[1 - \frac{1}{4}(1-w) - \frac{9}{64}(1-w)^2\right]$$
$$- \frac{z}{b}\frac{1}{1+\left(\frac{z}{b}\right)^2}\left[\frac{1}{4}(1-w) + \frac{9}{64}(1-w)^2 + \frac{3}{32}(1-w)^2\frac{1}{1+\left(\frac{z}{b}\right)^2}\right] \tag{18}$$

where $k^2 = 1 - w$.

Using the Huber-Mises-Hencky yield criterion and the derived equations (17) and (18), after transformations, we can obtain the relation (19) taking into account the thickness δ of the plastically deformed layer in a deformable body in contact with a non-deformable body.

$$F = \frac{\sqrt{2}}{3}\pi R_e b^2 (1$$
$$- w)\left\{\left[\left[\frac{\delta}{b}(1-v)\left(\frac{1+w}{w}E(\varphi,k) - 2F(\varphi,k)\right) + 1 - 2v\right.\right.\right.$$
$$- \frac{b^2w(1+w)(1-2v) - 2\delta^2(v(1+w)-1)}{2w\sqrt{(b^2w+\delta^2)(b^2+\delta^2)}}\Bigg]^2$$
$$+ \left[\frac{\delta}{b}\left(\frac{v-w}{w}E(\varphi,k) + (1-v)F(\varphi,k)\right) - \frac{1-2v}{2}\right.$$
$$+ \frac{w(b^2+\delta^2) - 2v(b^2w+\delta^2)}{2w\sqrt{(\delta^2w+\delta^2)(b^2+\delta^2)}}\Bigg]^2$$
$$+ \left[\frac{\delta}{b}\left(\frac{1-wv}{w}E(\varphi,k) - (1-v)F(\varphi,k)\right) + \frac{1-2v}{2}\right.$$
$$\left.\left.\left.+ \frac{b^2w^2(2v-1) + \delta^2(2(wv-1)+w)}{2w\sqrt{(b^2w+\delta^2)(b^2+\delta^2)}}\Bigg]^2\right\}^{-\frac{1}{2}}\right. \tag{19}$$

In turn, Eq. (19) after taking into account the equations (20)–(23)

$$\begin{cases} w = \dfrac{a^2}{b^2} < 1 \\ e = \sqrt{ab} \end{cases} \tag{20}$$

$$b = \frac{e}{\sqrt[4]{w}} \tag{21}$$

$$\frac{\delta}{b} = \frac{\delta}{e}\sqrt[4]{w} \tag{22}$$

$$\left(\frac{\delta}{b}\right) = \left(\frac{\delta}{e}\right)\sqrt{w} \tag{23}$$

we can transform it into Eq. (24) describing the thickness δ of the plastically deformed layer by the contact parameters $F(R_e e^2)^{-1} = f(w, \delta e^{-1})$

$$\frac{F}{R_e e^2} = \frac{\sqrt{2}}{3}\pi\frac{1-w}{\sqrt{w}}\left\{\left[\left[\frac{\delta}{e}\sqrt[4]{w}(1-\nu)\left(\frac{1+w}{w}E(\varphi,k)-2F(\varphi,k)\right)+1-2\nu\right.\right.\right.$$

$$\left.-\frac{w(1+w)(1-2\nu)-2\left(\frac{\delta}{e}\right)^2\sqrt{w}(\nu(1+w)-1)}{2w\sqrt{\left(w+\left(\frac{\delta}{e}\right)^2\sqrt{w}\right)\left(1+\left(\frac{\delta}{e}\right)^2\sqrt{w}\right)}}\right]^2$$

$$+\left[\frac{\delta}{e}\sqrt[4]{w}\left(\frac{\nu-w}{w}E(\varphi,k)+(1-\nu)F(\varphi,k)\right)+\frac{1-2\nu}{2}\right.$$

$$\left.+\frac{w\left(1+\left(\frac{\delta}{e}\right)^2\sqrt{w}\right)-2\nu\left(w+\left(\frac{\delta}{e}\right)^2\sqrt{w}\right)}{2w\sqrt{\left(w+\left(\frac{\delta}{e}\right)^2\sqrt{w}\right)\left(1+\left(\frac{\delta}{e}\right)^2\sqrt{w}\right)}}\right]^2 \tag{24}$$

$$+\left[\frac{\delta}{e}\sqrt[4]{w}\left(\frac{1-w\nu}{w}E(\varphi,k)-(1-\nu)F(\varphi,k)\right)+\frac{1-2\nu}{2}\right.$$

$$\left.\left.\left.+\frac{w^2(2\nu-1)\left(\frac{\delta}{e}\right)^2\sqrt{w}(2(w\nu-1)+w)}{2w\sqrt{\left(w+\left(\frac{\delta}{e}\right)^2\sqrt{w}\right)\left(1+\left(\frac{\delta}{e}\right)^2\sqrt{w}\right)}}\right]^2\right]\right\}^{-\frac{1}{2}}$$

here

$$E(\varphi,k) = arcctg\left(\frac{\delta}{e}\sqrt[4]{w}\right)\left(1-\frac{1}{4}(1-w)-\frac{3}{64}(1-w)^2\right)$$

$$+\frac{\delta}{e}\sqrt[4]{w}\frac{1}{1+\left(\frac{\delta}{e}\right)^2\sqrt{w}}\left[\frac{1}{4}(1-w)+\frac{3}{64}(1-w)^2+\frac{1}{32}(1-w)^2\frac{1}{1+\left(\frac{\delta}{e}\right)^2\sqrt{w}}\right] \tag{25}$$

$$F(\varphi,k) = arcctg\left(\frac{\delta}{e}\sqrt[4]{w}\right)\left(1-\frac{1}{4}(1-w)-\frac{8}{64}(1-w)^2\right)$$

$$+\frac{\delta}{e}\sqrt[4]{w}\frac{1}{1+\left(\frac{\delta}{e}\right)^2\sqrt{w}}\left[\frac{1}{4}(1-w)+\frac{9}{64}(1-w)^2+\frac{3}{32}(1-w)^2\frac{1}{1+\left(\frac{\delta}{e}\right)^2\sqrt{w}}\right] \tag{26}$$

where F is contact force; R_e is yield stress of the deformed material; ν is Poisson's ratio; E is Young's modulus; $= e = \sqrt{a \cdot b}$ is equivalent semi-axis of the contact ellipse (Hertzian semi-axis); a and b are minor and major semi-axis of the contact ellipse (Fig. 3), respectively; $w = a^2 b^2 < 1$ is dimensionless auxiliary coefficient.
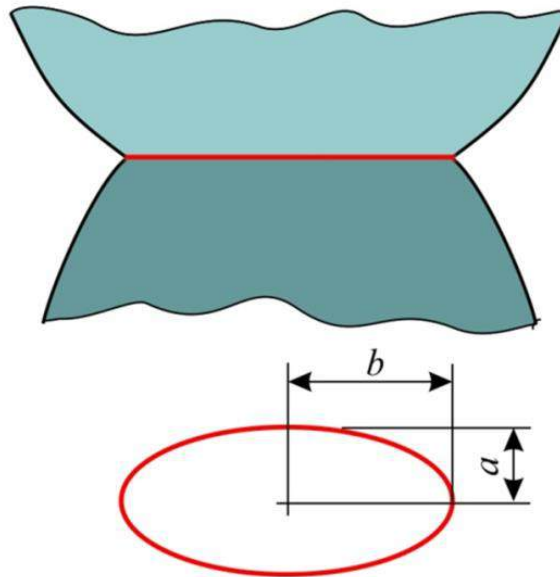
Fig. 3. Hertzian contact ellipse.

This equation concerns the general solution for the asymmetric stress state and was described by Mazur (2003). The solution to equation (24) for the case $a < b$ is a pencil of curves (each curve for a different value of w).

3. Results

Analytical calculations of the depth of the plastically deformed top layer were performed in the MathCAD program according to Eq. (24). The following data were assumed: diameter of the burnishing ball $D = 6.25$ mm, shaft diameter $d = 48$ mm, yield stress of shaft material $R_e = 450$ and $R_e = 900$ MPa, Young's modulus $E = 2.1 \times 10^5$ MPa and Poisson's ratio $\nu = 0.3$.

The results of contact force calculations using the asymmetric method were compared with the results obtained according to the classical (symmetric) solution (Jezierski, 1972) (Eq. (27)).

$$\frac{F}{R_e e^2} = \frac{4\pi}{3}\left[\frac{3}{1+\left(\frac{\delta}{e}\right)^2} + 2(1+\nu)\left(\frac{\delta}{e}\,arcctg\,\frac{\delta}{e} - 1\right)\right] \tag{27}$$

Results of numerical calculations of the contact forces and dimensions of half-axis of the contact ellipse obtained from the asymmetric and classical (symmetric) solutions are listed in Tables 1 and 2. The difference between the contact force values calculated using the asymmetric and symmetric solutions is 0.04–0.15% (Table 1) and 0.07–0.20% (Table 2), respectively. The difference between the values $e = a + b$ for both solutions does not exceed 0.11%. This is the result of the fact that the trace of the impression of a small diameter ball on the surface of a cylindrical roller is close to a circle (a ~ b). Figures 4a and 4b graphically present the influence of the depth of the plastically deformed top layer on the contact force for the yield stress of the roller material $R_e = 450$ MPa and $R_e = 900$ MPa, respectively. Approximation of the data points showed a power-law relationship between the depth of the plastically deformed top layer and the contact force.

Table 1. Results of numerical calculations of the contact forces and dimensions of half-axis of the contact ellipse obtained from the solution of the asymmetric case and the classical solution for a material with a yield strength of $R_e = 450$ MPa.

δ, mm	Asymmetric case				Classical solution	
	F, N	a, mm	b, mm	e, mm	F, N	$e = a + b$, mm
0.1	13.07	0.060	0.066	0.06296	13.05	0.06291
0/2	44.83	0.091	0.099	0.09495	44.80	0.09489
0.3	95.11	0.117	0.127	0.12200	95.04	0.12193
0.4	163.69	0.140	0.152	0.14621	163.60	0.14612
0.5	250.47	0.162	0.175	0.16848	250.35	0.16839

Table 2. Results of numerical calculations of the contact forces and dimensions of half-axis of the contact ellipse obtained from the solution of the asymmetric case and the classical solution for a material with a yield strength of R_e = 900 MPa.

δ, mm	Asymmetric case				Classical solution	
	F, N	a, mm	b, mm	e, mm	F, N	$e = a + b$, mm
0.1	34.23	0.083	0.090	0.08679	34.16	0.08669
0/2	104.58	0.121	0.131	0.12593	104.44	0.12582
0.3	212.96	0.153	0.166	0.15961	212.74	0.15949
0.4	358.68	0.182	0.198	0.18991	358.37	0.18977
0.5	541.38	0.209	0.227	0.21784	540.97	0.21770
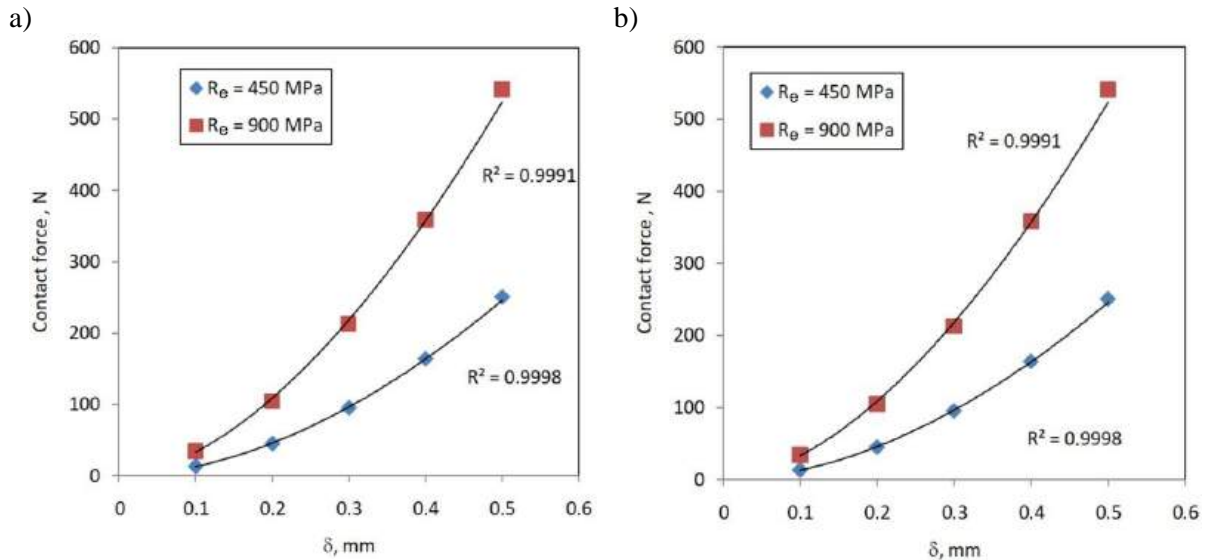
Fig. 4. Graphs of the relationship $F = f(\delta)$ obtained using the a) asymmetric and b) classical solution.

4. Conclusions

The depths of the plastically deformed top layer when burnishing with a small diameter ball ($D <$ 20 mm) and in the range of low contact forces, calculated using the asymmetric and classical solutions, are similar to each other. The difference in the burnishing force value determined using both methods does not exceed 0.2%. From the geometric point of view, the trace of the ball impression on the shaft has similar values of the semi-axis $a \sim b$. Therefore, for small values of the ball diameter, both methods provide similar results. The relationship between the depth of the plastically deformed top layer and the contact force with an accuracy of $R^2 > 0.999$ can be presented using a power equation in the form $F = u \times \delta^h$, where u and h are constants.

References

Belyaev, N. M. (1957). *Trudy po teorii uprugosti i plasticznosti* [*Works on the theory of elasticity and plasticity*]. Maszgiz.

Chodor, J., & Kukielka, L. (2014). Using nonlinear contact mechanics in process of tool edge movement on deformable body to analysis of cutting and sliding burnishing processes. *Applied Mechanics and Materials 474*, 339–344. https://doi.org/10.4028/www.scientific.net/AMM.474.339

Czechowski, K., & Kalisz, J. (2015). Wybrane aspekty procesu nagniatania [Selected aspects of the burnishing process]. *Mechanik*, *5-6*, 452–455. https://doi.org/10.17814/mechanik.2015.5-6.203

Czechowski, K., & Toboła, D. (2017). Gładkościowe nagniatanie ślizgowe stopów metali i kompozytów na osnowie metalowej [Slide finishing burnishing of metal alloys and metal matrix composites]. *Mechanik*, 7, 552–554. http://dx.doi.org/doi.org/10.17814/mechanik.2017.7.70

Dobrzyński, M., Javorek, L., Orłowski, K. A., & Przybylski, W. (2019). The effect of an active force while slide diamond burnishing of wooden shafts upon process quality. *Journal of Construction and Maintenance*, *1*(112), 7–15.

Dyl, T. (2010). Wpływ nagniatania na umocnienie elementów części maszyn okrętowych [The influence of burnishing on the surface layer strengthening ship machine]. *Zeszyty Naukowe Akademii Morskiej w Gdyni*, *64*, 36–42.

Dyl, T. (2011). Nagniatanie powierzchni płaskich elementów części maszyn okrętowych [The burnishing flat surfaces of machine parts ship]. *Zeszyty Naukowe Akademii Morskiej w Gdyni*, *71*, 2011, 38–48.

Dzierwa, A., Gałda, L., Tupaj, M., & Dudek, K. (2020). Investigation of wear resistance of selected materials after slide burnishing process. *Eksploatacja i Niezawodność-Maintenance and Reliability*, *22*(3), 432–439. https://doi.org/10.17531/ein.2020.3.5

Gałda, L., & Pająk, D. (2022). Analysis of the application of SIC ceramics as a tool material in the slide burnishing process. *Technologia i Automatyzacja Montażu*, *1*, 45–57. http://dx.doi.org/10.7862/tiam.2022.1.5

Huber, M. T. (1904). Właściwa praca odkształcenia jako miara wytężenia materiału [Specific work of strain as a measure of material effort]. *Czasopismo Techniczne*, *22*, 38–50, 61–62, 80–81.

Jezierski, J. (1972). *Obróbka maszynowa części maszyn zgniotem na zimno* [*Work hardening of machine parts*]. Prace Naukowe - Politechnika Warszawska: Mechanika, 19.

Jezierski, J., & Mazur, T. (2002). Analysis of the thickness of the plasticized zone in the surface burnishing process. *Archive of Mechanical Engineering*, *49*(2), 105–126.

Kaldunski, P., Patyk, R., Kukielka, L., Bohdal, L., Chodor, J., & Kulakowska, A. (2019). Numerical analysis and experimental researches of the influence of technological parameters burnishing rolling process on fatigue wear of shafts, *AIP Conference Proceedings*, *2078*, Article 020082. https://doi.org/10.1063/1.5092085

Kułakowska, A., Patyk, R., & Bohdal Ł. (2014). Zastosowanie obróbki nagniataniem w tworzeniu ekologicznego produktu [Application of burnishing process in creating environmental product]. *Annual Set The Environment Protection*, *16*, 323–335.

Mazur, T. (2003). Badania grubości warstwy wierzchniej odkształconej plastycznie po nagniataniu powierzchniowym [Testing the thickness of the plastically deformed surface layer after surface burnishing], [Unpublished doctoral dissertation]. Politechnika Radomska

Patyk, R., Kułakowska, A., & Nagnajewicz, S. (2017). Badanie wpływu głębokości nagniatania na chropowatość powierzchni wałków stalowych [Researches of the influence of burnishing depth on the surface roughness parameters of the steel shafts]. *Autobusy*, *12*, 1208–1211.

Przybylski W. (1987). *Technologia obróbki nagniataniem* [*Burnishing technology*]. Wydawnictwa Naukowo-Techniczne.

Przybylski, W. (2004). Nagniatanie stali o różnej twardosci narzędziami ceramicznymi [Burnishing of steel of various hardness with ceramic tools]. *Zeszyty Naukowe Politechniki Koszalińskiej*, *34*, 251–258.

Przybylski, W. (2016). Sliding burnishing technology of holes in hardened steel. *Advances in Manufacturing Science and Technology*, *40*(3), 43–51. https://doi.org/10.2478/amst-2016-001

Ryzyk, L. M., & Gradsztejn, I. S. (1964). *Tablice całek, sum, szeregów i iloczynów* [*Tables of integrals, sums, series and products*]. Wydawnictwo Naukowe PWN.

Sachin, B., Rao, C. M., Naik, G. M., & Puneet, N. P. (2021). Influence of slide burnishing process on the surface characteristics of precipitation hardenable steel. *SN Applied Sciences*, *3*, Article 223. https://doi.org/10.1007/s42452-021-04260-w

Skoczylas, A., & Zaleski, K. (2022). Study on the surface layer properties and fatigue life of a workpiece machined by centrifugal shot peening and burnishing. *Materials, 15,* Article 6677. https://doi.org/10.3390/ma15196677

Zaleski, K. (2018). *Technologia nagniatania dynamicznego* [*Dynamic burnishing technology*]. Wydawnictwo Politechniki Lubelskiej.

Zaleski, K., & Skoczylas, A. (2019). Effect of slide burnishing on the surface layer and fatigue life of titanium alloy parts. *Advances in Materials Science*, *19*(4), 35–45. https://doi.org/10.2478/adms-2019-0020

Ocena Głębokości Warstwy Odkształconej Plastycznie w Procesie Nagniatania Wału za Pomocą Nagniataka Ceramicznego

Streszczenie

Nagniatanie jest jedną z najbardziej efektywnych metod poprawy wytrzymałości warstwy wierzchniej wałów w efekcie umocnienia odkształceniowego materiału. W tym artykule przedstawiono teoretyczne podejście do określania grubości warstwy wierzchniej odkształconej plastycznie na podstawie teorii Bielajewa. Założono kontakt dwóch ciał z niesymetrycznym stanem naprężenia. Rozważano również rozwiązanie klasyczne. Celem badań było porównanie obliczonych wartości grubości warstwy odkształconej plastycznie wyznaczonych za pomocą tych dwóch metod. W obliczeniach rozważono nagniatanie wałów o średnicy 48 mm wykonanych ze stali o granicy plastyczności R_e = 450 MPa oraz R_e = 900 MPa. Do nagniatania wykorzystano nagniatak z końcówką ceramiczną Si_3N_4. Stwierdzono, że w zakresie małych sił nacisku obliczone wartości grubości warstwy umocnionej za pomocą rozwiązania niesymetrycznego i metodą klasyczną są zbliżone. Stwierdzono również, że zależność pomiędzy głębokością odkształconej plastycznie warstwy wierzchniej a siłą nacisku można wyjaśnić równaniem potęgowym z dokładnością R^2 > 0,999.

Słowa kluczowe: nagniatanie, warstwa odkształcona plastycznie, teoria Bielajewa, wały

Optimal Airfoil Selection for Small Horizontal Axis Wind Turbine Blades: A Multi-Criteria Approach

Temesgen Batu [1,*] , **Hirpa G. Lemu** [2] , **Besufekad Negash** [1] , **Eaba Beyene** [1] , **Dagim Tirfe** [1] , **Eyob Hailemichael** [3] , **Solomon Alemneh** [3]

[1] Centre of Armament and High Energy Materials, Institute of Research and Development, Ethiopian De-fence University, Bishoftu, Hora Lake Bishoftu, 1041, Ethiopia; bn.ird@etdu.edu.et (B. Negash), beyene.eaba@yahoo.com (E. Beyene), dagimasegidtirfe0286@gmail.com (D. Tirfe)

[2] Department of Mechanical and Structural Engineering and Materials Science, University of Stavanger (UiS), 4036 Stavanger, Norway; hirpa.g.lemu@uis.no

[3] Kombolcha Institute of Technology, Department of Mechanical Engineering, Wollo University, Dessie P.O. Box 1145, Ethiopia; eyobhailemichael@kiot.edu.et (E. Hailemichael), solomonalemneh16@gmail.com (S. Alemneh)

* Correspondence: temesgen.batu@kiot.edu.et

Abstract

Over the last century, the growing demand for clean energy has emphasized wind energy as a promising solution to address contemporary energy challenges. Within the realm of wind energy, the wind turbine plays a pivotal role in harnessing the kinetic energy of the wind and converting it into electrical power. Among the various components of the wind turbine system, turbine blades assume a critical role in capturing the wind's kinetic energy and converting it into rotational motion. Consequently, the design of wind turbine blades holds the utmost importance in determining the overall performance and efficiency of the entire wind turbine system. One essential aspect of blade design involves selecting an appropriate airfoil. Throughout history, numerous airfoil profiles have been developed for various applications. Notably, National Advisory Committee for Aeronautics (NACA) and National Renewable Energy Laboratory (NREL) airfoils have been tailored for aircraft and large-scale wind turbine blades, respectively. However, the quest for suitable airfoil types for small-scale wind turbine blades has been ongoing. This study delves into an examination of over 62 distinct NACA and NREL aerofoil types tailored for small horizontal-axis wind turbine blades. Employing specialized software, namely QBlade, specifically designed for modeling and simulating wind turbine blades, the study calculates key parameters such as power output, stress, deformation, and weight for each airfoil. Subsequently, based on the simulated data, the optimal airfoil is identified using the Technique for Order Preference by Similarity to Ideal Solution (TOPSIS) multi-criteria selection approach. This selection process takes into account simulation results pertaining to power output, stress, deformation, and weight. The decision-making process involving multiple criteria is facilitated using Excel and Python. The findings of this study reveal that among the 62 airfoil types under consideration, the NACA 0024, NACA 2424, and NACA 4424 airfoils emerge as the most suitable choices for small horizontal-axis wind turbine blades.

Keywords: wind energy, airfoil selection, horizontal axis wind turbine blades, multi-criteria approach

1. Introduction

The demand for Energy has been increasing significantly over the past years. Energy in the form of electricity has become a central commodity for the survival of human beings (Gopinath & Meher, 2018). Urbanization and rapid economic growth are the major factors for the rise in the demand of electricity over the past decades. By 2030, global electricity consumption is expected to reach 31657 TWh (Shahbaz et al., 2015). Previously the demand for electricity was met by the burning of fossil fuels which caused the environment to suffer as a consequence. This has resulted on a shift in the focus of the production and utilization of energy on clean and renewable energy sources. The use of renewable energy has fascinated the world's interest, as it can be used to meet current and future energy needs. Of all the available options for renewable energies, wind energy has become one of the
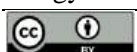
inevitably promising energy source options, owing to its cost-effectiveness, sustainability, and low environmental impact (Hsu et al., 2014; Liu, 2016).

An efficient generation of electricity from wind requires a well organised equipment and set of tools. The mass, shape and size of each part plays an important role on the process. One of the critical parts of a wind turbine is its blades. The shape of wind turbine blades has direct impact on both performance and cost of power production. This is because the efficiency of the wind turbine blades decide the con-version of kinetic energy associated with wind to mechanical energy (Torque) then power generation (Beig & Muyeen, 2016). The efficiency of the rotor in extracting power from the wind is a function of the aerodynamic characteristics of the airfoil sections used in the design of the rotor blades. The blade is made up of a number of different airfoil cross sectional aerodynamic shapes (Corke et al., 2015; Islam et al., 2019).

An airfoil is the foundation of wind turbine blade design, and accordingly, optimizing its design plays a key role in improving aerodynamic performance, noise control, and structural robustness of a rotor blade (Sudarsono et al., 2013). Figure 1 indicates how the airfoil distributed along the blade. For the last three decades, different airfoil was developed by different companies such as National Advisory Committee for Aeronautics (NACA), National Renewable Energy Laboratory (NREL) were used for wind turbine blades. But NACA series airfoil were designed for developing airplane wings. Also NREL has developed air-foils specifically designed for large scale wind turbine blade applications (Islam et al., 2019).
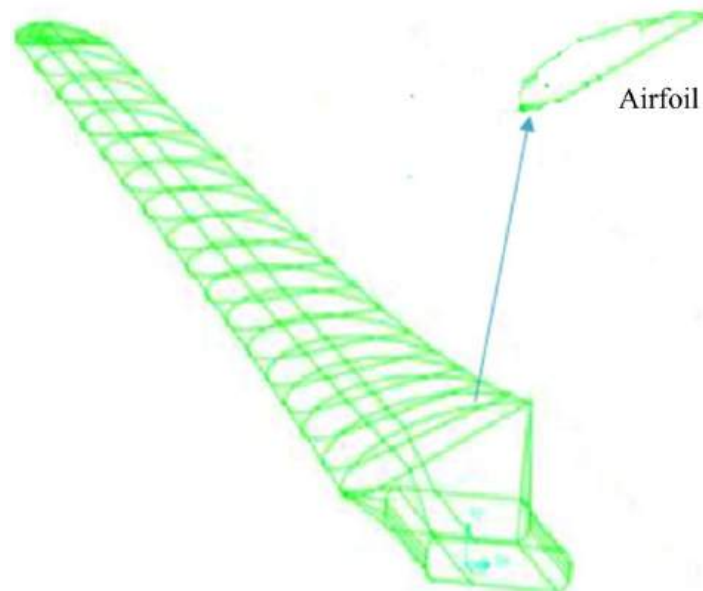
Fig. 1. Blade of wind turbine and its airfoil distribution (customized from Sudarsono et al., (2013)).

Both NACA and NREL have not developed initially for small scale wind turbines. While NACA airfoils have been widely used in various applications, including wind turbine blades, they also possess certain limitations and challenges. The NREL airfoils, such as the NREL S-series airfoils, are primarily designed and optimized for large-scale wind turbines (Islam et al., 2019). While these airfoils have been extensively tested and proven effective for utility-scale wind turbines, they may not be suitable for small-scale wind turbine blades due to several reasons (Osei et al., 2020) such as Reynold number, scale effects and structural considerations. Small-scale wind turbines typically operate at lower wind speeds, resulting in lower Reynolds numbers. But the NREL airfoils are optimized for higher Reynolds numbers typically encountered by large-scale turbines.

For small scale wind turbine, researchers have primarily focused on developing new airfoil (Noronha & Krishna, 2021; Osei et al., 2020; Wang & Li, 2021), selecting an appropriate airfoil from the developed airfoil such as NACA and NREL series (Islam et al., 2019) to enhance the efficiency of wind turbines. For instance, Islam et al. (Islam et al., 2019) presented a comparison study of different airfoils from the NACA and NREL airfoil families, aiming on suitability for small horizontal wind tur-bines, and finally showed that NACA airfoils have better average performance criteria whereas NREL airfoils have better stability criteria. For The comparisons, the criteria are: maximum glide ratio at lower and higher Reynolds number, difference between angle of attack between lower and higher Reynolds number and percentage deviation of maximum glide ratio from stall point. Noronha and Krishna (2021) conducted comparison of different airfoils based on the selected airfoils. Result were analyzed by using QBlade software with different Reynolds number (Re_c) and considering different

angles of attack (AOA) using Computational Fluid Dynamics and QBlade, and the result showed that SG6043 is the suitable airfoil for small horizontal axis wind turbine with low wind speed.

Selection of airfoils needs criteria for selecting an optimum one for wind turbine blades. Others have concentrated on selecting airfoils based on their properties. However, these selection methods fail to address the aforementioned challenges adequately. They merely prioritize the properties possessed by the airfoils without assessing their suitability and effectiveness for wind turbine blades. Unfortunately, this approach proves to be ineffective as certain airfoils were originally designed for diverse applications, such as aircraft, and operate under significantly different conditions. To overcome this limitation, the most effective strategy for airfoil selection is to empirically evaluate the performance of each airfoil in the context of wind turbine blades.

In the past, the selection of airfoils for small-scale wind turbines has often been limited to single-criterion decision-making, lacking in-depth assessments. However, in contemporary times, there is a growing trend towards employing multi-criteria decision-making (MCDM) techniques. These methods are increasingly utilized for determining preferences, such as selecting the most suitable wind turbine types, thereby addressing the limitations of previous approaches techniques (Rehman et al., 2020). MCDMs are also employed for material selection in wind turbine blade construction blades (Okokpujie et al., 2020), as well as across various other sectors. In the context of small-scale wind turbine blade design, the adoption of multi-criteria selection methods is becoming imperative. When it comes to airfoil selection criteria, MCDMs offer the advantage of simultaneously evaluating numerous parameters. These parameters may encompass aspects like lift-to-drag ratio, stall behavior, structural integrity, and manufacturing feasibility. These MCDM approaches involve the analysis and ranking of various airfoil designs through the application of mathematical models and decision matrices. This holistic approach enables a comprehensive evaluation of airfoil options, leading to more informed and effective decision-making processes.

Indeed, for small-scale wind turbines, the utilization of multi-criteria decision-making is essential when it comes to selecting an airfoil. With this in mind, our study focuses on evaluating various NACA and NREL airfoils to determine their compatibility with small horizontal-axis wind turbines. To conduct these assessments, we turned to QBlade software, which has been purposefully crafted for the analysis of wind turbines based on the blade element momentum theory. As a novelty, an extensive research of over 62 NACA and NREL aerofoil types tailored for small horizontal-axis wind turbine blades was carried out. Key parameters such as power output, stress, deformation, and weight for each airfoil were numerically assessed using QBlade program. Subsequent to the simulation phase, we rigorously scrutinized the results obtained from the software. To make an informed decision regarding the most suitable airfoils, we applied a multi-criteria decision-making approach known as the Technique for Order Preference by Similarity to Ideal Solution (TOPSIS). This approach has been tailored specifically to cater to the unique requirements and constraints associated with small-scale wind turbines, ensuring a methodical selection process for the most appropriate airfoils in this context.

2. Methodology

To achieve the overarching goals of this research paper, a logical flow diagram (Fig. 2) was developed to provide a structured framework. This diagram serves as a visual representation of the sequential steps and connections that will guide the research process and ensure the attainment of the desired objectives. Figure 2 illustrates the sequential process of our study. The initial step involves the modeling and simulation of all the chosen airfoils, during which we calculate essential parameters such as power out-put, weight, stress, and blade deflection for each airfoil. Following this, the second step encompasses the selection of the optimal airfoil from the pool of candidates. This selection is based on a comprehensive evaluation that takes into account the calculated power output, weight, stress, and deflection, employing a multi-criteria decision-making methodology known as TOPSIS.

2.1. NACA and NREL airfoil types

In this study, we incorporated a total of 50 NACA series airfoil types, along with 10 NREL variants, and an additional 2 distinct airfoil types. To obtain the essential x and y coordinate data for each of these airfoil profiles, we sourced this information from an open-source airfoil data repository available at http://airfoiltools.com/ as referenced in (AirfoilTools, 2013). This comprehensive dataset served as the foundation for our simulations and evaluations, enabling us to assess the suitability of these diverse airfoil profiles for our research on small horizontal-axis wind turbines.
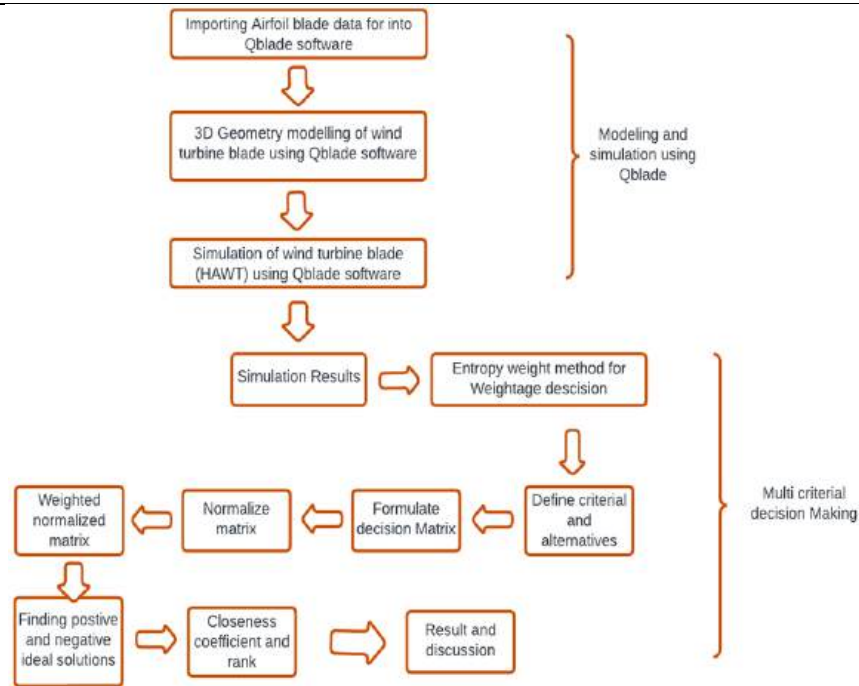
Fig. 2. Schematic flow diagram for methodology of the study.

Those airfoils have varying geometries, including differences in thickness, curvature, and camber distribution, leading to distinct aerodynamic performances. NREL's S807, S808, S809, S812, S816, S819, S823, S827, and S835, for instance, are designed by the NREL and are tailored for specific wind turbine applications, with variations in lift and drag characteristics. Similarly, AS5048 (18%) and NLR-7301 are airfoils optimized for particular aerodynamic efficiency and structural considerations. On the other hand, airfoils like NACA 63A010, 63-015A, 63-210, and 63-212 feature unique combinations of camber and thickness distributions, affecting their lift and drag performance across different angles of attack. Additionally, NACA airfoils such as 63-215, 63(2)-215 MOD B, 63-412, and 63-415 offer variations in thickness and camber to suit diverse aerodynamic requirements. Furthermore, NACA series airfoils like 64-008A, 64-012A, and 642-015 exhibit differences in thickness and camber for specific lift and drag characteristics at varying Reynolds numbers. Lastly, NACA airfoils such as 22112, 23012, and 23015 possess unique geometries optimized for specific applications, while others like NACA 0006, 0008, 0009, and 0010 feature variations in thickness and camber suitable for different aerodynamic conditions. These variations in airfoil geometries ultimately influence the aerodynamic performance, structural integrity, and overall efficiency of wind turbine blades.

2.2. Parameters for blade design for each airfoil

In this study, we employed existing parameters from small-scale wind turbine blades. The specific blade chosen for our airfoil analysis is part of a small horizontal-axis wind turbine (HAWT) utilized by the Department of Aerospace and Mechanical Engineering at the University of Notre Dame, Indiana, as detailed in (Corke et al., 2015). We utilized the wind turbine data to create a model of the blade geometry, which includes characteristics such as the chord length and twist angle.

The pertinent specifications of this turbine and its rotor geometry are comprehensively outlined in Table 1. The notations include the Reynolds number, which characterizes the flow regime of the air over the blade, as well as coefficients such as $c_d(\alpha)$ and $c_l(\alpha)$ representing the drag and lift forces as functions of the angle of attack (α) respectively. Additionally, parameters like the tip-speed ratio (λ), number of blades (B), and radius (R) of the blade are crucial in determining the efficiency and behavior of the turbine. Other important notations include V_{cut-in}, $V_{cut-rated}$, and $V_{cut-out}$, denoting the wind speeds at which the turbine starts generating electricity, reaches its rated power output, and shuts down to prevent damage, respectively. Hub heights indicate the elevations at which the turbines are installed, while the composition of the blade material is often described using terms like Glass/epoxy E. Furthermore, density (ρ) represents the mass per unit volume of air, influencing various aerodynamic and structural aspects of the turbine design.

Table 1. Characteristics of the University of Notre Dame wind turbines rotor, prepared on the basis of (Corke et al., 2015).

Parameter	Value
Re_c	0.5×10^6
$c_d(\alpha)$	$0.327 + 0.1059\alpha - 0.0013\alpha^2$
$c_l(\alpha)$	$0.006458 - 0.000272\alpha + 0.000219\alpha^2 - 0.0000003\alpha^3$
λ	$-2° \leq \alpha \leq 12°$
B	3
R	4.953 m
$V_{\text{cut-in}}$	3.0 m/s
$V_{\text{cut-rated}}$	11.6 m/s
$V_{\text{cut-out}}$	37 m/s
Hub heights	20 m
Glass/epoxy E	25 GPa
Density (ρ)	1915 kg/m^3

2.3. QBlade software for wind turbine blade modelling and simulation

2.3.1. QBlade

QBlade is an open-source tool developed at the Berlin Institute of Technology (TU Berlin) to assist in wind turbine blade design and simulation (Marten & Wendler, 2013). It is designed to be an all-in-one solution for aerodynamic wind turbine design and simulation. Unlike some other tools, it does not require data import from external sources or format conversions. QBlade offers various functionalities accessible through its graphical user interface (Marten & Wendler, 2013). Essentially, it's a collection of methods and tools for creating early-stage wind turbine blade designs.

For finite element simulations, it's crucial to consider the aerodynamic loads. The primary types of wind loads that significantly impact blade structural strength and stiffness are aerodynamic loads. These loads can be divided into tangential (F_T) and axial (F_N) force components, which can be calculated using the following equations:

$$F_N = L(\alpha) \cos\phi + D(\alpha) \sin\phi \tag{1}$$

$$F_T = L(\alpha) \sin\phi - D(\alpha) \cos\phi \tag{2}$$

Here, ϕ represents the flow angle, α is the angle of attack, $L(\alpha)$ and $D(\alpha)$ are the coefficients of lift force and trust force, respectively, and F_N and F_T are the normal and tangential forces, respectively.

2.3.2. Modeling and simulation process

The modeling and simulation were conducted in accordance with the following steps.

1) The turbine geometry data, as provided in the Table 1, was used to import the airfoil into QBlade for blade modeling.
2) Subsequently, the blade model was employed in nonlinear lifting line simulations within the software, using airfoil data obtained from an airfoils tool website.
3) The same input parameters, including radius, wind speeds, number of blades, tip speed ratio, and material properties, were applied to each analysis, except for the airfoil coordinates, which were imported.
4) The blade model was then imported into QFEM (QBlade's Finite Element Method module) to define the mechanical properties, utilizing glass fiber reinforced material properties outlined in Table 2.
5) The aerodynamic load, consisting of both tangential and normal forces, was specifically computed for an average wind speed of 11.6 m/s, representing the University of Notre Dame Wind Turbines rotor.
6) This aerodynamic load was then applied to the blade model to calculate stresses, total deformation, and the weight of the blade. For each airfoil the calculated results i.e. power, weight, stress and deformation was listed in Table A1 (Appendix A).

3. TOPSIS for multi-criteria selection

TOPSIS stands for "Technique of Order Preference Similarity to the Ideal Solution". It is a multi-criteria decision analysis (MCDA) method that was first introduced by Hwang and Yoon (1981). The

method is based on finding an ideal and an anti-ideal solution and comparing the distance of each one of the alternatives to those. It has been successfully applied in various instances and can be considered as one of the classical MCDA methods that has received a lot of attention from scholars and researchers (Papathanasiou & Ploskas, 2018).

One of the methods used for multi-criteria selection is TOPSIS. Of the numerous criteria decision-making (CDM) methods, TOPSIS is a useful technique for ranking and selecting a number of possible alternatives by measuring Euclidean distances. In this technique, a set of alternatives is compared based on the weights specified for each criterion. The results are then normalised and the geometric distance between each alternative and the ideal alternative are calculated. This method is used in different sectors for selecting things which have many conflicting criteria (Balioti et al., 2018).The method is simple and computationally efficient. The procedure of TOPSIS consists of a series of steps listed below (Fu, 2008).

Step 1: define/identify the decision criteria and alternatives.

The TOPSIS approach to the multi-criteria selection of airfoil geometry requires meeting additional decisions criteria and identification of alternatives. In this work, 62 airfoil geometries were considered based on the five decision criteria. The decision criteria are: i.e. power, weight, stress, deflection, and torsional frequency of turbine blades, and the alternatives are the airfoils listed in Table A1 (Appendix A).

Step 2: formulation and normalization of the decision matrix. The matrix listed in Table A1 (Appendix A), is normalized using Eq. (3).

$$r_{ij} = \frac{x_{ij}}{\sqrt{\sum_{i=1}^{m}(x_{ij})^2}}, \, i = 1, \ldots, m \text{ and } j = 1, \ldots, n \tag{3}$$

where: r_{ij} and x_{ij} are normalized value of the decision matrix element and original value of the decision matrix element, respectively; m is the number of alternatives or airfoil types and n is the number of decision criteria or attributes.

Step 3: weightage calculations for the attributes.

The third requirement is to assign weights to each of the five criteria to calculate the weighted normalized decision matrix. One of the appropriate methods used for weight calculation is an entropy method, which is used for the evaluation of weights for CDM. The entropy method uses the decision table to compute the weights regardless of the operator's choice. Entropy methods have gained much importance in recent years, as these methods reduce the decision makers' experiments as much as possible by implementing mathematical computation for determining the weights. In the entropy method, the higher the difference in performance values, the more weightage is considered, and the airfoils with similar performance are given lower weightage. The following is a common procedure for objective weight through entropy, which was listed as shown in steps 1–2. A detailed procedure of the entropy method is given with examples by Lotfi & Fallahnejad (2010).

Step 1: normalization of performance indices in decision matrix to obtain the project outcomes p_{ij}:

$$p_{ij} = \frac{x_{ij}}{\sum_{i=1}^{m} x_{ij}} \tag{4}$$

Step 2: computation of the entropy measure of project outcomes using the following equation:

$$E_j = -k \sum_{i=1}^{m} p_{ij} Ln p_{IJ}, \text{ in which } k = 1/ln \, (m) \tag{5}$$

where L is natural logarithm base, p_{IJ} is normalized project outcome.

Step 3: using the entropy concept to determine the objective weight w_j:

$$w_j = \frac{1 - E_j}{\sum_{i=1}^{n} 1 - E_j} \tag{6}$$

where w_j is objective weight.

Using the stepwise formulas listed, the entropy weights for the attributes and criteria would be computed.

Step 4: construction of the weighted normalized decision matrix.

A weighted normalized decision matrix is constructed using the weightage calculations obtained in step 3 for each criterion's attributes:

$$v_{ij} = w_j r_{ij}, j = 1, 2, \dots m, \ i = 1, 2, \dots n \tag{7}$$

where v_{ij} is weighted normalized decision matrix.

Step 5: calculation of the ideal best and ideal worst.

In this article the criteria (attributes) for power, the minimum value is the ideal worst, and the maximum value is the ideal best value. For stress, weight, and deflection, the maximum value is the ideal worst value, and the minimum value is the ideal best value.

Step 6: calculation of the Euclidean separation distance for each airfoil type.

Eq. (8) was used to calculate the Euclidean distance from the ideal best:

$$S_i^+ = \sqrt{\sum_{j=1}^{n} \left(v_{ij} - v_j^*\right)^2} \tag{8}$$

where S_i^+ is Euclidean distance from the ideal best and and v_j^* is ideal best value for criterion j.

Calculate the Euclidean distance from the ideal best using Eq. (9):

$$S_i^- = \sqrt{\sum_{j=1}^{n} \left(v_{ij} - v_j^-\right)^2} \tag{9}$$

where S_i^- is Euclidean distance from the ideal worst

Step 7: calculation of the relative closeness to the ideal solution or closeness coefficient C_i:

$$C_i = \frac{S_i^-}{S_i^+ + S_i^-} \tag{10}$$

Step 8: Rank of preference alternatives order. The solution with the highest value of R_i is the best solution. We developed Python code based on the TOPSIS steps for selecting an optimum airfoil. Additionally, we used Excel to verify the results and select the best alternative from the available options.

4. Results and discussion

The results and discussion are divided into two sets of analysis. In the first set, data for each airfoil was discussed comparatively to identify the best in terms of power output, stress and deflection created on the blade because of air-foil data variation, weight of the turbine blade due to airfoil data, and modal behavior of the blade. This procedure is repeated for all criteria, and the best solution is found for all airfoils. In the second analysis, the results of the TOPSIS analysis are briefly discussed. Details of these analyses are provided in the following sections.

4.1. Power output comparison

The 4.953 m wind turbine blade was modelled using the open-source tool QBlade software for each airfoil. The unsteady simulation was performed for HAWT in the time domain by using a QBlade for all airfoils. The power output and power coefficient were obtained from each airfoil with the same input parameters, such as wind speed $V_{hub} = 11.6$ m/s and a hub height of 20 m for 5 seconds. The power output obtained from simulation for the first five tops (maximum) and two minimums is listed in Table 2. After a detailed aerodynamic comparison based on power and power coefficient, it was concluded that NACA 6409, NACA 6412, and NACA 4412 are the most suitable airfoils for small horizontal axis wind turbines operating at low wind speeds.

Table 2. Results of selected output power.

Name of airfoil	NACA 6409	NACA 6412	NACA 4412	NACA 0012	NACA 4415
Power output (kW)	37.18	36.9732	36.4	36.3671	36.2179
Efficiency	0.47	0.4688	0.465	0.4649	0.4613

4.2. Comparison of weight of the blade

The QBlade software not only calculates critical parameters such as power output but also takes into account the weight of each blade when assessing different airfoil designs for wind turbines. It is worth noting that variations in airfoil data can lead to changes in blade size (Plaisier & Smeets, 2016). These size variations are directly related to the weight of the blades, which, in turn, have a significant impact on the aerodynamic power generated (Batu & Lemu, 2020). Table 3 provides a breakdown of the blade weights for the top-selected airfoils based on weight considerations. It is a well-known fact that optimizing wind turbine blade design to reduce the cut-in wind speed can lead to substantial performance enhancements (Batu et al., 2020; Eker et al., 2006). One effective approach to achieve this reduction is by minimizing the weight of the turbine blades. A lower blade weight, characterized by lower density, enables the wind blade to overcome friction and initiate rotation at lower cut-in wind speeds.

As depicted in Table 3, the weights of the wind turbine blades for the top five airfoils, ranging from minimum to maximum weight, are presented. For the sake of comparison, the last two airfoils with the maximum weight are also included. Based on these weight considerations, and after careful examination of the results, it would be advisable to consider NACA 0006, NACA 64-008A, and NACA 0008 as strong contenders for wind turbine blade applications. Furthermore, it's evident from the data that NACA airfoils outperform NREL airfoils in terms of weight considerations, further underlining their potential suitability for wind turbine blade design (Plaisier & Smeets, 2016).

Table 3. Results of selected weight of blade for best airfoils considering only weight

Name of airfoils	NACA 0006	NACA 64-008A	NACA 0008	NACA 1408	NACA 2408
Weight (kg)	44.9898	46.6282	47.2789	47.2844	47.29

4.3. Comparison of stress and deformation of the blade

Each air foil has a different shape and size. The shape and size of any structure may affect the stress-stain properties of that structure. When all the studied airfoils were applied to wind turbine blades, different stresses and deformations were obtained. The von Misses stress and deformation results for all the different airfoils listed in Table 4 were studied by targeting minimum stress to improve the life span of the blade. At a design stage of turbine blades, they are required to be low in weight. Moreover, safe stress and strain levels should satisfy the requirements of the specific application.

Table 4. Equivalent von mises stress and total deformation results of selected airfoils.

Name of airfoils	NACA 0024	NACA 2424	NACA 4424	NACA 23024	NACA23021
Von Mises stress (MPa)	499.04	502.62	505.59	505.63	689.78
Name of airfoils	**NACA 4421**	**NACA 4424**	**NACA 2424**	**NACA 0024**	**NACA 23024**
Deflection (mm)	0.4897	0.979	0.98527	0.98824	0.99

4.4. Selection of best air-foils using TOPSIS

4.4.1. Weightage calculations for the attributes

Using these listed stepwise formulas, the entropy weights for the attributes and criteria are computed and the results are shown in Table 5. This weight of the criteria is used to calculate the value and is used in step 4 of the TOPSIS methods for constructing weighted normalized decision matrixes.

Table 5. Weightage for all criteria

Power (kW)	Stress (MPa)	Weight (kg)	Deflection (mm)
0.251	0.251	0.248	0.249

4.4.2. Rank of preference

In our quest to identify the optimal airfoil for wind turbine blade applications, we took into account several crucial criteria, including power output, turbine blade weight, stress, and deflection. The outcomes of our TOPSIS analysis have been summarized in Table 6, ordered from the best-performing airfoil to the least. Our focus in this discussion is on the top fifty airfoils, as they represent the best candidates based on our evaluation.

Significantly, NACA 0024 emerges as the optimal selection, attaining the highest ranking in closeness coefficient (C_i) values among the airfoils considered. Following closely as the second-best

option across all criteria is NACA 2424. Additionally, NACA 4424 and NACA 23024 share the third position, indicating their equally strong suitability for small-scale wind turbine blade applications.

It's worth highlighting that our results diverge from single-objective selection methods used in prior research, such as SG6043 and SG6042 (Noronha & Krishna, 2021; Salgado et al., 2016), as well as from the most commonly employed airfoils for small-scale wind turbines, including NACA 0012, NACA 0015, NREL S825, and NREL S833 (Hazmoune et al., 2021).

Since the wind turbine works under complex operational conditions, we highly recommend the airfoil selected using multi-criteria decision-making methods. Our top recommendations, based on this approach, include NACA 0024, NACA 2424, NACA 4424, and others as listed in Table 6. These airfoils have demonstrated their strong suitability across a range of critical criteria, making them well-suited choices for small-scale wind turbine blade applications. The shapes of the top two airfoils, NACA 0024 and NACA 2424, are presented in Figure 3.

Table 6. Result of selected best aifoils using multi-criteria decisions.

Name of airfoil	Power output (kW)	Weight (kg)	Stress (MPa)	Deflection (mm)	C_i	Rank
NACA 0024	26.919	58.1058	499.04	0.9882	0.999996	1
NACA 2424	26.83	58.07	502.62	0.9853	0.999989	2
NACA 4424	29.393	57.95	505.59	0.979	0.999981	3
NACA 23024	23.825	58.03	505.63	0.99	0.999981	4
NACA 23021	27.624	56.2974	689.78	1.314	0.999371	5
NACA 0021	27.929	56.277	696.62	1.3156	0.999344	6
NACA 2421	33.389	56.298	697.47	1.3	0.999341	7
NACA 4421	35.597	56.3527	720.05	0.4897	0.999252	8
NREL's S835	33.359	55.4758	758.27	1.371	0.999095	9
NREL's S823	35.041	55.3279	815	1.438	0.998847	10
NREL's S827	31.943	53.0972	865	1.6016	0.998614	11
NREL's S808	34.769	55.0478	869.55	1.5285	0.998592	12
NREL's S819	33.023	54.8617	873.11	1.5583	0.998575	13
NREL's S812	34.06	53.7635	893	1.6194	0.998478	14
NREL's S809	32.19	53.7612	900.1	1.629	0.998442	15

a)

b)
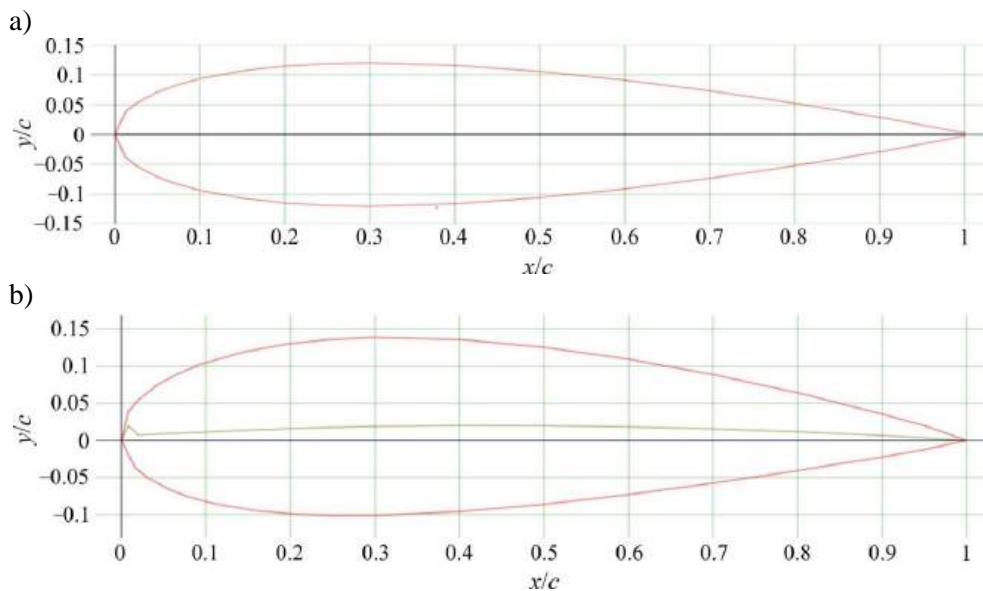
Fig. 3. Shape of the top selected airfoils by multicriteria decision-making methods: a) NACA 0024, b) NACA 2424.

5. Conclusions

One essential part of efficient wind turbine blade design is the selection of the best airfoil type. In this paper, NACA and NREL air-foils were studied for wind turbine blade application with the objective of minimum weight, stress, and maximum power. The airfoil data was taken from the airfoil tools site and the same input parameters like radius, wind speeds, number of blades, tip speed ratio, and material were used for each analysis, and except airfoil coordinates were imported. Performance of turbine blades was simulated using BEM-based finite element QBlade program. Multiple-criteria decision-making is needed to select the optimum airfoil based on the simulated results. The TOPSIS

method is adapted in this paper to effectively address the requirements of a multi-criteria airfoil selection problem, where four different yet important selection criteria were considered. These criteria are power output, stress, deflection of the blade, and weight of the turbine blade. The TOPSIS method, based on information entropy, is proposed as a multi-criteria decision for airfoil selection for 62 airfoil types. The simulation analyzes are the source of the conclusions listed below:

- Based on weight, NACA 0006 is recommended since it gives low weight.
- Based on power output and efficiency, NACA 6409 was recommended.
- With the objective of low stress and low deformation, maximum power output, and low weight of turbine blades, with a MCDM method (TOPSIS), the NACA 0024, NACA 2424, and NACA 4424 would be recommended.

For future research, we recommend expanding the study to include more airfoil types and refining our selection criteria. Additionally, integrating advanced simulation techniques and considering environmental factors could enhance our understanding. We also propose validating our findings by conducting experiments on the top 10 selected airfoils. By pursuing these avenues, we aim to develop more efficient wind turbine blades for sustainable energy production.

Appendix A

Table A1. Simulation results from QBlade software.

No.	Name of airfoil	Power output (Cp)	Weight of the turbine blades (kg)	Stress (MPa)	Deflection (mm)
1	NREL's S807	33.79	53.1091	1254.55	2.154
2	NREL's S808	34.7685	55.0478	869.55	1.52845
3	NREL's S809	32.19	53.7612	900.1	1.629
4	NREL's S812	34.06	53.7635	893	1.61974
5	NREL's S816	34.0063	53.5192	921.09	1.66795
6	NREL's S819	33.0243	54.8617	873.11	1.55833
7	NREL's S823	35.0407	55.3279	815	1.43798
8	NREL's S827	31.943	53.0972	865	1.60157
9	NREL's S835	33.359	55.4758	758.27	1.37096
10	AS5048 (18%)	33.8477	53.666	1080.63	1.9599
11	NLR-7301	31.3295	52.4296	1305.82	2.24668
12	NACA 63A010	25.68	48.3348	4843.6	8.13
13	NACA 63012A	27.55	49.7144	3080.28	5.196
14	NACA 63-015A	27.7907	51.7244	1732.6	3.027
15	NACA 63-210	30.294	47.4928	5249.39	8.49
16	NACA 63-212	30.09	48.8956	3282.38	5.389
17	NACA 63-215	32.1669	50.84	1875.93	3.16502
18	NACA 63(2)-215 MOD B	32.21939	51.2481	1718.21	2.908
19	NACA 63-412	33.1729	48.9256	3265.03	5.32476
20	NACA 63-415	35.15	50.8559	1874.88	3.14
21	NACA 64-008A	21.5667	46.6282	8809.18	14.6596
22	NACA 64-012A	27.5557	49.7144	3040.28	5.19693
23	NACA 642-015	26.5361	50.799	1867.09	3.19
24	NACA 22112	31.812	50.533	2804.48	4.83103
25	NACA 23012	32.7564	50.5177	2811.07	4.82641
26	NACA 23015	33.1298	52.5278	1606.14	2.82731
27	NACA 23018	31.9138	54.4149	1021.7	1.85241
28	NACA 23021	27.6235	56.2974	689.78	1.314
29	NACA 23024	23.8248	58.03	505.63	0.99
30	NACA 23112	32.6462	50.5469	2811.12	4.804
31	NACA 24112	33.36	50.55	2805.3	4.75497
32	NACA 25112	33.96	50.5626	2780.19	4.69773
33	NACA 0006	21.96	44.9898	18986.61	30.92
34	NACA 0008	23.1354	47.2789	8206.36	13.25
35	NACA 0009	29.39	48.2185	5979.9	10
36	NACA 0010	27.6	49.0013	4561.141	7.7193
37	NACA 0012	36.3671	50.5193	2817.38	4.831
38	NACA 0015	29.93	52.49	1611.25	2.83
39	NACA 0018	28.86	54.426	1021.45	1.85541
40	NACA 0021	27.929	56.277	696.62	1.31559
41	NACA 0024	26.919	58.1058	499.04	0.98824
42	NACA 1408	29.5393	47.2844	8294.58	13.729

Table A1. *Cont.*

43	NACA 1410	30.952371	48.9982	4532.52	7.62657
44	NACA 1412	30.59	50.4761	2836.54	4.846
45	NACA 2408	31.29	47.29	8041.49	13.249
46	NACA 2410	31.95	49.006	4475.1	7.49882
47	NACA 2411	34.66	49.65	3489.81	5.844
48	NACA 2412	32.5557	50.4949	2808.49	4.78
49	NACA 2414	34.393	51.8863	1897.09	3.28281
50	NACA 2415	34.25	51.5503	1596.98	2.78483
51	NACA 2418	34.49	54.4161	1021.65	1.8423
52	NACA 2421	33.389	56.298	697.47	1.3
53	NACA 2424	26.83	58.07	502.62	0.98527
54	NACA 4412	36.4	50.575	2667.36	4.5125
55	NACA 4415	36.2179	52.5847	1553.2	2.69
56	NACA 4418	36.1381	54.5096	901.44	1.4685
57	NACA 4421	35.5968	56.3527	720.05	0.4897
58	NACA 4424	29.3927	57.95	505.59	0.979
59	NACA 6409	37.18	48.2545	4682.89	7.5859
60	NACA 6412	36.9732	50.7167	2474.15	4.1
61	NACA747A315	31.73	51.1269	1744.01	2.994
62	NACA747A415	33.3	51.1516	1740.66	2.97278

References

AirfoilTools (2023, December 4). *Airfoil tools*. http://airfoiltools.com/

Balioti, V., Tzimopoulos, C., & Evangelides, C. (2018). Multi-criteria decision making using topsis method under fuzzy environment. *Proceedings*, *2*(11)*,* Article 637. https://doi.org/10.3390/proceedings2110637

Batu, T., & Lemu, H. G. (2020). Comparative study of the effect of chord length computation methods in design of wind turbine blade. In Y. Wang, K. Martinsen, T. Yu, & K. Wang, (Eds.), Advanced *Manufacturing and Automation IX. IWAMA 2019*. Lecture Notes in Electrical Engineering, 634 (pp. 106–115). Springer. https://doi.org/10.1007/978-981-15-2341-0_14

Batu, T., Lemu, H. G., & Sirhabizuh, B. (2020). Study of the performance of natural fiber reinforced compo-sites for wind turbine blade applications. *Advances in Science and Technology Research Journal*, *14*(2), 67–75. https://doi.org/10.12913/22998624/118201

Beig, A. R., & Muyeen, S. M. (2016). Wind energy. In M. H. Rashid (Ed.), *Electric renewable energy systems* (pp. 60-70). Elsevier Inc. https://doi.org/10.1016/B978-0-12-804448-3.00004-9

Corke, T. C., Nelson, R. C., & Dame, N. (2015). *Wind energy design* (1st ed.). CRC Press. https://doi.org/10.1201/b22301

Eker, B., Akdogan, A., & Vardar, A. (2006). Using of composite material in wind turbine blades. *Journal of Applied Sciences*, *6*(14), 2917–2921. https://doi.org/10.3923/jas.2006.2917.2921

Fu, C. (2008). Extended TOPSISs for belief group decision making. *Journal of Service Science and Management*, *1*, 11–20. https://doi.org/10.4236/jssm.2008.11002

Gopinath, G. S. S., & Meher, M. V. K. (2018). Electricity a basic need for the human beings. *AIP Conference Proceedings*, *1992*, Article 040024. https://doi.org/10.1063/1.5047989

Hazmoune, M., Lazaroiu, G., Ciupageanu, D. A., & Debbache, M. (2021, March 25-27). *Comparative study of airfoil profile effect on the aerodynamic performance of small scale wind turbines*. Proceedings of the 12th International Symposium on Advanced Topics in Electrical Engineering ATEE 2021, Bucharest, Romania. https://doi.org/10.1109/ATEE52255.2021.9425211

Hsu, Y., Wu, W., & Chang, Y. (2014). Reliability analysis of wind turbine towers. *Procedia Engineering*, *79*, 218–224. https://doi.org/10.1016/j.proeng.2014.06.334

Hwang, C. L., & Yoon, K. (1981). Multiple attribute decision making: methods and applications a state-of-the-art survey. Springer-Verlag. https://doi.org/10.1007/978-3-642-48318-9

Islam, M.R., Bashar, L. B., Saha, D. K., & Rafi, N. S. (2019). Comparison and Selection of Airfoils for Small Wind Turbine between NACA and NREL's S series Airfoil Families. *International Journal of Research in Electrical, Electronics and Communication Engineering*, *4*(2), 1-11. https://doi.org/10.5281/zenodo.3520469

Liu, W. (2016). Design and kinetic analysis of wind turbine blade-hub-tower coupled system. *Renewable Energy*, *94*, 547–557. https://doi.org/10.1016/j.renene.2016.03.068

Lotfi, F. H., & Fallahnejad, R. (2010). Imprecise shannon's entropy and multi attribute decision making. *Entropy*, *12*(1), 53–62. https://doi.org/10.3390/e12010053

Marten, D., & Wendler, J. (2013). QBLADE: An open source tool for design and simulation of horizontal and vertical axis wind turbines. *International Journal of Emerging Technology and Advanced Engineering*, 3(3), 264–269.

Noronha, N. P., & Krishna, M. (2021). Aerodynamic performance comparison of airfoils suggested for small horizontal axis wind turbines. *Materials Today: Proceedings*, *46*, 2450-2455. https://doi.org/10.1016/j.matpr.2021.01.359

Okokpujie, I. P., Okonkwo, U. C., Bolu, C. A., Ohunakin, O. S., Agboola, M. G., & Atayero, A. A. (2020). Implementation of multi-criteria decision method for selection of suitable material for development of horizontal wind turbine blade for sustainable energy generation. *Heliyon*, *6*, Article e03142. https://doi.org/10.1016/j.heliyon.2019.e03142

Osei, E. Y., Opoku, R., Sunnu, A. K., & Adaramola, M. S. (2020). Development of high performance airfoils for application in small wind turbine power generation. *Journal of Energy*, *2020*, Article 9710189. https://doi.org/10.1155/2020/9710189

Papathanasiou, J., & Ploskas, N. (2018). TOPSIS. In J. Papathanasiou, & N. Ploskas, (Eds.), *Multiple criteria decision aid. Methods, examples and Python implementation*s (pp. 1-30). Springer. https://doi.org/10.1007/978-3-319-91648-4_1

Plaisier, M. A., & Smeets, J. B. J. (2016). Object size can influence perceived weight independent of visual estimates of the volume of material. *Scientific Reports, 5*, Article 17719. https://doi.org/10.1038/srep17719

Rehman, S., Khan, S. A., & Alhems, L. M. (2020). Application of topsis approach to multi-criteria selection of wind turbines for on-shore sites. *Applied Sciences*, *10*(21), Article 7595. https://doi.org/10.3390/app10217595

Salgado, V., Troya, C., Moreno, G., & Molina, J. (2016). Airfoil selection methodology for small wind turbines. *International Journal of Renewable Energy Research*, *6*(4), 1410–1415. https://doi.org/10.20508/ijrer.v6i4.4642.g6930

Shahbaz, M., Loganathan, N., Sbia, R., & Afza, T. (2015). The effect of urbanization, affluence and trade openness on energy consumption: A time series analysis in Malaysia. *Renewable and Sustainable Energy Reviews*, 47, 683–693. https://doi.org/10.1016/j.rser.2015.03.044

Sudarsono, S., Purwanto, P., Soedarsono, J. W., & Munir, B. (2013). Utilization of Albizia wood (Albizia Falcata) and ramie fibers as wind turbine propeller modification of NACA 4415 standard airfoil. *Applied Mechanics and Materials*, *391*,41-45. https://doi.org/10.4028/www.scientific.net/AMM.391.41

Wang, Q., & Li, D. (2021). A new airfoil design method for wind turbine to improve maximum lift of airfoil. *Wind Engineering*, *45*(6), 1447-1458. https://doi.org/10.1177/0309524X20984428

Optymalny Dobór Profilu Łopatek Małych Turbin Wiatrowych o Osi Poziomej: Podejście Wielokryterialne

Streszczenie

W ciągu ostatniego stulecia rosnące zapotrzebowanie na czystą energię uwydatniło energię wiatrową jako obiecujące rozwiązanie umożliwiające sprostanie współczesnym wyzwaniom energetycznym. W dziedzinie energii wiatrowej turbina wiatrowa odgrywa kluczową rolę w wykorzystywaniu energii kinetycznej wiatru i przekształcaniu jej w energię elektryczną. Spośród różnych elementów systemu turbin wiatrowych, łopaty turbin odgrywają kluczową rolę w konwersji energii kinetycznej wiatru w ruch obrotowy. W związku z tym konstrukcja łopat turbin wiatrowych ma ogromne znaczenie przy określaniu ogólnej wydajności i efektywności systemu turbin wiatrowych. Jednym z istotnych aspektów konstrukcji łopaty jest dobór odpowiedniego profilu. Na przestrzeni ostatnich dekad opracowano wiele profili płatów do różnych zastosowań. Warto zauważyć, że profile NACA (National Advisory Committee for Aeronautics) i NREL (National Renewable Energy Laboratory) zostały dostosowane odpowiednio do łopat samolotów i wielkogabarytowych turbin wiatrowych. Trwają jednak poszukiwania odpowiednich typów profili do łopat małych turbin wiatrowych. W badaniu tym szczegółowo zbadano 62 różne typy profili NACA i NREL dostosowanych do łopat małych turbin wiatrowych o osi poziomej. Wykorzystując specjalistyczne oprogramowanie QBlade, opracowane specjalnie do modelowania i symulacji zachowania łopat turbin wiatrowych, w badaniach obliczono kluczowe parametry turbiny, takie jak moc wyjściowa, naprężenia, odkształcenia i masę każdego płata. Następnie, na podstawie symulowanych danych, zidentyfikowano optymalną geometrię płata przy użyciu wielokryterialnego podejścia TOPSIS (technika wyboru preferencji według podobieństwa do idealnego rozwiązania). W procesie wyboru odpowiedniej geometrii łopaty uwzględniono wyniki symulacji dotyczące mocy wyjściowej, naprężeń, odkształceń i masy. Proces podejmowania decyzji uwzględniający wiele kryteriów przeprowadzono za pomocą procedury Python w programie Excel. Wyniki badań wskazały, że spośród 62 rozważanych typów płatów, profile NACA 0024, NACA 2424 i NACA 4424 wydają się być najbardziej odpowiednim wyborem na łopaty małych turbin wiatrowych o osi poziomej.

Słowa kluczowe: energia wiatrowa, dobór profilu łopaty, łopaty turbin wiatrowych o osi poziomej, podejście wielokryterialne

Application of Categorical Boosting to Modelling the Friction Behaviour of DC05 Steel Sheets in Strip Drawing Test

Marek Szewczyk [1]* (iD), **Krzysztof Szwajka [1]** (iD), **Sherwan Mohammed Najm [2,3]** (iD), **Salwa O. Mohammed [2]** (iD)

[1] Department of Integrated Design and Tribology Systems, Faculty of Mechanics and Technology, Rzeszow University of Technology, ul. Kwiatkowskiego 4, 37-450 Stalowa Wola, Poland; kszwajka@prz.edu.pl (K. Szwajka)

[2] Kirkuk Technical Institute, Northern Technical University, 36001 Kirkuk, Iraq; sherwan@ntu.edu.iq (S.M. Najm), salwa@ntu.edu.iq (S. O. Mohammed)

[3] Department of Manufacturing Science and Engineering, Budapest University of Technology and Economics, Műegyetemrkp 3, 1111 Budapest, Hungary

* Correspondence: m.szewczyk@prz.edu.pl

Abstract

It is challenging to model the coefficient of friction, surface roughness, and related tribological processes during metal contact because of flattening, ploughing, and adhesion. It is important to choose the appropriate process parameters carefully when creating analytical models to overcome the challenges posed by complexity. This will ensure the production of sheet metal formed components that meets the required quality standards and is free from faults. This research analyses the impacts of nominal pressure, kinematic viscosity of lubricant, and lubricant pressure on the coefficient of friction and average roughness of DC05 deep-drawing steel sheets. The strip drawing test was used to determine the coefficient of friction. This work utilises the Categoric Boosting (CatBoost) machine learning algorithm created by Yandex to estimate the COF and surface roughness, intending to conduct a comprehensive investigation of process parameters. A Shapley decision plot exhibits the coefficient of friction prediction models via cumulative SHapley Additive exPlanations (SHAP) data. CatBoost has outstanding prediction accuracy, as seen by R^2 values ranging from 0.955 to 0.894 for both the training and testing datasets for the COF, as well as 0.992 to 0.885 for surface roughness.

Keywords: coefficient of friction, friction, sheet metal forming, steel sheet, surface roughness

1. Introduction

Sheet metal forming (SMF) is a metal processing technology that involves forming the material in the form of sheet metal in a way that allows obtaining a finished product with a given shape (Domitner et al., 2021; Venema et al., 2017). The use of the SMF processes allows for the quick and accurate production of components from sheet metal with a very complex shape, which is why it is widely used in many industries, including the automotive industry (Daniel el al., 2006; Spišák et al, 2016).

The deep drawing process involves forming the geometry of the finished product using a die and a punch, sometimes additionally at elevated temperature (Żaba et al., 2020). Therefore, an important phenomenon analyzed when designing metal processing using this method is the impact of selected process parameters on the surface quality of the finished product, energy consumption and tool durability (Çavuşoğlu et al., 2017). A phenomenon that has a direct impact on the nature of the deep drawing process is friction that occurs between the tools and the sheet metal surface, thereby causing wear of the mating surfaces (Bang et al., 2021).

The research carried out on the mapping of friction conditions in the sheet metal forming processes allows, using tribological tests, to simulate tribological phenomena in selected areas of the stamping

piece (Groche et al., 2019; Sigvant et al., 2019). This is related to the diversified nature of friction conditions in different areas of the stamping piece (Gali et al., 2013; Le et al., 2002; Wang et al., 2017), resulting from various values of stresses, strains and displacements. However, regardless of the analyzed area of the drawpiece, in order to prevent the negative effects of friction in the deep drawing process, various techniques are used to reduce the value of the coefficient of friction (COF). The most frequently used method to reduce friction between mating surfaces is the use of lubrication (Szewczyk et al., 2022). The lubricating substances used, due to the various parameters they must meet, are selected appropriately depending on the type of oil (natural oil, mineral oil, synthetic oil). (Carcel et al., 2005; Trzepieciński et al., 2022) and its kinematic viscosity (Bay et al., 2008; Lee et al., 2002). Another way to reduce friction in the deep drawing process is to properly select the material from which the tools are made (Kim et al., 2008; Shisode et al., 2021). In addition to the direct selection of the appropriate material from which the tools are made, a common way to reduce friction between the mating surfaces is to coat the tool surfaces, which, in addition to reducing the COF, can improve properties such as resistance to abrasion and high temperatures (Guillon et al., 2001; Severo et al., 2009).

The mentioned possibilities of modifying the friction pair were investigated, among others, by Żaba et al. (2023), who analysed the influence of the material of the friction pair based on the sheet material and modifying the countersamples' material were made. The strip samples were made of aluminium alloy EN AW-6061-T4, Inconel 625 alloy and AISI 321 stainless steel. Four sets of countersamples were made of polyurethane resin, differing in the percentage content of aluminium powder and fiber roving. A direct relationship between the COF values and the countersamples' was indicated. Another interesting phenomenon influencing the SMF process was investigated by Masters et al. (2013), who analyzed the influence of pre-stretched sheet metal strips made of aluminium alloys on the phenomenon of friction. Three grades of aluminium alloys often used in the automotive industry (EN AW-5754, EN AW-6111, EN AW-6451) which were pre-stretched to 2%, 5%, 10%, and 15% were tested. The die was made of ductile iron EN-JS2070, and lubrication was performed using wax greases (ALO70, AlubVS) and oil (MP404). As a result of the tests, it was shown that plastically pre-stretched strip sheets have an impact on the phenomenon of friction and the surface roughness of the finished product, indicating that increasing the value of the initial deformation increases the surface roughness of the finished product.

Analyzing the results of experimental research on the impact of selected parameters of the deep drawing process on COF and the surface quality of the finished product is possible thanks to the use of tools for performing statistical analyzes, i.e. artificial neural networks or machine learning algorithms. These methods allowing for the processing and analysis of information, but also enabling the construction of neural models with the help of which it is possible to predict friction phenomenon and surface quality based on the indicated values of process parameters. This article utilises the Categorical Boosting (CatBoost) machine learning technique, which has been recently created by Yandex researchers and engineers. It serves as an open-source library for gradient boosting on decision trees.

2. Material and methods

2.1. Test material

The material used in the tests was low-carbon steel sheet DC05. The chemical composition of DC05 steel meets the requirements of the PN-EN 10130:2009 standard. Due to its properties, primarily high deformability, this steel is often used in production of components using the sheet metal forming processes. The basic properties of the tested steel were determined by uniaxial tension testing of sheet metal strips cut at an angle of 0° to the rolling direction using a Zwick Roell Z030 testing machine equipped with an extensometer. As a result of the uniaxial tensile test, the results were obtained in the form of a relationship between the engineering stress and the true strain (Fig. 1). The values of basic mechanical parameters are presented in Table 1. The value of Young's modulus was automatically determined (regression method) by the software of testing machine.

In order to check the influence of selected parameters of the friction process on the value of the COF and the surface quality of the sheets, the surface roughness of the DC05 sheet was measured. For this purpose, a stationary profilometer from Hommel-Etamic T8000RC was used. The values of the roughness parameters are presented in Fig. 2. This figure also shows an isometric view of the sheet metal surface. The material ratio curve of DC05 sheet metal is shown in Fig. 3.

Based on the material ratio curve and the values of the parameters presented in Fig. 3, it can be seen that the DC05 sheet in the as-received condition is characterized by a very concentrated material density distribution, having over 17% of the material ratio at a depth of approximately 8 μm.
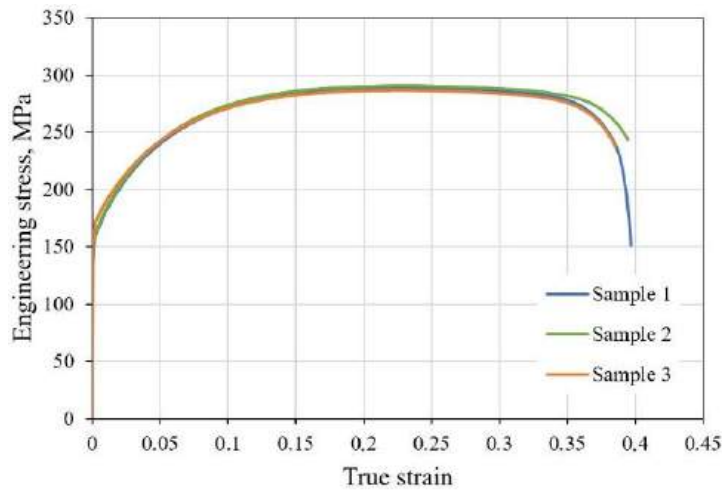
Fig. 1. The engineering stress - the true strain curve determined for samples made of DC05 sheet.

Table 1. Basic mechanical properties of DC05 steel.

Ultimate Tensile Stress R_m, MPa	Yield Stress $R_{p0.2}$, MPa	Young's Modulus E, GPa	Elongation A_{50}, %
289.1	162.5	163.2	25.9

Fig. 2. Isometric view of the topography of the DC05 steel sheet in the as-received state.

Fig. 3. The material ratio curve of DC05 sheet metal in the as-received state.

2.2. Experiment procedure
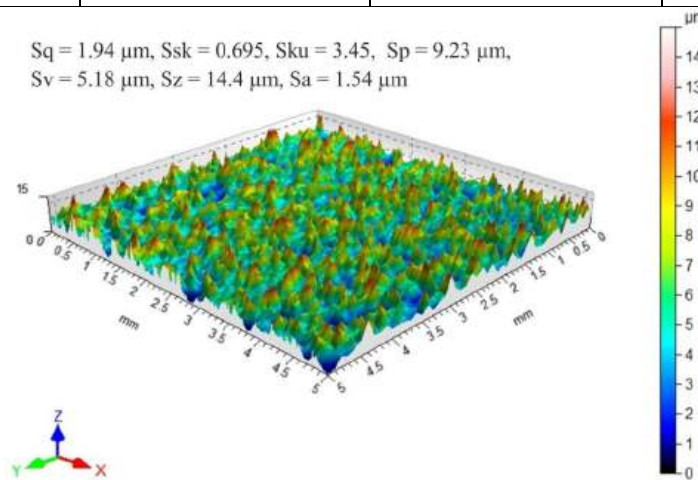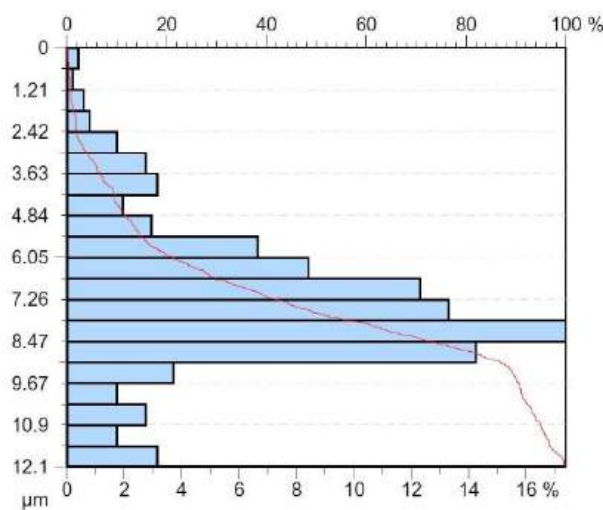
Research on the influence of process parameters such as nominal pressure, kinematic oil viscosity and lubrication pressure on coefficient of friction μ and surface quality of the finished product was carried out using a tribometer that allows to determine the COF, especially of sheet metals. The tribometer allows to simulate phenomena characteristic of the deep drawing process occurring in the area of the blankholder.

The friction tests were carried out using the test stand shown in Fig. 4. The presented test stand consisted of two measurement tracks. Measuring system of the Zwick Roell Z100 testing machine was used to recorded the force necessary to move the sheet metal strip. In turn, the second measurement track recorded the values of the clamping force, lubrication pressure and displacement of grip of tensile testing machine. The specimens for friction test were cut along the rolling direction of the sheet metal. The diagram of the test stand used in the research is shown in Fig. 5.

Fig. 4. Research stand.

Fig. 5. Diagram of the research stand.

When carrying out the strip drawing tests, variable values of the normal force were used. A Kistler force sensor type 9345B was used to measure the normal force, the value of which was selected in such a way as to correspond to the nominal pressures (p_n) of 2, 4, 6, 8 MPa. Lubrication with oils of different kinematic viscosity (η_k) values was considered. The influence of lubrication on COF and surface quality was also studied without the use of lubricant. The oils used in the tests were selected to have significantly different kinematic viscosity values, so it was decided to use two oils from the same manufacturer (Naftochem), with the commercial names S100 Plus and S300. Due to the fact that the oil manufacturer did not provide the kinematic viscosity value at the temperature at which the tests were carried out (20°C), additional tests were performed to determine the value of kinematic viscosity of oils at 20°C. The tests were carried out using an Ostwald viscometer. The kinematic viscosity of 360 mm^2/s for S100 Plus oil and 1135 mm^2/s for S300 oil was determined. Lubrication was carried out using variable oil pressure (p_o) of 0.6, 1.2, and 1.8 MPa generated using an Argo-Hytos hydraulic power unit. The values of the applied oil pressure were selected in such a way that there was no oil leakage from the contact zone.

As a result of the tests carried out using variable values of the process parameters, graphs of the changes in normal force (F_N) and the force needed to pull the sheet metal strip (F_T) were obtained (Fig. 6). The comparison of the values of these forces in accordance with the relationship presented in Fig. 6 allowed for the determination the changes in COF during the test (Fig. 7). The values of the COF for further analysis were determined as the average value from the stabilised values of forces, in accordance with the diagram shown in Fig. 7.
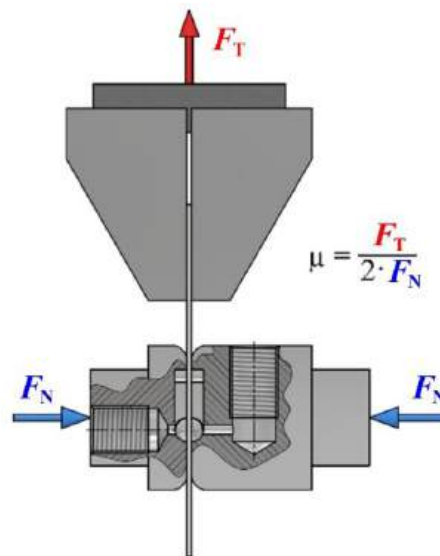

$$\mu = \frac{F_T}{2 \cdot F_N}$$

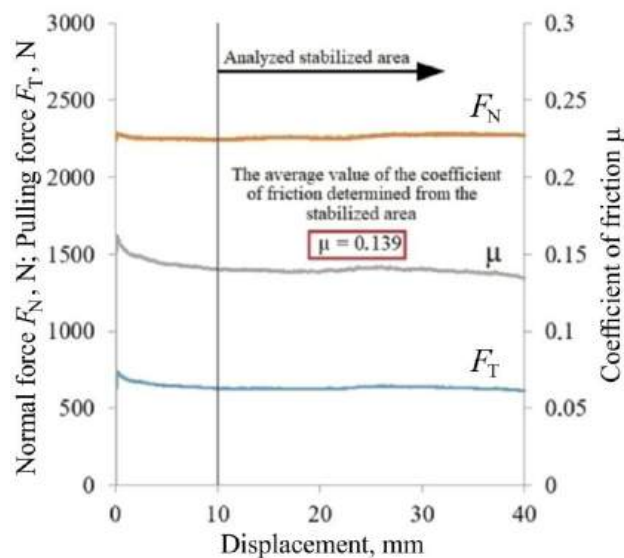**Fig. 6.** Diagram of drawing a strip of sheet metal.

Fig. 7. Change of the COF and force values during friction test (F_N = 4 MPa, p_o = 0.6 MPa, η_k = 1135 mm^2/s).

2.3. CatBoost

Categorical Boosting (CatBoost) is a sophisticated open-source programme created by Yandex researchers and engineers (Dorogush et al., 2018). Its purpose is to enhance decision tree gradients. One of its notable benefits is its ability to smoothly handle categorical data, avoiding the requirement for preprocessing or encoding such data into numbers (Ibragimov et al., 2019). In addition, CatBoost provides precise forecasts using its default settings, eliminating the need for customers to manually alter parameters (Nabipour et al., 2017). By default, CatBoost builds a total of 1000 trees. Each tree is totally symmetrical and binary, with a depth of six and two leaves. The learning rate is dynamically calculated by considering the properties of the dataset and the number of repetitions, with the goal of selecting an ideal value. Decreasing the number of iterations helps speed up the training process, but it requires increasing the learning rate for maximum performance.

3. Results and discussion

CatBoost has expertise in accurately anticipating a wide range of objectives using its default settings. The analysis demonstrated that CatBoost accurately predicted the COF, achieving R^2 values of 0.955 and 0.894 for the training and testing datasets, relative mean square error (RMSE) 0.004 and 0.005 respectively. Moreover, when it comes to predicting average roughness Sa, CatBoost demonstrated remarkable performance with R^2 values of 0.992 for the training dataset and 0.885 for the testing dataset, 0.017 and 0.053 as RMSE values respectively.

The coefficient of determination R^2 value was determined according to the following relationship (Najm & Paniti, 2023):

$$R^2 = \frac{SS_{\text{tot}} - SS_{\text{res}}}{SS_{\text{tot}}} \tag{1}$$

where SS_{tot} is the total sum of squares:

$$SS_{\text{tot}} = \sum_{i=1}^{n} \left(y_i^{\text{target}} - \bar{y}\right)^2 \tag{2}$$

$$\bar{y} = \frac{1}{n}\sum_{i=1}^{n}\left(y_i^{\text{target}}\right) \tag{3}$$

and SS_{res} is the sum of the squares of residuals:

$$SS_{\text{res}} = \sum_{i=1}^{n}\left(y_i^{\text{target}} - y_i^{\text{predict}}\right)^2 \tag{4}$$

After substituting equations (2) and (4) into equation (1), we get (Najm & Paniti, 2023):

$$R^2 = \frac{\sum_{i=1}^{n}\left(y_i^{\text{target}} - \bar{y}\right)^2 - \sum_{i=1}^{n}\left(y_i^{\text{target}} - y_i^{\text{predict}}\right)^2}{\sum_{i=1}^{n}\left(y_i^{\text{target}} - \bar{y}\right)^2} \tag{5}$$

Figures 8a and 8b illustrate the impact of each data point on the model's predictions. The X-axis displays SHAP values, representing the influence of each input features. The Y-axis depicts all the features, where red indicates high levels and blue indicates low ones. Features on the right positively impact prediction, whereas those on the left have a negative impact. Positive and negative pertain to the impact on the model's output, not its performance.
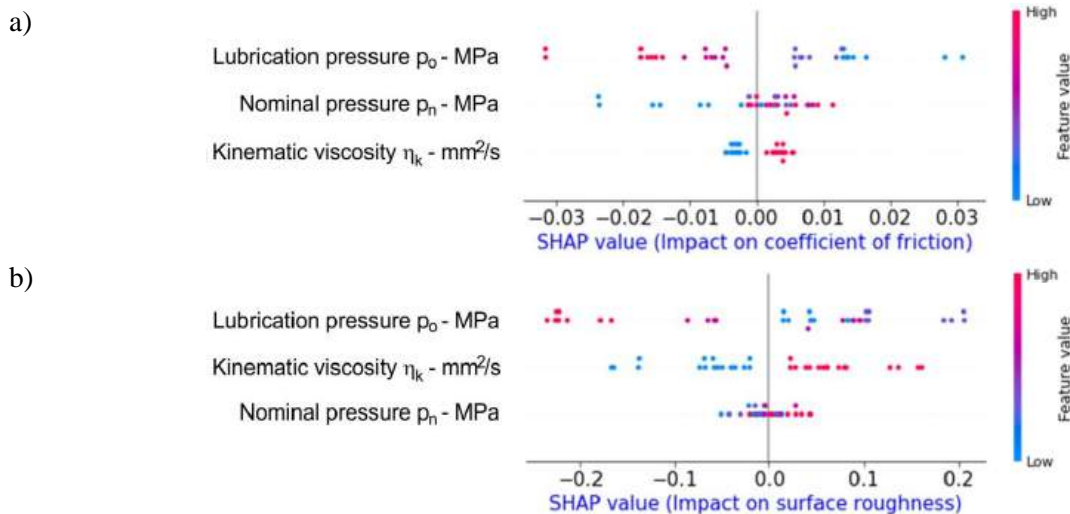

Fig. 8. Summary plot of SHAP value impact on a) coefficient of friction b) average roughness Sa.

A high lubricant pressure (depicted in red on the far left) decreases the estimated COF by about −0.03. If this attribute had not been included, the prediction would have been 0.03 or higher. The red point on the far right indicates a nominal pressure value of 0.01, implying that it lack results in a COF forecast below −0.01. The farther the distance a point is from the centre, the more significant the characteristic becomes.

Figure 9 shows the variation in SHAP values while predicting COF. Each line on the plot represents a unique model prediction. In Figure 10, the total positive feature values are presented. The representation is detailed in a SHAP decision plot (Fig. 10a), a SHAP bar plot (Fig. 10b), and SHAP force plots (Fig. 10c). The SHAP force plot offers extensive insights into the factors that have the most significant impact on the model's predictions for specific observations and displays the real values of the features.
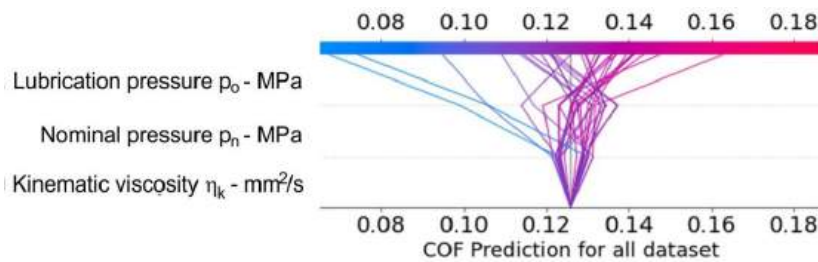
Fig. 9. All prediction values of COF using SHAP decision plot.
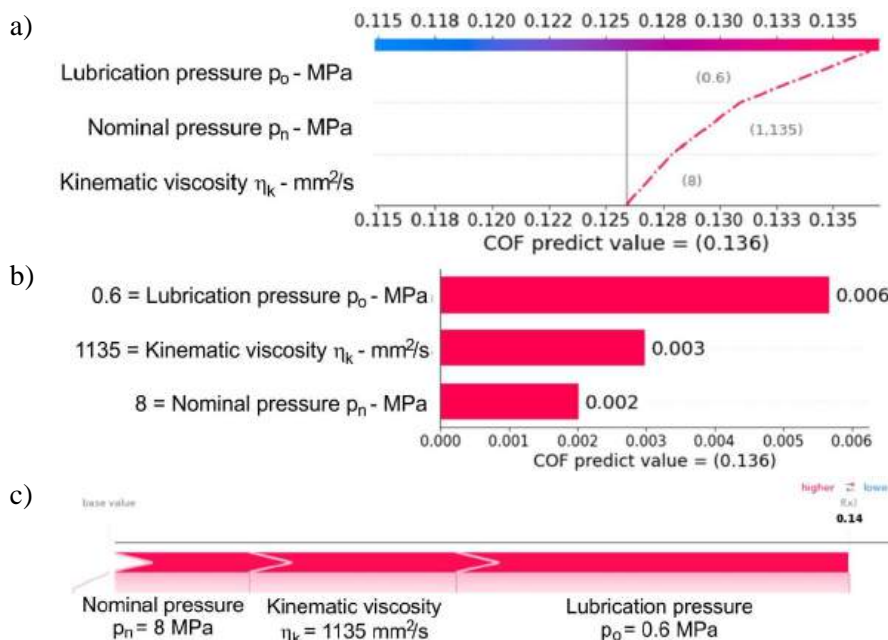
Fig. 10. Positive SHAP values using a) SHAP decision plot, b) SHAP bar plot, and c) SHAP force plot.

Figures 11 and 12 emphasise the significant factors that impact the COF and average roughness Sa, providing insights into their relative importance and how each feature influences the model's outcomes This approach evaluates the impact of each characteristic on each row of the dataset. Upon investigation, it is clear that changes in lubricant pressure significantly affect both COF and surface roughness, showing slight fluctuation. Kinematic viscosity has the most negligible impact on COF, whereas nominal pressure is the least significant factor in determining surface roughness.

Fig. 11. Relevance importance of various input factors on the coefficient of friction.

Fig. 12. Relevance importance of various input factors on the average roughness Sa.

4. Conclusions

The study used the CatBoost machine learning algorithm, created by Yandex researchers and engineers, to analyse and determine the factors affecting the coefficient of friction for three typ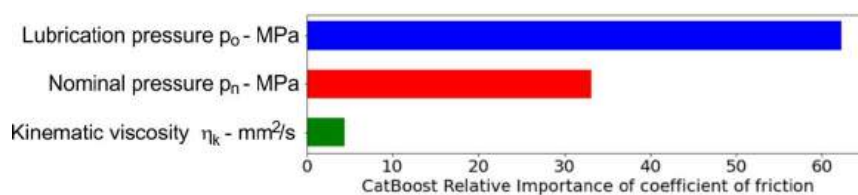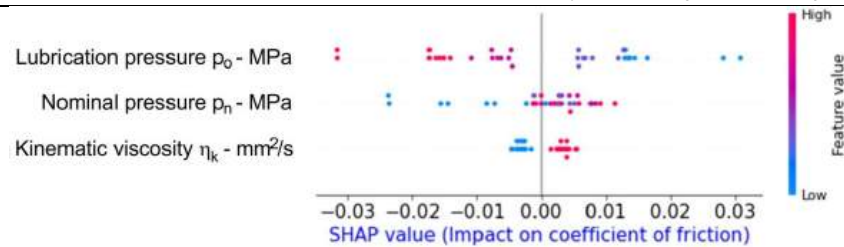es of deep-drawing quality steel sheets. The researchers visualised the COF prediction models using Shapley's decision plot, which incorporates cumulative SHAP. The study results in the following conclusions:

- CatBoost demonstrated good prediction accuracy for the coefficient of friction and average roughness, with R^2 values between 0.995 and 0.992 for the training dataset and between 0.894 and 0.895 for the testing dataset.
- This approach emphasises the uniqueness of each process condition and showcases the intricate interaction of many components, each producing varying impacts on individual results.
- The research highlights the substantial influence of variations in lubricant pressure on both COF and surface roughness, with only minor fluctuations seen. Kinematic viscosity of lubricant has the least effect on COF, whereas nominal pressure is the least important component affecting surface roughness.

References

Bang, J., Park, N., Song, J., Kim, H. G., Bae, G., & Lee, M. G. (2021). Tool wear prediction in the forming of automotive DP980 steel sheet using statistical sensitivity analysis and accelerated U-bending based wear test. *Metals*, *11*, 306. https://doi.org/10.3390/met11020306

Bay, N., Olsson, D. D., & Andreasen, J. L. (2008). Lubricant test methods for sheet metal forming. *Tribology International*, *41*, 844–853. https://doi.org/10.1016/j.triboint.2007.11.017

Carcel, A. C., Palomares, D., Rodilla, E., & Pérez Puig, M. A. (2005). Evaluation of vegetable oils as pre-lube oils for stamping. *Materials and Design*, *26*, 587–593. https://doi.org/10.1016/j.matdes.2004.08.010

Çavuşoğlu, O., Gürün, H. (2017). Statistical evaluation of the influence of temperature and surface roughness on aluminium sheet metal forming. *Transactions Famena*, *41*, 57–64. https://doi.org/10.21278/TOF.41305

Daniel, D., Guiglionda, G., Litalien, P., & Shahani R. (2006). Overview of forming and formability issues for high volume aluminium car body panels. *Materials Science Forum*, *519-521*, 795-802. https://doi.org/10.4028/www.scientific.net/MSF.519-521.795

Domitner, J., Silvayeh, Z., Shafiee Sabet, A., Öksüz, K. I., Pelcastre, L., & Hardell, J. (2021). Characterization of wear and friction between tool steel and aluminum alloys in sheet forming at room temperature. *Journal of Manufacturing Processes*, *64*, 774-784. https://doi.org/10.1016/j.jmapro.2021.02.007

Dorogush, A. V., Ershov, V., & Gulin, A. (2018). CatBoost: gradient boosting with categorical features support. http://arxiv.org/abs/1810.11363

Gali, O. A., Riahi, A. R., & Alpas, A. T. (2013). The tribological behaviour of AA5083 alloy plastically deformed at warm forming temperatures. *Wear*, *302*, 1257-1267. https://doi.org/10.1016/j.wear.2012.12.048

Groche, P., & Christiany, M., & Wu, Y. (2019). Load-dependent wear in sheet metal forming. *Wear*, *422-423*, 252-260. https://doi.org/10.1016/j.wear.2019.01.071

Guillon, O., Roizard, X., & Belliard, P. (2001). Experimental methodology to study tribological aspects of deep drawing Application to aluminium alloy sheets and tool coatings. *Tribology International*, *34*, 757–766. https://doi.org/10.1016/S0301-679X(01)00069-X

Ibragimov, B., & Gusev, G. (2019, December 8-14). *Minimal variance sampling in stochastic gradient boosting*. Proceedings of the 33rd Conference on Neural Information Processing Systems (NeurIPS 2019), Vancouver, Canada, pp. 1-11.

Kim, H., Han, S., Yan, Q., & Altan, T. (2008). Evaluation of tool materials, coatings and lubricants in forming galvanized advanced high strength steels (AHSS). *CIRP Annals*, *57*, 299–304.

https://doi.org/10.1016/j.cirp.2008.03.029

Le, H. R., & Sutcliffe, M. P. F. (2002). Measurements of friction in strip drawing under thin film lubrication. *Tribology International*, *35*, 123-128. https://doi.org/10.1016/S0301-679X(01)00104-9

Lee, B. H., Keum, Y. T., & Wagoner, R. H. (2002). Modeling of the friction caused by lubrication and surface roughness in sheet metal forming. *Journal of Materials Processing Technology*, *130-131*, 60-63. https://doi.org/10.1016/S0924-0136(02)00784-7

Masters L.G., Williams D. K., & Roy R. (2013). Friction behaviour in strip draw test of pre-stretched high strength automotive aluminium alloys. *International Journal of Machine Tools and Manufacture*, *73*, 17–24, https://doi.org/10.1016/j.ijmachtools.2013.05.002

Nabipour, M., & Keshavarz, P. (2017). Modeling surface tension of pure refrigerants using feed forward back-propagation neural networks. International journal of refrigeration, 75, 217–227. https://doi.org/10.1016/j.ijrefrig.2016.12.011

Najm, S.M., & Paniti, I. (2023). Investigation and machine learning-based prediction of parametric effects of single point incremental forming on pillow effect and wall profile of AlMn1Mg1 aluminum alloy sheets. *Journal of Intelligent Manufacturing*, *34*, 331–367. https://doi.org/10.1007/s10845-022-02026-8

Severo, V., Vilhena, L., Silva, P. N., Dias, J. P., Becker, D., Wagner, S., & Cavaleiro, A. (2009). Tribological behaviour of W–Ti–N coatings in semi-industrial strip-drawing tests. *Journal of Materials Processing Technology*, *209*, 4662–4667. https://doi.org/10.1016/j.jmatprotec.2008.11.040

Shisode, M., Hazrati, J., Mishra, T., Rooij, M., Horn, C., Beck, J., & Boogaard, T. (2021). Modelling boundary friction of coated sheets in sheet metal forming. *Tribology International*, *153*, 106554. https://doi.org/10.1016/j.triboint.2020.106554

Sigvant, M., Pilthammar, J., Hol, J., Wiebenga, J. H., Chezan, T., Carleer, B., & van den Boogaard, T. (2019). Fiction in sheet metal forming: influence of surface roughness and strain rate on sheet metal forming simulation results. *Procedia Manufacturing*, *29*, 512-519. https://doi.org/10.1016/j.promfg.2019.02.169

Szewczyk, M., & Szwajka, K. (2022). Analysis of the friction mechanisms of DC04 steel sheets in the flat strip drawing test. *Advances in Mechanical and Materials Engineering*, *94*, 51-61. https://doi.org/10.7862/rm.2022.4

Spišák, E., Majerníková, J., Duľová Spišáková, E., & Kaščák, Ľ. (2016). Analysis of plastic deformation of double reduced sheets. *Acta Mechanica et Automatica*, *10*(4), 271-274. https://doi.org/10.1515/ama-2016-0041

Trzepieciński, T., Szewczyk, M., & Szwajka, K. (2022). The use of non-edible green oils to lubricate DC04 steel sheets in sheet metal forming process. *Lubricants*, *10*, 210. https://doi.org/10.3390/lubricants10090210

Venema, J, Matthews, D. T. A., Hazrati, J., Wörmann, J. & Van den Boogaard, A. H. (2017). Friction and wear mechanisms during hot stamping of AlSi coated press hardening steel. *Wear*, *380-381*, 137-145. https://doi.org/10.1016/j.wear.2017.03.014

Wang, C., Ma, R., Zhao, J., & Zhao, J. (2017). Calculation method and experimental study of coulomb friction coefficient in sheet metal forming. *Journal of Manufacturing Processes*, *27*, 126–137. https://doi.org/10.1016/j.jmapro.2017.02.016

Żaba, K., Kuczek, Ł., Puchlerska, S., Wiewióra, M., Góral, M., & Trzepieciński, T. (2023). Analysis of tribological performance of new stamping die composite inserts using strip drawing test. *Advances in Mechanical and Materials Engineering*, *40*, 55–62. https://doi.org/10.7862/rm.2023.7

Żaba, K., Puchlerska, S., Pieja, T., & Pyzik, J. (2020). Process design for superalloys sheet rotary forming. *Materials Science Forum*, *985*, 91-96. https://doi.org/10.4028/www.scientific.net/MSF.985.91

Zastosowanie Wzbudzenia Kategorycznego do Modelowania Zachowania Tarciowego Blach Stalowych DC05 w Teście Ciągnienia Pasa Blachy

Streszczenie

Modelowanie współczynnika tarcia, chropowatości powierzchni i powiązanych procesów tribologicznych podczas kontaktu powierzchni blachy i narzędzi jest trudnym wyzwaniem ze względu na spłaszczanie, bruzdowanie i scepianie nierówności powierzchni. Podczas tworzenia modeli analitycznych ważne jest, aby ostrożnie wybierać odpowiednie parametry procesu. Zapewni to produkcję elementów formowanych z blachy spełniających wymagane standardy jakościowe i pozbawione wad. W pracy analizowano wpływ ciśnienia nominalnego, lepkości kinematycznej smaru i ciśnienia smaru na współczynnik tarcia i średnią chropowatość powierzchni blach stalowych głębokotłocznych DC05. Do wyznaczenia współczynnika tarcia wykorzystano

test przeciągania pasa blachy. W pracy tej wykorzystano algorytm uczenia maszynowego CatBoost, stworzony przez firmę Yandex, w celu oszacowania wartości współczynnika tarcia i chropowatości powierzchni. Przeprowadzono kompleksowe badania parametrów procesu tarcia. Modele przewidywania współczynnika tarcia na podstawie funkcji SHapley Additive exPlanations (SHAP) przedstawiono za pomocą wykresu decyzyjnego Shapleya. CatBoost charakteryzuje się wyjątkową dokładnością przewidywania potwierdzoną wartością R^2 w zakresie od 0.955 do 0.894 zarówno w przypadku zbiorów danych uczących, jak i testowych dla współczynnika tarcia, a także od 0.992 do 0.885 w przypadku średniej chropowatości powierzchni.

Słowa kluczowe: współczynnik tarcia, tarcie, kształtowanie blach, blacha stalowa, chropowatość powierzchni

Original Research

Frictional Characteristics of EN AW-6082 Aluminium Alloy Sheets Used in Metal Forming

Ján Slota [1,*] [iD], Ľuboš Kaščák [1] [iD], Lucian Lăzărescu [2] [iD]

[1] The Institute of Technology and Material Engineering, Faculty of Mechanical Engineering, Technical University of Košice, Mäsiarska 74, 040 01 Košice, Slovakia; lubos.kascak@tuke.sk (Ľ. Kaščák)

[2] Faculty of Industrial Engineering, Robotics and Production Management, Technical University of Cluj-Napoca, B-dul Muncii 103-105, 400641, Cluj-Napoca, Romania; lucian.lazarescu@tcm.utcluj.ro

* Correspondence: jan.slota@tuke.sk

Abstract

This article is devoted to testing EN AW-6082 aluminium alloy sheets in friction pair with NC6 (1.2063) tool steel. A special tribometer designed to simulate the friction conditions in sheet metal forming processes was used for friction testing. The research aimed to determine the influence of contact pressure, surface roughness of the tool, and lubrication conditions on the value of the coefficient of friction in the strip drawing test. Three grades of typical petroleum-based lubricants with kinematic viscosities between 21.9 and 97 mm^2/s were used in the tests. The surface morphologies of the sheet metal after the friction process were observed using a scanning electron microscope. A tendency for the coefficient of friction to decrease with increasing contact pressure was observed. LHL32 and 75W-85 oils lost their lubricating properties at a certain pressure value and with further increase in pressure, the coefficient of friction value tended to increase. The 10W-40 oil with the highest viscosity reduced the coefficient of friction more intensively than the LHL32 oil.

Keywords: EN AW-6082-T6, friction, sheet metal forming, strip drawing test

1. Introduction

A 6xxx-series Al-based alloy sheets are used for stamping aluminium profiles used in the aerospace, marine, automobile, and defence sectors (Dubey et al., 2023; Kaščák et al., 2021; Mukhopadhyay, 2012). Ensuring the desired quality of products is related to the phenomenon of friction (Tan & Liew, 2023). In each plastic forming process, there is metallic contact between the tool and the formed sheet. Apart from the phenomenon of friction, the second important problem in sheet metal forming is springback (Slota et al., 2017). Depending on the type of forming process (stamping, bending, spinning, incremental forming, etc.), there are different contact conditions, depending mainly on contact pressures (Mulidrán et al., 2023), sliding velocity (Luiz et al., 2023), temperature (Lukovic, 2019) and surface treatment (Nasake & Sakuragi, 2017).

Reducing friction can be easily achieved by using lubricants (Hol et al., 2017; Ludwig et al., 2010). Due to their widespread availability and relatively low cost, liquid oils are the most frequently used lubricants in sheet metal forming (Lachmayer et al., 2022). In addition to oils specifically intended for forming, oils intended for other purposes are also used (machine oils, hydraulic oils, gear oils, etc.). Dry film lubricants (Meiler et al., 2003) have also been developed. Understanding the phenomenon of friction in metal forming operations involves carrying out special tribological tests intended for modeling specific friction conditions in contact zone (Bay et al., 2008; Reichardt et al., 2020). For this reason, research on determining the coefficient of friction of sheet metal is somewhat limited. Chruściński et al. (2017) tested an EN AW-6060 sheet in friction pair with a countersample made of 100Cr6 steel under conditions of dry friction and titalite grease lubrication. A block-ring friction tester was used in investigations. Under lubrication conditions, a reduction in the coefficient of friction was observed by over 80% compared to dry friction conditions. Xu et al. (2018) investigated

the frictional performance of 6xxx-series aluminium alloy with various lubrication conditions in the draw bead friction test. It was found that the value of the pulling force of samples cut in the transverse direction relative to the sheet rolling direction was lower than of samples cut across the sheet rolling direction. Bellini et al. (2019) studied the effect of friction on the formability of EN AW-6060 aluminium alloy sheet. It was found that the distance between the specimen centre and the necking point effects on the friction coefficient value. Aiman and Syahrullail (2020) used the ring compression test to study the tribological performance of EN AW-6060 aluminium alloy sheets in the presence of palm oil-based lubricants and typical metal-forming lubricant. It was found that palm-oil base lubricant reduced the forming load however, its high friction lead to high surface roughness. Domitner et al. (2021) investigated friction between EN AW-6016 aluminium alloy sheets and 1.2343 tool steel using strip drawing test. They concluded that the coefficient of friction determined for as-delivered and naturally aged conditions did not differ significantly. An increase in sliding velocity resulted in a decrease in the intensity of the flattening of our asperities. Sabet et al. (2021) investigated the tribological condition of EN AW-6016-T4 aluminium alloy using the pin-on-plate test. Contact pressures between 4 and 16 MPa were considered. They found that the coefficient of friction decreased with increasing the sliding speed and the nominal contact pressure and sliding velocity. Hu et al. (2019) investigated the formation of a transfer layer between cast iron G3500 and EN AW-6082 aluminium alloy. It was concluded that the aluminium transfer increases with increasing sliding distance. Mohamed et al. (2017) studied the effect of friction on the formability of EN AW 6061-T4 aluminium alloy sheet under various lubrication conditions. The results of cup tests showed the significant effect of friction conditions on the formability of sheet metals. Reddy and Vadivuchezhian (2020) studied the effect of normal load on the coefficient of friction of EN AW-6082 aluminium alloy sheets under dry sliding conditions. The results of pin-on-disc tests revealed that the increase in wear volume resulting from an increase in normal load. Dubois et al. (2024) analysed the effect of lubrication (mineral oil, paraffin oil and mineral oil) and normal loads ranging from 5 to 600 N on the galling behaviour and coefficient of friction of EN AW-6082-T6 aluminium alloy sheets. Results of pin-on-disc tests showed the beneficial effect of liquid lubricants in limiting the galling phenomenon. Furthermore, it was found that onset of galling is sensitive to surface roughness on countersamples.

Tribological tests of the EN AW-6082 alloy under sheet metal forming conditions are limited. Therefore, this article is devoted to testing EN AW-6082 sheets in friction pair with NC6 (1.2063) tool steel. Strip drawing tests were performed using a special tribotester. The research campaign took into account various contact pressure conditions and various oils with kinematic viscosity of 21.9–97 mm^2/s.

2. Material and methods

2.1. Test material

The 1-mm-thick EN AW-6082-T6 aluminium alloy sheet used as test material. The mechanical properties of the sheets were determined three times in a uniaxial tensile test. Test samples were cut in three directions (0°, 45° and 90°) in relation to the sheet rolling direction. Three samples were tested for each condition. Selected mechanical properties are presented in Table 1. Basic surface roughness parameters of EN AW-6082-T6 sheet metal were measured using a T8000-RC (Hommel-Etamic) pro-filometer. The surface topography and bearing area curve of the workpiece surface are shown in Figs. 1a and 1b, respectively.

The values of the selected 3D roughness parameters are as follows: Sa = 0.141 μm, Sq = 0.178 μm, Sp = 0.559 μm, Sv = 0.880 μm, Sz = 1.44 μm, Sku = 3.29 and Ssk = –0.253. The morphology of surfaces of the sheet metals before and after friction testing were analysed using a scanning electron microscope (SEM). SEM micrograph of the surface of as-received sheet metal is presented in Fig. 2. The surface of the sheets is characterized by directional grooves as a result of the rolling process and surface cracks.

Table 1. Basic mechanical parameters of the test material.

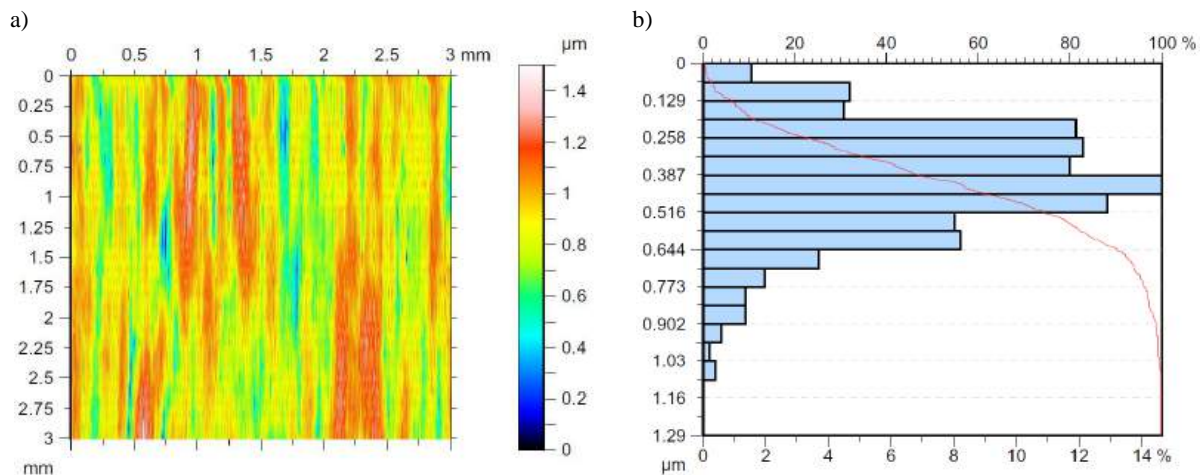| Sample orientation, °	Yield stress, MPa	Ultimate tensile stress, MPa	Elongation (A_{80}), %
0	314	342	13.7
45	307	337	14.2
90	313	341	12.0

a)

b)

Fig. 1. a) surface topography and b) bearing area curve of the sheet metal tested.
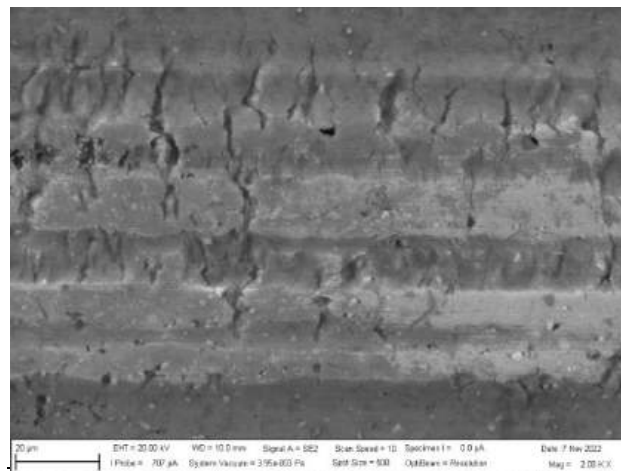
Fig. 2. SEM micrograph of the as-received EN AW-6068-T6 sheet metal.

2.2. Friction test

The tests were carried out by pulling a strip of sheet metal 240 mm long and 18 mm wide between two countersamples with a radius of rounding the working surface $R = 200$ mm. Specimens for friction test were cut along the sheet rolling direction. Sliding speed was 10 mm/min. The countersamples were made of NC6 steel (1.2063). The selected 3D roughness parameters of the countersamples are as follows: $Sa = 1.89$ μm, $Sq = 2.27$ μm, $Sp = 9.76$ μm, $Sv = 10.7$ μm, $Sz = 20.4$ μm, $Sku = 2.60$ and $Ssk = -0.585$. The surface topography and linear profilogram of the countersample surface are shown in Figs. 3 and 4, respectively.

Fig. 3. Topography of the surface of countersample.

Fig. 4. Linear profilogram of the surface of countersample.

The research tribotester (Fig. 5), the structure of which was presented by Haar (1996), was mounted in the lower gripper of the Zwick/R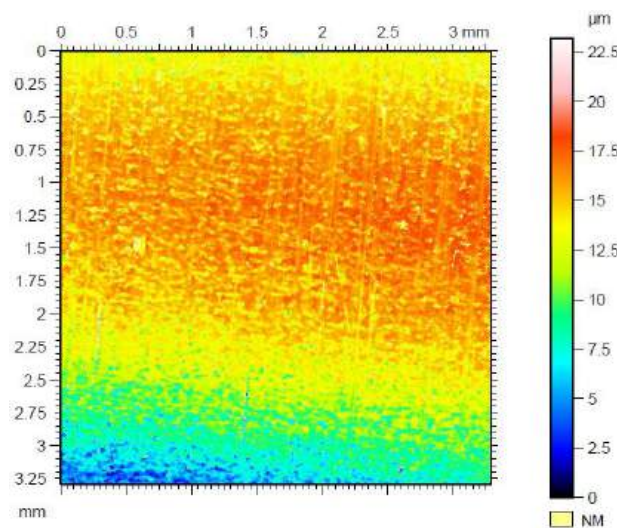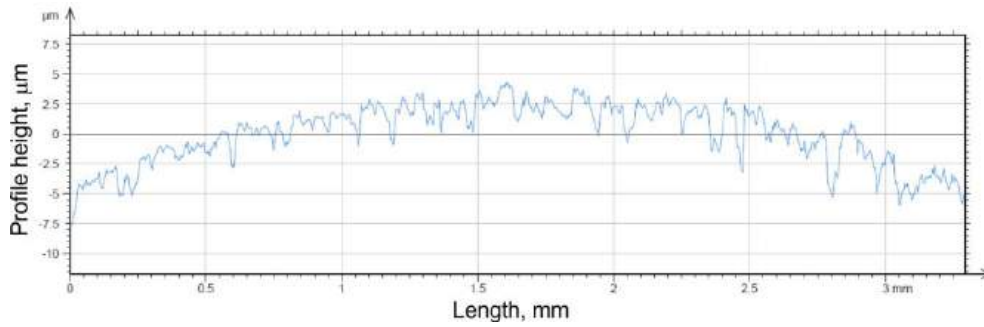oell Z100 testing machine. Meanwhile, the upper end of the sample was fixed in the upper gripper of the testing machine. The upper gripper of the testing machine can only move in the drawing direction (Fig. 5). The contact force F_N was exerted on the sample material by a spring with the known characteristic force = f(deflection). On the basis of shortening the spring length by tightening the set bolt (Fig. 5), the spring reaction force was obtained (from the force = f(deflection) characteristic), which is directly equal to F_N. Pulling force F_T was measured by the measuring system of the testing machine. Based on the values of the average friction force and the pulling force, the value of the coefficient of friction μ was determined from Eq. (1) (Jewvattanarak et al., 2016):

$$\mu = \frac{F_T}{2F_N} \tag{1}$$
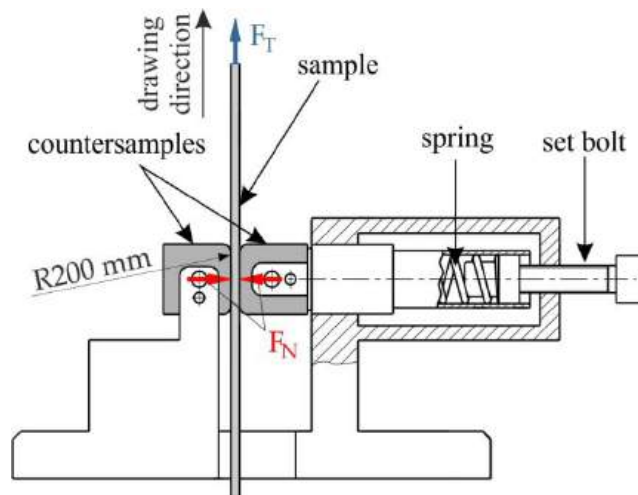
Fig. 5. Schematic diagram of the friction tribometer.

Friction tests were carried out under lubrication conditions with hydraulic oil LHL32 (kinematic viscosity 21.9 mm²/s, density 874.1 kg/m³), gear oil 75W-85 (kinematic viscosity 64.3 mm²/s, density 862.0 kg/m³) and engine oil 10W-40 (kinematic viscosity 97 mm²/s, density 870.0 kg/m³). Reference tests were performed for as-received surfaces of sheet metals. The tests assumed the value of contact pressures occurring in the blankholder zone in the deep-drawing process. Based on the values of contact forces, the average contact pressure was determined according to Eq. (2) (Haar, 1996):

$$p_{\text{mean}} = \frac{\pi}{4} \cdot \sqrt{\frac{\frac{F_N}{w} \cdot \frac{2E_1E_2}{E_2 \cdot (1-v_1^2) + E_1 \cdot (1-v_2^2)}}{2\pi R}} \tag{2}$$

where w is sample width; $E_1 = 200000$ MPa (Graba, 2020) and $E_2 = 69000$ MPa (6082-T6 Aluminum, 2023) are Young's moduli of steel countersample and sheet metal, respectively; $v_1 = 0.3$ MPa (6082-T6 Aluminum, 2023) and $v_2 = 0.33$ MPa (6082-T6 Aluminum, 2023) are Poisson's ratios of steel countersample and sheet metal, respectively.

3. Results and discussion

Figure 6 shows the influence of contact pressure on the coefficient of friction of the tested sheets. In the conditions of testing the sheet in the as-received state, a tendency was observed for the coefficient of friction to decrease from 0.28 for a contact pressure of 4.4 MPa to 0.24 for a contact pressure of 11.7 MPa. The tendency for the coefficient of friction to decrease with increasing contact pressure is the result of the non-linear relationship between the friction force and the contact force. A similar relationship was previously observed by Dou and Xia (2019), Sabet et al. (2021) and Xia et al. (2022). At low pressures, the dominant phenomenon is the flattening of the summits of the sheet metal asperities (Fig. 7) by the surface of the countersamples.
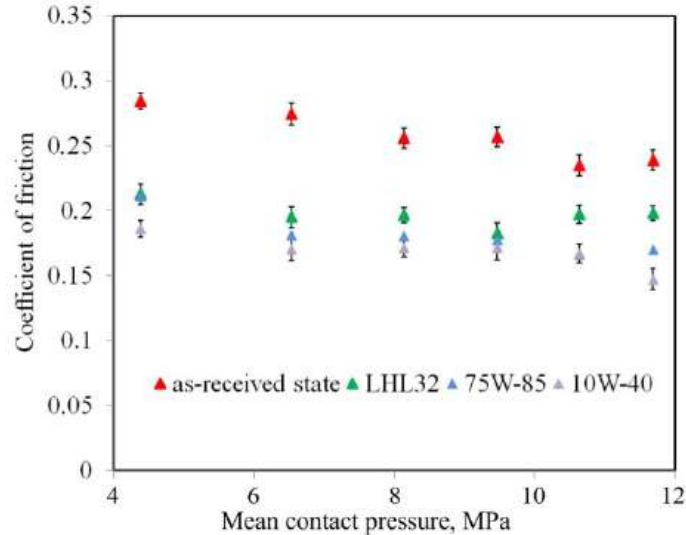

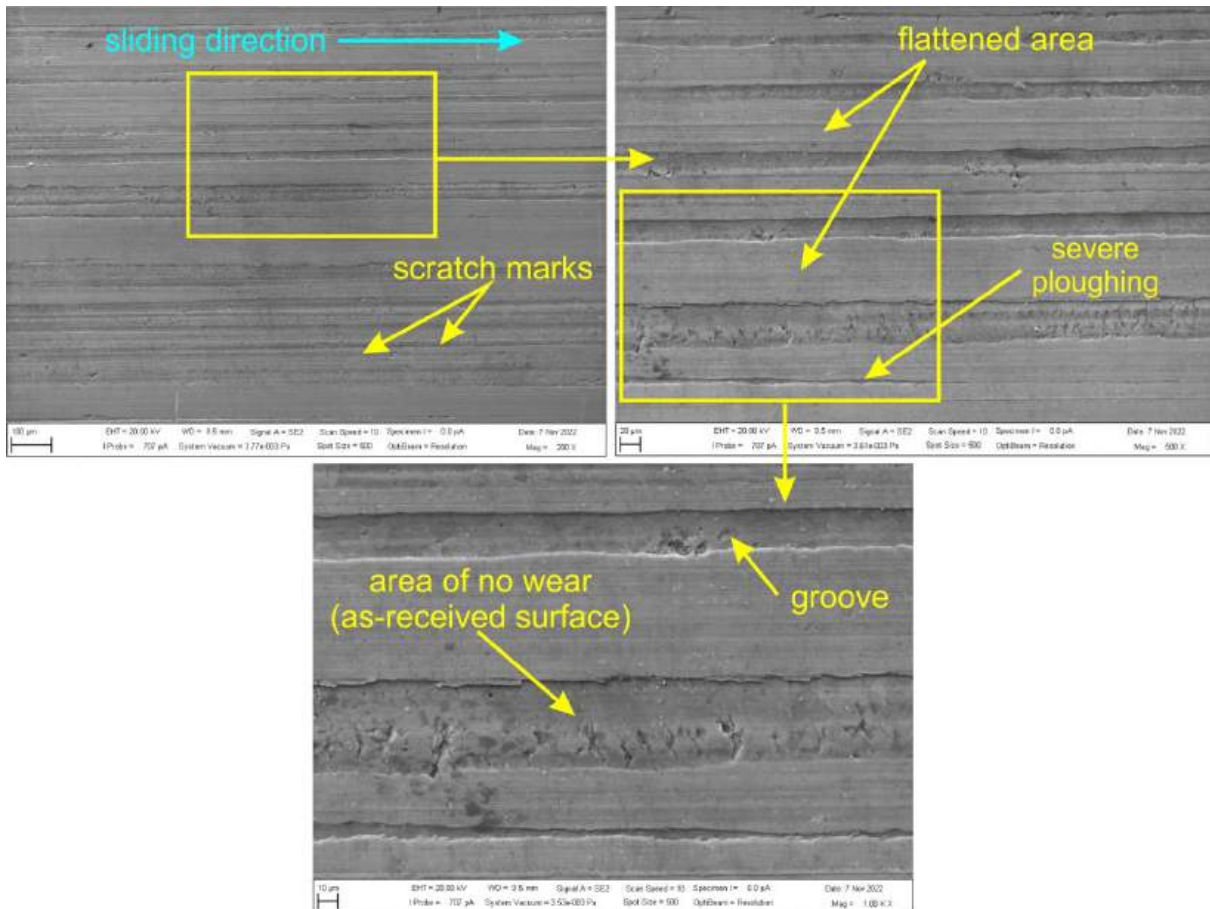**Fig. 6.** Effect of mean contact pressure on the coefficient of friction.

Fig. 7. View of the sheet metal surface after friction test (no lubrication, contact pressure 11.69 MPa).

Under lubrication conditions with LHL32 and 75W-85 oils, the coefficient of friction also tends to decrease with increasing pressure, but only up to a certain value of contact pressure, beyond which it tends to increase. However, when lubricating the sheet metal surface with 10W-40 oil, the value of the coefficient of friction decreases over the entire pressure range. Under lubricated conditions, friction occurs due to two mechanisms.

When the pressure is increased, the contact of the surface asperities intensifies, so that under unfavorable conditions a ploughing phenomenon may occur (Fig. 7). At the same time, greater contact pressure increases the pressure of the lubricant located in the valleys of surface asperities. Friction therefore results from the interaction of many mechanisms at the same time. Under lubricated conditions, the flattening phenomenon as a result of plastic deformation of the surface asperities under the influence of contact pressure was also observed (Fig. 8).

From the trend lines, it can be concluded that the 10W-40 oil provided the lowest coefficient of friction (Fig. 6). There is a clear influence of viscosity on the coefficient of friction. The higher the viscosity of the oil, the lower the coefficient of friction. It is also visible that under certain pressure during lubrication with LHL32 and 75W-85 oils, the lubricant film was broken, leading to an increase in the coefficient of friction. The 10W-40 oil with a higher viscosity than LHL32 and 75W-85 oils shows good lubricating properties in the entire range of pressures tested.
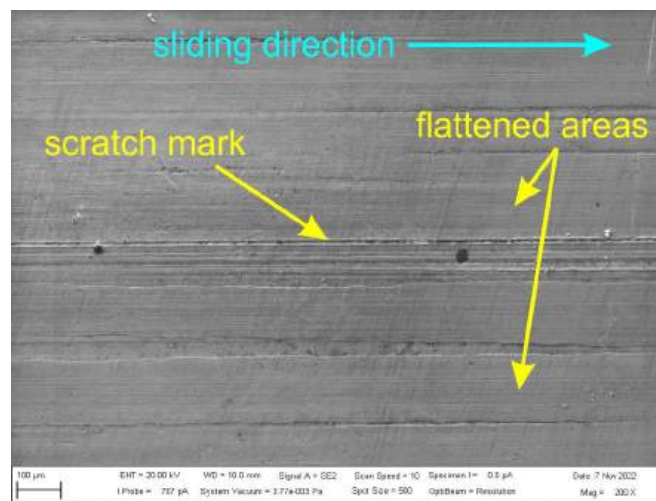

Fig. 8. View of the sheet metal surface after friction test (LHL32 lubricant, contact pressure 10.63 MPa).

An additional parameter, effectiveness of lubrication (EoL), was introduced to quantitatively assess the effect of lubrication on the coefficient of friction:

$$\text{EoL} = \left(1 - \left(\frac{\mu(\text{lubricated conditions})}{\mu(\text{dry friction})} \right) \right) \cdot 100\% \tag{3}$$

LHL32 oil shows a tendency to decrease lubrication efficiency with increasing contact pressure, although the lowest lubrication efficiency occurs for contact pressures in the range between 10.63 and 11.69 MPa (Fig. 9). Pressures of this value clearly led to the breakdown of the lubricating film and the intensification of the metallic interaction of the rubbing surfaces. It should be noted that LHL32 oil was characterized by the lowest value of kinematic viscosity. The lubrication efficiency of LHL32, 75W-85 and 10W-40 oils in the entire range of analyzed pressures is between 16.1 and 29%, between 25.8 and 34.1% and between 28.9 and 34.6%, respectively. At contact pressures between 10.63 and 11.69 MPa, 75W-85 and 10W-40 oils provided almost twice the EoL index. 75W-85 and 10W40 oils initially show an increased EoL index and then decrease to a minimum value of approximately 30 %. This is typical behaviour observed when rubbing a soft sheet metal and a hard tool. The continuous evolution of the surface topography produces a specific surface topography with valleys in which the lubricant is located. The increase in the EoL index for the 10W-40 grease under contact pressures of 11.69 MPa can be explained by the appropriate viscosity of the oil, which allowed the creation of a pressure cushion separating the rubbing surfaces.
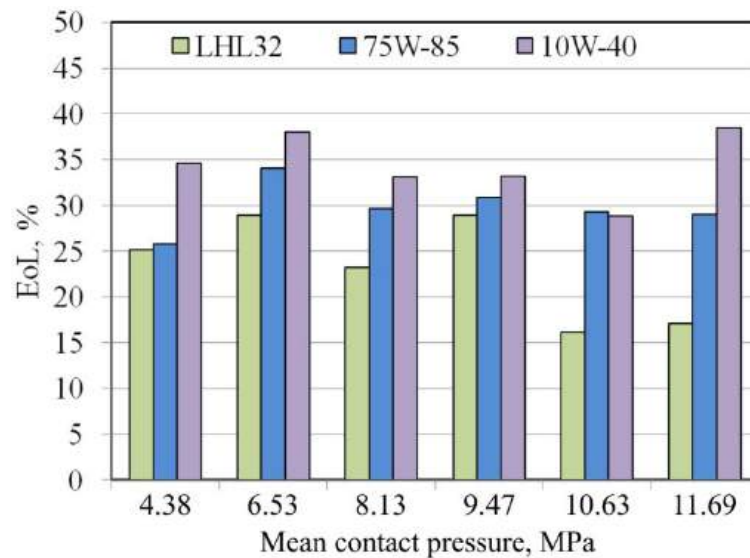
Fig. 9. Effect of mean contact pressure on the EoL index.

4. Conclusions

As a result of the friction tests carried out on the EN AW-6082-T6 sheets using the strip drawing test, a tendency for the coefficient of friction to decrease with the increase in contact pressure was observed. The values of the coefficient of friction of the sheets in the as-received state varied in the range between 0.235 and 0.284 for the considered range of contact pressures between 4.38 and 11.69 MPa. Under lubricated conditions with LHL32 and 75W-85 oils, the coefficient of friction also tends to decrease with increasing contact pressure, but only up to a certain value of contact pressure, beyond which it tends to increase (LHL32) or stabilise (75W-85). In the case of 10W-40 oil, which has the highest viscosity, it was found that the coefficient of friction decreased in the entire range of pressures considered. The basic friction mechanism observed during experimental tests was flattening the surface asperities of sheet metal as a result of plastic deformation. The as-received sheet metal showed longitudinal grooves resulting from the manufacturing process. As a result of the friction process, the bottoms of these grooves remained unchangeable, providing spaces containing lubricant. LHL32 oil showed the lowest EoL index between 16.1 and 29 % depending on the contact pressure.

The conducted research inspired the authors to expand the investigations to a wide range of contact pressures in the future. Sheets made of aluminium alloys are prone to seizing. It is also necessary to check the friction conditions for various sheet metal-tool material combinations. Another unexplored area is the influence of temperature generated in the contact zone on the friction behaviour of the sheet metal surface. There is a really limited number of articles published in this area.

Acknowledgments

References

6082-T6 Aluminum. (2023, January 10) https://www.makeitfrom.com/material-properties/6082-T6-Aluminum
Aiman, Y., & Syahrullail, S. (2020, July 13). Ring compression test of aluminum alloy AA6061 using palm mid olein as a metal forming lubricant. Proceedings of Mechanical Engineering Research Day MERD'22, (pp. 272-276). UTeM Press.

Bay, N., Olsson, D. D., & Andreasen J. L. (2008). Lubricant test methods for sheet metal forming. *Tribology International*, *41*(9-10), 844–853. https://doi.org/10.1016/j.triboint.2007.11.017

Bellini, C., Giuliano, G., & Sorrentino, L. (2019). Friction influence on the AA6060 aluminium alloy formability. *Frattura ed Integrità Strutturale*, *49*, 791–799. http://dx.doi.org/10.3221/IGF-ESIS.49.70

Chruściński, M., Wielowiejska-Giertuga, A., Garbiec, D., Rubach, R., & Ziółkiewicz, S. (2017). Badania tribologiczne materiałów przeznaczonych na elementy łożysk tocznych. *Obróbka Plastyczna Metali*, *4*, 239–250.

Domitner, J., Silvayeh, Z., Sabet, A. S., Öksüz, K. I., Pelcastre, L., & Hardell, J. (2021). Characterization of wear and friction between tool steel and aluminum alloys in sheet forming at room temperature. *Journal of Manufacturing Processes*, *64*, 774–784. https://doi.org/10.1016/j.jmapro.2021.02.007

Dou, S., & Xia, J. (2019). Analysis of sheet metal forming (stamping process): A study of the variable friction coefficient on 5052 aluminum alloy. *Metals*, *9*(8), Article 853. https://doi.org/10.3390/met9080853

Dubey, R., Jayagantham, R., Ruan, D., Gupta, N. K., Jones, N., & Velmurugan R. (2023). Energy absorption and dynamic behaviour of 6xxx series aluminium alloys: A review. *International Journal of Impact Engineering*, *172*, Article 104397. https://doi.org/10.1016/j.ijimpeng.2022.104397

Dubois, A., Filali, O., & Dubar, L. (2024). Effect of roughness, contact pressure and lubrication on the onset of galling of the 6082 aluminium alloy in cold forming, a numerical approach. *Wear*, *536-537*, 205179. https://doi.org/10.1016/j.wear.2023.205179

Graba, M. (2020). Characteristics of selected measures of stress triaxiality near the crack tip for 145Cr6 steel - 3D issues for stationary cracks. *Open Engineering*, *10*(1), 571–585. https://doi.org/10.1515/eng-2020-0042

Haar, R. (1996). Friction in sheet metal forming, the influence of (local) contact conditions and deformation [Doctoral dissertation, Universiteit Twente]. Universiteit Twente Repository. https://ris.utwente.nl/ws/portalfiles/portal/6079817/thesis_R_ter_Haar.pdf

Hol, J., Wiebenga, J. H., & Carleer, B. (2017). Friction and lubrication modelling in sheet metal forming: Influence of lubrication amount, tool roughness and sheet coating on product quality. *Journal of Physics: Conference Series*, *896*, Article 012026. https://doi.org/10.1088/1742-6596/896/1/012026

Hu, Y., Zheng, Y., Politis, D. J., Masen, M. A., Cui, J., & Wang L. (2019). Development of an interactive friction model to predict aluminum transfer in a pin-on-disc sliding system. *Tribology International*, *130*, 216–228. https://doi.org/10.1016/j.triboint.2018.08.034

Jewvattanarak, P., Mahayotsanun, N., Mahabunphachai, S., Ngernbamrung, S., & Dohda, K. (2016). Tribological effects of chlorine-free lubricant in strip drawing of advanced high strength steel. *Proceedings of the Institution of Mechanical Engineers, Part J: Journal of Engineering Tribology*, *230*(8), 974–982. https://doi.org/10.1177/1350650115622366

Kaščák, Ľ., Cmorej, D., Spišák, E., & Slota, J. (2021). Joining the high-strength steel sheets used in car body production. *Advances in Science and Technology Research Journal*, *15*(1), 184–196. https://doi.org/10.12913/22998624/131739

Lachmayer, R., Behrens, B. A., Ehlers, T., Müller, P., Althaus, P., Oel, M., Farahmand, E., Gembarski, P. C., Wester, H., & Hübner, S. (2022). Process-integrated lubrication in sheet metal forming. *Journal of Manufacturing and Materials Processing*, *6*(5), Article 121. https://doi.org/10.3390/jmmp6050121

Ludwig, M., Müller, C., & Groche, P. (2010). Simulation of dynamic lubricant effects in sheet metal forming processes. *Key Engineering Materials*, *438*, 171–178. https://doi.org/10.4028/www.scientific.net/KEM.438.171

Luiz, V. D., Santos, A. J. D., Câmara, M. A., & Rodrigues, P. C. D. M. (2023). Influence of different contact conditions on friction properties of AISI 430 steel sheet with deep drawing quality. *Coatings*, *13*(4), Article 771. https://doi.org/10.3390/coatings13040771

Lukovic, M. (2019). The influence of surface temperature on the coefficient of static friction. *The Physics Teacher*, *57*, 636–638. https://doi.org/10.1119/1.5135798

Meiler, M., Pfestorf, M., Geiger, M., & Merklein, M. (2003). The use of dry film lubricants in aluminum sheet metal forming. *Wear*, *255*(7-12), 1455–1462. https://doi.org/10.1016/S0043-1648(03)00087-5

Mohamed, M., Farouk, M., Elsayed, A., Shazly, M., & Hezagy, A. (2017). An investigation of friction effect on formability of AA 6061-T4 sheet during cold forming condition. *AIP Conference Proceedings*, *1896*, Article 080025. https://doi.org/10.1063/1.5008105

Mukhopadhyay, P. (2012). Alloy designation, processing, and use of AA6xxxx series aluminium alloys. *International Scholarly Research Notices*, *2012*, Article 165082. https://doi.org/10.5402/2012/165082

Mulidrán, P.; Spišák, E.; Tomáš, M.; Majerníková, J.; Bidulská, J.; & Bidulský, R. (2023). Impact of blank holding force and friction on springback and its prediction of a hat-shaped part made of dual-phase steel. *Materials*, *16*(2), Article 811. https://doi.org/10.3390/ma16020811

Nasake, T., & Sakuragi, K. (2017). Surface treatment of aluminium alloy for tribological applications. *KYB Technical Review*, *55*, 18–24.

Onuseit, V., Umlauf, G., Reichle, P., Barz, J. P., Tovar, G., & Hirth, T. (2020). Tribological system for cold sheet metal forming based on volatile lubricants and laser structured surfaces. *Dry Metal Forming Open Access Journal*, *6*, 128–165. https://doi.org/10.26092/elib/156

Reddy, I. S., & Vadivuchezhian, K. (2020). Sliding of various ductile materials (Al 6061, Al 6082) using pin on disc setup. *Materials Today: Proceedings*, *27*, 2688–2692. https://doi.org/10.1016/j.matpr.2019.11.248

Reichardt, G., Wörz, C., Singer, M., Liewald, M., Henn, M., Förster, D. J., Zahedi, E., Boley, S., Feuer, A., Onuseit, V., Weber, R., Graf, T., Umlauf, G., Reichle, P., Barz, J.P., Tovar, G., & Hirth, T. (2020). Tribological system for cold sheet metal forming based on volatile lubricants and laser structured surfaces. *Dry Metal Forming Open Access Journal*, *6*, 128-165. https://doi.org/10.26092/elib/156

Sabet, A. S., Domitner, J., Öksüz, K. I., Hodžić, E., Torres, H., Ripol, M. R., & Sammitsch, C. (2021). Tribological investigations on aluminum alloys at different contact conditions for simulation of deep drawing processes. *Journal of Manufacturing Processes*, *68*, 546–557. https://doi.org/10.1016/j.jmapro.2021.05.050

Slota, J., Šiser, M. & Dvorák, M. (2017). Experimental and numerical analysis of springback behavior of aluminum alloys. *Strength of Materials*, *49*, 565–574. https://doi.org/10.1007/s11223-017-9900-6

Tan, J. L., & Liew, K. W. (2023). Tribological behaviour and microstructure of an aluminium alloy-based g-SiC hybrid surface composite produced by FSP. *Lubricants*, *11*(3), Article 124. https://doi.org/10.3390/lubricants11030124

Xia, J., Zhao, J., & Dou, S. (2022). Friction characteristics analysis of symmetric aluminum alloy parts in warm forming process. *Symmetry*, *14*(1), Article 166. https://doi.org/10.3390/sym14010166

Xu, W., Gao, X., Zhang, B., Yang, L., Du, C., Zhou, D., Rawya, B., & Szymanski, M. (2018). Study on frictional behavior of AA 6XXX with three lube conditions in sheet metal forming. *SAE Technical Paper*, 2018-01–0810. https://doi.org/10.4271/2018-01-0810

Charakterystyka Tarciowa Blach ze Stopu Aluminium EN AW-6082 Stosowanych w Obróbce Plastycznej Metali

Streszczenie

Artykuł poświęcony jest badaniom tarciowym blach ze stopu aluminium EN AW-6082 w parze ciernej ze stalą narzędziową NC6 (1.2063). Do badań tarcia wykorzystano specjalny tribotester przeznaczony do symulacji warunków tarcia w procesach kształtowania blach. Celem badań było określenie wpływu nacisku kontaktowego, chropowatości powierzchni narzędzia i warunków smarowania na wartość współczynnika tarcia w próbie ciągnienia pasa blachy. Do badań wykorzystano trzy gatunki typowych smarów na bazie ropy naftowej o lepkości kinematycznej od 21,9 do 97 mm^2/s. Morfologię powierzchni blach po procesie tarcia obserwowano za pomocą skaningowego mikroskopu elektronowego. Zaobserwowano tendencję do zmniejszania się wartości współczynnika tarcia wraz ze wzrostem nacisku kontaktowego. Oleje LHL32 i 75W-85 przy określonej wartości nacisku kontaktowego traciły swoje właściwości smarne i wraz z dalszym wzrostem nacisku zaobserwowano zwiększanie się wartości współczynnika tarcia. Olej 10W-40 o najwyższej lepkości kinematycznej zapewnił większe zmniejszenie wartości współczynnika tarcia niż olej LHL32.

Słowa kluczowe: AW-6082-T6, tarcie, kształtowanie blach, test przeciągania pasa blachy

Original Research

Implementation of Technology for High-Performance Milling of Aluminum Alloys Using Innovative Tools and Tooling

Robert Ostrowski [1]* , **Marcin Szpunar [2]** , **Piotr Myśliwiec [1]** ,
Marek Zwolak [1] , **Marek Bujny [3]**

[1] Department of Materials Forming and Processing, Faculty of Mechanical Engineering and Aeronautics, Rzeszów University of Technology, al. Powstancow Warszawy 8, 35-959 Rzeszow, Poland; p.mysliwiec@prz.edu.pl (P. Myśliwiec), m.zwolak@prz.edu.pl (M. Zwolak)

[2] Doctoral School of the Rzeszów University of Technology, al. Powstancow Warszawy 12, 35-959 Rzeszow, Poland; d547@stud.prz.edu.pl

[3] Ultratech sp. z o.o., Fabryczna 4A, 39-120 Sedziszow Malopolski, Poland; m.bujny@ultratech.pl

* Correspondence: rostrows@prz.edu.pl

Abstract

The research described in the concerns the development and implementation of new clamping technologies used in machining, particularly for thin-walled structural components of aircraft and helicopters. Among other things, the performance of the Schunk Vero-S Aviation clamping system in machining landing gear beams from 7075 T6 aluminum alloy was analyzed, resulting in significant increases in production efficiency and improvements in the geometric quality of machined parts. During experimental research and implementation testing, special chucks were used on the Schunk Vero-S Aviation system for machining the chassis beam. The results showed an improvement in the quality and accuracy of machined parts compared to traditional clamping methods. Increased production efficiency by minimizing scrap and significantly better surface quality and geometric properties compared to conventional clamping. These studies were conducted as part of a project by Ultratech Sp. z o.o. which was implementing a project co-financed by European Funds "Development and implementation of an innovative clamping method for milling processing of thin-walled structural elements of helicopters and airplanes".

Keywords: non-rigid parts, thin-walled element, titanium and aluminium alloys, high-performance milling

1. Introduction

Proper semi-finished product selection for aircraft structural elements significantly affects the further technological process, including the efficiency. It is characteristic that in the field of lightweight alloys processing there is a tendency to simplify the design of semi-finished geometry products to reduce material usage. It is also common for technological processes to produce a product which weight of the finished element does not exceed 5% of weight of a semi-finished product (Cichosz, 2022). To reduce the cost of total part production, the time needed to prepare the semi-finished product is minimized due to of increase of the machining process performance from solid material (Oczoś & Kawalec, 2012).

Machine tools, cutting tools, process parameters and the type of fixtures objects play a significant role in this process (Zawada-Michałowska & Kuczmaszewski, 2020). Clamping technology in high-performance machining plays a very important role in the comprehensive optimization of process chains. It determines the times of auxiliary processes, enables the implementation of these processes and influences the quality of the workpiece. The current research evaluates three different reference
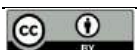
strategies in horizontal process chains and discusses the impact of fixture dynamics on workpieces. To achieve optimal performance in the parts supply chain, optimizing solutions for securing products during milling is crucial (Aurrekoetxea et al., 2022).

Important in the case of machining high-silicon silumins is to consider wear of applied cutting tools. The durability of tools, especially in automated machining on numerically controlled machine tools, mostly concerns elements used in the automotive industry (Pieśko & Kuczmaszewski, 2022). When machining high-silicon silumin alloys, tools with blades made of super-hard materials are used in this case - polycrystalline diamond due to its resistance to abrasive wear. For machining applications of 7075 aluminum alloys, in most cases fine-grained sintered carbide tools with appropriate coatings or polished flutes and appropriate cutting-edge microgeometry are used. The use of tools with PCD inserts for machining low-silicon aluminum alloys used in aerospace applications is intended to increase the efficiency of the cutting process by increasing the cutting speed and feed and improving the surface quality after machining (Ostrowski et al., 2013). The study presents a strategy for processing thin-walled elements.

The cutting process causes many technique problems, such as surface deformations and stresses, leading to increased production costs and extended production time. Various anti-vibration methods were used to avoid deterioration of the geometric quality of the surface and surface roughness. To minimize shape deviations and surface roughness, the machining strategy, cutting speed, cutting parameters, including feed per tooth and cutting depth, were optimized. These actions are aimed at reducing the cutting force perpendicular component to the machined surface, which is crucial for the quality of the final product (Bałon et al., 2017).

Many studies have been published on the selection of appropriate cutting parameters to avoid vibrations and a key aspect of high-performance machining is the transfer of this process into a digital space - Virtual MACHINING. Optimization and selection of parameters to create a digital twin of the process is a way cheaper solution not only because of the price of materials for prototype testing but also because of the use of costly machines for this purpose. The virtual machining system can be used independently or as an integral part of advanced CAM systems such as Siemens NX. The study presents an overview and example applications of a virtual high-performance machining system used in the aviation industry (Altintas, 2016).

Latest researches focus on developing methods and strategies that increase the precision of machining, minimizing deformations of thin-walled products and improving fastening technologies to prevent negative impacts of the production process on the final shape of products. These improvements are crucial for the final products to meet the stringent requirements of the aerospace industry. The problem mainly depends on the positioning of the coordinate system from which the next machining process is started. The published works provides a systematic review of cutting technologies for Aerospace Thin-Walled Components (ATWCs), including advanced tooling technology, prediction and control (or suppression) of machined surface integrity, deformation and cutting vibrations, as well as the use of Digital Twin (DT) technology in this process (Li et al., 2024).

Optimization requires dealing with references in the clamping and machining process. Performance aims for data consistency, providing a quick way to establish the defined relative positions of a workpiece in machining space at every stage of its production process. During designing the fastening of elements, a very important is to take into account the deformations of the processed products. The development of intelligent instrumentation that enables to critical process conditions identification, decrease impact of errors or compensation to minimize of defective parts was the subject of the work of a German team, as part of the European research project INTEFIX (2013). One of the milestones of the work concerned the development of instrumentation for identifying and actively limiting vibrations during milling of thin-walled elements. The next stage was related to compensation of workpiece distortions that occur during machining of large, thin-walled structural elements (Möhring & Wiederkehr, 2016).

Studies show that jigs and fixtures are key manufacturing equipment, fulfilling the tasks of positioning, supporting and fastening processed or joined components. A presentation of the current state of the concept of devices and fixtures, their categorization and an overview of their development over the last decade is described in the publication of the work of the WZL and RWTH Aachen University in Germany team (Fiedler et al., 2024).

Often, after machining of an element from semi-finished block e.g. aluminium alloy, it gets deformed after disassembly from the handle or devices. In practice, inception the technological process of production this type of parts is associated with a large number of operations, machining stages and

the use of various methods of releasing material stress, which inevitably arise during the removal of the allowance. It is economically unprofitable to use modern machining centers when the processing and setting time is lengthy due to conventional devices usage, which causes processes to be very expensive. Therefore, consideration must be given to the selection of clamping systems and the application of clamping force to the workpiece. Schunk Vero-S Aviation is a specialized system used in the aviation industry for mounting thin-walled, easily deformable parts during machining and assembly (Schiess Vero-S Aviation, 2020).

. This system enables rapid and precise part clamping that allows cycle times reduction and improved accuracy in machining. Schunk Vero-S Aviation offers many different clamping solutions to suit different types of elements. This system uses advanced techniques related to the zero-point concept, which allows for quick and easy exchange of parts. The Schunk Vero-S Aviation system includes elements such as mounting plates, processing tables, mounting screws, as well as various types of mounting tools and accessories. This system is valued in the aviation industry due to its reliability and high quality of workmanship.

In this work, an industrial implementation of Schunk Vero-S Aviation system is presented. This fixture system was selected as a replacement for conventional fixture types such as wedges, clamps, screws. To meet product requirements and reduce general part deformations a strategy of part machining was also taken into account.

2. Experimental

In accordance with the experimental plan, implementation tests were carried out on special product mounting fixtures based on the Schunk Vero-S Aviation system, intended for machining chassis beam parts made of 7075 T6 aluminium alloy, characterized by significant deformations during the conventional milling process. As a result of using this system, an increase in production efficiency and significantly better quality and geometric accuracy compared to traditional clamping were achieved. For example, let us consider the technological process of producing a sensitive part - a chassis beam made of 7075 T6 aluminium alloy at Ultratech, which has significant deformations when processed in a traditional way from a frame.

The Schunk Vero-S Aviation system was used as a clamping system. The main goal was to minimize part deformations during machining, increase cutting performance, efficiency and production costs reduction for one of the major parts of the aircraft - the landing gear beam. In the conventional technological process, the elements were attached directly to the machine table using clamps (Fig. 1). After machining the contour and shape with material removal of up to 4 mm, the cutting process was stopped, the stresses were released - the product was deformed, and the clamps were moved, after which the cutting process was continued. The aim of the test was to develop a clamping method of the product by attaching the parts using 9 modules (Fig. 2).

Machining was simulated in Siemens NX CAD/CAM software by selecting contour machining strategies. The parameters of the process as well as the tools were selected according to previous tests performed on the machine realizing the project.
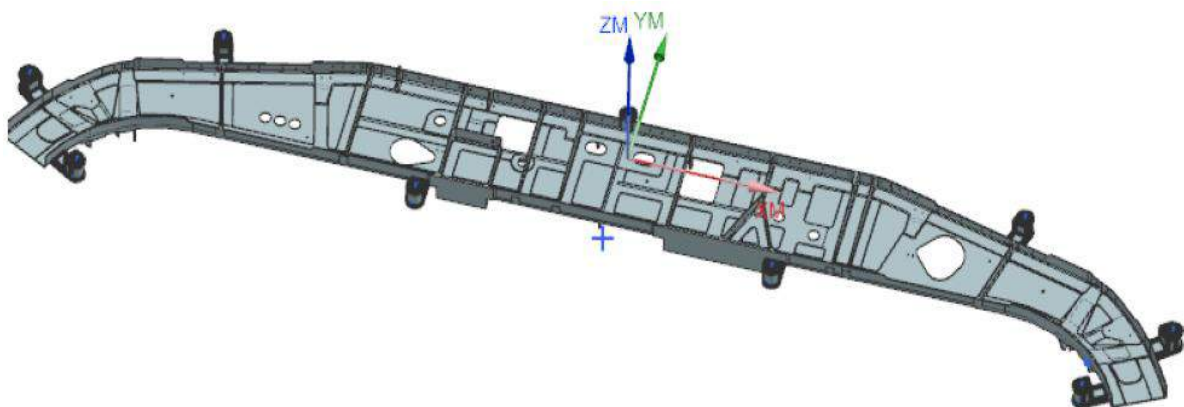

Fig. 1. CAD model of the manufactured part – traditional fixture method.
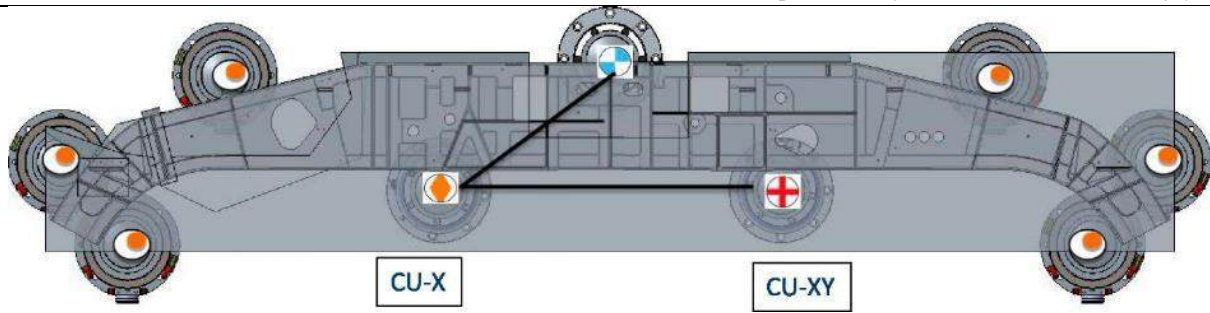
Fig. 2. Developed method of mounting beam-type parts using 9 mounting modules.

3. Results and Discussion

3.1 Comparison of fixture types

Highly efficient milling of thin-walled structural elements made of aluminum alloys using Schunk Vero-S Aviation equipment and lesser extent is a new approach to the production of these parts by milling processes. The use of this technology cannot be compared to milling in special devices or with vices enabling multi-sided milling. Because the first solution is a typical solution for the aviation and space industries solving inter-operational problems of part deformation resulting from the impact of the tool on the workpiece and the release of stresses resulting from the processes of producing semi-finished products. Compared to the current technology used at Ultratech company, we obtained a gain in changeover time of over 30% from the use of these devices (Table 1). In standard processing technology, in order to obtain the flatness of an element of the type presented in the article, the number of reinforcements was 4 and the time of a single changeover was up to 1 hour (setting the piece, using washers, measurements). When producing 2 pieces per month of a given element, in this case this beam, the cost of retooling is relatively high compared to the time required to produce the product individually. Application of Schunk Vero-S Aviation enables reduction of changeovers by up to 30%, using this flexible system, the loosening of the element is automatic and the measurement is made using a probe on a CNC machine. Schunk flexible chuck milling technology solves one of the biggest problems, which is eliminating the risk of human error. Manufacturing such a beam in accordance with tolerances and permissible deformations requires extensive experience of the operator and his cooperation with a CNC programming technologist. In the current traditional method, when retooling an element, the operator should follow the guidelines of the CAM programmer who included the beam fastening elements in his software to avoid collisions during high-performance milling.

Table 1. Benchmarking of used fixture equipment.

Parameter	Detail	Conventional (reference)	Schunk Vero-S1 Aviation
Comparison of unit times (including auxiliary times)	Reduction of changeover time	0%	−70%
Time for a single inter-operation changeover		About 1 hour	Approx. 5 minutes
Automatic loosening of elements and adjustment of the device		No	Yes
Elimination of deficiencies due to instrument	Shortage indicator	About 5%	Less than 1%
Elimination of human errors		No	Yes
Universal solution	Applicable to various products	No	Yes
Reducing the time that it takes for a product to enter the market	Save time and cost in instrument design and manufacturing	4 weeks - 128 hours - average equipment cost 20,000 for a 2.4 meters beam	Yes

Deformations at reference points

Comparison of quality indicators (deformations at reference points and the selected roughness parameter) of machining using traditional clamps - holders and Schunk Vero-S Aviation elements (for the same conditions and machining strategies performed at Ultratech):

1. Traditional clamps.
   Single deformations at the reference points were significant, reaching total values of up to 10 mm. Large deformations are the result of the lack of adequate stabilization and compensation of residual stresses during the machining process, which results in distortions of the finished parts. The allowance for this beam is 3 mm, so in order to produce an element in accordance with the standard, a lot of time must be spent on retooling (adjusting the device and fastening the deformed part for the next operation).
2. Schunk Vero-S Aviation.
   Deformations were minimal, between 0.15 and 1.46 mm, which is half the product approval tolerance. The Schunk Vero-S Aviation system, thanks to advanced clamping technology and stress compensation strategies, effectively reduces deformations, ensuring high machining precision.

Selected roughness parameter (Ra)

Measuring surface roughness after roughing is pointless because chip-breaking tools are used. Surface roughness is measured after finishing machining, where there is no such cutting resistance and machining is less efficient but provides a higher surface quality.

1. Traditional clamps.
   The average roughness parameter (Ra) was approximately 3.2 µm. Higher surface roughness may be the result of unstable mounting and suboptimal processing conditions, which affects the quality of the surface finish.
2. Schunk Vero-S Aviation.
   The average roughness parameter (Ra) was approximately 1.6 µm. Lower roughness indicates better surface finish quality, which is the result of stable fixture and optimized machining strategy, enabling more accurate and controlled surface machining.

The influence of tool vibrations and oscillations

In the case of this type of products, the surface roughness is not as important as the traces of tool vibrations. The main problem when milling aluminum alloys are vibrations of the tool, which affect the quality of the surface finish and may lead to undesirable deformations and reduced machining precision.

1. Traditional clamps.
   Significant tool scatters and vibration led to visible marks on the surface, which negatively affected the quality of the finish and required additional finishing operations.
2. Schunk Vero-S Aviation.
   Reducing vibrations and oscillations of the tool thanks to a more stable mounting allowed for better quality surfaces, minimizing the need for additional finishing operations and improving overall machining precision.

The use of the Schunk Vero-S Aviation system significantly improves the quality of machining by reducing deformation and minimizing traces of tool vibrations (Table 2), which is a key problem when milling aluminum alloys. Thanks to modern technological solutions, it is possible to achieve higher precision, quality of processing and reduced defects, which translates into better quality of finished products and efficiency of the production process.

Table 2. Fixture selection effect on key indicators for machined parts.

Indicator	Conventional	Schunk Vero-S Aviation
Deformations at the reference points of the product measured after complete machining	Up to 10 mm	Below 1.5 mm
Ra – surface roughness parameter	Average 3.2 µm	Average 1.6 µm
Traces of vibrations	Significant	Not significant

The main features of the tooling and milling technology in Schunk Vero-S Aviation holders are as follows:

1) Up to 95% of the metal volume is removed at the lowest possible number of settings.
2) Compensation of thermal expansion of workpieces and internal stresses without the use of washers and clamps, and at the same time eliminating human errors and related costs.
3) Positioning repeatability between roughing, finishing and control passes.

4) A new technological machining process that significantly reduces the time required for setting   and milling elements.

The instrumentation can be adapted to changes in the shapes of individual products very quickly and while keeping the basics intact - bases, zero points, without making expensive adjustments or adapting existing ones.

3.2 Machining details with Schunk Vero-S Aviation

Roughing was performed by milling in two operations (OP10, OP20). Finishing was performed on a specially designed vacuum device due to the very thin bottom of the product - 1.5 mm in the center of the part. The total height of the blank was 114 mm.

3.2.1. Fixture 1 - Milling operation OP10

The completed semi-finished product and the prepared fastening elements were mounted on a FIDIA multi-axis CNC machine (Fig. 3). OP10 machining programs were created in the Siemens NX CAM system and a test element was machined then measurements were made using a measurement probe on a CNC machine. The element was measured at individual points marked in the technical drawings.

Fig. 3. Developed method of mounting the blank on a CNC machine in OP10.

Milling strategy:
1) Pre-milling 20 mm from the upper reference surface:
   tool $\varnothing$20 mm, R = 3 mm - S-Carb APR-3 Kyocera SGS Precision Tools,
   v_c =1380 m/min, f_z = 0.08 mm/tooth,
   Stress release - loosening fasteners.
2) Pre-milling 20 mm of the outer contour:
   tool $\varnothing$20 mm, R = 3 mm - S-Carb APR-3 Kyocera SGS Precision Tools,
   v_c = 1380 m/min, f_z = 0.08 mm/tooth,
   Stress release - loosening fasteners.
3) Pre-milling of 47 mm pocket and contour:
   tool $\varnothing$20 mm, R = 3 mm - S-Carb APR-3 Kyocera SGS Precision Tools,
   v_c = 1380 m/min, f_z = 0.08 mm/tooth,
   Stress release - loosening fasteners.
4) Pre-milling 20 mm of the outer contour:
   tool $\varnothing$20 mm, R = 3 mm - S-Carb APR-3 Kyocera SGS Precision Tools,
   v_c = 1380 m/min, f_z = 0.08 mm/tooth,

A 6 mm of material was left on the outer contour (an allowance), without cutting the contour along its entire height (Fig. 4).

The measurements were made using an workpiece probe in the spots indicated in the Fig. 5, at points M1 and M2, after each milling operation and releasing the handles (1-4). The measurement results are presented in Table 3. The results were summed up to give the final dimension of the element's deformation from the reference point in the Z axis of the machine tool.

Fig. 4. Milling test performed on the CNC machine - operation OP10.

Fig. 5. Scheme of mounting the element in a side view and measuring the height of the element on the machine tool - after the OP10 operation at points M1 and M2.

Table 3. Results of element deviations in individual cuts after OP10 operation.

Measurement step	Measurement value at point M1, mm	Measurement value at point M2, mm
1	0.31	0.42
2	0.25	0.38
3	0.78	0.8
4	0	0
Total	1.34	1.6

3.2.2. Fixture 2 - Milling operation OP20

Figure 6 presents mounting for OP20. For this purpose, machining programs were created in the Siemens NX CAM system and a test element was machined while measurements were made using a workpiece probe on a CNC machine. The element was measured at individual points marked in the technical drawings.

Fig. 6. Developed method of mounting an element on a CNC machine in OP20.

Milling strategy:

1) Pre-milling 25 mm from the upper reference surface:
   tool ⌀20 mm, R = 3 mm - S-Carb APR-3 KYOCERA SGS Precision Tools,
   v_c = 1380 m/min, f_z = 0.12 mm/tooth,
   Relieving stress - loosening fasteners

2) Pre-milling 22 mm of pocket and contour:
   tool ⌀20 mm, R = 3 mm - S-Carb APR-3 KYOCERA SGS Precision Tools,
   v_c = 1380 m/min, f_z = 0.12 mm/tooth,
   Stress release - loosening fasteners.

3) Pre-milling 20 mm of the outer contour:
   tool ⌀20 mm, R = 3 mm - S-Carb APR-3 KYOCERA SGS Precision Tools,
   v_c = 1380 m/min, f_z = 0.12 mm/tooth,
   Stress release - loosening fasteners.

4) Pre-milling of a 20 mm pocket:
   tool ⌀20 mm, R = 3 mm - S-Carb APR-3 KYOCERA SGS Precision Tools,
   v_c = 1380 m/min, f_z = 0.12 mm/tooth,
   Stress release - loosening fasteners, zero-point shift + 3 mm.

5) Finish milling 3 mm from the product contour:
   Tool ⌀12 mm, R = 3.2 mm - S-Carb APF-3 KYOCERA SGS Precision Tools,
   v_c = 600 m/min, f_z = 0.08 mm/tooth,
   Stress release - loosening fasteners.

6) Finish milling 1 mm from the product contour:
   tool ⌀12 mm, R = 3.2 mm - S-Carb APF-3 KYOCERA SGS Precision Tools,
   v_c = 600 m/min, f_z = 0.08 mm/tooth,
   Stress release – zero-point shift +1 mm.

The finished part in operator OP20 (Fig. 7) has been submitted for verification. The measurement was made using a workpiece probe in the places indicated in the diagram below (Fig. 8), at point M1 and M2, after each milling operation and releasing the handles (1-6). Measurement step 7 was to completely release the piece from the holders. The measurement results are presented in Table 4. The results were summed up to give the final dimension of the element's deformation from the reference point in the Z axis of the machine tool.
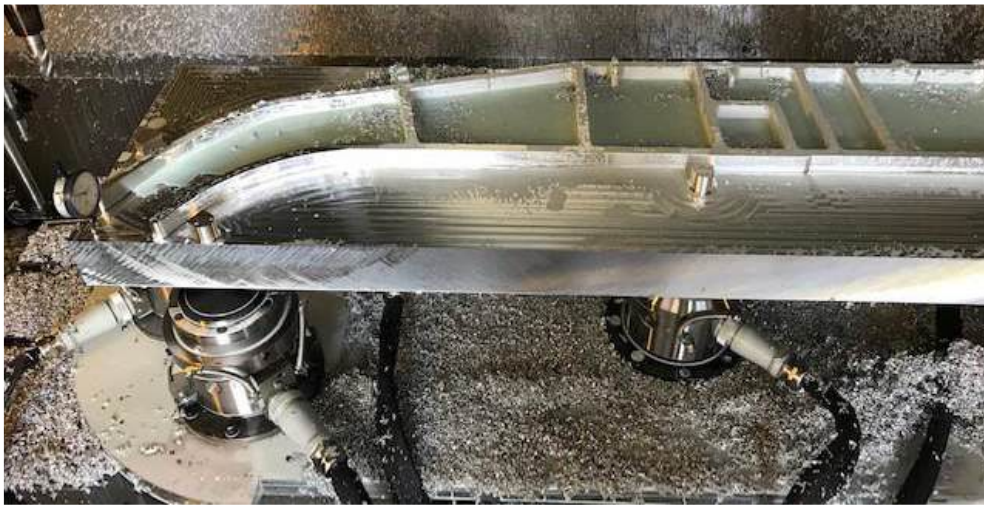

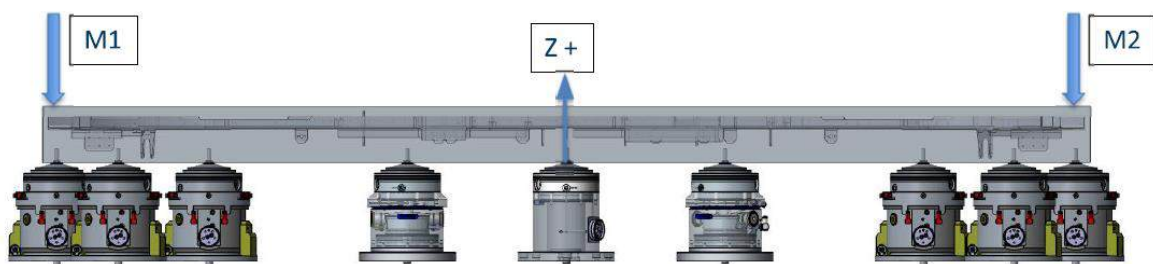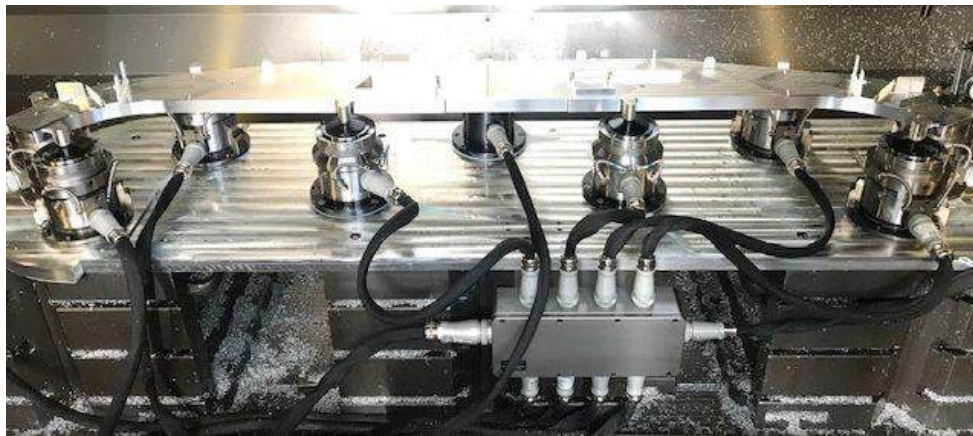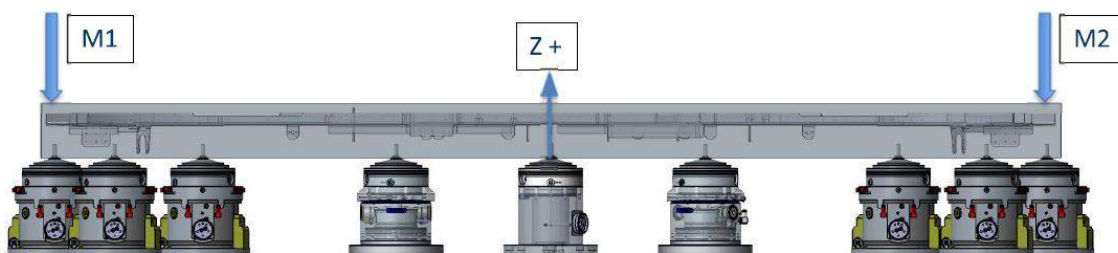**Fig. 7.** Milling test performed on the CNC machine - operation OP20.

Fig. 8. Scheme of mounting the element in a side view and measuring the height of the element on the machine tool - after the OP20 operation at points M1 and M2.

Table 4. Results of element deviations in individual cuts of OP20 operation.

Measuring step	Measurement value at point M1, mm	Measurement value at point M2, mm
1	0.39	0.79
2	3.7	4.45
3	0.05	0.4
4	1.4	1.85
5	0.75	0.45
6	1.1	0.9
7	0.8	0.8
Total	8.19	9.64

The purpose of the measurement was not to control the dimensions of the part, but to check whether the value of deformation (product deformation) after the machining operation would not be greater than the allowance left for the next operation - machining. The measurement is made only in the Z axis, because in this case the most important thing is to maintain the wall thickness at the bottom. In the event of a deformation greater than the expected allowance after rough machining, subsequent machining, after loosening the fasteners and allowing the product to deform, will lead to piercing/milling of the bottom of the structural element and will result in part being a scrap.

3.2.3. Fixture 3 - Milling operation OP30

For the third operation (OP30), the element was mounted as shown in Fig. 9. OP30 machining programs were created in the Siemens NX CAM system. The test part was manufactured and then measured with a workpiece probe on the CNC machine. The element was measured at individual points marked in the technical drawings. The element was mounted on a specially designed vacuum jig.
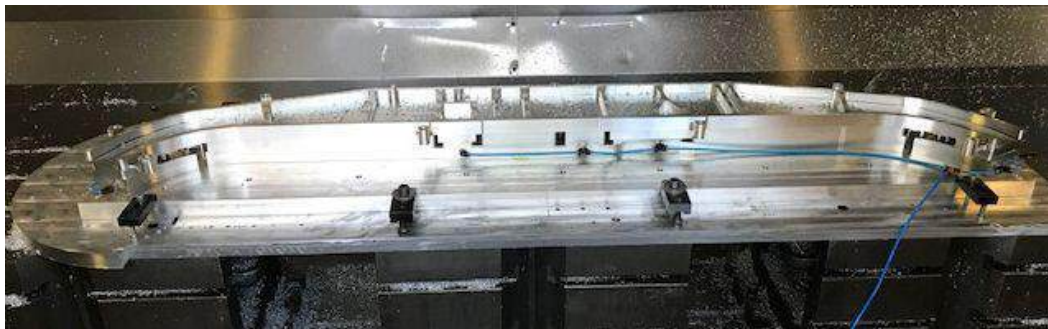
Fig. 9. A developed method of mounting an element on a CNC machine in OP30.

3.2.4. Finish milling strategy

Finishing contour milling in just a few steps. Since the OP30 was performed on a vacuum jig, the details of the subsequent operations were not described, as this was the finishing of the product and it did not have such an impact on the deformation of the product. For finishing operations, cylindrical face mills were used in the diameter range from 20 mm to 8 mm, depending on the geometry of the model (radius of rounding of the product).

After unfastening the mounting clamps (standard claws), the part (Figs. 10 and 11) was deformed by approximately 1 mm in the Z axis. Finally, the achieved part deformation was measured (Fig. 12) and deviations met the range of requirements, 3 mm tolerance band.

Fig. 10. View of toolpaths finish milling operations performed on a vacuum fixture in NX CAD/CAM.

Fig. 11. Machined part by the CNC machine - operation OP30 - side view of the element.

Fig. 12. Final measurement results of manufactured part after unclamping from the fixture.

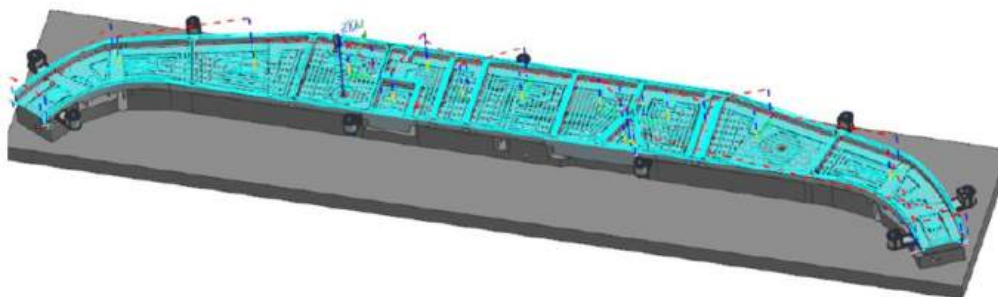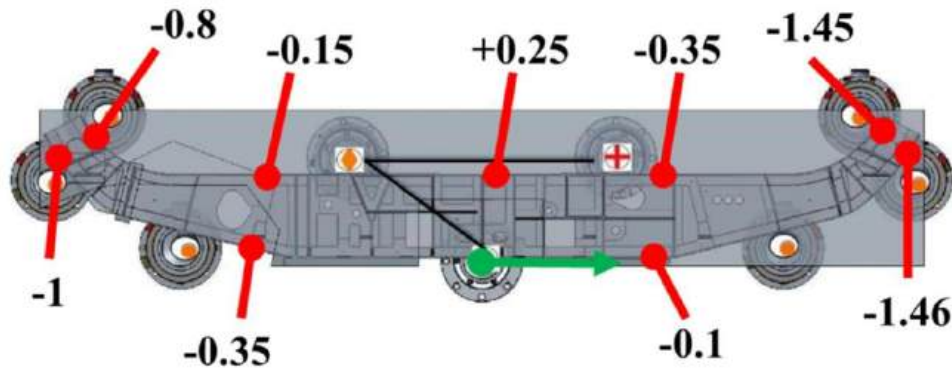The proposed Schunk Vero-S Aviation mounting system significantly contributes to achieving acceptable results by reducing deformation, reducing oscillations and vibrations, optimizing the machining process, improving roughness parameters and reducing production costs. These benefits translate into higher quality and efficiency in the production of unstable aluminum parts, meeting the requirements of the modern aerospace industry and other industries requiring precision machining.

In standard milling with positioned workpiece using special devices such as a frame or clamps (to have access to the processing of both sides of the part), after complete milling and removing the element from the device, the element is deformed, and the deformations reach up to several millimeters or centimeters depending on the dimensions product (beam) ranging from 0.5 to several meters. In most cases, due to the lack of experience of the manufacturing team, the milled product does not pass quality control. Due to costs, this element is stretched, bent and straightened to meet the acceptance requirements, but this must require the recipient's acceptance. As this element is a structural element, assembled by hand using riveting techniques, slight deformations are allowed for this 2.4 meter long beam tested, with a maximum deformation of 3 mm allowed, assuming that installers are able to fasten and adjust the element by hand during installation usually riveting process. Multi-axis high-performance milling technologies are also used in vices, gripping the base of an aluminum block, which is connected to the product using additional bridges cut off in the final operation. Due to the local mounting of the product in relation to the frame, the entire product is deformed, which causes subsequent operations to mill the deformed product according to the CAM program - a 3D model that does not take into account its deformation, thus causing a shortage. There is research on predicting these deformations and adapting appropriate 3D models to perform the technological process in a CAM system. Unfortunately, changing 3D models in this way is very complicated. The tested solution does this automatically, loosening the product between operations, giving it free to deform. Finishing was performed on an element that is no longer subject to further deformation.

Machining techniques and the technological history of semi-finished products influence the deformations of thin-walled elements made of aluminum alloy after milling. Milling in the direction perpendicular to the rolling direction results in larger deformations than milling in the parallel direction (Zawada-Michałowska et al., 2020a). The initial residual stress in the blank is a major factor leading to machining deformation, and uneven milling during the machining process, caused by the variation in local cutting depth resulting in uneven material removal thickness, contributes to machining deformation (Zheng et al., 2023).

Avoiding deformation in aluminum elements can be achieved through the optimization of milling parameters, selection of appropriate milling strategies, and control of machining conditions. Analysis of the influence of milling parameters on milling forces, milling temperature, and machining deformation has shown that the optimized milling parameters are able to be determined, which significantly

reduce machining deformation and improve the machining quality of thin-walled parts (Yang et al., 2022). It was found that post-machining deformation of thin-walled elements can be minimized by using a selected milling strategy and its combination with pre-machining (or lack thereof) (Zawada-Michałowska et al., 2020b). The other results indicates that post-deformation annealing to increase ductility suggests a potential approach for minimizing deformation (Zrník et al., 2014).

4. Summary

In the current scientific publication, the key was to analyze in detail the occurrence of deformations during the machining process of thin-walled structural component. Deformations of approximately 1.6 mm were observed in OP10 operation and identified to be as expected and considered acceptable. This happens due to the stresses of the part caused by the forces, which are typical to roughing operations when machining this kind of thin-walled part. Additionally, the direction of the shift was consistent with the predictions, which confirms the correctness of the machining strategy used at this stage.

Much greater challenges were encountered when milling the other side of the part, where deformations of 9 mm in one direction were observed. Such a large deviation from the predicted values was not expected and indicates potential problems with the milling process, which may require further analysis and technological optimization. A deviation of 9 mm is the total value of individual deviations in each milling operation in the OP20 fixture. The analysis requires looking at individual milling operations, i.e. machining parameters and the resulting deformation of the part. The solution to these situations is either to reduce the machining parameters of cutting speed and feed, which will adversely affect the machining time, or to increase the allowance remaining for subsequent milling operations. Increasing the allowance will increase the thickness of the product, which may reduce its deformation. After the third operation (OP30) was measured and the deformation values of the entire product were given and are within its manufacturing tolerance of 3 millimeters. The fact that the element was partially deformed during individual operations and the handle adapted to the deformed element and was reattached, after which it was processed. This value of 9 mm is the predictable total deformation value of the element in the event that we did not loosen the handles for subsequent operations and the handles did not adapt to this part.

In operation OP20, which included the finishing process, further deformation and movement of the component was observed. This type of movement occurring during the finishing stage is usually undesirable as it can significantly affect the quality of the final product. Normal process conditions should not lead to any displacement, so these results suggest that there is a need to review and potentially revise both the clamping method and the machining process parameters. Tests showed that the fastening system was operated close to the limits of its maximum movement capabilities (+/- 6 mm). In response to this, an additional pad was added for the pin extensions, which increased the Z-direction movement capabilities on the four 3D modules at the end of the part. This step was necessary to provide greater flexibility and precision in the final stages of machining.

The main purpose of using the proposed Schunk Vero-S Aviation fastening system was to minimize the deformation of the product after processing in individual operations. The measurement results of the final product after operation OP30 confirm the advisability of this use. Traditional fastening methods often lead to significant deformations, which results in parts failing quality control and requiring costly and labor-intensive manual corrections. The Schunk Vero-S Aviation system is designed to provide a more stable fixture that allows parts to move freely between operations, minimizing stress accumulation and reducing deviation, resulting in higher machining precision and better-quality finished products. The purpose of this test was to show how large element deviations can be during high-performance milling of thin-walled structural elements. Despite the deviations between operations, thanks to this system which adapted to the deformed product and stabilized it by appropriately fixing it for further operations.

Thanks to the use of this system, we avoided to achieve scrap part which can be caused by the fact that the thickness of the bottom of the beam was 1.5 millimeters, and after milling and measuring the product, analyzing the allowances left, we came to the conclusion that it was necessary to shift the coordinate system for NC code for the workpiece on CNC machines to maintain this thickness of the bottom of the beam. Hence, in the second operation OP20 there is an entry about shifting the zero (coordinate system) by one millimeter.

5. Conclusions and feature prospects

The experiments performed show that both the tools and cutting parameters were appropriately selected and did not negatively affect the deformation of the parts. This indicates their application in the context of the processing methods used in CAM software for thin-walled parts. These results highlight the importance of continuously monitoring and adapting machining techniques and fastening methods to minimize the risk of deformation and ensure high quality of final products, especially in the context of demanding industrial production.

The most important point for the future of component production is to reduce the deformation in the OP20 operation and allow the part to move more freely in the OP10 operation.

- Process the material as much as possible in OP10, one of the keys one's points will be to machine the outer contour along the entire height of the board in OP10 was recommended.
- Quality check of the raw material - semi-finished product.

An alternative strategy option could be to machine the part in 4 operations:

- OP10 - milling of the first side (clamping side for vacuum equipment) and complete outer contour throughout,
- OP20 - milling the second side with an allowance of 5-6 mm,
- OP30 - finishing the first side of the part on VERO-S Aviation,
- OP40 - finishing the other side on the special fixing vacuum jig.

Acknowledgments

References

Altintas, Y. (2016). Virtual high performance machining. *Procedia CIRP*, *46*, 372–378. https://doi.org/10.1016/j.procir.2016.04.154

Aurrekoetxea, M., Llanos, I., Zelaieta, O., & de Lacalle, L. N. L. (2022) Towards advanced prediction and control of machining distortion: a comprehensive review. *International Journal of Advanced Manufacturing Technology*, *122*, 2823–2848. https://doi.org/10.1007/s00170-022-10087-5

Bałon, P., Rejman, E., Smusz, R., & Kiełbasa, B. (2017). Obróbka z wysokimi prędkościami skrawania cienkościennych konstrukcji lotniczych. *Mechanik, 8-9,* 726-729. https://doi.org/10.17814/mechanik.2017.8-9.105

Cichosz, P. (2022) *Nowoczesne procesy obróbki skrawaniem*. Wydawnictwo Naukowe PWN.

Fiedler, F., Ehrenstein, J., Höltgen, C., Blondrath, A., Schaper, L., Göppert, A., & Schmitt, R. (2024). Jigs and fixtures in production: A systematic literature review. *Journal of Manufacturing Systems*, *72*, 373–405. https://doi.org/10.1016/j.jmsy.2023.10.006

INTEFIX (2013). INTElligent FIXtures for the manufacturing of low rigidity components. Grant agreement ID: 609306.

Li, Z., Zeng, Z., Yang, Y., Ouyang, Z., Ding, P., Sun, J., & Zhu, S. (2024). Research progress in machining technology of aerospace thin-walled components. *Journal of Manufacturing Processes*, *119*, 463-482. https://doi.org/10.1016/j.jmapro.2024.03.111

Möhring, H. C., & Wiederkehr, P. (2016). Intelligent fixtures for high performance machining. *Procedia CIRP*, *46*, 383-390. https://doi.org/10.1016/j.procir.2016.04.042

Oczoś, K. E., & Kawalec, A. (2012). *Kształtowanie metali lekkich*. Wydawnictwo Naukowe PWN.

Ostrowski, R., Tyczyński, P., & Śliwa, R. (2013, November 5-7). Development of tools with blades based on diamond materials for the aviation industry AIRTEC 2013 - 8th International Conference „Supply on the wings" Frankfurt, Germany.

Pieśko, P., & Kuczmaszewski, J. (2022), *Obróbka elementów cienkościennych narzędziami o obniżonej sztywności*. Wydawnictwo Politechniki Lubelskiej.

Schiess Vero-S Aviation (2020, May 30). Reduzierung der Rüstzeiten in der Großteilebearbeitung. https://www.zerspanungstechnik.com/bericht/werkstueckspannung/reduzierung_der_ruestzeiten_in_der_groteilebearbeitung-2018-06-26

Yang, S., Yin, T., & Wang, F. (2022). Research on finite element simulation and parameters optimization of milling 7050-T7451 aluminum alloy thin-walled parts. *Recent Patents on Engineering*, *16*(1), 82–93. https://doi.org/10.2174/1872212114999200902153633

Zawada-Michałowska, M., & Kuczmaszewski, J. (2020). *Odkształcenia elementów cienkościennych po frezowaniu*. Wydawnictwo Politechniki Lubelskiej.

Zawada-Michałowska, M., Kuczmaszewski, J., Legutko, S., & Pieśko, P. (2020a). Techniques for thin-walled element milling with respect to minimising post-machining deformations. *Materials*, *13*(21), Article 4723. https://doi.org/10.3390/ma13214723

Zawada-Michałowska, M., Kuczmaszewski, J., & Pieśko, P. (2020b). Pre-machining of rolled plates as an element of minimising the post-machining deformations. *Materials*, *13*(21), Article 4777. https://doi.org/10.3390/ma13214777

Zheng, Y., Hu, P., Wang, M., & Huang, X. (2023). Prediction model for the evolution of residual stresses and machining deformation of uneven milling plate blanks. *Materials*, *16*(18), Article 18. https://doi.org/10.3390/ma16186113

Zrník, J., Cieslar, M., & Slama, P. (2014). Structure development and deformation behaviour of pure aluminium processed by constrained groove pressing. *Materials Science Forum*, *794–796*, 882–887. https://doi.org/10.4028/www.scientific.net/MSF.794-796.882

Wdrożenie Technologii Wysokowydajnego Frezowania Stopów Aluminium z Wykorzystaniem Innowacyjnych Narzędzi i Oprzyrządowania

Streszczenie

Badania opisane w artykule dotyczą rozwoju i wdrażania nowych technologii mocowania stosowanych w obróbce skrawaniem, szczególnie w przypadku cienkościennych elementów konstrukcyjnych samolotów i śmigłowców. Przeanalizowano m.in. wydajność systemu mocowania Schunk Vero-S Aviation w obróbce belek podwozia ze stopu aluminium 7075 T6, co umożliwiło w znacznym stopniu wzrost wydajności produkcji i poprawą jakości geometrycznej obrabianych części. Podczas badań eksperymentalnych i testów wdrożeniowych zastosowano specjalne uchwyty w systemie Schunk Vero-S Aviation do obróbki belki podwozia. Wyniki wykazały poprawę jakości i dokładności obrabianych części w porównaniu z tradycyjnymi metodami mocowania. Zwiększona wydajność produkcji poprzez zminimalizowanie ilości odpadów w postaci braków i znacznie lepszą jakość powierzchni po frezowaniu, oraz właściwości geometryczne w porównaniu do konwencjonalnego mocowania za pomocą zacisków czy imadeł. Badania te zostały przeprowadzone w ramach projektu przez firmę Ultratech Sp. z o.o., która realizowała projekt dofinansowany z Funduszy Europejskich "Opracowanie i wdrożenie innowacyjnej metody mocowania do obróbki frezarskiej cienkościennych elementów konstrukcyjnych helikopterów i samolotów".

Słowa kluczowe: części niesztywne, element cienkościenny, stopy tytanu i aluminium, wysokowydajne frezowanie

Original Research

The Influence of the Variability of the Support of the Mortar Base Plate on the Quality of the Results Obtained in the Process of Its Numerical Design

Piotr Bieniek [1] iD **, Mirosław Tupaj [2]** iD **, Krzysztof Szwajka [3]*** iD

[1] Doctoral School of Rzeszow University of Technology, al. Powstańców Warszawy 12, 35-959 Rzeszów, Poland; p.bieniek10@gmail.com

[2] Department of Integrated Technology Component Manufacturing and Production Organization, Faculty of Mechanics and Technology, Rzeszow University of Technology, ul. Kwiatkowskiego 4, 37-450 Stalowa Wola, Poland; mirek@prz.edu.pl

[3] Department of Integrated Design and Tribology Systems, Faculty of Mechanics and Technology, Rzeszow University of Technology, ul. Kwiatkowskiego 4, 37-450 Stalowa Wola, Poland; kszwajka@prz.edu.pl

* Correspondence: kszwajka@prz.edu.pl

Abstract

Due to the high costs associated with the purchase of ammunition and firing in certified training ground centers, tests of retaining plate deformations are increasingly replaced by computer simulations using numerical models. Computer programs usually use a single-parameter subsoil model (Winkler-Zimmermann) for calculations, which requires providing the subgrade susceptibility coefficient. The subgrade compliance coefficient is intended to determine the mutual reaction of the subgrade and the structure due to the pressure exerted on the soil by the retaining slab, which settles. When designing slabs in computer programs, it is assumed that the substrate compliance coefficient is constant. Determining the impact of the soil on the retaining slab is important when analyzing its deformations. The subject of the work was the analysis of the influence of ground support on the results obtained during modeling of the retaining slab. In order to obtain data for FEM analysis and validation, the actual strains occurring on the thrust plate were measured using strain gauge rosettes. The plate deformations were measured during field shooting tests. In order to vary the influence of supporting the slab on the ground and obtain reliable stress values on the slab surface, a method of successive iterations was proposed. Calculations are performed using this method until the error is smaller than the assumed one.

Keywords: mortar base plate, strain measurement, finite element method

1. Introduction

When measuring the value of strains (stresses) during field shooting tests, the high costs associated with purchasing ammunition and carrying out such tests in a certified research center should be taken into account. The data obtained from real measurements are the most reliable, but the development of technology and economic considerations are increasingly reduced to performing computer simulations on computational models.

The issues of interaction between the mortar base plate and the ground are not widely described in world literature. The first and at the same time the most frequently used measurement method is the measurement of deformation using strain gauges (Szwajka et al., 2022). The main emphasis in research is on the analysis of the stress and strength of the mortar itself (Bartnik et al., 2021, Zhang et al., 2016). The quality requirements for mortars stipulate the possibility of firing from them after placing on grounds with a wide range of properties. Any proper interaction of the mortar and the terrain is largely dependent on the latter's deformation modulus (Gomez & Spencer, 2019; Lee & Park, 2015).

The main assumption of Finite Element Method (FEM) is the discretization of a continuous geometric model by dividing it into a finite number of elements connecting at nodes. The effect of this

division is also the transformation of a system with an infinite number of degrees of freedom into a form with a specific number of degrees of freedom (Kleiber, 1989). In the case of calculations using FEM, all other physical quantities operating in the system in the form of continuous functions, such as loads, restraints, displacements and stresses, are also discretized. The result of discretization of a specific physical quantity is the pursuit of a maximum approximation of its discrete and continuous form through the use of approximation methods (Dacko et al., 1994). The complexity of the finite element method and its approximate nature place significant demands on the software user. A necessary condition for obtaining correct results is to define the appropriate computational model based on the specificity and fundamentals of finite elements (Kacprzyk et al., 2011). The basic advantages of using FEM software include undertaking increasingly complex designs and analyzes of structures for which analytical solutions are not available, and easy consideration of many variants of loads, boundary conditions, types of materials, and shapes of individual parts. Moreover, FEM programs enable automatic data conversion, preventing possible errors or time-consuming calculations, and creating reports on the analyzes performed (Anitescu et al., 2019; Bielski, 2010). The thematic reference to the characterized finite element method are publications by Wang (2019) and Wang et al. (2020), in which the computational models are mortar retaining slabs. The final effect of design optimization is the ability to make boards from light composite layers.

Another example of the use of FEM on a computational model in the form of a mortar thrust plate is the work (Ristić et al., 2009), in which the Pro/Engineer Wildfire software was used. Based on the simulations performed, the stresses occurring on the retaining plate of a 120 mm mortar were analyzed for soft, medium and hard ground. In this work, an attempt was made to compare the simulation with real measurements, however, the insufficiently well-prepared strain gauge installation and its location provided rudimentary results from shooting tests.

The work (Wang & Yang, 2021) presents a topographic design of the retaining plate of a 120 mm mortar based on the finite element method. The model of a trapezoidal-pyramidal plate was subjected to optimization of the dynamic topology of its continuous structure based on the results obtained from laboratory tests. For this purpose, a station was created enabling the impact load on the thrust plate to be applied and this force to be measured. The results obtained from the analyzes provided the basis for optimizing the original model.

The issue of the interaction of the mortar retaining plate with the ground is not widely described in world literature. The main emphasis in the research is placed on the analysis of stresses and strength of the mortar itself. Therefore, the study presents a comparison of the stresses on the mortar retaining plate obtained during the tests carried out using strain gauge measurements with the stress results obtained using FEM. A function was assumed that determines the influence of the elastic substrate on the deformations of the retaining plate. The research is complemented by the results of calculations of the plate model using the finite element method in the MIDAS program. Problems related to the cooperation of the ground and the structures resting on it are an important aspect of strength analysis. There is no detailed research in the literature regarding, among others, deformations of retaining plates on an elastic base. As previously mentioned, a very important issue in the FEM analysis of plates is their interaction with the substrate on which they rest, which are loaded not only with static, but above all dynamic forces.

Due to the specific nature of military products with closely guarded design solutions, the literature review in the area of stress measurement methods and computer simulations in relation to testing mortar thrust plates is significantly limited. Based on the literature, the concept of the work undertaken was to find effective methods to replace the firing of a retaining plate in laboratory conditions and to reduce the costs associated with shooting tests. Due to the lack of correlation between the actual deformations occurring on the retaining plate during the shot and numerical simulations on the computational model of the plate, this work was undertaken to analyze the state of stress and compare the values obtained from strain measurements and as a result of strength analyzes carried out using the finite elements.

2. Material and methods

2.1. Mortar base plate

The subject of the research was the retaining plate of a 98 mm mortar used to support the mortar barrel and to slow down the recoil during firing by transferring energy to the ground. It was made of heat-treated 30HGSA steel. 30HGSA steel is characterized by high hardenability, strength and wear

resistance. Due to the decrease in strength properties after exceeding a certain thickness, it is used to produce elements up to 60 mm. It is steel intended for heat treatment consisting of hardening and tempering. After thermal improvement, it obtains excellent strength parameters, while maintaining optimal other properties. Steel is used primarily for highly loaded machine parts and heavy structures subject to heavy loads. Table 1 lists its mechanical properties. The resistance plate used in the research is part of the equipment of soldiers. We had no influence on its shape.

Table 1. Basic mechanical properties of 30HGSA steel.

Ultimate Tensile Stress R_m, MPa	Yield Stress R_e, MPa	Young's Modulus E, GPa	Elongation A_{50}, %
1070	820	210	10

The technology for making the retaining plate was cold-formed sheet metal, 5 mm thick, in the shape of a circle with stiffening embossments. The sheet is then connected to the ball socket, reinforcing ribs and plates as well as stiffening and transport elements by welding with 3.5 mm thick fillet welds. After welding, the plate was heat treated. Figure 1 shows the retaining plate of a 98 mm mortar from both sides.
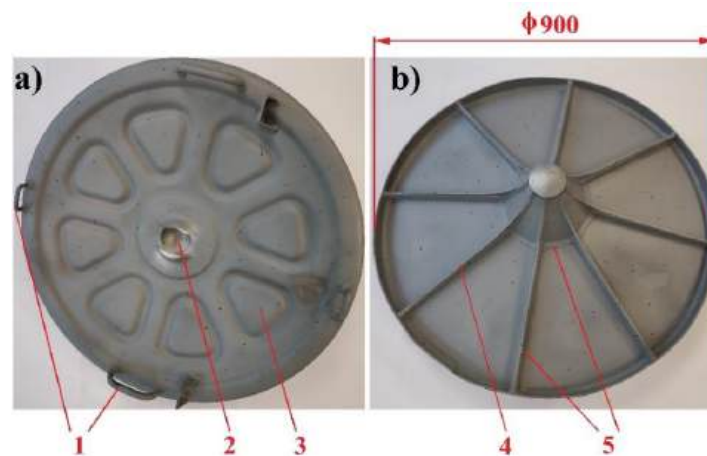
Fig. 1. Mortar base plate: a) – view from above, b) – view from below, consisting of: 1 – transport handles, 2 – ball socket, 3 – stiffening embossments, 4 – strengthening ribs, 5 – welded joints.

2.2. Experiment procedure

During the firing range tests, the deformations occurring on the thrust plate and the pressure of the gunpowder gases in the mortar barrel were measured. The firing was conducted from the ground at a barrel elevation angle of 45º with smoke projectiles on reinforced propellant charges (Fig. 2).
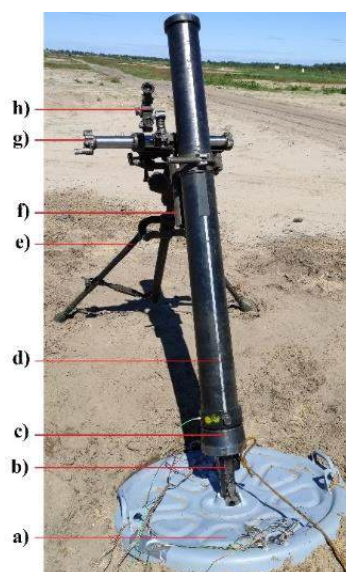
Fig. 2. 98 mm caliber mortar consisting of: a) base plate, b) ball shaft, c) lock, d) barrel, e) bipod, f) recoil dampeners, g) lifting and directional mechanism, h) sight.

Ten strain gauge rosettes were used to measure deformations on the thrust plate during firing from a 98 mm mortar, allowing measurement in three directions: 0°, 45° and 90°. Strain gauge rosettes were placed on the supporting plate in such a way as to enable obtaining as much data as possible regarding the loads acting on various areas of the supporting plate during the shot. Preliminary shooting tests (in the form of pilot tests) showed that the greatest loads on the plate occur in its lower area, and the smallest in the upper area. A symmetrical stress distribution in the vertical system was also observed, on the basis of which the arrangement of strain gauge rosettes on the retaining plate was determined, graphically shown in Fig. 3.
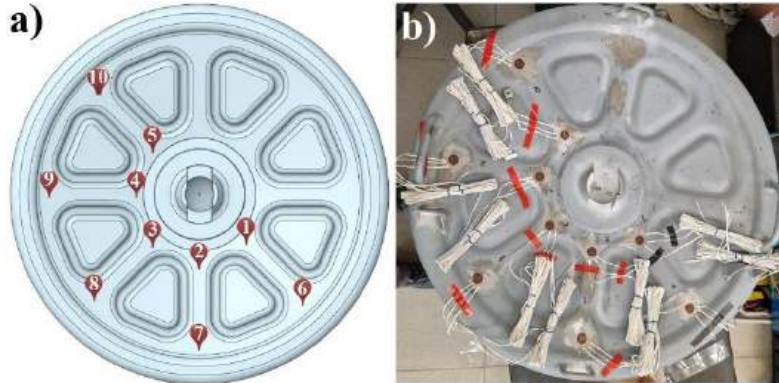
Fig. 3. Location of strain gauge rosettes on: a) 3D model of the plate, b) mortar base plate intended for field tests.

The strain gauge installation was made on the outside of the thrust plate, due to the direction of the shot force, but also due to the impossibility of securing the strain gauges if they were mounted on the side in contact with the ground. The installation consisted of 10 KYOWA rosettes, type KFGS-10-120-D17-11 L3M3S, glued using CC-33A glue from KYOWA. The frequency response of the strain gauge rosettes was 1200 Hz. The signals were recorded at a frequency of 19,200 Hz using an HBM amplifier – QuantumX MX1615B model and dedicated HBM computer software. Then, the signals were filtered to remove interference. The strain gauge rosettes used for the measurement worked in a Wheatstone quarter-bridge. Along with recording the deformations, a measurement of the pressure of the gunpowder gases was carried out in parallel, synchronized in an identical time interval using the Piezotronics 482C PCB signal conditioner. Figure 4 shows a diagram of the measurement track used during the firing range tests.
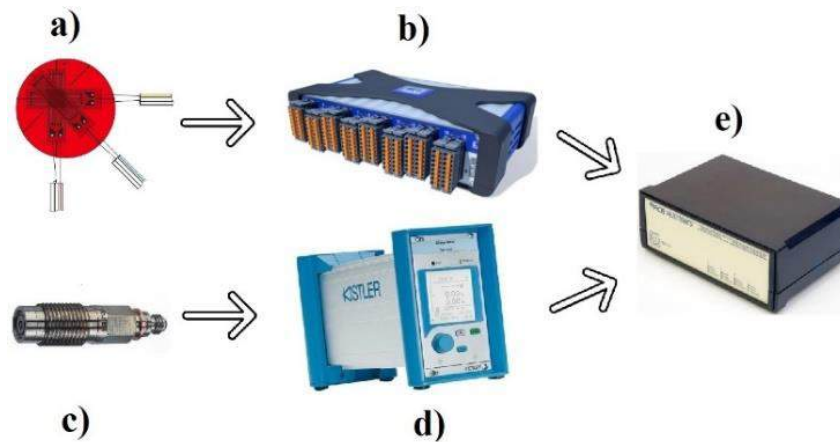
Fig. 4. Diagram of the measurement path consisting of: a) KYOWA strain gauge rosettes, b) HBM MX1615B measurement amplifier, c) Kistler 6215 piezoelectric sensor, d) Kistler 5015A charge amplifier, e) Piezotronics 482C PCB signal conditioner.

3. Results and discussion

During firing, the maximum deformation values were measured on the retaining plate of the 98 mm mortar using ten strain gauge rosettes, and the pressure of the powder gases in the mortar barrel was measured using a piezoelectric sensor. Examples of the recorded maximum signals for the R1 rosette are shown in Fig. 5a, while the pressure course over time is shown in Fig. 5b.
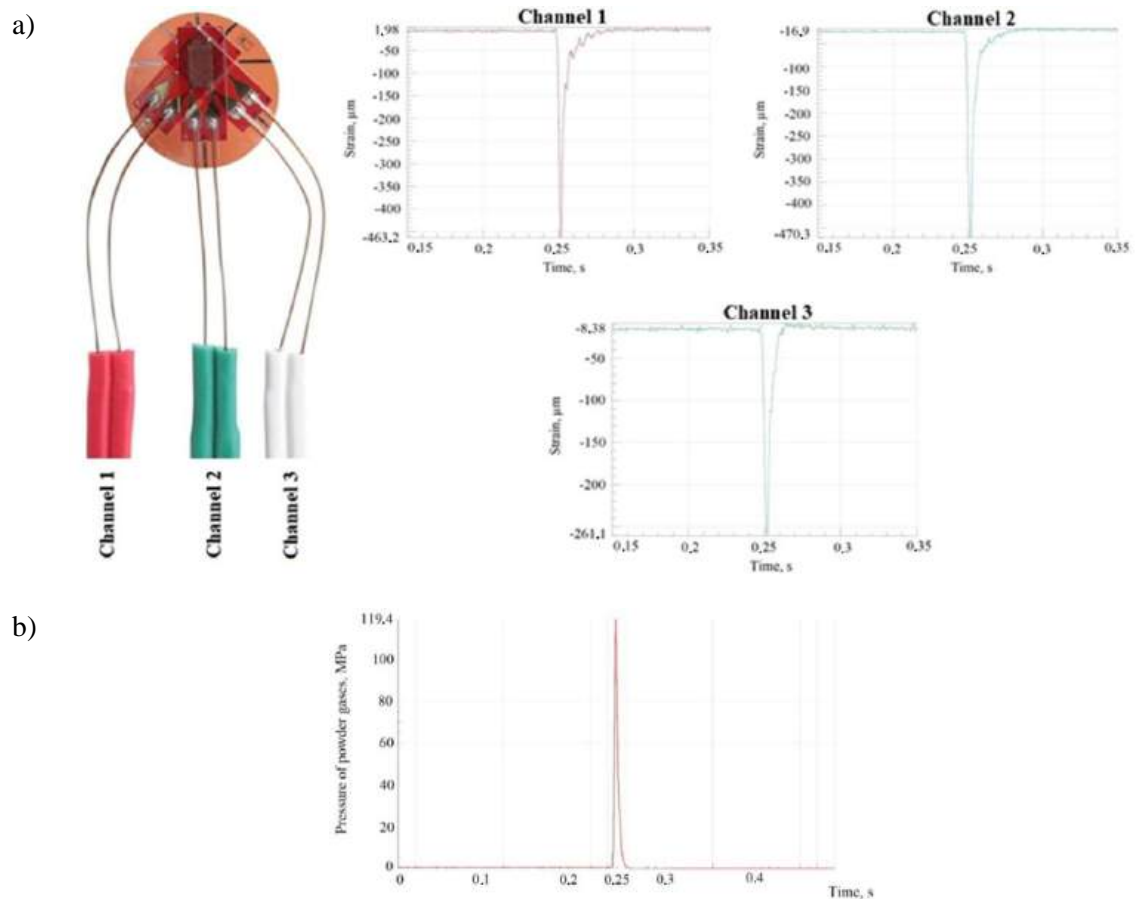
Fig. 5. a) maximum strain curves for rosette R1 and b) the course of the pressure of gunpowder gases over time.

When conducting strength analyses, the measurement results were reduced to reduced stresses in accordance with the Huber-Mises-Hencky (H-M-H) hypothesis. In the calculation program, the stresses for individual directions were converted into reduced stresses using the Von Mises module. Below is an iterative summary of the results obtained in three subsequent analyses, which allowed to obtain the correct final result of the analyses. The elements used to represent the stiffness of the soil were Bush elements. These are elements that are characterized by elasticity and damping. In the calculations, they were used as elements whose dominant component is stiffness. There is a node at each end of the bush element (this is a 1D element). One of the nodes is adjacent to the surface of the elements from which the numerical model of the plate is built. The second node is automatically supported.

The next stage was to determine the estimated values of soil stiffness, which will be expressed in N/mm. Converting the stiffness into these units is necessary because it is in them that the stiffness is defined in the Midas NFX calculation program. An axisymmetric model was prepared for this task. By assigning material parameters (Young's modulus, Poisson's ratio) determined from standard PN-81 B-03020 that describe various types of soil, a model was created into which a triangular indenter was pressed, which was supposed to approximately reproduce the shape of the plate (test this, to a large extent, looked like a microhardness test). Then, after applying the assumed force to the indenter, the indentation value was read. In this way, the stiffness parameter (N/mm) was obtained from the material parameters. This allowed us to determine the approximate order of magnitude of the individual stiffnesses that the Bush-type elements that support the model should have.

The initial assumption for modeling the structure of the mortar support plate in the numerical model in iteration 1 included the full support of the plate on the ground, both surface and edge parts, with constant soil stiffness conditions. Below is a summary of the stiffness of spring elements representing elastic support conditions:

- stiffness on surfaces 200 N/mm,
- stiffness at the edges 1400 N/mm.

The envelopes of stress values in individual views for 2D shell elements for top and bottom surfaces are shown in Figure 6.

Fig. 6. Stress values in the envelope from strain gauge measurement points (first iteration): a) upper view, b) side view.

A comparison of the results of numerical analyzes and the results obtained during measurements at reference measurement points is shown in Fig. 7.

Fig. 7. Graphical summary of results obtained from numerical analyzes and measurements (first iteration).

The initial assumption for modeling the structure of the mortar support plate in the numerical model in iteration 2 included half of the support of the surface parts of the plate on the ground and full support of the edge parts of the plate on the ground, with constant soil stiffness conditions. Figure 8 presents a summary of the stiffness of spring elements representing elastic support conditions:
- stiffness on surfaces 200 N/mm,
- stiffness at the edges 1400 N/mm.

Fig. 8. Stress values in the envelope from strain gauge measurement points (second iteration): a) upper view, b) side view.

A comparison of the results of numerical analyzes and the results obtained during measurements at reference measurement points is shown in Fig. 9.
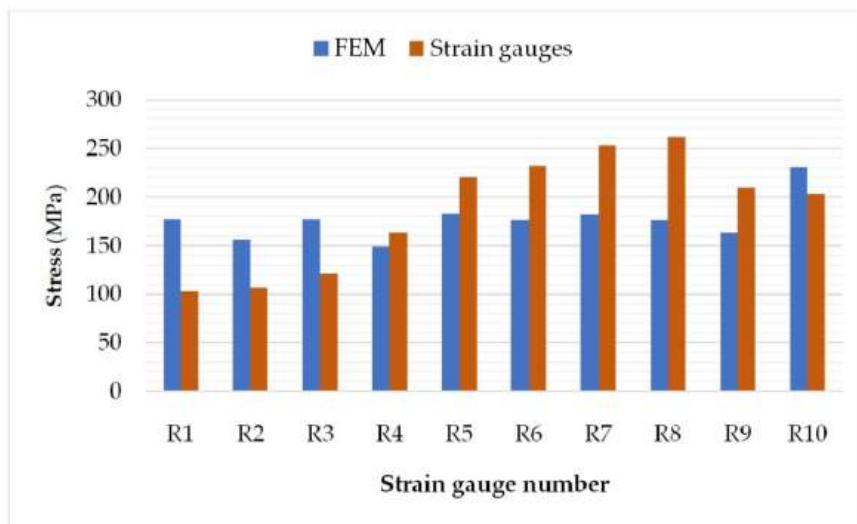
Fig. 9. Graphical summary of results obtained from numerical analyzes and measurements (second iteration).

The initial assumption for modeling the structure of the mortar support plate in the numerical model in iteration 3 took into account only the medial area of the support of the surface parts of the plate on the ground and the full support of the edge parts of the plate on the ground, with constant soil stiffness conditions. Figure 10 presents a summary of the stiffness of spring elements representing elastic support conditions:
- stiffness on surfaces 200 N/mm,
- stiffness at the edges 1400 N/mm.

A comparison of the results of numerical analyzes and the results obtained during measurements at reference measurement points is shown in Fig. 11.

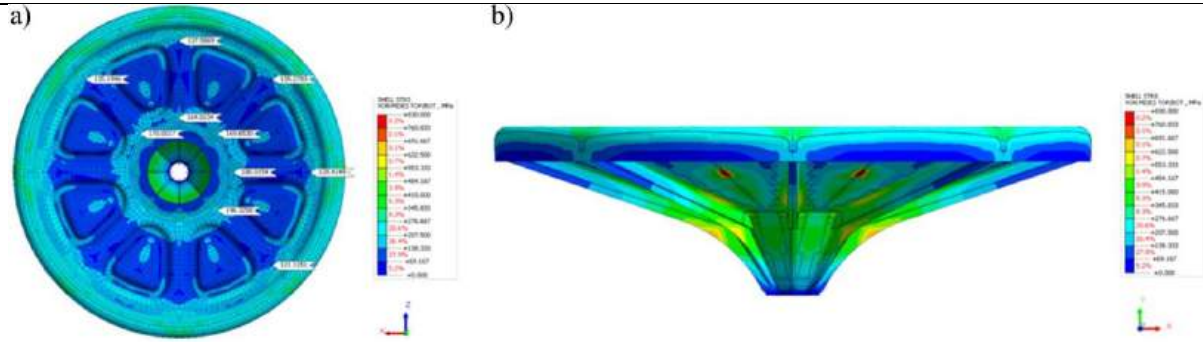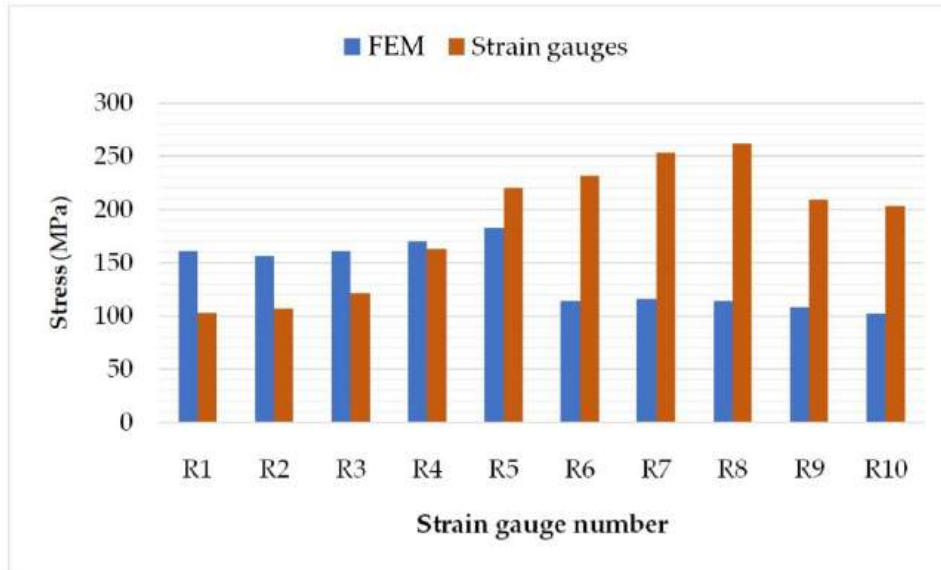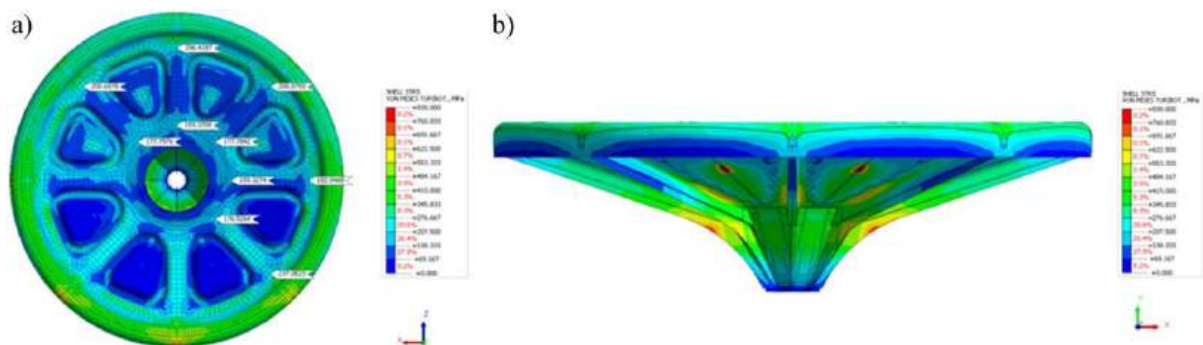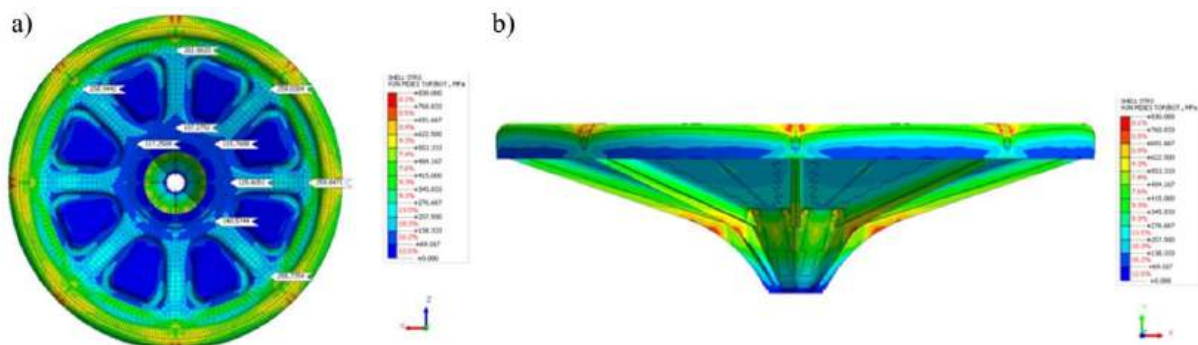**Fig. 10.** Stress values in the envelope from strain gauge measurement points (third iteration): a) upper view, b) side view.
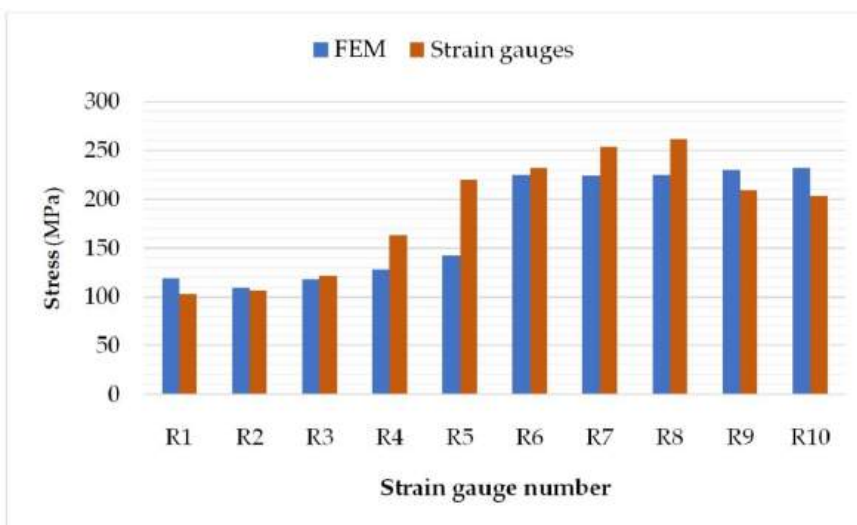

Fig. 11. Graphical summary of results obtained from numerical analyzes and measurements (third iteration).

4. Conclusions

This study proposes a continuum base plate topology optimization problem under quality and engineering constraints. The modeling method used for the mortar base plate was proven to be accurate and feasible through test verifications. In this case, topology optimization was performed on the mortar base plate structure using a force transmission path based on base plate stress analysis. The base plate optimization model could meet the requirements of structural stiffness and strength, shooting stability and lightweight structure. Thus, this study provides a benchmark for performance improvement and structural optimization design of the base plate.

The highest stress values were observed on the outer circumference of the mortar plate. This is due to the shape of the outer ring of the plate. It sinks into the ground and acts as a block to the movement of the mortar plate.

The case of obtaining the results of individual analyzes was limited to the ground, which was fill sand and shot at an angle of 45°. The iterative comparison of the results obtained in three subsequent analyzes allowed to obtain the final effect of the analyses, allowing obtaining satisfactory results, consistent with the results obtained from strain gauge measurements. The process of obtaining the final results was an iterative process, which included many computational approaches with each change of the calculation assumptions, in particular the slab support conditions.

References

Anitescu, C., Atroshchenko, E., Alajlan, N., & Rabczuk, T. (2019). Artificial neural network methods for the solution of second order boundary value problems. *Computers, Materials & Continua*, *59*(1), 345–359.

Bartnik, G., Józefiak, K., Superczyńska, M., Czerwińska, M., Krajewski, W., Legieć, J., Kuśnierz, T., Magier, M. (2021). The use of geotechnical methods to determine the deformation parameters of the ground in terms of operation and safety of mortar use. *Materials*, 14(23), Article 7237. https://doi.org/10.3390/ma14237237

Bielski, J. (2010). *Introduction to engineering applications of the finite element method*. The publishing house of the Krakow University of Technology.

Dacko, M, Borkowski, W, Dobrociński, S, Niezgoda, T., & Wieczorek, M. (1994). Finite element method in structural mechanics. Arkady.

Gomez, F., & Spencer, B. F. (2019). Topology optimization framework for structures subjected to stationary stochastic dynamic loads. *Structural and Multidisciplinary Optimization*, *59*, 813–833. https://doi.org/10.1007/s00158-018-2103-3

Kacprzyk, Z., Maj, M., Pawłowska, B., & Sokół, T. (2011). *Finite element method manual* (2nd ed.). Warsaw University of Technology Publishing House.

Kleiber, M. (1989). *Introduction to the finite element method*. State Sci. Pub. House.

Lee, H. -A., & Park, G. -J. (2015). Nonlinear dynamic response topology optimization using the equivalent static loads method. *Computer Methods in Applied Mechanics and Engineering*, *283*, 956–970. https://doi.org/10.1016/j.cma.2014.10.015

Ristić, Z., Kari, A., & Bajević, M. (2009). Dynamic analysis of the mortar base model using the Pro/engineer software package. *Vojnotehnički Glasnik*, *57*(1), 81–89. http://dx.doi.org/10.5937/vojtehg0901081R

Szwajka, K., Szewczyk, M., & Trzepieciński, T. (2022). Experimental Compaction of a High-Silica Sand in Quasi-Static Conditions. *Materials*, *16*(1), Article 28. https://doi.org/10.3390/ma16010028

Wang, X. (2019). *Optimal design of a large caliber mortar base plate structure*. Nanjing University of Technology.

Wang, F., Yang, G., Wang, D., Ge, J., Yu, Q., & Li, Z. (2020). Research on the test and lightweight design of a mortar base plate. *Vibration and Shock*, *39*(17), 76–81. https://doi.org/10.13465/j.cnki.jvs.2020.17.011

Wang, F., & Yang, G. (2021). Topological design of a mortar base plate under impact loads. *Shock and Vibration*, *2021*(1), 1-13. https://doi.org/10.1155/2021/8845019

Zhang, X., Liu, S., Peng, K. et al. (2016). Topological optimization design for mortar's base plate. *Journal of Ordnance Equipment Engineering, 4*, 33–35.

Wpływ Zmienności Podparcia Płyty Oporowej Moździerza na Jakość Uzyskanych Wyników w Procesie Jej Projektowania Numerycznego

Streszczenie

Ze względu na wysokie koszty związane z zakupem amunicji oraz realizacją ostrzału w certyfikowanych ośrodkach poligonowych badania odkształceń płyty oporowej są coraz częściej zastępowane symulacjami komputerowymi za pomocą modeli numerycznych. Programy komputerowe wykorzystują przeważnie do obliczeń jednoparametrowy model podłoża (Winklera-Zimmermanna), w którym wymaga się podania współczynnika podatności podłoża. Współczynnik podatności podłoża gruntowego ma na celu określenie wzajemnej reakcji podłoża i konstrukcji, przez nacisk wywierany na grunt przez osiadającą płytę oporową. Przy projektowaniu płyt w programach komputerowych zakłada się, że współczynnik podatności podłoża jest stały. Określenie oddziaływania gruntu na płytę oporową jest istotne przy analizie jej odkształceń. Przedmiotem pracy była analiza wpływu sposobu podparcia płyty oporowej o podłoże gruntu na uzyskane wyniki w trakcie jej modelowania. W celu uzyskania danych do analizy i walidacji MES, przeprowadzono pomiar rzeczywistych odkształceń występujących na płycie oporowej za pomocą rozet tensometrycznych. Pomiaru odkształceń płyty dokonano podczas poligonowych badań strzelaniem. W celu uzmiennienia wpływu podparcia płyty o podłoże oraz uzyskania miarodajnych wartości naprężeń na powierzchni płyty, zaproponowano metodę kolejnych iteracji. Metodą tą są wykonywane obliczenia do chwili uzyskania błędu mniejszego od założonego.

Słowa kluczowe: płyta oporowa moździerza, pomiar odkształceń, metoda elementów skończonych

Original Research

An Experimental Study on Electricity Generator Emissions and Their Environmental Impact in Kirkuk City

Maral Mahmood Husain ⓘ

Renewable Energy Research Center-Kirkuk, Northern Technical University, 36001 Kirkuk, Iraq

Correspondence: maralmahmood0@ntu.edu.iq

Abstract

This article evaluated the environmental impact of emissions from private electric generators, focusing on the amount of toxic gas they contribute to the surrounding environment. In the research, the number of generators used in the study was fifteen diesel-powered generators confined within specific residential areas in the city of Kirkuk (Iraq). The study included a field survey and measurements using air pollution standards. The amounts of HCl, H_2S, SO_2, NO_2, NO, CO_2, CO, O_2, temperature, and relative humidity in the exhaust gases to illustrate the pollutants and compare them to the normal case were measured. It was found that the concentrations varied depending on the generators' parameters and they were high. The diffraction values were distinguished in location A4 (generator manufacturing company – Scania, generating capacity 250 kVA, voltage 200 V, number of residential units consumed - 500), which was characterized by higher concentrations of contaminants than in the standard case. In the remaining cases, this was due to a variety of factors, including the generator's operational age and the higher number of houses it served compared to its generating capacity, which exceeded its design limit.

Keywords: electricity generators, environmental pollution's impact, internal combustion engines, pollutant concentration

Nomenclature and abbreviations

BDC	Bottom dead centre	LEL	Lower explosive limit
CO	Carbon monoxide	NO	Nitrogen monoxide
CO_2	Carbon dioxide	NO_2	Nitrogen dioxide
DCA	Digital communication analyzer	NO_x	Nitrogen oxide
EPA	Environmental Protection Agency	O_3	Trioxygen
H_2O	Water	PM	Particulate matter
H_2S	Hydrogen sulphide	RH	Relative humidity
HC	Hydrocarbon	SO_2	Sulphur dioxide
HCl	Hydrogen chloride	T	Temperature
IAQ	Indoor air quality	TDC	Top dead centre

1. Introduction

The electricity crisis in Iraq necessitated the urgent use of electrical generators, and the scarcity of electrical energy compelled citizens to supply electricity to houses, shops, public places, restaurants, hotels, and other uses. The large number of generators located in our residential areas and across Iraqi cities naturally generate these negative effects. Mohammed (2009) looked at how private electricity generators pollute the environment by releasing harmful gases and making noise in certain residential areas of Kirkuk. Vehicle exhausts and the burning of oily waste pollute the city of Kirkuk. The total chemical analyses revealed higher concentrations of polluting elements like lead, cadmium, copper, and

This is an Open Access article distributed under the terms of the Creative Commons Attribution License CC BY 4.0 (https://creativecommons.org/licenses/by/4.0/)

zinc in the samples collected from Kirkuk's main streets and the western side of the Khasa River. Mohammed (2009) collected the samples from the east side of the river. This is due to the heavy traffic on the western side of the river, as well as its proximity to the North Oil Company (Mohammed, 2009). If we classify environmental pollution into two categories that affect the environment surrounding generators, they are air pollution and noise pollution. Generators cause varying levels following pollutants: (soot, Pb, SO_2, NO, and CO). Diesel generators produce about 10% of the carbon monoxide that gasoline generators do when in use. This is higher than the national limit (35 ppm) for gasoline generators. Diesel does not contain any lead compounds, but using a gasoline generator increased the amount of lead to exceed the proposed national limit of 1.5 g/m^3. The concentrations of SO_2 pollutants produced by gasoline generators are deficient compared to those of SO_2 pollutants produced by diesel generators and are higher than the national limit (0.1 ppm) in the case of a diesel generator. Regarding the group of suspended particles in diesel generators, we notice that their amount in the gasoline generator is less than in the diesel generator, as the main problem with diesel engines is smell and smoke.

When Al Kizwini et al. (2013) doubled the distance, he observed a decrease or increase in the sound pressure level in the range of 6-7 dBA, indicating noise pollution. Researchers looked into how electric generators in Baghdad's Al-Karrada area affected the environment and found that the levels of gases (CO, NO_2, SO_2, and H_2S) were much higher than what was considered to be a pollutant. There are decreases when moving away from the emission source and at distances (2 m, 5 m, 10 m), which indicates the state of diffusion of these gases when moving away from the emission source. The study attributed the clear differences in gas concentrations emitted from the generators to their type and generating capacity. Research has demonstrated that the age factor of the generator significantly influences the variations in gas concentrations emitted from generators (Areaj kh airy alrawi Rana hazim, 2018). A study mapping the dispersion of air pollutant particles in urban areas above Kirkuk using a geographic information system was added. The results showed that there is a weak linear relationship between metrological factors and most pollutants (Salah et al., 2014). The air pollution maps distributed through ArcGIS analysis showed that the pollutants with the highest concentrations were near and around oil fields and refineries. The researcher's Arc GIS air pollution analysis maps can serve as a foundation for the appropriate placement of air pollution measuring stations. The researchers looked at levels of NO, HC, CO_2, and CO, as well as compared them to the pollution limits in Iraq. In April, the Al'Asraa-w al-Mafqudin area had the highest level of CO gas, surpassing the allowed limits. The highest concentration of CO_2 gas was in March, in the Rahim Awa area, at 450 ppm. The same month saw the highest concentration of NO gas at 3.5 ppm, while the Al'Asraa-w al-Mafqudin and Rahim Awa areas in April had the highest concentration of HC gas at about 1.8 ppm. Calculating the noise level values for these generators was the second determinant. The highest average value of equivalent noise was 102.55 DCA in the Rahim Awa area, which exceeded the limits permitted by the U.S. Environmental Protection Agency (EPA), while the lowest average value of equivalent noise was 91.02 DCA in the Tisein area (Ali, 2019). Pollution problems, in general, are considered very important for research studies. The use of electrical generators in Koya city, located in northern Iraq, significantly impacted pollution levels. An actual examination and study of various generators, their types, and the distribution of gases (CO_2, NO_X, SO_2, CO, and particle solids) from 2009 to 2017 was conducted. The correlation between these generators and fuel consumption, indicated that energy production in 2009 was 23850 MW, but it increased to 49635 MW in 2017. The number of generators increased, leading to excess energy production and a clear increase in the percentage of pollutants. Eight years later, as a result of the increase in electrical energy production, pollutants increased rapidly. It was 6,695 Mg in 2009 and rose to 13,933 Mg in 2017 (Abbas et al., 2019). The concentrations of carbon dioxide, carbon monoxide, and particulate matter (PM2.5) emitted from the exhaust of gasoline-powered electric generators in a city in Nigeria are 710 ± 19.1, 83 ± 4.0, and 83 ± 4.1 ppm, respectively. Average concentrations of carbon dioxide and PM2.5 are higher than those recommended by the World Health Organisation (Giwa et al., 2023). Some studies aimed to evaluate the concentration of heavy metals (Cd, Co, Cr, Cu, Ni, Pb, and Zn) and their environmental risks in the soil adjacent to electric power generators. For example, in the city of Ramadi in Iraq, soil samples from a depth of 20 cm showed average concentrations of the elements. AL-Heety et al. (2021) arranged the intense elements in descending order: Ni is very intense (354.56 mg/kg), Cd is intense (255.31 mg/kg), Co is heavy (207.77 mg/kg), Zn is heavy (88.69 mg/kg), Cu is light (25.73 mg/kg), Cr is light (17.43 mg/kg), and Pb is light (12.0 mg/kg). They conducted a study to evaluate the noise levels of fifty (50) diesel generator sets used for street lighting in Kano city. They measured the noise levels at the point source (0 m) and at a distance of 10.5 m from the source, which ranged from about 55 to 103 dB. The permissible noise limits are 55

dB, and the noise levels decreased as the distance from the noise source decreased. A high level of noise affects human health negatively; it may cause irritability and aggression, high blood pressure, high stress levels, tinnitus, hearing loss, and sleep disturbance, which can hinder cognitive development in children (Safiyanu & Mohammed, 2020). The concentration of air pollutants (CO, NO_2, SO_2, O_3, PM10, and PM2.5) in four Iraqi cities (Najaf, Muthanna, Maysan and Kirkuk) from September 1, 2019 to September 31, 2020, using the AirQ+ programme to assess the health impact of air pollutants was studied. The results showed that the average daily concentration of carbon dioxide and nitrogen dioxide in the four cities is much higher than the air quality specifications set by the World Health Organisation, while PM10 and PM2.5 were among the air pollutants that exceeded the special air quality standards compared to other pollutants. Muthanna's dust storms and Baghdad's high population contribute to the lower air quality compared to other cities. Abbas and Abbas (2021) found that the high emissions of air pollutants are due to industry, transportation, and electricity generation activities. Increased combustion of fossil fuels in industrial activities, such as cement manufacturing plants, and wind and dust storms heavily pollute Iraq's air. These pollutants exceed national and international standards, potentially causing diseases. Researchers studied the impact of antioxidant additions on nitrogen oxide emissions and smoke in a diesel engine using four types of antioxidants. Results showed a reduction in nitrogen oxide emissions at rates of 5.7%, 7.3%, 7.2%, and 11.3%. Carbon monoxide concentrations ranged from 0.3 ppm to 11.2 ppm, exceeding permissible levels. The north eastern part of the city had the lowest concentration, while traffic lights displayed the highest concentration. Traffic intersections near Qalaa Kirkuk, Kirkuk University, Ras Domiz, the car dealer area, Khabat Bridge, and the Kirkuk Health Department recorded high concentrations of pollutants (Al-Kasser, 2021; Dhahad & Fayad, 2020; Mohamedali et al., 2020). The analysis of sulphur dioxide (SO_2) emissions revealed that the American invasion began in 2006, coinciding with the closure of most factories and the curtailment of human activities, including transportation. Sulphur dioxide values increased across all stations from 2006 to 2009 (Abbas & Rajab, 2022). When comparing five areas of Kirkuk Governorate with the Yayci area, due to its relative lack of vehicle movement, the results of measuring the concentrations of carbon monoxide and hydrocarbons emitted from car exhausts revealed that the beginning of the Martyrs' Bridge (the Citadel) recorded the highest rate of carbon monoxide pollution at 5.570 ppm, while the Kirkuk entrance checkpoint on June 1 recorded the highest rates of hydrocarbon pollution at 15.187 ppm (Al-Shwany & Al-Karkh, 2022). When comparing the emissions of carbon dioxide and air pollutants from the exhaust gases of a specific group of electric generators, it appears that the 2.5 kVA petrol generator produces the maximum quantity of pollutants, followed by the 0.7 kVA generator. On the other hand, the 8.8 kVA diesel generator emits the lowest amount of pollutants. With the exception of carbon dioxide, other pollutants had a high percentage, and overall, all generators produce a significant amount of pollutants, especially carbon dioxide (Oriakpono & Ohabuike, 2022). Several studies assessed the impact of noise from electrical power generators on physiological parameters, kidney function, and oxidative stress in a group of 30 workers in the city of Najaf, as well as a control group of 30 individuals not subjected to the same stress. The morning period revealed decibel levels exceeding the recommended limits. These levels are determined by Iraqi standards and the World Health Organization. There was also no significant change in the average creatine and urea levels in the blood compared to the control group. There is a significant decrease ($P \geq 0.05$) in the level of glutathione for workers in electric generators. In addition, headaches (50%) and discomfort (39%) were the most common types of noise-induced symptoms among people working with generators (AL-Hakkar & AL-Maraashi, 2023).

The current research includes a study to evaluate the environmental impact of a group of electricity generators located in different residential areas. Generators with varying generating capacities run on diesel and provide service to a variety of households. The study by graphically recording field surveys of generators and comparing them with data was conducted.

2. Commercial generators

The destructive consequences of the war, the damage to the country's electricity system, and the persistently insufficient level of power provision have driven the widespread installation of generators in Iraqi cities. While it provided a remedy for the electrical shortage, it also provided a path to another, far worse predicament: pollution. Pollution is a direct consequence of the generator's operation through a specific process.

2.1. How do electric generators work?

In order to know and determine the concentration of pollutants emitted from the exhaust gases of electric generators, it is necessary to know the mechanism of operation of these generators. The principle of operation of the generator does not differ from the principle of operation of a car. Both use fuel (gasoline or diesel), with the car producing kinetic energy to move and the generator generating electrical energy. Internal combustion engines function as heat engines, burning fuel and an oxidizer, typically air, within a combustion chamber. Diesel engines rely on self-combustion, which involves compressing the air inside the cylinder, raising its temperature, and injecting diesel that ignites automatically. While gasoline engines need an electric spark to ignite the fuel-air mixture, the expansion of gases with high pressure and temperature resulting from combustion in an internal combustion engine exerts a direct force on some engine components. The piston absorbs this force. The piston converts thermal energy into mechanical energy, causing the part under force to move. These generators export gaseous pollutants resulting from the combustion of fuel to the outside atmosphere through the outlet of the exhaust pipe or any outlet in its path. These pollutants include some gases and hydrocarbons, which are considered dangerous and contribute significantly to human exposure to pollution risks (Al-Ashri, 2010). Diesel engines operate on diesel fuel. They inject fuel at high pressure into the cylinder, which contains air at a temperature equal to the fuel's self-ignition temperature. Diesel engines' fuel devices differ from gasoline engines' due to their different thermal cycles and fuel types.

Incomplete combustion of fuel leads to the formation of very fine carbon residues that have a very bad effect, especially on small engines with high speeds. Incomplete combustion may be the result of not adjusting the fuel injection timing or using fuel that contains a high percentage of impurities.

The diesel engine operates in harsher working conditions than other engines, and its operating efficiency depends to a large extent on the cleanliness of the fuel entering the injection pump and sprayers. Dirt, impurities, and dust are considered the main causes of corrosion in the injection system (Stone, 1999).

2.2. The engine's strokes and exhaust system

In four-stroke diesel engines, the strokes alternate as follows: (Intake stroke), a vacuum is created inside the cylinder during the intake stroke when the piston travels from the top dead centre (TDC) to the bottom dead centre (BDC). Due to atmospheric pressure, the intake valve opens, letting fresh air into the cylinder. Diesel engines, in contrast to petrol engines, simply suck in air-not an air-fuel mixture-during this stroke. During the compression stroke, when the piston returns to TDC from BDC, the air inside the cylinder is compressed. Throughout this procedure, the intake valve closes. Both the temperature and pressure of compressed air rise noticeably. High compression ratios, which warm the air to a temperature high enough to ignite diesel fuel when it is injected, are characteristics of diesel engines. During the power stroke), fuel is fed into the heated, compressed air inside the cylinder after the compression stroke. An explosion results from the gasoline igniting when it comes into touch with the heated air. Mechanical effort is produced as a result of this explosion forcing the piston downward from TDC to BDC. This stroke generates power, which is used to move the car or carry out other mechanical operations. During the exhaust stroke, after the power stroke, the exhaust valve opens as the piston returns from BDC to TDC. Through the exhaust valve, the combustion gases are released from the cylinder during this movement. The exhaust valve closes and the cycle restarts with the intake stroke when the piston reaches TDC.

To generate the required kinetic energy, the engine repeats these runs in each cylinder. The gases pass through the exhaust system until they reach the outside air. The system extracts the exhaust gases from the engine, slows down their velocity, muffles the noise from the intense pressure bursts during exhaust discharge, and extinguishes any carbon part glowing from the engine before it leaves the atmosphere (Stone, 1999).

2.3. Exhaust gas products

An ideal mixing ratio, when achieved, yields harmless combustion products like carbon dioxide, nitrogen gas, and water vapor. However, the variable mixing ratios of engines make it challenging to control ideal combustion, potentially producing unwanted secondary gases. desirable and harmful to humans.

The burning of diesel fuel produces a variety of gases and particulates that make up the exhaust fumes from an internal combustion engine. These elements, which comprise both gaseous and solid

emissions, are produced by intricate chemical reactions that occur during combustion. Carbon dioxide (CO_2) is one of the main byproducts of full combustion. Carbon dioxide is created during combustion when the carbon in the diesel fuel combines with oxygen from the surrounding air. Although this gas is a significant greenhouse gas that contributes to climate change and global warming, it is not harmful in low doses. It makes up a significant amount of the exhaust gases. Water (H_2O) is created when oxygen interacts with the hydrogen atoms in diesel fuel. Usually harmless, water vapor in the exhaust manifests as steam and is most noticeable when the engine is cold. Nitrogen (N_2) is the main component of the exhaust gases when it leaves the engine and makes up a large portion of the intake air. Since nitrogen is inert, it does not immediately cause pollution. Oxygen (O_2) in the exhaust indicates either incomplete combustion or efficient combustion with surplus air. Its focus aids in the analysis of combustion efficiency and is applied to engine management systems' feedback control. Nitrogen oxides (NO_x) are created in the combustion chamber at high temperatures and pressures . Mainly nitrogen dioxide (NO_2) and nitric oxide (NO) are created. These circumstances allow for the reaction of oxygen and nitrogen in the air. NO_x emissions are harmful chemicals that lead to smog, acid rain, and respiratory problems. Carbon monoxide (CO) is one of byproduct of incomplete combustion. When there is not enough oxygen in the fuel to completely convert the carbon in it to carbon dioxide, it develops. At high concentrations, CO is a toxic gas that can have a fatal effect on health. Unburned hydrocarbons (HCs) that remain after a fuel burns partially are known as unburned fuel. These can contain several organic chemicals, some of which are dangerous air pollutants and can lead to the development of ground-level ozone (smog). Unburned hydrocarbons are a sign of poor combustion. Diesel exhaust contains particulate matter (PM), which consists of carbon particles called soot as well as other solids including metal pieces and sulfates. Because PM can enter the lungs deeply and cause respiratory and cardiovascular issues, it is very worrying. When sulphur compounds found in diesel fuel burn, sulphur dioxide (SO_2) is produced. The fuel's sulphur concentration determines how much SO_2 is released into the exhaust. Acid rain is preceded by SO_2, which is harmful to respiratory health. Formaldehyde and acrolein (aldehydes) are two examples of aldehydes that result from incomplete combustion. Certain substances are categorized as carcinogens and can irritate the eyes and respiratory system. Their existence in the exhaust signifies inadequate combustion circumstances.

The white fog in the exhaust gases that appears when the engine is running and its temperature has not yet risen, or in the winter, is considered normal. However, its exit with the hot engine exhaust gases and during warm weather conditions indicates water leaking into the cylinder. The appearance of blue smoke also indicates that burning oil is leaking. Due to the lack of valve tightness in the combustion chamber lacks valve tightness, black smoke indicates that the fuel-air mixture is rich, meaning there is a high percentage of fuel in it (Stone, 1999).

3. Experimental work

Pollution has become inevitable today, and the operation of electric generators causes two types of direct pollution: gaseous pollution resulting from the combustion of fossil fuels when operating generators and noise pollution, in addition to other indirect types of pollution. The current research dealt with the pollution resulting from gases emitted from the generators selected for the study, which numbered fifteen electrical generators with varying generating capacities that provide service to a specific number of houses. Table 1 provides codes of the generators based on their respective areas of operation. The values recorded in the month of December represented the average reading of a total of readings that lasted for one continuous hour, with a reading every ten minutes.

A field survey at the generators, recording the values of pollutants released into the external environment was conducted. Measuring instruments shown in Fig. 1, were used for measurements at a distance of one meter from the exhaust nozzle. To get a good idea of how well the generators were working in the study areas, it was found out how much carbon monoxide (CO), carbon dioxide (CO_2), nitrogen oxide (NO), nitrogen dioxide (NO_2), sulphur dioxide (SO_2), hydrogen sulphide (H_2S), and hydrogen chloride (HCl) were in the air, along with the temperature (T) and relative humidity (RH). The readings in ppm units were recorded and compared with the values of the standard case, as shown in Table 2.

Table 1. Generator specifications used in the field survey process.

Zone	Code	Generator manufacturing company	Generating capacity (kVA)	Voltage (V)	Number of residential units consumed
Wahid Adhar quarter	A1	Volvo	250	220	188
	A2	Volvo	200	200	200
Aldubaat quarter	A3	Volvo	290	200	200
Eadn quarter	A4	Scania	250	200	500
	A5	Volvo	300	235	400
Almuealimin quarter	B1	Scania	400	217	680
	B2	Scania	400	220	600
Gharnata quarter	B3	Scania moma	315	235	350
	B4	Scania	1100	220	800
	B5	Scania	250	220	400
Alasraa quarter	C1	Scania	290	230	400
	C2	Volvo	190	220	198
Aleaskariu quarter	C3	Volvo	250	220	344
	C4	Volvo	350	220	340
Aleaskariu quarter	C5	Scania moma	315	235	355

Fig. 1. Measuring instruments used in the field survey of pollutant samples: a) Dräger X-am 2000 gas detector, b) air quality monitor model TSI Q-Trak Model 7565 and c) GrayWolf meter for indoor air quality (IAQ) measurements.

Table 2. Values of chemical individuals and environmental conditions in a standard case.

Sequence	Parameter	Standard delimiter
	Chemical compounds	
1	CO	2.8 ppm
2	CO_2	250 ppm
3	O_2	24.2%
4	NO	2.7 ppm
5	NO_2	0.01 ppm
6	SO_2	0
7	H_2S	0
8	HCl	12.3 ppm
	Environmental conditions	
9	T	7.8 °C
10	RH	75.4%

Results were obtained under natural conditions in a public park approximately a kilometer away from the generator sites. These values were adopted as a standard parameter and named it the standard case. Through it, the number of pollutants added to the air surrounding was studied.

As for the specifications of the standards used in Table 2, the Dräger X-am 2000 gas detector is a dependable and effective gas detector with strong detection powers for flammable gases, carbon monoxide, hydrogen sulphide, and oxygen. This safe industrial design that is ideal for hard industrial applications and delivers accurate measurements makes it a great option for assuring safety in locations where gas risks are present. The operational parameters of Dräger X-am 2000 gas detector are as follows:

- O_2: range 0 - 25% volume and accuracy $\pm$ 0.2% volume,
- CO: range 0 - 2000 ppm and accuracy $\pm$ 2 ppm,
- H_2S: range 0 - 100 ppm and accuracy $\pm$ 1 ppm,
- Lower Explosive Limit (LEL) Range 0-100% LEL and accuracy $\pm$ 2% LEL.

The sophisticated and trustworthy air quality monitor model TSI Q-Trak Model 7565 is a tool for assessing air quality. It has excellent accuracy in measuring temperature, relative humidity, and carbon dioxide and carbon monoxide. Its sophisticated capabilities, such as data logging and analysis, along with its portable design make it a vital tool for maintaining safe and healthy settings. The operational parameters for measurement CO_2 concentration are range 0 - 5000 ppm and accuracy ± 50 ppm.

An innovative, trustworthy tool for gauging indoor air quality is the GrayWolf meter. It properly measures nitrogen oxides, sulphur oxides, carbon oxides, volatile organic compounds, hydrogen sulphide, hydrogen chloride in the air, humidity and temperature. Because of its lightweight form and sophisticated functions like data logging and analysis, it is an essential tool for maintaining safe and healthy indoor settings. The operational parameters of GrayWolf meter are as follows

- temperature (T): range -15 to +70 °C and accuracy: ± 0.3 °C,
- relative humidity (RH): range 0 - 100% and accuracy ± 2% RH,
- volatile organic compounds: range 5 – 20000 ppb,
- CO_2: range 0 - 50000 ppm and accuracy ± 150 ppm.

4. Results and discussion

The extracted figures for the state values collected from electric generators and their comparison with the standard state values are presented in Figs. 2-3.

Figure 2a shows that all cases had CO concentration values higher than the standard case, which was 2.8 ppm. The values of CO content varied, as it reached 51.5 ppm in the case, followed by case A5, which was 49.7 ppm, and case A3, which reached 41.3 ppm. The different types of generators, their operational age, and the number of houses they serve compared to their operational capacity account for the difference in values.

Figure 2b show the presence of CO_2 gas in some cases, either within reasonable limits or less than the standard case of 250 ppm. However, a significant CO_2 increase in case A4, reaching 470 ppm, can be attributed to the superior combustion process.
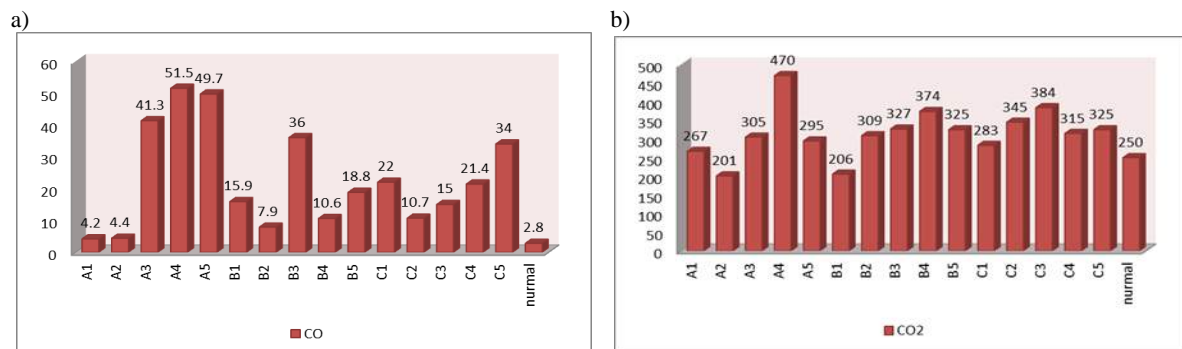
Fig. 2. a) CO and b) CO_2 gas concentrations.

NO_2 gas was not present in case A3 but was present in the other cases, but in very small or almost nonexistent amounts (Fig. 3a). The generator's lifetime caused case A4 to have a diffraction value of 1.96 ppm, followed by case A5, which reached 0.25 ppm.

In Figure 3b, one can see the diffraction of the NO gas value in case A4 is 51.8 ppm, followed by case A5, which is 16.2 ppm. As for the remaining cases, NO_2 content was within the standard range of 2.7 ppm.

Fig. 3. a) NO_2 and b) NO gas concentrations.

Figure 4a reveals the absence of the compound SO_2 in the standard case and in most of the remaining cases, with the exception of cases A3 and A4, which reached 0.5 ppm and 0.9 ppm, respectively. The high gas values in case A4 reflect the generator's high consumption compared to its counterparts, indicating its long operating life. In case A3, the number of houses it serves exceeds its generating capacity in comparison to the remaining cases.

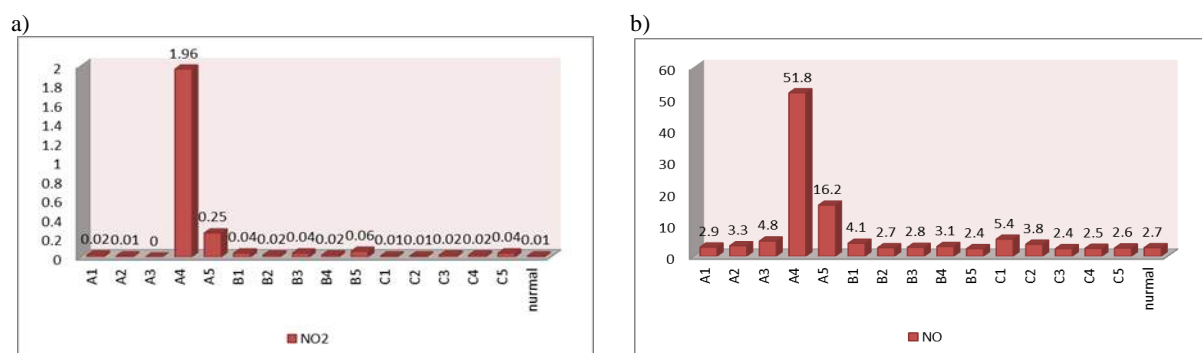H_2S was present and diffracted in case A4, which was 0.09 ppm, but it was not present in most of the other cases (Fig. 4b). Some of the other cases were different because they had H_2S, even if it was only a small amount. The lowest values of H_2S content were in cases A3 and A5, which amounted to 0.02. ppm. This compound is flammable and has a foul odor resembling moldy, colorless eggs. Heat can separate the gas emissions associated with petroleum extraction. It naturally contains different proportions of natural gas and oil, resulting from garbage fermentation or corpse decomposition. The H_2S is toxic and may cause death when exposed to low concentrations (Areaj kh airy alrawi Rana hazim, 2018). Therefore, workers exposed to the gas must review the risks and methods of dealing with it in the context of their work.
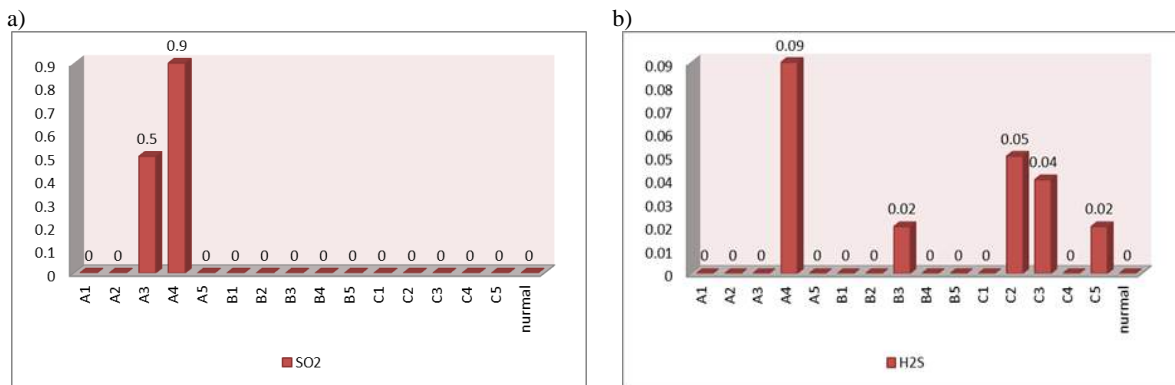

Fig. 4. a) SO_2 and b) H_2S gas concentrations.

Figure 5a reveals an increase in the HCl values across all cases. The highest value was in case A4 which reached 13.7 ppm, followed by case A5, which reached 4.6 ppm, while the standard case was 12.3 ppm. In all cases, high HCl content indicate a general presence of gas. Chemical reactions in nature, such as the interaction of chlorine-containing minerals with organic acids in the soil, as well as industrial and human activities, produce gas in the atmospheric air (Stone, 1999).

Figure 5b shows that the standard case's oxygen content increased to 24.2%, while all other cases showed a decrease, ranging from 20.9% to 22.5%. This indicates a deficiency in pure oxygen essential for the health of those present in those atmospheres, posing a threat to the health of those who operate and manage generators.
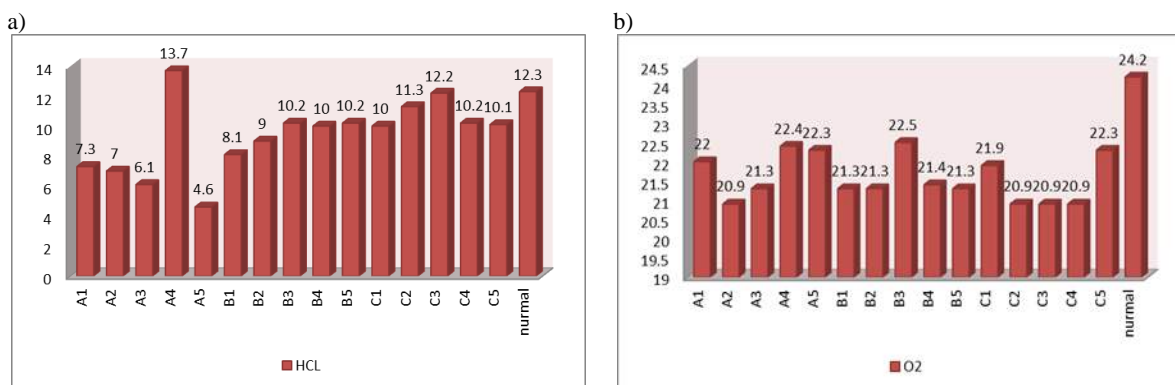
Fig. 5. a) HCl and b) O_2 gas concentrations.

Figure 6a shows the rise in exhaust temperatures relative to the air temperature in the standard case, which reached 7.8 °C. The temperature of the case A4 rose to 40 °C, followed by the case A3, which reached 32.2 °C. This was characterised by a relatively noticeable increase as a natural product of the generator (Stone, 1999). It should be noted that hot exhaust gases indirectly raise the temperature of the surrounding environment of the generators.

Figure 6b displays the monitored humidity percentage. All percentages are high, with the standard case (75.4%) being the highest.
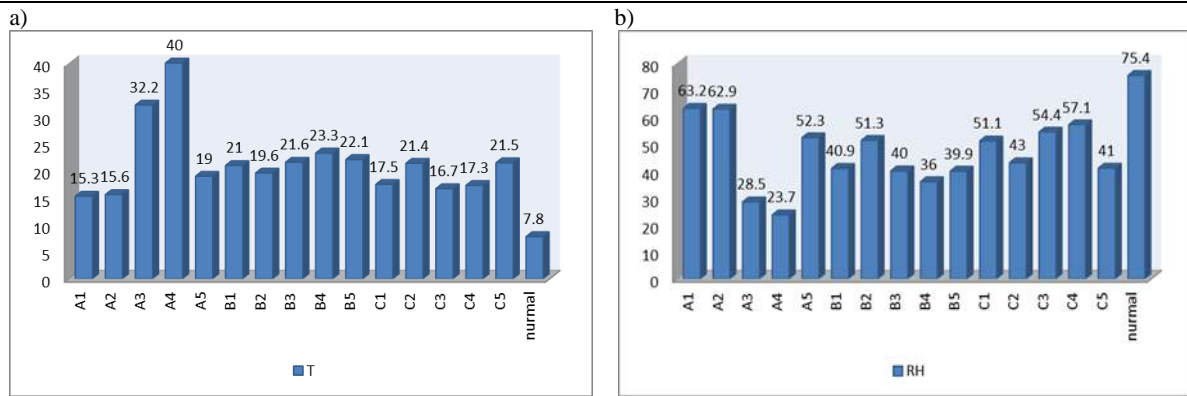
Fig. 6. a) temperature (T) and b) relative humidity (RH%) values.

5. Conclusions

From the above, it is clear that in order to determine the amount of toxic gases added to the atmosphere around us, we must compare the values for the standard case with the values obtained from generator exhaust. The polluted gases measured were as follows: HCl, H_2S, SO_2, NO_2, NO, CO_2 and CO. The measured contents of the mentioned chemical compounds were compared with the standard case: HCl = 12.3 ppm, H_2S = 0 ppm, SO_2 = 0 ppm, NO = 2.7 ppm, NO_2 = 0.01 ppm, CO_2 = 250 ppm, and CO = 2.8 ppm. The measured O_2 concentration and a temperature were 24.2% and 7.8 °C, respectively. The generators recorded the highest readings for gases at 13.7 ppm (HCl), 0.09 ppm (H_2S), 0.9 ppm (SO_2), 51.8 ppm (NO), 1.96 ppm (NO_2), 470 ppm (CO_2), and 51.5 ppm (CO). The highest values of O_2 concentration, relative humidity and a temperature were 20.9%, 75.4% and 40 °C, respectively.

The measured values reveal that the case A4 stands apart from its peers. This is because the generator's long operational life and consumable parts contributed to an increase in the toxic gases it exhaled. Additionally, the number of houses it served was large and not in line with its design capacity. This can be seen when comparing similar to the other cases in Table 2. The situation led to an increase in the engine's load, which in turn generated and expelled more gases from the exhaust.

6. Recommendations

1) It is critical to repair the central electrical networks and restore their efficiency to eliminate the need for private electrical generators.
2) It is suggested to conduct a study to establish central committees that will hold generators responsible for exceeding their engine's designed capacity, levy significant financial penalties if the generator exceeds its lifespan, and keep a close watch on nearby locations to prevent any diesel waste leaks. Operating oils can contaminate the soil around the generator.
3) It is suggested to installing filters for generator exhausts to reduce the impact of environmentally polluting gases.
4) Keep the generator as far away from residential neighborhoods as possible.
5) It is suggested to investigate the possibility of reducing the number of generators by merging them when there are too many in a single residential area.
6) Continuous maintenance and lubrication is needed to ensure a reduction in the emission of pollutants that increase due to poor operation.
7) It is suggested to study the possibility of placing electrical generators near a concentration of shade trees to benefit from them as networks for suspended particles and to create an environment in which large quantities of oxygen are present, necessary to oxidase air pollutants.
8) Generator owners should be forced to purchase silent generators with modern specifications if they replace the generator at the end of its operational life.
9) Renewable energy sources for residential buildings, such as solar cells, should be relied upon, especially since they are currently available in local markets, and using them as an alternative to electrical generator sources.

References

Abbas, H. H., Ibraheem, F. H., & Maaroof, A. A. (2019). Pollution problems in Koya City due to private electrical generators. *Aro-The Scientific Journal of Koya University*, 7(2), 38–46. https://doi.org/10.14500/aro.10538

Abbas, N. M., & Rajab, J. M. (2022). Sulfur Dioxide (SO_2) anthropogenic emissions distributions over Iraq (2000-2009) using MERRA-2 data. *Al-Mustansiriyah Journal of Science*, 33(4), 27–33. https://doi.org/10.23851/mjs.v33i4.1187

Abbas, T. R., & Abbas, R. R. (2021). Assessing health impact of air pollutants in five Iraqi cities using AirQ+ model. *IOP Conference Series: Materials Science and Engineering*, 1094(1), Article 12006. https://doi.org/10.1088/1757-899X/1094/1/012006

Al Kizwini, S. S, Khadim, I. A., & Rasha, S. M. (2013). Environmental pollution study of the impact of electric generators on the surrounding environment (case study: home generators). *Journal of Babylon University, Engineering Sciences*, 21, 1-17.

Al-Ashri, R. A. (2010). *Internal combustion engine (engine auxiliaries)* (1st ed.). Almaerifa Library: Alexandria Egypt.

AL-Hakkar Z. M., & AL-Maraashi, D. M. (2023). Study effect of noise pollution from electric generators on human health in Al-Najaf Al-Ashraf City. *Al-Kut University College Journal*, 50, 50–59.

AL-Heety, L. F. D., Hasan, O. M., & Al-Heety, E. A. M. S. (2021). Heavy metal pollution and ecological risk assessment in soils adjacent to electrical generators in Ramadi city, Iraq. *Iraqi Journal of Science*, 62(4), 1077–1087. https://doi.org/10.24996/ijs.2021.62.4.4

Al-Kasser, M. K. (2021). Air pollution in Iraq sources and effects. *IOP Conference Series: Earth and Environmental Science*, 790(1), Article 12014. https://doi.org/10.1088/1755-1315/790/1/012014

Al-Shwany, T. M. K., & Al-Karkh, R. M. S. (2022). Assessment of pollutants emitted by automobile exhaust on some physiological variables of the exposed people in the city of Kirkuk. *International Journal of Health Science*, 6(S6), 5499-5513. https://doi.org/10.53730/ijhs.v6nS6.10825

Ali, S.M. (2019). Study the environmental effects of private electrical generators for some locations in Kirkuk city. *Sulaimania Journal For Engineering Sciences*, 6(1), 136–147. https://doi.org/10.17656/sjes.10082

Areaj kh airy alrawi Rana hazim (2018). Impact environment of electric generation in Baghdad city-alkarada district 903. *Journal of Education College Wasit University*, 1(14), 294–314. https://doi.org/10.31185/eduj.Vol1.Iss14.386

Dhahad, H. A., & Fayad, M. A. (2020). Role of different antioxidants additions to renewable fuels on NO_X emissions reduction and smoke number in direct injection diesel engine. *Fuel*, 279, Article 118384. https://doi.org/10.1016/j.fuel.2020.118384

Giwa, S. O., Nwaokocha, C. N., & Samuel, D. O. (2023). Off-grid gasoline-powered generators: pollutants' footprints and health risk assessment in Nigeria. *Energy Sources, Part A: Recovery, Utilization, and Environmental Effects*, 45(2), 5352–5369. https://doi.org/10.1080/15567036.2019.1671555

Mohamedali, S. A., Ameen, M. H., & Saeb, A. (2020, February 21-23). Repercussion of petroleum industry and vehicle emissions on Kirkuk air quality using GIS. Proceedings of the 10th International Conference on Research in Engineering, Science, and Technology, (pp. 21–23). Diamond Scientific Publishing.

Mohammed, F. A. (2009). Pollution caused by vehicle exhausts and oil trash burning in Kirkuk city. *Iraqi National Journal of Earth Science*, 9(2), 39–48.

Oriakpono, O. E., & Ohabuike, U. C. (2022). Determination and comparison of CO2 and air pollutants emitted from the exhaust gas of selected electric generators. *Sultan Qaboos University Journal for Science*, 27(1), 1–18. https://doi.org/10.53539/squjs.vol27iss1pp1-18

Safiyanu, U., & Mohammed, K. (2020). Assessment of noise levels from diesel generators used for street lighting. *African Journal of Earth and Environmental Sciences*, 2(2), 617–622. https://doi.org/10.11113/ajees.v3.n1.104

Salah, S. A. H., Bahaa, Z., & Hasan, G. (2014). Mapping dispersion of urban air particulate matter over Kirkuk city using geographic information system. *Journal of Environment and Earth Science*, 4(8), 80–87.

Stone, R. (1999). Introduction to internal combustion engines (Vol. 3). Red Globe Press London. https://doi.org/10.1007/978-1-349-14916-2

Badania Eksperymentalne Emisji Spalinowych Generatorów Elektryczności i Ich Wpływu na Środowisko w Mieście Kirkuk

Streszczenie

W artykule oceniono wpływ emisji z prywatnych generatorów elektrycznych na środowisko, koncentrując się na ilości toksycznych gazów, jakie emitują one do otaczającego środowiska. W badaniach wykorzystano piętnaście generatorów zasilanych olejem napędowym, rozmieszczonych w określonych obszarach mieszkalnych miasta Kirkuk (Irak). Analizy obejmowały badania terenowe i pomiary z wykorzystaniem norm

zanieczyszczeń powietrza. Zmierzono zawartość HCL, H_2S, SO_2, NO_2, NO, CO_2, CO, O_2 oraz temperaturę i wilgotność względną w spalinach, aby zbadać zanieczyszczenia i porównać je z przypadkiem standardowym. Stwierdzono, że stężenia te zmieniały się w zależności od parametrów generatorów i były na wysokim poziomie. Wartości dyfrakcyjne wyróżniono w lokalizacji A4 (producent generatora – Scania, zdolność wytwórcza 250 kVA, napięcie 200 V, liczba obsługiwanych mieszkań – 500), która charakteryzowała się większymi stężeniami zanieczyszczeń niż w przypadku standardowym. W pozostałych przypadkach było to spowodowane różnymi czynnikami, m.in. okresem eksploatacyjnym generatora oraz większą liczbą obsługiwanych przez niego domów w stosunku do jego mocy wytwórczej, co przekraczało limit projektowy.

Słowa kluczowe: generatory prądu elektrycznego, wpływ zanieczyszczeń na środowisko, silniki spalinowe wewnętrznego spalania, stężenie zanieczyszczeń

Review

Current Possibilities for Recycling Industrial Metallic Wastes: Potential of KOBO Extrusion Process

**Damian Kołodziejczyk [1] , Romana Ewa Śliwa [1,2,*], Marek Zwolak [1,2] ,
Aleksandra Wędrychowicz [1,3]**

[1] Rzeszów University of Technology, al. Powstańców Warszawy 12, 35-959 Rzeszów, Poland;

[2] Department of Materials Forming and Processing, Faculty of Mechanical Engineering and Aeronautics, Rzeszów University of Technology, al. Powstańców Warszawy 8, 35-959 Rzeszów, Poland; m.zwolak@prz.edu.pl (M. Zwolak)

[3] Doctoral School in Rzeszów University of Technology, al. Powstańców Warszawy 12, 35-959 Rzeszów; d533@stud.prz.edu.pl

* Correspondence: rsliwa@prz.edu.pl

Abstract

The paper addresses the issue of utilizing industrial wastes considering the current legal regulations in Poland and the European Union. The importance of recycling was highlighted, with particular emphasis on metal elements whose natural deposits are limited. A comparison was made between primary methods of metal extraction and metal recovery (from secondary sources) using solid-state recycling methods without melting. An analysis of some methods for recycling industrial metallic wastes was conducted. Special attention was given to metal chips and the accompanying lubricating and cooling substances. An innovative recycling process was presented – the KOBO extrusion of metallic wastes in the form of chips, with example research results and a list of benefits from using this process for the production of metal profiles.

Keywords: recycling, post-production wastes, utilizing industrial wastes, legal regulations, KOBO extrusion

1. Introduction

The current state of legal regulations concerning waste utilization, in reference to numerous publications on metal recycling (Waste Management in the European Union, Circular Economy, Recycling), demonstrates the possibilities for their use and provides a basis for assessing the selection of recycling methods and their effects. This is crucial from the perspective of the types of metallic materials and the nature and properties of industrial wastes.

The growing global population results in increased metal consumption, leading to the generation of larger quantities of waste (Zante et al., 2024). According to the European Parliament directive, waste is defined as any substance or object which the holder disposes of or is required to dispose of pursuant to the provisions of national law in force (European Parliament and the Council of the European Union, 2008). All EU members must adhere to the waste hierarchy presented in Fig. 1 (European Parliament and the Council of the European Union, 2008; Grabas, 2015).

First and foremost, waste generation should be prevented. If this is not possible, waste should be prepared for reuse, recycled, recovered in some other way, or disposed of (European Parliament and the Council of the European Union, 2008). Waste processing aims to meet the demand for secondary raw materials while increasing the security of raw material supply and stimulating innovative solutions (Nowicka, 2020). The European Commission mandates the increased use of recycled secondary raw materials in new products (European Commission, 2020a). The sustainable use of materials and the reduction of negative environmental impact are ensured by applying a circular economy (McKinsey & Company, 2016; Ellen MacArthur Foundation, 2013). The circular economy model is presented in Fig. 2.
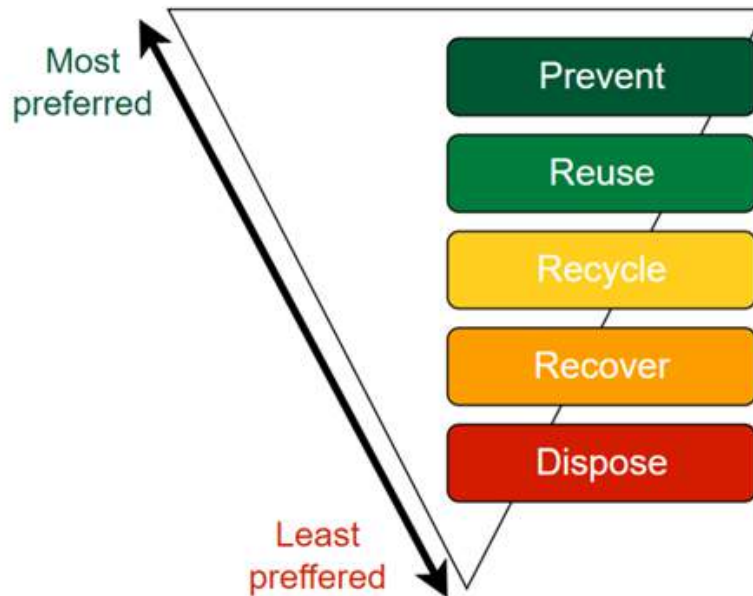
Fig. 1. Waste hierarchy in the EU (Grabas, 2015).

Fig. 2. Circular economy model (European Parliament, 2023).

The transition from the current linear economy to a circular economy brings long-term benefits (Kwiecień, 2018; Nowicka, 2020). This shift aims to achieve a 55% reduction in greenhouse gas emissions by 2030 and zero pollution by 2050 (Fetting, 2020), while it is forecasted that by then, the consumption of natural resources will double (Pietrzyk-Sokulska, 2016; European Commission, 2021). To reach these goals, Europe needs a competitive, green, and more digitalized industry (European Commission, 2020b). It is anticipated that the value of the global green market will be around 2 trillion dollars by 2028. By 2030, the circular economy could be worth as much as 4.5 trillion dollars (Degórski, 2018).

An essential part of the circular economy is the development of new, eco-friendly, and innovative solutions as well as technological transformation (Degórski, 2018; Nowicka, 2020; Zante et al., 2024). The industrial sector is responsible for 50% of total pollution emissions (European Commission,

2024). In the EU, industrial processes and product use accounted for approximately 9.10% of greenhouse gas emissions in 2019 (European Parliament, 2018). It is also estimated that 23% of global greenhouse gas emissions arise from the extraction and processing of natural resources. The application of eco-design ensures easier recycling at later stages (Nowicka, 2020). In highly developed countries, recycling rates can reach up to 50% (Pietrzyk-Sokulska, 2016).

Recycling is the process of recovering waste, whereby waste becomes a useful product again (European Parliament and the Council of the European Union, 2008). It is estimated that until a few years ago, 92% of raw materials used only once were disposed of (Degórski, 2018). Increased consumption leads to the exploitation of natural resources (Kwiecień, 2018). As a result, non-renewable raw materials are depleting and could eventually disappear completely (Degórski, 2018; Pietrzyk-Sokulska, 2016). Therefore, secondary raw materials from the recovery process, which can be reused in production, are gaining importance (Pietrzyk-Sokulska, 2016). Although metal recovery is challenging due to the varied composition of materials withdrawn from use (European Parliament and the Council of the European Union, 2008), recycling leads to reduced operational costs (Kwiecień, 2018) and is a less energy-intensive process compared to sourcing raw materials from primary sources (Pietrzyk-Sokulska, 2016). Recovery also ensures resource security and competitiveness in the EU by reducing dependency on raw material imports from other countries (Degórski, 2018; Pietrzyk-Sokulska, 2016).

Manufacturing metal products generates a large amount of waste (chips, scraps, defective products, or those not meeting standards). The most common method of recycling this waste is melting it down. However, this process has a significant limitation. Scrap in the form of chips undergoes oxidation during the melting process, resulting in the loss of a substantial portion of the material, even up to 60% (Dybiec, 2010), which makes this method inefficient despite the preliminary briquetting before melting (Tucholski, 2013).

There is also the aspect of environmental pollution due to the presence of lubricants, coolants, and other substances used in the production of metal products (Dybiec & Kabalak, 2009).

A key aspect in choosing a recycling method is considering all factors that influence the positive outcome of the process. These include preparation and implementation costs, environmental impact (expected to have no negative impact), and the benefits of using the chosen method and the potential for using post-recycled products.

2. Methods of recycling industrial metallic wastes

Metals, which constitute 4% of all waste globally (Maloney et al., 2020), can be recycled multiple times without losing their properties and quality (Born & Ciftci, 2024; Dubreuil et al., 2010). Recycling ferrous metals consumes 74% less energy, 40% less water, and generates 58% less carbon dioxide emissions compared to extraction from ores. In contrast, recycled aluminum uses 90-95% less energy, while copper recycling requires 85% less energy than production from ores (Krall et al., 2024; Maloney et al., 2020).

Table 1 presents the end-of-life recycling input rates for the EU. The recycling rates for the listed materials vary significantly. The very low rates for some of them are attributed to (European Commission, Joint Research Centre, 2018):

- the unprofitability of recycling,
- the lack of appropriate recycling technology,
- use in long-lasting products,
- increasing demand for these materials.

Alloys of aluminum and iron, which are widely used in industrial production processes, are easy to recover and separate using mechanical sorting and pyrometallurgical processes. However, pyrometallurgical recovery methods consume a significant amount of energy. Hydrometallurgical methods generate considerable waste and require large quantities of water and other chemicals. Both hydrometallurgical and pyrometallurgical methods also produce hazardous gases and wastewater, whose treatment can be costly (Li et al., 2022; Zante et al., 2024).

Aluminum and its alloys can be recycled using conventional remelting methods as well as innovative solid-state recycling methods or without remelting (Gronostajski et al., 2000; Rietdorf et al., 2024). During remelting, liquid aluminum should be treated as a hazardous material due to its high susceptibility to fires and explosions (Dion-Martin et al., 2021; Park et al., 2022).

Table 1. End-of-life recycling input rates for the EU (European Commission. Joint Research Centre, 2018).

Element	End-of-life recycling input rates	Element	End-of-life recycling input rates
Li	0%	Pd	9%
Be	0%	Pr	10%
K	0%	Ru	11%
Sc	0%	Pt	11%
Ga	0%	Mn	12%
Si	0%	AI	12%
Nb	0%	Mg	13%
In	0%	Ir	14%
Dy	0%	Cu	17%
Be	0.6%	P	17%
F	1%	Ti	19%
He	1%	Au	20%
Te	1%	Cr	21%
Ba	1%	Tb	22%
HF	1%	Sb	28%
Ta	1%	Mo	30%
Bi	1%	Fe	31%
La	1%	Zn	31%
Ce	1%	Y	31%
Nd	1%	Sn	32%
Sm	1%	Ni	34%
Gd	1%	Co	35%
Ho	1%	Eu	38%
Tm	1%	W	42%
Yb	1%	V	44%
Lu	1%	Re	50%
S	5%	Ag	55%
Rh	9%	Pb	75%

During the manufacturing process of metal products, significant amounts of waste are generated in the form of chips (Pawłowska & Śliwa, 2017). Aluminum chips can be divided into those resulting from machining or abrasive processes (Lee et al., 2017). Aluminum chips constitute 13.7% and steel chips 14.6% of the waste in the manufacturing industry worldwide (Dhiman et al., 2021). One study showed that cooling and lubricating substances account for about 20% of industrial chips (Rietdorf et al., 2024). Depending on the machining process used, the volume of chips compared to the volume of the machined material is 15 to 30 times greater. The geometry of the chips depends on the cutting speed, cutting depth, the tool used, and the properties of the material from which the workpiece is made (Lee et al., 2017). The burning of residual oils, emulsions, and coolants on the surface of the chips during remelting releases very dangerous gases (Rietdorf et al., 2024; Topolski et al., 2021).

Cooling and lubricating fluids used in machining can be divided into straight oils, soluble oils (emulsions), synthetic fluids, and semi-synthetic fluids. Metal chips can be separated from the lubricating and cooling agents. Table 2 presents some methods for separating lubricating and cooling fluids from chips. Magnetic separation is characterized by low maintenance costs and small size of the separator but it can only be used for materials exhibiting magnetic affinity. Centrifugal separation works well with oils but has a low fluid flow rate, making it difficult to remove large amounts of fluid. Membrane application removes bacteria and it is easy to use, but it has a slow filtration time and high membrane costs. The chemical method effectively removes organic substances but requires a large amount of space, is costly, and generates a large amount of waste. The biological method generates a small amount of waste and effectively dissolves organic substances, but it requires specialized equipment. (Lee et al., 2017).

Table 2. Advantages and disadvantages of recycling methods for cooling and lubricating fluids mixed with metal chips (Lee et al., 2017).

Method	Advantages	Disadvantages
Magnetic separation	Low maintenance costs and small size of the separator	Can only be used for materials with magnetic affinity.
Centrifugal separation	Effective removal of oils from chips	Low fluid flow rate makes it difficult to remove large quantities of fluids
Membrane application	Removes bacteria and is easy to use	Slow filtration time and high membrane costs
Chemical	Effectively removes organic substances	Requires a large amount of space, is costly, and generates a large amount of waste
Biological	Generates a small amount of waste and effectively dissolves organic substances	Requires specialized equipment

Materials such as titanium (Ti) and its alloys, nickel (Ni) and its alloys, and other superalloys present challenges in recycling because they require high processing forces and are difficult to machine. These high forces often lead to damage of die components or tools. Therefore, it is necessary to develop new technologies or innovatively use existing technologies to ensure sustainable and efficient recycling of metal chips (Dhiman et al., 2021).

Machining materials such as titanium generates a very large amount of waste in the form of chips. It is estimated that the mass of chips compared to the total mass of the machined object constitutes 55% (Dhiman et al., 2021). In specific cases, such as the production of biomedical or aerospace parts from titanium, the waste in the form of chips can even constitute up to 80% (Topolski et al., 2017).

Recycling aluminum and its alloys from the secondary market allows for the savings of up to 20 times more energy compared to obtaining it through extraction (Krall et al., 2024; Shamsudin et al., 2016). The use of metal remelting processes is inefficient due to oxidation and the formation of waste in the form of slags (Rietdorf et al., 2024). Recycling chips using conventional remelting is characterized by a recovery rate of about 60% (Rietdorf et al., 2024; Shamsudin et al., 2016).

On the other hand, direct conversion methods (DCM) transform metal chips (MC) into briquettes, which are easy to handle and process further. Processing materials such as aluminum (Al), magnesium (Mg), and copper (Cu) using DCM is feasible due to lower force requirements. Despite many advantages of direct conversion methods, chips have certain limitations. The disadvantages of using some conventional and unconventional metal recycling methods are presented in Fig. 3 (Dhiman et al., 2021).
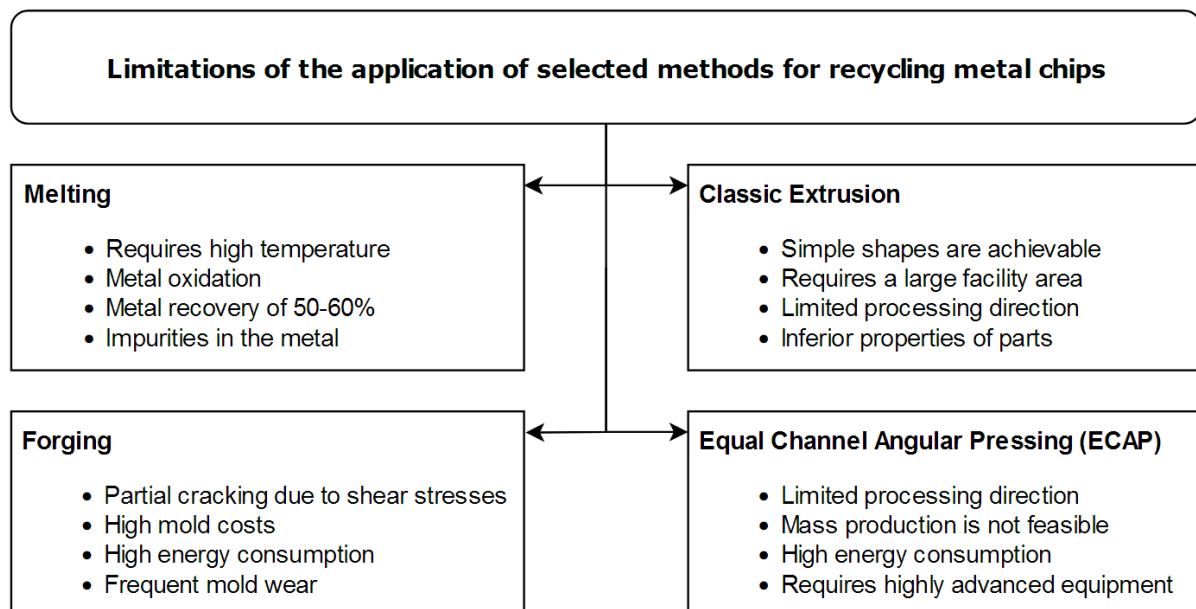
Fig. 3. Limitations of the application of selected direct conversion methods for recycling metal chips (Dhiman et al., 2021).

Equal Channel Angular Pressing (ECAP) is characterized by limited processing direction, high energy consumption, the need for advanced equipment, and is not suitable for mass production. Melting generates high temperatures, leading to metal oxidation, introduces impurities, and achieves metal

recovery rates of only 50-60%. Classic extrusion allows for the formation of simple shapes but requires a large facility area, it has a limited processing direction, and produces parts with inferior properties. Forging is costly due to the use of dies that wear out quickly, it consumes a lot of energy, and can cause partial material cracking (Dhiman et al., 2021; Lee et al., 2017).

Considering that significant amounts of industrial waste, primarily chips, are generated during the machining of metals, especially aluminum and magnesium alloys (Table 3), the issue of proper management of this waste, including the use of recycling processes, is very important.

Table 3. Standard chips forms acc. to ISO 3685.

1 Ribbon chips	2 Tubular chips	3 Spiral chips	4 Washer type helical chips	5 Conical helical chips	6 Arc chips	7 Elemental chips	8 Needle chips
1.1 Long	2.1 Long	3.1 Flat	4.1 Long	5.1 Long	6.1 Connected		
1.2 Short	2.2 Short	3.2 Conical	4.2 Short	5.2 Short	6.2 Loose		
1.3 Snarled	2.3 Snarled		4.3 Snarled	5.3 Snarled			

Chips, which are waste generated in the machining of aluminum and magnesium alloys in the aerospace and automotive industries—such as turning, milling, drilling, reaming, tapping, and cutting—can serve as a source for recovering input material for use in other shaping technologies, primarily plastic deformation processes.

In the machining process of aluminum alloys, the same types of chips can be produced as when processing other materials. The most commonly encountered chips are ribbon chips and spiral chips, along with their variations. The type of chip is influenced by the shape of the cutting edge (chip breaker) and the cutting parameters.

The cutting temperature has an indirect effect on the chip formation. While machining with emulsions as cutting fluids results in long spiral chips, machining the same alloy dry under the same cutting parameters produces short spiral chips (Feld, 1984).

During the machining of magnesium alloys, short chips are most commonly produced (due to the formation of serrated chips), which are easy to remove from the machine tool (Kłonica et al., 2015; Oczoś, 2009).

The KOBO (Korbel and Bochniak method of plastic forming) extrusion process (Korbel & Bochniak, 1998) is one of the very promising recycling methods as it helps eliminate the previously described limitations of recycling metal chips. This method allows for the consolidation of chips into a solid material through pressing of scrap at low-temperature(Korbel et al., 2016). The melting stage is replaced by hot extrusion, resulting in the direct remelting of waste (Dybiec, 2008). An additional advantage of recycling using the KOBO method is the preservation of the mechanical and plastic properties of the alloy, and in some cases, even achieving better parameters than those of solid material (Bochniak et al., 2023; Dybiec, 2007; Xu et al., 2012; Watanabe et al., 2001). Low-temperature consolidation minimizes material losses and energy consumption by as much as five times (Chmura & Gronostajski, 2000).

Characterizing waste from metallic materials in terms of type, material properties, geometric forms, mechanical properties, and the type and properties of industrial impurities (such as lubricants, oils, and emulsions) is essential for developing the input material preparation for the KOBO extrusion process (Bochniak, 2009) and for selecting the parameters of that process.

Chips, as a specific type of waste, have the largest quantitative, volumetric, weight, and percentage share in the overall metallic waste. They are characterized by specific features resulting from:

- the types of metallic materials and their origin from a given machining technology,
- geometry (shape and size),
- the potential for consolidation (forming input materials for subsequent processing steps, including the KOBO extrusion process).

Chips represent a significant potential as a relatively inexpensive input material for further plastic processing. The geometry of the chips affects the consolidation process (Topolski et al., 2021), as their characteristics lead to interlocking, adhesion, and blockage. In briquettes, there is a smaller number of voids, but the connections between chips are weaker, making it difficult to form strong bonds. Thick chips create a structure that is more challenging to undergo elastic and plastic deformation. A properly prepared preliminary consolidation process for chips into briquettes is crucial (as illustrated in Fig. 4).
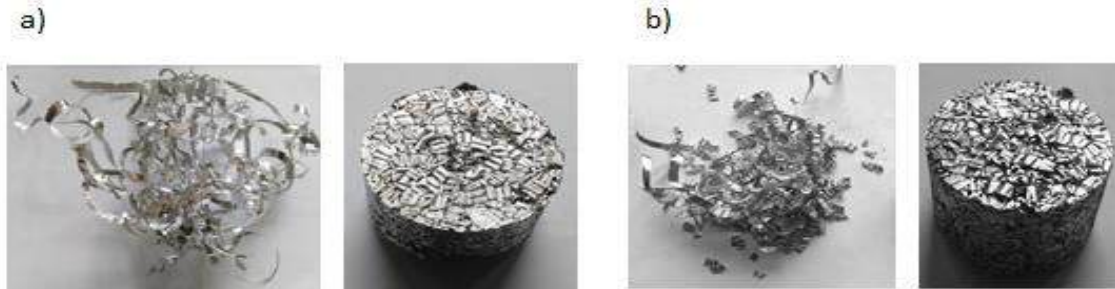
Fig. 4. Post-processing chips of a) 2024 alloy and b) 7075 alloy in fragmented and briquetted forms.

An example of a promising and energy-efficient recycling process for fragmented metallic fractions (wastes and chips) is the KOBO extrusion process (Bochniak, 2009; Pawłowska et al., 2019; Topolski & Ostachowski, 2021). Selected sample results from the KOBO process show that pre-consolidated billets in the form of briquettes can be effectively processed through KOBO extrusion when the following parameters are appropriately selected:

- Reverse die rotation angle (2-8 degrees).
- Die oscillation frequency (2-10 Hz).
- Extrusion rate (adjusted to the extrusion ratio and type of metal being extruded).
- Input material at room temperature (without preheating the input material).
- Extrusion ratio.

The KOBO method is characterized by its ability to achieve excellent mechanical properties in the products, which are optimal at room temperature deformation and offer superplasticity at higher temperatures (Bochniak et al., 2023). The preparation and execution of the KOBO process are schematically presented in Fig. 5. The KOBO extrusion press is shown in Fig. 6.

POST-PROCESSING METAL CHIPS   BRIQUETTING   EXTRUSION USING KOBO METHOD
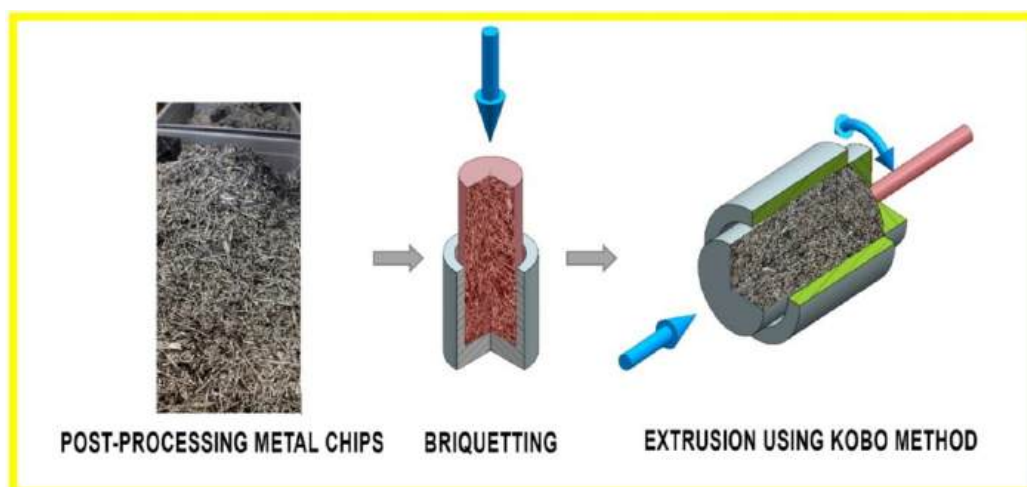
Fig. 5. Scheme of the preparation and execution of the KOBO extrusion process.

The extrudates obtained through this method demonstrated very positive characteristics, as confirmed by the results of mechanical property tests, including tensile testing results (Fig. 5) and the

analysis of the micro and macrostructure examined on the cross-section of the extruded part, e.g. Fig. 6. Comparison of mechanical properties of extruded solid billets and consolidated industrial chips by the KOBO method is presented in Fig. 7.

a)   b)
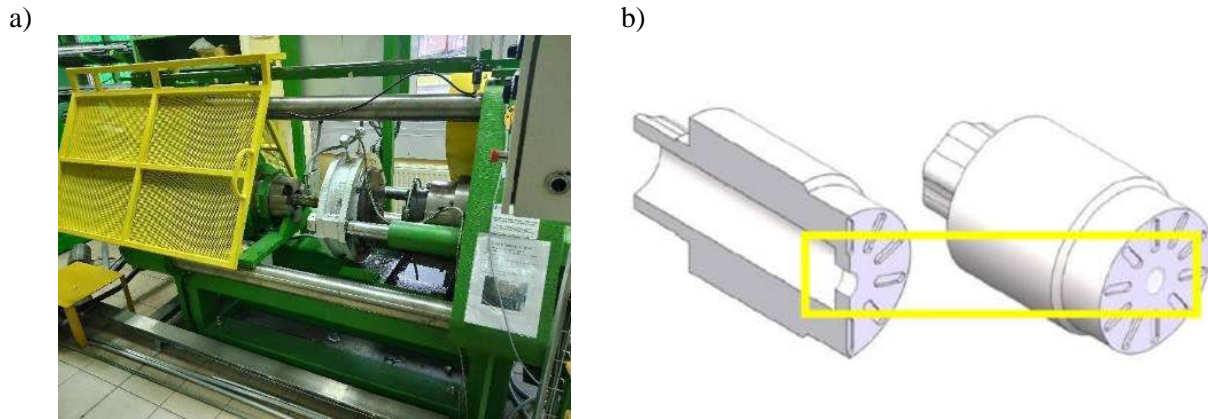
Fig. 6. Laboratory stand: a) KOBO extrusion press, b) dies used in the KOBO process.

a)

b)
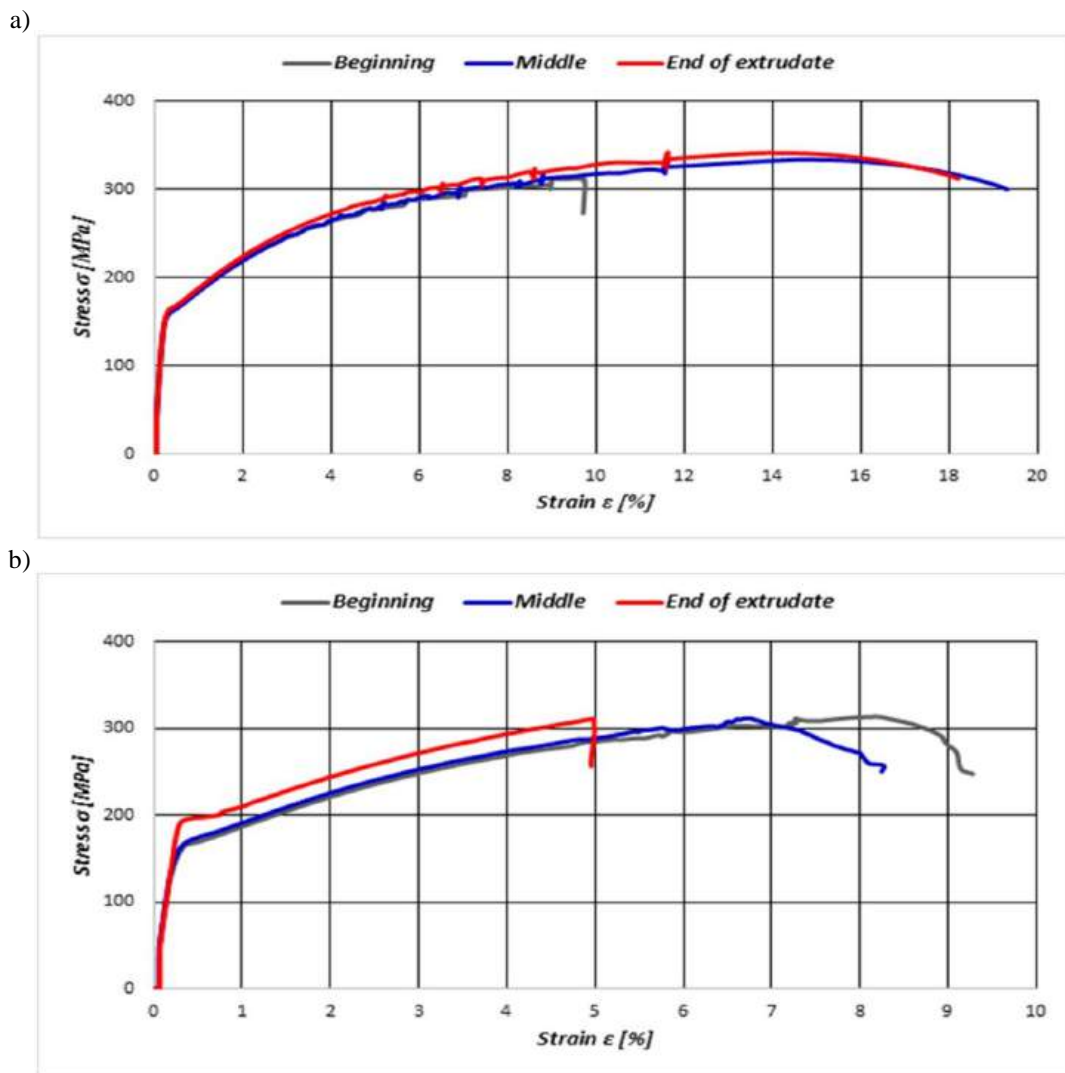
Fig. 7. Comparison of mechanical properties of extruded solid billets and consolidated industrial chips by the KOBO method
a) Tensile curves for φ = 10 mm rods obtained by KOBO method consolidation of industrial chips from aluminum alloy 2024
b) Tensile curves for φ = 10 mm rods from aluminum alloy 2024 – solid billet.

It is important to note the uniform values of the mechanical properties of the extruded product (homogeneity of properties along the length of the extrudate) in the case of product extruded from briquetted chips compared to profile extruded using solid billets (see Table 4). This allows for the

production of 'long' products with any desired cross-sectional shape (profile), as stated in the publication (Korbel et al., 2016).

Table 4. Comparison of the properties of the compact during the KOBO extrusion (samples taken from the beginning, middle, and end of extrudate) using input in the form of briquetted chips, and input in the form of solid billets.

Chips				Solid billet			
Alloy / features	UTS [MPa]	YS [MPa]	A [%]	Alloy / features	UTS [MPa]	YS [MPa]	A [%]
2024 – in the beginning	290	161	9.2	2024 – in the beginning	286	163	9.7
2024 – in the middle	299	165	19.3	2024 – in the middle	292	171	8.2
2024 – at the end	306	171	18.2	2024 – at the end	296	196	4.9

The results of plastic deformation of the input material in the form of briquetted chips, assessed on the basis of the analysis of the internal structure of the extruded profile, indicate a satisfactory consolidation effect close to full consolidation (Fig. 8).
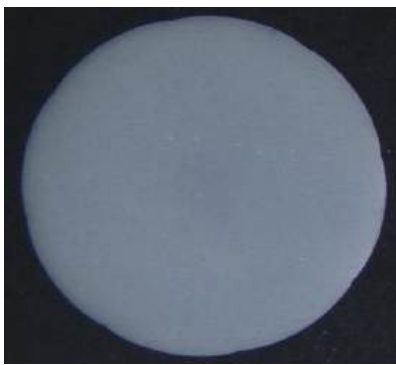
a)   b)
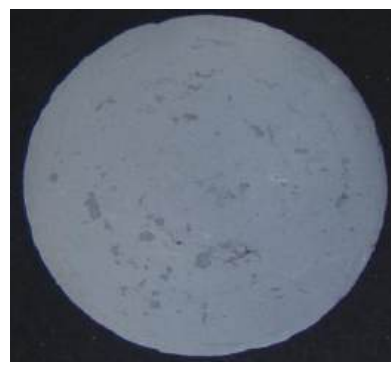
Fig. 8. Macrostructure of the sample from aluminum 2024 alloy a) from the extrusion obtained in the KOBO process using a solid billet, b) from the extrusion obtained in the KOBO process using briquetted chips.

The presented examples of research results regarding the effect of using the KOBO extrusion process for recycling industrial wastes, primarily chips from metallic materials, confirm the validity of employing this process for this purpose.

3. Summary

The demonstrated and documented necessity for seeking and implementing recycling processes in the global economy justifies conducting research aimed at material savings across various industries, minimizing energy consumption, and avoiding adverse environmental impacts. This is particularly relevant for metallic materials, which, in the form of various types of industrial waste, pose a significant recycling challenge. Chips from machining processes represent a large portion of this waste. Their recycling can be achieved through the innovative low-temperature KOBO extrusion, which is a low-energy process that ensures favorable properties of the obtained products.

All types of investigated metal chips that were consolidated and plastically deformed in the KOBO extrusion process led to the production of rods, regardless of the cleanliness and properties, type of chips, as well as their shape and thickness. It has been shown that despite significant differences in the properties of the chips, the KOBO extrusion process allowed for the conversion of chips into solid material.

It has been demonstrated that all rods produced after recycling possess a solid, monolithic structure in the raw state, which is homogeneous, consolidated, and nearly fully dense. No significant macro or micro defects such as cracks, porosity, or discontinuities were observed.

Using the method of large plastic deformation through the KOBO extrusion process, it is possible to modify the material via strengthening to such an extent that the values of its mechanical properties exceed those obtained after heat treatment.

References

Bochniak, W. (2009). *Teoretyczne i praktyczne aspekty plastycznego kształtowania metali*. Wydawnictwo AGH.

Bochniak, W., Ostachowski, P., Korbel, A., & Łagoda, M. (2023). Potential of the KOBO extrusion process for nonferrous metals in the form of solids and chips. *The International Journal of Advanced Manufacturing Technology, 127*(1–2), 733–750. https://doi.org/10.1007/s00170-023-11596-7

Born, K., & Ciftci, M. M. (2024). The limitations of end-of-life copper recycling and its implications for the circular economy of metals. *Resources, Conservation and Recycling, 200*, Article 107318. https://doi.org/10.1016/j.resconrec.2023.107318

Chmura, W., & Gronostajski, J. (2000). Mechanical and tribological properties of aluminium-base composites produced by the recycling of chips. *Journal of Materials Processing Technology, 106*(1–3), 23–27. https://doi.org/10.1016/S0924-0136(00)00632-4

Degórski, M. (2018). Gospodarka o obiegu zamkniętym circular economy – nowe podejście w rozumieniu relacji człowiek–środowisko. *Studia Komitetu Przestrzennego Zagospodarowania Kraju PAN, 183*, 27–35.

Dhiman, S., Joshi, R. S., Singh, S., Gill, S. S., Singh, H., Kumar, R., & Kumar, V. (2021). A framework for effective and clean conversion of machining waste into metal powder feedstock for additive manufacturing. *Cleaner Engineering and Technology, 4*, Article 100151. https://doi.org/10.1016/j.clet.2021.100151

Dion-Martin, O., Desmeules, J.F., & Dumont, R. (2021). Molten aluminium transfer: Review and comparison of different technologies. In L. Perander (Ed.), *Light Metals 2021* (pp. 769–777). Springer International Publishing. https://doi.org/10.1007/978-3-030-65396-5_101

Dubreuil, A., Young, S. B., Atherton, J., & Gloria, T. P. (2010). Metals recycling maps and allocation procedures in life cycle assessment. *The International Journal of Life Cycle Assessment, 15*(6), 621–634. https://doi.org/10.1007/s11367-010-0174-5

Dybiec, H. (2007). Plastic consolidation of metallic powders. *Archives of Metallurgy and Materials, 52*(2), 161-170.

Dybiec, H. (2008). *Submikrostrukturalne stopy aluminium*. AGH Uczelniane Wydawnictwa Naukowo-Dydaktyczne.

Dybiec, H. (2010). Alternatywny proces recyklingu trudno przerabianych złomów z metali lekkich. *Metalurgia'2010: Konferencja Sprawozdawcza Komitetu Metalurgii PAN, Krynica Zdrój*. https://badap.agh.edu.pl/publikacja/66788

Dybiec, H., & Kabalak, A. (2009). Ocena możliwości odzysku chłodziw z wiórów po obróbce skrawaniem stopów aluminiowych na drodze obróbki termicznej. *Ochrona Powietrza i Problemy Odpadów*, *43*(4), 137-142.

Ellen MacArthur Foundation. (2013). *Towards the circular economy: Economic and business rationale for an accelerated transition* (Vol. 1). https://www.ellenmacarthurfoundation.org/towards-the-circular-economy-vol-1-an-economic-and-business-rationale-for-an

European Commission, Joint Research Centre. (2018). *Towards recycling indicators based on EU flows and raw materials system analysis data: Supporting the EU 28 raw materials and circular economy policies through RMIS*. Luxembourg: Publications Office of the European Union. https://data.europa.eu/doi/10.2760/092885

European Commission. (2020a). *A new circular economy action plan*. https://environment.ec.europa.eu/strategy/circular-economy-action-plan_en

European Commission. (2020b). *A new industrial strategy for Europe*. https://eur-lex.europa.eu/legal-content/EN/TXT/?uri=CELEX:52020DC0102

European Commission. (2021, July 15). *Zero pollution action plan - 2050: A healthy planet for all*. https://environment.ec.europa.eu/publications/zero-pollution-action-plan-2050-healthy-planet-all_en

European Commission. (2024). *Industrial emissions and safety*. https://environment.ec.europa.eu/topics/industrial-emissions-and-safety_en

European Parliament and the Council of the European Union. (2008). *Directive 2008/98/EC on waste and repealing certain directives (Text with EEA relevance)*, OJ L 312. http://data.europa.eu/eli/dir/2008/98/oj/eng

European Parliament. (2018). Greenhouse gas emissions by country and sector (infographic). https://www.europarl.europa.eu/topics/en/article/20180301STO98928/greenhouse-gas-emissions-by-country-and-sector-infographic

European Parliament. (2023). Circular economy: Definition, importance, and benefits. https://www.europarl.europa.eu/topics/en/article/20151201STO05603/circular-economy-definition-importance-and-benefits

Feld, M. (1984). *Obróbka skrawaniem stopów aluminium*. Wydawnictwa Naukowo-Techniczne.

Fetting, C. (2020). *The European Green Deal*. European Sustainable Development Network. https://www.esdn.eu/fileadmin/ESDN_Reports/ESDN_Report_2_2020.pdf

Grabas, M. (2015). *Waste management*. Oficyna Wydawnicza Politechniki Rzeszowskiej.

Gronostajski, J., Marciniak, H., & Matuszak, A. (2000). New methods of aluminium and aluminium-alloy chips recycling. *Journal of Materials Processing Technology, 106*(1–3), 34–39. https://doi.org/10.1016/S0924-0136(00)00634-8

Kłonica, M., Kuczmaszewski, J., Zaleski, K., Matuszak, J., Pieśko, P., Włodarczyk, M., Pałka, T., Rusinek, R., & Zagórski, I. (2015). *Obróbka skrawaniem stopów aluminium i magnezu*. Politechnika Lubelska.

Korbel, A., Bochniak, W., Śliwa, R., Ostachowski, P., Łagoda, M., Kusion, Z., & Trzebuniak, B. (2016). Low-temperature consolidation of machining chips from hardly-deformable aluminum alloys. *Obróbka Plastyczna Metali, 27*(2), 133-152.

Korbel, A., & Bochniak, W. (1998). Method of plastic forming of materials. U.S. Patent No. 5,737,959. European Patent No. 737,959.

Krall, P., Weißensteiner, I., & Pogatscher, S. (2024). Recycling aluminum alloys for the automotive industry: Breaking the source-sink paradigm. *Resources, Conservation and Recycling, 202*, Article 107370. https://doi.org/10.1016/j.resconrec.2023.107370

Kwiecień, K. (2018). Gospodarka o obiegu zamkniętym – wyzwania dla przedsiębiorstw. *Gospodarka w Praktyce i Teorii, 52*(3), 47–59. https://doi.org/10.18778/1429-3730.52.04

Lee, C. M., Choi, Y. H., Ha, J. H., & Woo, W.-S. (2017). Eco-friendly technology for recycling of cutting fluids and metal chips: A review. *International Journal of Precision Engineering and Manufacturing-Green Technology, 4*(4), 457–468. https://doi.org/10.1007/s40684-017-0051-9

Li, F. Q., Wang, P., Chen, W., Chen, W. Q., Wen, B., & Dai, T. (2022). Exploring recycling potential of rare, scarce, and scattered metals: Present status and future directions. *Sustainable Production and Consumption, 30*, 988–1000. https://doi.org/10.1016/j.spc.2022.01.018

Maloney, M. M., Grimm, S. D., & Anctil, R. (2020). Atlas international business case: Examining globalization and economic indicators for the scrap metal recycling industry. *Journal of Accounting Education, 51*, Article 100661. https://doi.org/10.1016/j.jaccedu.2020.100661

McKinsey & Company. (2016). *The circular economy: Moving from theory to practice*. McKinsey Center for Business and Environment.

Nowicka, K. (2020). Zielone łańcuchy dostaw 4.0. In J. Gajewski & W. Paprocki (Eds.), *Polityka klimatyczna i jej realizacja w pierwszej połowie XXI wieku* (pp. 114-135). Sopot: Centrum Myśli Strategicznych.

Oczoś, K. E. (2009). Rozszerzanie granic stosowalności stopów magnezu. *Mechanik, 82*(5–6), 388-400.

Park, H., Nam, K., & Lee, J. (2022). Lessons from aluminum and magnesium scraps fires and explosions: Case studies of metal recycling industry. *Journal of Loss Prevention in the Process Industries, 80*, Article 104872. https://doi.org/10.1016/j.jlp.2022.104872

Pawłowska, B., & Śliwa, R. E. (2017). Recykling wiórów aluminium metodą KOBO. *Obróbka Plastyczna Metali, 28*(4), 301–316.

Pawłowska, B., Śliwa, R. E., & Zwolak, M. (2019). Possibilities to obtain products from 2024 and 7075 chips in the process of consolidation by KoBo extrusion. *Archives of Metallurgy and Materials*, 1213–1221. https://doi.org/10.24425/amm.2019.130083

Pietrzyk-Sokulska, E. (2016). Recykling jako potencjalne źródło pozyskiwania surowców mineralnych z wybranych grup odpadów. *Zeszyty Naukowe Instytutu Gospodarki Surowcami Mineralnymi i Energią PAN, 92*, 141-162.

Rietdorf, C., Ziehn, S., Giunta, S. M., Miehe, R., & Sauer, A. (2024). Environmental assessment of metal chip recycling – Quantification of mechanical processing's global warming potential. *Procedia CIRP, 122*, 241–246. https://doi.org/10.1016/j.procir.2024.02.009

Shamsudin, S., Lajis, M., & Zhong, Z. W. (2016). Evolutionary in solid state recycling techniques of aluminium: A review. *Procedia CIRP, 40*, 256–261. https://doi.org/10.1016/j.procir.2016.01.117

Topolski, K., & Ostachowski, P. (2021). Solid state processing of titanium chips by an unconventional plastic working. *Journal of Materials Research and Technology, 13*, 808–822. https://doi.org/10.1016/j.jmrt.2021.04.037

Topolski, K., Bochniak, W., Łagoda, M., Ostachowski, P., & Garbacz, H. (2017). Structure and properties of titanium produced by a new method of chip recycling. *Journal of Materials Processing Technology, 248*, 80–91. https://doi.org/10.1016/j.jmatprotec.2017.05.005

Topolski, K., Jaroszewicz, J., & Garbacz, H. (2021). Structural aspects and characterization of structure in the processing of titanium Grade 4 different chips. *Metals, 11*(1), 101. https://doi.org/10.3390/met11010101

Tucholski, G. (2013). Chips versus briquettes: How the aluminium industry can effectively and efficiently recycle scrap. *International Aluminium Journal, 89*(1/2), 87-88.

Watanabe, H., Moriwaki, K., Mukai, T., Ishikawa, K., Kohzu, M., & Higashi, K. (2001). Consolidation of ma-
chined magnesium alloy chips by hot extrusion utilizing superplastic flow. *Journal of Materials Science,
36*, 5007–5011. https://doi.org/10.1023/A:1017937205871

Xu, H., Ji, Z., Hu, M., & Wang, Z. (2012). Microstructure evolution of hot pressed AZ91D alloy chips reheated
to semi-solid state. *Transactions of Nonferrous Metals Society of China, 22*(12), 2906–2912.
https://doi.org/10.1016/S1003-6326(11)61549-5

Zante, G., Elgar, C. E., Hartley, J. M., Mukherjee, R., Kettle, J., Horsfall, L., Walton, A., Harper, G. J., & Ab-
bott, A. P. (2024). A toolbox for improved recycling of critical metals and materials in low-carbon technolo-
gies. *RSC Sustainability, 2*(2), 320-347. https://doi.org/10.1039/d3su00390f

Obecne Możliwości Recyklingu Przemysłowych Odpadów Metalowych: Możliwości Procesu Wyciskania KOBO

Streszczenie

Praca dotyczy problematyki wykorzystania odpadów w świetle obowiązujących regulacji prawnych w Polsce
i Unii Europejskiej. Wskazano istotę recyklingu, ze zwróceniem szczególnej uwagi na pierwiastki metali,
których złoża naturalne są ograniczone. Wskazano porównanie pierwotnych metod wydobycia metali oraz
odzysk metali (pochodzących ze źródeł wtórnych) z wykorzystaniem metod recyklingu w stanie stałym oraz
bez przetopu. Dokonano analizy niektórych sposobów recyklingu poprodukcyjnych odpadów metalowych.
Szczególną uwagę zwrócono na metalowe wióra oraz towarzyszące im substancje smarno-chłodzące. Zapre-
zentowano innowacyjny proces recyklingowy – wyciskanie KOBO odpadów metalowych w postaci wiórów,
przykładowe wyniki badań oraz wykaz korzyści płynących z wykorzystania tego procesu do produkcji kształt-
towników metalowych.

Słowa kluczowe: recykling, odpady poprodukcyjne, wykorzystanie odpadów przemysłowych, regulacje
prawne, wyciskanie KOBO

Original Research

The Effect of Varnishing and Soaking on Formability of the AW-5052-H28 Aluminium Alloy Sheets in Erichsen Cupping Test

Krzysztof Żaba * [ID], Łukasz Kuczek [ID], Maciej Balcerzak [ID]

Department of Metal Working and Physical Metallurgy of Non-Ferrous Metals, Faculty of Non-Ferrous Metals, AGH—University of Science and Technology, al. Adama Mickiewicza 30, 30-059 Cracow, Poland; lukasz.kuczek@agh.edu.pl (Ł. Kuczek), maciejbalcerzak1@gmail.com (M. Balcerzak)

* Correspondence: krzyzaba@agh.edu.pl

Abstract

This article presents the results of experimental tests on the stretch-forming ability of 0.21-mm-thick AW-5052-H28 aluminium alloy sheets used in the production of pull-off cups. Erichsen test under various tribological conditions (dry friction, lubrication with graphite lubricant) was used to assess the sheet formability. Punches with a various diameter of the spherical end (8 and 20 mm) were used in the tests. The effect of soaking conditions and varnishing variants on the value of Erichsen indices IE and IE_{11} was investigated. The sheets were soaked for 13 minutes at various temperatures: 185°C, 190°C and 200°C. In test conditions without lubrication, the lowest value of the IE index = 3.3 mm was observed for sheets in as-received state and for samples after soaking. However, the highest values of the Erichsen index in tests without lubrication were measured for varnished samples and repeatedly soaked. The tests conducted under lubrication conditions with graphite grease revealed usually higher values of the IE index compared to testing conditions without the use of grease. The values of the IE_{11} index were approximately twice lower than the IE indices. Observation of the bulge surface revealed a smooth surface, which means that the material is characterised by a fine-grained microstructure.

1. Introduction

Formability of sheet metal is a property that allows the material to be deformed without the risk of cracking. The ability of metallic materials to undergo plastic deformation is limited due to the microstructure of material depending on their chemical composition. Metals with high elongation are characterised by good formability resulting from the phenomenon of strain hardening (Sobota, 2017). The deformability of sheet metal can be assessed using various tests. Many tests have been developed to test deformability, however, the most commonly used are (Banabic et al., 2000; Reddy et al., 2020): the Swift cup test, the Olsen test, the Fukui conical cup test, the hydraulic bulging test, the hole expansion test, the limiting dome height test and the Erichsen deep-drawing test.

Owing to the requirements posed by the market, manufacturers of packaging closures must ensure the appropriate style of the closures offered (Marsh and Bugusu, 2007). The most popular form of personalisation of closures is the application of lithography to the surface of the closure. The print is done with inks that require high temperatures to dry them. The number of sheet-heating processes depends on the quality requirements and customer requirements. Ensuring adequate reliability of the production process of packaging closures made it necessary to study the input material, the effect of soaking and varnishing variants on strength and microstructural properties. Plastic working of aluminium alloys is problematic due to the presence of build-up on forming tools and galling behaviour (Devenport et al., 2023; Zheng et al., 2023). One of the methods of improving the forming process is the use of coatings on tools characterised by a low coefficient of friction (CoF) and high resistance to

wear (Bang et al., 2021; Bang et al., 2022). Tool surface parameters, such as CoF, hardness or the tendency to gall are very important to ensure the proper course of the production process. In industries using aluminium alloy sheets, particular emphasis is placed on product quality. Excessive wear from punching and forming tools creates a risk of fluctuations in the stability of the production process (Fernandes et al., 2017).

Packaging closures are most often made of aluminium alloy AW-5052-H28 (AlMg2.5). This alloy belongs to the 5xxx group of Al-Mg aluminium alloys with a magnesium content of 3-5 wt.%. 5xxx series alloys are medium-strength, reaching a strength of 300 MPa (Leśniak et al., 2014). Their usefulness in the packaging industry is particularly related to high corrosion resistance. Increasing expectations regarding the strength of products made of aluminium alloys of the 5xxx series, combined with their surface treatment, require complex mechanical and tribological tests, e.g. in order to analyse the suitability of selected coating materials and adapt them to specific operating conditions (He et al., 2022; Yamamoto and Nonaka, 2022).

The most important property of sheet metal determining its suitability for forming is stretch-forming ability (Wankhede and Suresh, 2020). Aluminium alloys have been the subject of many studies focused on analyzing the impact of friction and the type of heat treatment on formability. He et al. (2022) tested 1.2-mm-thick AW-5052-H24 aluminium alloy sheet using Erichsen test. It was found that the bulging property of test sheets could be improved by choosing good lubrication conditions. Singh et al. (2017) studied the formability of AW-1200 aluminium alloy sheets and they found that the formability could be increased by controlling the soaking temperature of sheet metals. Sekhar (2019) investigated the formability of 1-mm-thick AW-5052-H32 aluminium alloy sheets by developing a forming limit diagram. Results of Erichsen test revealed that the formability has been improved by soaking. Sravanathi et al. (2015) analysed the formability of AW-5052-H32 aluminium alloy sheets under dry conditions, grease lubrication and soaked condition. The samples after soaking showed enhanced good drawability compared to other test conditions. Subramani et al. (2018) used Using Design of Experiments (DOE) to explore the formability of 1-mm-thick AW-5052 aluminium alloy sheets (temper not specified). It was observed that normal anisotropy and the strain hardening exponent were the most influencing factors in determining the sheet formability. Yamashita et al. (2021) analysed the effect of strain rate on formability of the AW-5052-H34 sheet with thickness of 0.5 mm. The forming limit strains were larger under quasi-static condition in the linear path.

To the best of the authors' knowledge, tests on the deformability of thin sheets of the AW-5052 alloy in the H28 temper condition have not been carried out so far. This article presents the results of testing this sheet using the Erichsen test. In order to enhance novelty, the tests were carried out for sheets subjected to soaking in various conditions and varnishing the sheet metal surface using various varnishes.

2. Experimental

2.1. Material

In the investigations the 0.21-mm-thick AW-5052-H28 aluminium alloy sheets were tested. These sheets are commonly used to produce pull-off caps. The chemical composition of the EN AW-5052-H28 aluminium alloy (in wt.%) is Si (0.4), Fe (0.5), Cr (0.3), Zn (0.2), Cu (0.1), Ti (0.1), Mg (1.6-2.5), Mn (0.5-1.1) and Al (balance). The basic mechanical properties of tested sheets in the as received state (Table 1) were determined on the basis of a uniaxial tensile test according to EN ISO 6892-1 (2020) standard. Zwick/Roell Z020 (Zwick/Roell Group, Ulm, Germany) testing machine was used to determine mechanical properties of the test material. Sheet metal strips were cut along three directions from sheets at an angle of 0°, 45° and 90° with respect to the rolling direction of the sheet metal. Tests were performed in three replications. The parameters presented in the Table 1 represent average values from three samples.

Sheet metal processing before the pull-off cups (Fig. 1) forming process involves heat treatment and varnishing the sheet metal surface using various varnishes. The methods of preparing the analysed sheet metals and denotation of the samples are presented in Table 2.

Table 1. Basic mechanical properties of AW-5052-H28 aluminium alloy sheets.

Sample orientation, °	$R_{p0.2}$, MPa	Ultimate tensile strength (UTS) R_m, MPa	A, %
0	279.7	315.0	5.0
45	276.0	311.0	5.7
90	283.7	319.7	5.5

Fig. 1. Geometric model of an example pull-off cup.

Table 2. Denotation of samples and parameters of surface treatment.

Sample denotation	Surface treatment
S1	No treatment (as-received state)
S2	Varnishing with adhesive varnish Salchi VI1106 and soaking at 200°C for 13 minutes
S3	Varnishing with adhesive varnish Salchi VI1106 and coating varnish Salchi ANC6001, soaking at 200°C for 13 minutes and at 190°C for 13 minutes
S4	Varnishing with adhesive varnish Salchi VI1106, coating varnish Salchi ANC6001 and overprint varnish Salchi VE2028, soaking at 200 °C for 13 minutes, at 190 °C for 13 minutes and at 185 °C for 13 minutes
S5	Soaking at 200°C for 13 minutes
S6	Soaking at 200°C for 13 minutes and at 190°C for 13 minutes
S7	Soaking at 200°C for 13 minutes, at 190°C for 13 minutes and at 185°C for 13 minutes

Only one side of the sheet is varnished. In order to better identify the sides of the sheet metal, this article assumes that the varnished surface will be referred to as 'inner side' and 'outer side' for non-varnished surface.

Mean roughness Ra and ten point height of irregularities Rz were measured on both sides of the sheet metals on a T1000 (Hommel-Etamic Jenoptik, Jena, Germany) roughness-measuring instrument. A measuring length of 4.8 mm was assumed. Surface roughness parameters were measured in three directions (0°, 45° and 90°) relative to the sheet rolling direction. Table 3 shows the average values of the Ra and Rz parameters measured on both sides of the sheets.

Table 3. Selected surface roughness parameters of the sheet metals.

Sample denotation	Ra, µm		Rz, µm	
	Inner side	Outer side	Inner side	Outer side
S1	0.24	0.22	1.49	1.38
S2	0.42	0.23	2.27	1.53
S3	0.43	0.72	2.15	4.31
S4	0.40	0.18	2.00	1.02
S5	0.26	0.25	1.63	1.53
S6	0.25	0.25	1.68	1.51
S7	0.24	0.25	1.55	1.52

2.2. Erichsen test

The Erichsen test was performed on a universal-sheet metal testing machine (Fig. 2), model 142-40 (Erichsen GmbH & Co. KG, Hemer, Germany). Tests were conducted according to the recommendations of the EN ISO 20482 (2014) standard. The research was carried out using two sets of tools differing in the distance between individual indentations (Table 4). In the case of a tool with a diameter of the spherical end of the punch of 20 mm, tests were carried out with graphite lubricant and without lubricant on the surfaces of contact between the sheet metal and the punch. The Erichsen index IE was also determined depending on the surface of the sheet metal (inner or outer) that was in contact with the punch. The tests were carried out at a constant punch speed of 10 mm/min. The average Erichsen index values for a given material were determined from three measurements.

Fig. 2. Universal-sheet metal testing machine, model 142-40.

Table 4. Geometric parameters in the Erichsen test.

Erichsen index	Diameter of the spherical end of the punch, mm	Bore diameter of the die, mm	Distance between individual indenta-tions, mm	Dimensions of samples, mm	
				Thickness	Width
IE	20	27	90	~0.22	90
IE_{11}	8	11	40	~0.22	40

3. Results and discussion

The results of measuring the Erichsen index of the AW-5052-H28 aluminium alloy sheets depending on the friction conditions (without lubrication and with graphite grease) are shown in Fig. 3. The tests were carried out for one side of the sheet, identical to the side that is in contact with the punch during its forming. Slight differences were found between the obtained Erichsen index values. Due to smaller standard deviations (SD = 0.06-0.1 mm), it was found that the results obtained in tests carried out without lubrication were more reliable. Samples S1, S5 and S6 were characterized by the lowest value of the IE index (IE = 3.3 mm). However, the highest Erichsen index values in tests without lubrication were measured for samples S3 and S4. This means that these sheets are characterised by the highest formability among the analyzed samples.

Similar results were obtained when testing with graphite grease. The Erichsen index values in this case were usually higher than the results obtained in tests without the use of lubricant (Fig. 3), which was related to lower friction between the sheet and the punch. The exception was sample S4, which showed lower indentation depth under lubrication conditions, but a large standard deviation (SD) was obtained (SD = 0.35 mm). The values of standard deviations in tests using graphite grease were between 0.1 (sample S6) and 0.42 mm (sample S1).
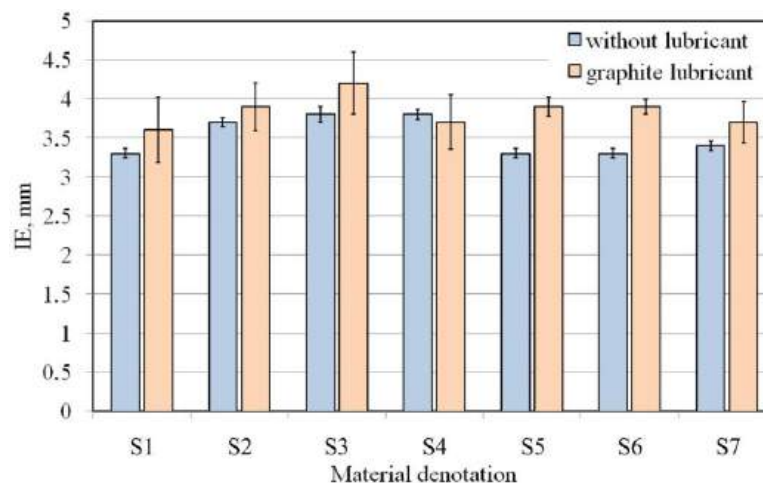
Fig. 3. Erichsen index IE values depending on the type of sample.

Based on the Erichsen test, it is possible to qualitatively determine the grain size of the sheet and the homogeneity of the material. In all cases, a smooth surface of the bulge was found, which means that the material is characterized by a fine-grained microstructure (Fig. 4). At the same time, the character of the crack differed from that of an arc, which may indicate the banded microstructure of the tested materials.
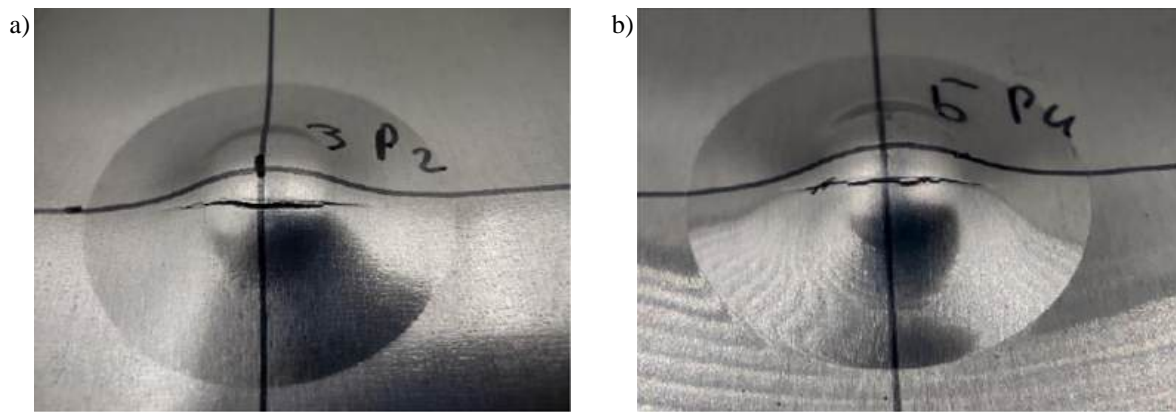
Fig. 4. View of samples deformed using punch with a diameter of the spherical end of 20 mm for samples a) S3 and b) S6.

The influence of the side of the tested sheet that was in contact with the punch during the Erichsen test was also analyzed. It was found that the values of the Erichsen index measured on both sheet sides are similar (Fig. 5). The largest discrepancies of 0.2 mm were observed for samples S1 and S5. This is a difference within the measurement error. The highest value of the IE index (3.8 mm) was found for the sample S3, and the lowest (3.3 mm) for the sample S1. Changing the side of the material in contact with the punch did not change the quality of the bulge surface or the character of the cracks. For sample S3, the value of the SD during tests on the outer side of the sheet was 0.1 mm. For the remaining samples, SD = 0.01 mm was obtained. During tests of samples at the inner side, for samples S4-S7 much larger values of SD between 0.12 mm and 0.15 mm were observed.
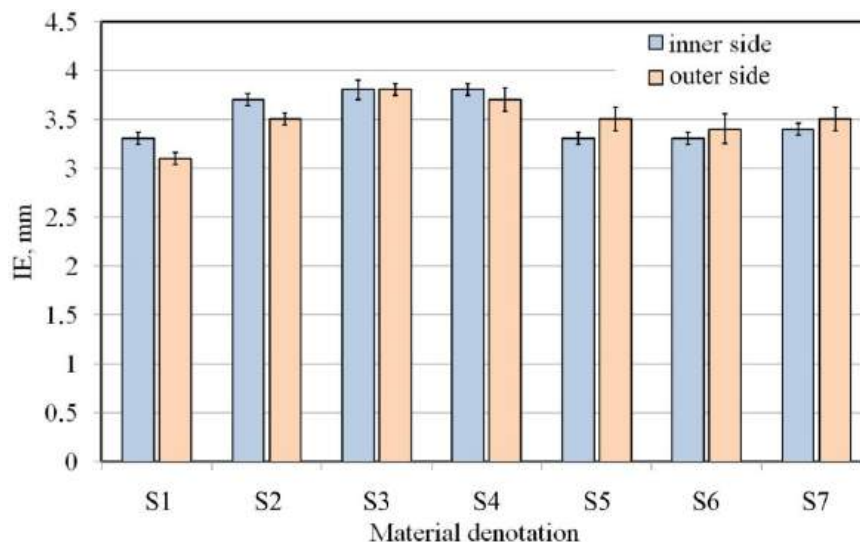
Fig. 5. Values of Erichsen index IE depending on the test side of sheet metal.

Due to the small thickness of the tested sheet metal, the Erichsen test (IE_{11}) was performed using a punch with a diameter of the spherical end of the punch of 8 mm. Under dry friction conditions, slight differences were found in the results obtained with the highest formability ($IE_{11} = 0.22$ mm) determined for samples S2-S4 (Fig. 6). The use of lubricant slightly changed the values of IE_{11} index obtained for non-lubricated conditions. Sample S3 exhibit the maximum formability ($IE_{11} = 2.3$ mm). The character of the change in the Erichsen index IE_{11} coincides well with the values obtained in the same test, but using a punch with a diameter of the spherical end equal to 20 mm (Fig. 7). The IE_{11} index values are approximately twice smaller than the IE index values. Regardless of the material analysed and the test conditions, in the test using a punch with a diameter of the spherical end equal to 8 mm (Fig. 8), the character of the cracks was similar to that obtained using a punch with a diameter of the spherical end equal to 20 mm (Fig. 4).

The effect of soaking temperature on the mechanical properties (yield stress, UTS and elongation) of the sheet metals was the subject of a previous article (Czapla et al., 2023). It was found that soaked and/or lacquered samples showed a decrease in yield stress and UTS compared to as-received sample.
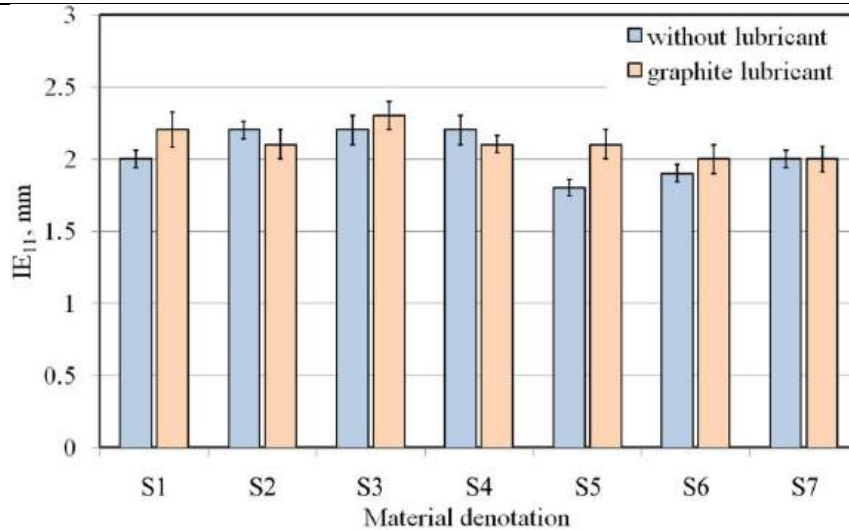
Fig. 6. Erichsen index IE$_{11}$ values depending on the type of sample.
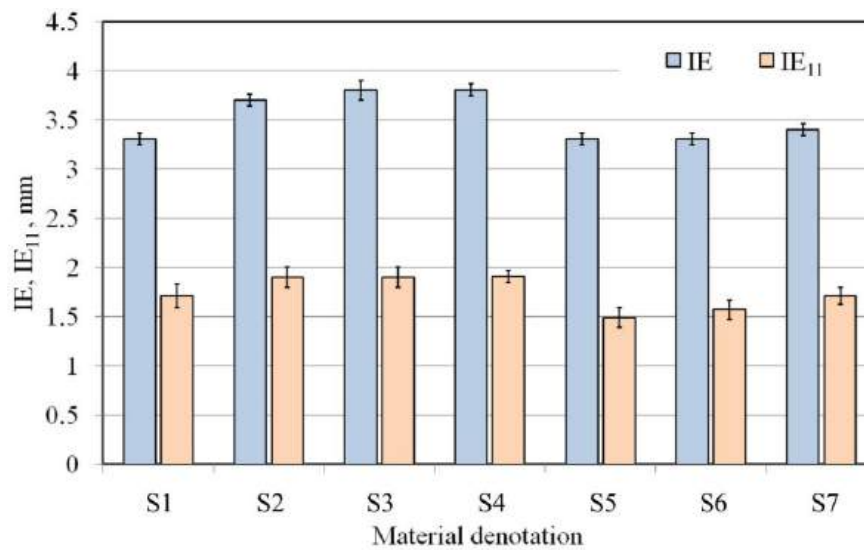
**Fig. 7.** Comparison of the Erichsen indices IE and IE$_{11}$ obtained in non-lubricated conditions.
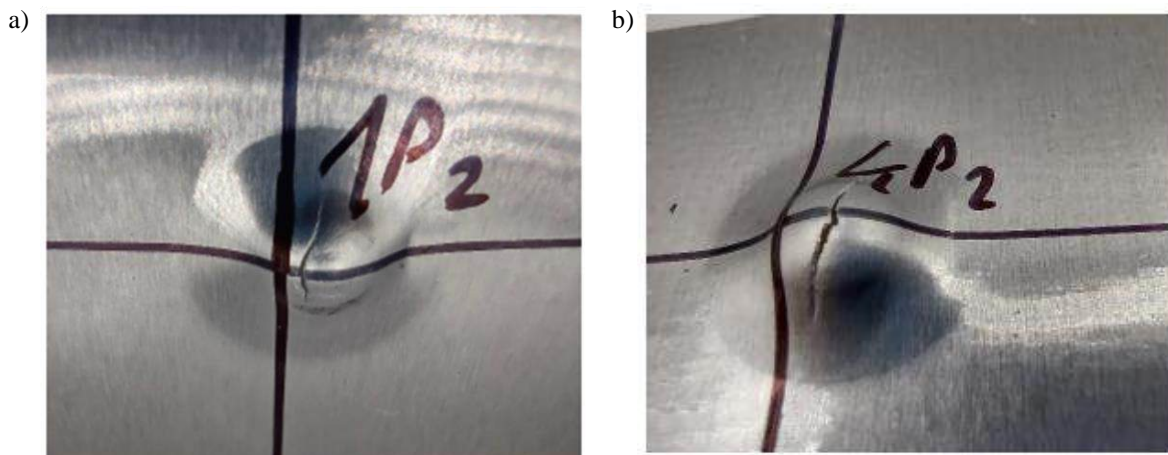
Fig. 8. View of samples deformed using punch with a diameter of the spherical end of 8 mm for samples a) S3 and b) S6.

4. Conclusions

This article presents the results of experimental tests on the stretch-forming capacity of AW-5052-H28 aluminium alloy sheets used in the production of pull-off cups. The Erichsen test was used to assess the formability of varnished and soaked sheet metals. Punches with a various diameter of the spherical end (8 and 20 mm) were considered in the investigations. The following main conclusions were obtained:

- Slight differences were found between the obtained values of Erichsen indices IE and IE_{11} during formability tests without lubricant and with graphite grease. However, smaller standard deviation values (SD = 0.06-0.1 mm) were found in tests carried out without lubrication.
- The lowest value of the IE index = 3.3 mm was observed for sheets in the as-received state and for soaked sheets (samples S5 and S6).
- In non-lubricated conditions, varnished and soaked sheets showed the greatest tendency to stretch-forming.
- Bulged specimens were characterized by a smooth surface, which confirms the fine-grained microstructure of the workpiece material.
- For specific samples, the values of the IE_{11} indices were approximately twice lower than the IE indices.
- Qualitatively similar IE indices were obtained when testing sheet metals on the inner and outer sides. Similarly, the quality of the bulge surface and the character of the cracks were similar on both sides of the sheet.
- Varnished (Salchi VI1106 + Salchi ANC6001) and soaked (200°C for 13 minutes and 190°C for 13 minutes) sample exhibit the maximum IE_{11} index of 2.3 mm.

References

Banabic, D., Bunge, H. J., Pöhlandt, K., & Tekkaya, A. E. (2000). *Formability of metallic materials*. Springer-Verlag. https://doi.org/10.1007/978-3-662-04013-3

Bang, J., Kim, M., Bae, G., Kim, H. G., Lee, M. G., & Song, J. (2022). Efficient wear simulation methodology for predicting nonlinear wear behavior of tools in sheet metal forming. *Materials*, *15*(13), Article 4509. https://doi.org/10.3390/ma15134509

Bang, J., Park, N., Song, J., Kim, H. G., Bae, G., & Lee, M. G. (2021). Tool wear prediction in the forming of automotive DP980 steel sheet using statistical sensitivity analysis and accelerated U-bending based wear test. *Metals 11*(2), Article 306. https://doi.org/10.3390/met11020306

Czapla, K., Żaba, K., Kot M., Nejman, I., Madej, M., & Trzepieciński T. Tribological performance of anti-wear coatings on tools for forming aluminium alloy sheets used for producing pull-off caps. *Materials*, 2023, *16*(19), 6465. https://doi.org/10.3390/ma16196465

Devenport, T. M., Griffin, J. M., Rolfe, B. F., & Pereira, M. P. (2023). Friction and wear in stages of galling for sheet metal forming applications. *Lubricants*, *11*(7), Article 288. https://doi.org/10.3390/lubricants11070288

EN ISO 20482. (2014). Metallic materials—Sheet and strip Erichsen cupping test. International Organization for Standardization.

EN ISO 6892-1. (2020). Metallic materials—Tensile testing—Part 1: Method of test at room temperature. International Organization for Standardization.

Fernandes, L., Silva, F. J. G., Andrade, M. F., Alexandre, R., Baptista, A. P. M., & Rodrigues, C. (2017). Improving the punch and die wear behavior in tin coated steel stamping process. *Surface and Coatings Technology*, *332*, 174-189. https://doi.org/10.1016/j.surfcoat.2017.06.086

He, H., Yang, T., Ren, Y., Peng, Y., Xue, S., & Zheng, L. (2022). Experimental investigation on the formability of al-mg alloy 5052 sheet by tensile and cupping test. *Materials*, *15*(24), Article 8949. https://doi.org/10.3390/ma15248949

Leśniak, D., Rękas, A., Libura, W., & Zasadziński, J. (2014). Badania odkształcalności stopów aluminium serii 5xxx o wysokiej zawartości Mg w procesie półprzemysłowego wyciskania. *Obróbka Plastyczna Metali*, 25(3), 159-167.

Marsh, K., & Bugusu, B. (2007). Food packaging—Roles, materials, and environmental issues. *Journal of Food Science*, *72*(3), 39-55. https://doi.org/10.1111/j.1750-3841.2007.00301.x

Reddy, A. C. S., Rajesham, S., Reddy, P. R., & Umamaheswar, A. C. (2020). Formability: A review on different sheet metal tests for formability. *AIP Conference Proceedings*, *2269*(1), 2020, Article 030026. https://doi.org/10.1063/5.0019536

Sekhar, R. A. (2019). Determining the formability of AA5052 sheets in annealed and H32 condition. *Journal of Physics: Conference Series*, 1355, Article 012044. https://doi.org/10.1088/1742-6596/1355/1/012044

Singh, M., Choubey, A. K., & Sasikumar, C. (2017). Formability analysis of aluminum alloy by Erichsen cupping test method. *Materials Today Proceedings*, *4*(2), 805–810. https://doi.org/10.1016/j.matpr.2017.01.089

Sobota, J. (2017). Umocnienie odkształceniowe stopów aluminium serii 6xxx. *Rudy i Metale Nieżelazne*, *62*(6), 20-24.

Sravanthi, G., & Nethala, Y. V. K. K. (2015). Analysis of formability on aerospace grade aluminum alloys. *International Journal of Engineering Research & Technology*, *4*(10), 236-260.

Subramani, K., Alogarsamy, S. K., Chinnaiyan, P., & Chinnaiyan, S. N. (2018). Studies on testing and modelling of formability in aluminium alloy sheet forming. *Transactions of Famena*, *42*(2), 67-82. https://doi.org/10.21278/TOF.42206

Wankhede, P., & Suresh, K. (2020). A review on the evaluation of formability in sheet metal forming. *Advances in Materials and Processing Technologies*, *6*(2), 458-485. https://doi.org/10.1080/2374068X.2020.1731229

Yamamoto, S., & Nonaka, T. (2022). Electrostatic and tribological properties of hydrogenated diamond-like carbon on anodic aluminium oxide. *Surface and Coatings Technology*, *441*, Article 128530. https://doi.org/10.1016/j.surfcoat.2022.128530

Yamashita, M., Komuro, S., & Nikawa, M. (2021). Effect of strain-rate on forming limit strain of aluminum alloy and mild steel sheets under strain path change. *International Journal of Automation Technology*, *15*(3), 343-349. https://doi.org/10.20965/ijat.2021.p0343

Zheng, K., He, Z., Qu, H., Chen, F., Han, Y., Zheng, J. H., & Li, N. (2023). A novel quench-form and in-die creep age process for hot forming of 2219 thin aluminum sheets with high precision and efficiency. *Journal of Materials Processing Technology*, *315*, Article 117931. https://doi.org/10.1016/j.jmatprotec.2023.117931

Wpływ Lakierowania i Wygrzewania na Odkształcalność Blach ze Stopu Aluminium AW-5052-H28 w Próbie Tłocznosci Erichsena

Streszczenie

W tym artykule przedstawiono wyniki badań eksperymentalnych odkształcalności blach ze stopu aluminium AW-5052-H28 o grubości 0.21 mm stosowanych do produkcji kapsli zawierających zawleczkę. Tłoczność blachy określono metodą Erichsena w warunkach tarcia suchego i smarowania smarem grafitowym. Wykorzystano stemple o średnicy sferycznej końcówki 8 oraz 20 mm. Badano wpływ warunków lakierowania i wygrzewania na wartość wskaźników Erichsena IE oraz IE_{11}. Wygrzewanie blach przeprowadzano w czasie 13 minut i w różnej temperaturze: 185°C, 190°C oraz 200°C. W warunkach bez smarowania najmniejszą wartością wskaźnika IE = 3,3 mm charakteryzowały się blachy w stanie dostawy oraz próbki po wygrzewaniu. Natomiast najwyższe wartości wskaźnika Erichsena w badaniach bez smarowania zmierzono dla próbek lakierowanych oraz wielokrotnie wygrzewanych. Testy przeprowadzone w warunkach smarowania smarem grafitowym ujawniły przeważnie większe wartości wskaźnika IE w porównaniu do warunków testowania bez użycia smaru. Wartości wskaźnika IE_{11} były około dwukrotnie mniejsze niż wskaźnika IE. Obserwacja powierzchni wytłoczenia pozwoliła stwierdzić gładką powierzchnię, co oznacza, że materiał charakteryzował się drobnoziarnistą mikrostrukturą.

Słowa kluczowe: stop aluminium, wygrzewanie, test Erichsena, odkształcalność, blacha

Review

A Review of Generative Design Using Machine Learning for Additive Manufacturing

Parankush Koul (iD)

Department of Mechanical and Aerospace Engineering, Illinois Institute of Technology, 60616 Chicago, Illinois, United States of America

Correspondence: pkoul2.iit@gmail.com

Abstract

This review explores how generative design is combined with machine learning (ML) to achieve additive manufacturing (AM) and its societal transformative effect. Generative design uses complex algorithms to automate the process of designing best-fit designs, mass customization, and customization to suit specific customer requirements with high efficiency and quality. The scalability and predictability of artificial intelligence (AI) models make handling huge data easy and enable scale-up of production without compromising quality. This paper also focuses on how generative design can help accelerate innovation and product creation because it empowers designers to play in a wider space of design and provide solutions that cannot be reached with traditional techniques. AI integration with existing production processes is also vital to real-time manufacturing optimization—further increasing overall operational effectiveness. Additionally, the emergence of sophisticated predictive models like gradient boosting regression shows how ML can enable better accuracy and robustness of 3D printing operations to achieve quality standards of the outputs. This paper ends with what generative design and ML hold for the future of AM and how designing continues to be improved and modified to match changing industry requirements.

Keywords: Generative Design, Machine Learning, Additive Manufacturing, Lightweight Design, Optimization

1. Introduction

Manufacturing has experienced major shifts due to the introduction of AM technologies. AM fabricates components layer by layer and, unlike subtractive manufacturing, creates complex geometries impossible using traditional techniques. These have stimulated the increasingly fashionable concept of combining ML to streamline the design process, resulting in the increasingly mainstream concept of generative design. Generative design makes use of algorithms utilizing ML to generate vast design possibilities that guarantee both high performance and optimization of materials and cost (Kumar et al., 2022).

Generative design is defined as an ability to model evolutionary mechanisms, enabling systems to evolve designs in response to performance demands and limitations. It uses AI and in particular ML to optimize the design stage, allowing engineers and designers to discover as many possible solutions as possible in a fraction of the time required by the conventional approach (Ng et al., 2024). The combination of generative design and ML further enhances the innovation of design, and it enables AM parts to be customized in order to further extend the capabilities of modern manufacturing (Lee et al., 2023).

Many recent studies have highlighted techniques and models that combine generative design and ML to develop AM materials and optimize AM processes (Jin et al., 2020; Wang et al., 2022). Both of these techniques rely on the increased predictive power of ML algorithms that are able to detect patterns in large datasets produced during AM, helping to guide design decisions that result in enhanced functional and structural properties of the parts (Wang et al., 2020). The application of ML methods

to generative design will potentially change the way goods are designed, tested, and manufactured in the manufacturing industry.

Furthermore, the ML use in generative design goes beyond aesthetic or geometric developments to cover important operational parameters and constraints essential to AM, including material properties, process behavior, and environment (Ciccone et al., 2023). This deep dive of generative design methods employing ML for AM will shed light on the cutting-edge techniques, challenges, and future of this novel synthesis for the market (Johnson et al., 2020; Regenwetter et al., 2022).

In conclusion, the combination of generative design and ML marks a revolution in AM with an ability to innovate design creativity, efficacy, and effectiveness while also addressing AM's unique challenges. In our further parts of this retrospective, we'll be exploring the roles, trends, and disruptive potential of these developments in the context of today's manufacturing environments.

2. Methodologies to Implement ML in Generative Design for AM (DfAM)

When applying ML to generative DfAM, there are a number of techniques used for designing and manufacturing better. All of these approaches are beneficial and have their own uses to be efficient, cost-effective, and innovative.

- Data Collection and Preprocessing: To make ML work in generative design, rigorous data collection and processing are the essential first steps. This is based on the collection of pertinent datasets that cover all sorts of parameters, such as material characteristics, geometry constraints, and performance parameters. It is such large datasets that help ML models to learn from various examples and predict more accurately. Preprocessing also denoises and normalizes the data, which removes noise and anomalies and improves the performance of the model (Chinchanikar & Shaikh, 2022).

- Feature Engineering: Feature engineering is used to transform inputs into ML models. With a bit of research and choosing the right features (such as dimensional parameters and material properties), the designers can significantly impact how the model performs. Well-done feature engineering makes the model generalizable so that it can correctly predict new designs based on the patterns learned from the training data (Wang et al., 2020).

- Model selection: The right ML model is also critical for the generative design. Algorithms like support vehicle machines (SVM), neural networks, decision trees, and others have strengths and weaknesses depending on the design problem difficulty. Model readability, computer speed, and the possibility of processing high-dimensional data are also aspects of selection. This phase makes sure that the model is correct for the application of the AM process (Jin et al., 2020).

- Training and validation: Then train the ML model that one chooses from collected and preprocessed data to train the model to learn the relationships between design parameters and results. At the time of training, the model must be checked against another dataset in order not to overfit the training data (and result in low performance on unseen data). Each validation session can refine the model parameters and make it work best, which ultimately makes it better to use for generative design (Johnson et al., 2020).

- Optimization algorithms: Optimization algorithms are essential to generative design by iteratively fine-tuning design solutions for specified goals. After the design space is determined, these algorithms check a number of parameters in parallel to find the best configurations that are at par with the required performance. Some of the commonly used optimization algorithms are genetic algorithms and gradient descent to direct the ML models to the best design solutions for increasing the efficiency of AM (Soori et al., 2024).

- Integration with Simulation Tools: Combining ML models with simulation tools enables designers to compare how the generated designs perform in various conditions before going to production. This combination enables the design to be tested and validated in virtual space without large-scale real-world prototypes. These simulations can be helpful in getting insights and running iterations and updates at speed that helps make generative design easier (Regenwetter et al., 2022).

- Continuous learning and adaptation: Implementing a continuous learning system is essential to keep the ML model up to date. It is a method where we regularly update the model with new information and results from AM. With more information—either from experiments or feedback from users—the model can scale changes in design, material properties, or produc-

tion process. This flexibility makes the model more efficient over time and adapts to industry changes (Williams, 2022).

- Postprocessing and analysis: The designs produced, and performance measures have to be processed after-the-fact to assess the effectiveness of imposed methodologies. This step will be looking at the outputs produced by the ML model to see which designs perform best under which conditions. Weight, strength and manufacturability are calculated to determine which design to proceed with. By analyzing outcomes closely, designers will have a better idea of how to improve their method and how to implement ML in generative design in the future (Vaneker et al., 2020).

- User Interface and Visualization: User interface and visualization tools are important for communicating between designers and generative designers. These interfaces let the user feel free to easily tweak design settings, view results, and learn more about the effects of variables. Powerful visualization is what makes complex data digestible and so can make the design decisions easier (Guo et al., 2022).

- Deployment and Feedback Mechanisms: The last phase is to use the ML solutions in real-world AM environments and build feedback loops for data gathering. This is the step where companies can measure the impact of the implemented methods and learn from production results. Feedback loops are the way to iteratively improve in order to keep advancing the ML models and the generative design processes they're backed by (Babu et al., 2022).

3. Benefits and Applications of ML in Generative DfAM

3.1. Benefits

The first advantage of applying ML to generative designs is better design optimization. It is also fast enough for ML algorithms to mine the large amount of data and detect the optimal design parameters that human minds cannot. With the help of historical performance data, ML can suggest weight and structure reduction designs that enhance the efficiency and performance of manufactured assemblies (Jin et al., 2020).

An additional benefit is the time savings on design. While ML algorithms can do most of the work, designers must spend time on it. They can, for example, quickly iterate on design variations and anticipate results, reducing product development time by hundreds of percentage points (Wang et al., 2020). This allows engineers and designers to work on things that matter instead of wasting so much time on tedious calculations and tinkering.

Save money—this is a key benefit of including ML into AM generative design. In designing to make the most of AM, ML helps avoid material waste and costs. Smart design algorithms, for instance, can propose building solutions that require less material while still performing—saving huge amounts in the manufacturing process (Westphal & Seitz, 2024). This efficiency can be used to lower the cost of AM for niche use cases that call for customized parts.

In addition, improved material performance is another big advantage of using ML in design. ML can anticipate how different materials will behave under different conditions, so we can make components lighter but more robust as well. With the right material selection and consumption optimized through predictive modeling, manufacturers can improve the overall quality and life of their products (Regenwetter et al., 2022).

Last but not least, ML allows for the integration of multidisciplinary expertise in design. Incorporating input from other areas of knowledge, including mechanical engineering and materials science, can help ML create novel design alternatives that demonstrate a more general understanding of the AM's needs and limitations. It is through this ambivalent methodology that we can see design innovation break the limitations of what is already possible with conventional means (Bendoly et al., 2023).

3.2. Applications

Topology optimization (TO) is one of the main use cases of ML in generative design. ML algorithms are used to calculate the optimal physical configuration of buildings according to performance constraints. The algorithms study the design and materials in use to identify the best practices for producing structures that are both usable and efficient, which are necessary for light and strong parts in aerospace and automotive designs (Jin et al., 2020).

ML is also used for designing space exploration, where ML is used to automate the journey through different designs. Algorithms evaluate multiple parameters at once, and the most promising design solutions are found much more quickly than with any other means. It can bring out the design more imaginatively and more innovatively, making AM technologies more efficient (Chaudhari & Selva, 2023).

Predictive maintenance, another important ML use in generative design, is another one. Analyzing AM process data, ML algorithms will detect part failures or defects in advance of them occurring so that corrective action can be taken prior to them happening. This makes components created through generative design durable and secure, and it can drastically mitigate unexpected outages (Nyamekye et al., 2024).

In customizing and personalizing products, ML is also very helpful. ML in the healthcare sector can be used to design customized surgical implants or prostheses using patients' information. Automated design algorithms adjust the parameters based on one's needs to get the final result that is not just custom but also performance optimized (Westphal & Seitz, 2024).

Finally, ML helps in better simulation of some generative design cases. ML makes realistic simulations of the operation of parts at different temperatures that can help engineers verify designs before they're actually built. This is not only more time efficient for designing but also for checking that the end product is quality and functional—thus reducing the risk involved in launching new designs into the market (Regenwetter et al., 2022).

4. Past Projects in Manufacturing Companies Implementing ML for Generative Design in AM

The manufacturing environment has changed the build products with advanced technologies, especially ML and AM. Of all these developments, generative design is the one that has brought the capabilities of product design and manufacturing into the modern day. In this article, we want to share some of the earlier projects done by big-name manufacturing organizations that have implemented ML in AM for generative design. These efforts are proving both the promise of combining generative design and ML, and the impact these technologies can have across multiple industries. From aircraft to medical devices, Autodesk, General Motors (GM), Lockheed Martin, and NASA have all shown promising successes focused on designing parts more efficiently, automating production processes, and improving overall manufacturing efficiency. By explicating these projects, we can recognize how profoundly ML and generative design are still changing the way we build products.

4.1. Generative Design for 3D Printing at Autodesk (2018)

Autodesk introduced generative design for 3D printing, using an algorithm that reduces design repeats. Using this technology, engineers and designers can design any potential variety of solutions that fulfill some performance requirements, and it will help in reducing cost and being creative while designing products. Generic design tools allow one to generate thousands of designs at a moment's notice, creating lighter, stronger and more material-efficient parts than traditional ones. This ability comes in handy especially for applications like aerospace and automotive where optimal components are required. Autodesk's efforts in building complex scale 3D-printed building components with partners such as Acciona are just the beginning of applications of this technology (Toro, 2024). Introducing AI in the design flow is Autodesk's way to transform the creation process for products by going beyond traditional processes to build a more creative design world.

4.2. GM - Project Dreamcatcher (2018)

GM collaborated with Autodesk to use generative design to develop automotive parts, including low-slung seat brackets. In this collaboration, AI algorithms examined multiple design variants that maximize strength and lightness. Its generative design tools enable engineers to enter constraints and requirements that result in creative designs otherwise impossible by conventional methods (Beesley, 2020; Kvernvik, 2018).

4.3. Lockheed Martin – Spacecraft Components (2018)

Lockheed Martin also employed generative design in the design of components for spacecraft; AM is coupled with generative design for part optimization. The firm employed this technology, for

instance, to build sophisticated brackets and other structures that are needed to run the satellite. Through the use of computer algorithms, to look at design options, Lockheed Martin developed high-fidelity aerospace-grade components that are also lightweight and affordable (Werner, 2018). This flexibility is important as the aviation industry becomes more advanced and efficient in designs that would otherwise be difficult to fabricate by conventional manufacturing.

4.4. NuVasive - Titanium Implants (2018)

NuVasive   transformed spinal implant technology by ML-based generative design within AM. The Modulus titanium implants, created using proprietary optimization software, are organic and porous, mimicking natural bone in order to support osseointegration and minimize stress shielding (Mattias, 2024; Mazer, 2017). Hence, this process of generative design leads to the development of light and unsymmetric structures not possible with conventional approaches, leading to improved surgical performance and healing outcomes (Mattias, 2024). NuVasive highlights the ability of generative design to compare many designs rapidly, maximizing performance requirements while maintaining structural integrity (Christian, 2018). This same dedication to innovation can be found in these implants, which are a great advancement in introducing cutting-edge technology to medical devices (Mattias, 2024; Mazer, 2017). And thus, NuVasive is revolutionizing spine surgery through these new, patient-centric design techniques.

4.5. NASA's Utilization of ML-Driven Generative Design in AM for Aerospace Applications (2018)

NASA has implemented ML-based design into AM, which will transform aerospace component production. This is what enables AI to create optimized designs that meet given needs effectively. Since 2018, NASA has been using generative design to achieve remarkable improvements, such as cutting component weights by up to half and reducing development times from months to days (Rivera, 2024). The EXCITE mission highlighted new techniques where AI and AM have produced seemingly nonstandard structures that are structurally sound and functional in use (Rivera, 2024; Rosen, 2023). As Ryan McClelland explained, generative design makes it fast—creating 30-40 designs in an hour, maximizing mass and performance. This innovative technology can be used not only for better design but also to drastically reduce production costs, which was a revolutionary step in aerospace engineering (Rivera, 2024).

4.6. Airbus - Lightweight Aircraft Interior Components (2019)

Airbus is currently using generative design to create lightweight aircraft parts like the bionic partition for their A320 plane. The partition was created in Autodesk's generative design software and was 45% lighter than conventional components without compromising structure. Airbus is able to can design parts that will lead to less fuel and better performance from the aircraft by adopting generative design techniques. This project fits into their aerospace sustainability agenda and strives to lower the ecological footprint of aviation (Deplazes, 2019).

4.7. GE Aviation - Aircraft Engine Components (2019)

GE Aviation uses generative design to optimize the internal parts of its aircraft engines, including fuel nozzles. The first 3D-printed fuel nozzle derived from generative design principles was launched by GE for weight reduction and performance enhancement. The algorithms let engineers test and prototype thousands of possible designs very quickly, making them lighter and more energy-efficient under load. These advancements underscored GE's strategy of using cutting-edge manufacturing processes to optimize the aviation marketplace (Markovic, 2022).

4.8. Leveraging ML for AM in Boeing's Aircraft Design (2021)

Boeing also used ML to design AM process improvements for aircraft manufacturing (by much since 2021), optimizing component designs through the use of ML algorithms and making them to produce higher complexity geometries than traditional manufacturing processes could do (Warde, 2023). This option lowered the weight, enhanced performance, and improved production efficiency. Exhibits such as MEDAL, which used ML to improve AM characteristics of metal alloys, enabled

Boeing to accelerate the time and costs of production (Warde, 2023). Further, Boeing's partnerships with academia, including MIT, have spawned education initiatives that developed worker capabilities in AM and ML that reflected the rising use of AM and ML in aerospace. On the whole, Boeing's adoption of ML in AM was a major step in a journey towards new and efficient production in the aerospace sector.

Overall, ML for generative design in AM is something that has revolutionized the production possibilities of all sectors. In projects carried out by some of the largest firms—Autodesk, GM, Lockheed Martin, NuVasive, and Boeing—we could see the tremendous advantages of this technological co-design, such as higher efficiency, decreased material use, and structural optimization. Such previous projects provided a framework for future innovation and served as a model for other industries that seek to leverage technology for better products and manufacturing processes.

5. Overview of Past Research on Generative Design using ML for AM

The amount of research on generative DfAM using ML has grown dramatically in the past 10 years, with a peak in publications in 2020–2021. This trend is part of an increasing use of AI to innovate and improve AM design practices, which has remained consistent but at a somewhat lower rate ever since. Fig. 1 shows how the field has changed over the time from 2013 to 2024 (n = number of articles per year).
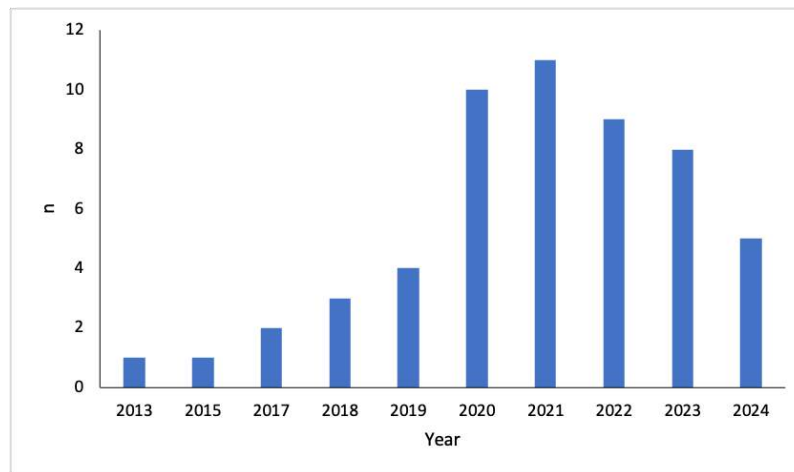
Fig. 1. Number of articles on Generative Design using ML for AM *vs*. year.

Different publishers have been responsible for publicizing this research. In Table 1 below, we have listed publishers and articles in this paper they have published.

5.1. Design and Performance Enhancement

Gu et al. (2018) used ML to build generative designs for hierarchical materials and showed that their ML-optimized designs improved mechanical properties to about 25 times tougher than traditional materials and were computationally fast, screening billions of designs in a matter of hours. A generative design optimization strategy by Strömberg (2019) combined TO and cellular lattices with massive increases in AM design efficiency using material layout optimization and support vector machines for prediction has been described. Goguelin (2019) focused on AM-specific generative design methods and showed how advanced computation enabled part geometries, performance, and better use of materials. In that research, it was shown that generative design resulted in enhanced strength-to-weight ratios and helped design difficult geometries previously unimaginable using classical techniques, making it applicable in fields from aerospace to automobile.

Hyunjin (2020) investigated how artificially generated generative design systems can radically alter the manufacturing process. This a study affirmed that AI and human designers work collaboratively to determine the best design choices and materials for an optimal product, implying an important paradigm shift to AI-based approaches in future product design. Ricotta et al. (2020) proposed a generative parametric model algorithm for elbow orthoses, which highlighted the role of 3D capture and modeling of structures in order to customize and predict orthopaedic device customization. They showed that it was feasible to use selective laser sintering (SLS) technology and found that generative algorithms could bypass the limitations of traditional CAD, making design easier.

Table 1. Number of articles on Generative Design using ML for AM by Publisher

Publisher	Number of articles reviewed
Springer	9
Elsevier	7
MDPI	7
arXiv (Cornell University)	4
IOP Publishing Ltd	4
ASME	3
Emerald	2
ACM	1
AIP Publishing	1
Cambridge University Press	1
CIMNE	1
eCAADe	1
IASDR	1
IEEE	1
IJECE	1
IJMRET	1
JETIR	1
Justia	1
MATEC	1
Royal Society of Chemistry	1
Taylor & Francis Group	1
Toronto Metropolitan University	1
UIKTEN	1
University of Bath	1
Wiley	1
Total	**54**

The same goes for Aman (2020), who studied the optimization and performance enhancement of bracket design using Autodesk Fusion 360; they differentiated generative design from optimization: iterative solutions verified via stress, heat and buckling simulation resulted in successful design implementation into workable assemblies.

Ntintakis and Stavroulakis (2020) talked about the latest developments in generative design, for instance, soft robot actuators. Their work demonstrated how generative design was able to generate complex forms in a way that conventional manufacturing wasn't able to produce, validating their models through finite element analysis (FEA) and exploring the effects of material choice on actuator behavior. Kumaran and Senthilkumar (2021) utilized generative design and optimization of topology to analyze industrial robot arms and showed that AM such as powder bed fusion and direct energy deposition (DED) can be used to solve structural complexity and weight and provide for efficient repair mechanisms. The generative design strategy of Yadav et al. (2021) was used to enhance Unmanned Aerial Vehicle (UAV) frame designs, showing the ability of AM to design complex geometries in response to performance needs by using FUSION 360 software.

Ricotta et al. (2021) specifically developed a generative algorithm for creating elastic shapes for orthopedic use and created an optimized elbow orthosis, better fitting and performing than previous designs based on Finite Element Method (FEM) simulations. Barbieri and Muzzupappa (2022) have examined generative design and TO to its full extent by redesigning mechanical parts of a Formula Student racing car and finding impressive performance gains. They showed that generative design outperformed TO for mass reduction and safety factors, showing that generative design could design light and strong structures. Watson et al. (2023) instead created a generative design approach for space-frame systems especially to optimize efficiency. They implemented formal TO techniques and generated high-performance designs by using a parameterization strategy that transformed voxel data into manageable models. In the paper, they claimed that six plausible topologies were generated while taking into account restrictions of certain input parameters.

5.2. Robust Material Design

Nordin et al. (2013) researched generative design systems that used nature-based algorithms to create sophisticated, mass-produced objects, showing the ability to combine form and function across a range of manufacturing processes, including CNC milling and AM. Jiang et al. (2020) developed a parallel trend by carrying out an ML-integrated design system that optimized design parameters

of customized products (for example, a tunable mechanical performance ankle brace). Their example showed that ML made a big impact in design and gave us a detailed insight on how design decisions affect performance. Almasri et al. (2020) used a dual-discriminator generative adversarial network (GAN) to apply mechanical and geometrical constraints to AM design. That method effectively maximized topology, leading to mechanically reliable designs following sophisticated constraints.

Goudswaard et al. (2021) developed a neural network capability profile to improve filament deposition modeling (FDM) and showed that their generative design algorithm was capable of accurately predicting mechanical values such as ultimate tensile strength (UTS) and tensile modulus (E), with low prediction errors, and verifying the capability profile via successful load-bearing part designs. Siegkas (2022) used GANs to generate dense 3D porous architectures similar in nature to forms found in the natural world, showing how AM could benefit from biomimetic designs, despite observed differences in mechanical performance due to resolution variations in image generation. Felbrich et al. (2022) pioneered by integrating generative design software and deep reinforcement learning for robot autonomy in AM, establishing the critical role of geometric state representation and task-specific training approaches for complex structure construction.

Zhang et al. (2022) created a probabilistic ML-based prediction system for DED of about 1,150 tensile test specimens. Their findings showed that probabilistic modeling reduced the time and cost of validation of material systems to less than 0.5 for most properties with an R2 of over 0.5, and it also tackled dataset sparsity and aleatory uncertainty. Junk and Rothe (2022) focused on ultra-lightweight automobile parts using generative design and fiber-reinforced AM. Their findings showed dramatic decreases in cost and weight, with a safety factor of 1.44 in mechanical tests, though they do leave some room for improvements in fiber reinforcement design. Dheeradhada et al. (2022) expanded the domain of design of experiments (DoE)-informed design with ML that allowed higher manufacturing accuracy and a reduction of model uncertainty by 25%.

Milone et al. (2023) designed a shape optimization algorithm for hip replacement prostheses that increases volume and mass by 20% and maximum von Mises stress by 39%, indicating durability and performance. Awd et al. (2024) studied how manufacturing metadata can be integrated into ML models to predict fatigue properties in metamaterials, showing that mechanistic functions can quantify the influence of defects on fatigue lifetime to design better materials. Cao et al. (2024) used an image-based GAN algorithm to study microstructures in metal AM, which was able to produce high-resolution images very similar to actual microstructures and enable better material property measurements.

Headley et al. (2024) presented an augmented ML technique in AM of thermoelectric materials and reported over 99% density and shorter build times on bismuth telluride parts that allowed for improved process parameters without degradation in quality.

5.3. AM Process Automation and Optimization

Mostafavi et al. (2015) continued this by developing the Informed Design-to-Robotic-Production (D2RP) system for material deposition in robotic 3D printing. Their work forged a relationship between design and production, improving the performance of architecture with smart management of porosity. In contrast, Tutum et al. (2018) addressed functional generative design by using a variational autoencoder and surrogate modeling to optimize complex 3D-printed springs. They found both strength of the generated geometries and applicability of the method for other functional design challenges. Nguyen et al. (2018) developed a mixed generative-discriminative inverse materials design method that efficiently predicted design parameters with imperfect information, making the materials design process faster and more effective.

Ko et al. (2019), by comparison, introduced an ML-based system of continuous knowledge engineering in AM with the focus on design and manufacturing data-driven insights. The results they produced revealed that the algorithm could be used to automate the rule generation from AM data to significantly enhance part quality using intelligent decision-making. Jaisawal and Agrawal (2021) described many different techniques of generative design in detail, sorting by techniques and stressing the need to use computing power to come up with multiple design options during the multidimensional planning phase of product design. Their article emphasized the multidisciplinary-ness of generative design. Alternatively, Sotomayor et al. (2021) had an emphasis on reducing DfAM workflow with the help of advanced design tools and highlighted some optimization techniques such as topology and lattice infill optimization that complemented material efficiency and performance.

Ko et al. (2021) targeted establishing AM design rules with a data-driven approach leveraging ML and knowledge graphs to learn more about AM processes and consequences, resulting in LPBF-specific design rules. Grierson et al. (2021) also discussed the broad effects of ML on AM by noting its positive role in technological adoption but admitting to the limitations of existing applications, including the need for more powerful, field-tested ML packages and generalizable models for process parameter optimization. On the contrary, Hsu et al. (2022) had developed a novel approach that translated natural language input into 3D-designed material via a mixture of GANs and contrastive language-image pre-training. Their work demonstrated the effective design of materials of variable rigidity and showed potential to apply material science more broadly, but they were more concerned with the amputation of language to matter.

Sandeep et al. (2022) assessed ML's role in AM, which highlighted the potential to maximize design, production, and defect detection and identified a lack of research about ML's repair and restoration applications. In a related article, Staub et al. (2022) proposed a ML-based technique for AM to detect problematic geometrical features with a success rate of 88% in detecting hard-to-manufacture geometries. This showed ML's ability to optimize manufacturability through custom scanning techniques. Ajayi et al. (2023) demonstrated a new 3D-VAE-SDFGAN method to create 3D forms from 2D pictures that scalably and visibly outperformed previous approaches, indicating that the use of ML for designing might be the future.

Pilagatti et al. (2023) analyzed GD and AM's integration in the space industry, recommending a process that automated the design selection cycle and reduced project duration. Trovato et al. (2023) identified other general trends of ML in AM design, separating use cases into geometrical design, process setup, and process monitoring. They highlighted the disadvantages of AM, such as cost and dimensional tolerances, and advocated ML as a way to improve the design process. Ng et al. (2024) also discussed ML applications in AM with detailed coverage of how ML has been used to identify pattern complexity and reverse-engineer design workflows to significantly improve production productivity and quality assurance.

5.4. New Use Cases

Oh et al. (2019) combined deep generative models with TO to build a system that produced performant designs through a case study that confirmed the effectiveness of the system over earlier generative approaches. Ghiasian and Lewis (2020) proposed a design recommender engine that used ML to convert legacy part inventories into AM. Their findings showed marked enhancements in design ease for AM, which also highlighted how ML could inform efficient design adjustments and improve manufacturing practices. Jin et al. (2020) turned to ML's capabilities to mitigate AM issues, including build deviations and material property differences. They detailed the use of ML algorithms for geometrical design, process parameter tuning, and in-place anomaly detection with a roadmap for enhancing manufacturing efficiency.

Pollák et al. (2020) demonstrated the use of generative design software for robotic 3D printing by showing the flexibility and speed of rapid prototyping with Rhinoceros and Grasshopper-based programs, allowing to go from design to simulation without friction. Junk and Burkart (2021) evaluated CAD software, Fusion 360, Solid Edge, and CogniCAD, in generative design terms: Fusion 360 and Solid Edge both produced the same design, but CogniCAD was far different, with user interfaces, calculation times, and design considerations varying across systems. Nebot et al. (2021) proposed a novel generative design approach that combines 3D morphing with genetic algorithms for breaking the cycle of traditional design obsession, but their conceptual process never got applied, setting a precedent for the coming years.

Yoo et al. (2021) examined how deep learning can be implemented within CAD/CAE for generative design and developed a formal model to automate 3D CAD model creation and analysis for a high-productivity conceptual design workflow using an example. Kanagalingam et al. (2023) were more interested in generative design as applied in medical implants—high tibial osteotomy fixation plates. Then, they presented an AM workflow that combined generative design and detailed design with significant enhancements in surface finish and geometric precision with the help of advanced post-processing. Marino (2023) analyzed drone frame optimization through generative design and AI algorithms and found that a square-type frame with load distribution was the most suitable one for PEEK 3D printing.

5.5. Challenges and Limitations

Yao et al. (2017) proposed a mixed ML solution that recommended AM design features, which could assist the novice designers by computing support for AM. Guerguis et al. (2017), in contrast, addressed the algorithmic design of massive AM architecture, which demonstrated that 3D printing was able to make architecture more energy efficient. In 2020, Cunningham et al. (2020) utilized a sparsity-preserving genetic algorithm paired with generative neural networks to create various useful 3D models. This strategy was successful in their discovery of latent space, and they could produce designs with a functional advantage while remaining close to the human models so as to allow for a transition from design innovation to experimental testing.

Peles et al. (2023) used GAN for structural analysis of additively made parts and showed that the technique could reliably predict melt pool boundaries and defects from optical photos. They found that melt pool geometries were positively skewed in their area probability distribution, indicating a strong use of deep learning for structural information in AM. Lastly, Peckham et al. (2024) in their paper also pointed out that generative design in AM has some randomness; performance varies as much as 592% from design to design, which warrants better user training and learning of generative design tooling to enhance the design results.

6. Conclusions

As ML is already used in AM generative design, the production capability can grow across industries and scale. ML-driven generative design could provide new opportunities for production, allowing them to generate complex geometries that would not be achievable with conventional manufacturing. It allowed not only design accuracy but material consumption to be maximized for more effective manufacturing. Generative design helped to be sustainable by reducing material waste with algorithms and iterative optimization. This solution provides clear environmental benefits, for example, in the case of aerospace, where lightweight materials mean a reduction in fuel usage and associated environmental impacts. Optimization for a specific performance need (like strength, weight, etc.) leads to lightweight and economical designs. Not only does this lower production costs, but it also increased the overall performance of final products, which is what makes generative design such a powerful resource for manufacturers. Past innovations of the pioneers of a specific industry set the example for future innovation. The continuous adoption of ML in generative design should address underlying production efficiency and variability issues leading to reliable and innovative manufacturing technologies. The paper concludes that the convergence of generative design and ML isn't a mere technological solution but a force of change that can yield future more sustainable, efficient, and novel forms of manufacturing.

7. Future Scope

The potential for generative design coupled with ML in AM is huge for creativity and efficacy. The following are some of the most promising future directions:

- Advanced Predictive Models: Future research will have to focus on building better ML models capable of predicting the quality of 3D printed items with better precision. For example, gradient boosting regression (which achieved an R-2 score of 0.954) with improvement of models may enable one to better optimize construction orientation and component dispersion and deliver high-quality outputs during production.
- Integration with Production Management: It is essential to integrate AI models in the current manufacturing process. Moving forward, efforts need to focus on building flexible systems that support multiple data science tools and frameworks like TensorFlow and ONNX. This would also enable the telemetry between AI models and production sites in real time, enabling manufacturing automation in real-time.
- Sustainability Programs: With companies' awareness of sustainability, generating design could also be key to reducing waste and materials. The research needs to investigate even more advanced algorithms that further increase resource efficiency, along with environmentally friendly manufacturing processes in other sectors.
- Industry-Level Applications: Although current applications for aerospace and automotive are incredible, there is significant potential for generative design and ML to be applied in many

other fields, such as healthcare, consumer products, and construction. Analyzing these new areas could result in new products tailored to specific industrial issues.

- Academic Partnerships: Collaborations between leaders from industry and academic organizations could enable a skilled workforce capable of AM/ML. Such efforts as Boeing's and MIT's might help to lay the skills and knowledge base to drive further developments in the industry.

The future of generative design in AM through ML is truly endless and promises more predictive power, sustainability, and expanded domain application. This potential will require a sustained commitment to research and collaboration.

Acknowledgments

References

Ajayi, E. A., Lim, K. M., Chong, S. C., & Lee, C. P. (2023). Three-dimensional shape generation via variational autoencoder generative adversarial network with signed distance function. *International Journal of Electrical and Computer Engineering*, *13*(4), 4009-4019. https://doi.org/10.11591/ijece.v13i4.pp4009-4019

Almasri, W., Bettebghor, D., Ababsa, F., & Danglade, F. (2020). Shape related constraints aware generation of mechanical designs through deep convolutional GAN. *arXiv (Cornell University)*. https://doi.org/10.48550/arxiv.2010.11833

Aman, B. (2020). Generative design for performance enhancement, weight reduction, and its industrial implications. *arXiv (Cornell University)*. https://doi.org/10.48550/arxiv.2007.14138

Awd, M., Saeed, L., Münstermann, S., Faes, M., & Walther, F. (2024). Mechanistic machine learning for metamaterial fatigue strength design from first principles in additive manufacturing. *Materials & Design*, *241*, Article 112889. https://doi.org/10.1016/j.matdes.2024.112889

Babu, S. S., Mourad, A. I., Harib, K. H., & Vijayavenkataraman, S. (2022). Recent developments in the application of machine-learning towards accelerated predictive multiscale design and additive manufacturing. *Virtual and Physical Prototyping*, *18*(1), 1–47. https://doi.org/10.1080/17452759.2022.2141653

Barbieri, L., & Muzzupappa, M. (2022). Performance-driven engineering design approaches based on generative design and topology optimization tools: a comparative study. *Applied Sciences*, *12*(4), Article 2106. https://doi.org/10.3390/app12042106

Beesley, C. (2020, November 12). *Generative design is out of the lab and being used in the field*. GovDesignHub. https://govdesignhub.com/2018/06/28/generative-design-is-out-of-the-lab-and-being-used-in-the-field/

Bendoly, E., Chandrasekaran, A., Lima, M. D. R. F., Handfield, R., Khajavi, S. H., & Roscoe, S. (2023). The role of generative design and additive manufacturing capabilities in developing human–AI symbiosis: Evidence from multiple case studies. *Decision Sciences*, *55*(4), 325–345. https://doi.org/10.1111/deci.12619

Cao, Z., Liu, Y., Kruzic, J. J., & Li, X. (2024). An image-driven machine learning method for microstructure characterization in metal additive manufacturing: generative adversarial network. *IOP Conference Series: Materials Science and Engineering*, 1310(1), Article 012015. https://doi.org/10.1088/1757-899X/1310/1/012015

Chaudhari, A. M., & Selva, D. (2023). Evaluating designer learning and performance in interactive deep generative design. *Journal of Mechanical Design*, *145*(5), Article 051403. https://doi.org/10.1115/1.4056374

Chinchanikar, S., & Shaikh, A. A. (2022). A review on machine learning, big data analytics, and design for additive manufacturing for aerospace applications. *Journal of Materials Engineering and Performance*, *31*, 6112–6130. https://doi.org/10.1007/s11665-022-07125-4

Christian, B. (2018, April 17). This remarkable spinal implant was created by an algorithm. WIRED. https://www.wired.com/story/nuvasive-automated-design-spinal-implant-artificial-intelligence/

Ciccone, F., Bacciaglia, A., & Ceruti, A. (2023). Optimization with artificial intelligence in additive manufacturing: a systematic review. *Journal of the Brazilian Society of Mechanical Sciences and Engineering*, *45*, 1-22. https://doi.org/10.1007/s40430-023-04200-2

Cunningham, J. D., Shu, D., Simpson, T. W., & Tucker, C. S. (2020). A sparsity preserving genetic algorithm for extracting diverse functional 3D designs from deep generative neural networks. *Design Science*, *6*, Article e11. https://doi.org/10.1017/dsj.2020.9

Deplazes, R. (2019, November 19). *Autodesk and Airbus Demonstrate the Impact of Generative Design on Making and Building*. Autodesk News. https://adsknews.autodesk.com/en/news/autodesk-airbus-generative-design-aerospace-factory/

Dheeradhada, V. S., Kumar, N. C., Gupta, V. K., Dial, L., Vinciquerra, A. J., & Hanlon, T. (2022). *Machine learning assisted development in additive manufacturing* (Patent 11511491). US Patent for Machine learning assisted development in additive manufacturing. https://patents.justia.com/patent/11511491

Felbrich, B., Schork, T., & Menges, A. (2022). Autonomous robotic additive manufacturing through distributed model-free deep reinforcement learning in computational design environments. *Construction Robotics*, *6*(1), 15-37. https://doi.org/10.1007/s41693-022-00069-0

Ghiasian, S. E., & Lewis, K. (2020). A machine learning-based design recommender system for additive manufacturing. In *International design engineering technical conferences and computers and information in engineering conference* (Vol. 84003, p. V11AT11A025). American Society of Mechanical Engineers. https://doi.org/10.1115/DETC2020-22182

Goguelin, S. (2019). *Generative part design for additive manufacturing* [Doctoral dissertation, University of Bath].

Goudswaard, M., Hicks, B., & Nassehi, A. (2021). The creation of a neural network based capability profile to enable generative design and the manufacture of functional FDM parts. *The International Journal of Advanced Manufacturing Technology*, *113*, 2951-2968. https://doi.org/10.1007/s00170-021-06770-8

Grierson, D., Rennie, A. E., & Quayle, S. D. (2021). Machine learning for additive manufacturing. *Encyclopedia*, *1*(3), 576-588. https://doi.org/10.3390/encyclopedia1030048

Gu, G. X., Chen, C. T., Richmond, D. J., & Buehler, M. J. (2018). Bioinspired hierarchical composite design using machine learning: simulation, additive manufacturing, and experiment. *Materials Horizons*, *5*(5), 939-945. https://doi.org/10.1039/C8MH00653A

Guerguis, M., Eikevik, L., Obendorf, A., Tryggestad, L., Enquist, P., Lee, B., Johnson, B., Post, B.K., & Biswas, K. (2017). Algorithmic design for 3D printing at building scale. *International Journal of Modern Research in Engineering and Technology*, *1*(6), 1-10. https://www.osti.gov/biblio/1351781

Guo, S., Agarwal, M., Cooper, C., Tian, Q., Gao, R. X., Guo, W., & Guo, Y. (2022). Machine learning for metal additive manufacturing: Towards a physics-informed data-driven paradigm. *Journal of Manufacturing Systems*, *62*, 145–163. https://doi.org/10.1016/j.jmsy.2021.11.003

Headley, C.V., del Valle, R.J.H., Ma, J., Balachandran, P., Ponnambalam, V., LeBlanc, S., Kirsch, D., & Martin, J.B. (2024). The development of an augmented machine learning approach for the additive manufacturing of thermoelectric materials. *Journal of Manufacturing Processes*, *116*, 165-175. https://doi.org/10.1016/j.jmapro.2024.02.045

Hsu, Y. C., Yang, Z., & Buehler, M. J. (2022). Generative design, manufacturing, and molecular modeling of 3D architected materials based on natural language input. *APL Materials*, *10*(4), 041107. https://doi.org/10.1063/5.0082338

Hyunjin, C. (2020). A study on application of generative design system in manufacturing process. In *IOP Conference Series: Materials Science and Engineering*, *727*(1), Article 012011. https://doi.org/10.1088/1757-899X/727/1/012011

Jaisawal, R., & Agrawal, V. (2021). Generative Design Method (GDM)–a state of art. In *IOP Conference Series: Materials Science and Engineering*, *1104*(1), Article 012036. https://doi.org/10.1088/1757-899X/1104/1/012036

Jiang, J., Xiong, Y., Zhang, Z., & Rosen, D. W. (2022). Machine learning integrated design for additive manufacturing. *Journal of Intelligent Manufacturing*, *33*(4), 1073-1086. https://doi.org/10.1007/s10845-020-01715-6

Jin, Z., Zhang, Z., Demir, K., & Gu, G. X. (2020). Machine learning for advanced additive manufacturing. *Matter*, *3*(5), 1541-1556. https://doi.org/10.1016/j.matt.2020.08.023

Johnson, N., Vulimiri, P., To, A., Zhang, X., Brice, C., Kappes, B., & Stebner, A. (2020). Invited review: Machine learning for materials developments in metals additive manufacturing. *Additive Manufacturing*, *36*, 1–30. https://doi.org/10.1016/j.addma.2020.101641

Junk, S., & Burkart, L. (2021). Comparison of CAD systems for generative design for use with additive manufacturing. *Procedia CIRP*, *100*, 577-582. https://doi.org/10.1016/j.procir.2021.05.126

Junk, S., & Rothe, N. (2022). Lightweight design of automotive components using generative design with fiber-reinforced additive manufacturing. *Procedia CIRP*, *109*, 119-124. https://doi.org/10.1016/j.procir.2022.05.224

Kanagalingam, S., Dalton, C., Champneys, P., Boutefnouchet, T., Fernandez-Vicente, M., Shepherd, D. E., & Thomas-Seale, L. E. (2023). Detailed design for additive manufacturing and post processing of generatively designed high tibial osteotomy fixation plates. *Progress in Additive Manufacturing*, *8*(3), 409-426. https://doi.org/10.1007/s40964-022-00342-2

Ko, H., Witherell, P., Lu, Y., Kim, S., & Rosen, D. W. (2021). Machine learning and knowledge graph based design rule construction for additive manufacturing. *Additive Manufacturing*, *37*, Article 101620. https://doi.org/10.1016/j.addma.2020.101620

Ko, H., Witherell, P., Ndiaye, N. Y., & Lu, Y. (2019). Machine learning based continuous knowledge engineering for additive manufacturing. In *2019 IEEE 15th international conference on automation science and Engineering (CASE)* (pp. 648-654). IEEE. https://doi.org/10.1109/COASE.2019.8843316

Kumar, S., Gopi, T., Harikeerthana, N., Gupta, M. K., Gaur, V., Krolczyk, G. M., & Wu, C. (2022). Machine learning techniques in additive manufacturing: a state of the art review on design, processes and production control. *Journal of Intelligent Manufacturing*, *34*, 21–55. https://doi.org/10.1007/s10845-022-02029-5

Kumaran, M., & Senthilkumar, V. (2021). Generative design and topology optimization of analysis and repair work of industrial robot arm manufactured using additive manufacturing technology. In *IOP Conference Series: Materials Science and Engineering*, *1012*(1), Article 012036. https://doi.org/10.1088/1757-899X/1012/1/012036

Kvernvik, M. (2018, May 14). *General Motors applies Autodesk generative design software to develop future vehicles*. TCT Magazine. https://www.tctmagazine.com/additive-manufacturing-3d-printing-news/gm-teams-up-autodesk-generative-design-vehicle/

Lee, J., Park, D., Lee, M., Lee, H., Park, K., Lee, I., & Ryu, S. (2023). Machine learning-based inverse design methods considering data characteristics and design space size in materials design and manufacturing: a review. *Materials Horizons*, *10*, 5436–5456. https://doi.org/10.1039/d3mh00039g

Marino, S. O. (2023, June 7). Generative design for 3D printing of advanced aerial drones (Version 1). Toronto Metropolitan University. https://doi.org/10.32920/23330861.v1

Markovic, N. (2022, February 12). *General electric collaboration targets jet engine efficiency with generative design*. Autodesk Research. https://www.research.autodesk.com/blog/general-electric-collaboration-targets-jet-engine-efficiency-with-generative-design/

Mattias. (2024, November 12). *How generative design and 3D printing fuels innovation*. Addinor. https://addinor.eu/articles/how-generative-design-and-3d-printing-fuels-innovation/

Mazer, S. (2017, October 18). *NuVasive Launches New 3D-Printed Porous Titanium Implant In Expanding Advanced Materials Science Portfolio*. NuVasive. https://www.nuvasive.com/news/nuvasive-launches-new-3d-printed-porous-titanium-implant-expanding-advanced-materials-science-portfolio/

Milone, D., D'Andrea, D., & Santonocito, D. (2023). Smart design of hip replacement prostheses using additive manufacturing and machine learning techniques. *Prosthesis*, *6*(1), 24-40. https://doi.org/10.3390/ prosthesis6010002

Mostafavi, S., Bier, H., Bodea, S., & Anton, A. M. (2015). Informed design to robotic production systems: developing robotic 3D printing system for informed material deposition. In *33rd International Conference on Education and research in Computer aided Architectural Design in Europe* (pp. 287-296). eCAADe (Education and Research in Computer Aided Architectural Design in Europe) and University of Ljubljana. https://pure.hud.ac.uk/en/publications/informed-design-to-robotic-production-systems-developing-robotic-

Nebot, J., Peña, J. A., & López Gómez, C. (2021). Evolutive 3D modeling: A proposal for a new generative design methodology. *Symmetry*, *13*(2), 338. https://doi.org/10.3390/sym13020338

Ng, W. L., Goh, G. L., Goh, G. D., Ten, J. S. J., & Yeong, W. Y. (2024). Progress and opportunities for machine learning in materials and processes of additive manufacturing. *Advanced Materials*, *36*(34), Article 2310006. https://doi.org/10.1002/adma.202310006

Nguyen, P., Tran, T., Gupta, S., Rana, S., & Venkatesh, S. (2018). Hybrid generative-discriminative models for inverse materials design. *arXiv (Cornell University)*. https://doi.org/10.48550/arxiv.1811.06060

Nordin, A., Hopf, A., & Motte, D. (2013). Generative design systems for the industrial design of functional mass producible natural-mathematical forms. In *5th International Congress of International Association of Societies of Design Research-IASDR'13* (pp. 2931-2941). International Association of Societies of Design Research (IASDR). https://portal.research.lu.se/en/publications/generative-design-systems-for-the-industrial-design-of-functional

Ntintakis, I., & Stavroulakis, G. E. (2020). Progress and recent trends in generative design. *MATEC Web of Conferences*, 318, Article 01006. https://doi.org/10.1051/matecconf/202031801006

Nyamekye, P., Lakshmanan, R., & Piili, H. (2024). Effect of computational generative product design optimization on part mass, manufacturing time and costs: Case of laser-based powder bed fusion. In *Computational methods in applied sciences* (Vol. 59, pp. 257–273). https://doi.org/10.1007/978-3-031-61109-4_17

Oh, S., Jung, Y., Kim, S., Lee, I., & Kang, N. (2019). Deep generative design: Integration of topology optimization and generative models. *Journal of Mechanical Design*, *141*(11), Article 111405. https://doi.org/10.1115/1.4044229

Peckham, O., Elverum, C. W., Hicks, B., Goudswaard, M., Snider, C., Steinert, M., & Eikevåg, S. W. (2024). Investigating and characterizing the systemic variability when using generative design for additive manufacturing. *Applied Sciences*, *14*(11), Article 4750. https://doi.org/10.3390/app14114750

Peles, A., Paquit, V. C., & Dehoff, R. R. (2023). Deep-learning quantitative structural characterization in additive manufacturing. *arXiv (Cornell University)*. https://doi.org/10.48550/arXiv.2302.06389

Pilagatti, A. N., Atzeni, E., & Salmi, A. (2023). Exploiting the generative design potential to select the best conceptual design of an aerospace component to be produced by additive manufacturing. *The International Journal of Advanced Manufacturing Technology*, *126*(11), 5597-5612. https://doi.org/10.1007/s00170-023-11259-7

Pollák, M., Töröková, M., & Kočiško, M. (2020). Utilization of generative design tools in designing components necessary for 3D printing done by a robot. *TEM Journal*, *9*(3), 868-872. https://doi.org/10.18421/tem93-05

Regenwetter, L., Nobari, A. H., & Ahmed, F. (2022). Deep generative models in engineering design: A review. *Journal of Mechanical Design*, *144*(7), Article 071704. https://doi.org/10.1115/1.4053859

Ricotta, V., Campbell, R. I., Ingrassia, T., & Nigrelli, V. (2020). Additively manufactured textiles and parametric modelling by generative algorithms in orthopaedic applications. *Rapid Prototyping Journal*, *26*(5), 827-834. https://doi.org/10.1108/RPJ-05-2019-0140

Ricotta, V., Campbell, R. I., Ingrassia, T., & Nigrelli, V. (2021). Generative design for additively manufactured textiles in orthopaedic applications. In *Advances on Mechanics, Design Engineering and Manufacturing III: Proceedings of the International Joint Conference on Mechanics, Design Engineering & Advanced Manufacturing, JCM 2020, June 2-4, 2020* (pp. 241-248). Springer International Publishing. https://doi.org/10.1007/978-3-030-70566-4_39

Rivera, L. (2024, January 18). *NASA revolutionizes component fabrication with generative design*. GovDesignHub. https://govdesignhub.com/2024/01/18/nasa-revolutionizes-component-fabrication-with-generative-design/

Rosen, L. (2023, February 19). *NASA has jumped on the generative AI design and manufacturing bandwagon*. 21st Century Tech Blog. https://www.21stcentech.com/nasa-jumped-generative-ai-design-manufacturing-bandwagon/

Sandeep, R., Jose, B., Kumar, K. G., Manoharan, M., & Arivazhagan, N. (2022). Machine learning applications for additive manufacturing: State-of-the-art and future perspectives. In *Industrial Transformation* (pp. 25-44). CRC Press. http://dx.doi.org/10.1201/9781003229018-2

Siegkas, P. (2022). Generating 3D porous structures using machine learning and additive manufacturing. *Materials & Design*, *220*, Article 110858. https://doi.org/10.1016/j.matdes.2022.110858

Soori, M., Jough, F. K. G., Dastres, R., & Arezoo, B. (2024). Additive manufacturing modification by artificial intelligent, machine learning and deep learning, A review. *Chinese Journal of Mechanical Engineering Additive Manufacturing Frontiers*, pp. 1–32. https://www.researchgate.net/profile/Mohsen-Soori/publication/384200665_Additive_manufacturing_modification_by_artificial_intelligent_machine_learning_and_deep_learning_A_Review/links/66ee4a3397a75a4b483bd564/Additive-manufacturing-modification-by-artificial-intelligent-machine-learning-and-deep-learning-A-Review.pdf

Sotomayor, N. A. S., Caiazzo, F., & Alfieri, V. (2021). Enhancing design for additive manufacturing workflow: Optimization, design and simulation tools. *Applied Sciences*, *11*(14), Article 6628. https://doi.org/10.3390/app11146628

Staub, A., Brunner, L., Spierings, A. B., & Wegener, K. (2022). A machine-learning-based approach to critical geometrical feature identification and segmentation in additive manufacturing. *Technologies*, *10*(5), Article 102. https://doi.org/10.3390/technologies10050102

Strömberg, N. (2019). A generative design optimization approach for additive manufacturing. In *Sim-AM 2019: II International Conference on Simulation for Additive Manufacturing* (pp. 130-141). CIMNE. http://hdl.handle.net/2117/334593

Toro, R. B. (2024, November 12). *First concrete, large-scale, 3D-printed building elements using generative design*. Autodesk University. https://www.autodesk.com/autodesk-university/class/First-Concrete-Large-Scale-3D-Printed-Building-Elements-Using-Generative-Design-2018

Trovato, M., Belluomo, L., Bici, M., Campana, F., & Cicconi, P. (2023). Machine learning trends in design for additive manufacturing. In *International Conference of the Italian Association of Design Methods and Tools for Industrial Engineering* (pp. 109-117). Cham: Springer Nature Switzerland. https://doi.org/10.1007/978-3-031-52075-4_14

Tutum, C. C., Chockchowwat, S., Vouga, E., & Miikkulainen, R. (2018). Functional generative design: An evolutionary approach to 3D-printing. In *Proceedings of the Genetic and Evolutionary Computation Conference* (pp. 1379-1386). https://doi.org/10.1145/3205455.3205635

Vaneker, T., Bernard, A., Moroni, G., Gibson, I., & Zhang, Y. (2020). Design for additive manufacturing: Framework and methodology. *CIRP Annals*, *69*(2), 578–599. https://doi.org/10.1016/j.cirp.2020.05.006

Wang, C., Tan, X., Tor, S., & Lim, C. (2020). Machine learning in additive manufacturing: State-of-the-art and perspectives. *Additive Manufacturing*, *36*, Article 101538. https://doi.org/10.1016/j.addma.2020.101538

Wang, Z., Yang, W., Liu, Q., Zhao, Y., Liu, P., Wu, D., Banu, M., & Chen, L. (2022). Data-driven modeling of process, structure and property in additive manufacturing: A review and future directions. *Journal of Manufacturing Processes*, *77*, 13–31. https://doi.org/10.1016/j.jmapro.2022.02.053

Warde, S. (2024, November 12). *Data-driven Additive Manufacturing: AMRC, Boeing, Constellium, GE Additive*. Intellegens. https://intellegens.com/data-driven-additive-manufacturing-with-amrc-and-boeing/

Watson, M., Leary, M., Downing, D., & Brandt, M. (2023). Generative design of space frames for additive manufacturing technology. *The International Journal of Advanced Manufacturing Technology*, *127*(9), 4619-4639. https://doi.org/10.1007/s00170-023-11691-9

Werner, D. (2018, November 1). *Lockheed Martin extends additive manufacturing to key spacecraft components*. SpaceNews. https://spacenews.com/lockheed-martin-extends-additive-manufacturing-to-key-spacecraft-components/

Westphal, E., & Seitz, H. (2024). Generative artificial intelligence: analyzing its future applications in additive manufacturing. *Big Data and Cognitive Computing*, *8*(7), Article 74. https://doi.org/10.3390/bdcc8070074

Williams, G. (2022). *Towards the next-generation of engineering design artificial intelligence: a framework for additive manufacturing machine learning development* [PhD dissertation, Pennsylvania State University]. https://etda.libraries.psu.edu/files/final_submissions/26721

Yadav, V.D., Yadav, P., & Francis, V. (2021). Application of generative design approach for optimization and additive manufacturing of UAV's frame structure. *Journal of Emerging Technologies and Innovative Research (JETIR), 8(*4), 1194-1201.

Yao, X., Moon, S. K., & Bi, G. (2017). A hybrid machine learning approach for additive manufacturing design feature recommendation. *Rapid Prototyping Journal*, *23*(6), 983-997. https://doi.org/10.1108/RPJ-03-2016-0041

Yoo, S., Lee, S., Kim, S., Hwang, K. H., Park, J. H., & Kang, N. (2021). Integrating deep learning into CAD/CAE system: generative design and evaluation of 3D conceptual wheel. *Structural and Multidisciplinary Optimization*, *64*(4), 2725-2747. https://doi.org/10.1007/s00158-021-02953-9

Zhang, Y., Karnati, S., Nag, S., Johnson, N., Khan, G., & Ribic, B. (2022). Accelerating additive design with probabilistic machine learning. *ASCE-ASME Journal of Risk and Uncertainty in Engineering Systems, Part B: Mechanical Engineering*, *8*(1), Article 011109. https://doi.org/10.1115/1.4051699

Przegląd Projektowania Generatywnego z Wykorzystaniem Uczenia Maszynowego w Produkcji Przyrostowej

Streszczenie

W niniejszym artykule przeglądowym zbadano, w jaki sposób projektowanie generatywne jest łączone z uczeniem maszynowym w celu realizacji produkcji przyrostowej i jej transformacyjnego wpływu na społeczeństwo. Projektowanie generatywne wykorzystuje złożone algorytmy w celu automatyzacji procesu projektowania najlepiej dopasowanych struktur, masowej personalizacji i dostosowywania do konkretnych wymagań klienta przy zachowaniu wysokiej wydajności i jakości. Skalowalność i przewidywalność modeli sztucznej inteligencji (ang. Artificial Intelligence - AI) ułatwiają obsługę dużych ilości danych i umożliwiają skalowanie produkcji bez uszczerbku dla jakości. Niniejszy artykuł koncentruje się również na tym, w jaki sposób projektowanie generatywne może pomóc przyspieszyć innowacje i wytwarzanie wyrobów, ponieważ umożliwia projektantom działanie w szerszej przestrzeni projektowania i dostarczanie rozwiązań, których nie można osiągnąć za pomocą tradycyjnych technik. Integracja AI z istniejącymi procesami produkcyjnymi ma również kluczowe znaczenie dla optymalizacji produkcji w czasie rzeczywistym — co dodatkowo zwiększa ogólną skuteczność operacyjną. Ponadto pojawienie się zaawansowanych modeli predykcyjnych, takich jak regresja z pobudzeniem gradientowym (ang. gradient boosting regression), pokazuje, w jaki sposób uczenie maszynowe może zapewnić lepszą dokładność operacji drukowania 3D w celu zapewnienia standardów jakościowych wyrobów. Artykuł zakończono omówieniem projektowania generatywnego i uczenia maszynowego w aspekcie rozwoju przyszłościowego wytwarzania przyrostowego oraz sposobów, według których projektowanie może być udoskonalane i modyfikowane, tak aby dostosowywać się do zmieniających się wymagań przemysłu.

Słowa kluczowe: projektowanie generatywne, uczenie maszynowe, wytwarzanie przyrostowe, projektowanie struktur lekkich, optymalizacja

Calculation Methods for Volute Parameters Used in the Conceptual Design of Radial and Axial-Centrifugal Compressors

Stanisław Antas [iD]

Faculty of Mechanical Engineering and Aeronautics, Rzeszów University of Technology, al. Powstańców Warszawy 8, 35-959 Rzeszów

Correspondence: santas@prz.edu.pl, tel.: +48 17 865 1501

Abstract

In many designs of a single-stage radial and axial-centrifugal compressors of the turboprop and turboshaft aviation engines, a properly formed collector placed after a vaneless or vaned radial diffuser, is used to decrease velocity and to increase static pressure of an air stream. The spiral diffuser is one of the main diffuser types. A volute is a channel with a different form of transverse sections that gradually expands in the direction of rotor rotation and includes preceding diffuser with a cylindrical inlet hole. Its geometrical parameters should be properly selected to ensure the correct operation of the scroll. This paper presents two main methods of calculation of geometrical parameters of the spiral diffuser: free vortex design (constant angular momentum principle) and constant mean velocity design. Mentioned methods (recommended for use in the conceptual design of a compressor) are based on energy equation - steady flow energy equation, equation of continuity, first law of thermodynamics, Euler's moment of momentum equation, gas dynamics functions and definitions used in theory of turbomachinery. A detailed analysis of geometrical parameters of different types of collectors were conducted. This paper also provides a review of experimental research results of total pressure loss coefficient in the volute and proposed method of determining air stream parameters at volute outlet.

Keywords: turbine engine, compressor, collector

Nomenclature

a	speed of sound	R_{sr}	radius of spiral axis for volute, measured from impeller axis of rotation to centre of gravity of the cross-section
b	passage width of vaneless, vaned diffuser or volute		
c	absolute velocity	T	static temperature
c_r	radial velocity komponent	α	angle of absolute velocity from tangential
c_u	tangential velocity komponent	Δ	height of threshold
D	duct diameter of a volume	ρ	gas density
F	surface area	λ	Laval number
F_φ	surface area of collector in radial section at angle φ	φ	polar angle (volute azimuth angle) measured from spiral volute tongue towards impeller rotation to the considered radial cross section
h	volute Weight		
$\dot{m}$	mass flow rate		
N	polytropic exponent/rotational speed	ξ_{sp}	total pressure loss coefficient
p	static pressure	ϑ	volute sidewalls angle
r	radius of circular volute passage at radial cross-section		
R	radius of an infinitesimal section for volute passage measured from impeller axis of rotation		
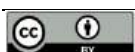
Subscripts

2	impeller exit	$/_{\text{śr}}$	mean
3	vaneless diffuser exit	$/_{\text{SR}}$	centrifugal compressor parameter
4	vaned diffuser exit	$/_{\text{w}}$	inner
5	volute exit	$/_{\text{z}}$	outer
6	exit cone discharge condition	$*/$	stagnation parameter
$/_{\text{kr}}$	critical		

1. Introduction

In a centrifugal compressor impeller, an effective work is supplied to the working medium, in which a significant proportion of this work is the increase of kinetic energy of the stream ($c_2 >> c_1$). At the total pressure ratio $\pi_{SR}^* \approx 4$ the absolute velocity at the exit from the impeller reaches the value $C_2 \approx 420$ m/s ($M_{C2} \approx 1,1$), whereas for higher values of the stagnation pressure ratio $\pi_{SR}^* \approx 8,5$ absolute velocity is greater and is equal to $C_2 \approx 525$ m/s, what corresponds to a Mach number $M_{C2} \approx 1,2$. Supersonic flow velocities at the impeller exit require to use efficiently operating diffusers in the design of centrifugal compressor for diffusing the air flow to the velocity necessary for the proper operation of the combustion chamber – usually $C_B \leq 120 \div 160$ m/s ($0,1 < M_B \leq 0,3$).A spiral diffuser also called collector or volute (Fig.1) is a classic design of a diffuser, which can be found in a number of turboprop engines designs (Allison 250 – B15, Allison 250 – B17) as well as turboshaft engines (GTD – 350, Allison 250 – C20) with mixed-flow compressor, and turboprop (RR500TP) and turboshaft engines equipped with single-stage centrifugal compressor (Allison 250 – C28, Allison 250 – C30, RR300).

Fig. 1. Axial-centrifugal compressor of turboshaft engine GTD-350 - a gift from WSK PZL Rzeszów to the Rzeszów University of Technology: 1 – double jet collector.

In case of low pressure ratio of the centrifugal compressor module $\pi_{SR}^* < 2,5$ the volute is preceded by a vaneless diffuser. At higher pressure ratio values $\pi_{SR}^* > 2,5$ volute is placed after the vaned diffuser which is preceded by vaneless diffuser (Antas, 2023). In the design practice, there are two main methods used to calculate diffuser's geometrical parameters (Baloni et al., 2012; Ris, 1951; Yahya, 2012):

1) the method based on the law of constant angular momentum (flow without friction – free vortex, constant circulation),
2) the method based on the assumption of constant mean velocity in the volute.

In the methods mentioned above axisymmetrical nature of flow is assumed.

It should be noticed, that in the available literature on the subject lacks publications concerning comprehensive analysis of geometrical parameters of collectors as well as determination of thermal and kinematic parameters of the stream flowing through diffuser (Antas, 2014; Dmitriewskij, 1960; Japikse, 1990, Japoikse, 1996; Reunaunen, 2001; Walczak, 1999; Yahya, 2012).This article is a first publication in the world concerning those problems. According to Van den Braembusshe and Hände (1990) spiral diffuser is probably the most neglected component of the centrifugal compressor in relation to theoretical and experimental studies but, according to the author of this article, the pipe diffuser and controlled –contour diffuser are equally neglected (Antas, 2014, 2019). The geometrical parameters of the volute are (Figs. 2-8):

- inner radius of volute, equal to the outer radius of the preceding diffuser - vaneless: $R_w = R_3 = D_3/2$ or vaned: $R_w = R_4 = D_4/2$,
- outer radius: $R_z = R_z(\varphi) = var$
- mean radius from the impeller axis to the centroid of volute passage: $R_{śr} = R_{śr}(\varphi) = var.$

All above mentioned radii are measured from the impeller axis.

- width or chord of spiral diffuser: $b = idem$ or: $b = b(\varphi) = var,$
- volute height: $h = h(\varphi) = var.$

A volute is a passage with differently shaped cross-sectional areas, which are progressively increasing in the direction of impeller rotation (i.e. diffuser) with a spiral-shaped axis surrounding vaneless gap or vaned diffuser. In practice, most commonly used collectors are (Cumpsty, 1989; Japikse, 1996):

- single jet – a type of a collector, in which single volute surrounds a diffuser along the circumference i.e. at an azimuth angle $\varphi = 2\pi = 360^0$.
- double jet – a kind of volute, in which two collectors are placed on the circumference of a diffuser, each covering half of the circumference at an azimuth angle $\varphi = 2\pi/2 = 180^0$, dividing airflow in the same ratio.
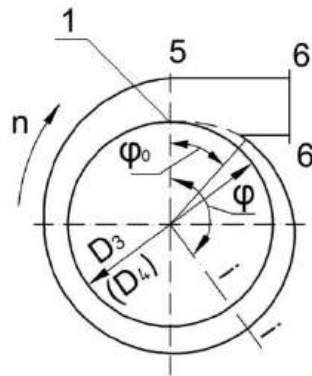

Fig. 2. Single jet scroll (single spiral diffuser).

In Fig.2. and 3. „1" indicates initial segment of a collector located at radius R_3 or R_4, which has coordinate $\varphi = 0$. It corresponds to the collector section with a zero area. Depending on the position of diffuser's wall contour in relation to the axis of vaneless or vaned diffuser, the following volutes can be distinguished (Fig. 4):
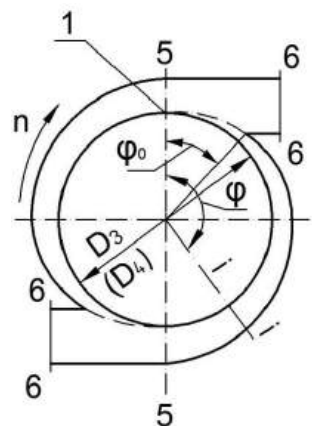
- symmetrical,
- asymmetrical.

Fig. 3. Double jet collector (double spiral diffuser).

During the design process of collectors the aim is to ensure, that along the inlet section of a collector, the static pressure is approximately constant. Fulfilling the requirement plays an important role in the compressor operation, especially when the volute is preceded by diffuser vane ring or impeller. Otherwise, airflow pulsations will be formed, which can cause flow separation and associated significant losses, and in addition diffuser or impeller blade vibration, threatening the compressor operation reliability (Tuliszka, 1976).
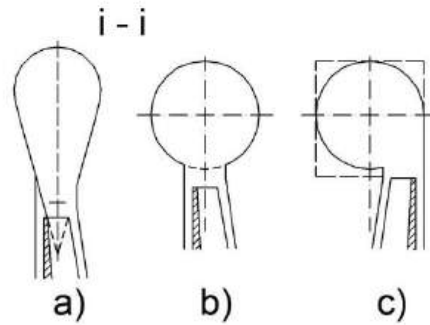
Fig. 4. Shapes of radial sections of the collector (i-i): (a) - symmetrical with an oval section, (b) - symmetrical with a circular section, (c) - asymmetric with a circular or rectangular section.

2. Continuous circulation (free vortex) method

Assuming that flow has axisymmetric nature and is held with no wall friction, then according to Euler's equation the angular momentum is constant, and the change of the absolute velocity in the tangential direction can be determined using a formula:

$$C_u R = C_{4u} R_4 = K = idem \tag{1}$$

if compressor comprises a vaned diffuser - or:

$$C_u R = C_{3u} R_3 = K = idem \tag{2}$$

if compressor comprises only a vaneless diffuser.

The working medium flowing from the vaneless or vaned diffuser is collected in volute starting from cross-section with the coordinate $\varphi = 0$. Through the radial cross-section of the collector (i-i) with the coordinate φ [rad] a mass flow is flown depending on positioning in the compressor:

- when a vaned diffuser is placed before the spiral diffuser

$$\dot{m}_\varphi = \dot{m} \frac{\varphi}{2\pi} = 2\pi R_4 b_4 c_{4r} \rho_4 \frac{\varphi}{2\pi} \tag{3}$$

- or, if a spiral-shaped diffuser is placed after the vaneless diffuser

$$\dot{m}_\varphi = \dot{m} \frac{\varphi}{2\pi} = 2\pi R_3 b_3 c_{3r} \rho_3 \frac{\varphi}{2\pi} \tag{4}$$

We consider the flow through the collector installed directly after the vaneless (slot) diffuser. We take into account different types of volute design.

2.1. Circular volute

The mass flow rate flowing through the radial cross-section of the collector with the coordinate φ can be written using the tangential absolute flow velocity component C_u in the collector, the cross-section area $F = \pi r^2$ and the density ρ_3, which is assumed to be constant for the whole section area F. Then, according to the author of monograph (Kholscevnikov, 1970) - (Fig. 5):

$$\dot{m}_\varphi = \rho_3 \iint_F C_u dF = \rho_3 \iint_F C_u R \frac{dF}{R} = \rho_3 C_{3u} R_3 \int_{R_3}^{R_z} \frac{b(r)dR}{R} = K\rho_3 \int_{R_3}^{R_z} \frac{b(r)dR}{R} \tag{5}$$

The equation can be written as:

$$\dot{m}_\varphi = \dot{m} \frac{\varphi}{2\pi} = K\rho_3 \int_{R_3}^{R_z} \frac{b(r)dR}{R} \tag{6}$$

therefore:

$$\varphi = \frac{2\pi}{\dot{m}} K \rho_3 \int_{R_3}^{R_z} \frac{b(r)dR}{R} \tag{7}$$

By denoting the collector cross-section radius with „r", the relation between chord b and radius (Fig.6) can be written as: $\left(\frac{b}{2}\right)^2 + c^2 = r^2$, where: $c = (R - R_3 - r)$, thus:

$$\left(\frac{b}{2}\right)^2 = r^2 - (R - R_3 - r)^2 \tag{8}$$

or:

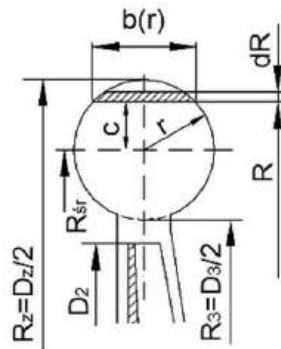$$b = 2\sqrt{r^2 - (R - R_3 - r)^2} \tag{9}$$

Fig. 5. Schematic designations in the circular collector of the radial compressor: Rśr - radius of the spiral axis, R_3 - inner radius of the collector (R_3 = idem), Rz - outer radius of the collector (Rz = var), b (r) - chord of the collector, r - the collector cross-section radius

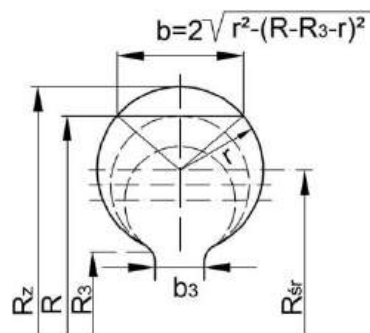**Fig. 6.** Spiral collector with a circular section

Therefore:

$$\varphi = \frac{2\pi}{\dot{m}} K\rho_3 \int_{R_3}^{R_z} \frac{2\sqrt{r^2 - (R - R_3 - r)^2}}{R} dR$$
$$= \frac{2\pi}{\dot{m}} K\rho_3 \int_{R_3}^{R_3+2r} \frac{2\sqrt{r^2 - (R - R_3 - r)^2}}{R} dR = \tag{10}$$
$$\frac{4\pi^2}{\dot{m}} K\rho_3 \left[(R_3 + r) - \sqrt{(R_3 + r)^2 - r^2} \right]$$

The above equation, obtained as a result of complex equations' transformations, determines relation between the angle φ and the radius r of the circular cross-section, as well as the volute shape. Solving the above quadratic equation in relation to „r" the following relation is obtained:

$$r = \frac{\varphi \dot{m}}{4\pi^2 K\rho_3} + \sqrt{R_3 \frac{\varphi \dot{m}}{2\pi^2 K\rho_3}} \tag{11}$$

By specifying the angle φ, the radius r can be determined (the angle is expressed in [rad]). If the angle φ in the relation (11) is expressed in degrees, then:

$$\varphi^{\circ} = 57.3 \cdot \varphi \tag{12}$$

Whereas, formula (11) for radius of the collector cross-section is:

$$r = \frac{\varphi^{\circ} \dot{m}}{4\pi^2 K \rho_3 \cdot 57.3} + \sqrt{R_3 \frac{\varphi^{\circ} \dot{m}}{2\pi^2 K \rho_3 \cdot 57.3}} \tag{13}$$

For the following case, if the angle φ in the equation (11) is expressed in radians, the diameter of the circular collector is:

$$D = 2r = \frac{\varphi \dot{m}}{2\pi^2 K \rho_3} + \sqrt{2R_3 \frac{\varphi \dot{m}}{\pi^2 K \rho_3}} \tag{14}$$

While, if the angle φ is expressed in degrees:

$$D = 2r = \frac{\dot{\varphi^{\circ}} \dot{m}}{2\pi^2 K \rho_3 \cdot 57.3} + \sqrt{2R_3 \frac{\varphi^{\circ} \dot{m}}{\pi^2 K \rho_3 \cdot 57.3}} \tag{15}$$

Collector's external radius in random cross-section (i-i):

$$R_z = R_3 + D \tag{16}$$

If a volute is preceded by a vaned diffuser, then in the above relations the following should be substituted:

$$R_3 \equiv R_4 \tag{17}$$

$$\rho_3 \equiv \rho_4 \tag{18}$$

$$K = C_{4u} R_4 \tag{19}$$

$$\dot{m} = 2\pi R_4 b_4 c_{4r} \rho_4 \tag{20}$$

The radius of the volute's central axis is then:

$$R_{sr} = R_3 + r \tag{21}$$

or if a circular collector is preceded by a vaned diffuser:

$$R_{sr} = R_4 + r \tag{22}$$

2.2. Constant-width volute (rectangular)

In this case $b(r) = b = idem$ (Fig. 7). Therefore equation (7) for the angle φ expressed in radians can be rewritten as:

$$\varphi = \frac{2\pi}{\dot{m}} K \rho_3 \int_{R_3}^{R_z} \frac{b(r)dR}{R} = \frac{2\pi}{\dot{m}} K \rho_3 b R|_{R_3}^{R_z} = \frac{2\pi}{\dot{m}} K \rho_3 b (ln\, R_z - ln\, R_3) = \frac{2\pi}{\dot{m}} K \rho_3 b\, lnR\, \frac{R_z}{R_3} \tag{23}$$

Therefore:

$$\frac{R_z}{R_3} = e^{\frac{\dot{m}\varphi}{2\pi K b \rho_3}} \tag{24}$$

and finally:

$$R_z = R_3 e^{\frac{\dot{m}\varphi}{2\pi K b \rho_3}} \tag{25}$$

In this case the curve that determines external contour of spiral diffuser is a logarithmic spiral.
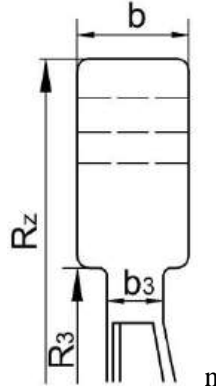

Fig. 7. Spiral collector with a rectangular cross-section.

According to equation (23):

$$\varphi = \frac{2\pi}{\dot{m}} K \rho_3 b \ln \frac{R_z}{R_3}$$

and using the formula (2) (or (1) and from the relation:

$$\dot{m} = 2\pi R_3 b_3 C_{3r} \rho_3 \tag{26}$$

or the relationship (20):

$$\dot{m} = 2\pi R_4 b_4 C_{4r} \rho_4$$

this gives:

$$\varphi = \frac{2\pi R_3 b C_{3u} \rho_3}{2\pi R_3 b_3 C_{3r} \rho_3} \ln \frac{R_z}{R_3} = \frac{C_{3u} b}{C_{3r} b_3} \ln \frac{R_z}{R_3} \tag{27}$$

but:

$$\ln x \cong 2.3 \log x \tag{28}$$

therefore:

$$\varphi \cong 2.3 \frac{C_{3u} b}{C_{3r} b_3} \log \frac{R_z}{R_3} \tag{29}$$

or in degrees:

$$\varphi^{\circ} = 57.3 \cdot \varphi \cong 132 \frac{C_{3u} b}{C_{3r} b_3} \log \frac{R_z}{R_3} \tag{30}$$

If a spiral volute is preceded by a vaned diffuser the following relations are received:

$$R_z = R_4 e^{\frac{\dot{m}\varphi}{2\pi K b \rho_4}} \tag{31}$$

where: $K = C_{4u}R_4, \dot{m} = 2\pi R_4 b_4 C_{4r}\rho_4$

and:

$$\varphi = \frac{2\pi}{\dot{m}} K \rho_4 b \ln\frac{R_z}{R_4} \tag{32}$$

$$\varphi = \frac{C_{4u}b}{C_{4r}b_4} \ln\frac{R_z}{R_4} \tag{33}$$

$$\varphi \cong 2{,}3 \frac{C_{4u}b}{C_{4r}b_4} \log\frac{R_z}{R_4} \tag{34}$$

$$\varphi^\circ = 132 \frac{C_{4u}b}{C_{4r}b_4} \log\frac{R_z}{R_4} \tag{35}$$

The equation (25) can be simplified by deployment of it in series, and then:

$$R_z = R_3 \left[1 + \frac{\dot{m}}{2\pi K b \rho_3}\varphi + \left(\frac{\dot{m}}{2\pi K b \rho_3}\right)^2 \frac{\varphi^2}{2} + \cdots \right] \tag{36}$$

and omitting expressions in the power factor greater than one (higher order negligible):

$$R_z = R_3 + R_3 \frac{\dot{m}}{2\pi K b \rho_3}\ \varphi \tag{37}$$

or taking into account formulas (2) and (26):

$$R_z = R_3 + R_3 \frac{C_{3r}b}{C_{3u}b_3}\ \varphi \tag{38}$$

then:

$$\varphi \cong \frac{R_z - R_3}{R_3} \frac{C_{3u}b}{C_{3r}b_3} \tag{39}$$

or expressed in degrees:

$$\varphi^\circ = 57.3\ \frac{R_z - R_3}{R_3} \frac{C_{3u}b}{C_{3r}b_3} \tag{40}$$

The equation (37) gives less accurate results and presents Archimedean spiral. The radius of the central axis of the rectangular cross-section volute is:

$$R_{sr} = R_3 + \frac{R_z - R_3}{2} = \frac{R_z + R_3}{2} \tag{41}$$

2.3. Square volute

For a volute with square cross-section (Fig. 8) the following relation can be written:

$$b = R_Z - R_3 \tag{42}$$

Because the angle φ is determined by the formula (7):

$$\varphi = \frac{2\pi}{\dot{m}} K\rho_3 \int_{R_3}^{R_z} \frac{b(r)dR}{R}$$

therefore after taking into account the relation $b(r) = b = idem$ the following relation – as for a rectangular volute – is obtained (23):

$$\varphi = \frac{2\pi}{\dot{m}} K\rho_3 b \ln\frac{R_z}{R_3}$$

And after using the formula (42):

$$\varphi = \frac{2\pi}{\dot{m}} K\rho_3 (R_z - R_3) \ln\frac{R_z}{R_3} \tag{43}$$

or in degrees, applying the relation for a rectangular volute (35):

$$\varphi° = 132 \frac{C_{3u}b}{C_{3r}b_3} \log\frac{R_z}{R_3}$$

therefore using the relation (42):

$$\varphi° = 132 \frac{C_{3u}(R_z - R_3)}{C_{3r}b_3} \log\frac{R_z}{R_3} \tag{44}$$
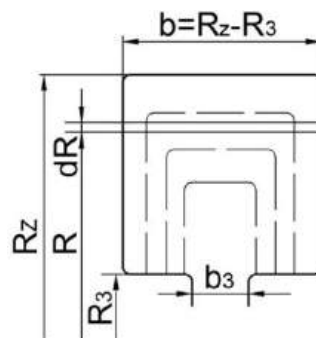

Fig. 8. Spiral collector with a square cross-section.

The volute passage width (height) $b = R_z - R_3$ – eq. (42) can be determined by integrating at the volute discharge (exit) cross-section ($b = b_{wyl} = b_5$). Assuming that in this cross-section on the radius of the volute spiral axis

$$R_{5sr} = R_3 + b/2 \tag{45}$$

the flowing airflow reaches the following velocity:

$$C_{5usr} = \frac{C_{3u}R_3}{R_{5sr}} \tag{46}$$

or generally:

$$C_u = \frac{C_{3u}R_3}{R} \tag{47}$$

while infinitesimal mass flow rate:

$$d\dot{m} = \rho_3 C_u b dR \tag{48}$$

therefore:

$$\dot{m} = \rho_3 \int_{R_3}^{R_z} C_u b dR = \rho_3 \int_{R_3}^{R_3+b} C_u b R_3 \frac{dR}{R} \tag{49}$$

then:

$$\dot{m} = \rho_3 b C_{3u} R_3 \ln \frac{R_3 + b}{R_3} \quad or \quad \dot{m} = K \rho_3 b \ln \frac{R_3 + b}{R_3} \tag{50}$$

This equation is solved using the method of successive approximations. The value of the left side of the equation is known and is written by the equation (26). The width or height of volute's passage with square cross-section can also be approximated. Taking into account, that in the spiral volute cross-section (5-5) in its axis, the flowing airflow velocity is determined by the relation (46), then after using this formula we receive:

$$C_{5usr} = \frac{C_{3u} R_3}{R_3 + \frac{b}{2}} \tag{51}$$

The mass airflow rate flowing through this cross-section (5-5) is accordingly ($\rho_{5sr} = \rho_3$):

$$\dot{m} = \dot{m}_5 = \rho_3 C_{5usr} F_5 \tag{52}$$

therefore:

$$\dot{m} = \rho_3 \frac{C_{3u} R_3}{R_3 + \frac{b}{2}} b^2 \tag{53}$$

On the other hand, it is known that mass flow rate is determined by the formula (26), then:

$$2\pi R_3 b_3 C_{3r} = \frac{C_{3u} R_3}{R_3 + \frac{b}{2}} b^2 \tag{54}$$

Solving the above quadratic equation with respect to „b" the following is obtained:

$$b = \frac{\pi}{2} b_3 \frac{C_{3r}}{C_{3u}} + \sqrt{\left(\frac{\pi b_3 c_{3r}}{2 c_{3u}}\right)^2 + \left(\frac{\pi b_3 c_{3r}}{c_{3u}}\right)} \tag{55}$$

Note: In case of a single jet volute in above relations it should be considered, that: $\dot{m} = \dot{m}$; $\varphi = 0 \dots 2\pi$; or $\varphi^° = 0 \dots 360°$, whereas for a double spiral diffuser: $\dot{m} = \frac{\dot{m}}{2}$; $\varphi = 0 \dots \pi$; or $\varphi^° = 0 \dots 180°$.

3. Constant mean velocity method

The second type of method for calculating the geometrical parameters of volutes is based on the assumption of the mean velocity flow value in the considered spiral diffuser cross-section (Ris, 1951; Yahya, 2012).

3.1. Trapezoidal or oval cross-section volute (pear-shaped)

By determining the volute cross-section corresponding to the angle φ expressed in radians by F_φ, then assuming mean airflow velocity value in this cross-section, for single-jet volute the following relation is obtained:

$$F_\varphi = \frac{\dot{m}_\varphi}{\rho_3 \cdot c_{sr}} \tag{56}$$

or:

$$F_\varphi = \frac{\dot{m}\varphi^\circ}{\rho_3 \cdot 360 \cdot c_{sr}} \tag{57}$$

while, for a double jet collector this formula can be written as:

$$F_\varphi = \frac{\dot{m}\varphi^\circ}{\rho_3 \cdot 180 \cdot c_{sr}} \tag{58}$$

Expressing the surface area of a collector in radial section by F_φ as function of given geometrical parameters i.e. $F_\varphi = f(b_3, \vartheta, h)$ – for the trapezoidal volute and $F_\varphi = f(b_3, \vartheta, h_c))$ – for the oval volute, the following h and h_c parameters respectively can be determined from the continuity equation (Fig. 9).
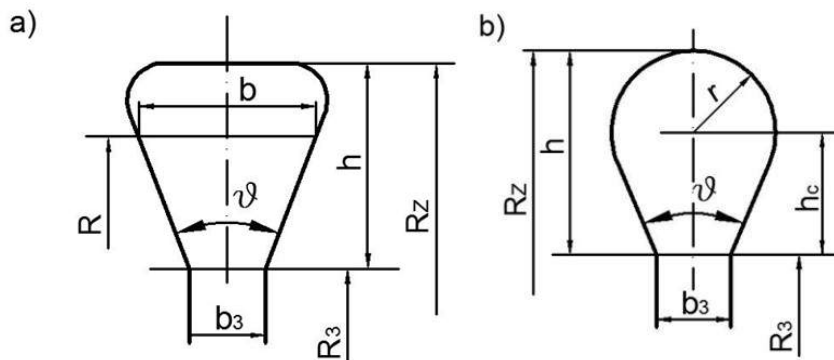

Fig. 9. Schematic designations in the trapezoidal (a) and oval (b) collector: h - the volute height, ϑ – the divergence angle of the lateral walls of the volute.

In case of trapezoidal scroll cross-section, the volute's height $h = R_z–R_3$, corresponding to the angle φ, is related to the radial section area F_φ by a quadratic equation:

$$F_\varphi = tg\frac{\vartheta}{2}h^2 + b_3 \cdot h \tag{59}$$

hence:

$$h = -\frac{b_3}{2\,tg\frac{\vartheta}{2}} + \sqrt{\left(\frac{b_3}{2\,tg\frac{\vartheta}{2}}\right)^2 + \frac{F_\varphi}{tg\frac{\vartheta}{2}}} \tag{60}$$

then, for a single-jet collector the following relation is obtained:

$$h = -\frac{b_3}{2\,tg\frac{\vartheta}{2}} + \sqrt{\left(\frac{b_3}{2\,tg\frac{\vartheta}{2}}\right)^2 + \frac{\dot{m}\varphi^\circ}{\rho_3 \cdot 360 \cdot c_{sr} \cdot tg\frac{\vartheta}{2}}} \tag{61}$$

or:

$$h = -K_1 + \sqrt{K_1^2 + \frac{K_2\,\varphi^\circ}{c_{sr}}} \tag{62}$$

where:

$$K_1 = \frac{b_3}{2\,tg\frac{\vartheta}{2}} \tag{63}$$

$$K_2 = \frac{\dot{m}}{\rho_3 \cdot 360 \cdot tg\frac{\vartheta}{2}} \tag{64}$$

The corrective coefficient $K_F = 1.05 \div 1.1$ (Ris, 1951), shall be inserted in order to take into consideration decreasing of volute's cross-section surface area, as a result of corners rounding, so then:

$$K_2 = \frac{\dot{m}K_F}{\rho_3 \cdot 360 \cdot tg\frac{\vartheta}{2}} \tag{65}$$

Width of the spiral diffuser with a trapezoid contour for any radius R value of cross-section can be determined by geometrical relation:

$$b = b_3 + 2(R - R_3)\,tg\frac{\vartheta}{2} \tag{66}$$

For an oval spiral diffuser (Fig. 9b) the distance value h_c if the center of the circle with radius r from inlet radius R_3, corresponding to the polar angle φ, is related to the cross-section of the volute passage F_φ by the following quadratic equation:

$$F_\varphi = \left(\frac{\pi}{2}tg^2\frac{\vartheta}{2} + tg\frac{\vartheta}{2}\right)h_c^2 + \left(\frac{\pi}{2}b_3\,tg\frac{\vartheta}{2} + b_3\right)h_c + \frac{\pi}{8}b_3^2 \tag{67}$$

After solving the above quadratic equation and transformations the following is obtained (Podobuiev & Selezniev, 1957):

$$h_c = -K_1 + \sqrt{\frac{K_1^2\,tg\frac{\vartheta}{2} + F_\varphi}{K_3}} \tag{68}$$

or, having regard to the relation F_φ for a single-jet volute, this gives:

$$h_c = -K_1 + \sqrt{\frac{K_1^2 + \frac{K_2'\varphi°}{c_{sr}}}{K_3}} \tag{69}$$

where:

$$K_1 = \frac{b_3}{2\,tg\frac{\vartheta}{2}} \tag{70}$$

$$K_2' = \frac{\dot{m}}{\rho_3 \cdot 360} \tag{71}$$

$$K_3 = \frac{\pi}{2}tg^2\frac{\vartheta}{2} + tg\frac{\vartheta}{2} \tag{72}$$

The other geometric parameters of the volute are determined by relations:

$$r = (h_c + K_1)\,tg\frac{\vartheta}{2} \tag{73}$$

$$h = h_c + r \tag{74}$$

$$R_z = R_3 + h \tag{75}$$

3.2. Circular cross-section volute

For any cross-section of a single-jet volute the section is:

$$F_\varphi = \frac{\pi D^2}{4} \tag{76}$$

then according to the formula (56):

$$\frac{\pi D^2}{4} = \frac{\dot{m}_\varphi}{\rho_3 \; c_{sr}} \tag{77}$$

hence, the volute diameter is:

$$D = 2\sqrt{\frac{\dot{m}_\varphi}{\pi \rho_3 \; c_{sr}}} \tag{78}$$

or according to the equation (57):

$$\frac{\pi D^2}{4} = \frac{\dot{m}\varphi^\circ}{\rho_3 \; c_{sr} 360} \tag{79}$$

whence:

$$D = \sqrt{\frac{\dot{m}\varphi^\circ}{90 \pi \rho_3 \; c_{sr}}} \tag{80}$$

And for a double jet volute according to the relation (58):

$$D = \sqrt{\frac{\dot{m}\varphi^\circ}{45 \pi \rho_3 \; c_{sr}}} \tag{81}$$

In case of a volute installed at the vaneless diffuser exit a constant value of the average airflow velocity can be assumed along the whole scroll $c_{sr} = (0.7 \div 0.8)c_3$. The divergence angle of the lateral walls recommended for trapezoidal and oval collector is between $\vartheta = 45 \div 60°$ (Podobuiev & Selezniev, 1976; Ris, 1951).

4. Flow parameters at the volute exit

The stagnation pressure loss at the volute depends on placing the spiral diffuser in the compresor passage, therefore depending on the design type, it is determined from the following relations:
- for a volute installed at the impeller exit (compressor without vaneless and vaned diffuser):

$$\Delta p_{2,5}^* = \xi_{sp} \frac{\rho_2 \cdot c_2^2}{2} \tag{82}$$

- for a volute preceded by a vaneless diffuser:

$$\Delta p_{3,5}^* = \xi_{sp} \frac{\rho_3 \cdot c_3^2}{2} \tag{83}$$

- for a volute installed at a vaned diffuser exit:

$$\Delta p_{4,5}^* = \xi_{sp} \frac{\rho_4 \cdot c_4^2}{2} \qquad\qquad (84)$$

The issue of determining the total pressure loss coefficient in the spiral diffuser ξ_{sp}, experimentally determined, was the subject of consideration only in a few papers (Abduraszilow et al., 1974; Bajle, 1981; Biełousov et al., 2003; Eckert, 1959; Japikse, 1990; Tuliszka, 1976; Walczak, 1999; Witkowski, 2004). However, this issue can avoided, or at least the uncertainty reduced, by using numerical simulations to estimate losses for the considered configuration.

According to Abduraszilow et al. (1974) the total pressure loss coefficient value in a volute (Fig. 10) depends on the location of a spiral diffuser in a compressor passage and on the absolute velocity angle of α (α_2, α_3) at collector inlet. Due to high values of the total pressure loss coefficient in the centrifugal compressors of turbine engines, the volute is not installed directly behind the rotor exit.

The most complex analysis of total pressure loss coefficient changes in a spiral diffuser as a function of the angle of absolute velocity of stream outflow from vaneless diffuser α_3 was introduced in the paper by Walczak (1999) – Fig.11. This angle value is related with compressor's operating point from surge mass flow rate ($\dot{m}_{min}$) to maximum mass flow rate ($\dot{m}_{max}$).
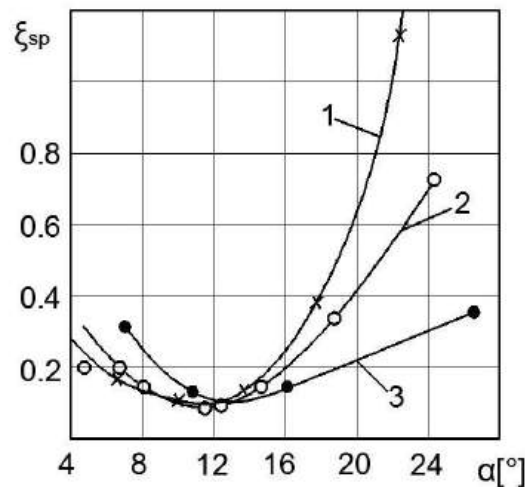

Fig. 10. Changes of the total pressure loss coefficient in the collector vs. angle of absolute velocity at the collector inlet. 1, 2 - the volute mounted at the outlet of the impeller , 3 - the volute preceded by a vaneless diffuser.

The analysis shown in the Fig. 10 and Fig. 11 show that discrepancies between the results of the research of individual authors are considerable. In order to avoid doubts regarding to the reliability of the research results, it is recommended to conduct extensive additional experimental researches based on measurements of pressure, temperature and velocity at volute's inlet and exit cross-section, avoiding completing the researches with velocity calculations in control cross-sections.
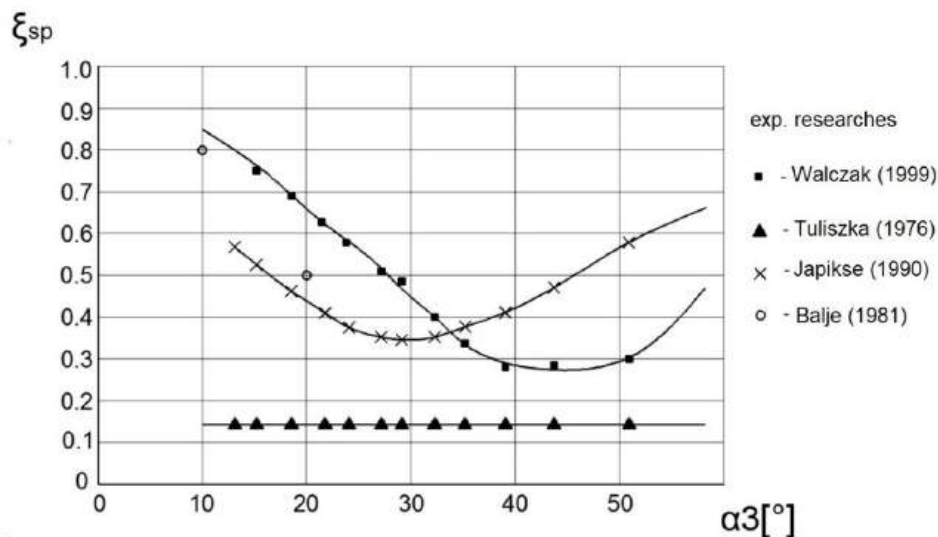

Fig. 11. The variation of the total pressure loss coefficient in the collector vs. angle of absolute velocity α_3 at the collector inlet (Walczak, 1999).

According to Tuliszka (1976) the total pressure loss coefficient in a spiral diffuser has a constant value regardless of the angle α_3, and its value is definitely lower. Similar recommendations are given in the paper by Biełousov et al. (2003) by, while ($\xi_{sp}=0.06\div0.15$) and in the monograph by Witkowski (2004) (where $\xi_{sp}=0.22$).

- Stagnation pressure p_5^* at the volute exit cross-section (5-5) is defined according to the design of a centrifugal compressor. Thus, in the case of collector placed at impeller's exit and behind a vaneless diffuser the following is obtained:

$$p_5^* = p_2^* - \Delta p_{2,5}^* \tag{85}$$

$$p_5^* = p_3^* - \Delta p_{3,5}^* \tag{86}$$

while, in case of the collector preceded by a vaned diffuser:

$$p_5^* = p_4^* - \Delta p_{4,5}^* \tag{87}$$

- The stagnation temperature at the exit cross-section is:

$$T_5^* = T_2^* = T_3^* = T_4^* \tag{88}$$

- The absolute airflow velocity at the exit cross-section of a volute preceded by a vaneless diffuser is given by the equation (46):

$$c_5 = c_{5usr} = \frac{c_{3u} \cdot R_3}{R_{sr5}} \tag{}$$

- The critical speed of sound:

$$a_{kr5} = \sqrt{\frac{2 \cdot k \cdot R}{k+1} T_5^*} \tag{89}$$

- Laval number of the absolute velocity for stream outflow from the volute:

$$\lambda_5 = \frac{c_5}{a_{kr5}} \tag{90}$$

- Gasdynamics function of pressure:

$$\Pi(\lambda_5) = (1 - \frac{k-1}{k+1}\lambda_5^2)^{\frac{k}{k-1}} \tag{91}$$

- Static pressure:

$$p_5 \equiv p_{\varphi=2\pi} = \Pi(\lambda_5) \cdot p_5^* \tag{92}$$

- Static temperature:

$$T_5 \equiv T_{\varphi=2\pi} = T_3^* - \frac{c_5^2}{\frac{2 \cdot k \cdot R}{k+1}} \tag{93}$$

or:

$$T_5 = \tau(\lambda_5) \cdot T_5^* \tag{94}$$

where, gasdynamics function of temperature

$$\tau(\lambda_5) = 1 - \frac{k-1}{k+1}\lambda_5^2 \tag{95}$$

Friction work losses in a volute preceded by vaneless diffuser

$$l_{r3,5} = \xi_{sp}\frac{c_3^2}{2} \tag{96}$$

- The polytrophic exponent of the compression in a volute $n \equiv n_{3,5}$ is determined from the relation (First Law of Thermodynamics):

$$l_{r3,5} = \left(\frac{k}{k-1} - \frac{n}{n-1}\right)R(T_5 - T_3) \tag{97}$$

or from the polytrophic process equation:

$$\frac{n}{n-1} = \frac{ln\frac{p_5}{p_3}}{ln\frac{T_5}{T_3}} \tag{98}$$

usually: n=1.9÷2.0

- The single jet volute's exit radius – for $\varphi = 2\pi$ from the equation (11) results from:

$$r_5 = \frac{\dot{m}}{2\pi \cdot K \cdot \rho_3} + \sqrt{\frac{R_3 \cdot \dot{m}}{\pi \cdot K \cdot \rho_3}} \tag{99}$$

- The mean volute exit radius:

$$R_{sr5} = R_3 + r_5 \tag{100}$$

Checking the value of the single jet circular volute exit radius could be performed in the following sequence:

- Static pressure:

$$p_5 = p_3 \left(\frac{T_5}{T_3}\right)^{\frac{n}{n-1}} \tag{101}$$

- Ratio of stagnation pressures at the collector:

$$\sigma_{3,5} = 1 - \xi_{sp}\frac{k \cdot \lambda_3^2}{k+1}(1 - \frac{k-1}{k+1}\lambda_3^2)^{\frac{k}{k-1}} \tag{102}$$

- Stagnation pressure:

$$p_5^* = \sigma_{3,5} \cdot p_3^* \tag{103}$$

- Mass flux density gasdynamics function:

$$q(\lambda_5) = \lambda_5(1 - \frac{k-1}{k+1}\lambda_5^2)^{\frac{k}{k-1}}(\frac{k+1}{2})^{\frac{k}{k-1}} \tag{104}$$

- Surface area of the volute exit:

$$F_5 = \frac{\dot{m}\sqrt{T_5^*}}{s \cdot p_5^* \cdot q(\lambda_5)} \tag{105}$$

where constant in the continuity equation for air: $s = 0,0404(\frac{J}{kgK})^{-0.5}$

- Single jet volute exit radius:

$$r_5 = \sqrt{\frac{F_5}{\pi}} \qquad (106)$$

5. Discussion

The considerations presented in this paper regarding selection of cross section areas $F = F(\varphi)$ for typical scroll shapes were conducted on the basis of the inviscid medium model – equation (5). However the losses occurring in the volute cause corresponding pressure decreases. According to Eckert (1959) it is recommended to apply additional delay of the medium, that is additional increase of radial section F, so that in this manner take into consideration the influence of friction and separation in the volute tongue area (from $\varphi = 0 \; to \; \varphi = \varphi_0$).

However, there is no uniform view on the method of volute design presented above, as e.g. studies by Reunanen (2001) on spiral diffusers show that the volutes designed on the basis of inviscid medium model operate in the best way. Therefore it seems to be a little safer to adopt collector design principle on the basis of the equation (7) and not to introduce corrections resulting from pressure losses, although the method of B. Eckert is also allowable and appropriate. It is recommended to compile calculated volute parameters in the aggregate chart.

The flow through spiral diffuser can be treated to some extent as a flow through curved passage. As with any type of flow as in this passage, secondary flows arise in it (induced, knee flow), marked schematically in the Fig. 12. The flow through these diffusers was examined experimentally by Krantz using a fluid as a working medium. As a result of these researches it was stated, that particle tracks are not spiral, but helical. This causes, that the path by which working medium is flowing is several times greater than volute axis distance (Hariharan & Govardhan, 2015; Tuliszka, 1976).
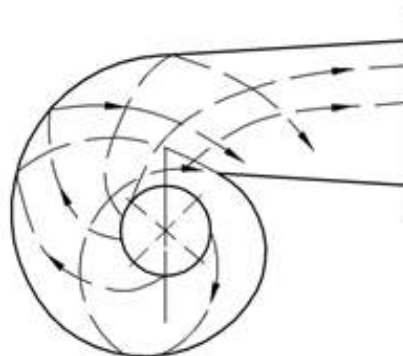

Fig. 12. Medium flow through a collector (Cumpsty, 1989).

In case of symmetrical collectors the introduction of a symmetrical flow leaving a vaneless or vaned diffuser, so heading toward the center line, intensifies the secondary flow and simultaneously increases losses. If the stream outflowing from the diffuser is introduced tangentially to the volute – Fig. 13. – then with unilaterally formed spiral diffuser, the double vortex can be reduced to single vortex, which causes smaller losses (Cumpsty, 1989).

Centrifugal compressor stage characteristics with three different volutes formed symmetrically are shown in the Figure 14 (symmetrical spiral diffuser a and b) and asymmetrical (volute c). Escher-Wyss researches show that volutes with asymmetrical stream inlet operates with lower losses, therefore this type of design, if there are no other design or technological considerations, is recommended for centrifugal compressors.

The problem of asymmetrical delivery of working fluid to the collector was subject of few theoretical and experimental researches. According to Reunanen (2001) the shape of volute passage cross-section satisfying the condition of symmetrical and asymmetrical working fluid delivery are equivalent in terms of operation of the centrifugal compressor. It should be noticed, that asymmetrical volute in case of rectangular or square contour (Fig. 15) does not create additional designing problems, where as in a circular-shaped diffuser, asymmetrical working fluid delivery causes creation of threshold of height Δ – Fig. 15.b (Cumpsty, 1989; Pan et al., 1999).
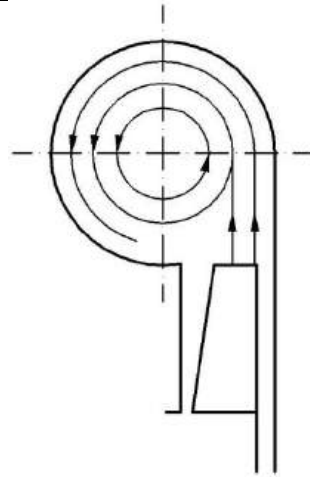
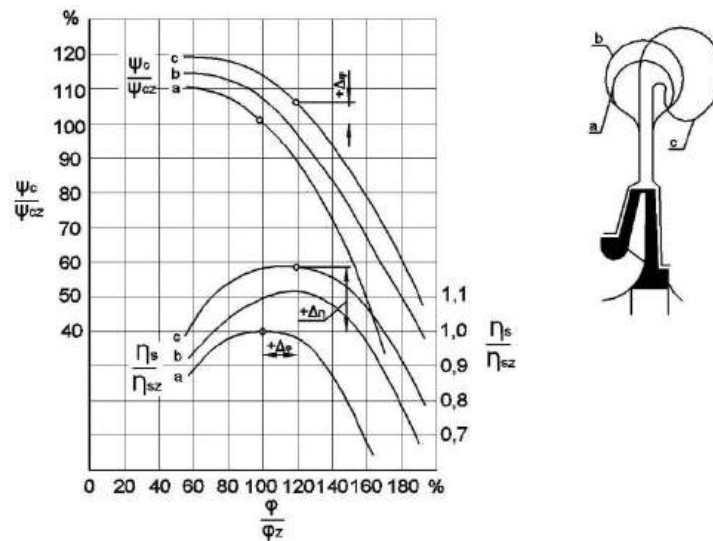**Fig. 13.** The stream lines in the cross-section of the asymmetrical collector (Tuliszka, 1976).

Fig. 14. Effect of the volute shape on characteristics and efficiency of the radial compressor stage (test results of Escher-Wyss Zurich); ψ_c - the pressure rise coefficient, η_s - isentropic efficiency, φ – flow coefficient (subscript z refers to the nominal operating conditions) (Eckert, 1959).
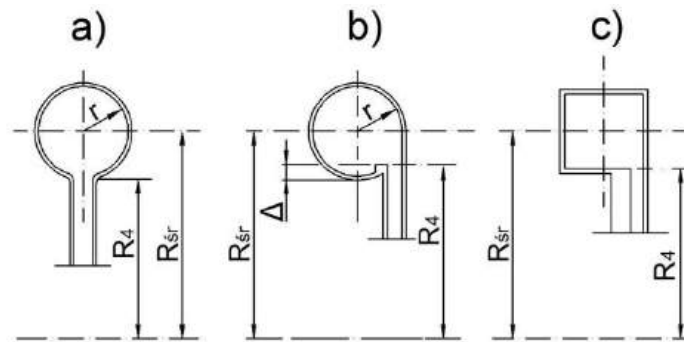
Fig. 15. Designation of geometrical parameters of the volute with a circular contour: a) symmetric, b) asymmetric and c) asymmetric with a rectangular section.

The radius from impeller axis to the centroid of the symmetrical volute with a circular contour, preceded by vaned diffuser in accordance with formula (14) is $R_{sr} = R_4 + r$, therefore the difference:

$$R_{sr} - r = R_4 \tag{107}$$

has a constant value.

In case of asymmetrical spiral diffuser with a circular cross-section the above equation is not fulfilled, because the threshold height is:

$$\Delta = R_4 - (R_{sr} - r) \tag{108}$$

whereas according to research conducted by Pan et al. (1999) the difference $(R_{śr} - r)$ is linear function of angle $\varphi°$ expressed in degrees, i.e.:

$$(R_{sr} - r) = a + b\varphi^o \tag{109}$$

where constants: a = 0.0823 m, b = 2.33 10^{-5} m/^{0}.

The design of a compressor with specific technical conditions can be divided into three stages. The first stage, covered by the conceptual design, includes determining the number of stages and their load, appropriate selection of speed at a set radius in individual stages, determining the flow channel in a meridional cross-section, assessing the density and profiling of the compressor rim. Many processes cannot be explained using one- and two-dimensional models, but such models, together with the cylindrical flow model, allow obtaining flow equations that, despite numerous simplifications, provide sufficient accuracy for the initial quantitative analysis of flows in aircraft turbomachines. These methods are commonly used to determine the initial geometry of the flow channel of turbomachines at the stage of design assumptions. The second stage, which is the preliminary design of the assembly, includes a more accurate calculation of the flow kinematics and the parameters of the thermodynamic state in the gaps between the rims. In these calculations, an axisymmetric model of gas flow through the turbomachine rims is usually assumed. The third stage, covered by the technical design, includes a detailed quantitative analysis of the flow of the medium through the individual rims of the fluid-flow machine stages. In the calculations for the technical design, it is recommended to use two-dimensional and three-dimensional flow models of the viscous or inviscid medium. The Navier-Stokes or Euler equations are used for quantitative analysis. It is advisable to analyse both a two- and three-dimensional flow models and to use them in the order of increasing complexity.

6. Summary

Although experimental studies of spirals of different geometry were performed as early as the 1940s, these studies were limited due to high production costs. In recent years, numerical simulations have provided significant progress in the analysis of spirals of different designs. An example is the work of Hottois et al. (2023), which presents an adjoint-based optimization of a volute of the SRV2-O compressor based on computational fluid dynamics modeling. Due to the high instrumentation costs, experimental analysis of volute is the domain of large industrial companies, which do not provide research results due to legal regulations. For this reason, the total number of studies in the open literature concerning the volute geometry is small (Heinrich & Schwarze, 2016). The shape optimization of radial compressors mainly focuses on improving the impeller. However, as indicated by Hottois et al. (2023) the volute plays a key role in the overall performance of the compressor.

The geometrical parameters of the volute should be properly selected to ensure the correct operation of the diffuser. The constant mean velocity design and free vortex design presented in this work are recommended for use in the conceptual design of a compressors. The selection of the cross-section of typical scroll shapes presented in this article was based on the inviscid medium model. A detailed analysis of geometrical parameters of different types of collectors and proposed method of determining air stream parameters at volume outlet may be helpful for compressor designers.

References

Abduraszilow, S. A. et al. (1974). *Pumps and compressors*. Niedra (in Russian).

Antas, S. (2014). Pipe diffuser for radial and axial-centrifugal compressor. *International Journal of Turbo & Jet-Engines*, 31(1), 29-36. https://doi.org/10.1515/tjj-2013-0031

Antas, S. (2019). Exhaust system for radial and axial-centrifugal compressos with pipe diffuser. *International Journal of Turbo & Jet-Engines*, *36*(3), 297-304. https://doi.org/10.1515/tjj-2016-0068

Antas, S. (2023). *Theory of turbomachines for aviation turbine engines*. Publishing House of Rzeszów University of Technology (in Polish).

Aungier, R. H. (2000). *Centrifugal compressors*. ASME Press.

Balje, O. E. (1981). *Turbomachines. A guide to design selection and theory*. Wiley-Interscience.

Baloni, B. D., & Channiwala, S. A. (2013). Design and analysis of volute casing: A review. In *Proceedings of ASME Turbo Expo 2012: Turbine Technical Conference and Exposition*, paper no. GT 2012-68056 (pp. 657-664). https://doi.org/10.1115/GT2012-68056

Baloni, B. D., Channiwala, S. A., & Mayavanshi, V. K. (2012). Pressure recovery and loss coefficient variations in the two different centrifugal blower volute designs. *Applied Energy*, *90*, 335-343. https://doi.org/10.1016/j.apenergy.2011.02.016

Biełousov, A. N., Musatkin, N. F., & Radko, W. M. (2003). *Theory and calculations of aircraft turbo-machines*. Samarski Gosudarstvenni Aerokosmiceski Institut (in Russian).

Cumpsty, N. A. (1989). *Compressor aerodynamics*. Longman Scientifics and Technical.

Dmitriewskij, W. I. (1960). *Gasdynamics calculations and design of radial compressor stage*. Technical report No. 137. CIAM (in Russian).

Eckert, B. (1959). *Axial and radial compressors. Application, theory, calculation*. PWT (in Polish).

Hariharan, C., & Govardhan, M. (2015). Effect of inlet clearance on the aerodynamic performance of centrifugal blower. *International Journal of Turbo & Jet-Engines*, *33*, 215-228. https://doi.org/10.1515/tjj-2015-0026

Heinrich, M., & Schwarze, R. (2016). Genetic algorithm optimization of the volute shape of a centrifugal compressor. International Journal of Rotating Machinery, Article 4849025. https://doi.org/10.1155/2016/4849025

Hottois, R., Châtel, A., & Verstraete, T. (2023). Adjoint-based design optimization of a volute for a radial compressor. *International Journal of Turbomachinery Propulsion and Power*, *8*(4), Article 41. https://doi.org/10.3390/ijtpp8040041

Japikse, D. (1990). *Centrifugal compressor design and performance*. Concepts ETI Inc. Norwich, Vermont, Course held at Borsing GmbH Berlin.

Japikse, D. (1996). *Centrifugal compressor design and performance*. Concepts ETI Inc.

Kholscevnikov, K. V. (1970). *Theory and calculations of aircraft turbo-machines*. Masinostrostrojenije (in Russian).

Pan, D., Whitfield, A., & Wilson, M. (1999). Design considerations for the volutes of centrifugal fans and compressors. *Proceedings of the Institution of Mechanical Engineers, Part C: Journal of Mechanical Engineering Science, 213*(4), 401-410. https://doi.org/10.1243/0954406991522356

Podobuiev, J. S., & Selezniev, K. P. (1957) *Theory and calculations of axial and radial compressors*. Maszgiz (in Russian).

Reunanen, A. (2001). Experimental and numerical analysis of different volutes in a centrifugal compressor [D.Sc. Thesis, Lappeemranta University of Technology].

Ris, W. F. (1951). *Radial compressors*. Maszgiz (in Russian).

Tuliszka, E. (1976). *Compressors, blowers and fans*. WNT (in Polish).

Van den Braembusshe, R. A., & Hände B. M. (1990). Experimental and theoretical study of the swirling flow in centrifugal compressor volutes. *Journal of Turbomachinery*, *112*(1), 38-43. https://doi.org/10.1115/1.2927418

Walczak, J. (1999). *Radial compressors and fans. Theory, an investigations and optimization of compressor stage*. Publishing House of Poznan Society of Friends for Sciences (in Polish).

Wen, X., Mao, Y., Yang, X., & Qi, D. (2016). Design method for the volute profile of a squirrel cage fan with space limitation. *Journal of Turbomachinery*, *138*(8), Article 081001. https://doi.org/10.1115/1.4032537

Witkowski, A. (2004). *Rotary compressors. Theory, design, exploitation*. Publishing House of Silesian University of Technology (in Polish).

Yahya, S. M. (2012). *Turbines compressors and fans* (4th Ed.). Tata McGraw Hill Education Private Limited.

Metody Obliczeniowe Parametrów Spirali Stosowane w Projektowaniu Koncepcyjnym Sprężarek Promieniowych i Osiowo-Odśrodkowych

Streszczenie

W wielu projektach jednostopniowych sprężarek promieniowych i osiowo-odśrodkowych silników lotniczych turbośmigłowych i turbowałowych, odpowiednio uformowany kolektor umieszczony za bezłopatkowym lub łopatkowym dyfuzorem promieniowym, jest stosowany do zmniejszenia prędkości i zwiększenia ciśnienia statycznego strumienia powietrza. Dyfuzor spiralny jest jednym z głównych typów dyfuzorów. Spirala to kanał o zmiennym przekroju poprzecznym, który stopniowo rozszerza się w kierunku obrotu wirnika i obejmuje poprzedzający go dyfuzor z cylindrycznym otworem wlotowym. Jego parametry geometryczne powinny być odpowiednio dobrane, tak aby zapewnić prawidłową pracę spirali. W artykule przedstawiono dwie główne metody obliczania parametrów geometrycznych dyfuzora spiralnego: projektowanie swobodnego wiru (zasada stałego momentu pędu) i projektowanie według stałej średniej prędkości. Wymienione meto-

dy (zalecane do stosowania w projektowaniu koncepcyjnym sprężarki) opierają się na równaniu energii - równaniu energii przepływu ustalonego, równaniu ciągłości, pierwszej zasadzie termodynamiki, równaniu momentu pędu Eulera, funkcjach dynamiki gazów i definicjach stosowanych w teorii maszyn wirnikowych. Przeprowadzono szczegółową analizę parametrów geometrycznych różnych typów kolektorów. W artykule przedstawiono również przegląd wyników badań eksperymentalnych współczynnika strat ciśnienia całkowitego w spirali oraz zaproponowano metodę określania parametrów strumienia powietrza na wylocie spirali.

Słowa kluczowe: silnik turbinowy, sprężarka, kolektor

Original Research

The Effect of the Drawing Die Radius in the Bending Under Tension Test on the Frictional Behaviour of AISI 430 Steel and AW-1100 Aluminium Alloy Sheets

Eduarda Soares Oliveira [iD], **Juliana Rodrigues Damasceno** [iD], **Almir Silva Neto** [iD],
Erriston Campos Amaral [iD], **Karina Aparecida Martins Barcelos Gonçalves** [iD],
Valmir Dias Luiz * [iD]

Department of Metallurgy and Chemistry, Centro Federal de Educação Tecnológica de Minas Gerais, R. 19 de Novembro, 121, Centro Norte, Timóteo 35180-008, MG, Brazil; eduardaoliveiraduda1307@gmail.com (E.S. Oliveira), julianarodriguesdamasceno963@gmail.com (J.R.D. Damasceno), almir.sneto@cefetmg.br (A.S. Neto), erriston.campos@cefetmg.br (E.C. Amaral), karinabarcelos@cefetmg.br (K.A.M.B. Gonçalves)

* Correspondence: valmir@cefetmg.br

Abstract

Friction is an unfavourable phenomenon in sheet metal forming processes because it increases the forming force, reduces the surface quality of the drawpieces and affects the increased wear of the forming tools. This article presents the results of experimental studies on friction occurring due to the drawing die radius. The test materials used were 0.8-mm-thick strip samples made of AISI 430 steel and AW-1100 aluminium alloy sheets. A special bending under tension friction-test simulator was used to carry out the tests. Countersamples (pins) with different radii in the range of 1.5 mm to 13.5 mm were used. The tests were carried out at room temperature under mineral-based oil lubrication conditions. The friction tests were supplemented by determining the hardness and measuring the surface roughness (parameters Ra, Rq and Rt) of the samples. Based on the results, it was found that the coefficient of friction increased with a decrease in the bending pin radius, however, this behaviour changed above a critical radius (4.5 mm), after which the coefficient of friction increased with an increase in the pin radius. Furthermore, the AW-1100 aluminium alloy strip had a higher coefficient of friction than the AISI 430 steel strip.

Keywords: AW-1100 aluminium alloy, AISI 430 steel, coefficient of friction, bending under tension test, sheet metal forming

1. Introduction

Deep drawing is one of the most widely used manufacturing processes in sheet metal forming, making it is possible to manufacture products with very complex geometry in contrast to other processes, such as machining and casting. During the deep drawing process, a flat sheet called a blank is plastically deformed to achieve its final shape (Pereira et al., 2024). However, this deformation is not uniform and the surface of the sheet is subject to the occurrence of phenomena caused by friction and wear, such as scratches, debris, cracks, delamination and plastic deformation of the asperities (Arinbjarnar & Nielsen, 2023). One way to reduce the unfavourable impact of friction is to use lubricants in liquid, gaseous or solid forms (Semiatin, 2006). Traditionally, petroleum-based lubricants are used in the metal forming industry. However, in the last decade there has been an interest in edible and non-edible green oils (Carcel et al., 2005; Więckowski et al., 2020). The use of environmentally friendly lubricants with a high degree of biodegradability is consistent with the concept of sustainable industry (Antonicelli et al., 2024). Efficient lubrication is necessary to mitigate the deleterious effects of friction and wear. Current literature on this subject argues that friction-related aspects are of great concern, as they have a considerable influence on productivity, product quality and die wear, because during material processing, friction and lubrication are influenced by many factors, such as sheet
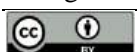
properties, temperature, surface finish, contact pressure, sliding speed, lubricant characteristics, die radius, among others (Luiz et al., 2023; Trzepieciński & Lemu, 2020). The main parameters influencing the physico-mechanical phenomena in the contact zone in sheet metal forming are shown in Fig. 1.
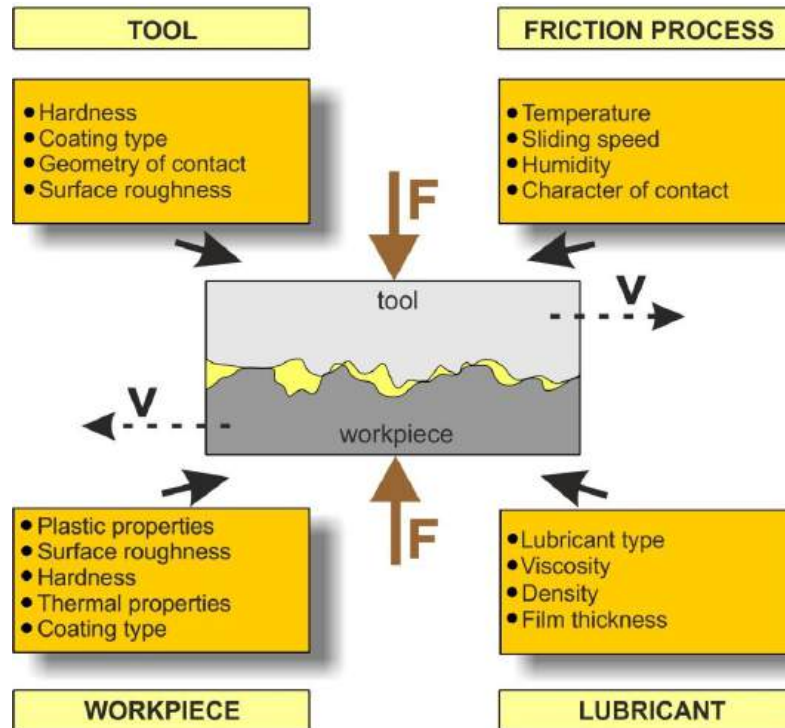

Fig. 1. The main elements of the tribological system in sheet metal forming.

Due to the complexity of the friction phenomenon in deep drawing processes, many tribological tests have been developed that reproduce friction in specific areas of the stamping tool in sheet metal forming. In addition to the commonly known strip drawing test, the bending under tension (BUT) test simulates friction conditions on the drawing die radius. In recent years, many scientists have been extending the knowledge about the influence of the tool radius, tool preheat temperature and sliding speed on the drawing die radius on the force parameters of the forming process, sheet metal formability and surface quality of the drawpieces. Andreasen et al. (2006) developed a sensitive torque transducer in which friction around the tool radius can be directly measured. The effect of the drawing speed on the tribological performance of AISI 316 stainless steel was studied. It was found that increasing the drawing speed from 10 mm/s to 50 mm/s significantly reduced friction stress. Ayllón et al. (2017) used the BUT test to model material deformation during the single-point incremental forming (SPIF) process of Ti-6Al-4V (Grade 5) titanium alloy. Both experimental and finite element-based approaches reproduced a realistic situation from the point of view of the lubrication regime occurring in SPIF. Vega et al. (2017) investigated ammonium-based protic ionic liquids as lubricant fluids for sheet metal forming. They found that protic ionic liquids showed a performance similar to that of the mixed lubrication regime. Folle and Schaeffer (2016) proposed a method for measuring the contact pressure in the BUT test using a pressure sensitive film. The results revealed that the area of contact between the sheet and the pin will always be smaller than the area calculated geometrically. Similar results were obtained by Kim et al. (2004) and Pereira et al. (2009). Coubrough et al. (2002) evaluated the contact pressure using a film of piezoelectric material in the BUT test. The change in the electric current voltage was proportional to the pressure value on the pin. Ceron et al. (2014) proposed the tribometer for analysing the effect of temperature on the frictional behaviour of DP800 steel in the BUT test. It was concluded that the proposed methodology can effectively predict the interface temperature in the test tool.

In recent years, there has been an increasing application of stainless steel and aluminium alloys in situations where corrosion resistance and weight reduction are desired. However, friction between the sheet metal and the die during stamping has also had a major impact on the formability of these materials (Gao et al., 2024). Although the influence of contact pressure and sliding speed on the coefficient of friction (CoF) has been intensively investigated, the study of the influence of the die geometry in terms of curvature is limited (Evin et al., 2014). Some authors (Dilmec & Arap, 2016; Kim et al., 2012; Zhao et al., 2021) have reported different coefficients of friction between flat and curved surfac-

es, but have not analysed the causes of this behaviour in depth. For this, several tribological tests have been used to simulate friction phenomena in specific regions of stamped parts, for example, the BUT test, which simulates the contact region of the deep drawing die radius. In this region, the mutual effect of the bending and stretching forces dominates the tribocontact (Luiz et al., 2023; Luiz & Rodrigues, 2022). Therefore, this study aims to investigate the influence of the radius of the stamping die on the tribological behaviour of AISI 430 steel and AW-1100 aluminium alloy sheets, both of 0.8 mm thickness. Eight different bending pin radii (1.5–13.5 mm) were used in the BUT test, the coefficient of friction was determined and the experimental results were compared with each other. In addition, variations in the hardness of the sheets and the roughness parameters (Ra, Rq and Rt) were also analysed.

2. Materials and methods

2.1. Test material

In this study, 0.8-mm-thick metal strips with a width of 25 mm and a length of 770 mm, cut from AISI 430 ferritic stainless steel and AW-1100 aluminium alloy sheets along the rolling direction, were used as test materials. The test materials can be strengthened by the work hardening phenomenon. Both materials have high electrical conductivity, thermal conductivity, corrosion resistance, and workability. Uses include decorative panels and household utensils. The quality requirements for the chemical composition of these metal sheets are presented in Tables 1 and 2.

The basic mechanical properties of the metal strips (Table 3) were determined using a universal tensile testing machine (Emic, model DL30000 with capacity of up to 300 kN) at room temperature, according to the American Society for Testing and Materials (2021) standard. Flat dog-bone specimens with dimensions as specified in the American Society for Testing and Materials (2021) standard, with 50 mm gauge length, were used in the tests.

Table 1. Chemical composition of AISI 430 steel sheets (wt.%).

C	Ni	Si	Mn	Cr	S	P	Fe
≤0.12	≤0.75	≤1.0	≤1.0	16-18	≤0.03	≤0.04	balance

Table 2. Chemical composition of AW-1100 aluminium alloy sheets (wt.%).

Mn	Zn	Si+Fe	Cu	Other	Al
0.05	0.10	0.95	0.05-0.2	0.15	balance

Table 3. Mechanical properties of test materials.

Material	Yield stress $R_{p0.2}$, MPa	Ultimate tensile strength R_m, MPa	Elongation after fracture A_{50}, %
AISI 430	316	465	33
AW-1100	93	115	5

The hardness of the metal strips in the as-received state was measured using a Vickers micro-hardness meter (Shimadzu, model HMV-2T), with a test load of 1.96 N for a time of 15 s. The average hardness found for the AISI 430 steel and AW-1100 aluminium sheets was 120.6 and 44.1 HV, respectively. Furthermore, with the aid of a portable surface roughness tester (Tesa Rugosurf 20), the basic height parameters of the geometric structure of the strip surfaces were determined: the arithmetic mean roughness Ra, the root-mean-square roughness Rq and the total height of the roughness profile Rt. The surface roughness parameters were determined according to the International Organization for Standardization (2021) standard. The average values found for these parameters on the surface of the AISI 430 steel strip, in the as-received state, were 0.09, 0.15 and 1.08 μm, respectively. For the AW-1100 aluminium sheet, these were 0.76, 0.93 and 5.70 μm, respectively. The bending pins (counter-samples) were machined from VND steel (DIN: 1.2510) and heat treated (quenching at 800°C + oil cooling + 2 consecutive tempering passes at 260°C) to increase wear resistance. VND steel is typically used to produce woodworking tools, cutting tools, measuring instruments, and guide pins as well as tools and dies in general.

The quality requirements for the chemical composition of VBD steel are presented in Table 3. The requirements for the basic mechanical properties are equal to (ABNT VND, 2024): $R_{p0.2} \geq 681$ MPa, $R_m \geq 779$ MPa, $A = 32\%$. After being treated and polished, the hardness was on average 760 HV and the roughness parameters were Ra = 0.27 μm, Rq = 0.36 μm and Rt = 2.28 μm, respectively.

Table 3. Chemical composition of VND steel (wt.%), prepared on the basis of ABNT VND (2024).

Mn	S (min.)	V (max.)	Si	W	C	Fe
1.25	0.5	0.12	0.25	0.50	0.95	balance

2.2. Bending under tension test

The friction simulation test used in this study was the BUT test. This test is capable of simulating the mechanics of plastic deformation and the friction phenomenon of a metal sheet sliding under the radius of the tool in deep drawing processes (Fig. 2a). It consists of bending and sliding a metal strip with a certain thickness t over a pin with a predetermined radius R (Fig. 2b). During the kinematics of the movement, a front tension force F_1 is applied to one end of the metal strip, while the other and is subjected to a back tension force F_2. Figs. 3a and 3b show the friction test stand, as well as the tool holder (die) and some of the bending pins used during the tests, respectively.
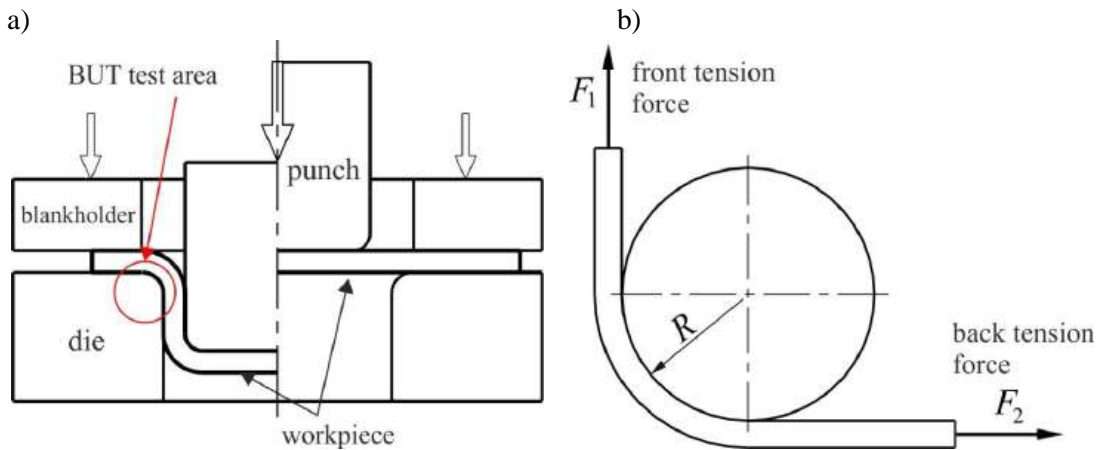
a)   b)

Fig. 2. a) BUT test area and b) the forces acting on the strip sample in the BUT test.

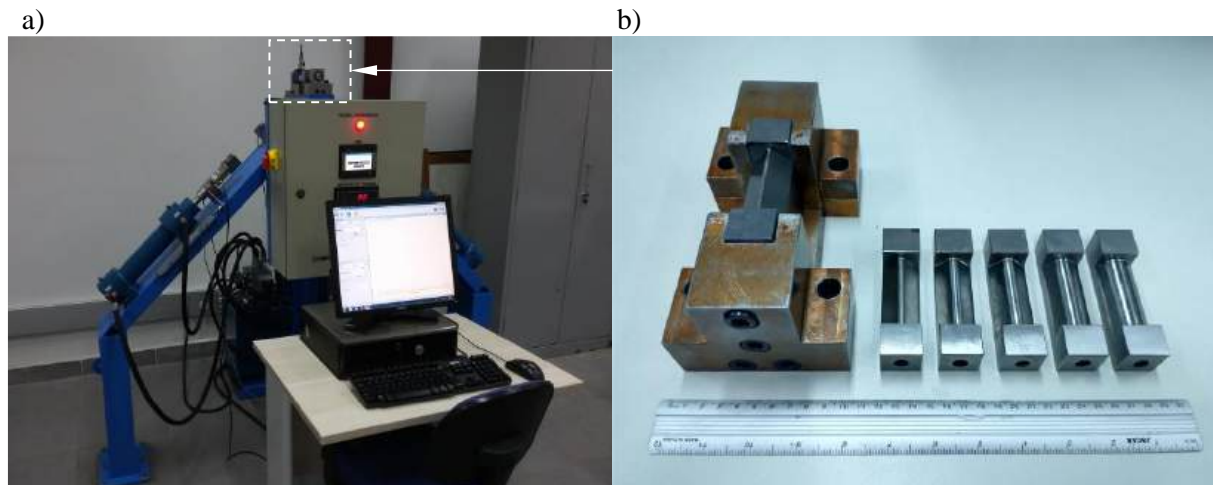a)   b)

Fig. 3. a) the friction simulator and b) the tool holder and the bending pins.

The tests were carried out under lubricated conditions with a sliding speed of 5 mm/s. Pins with the following radii were used: 1.5, 3.0, 4.5, 6.0, 7.5, 9.0, 10.5, 13.5 mm. All countersamples had the same surface roughness as defined in Section 2.1. It is worth noting that for each new test, the contact surfaces were cleaned with acetone and then a mineral-based lubricating oil (kinematic viscosity of 120 mPa·s and density of 0.894 g/cm^3) typical for cold forming was applied abundantly to the strip/pin contact interface. The coefficient of friction (CoF) was determined according to Eq. (1) (Sulonen et al., 1981):

$$\mu = \frac{2}{\pi}\left(1 + \frac{t}{2R}\right) ln\left(\frac{F_1 - F_b}{F_2}\right) \tag{1}$$

where F_b is the bending force, which is determined by Eq. (2) (Swift, 1948):

$$F_b = \frac{R_{p0.2} \cdot t^2 \cdot w}{2R} \qquad (2)$$

where $R_{p0.2}$ is the yield stress of the metal strip, w is its width and R is the radius of the bending pin.

3. Results and discussion

Figure 4 shows the behaviour of the CoF of the AISI 430 steel and AW-1100 aluminium alloy strips as a function of the bending pin radius during the BUT test. It was found that for both materials, the value of the CoF decreased with the increase in the radius of the bending pin. However, this behaviour changed after a critical radius (4.5 mm), at which the value of the coefficient of friction increased. Nanayakkara et al. (2005) observed a similar behaviour for galvanised steel sheets subjected to the BUT test, concluded that after a critical bending radius, the tribosystem changed its lubrication regime from mixed to hydrodynamic. Current literature explains that this change may be related to the variation in contact pressure and increased surface roughness of the sheet metal due to plastic deformation by stretching. Deformation of the sheet metal causes a change in its mechanical properties due to the work hardening phenomenon (Parsa & Ahkami, 2008). Generally, contact pressure tends to increase as the radius of the pin decreases and, furthermore, it is not uniformly distributed on the contact surface (Andreasen et al., 2006; Kim et al., 2012). Under these conditions, the ability of the lubricant to separate the contact surfaces and stabilise friction is reduced.
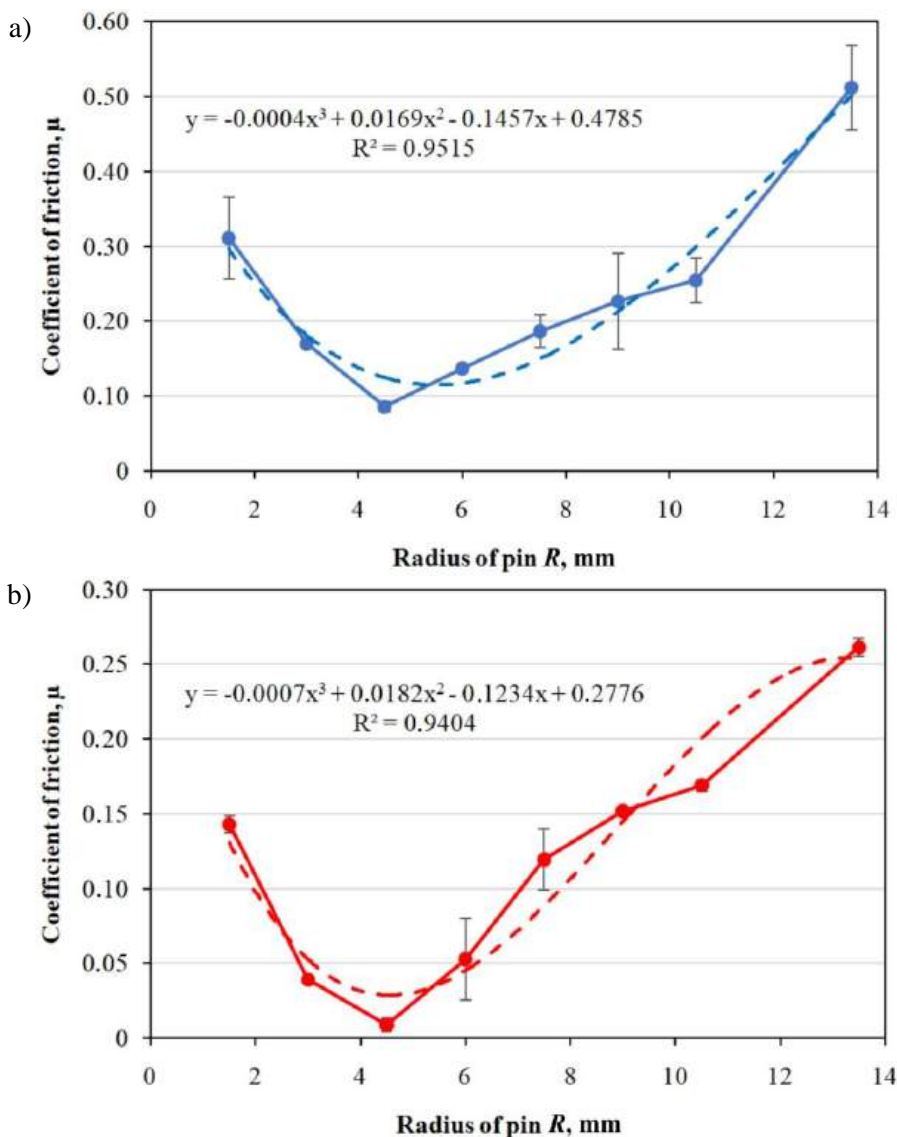

Fig. 4. Effect of the bending pin radius R on the value of the coefficient of friction (μ) of a) AW-1100 aluminium alloy and b) AISI 430 steel strips subjected to the BUT test.

At higher pressures, the lubricant film may be expelled from the contact zone or rupture, which increases the mechanical interaction between the surface asperities through flattening and ploughing mechanisms and, consequently, the resistance to friction is increased (Roizard et al., 1999). Increased frictional resistance on the drawing die radius can cause premature cracking of the drawpiece due to increased sheet metal deformation resistance in the punch impact area. Such cracking most often occurs in the area of the punch drawing radius (Seo et al., 2018).

In addition, it is possible to observe in Fig. 4a that the value of the friction coefficient of the AW-1100 aluminium strip was higher compared to that of the AISI 430 steel strip. This behaviour can be attributed to the greater surface roughness of the aluminium strip, as shown in Fig. 5. However, it can be observed in Fig. 5 that, from a radius of approximately 7.5 mm, the difference in surface roughness parameters tended to decrease. Most likely, the lower intensity of the mutual effect of bending/stretching at larger radii and the more uniform lubrication regime were the cause of this behaviour. The surface roughness parameters of the samples were measured in the middle section of the sample in the area of contact with the pin surface, in the direction transverse to the strip pulling direction. In fact, it can be seen in Fig. 4 that for larger radii the difference between the values of the CoF for the metal strips was ~1.5–2.0 times greater, while for smaller radii it was ~2.2–9.6 times greater, supporting the discussions above. For the AW-1100 sheet with pin radii greater than 7.5 mm, and for the AISI 430 sheet with pin radii greater than 10.5 mm, both parameters Ra and Rq increase rapidly. Probably, for the small pin radii, the increase in surface roughness caused by sample elongation is compensated for by the phenomenon of the flattening out of the surface asperities.
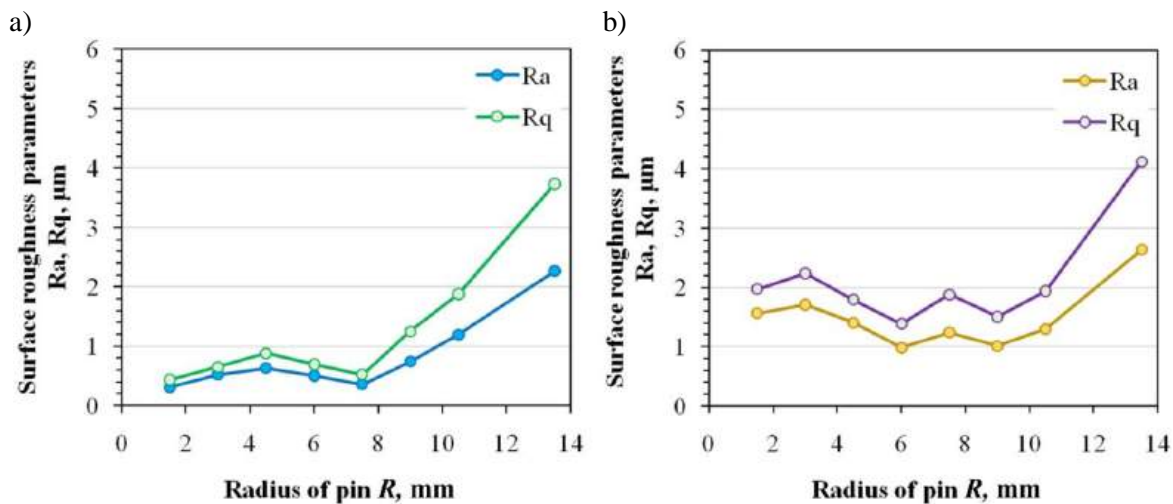
a)   b)

Fig. 5. Effect of the bending pin radius (R) on the Ra and Rq parameters of a) AW-1100 aluminium alloy and b) AISI 430 steel strips subjected to the BUT test.

The AW-1100 alloy sheet showed a greater increase in the Rt parameter compared to the AISI 430 sheet (Fig. 6). It is worth noting that this parameter represents the sum of the maximum peak height and the maximum valley depth of the profile along the evaluation length. In contrast to the Ra and Rq parameters, it should be taken into account that the Rt parameter is significantly affected by scratches, contamination and measurement noise due to its use of peak values. The increase in the CoF due to contact pressure, even under lubricated conditions, causes changes mainly in the surface topography of the aluminium sheet, which is softer compared to the tool hardness. Moreover, AW-1100 sheet metal is a material with much lower hardness than the steel countersample, therefore its surface tends to show greater topographic changes, such as greater wear and deeper scratches. The hard tool asperities cause ploughing of the surface of the soft aluminium strip, creating deep scratches, which increases the Rt parameter value. At larger radii, the real contact area between the strip sheet and the pin is larger, which usually results in a larger increase in the Rt value compared to smaller radii. The influence of the radius of the pin on the change in the total height of the roughness profile for steel (Fig. 6b) is not as stable as shown in Fig. 6a. Due to the complex influence of pressure, the radius of the pin, the sheet metal properties and the lubrication regime on the change in the sheet surface topography at pin radii of 9 and 10.5 mm, a beneficial reduction in the real pressures could have occurred. A larger pin radius, with the same cross-section of the strip sheet, causes a reduction in the real contact pressures.

The behaviour of the hardness values shown in Fig. 7 supports the aforementioned statements, where, on average, a lower hardness value is noted for the aluminium strip, even though it presents an

approximately constant increase in hardness throughout the range of radii tested (Fig. 7a). In contrast, for smaller radii, it is observed that the AISI 430 steel strip tended to present a smaller increase in hardness. Since the metal strips are subjected to bending and stretching during the BUT test, at larger radii, the mutual effect of these stresses is less intense, attenuating the effect of work hardening and, consequently, the hardness value. Furthermore, it is observed that the AISI 430 steel strip tended to present a hardness very similar to its hardness in the as-received state (Fig. 7b), which indicates that its asperities did not undergo such a significant variation in mechanical properties. In addition, a larger pin radius causes less of a bending effect on materials compared to smaller radii. This produces smaller deformations in the thickness of the strip sample.
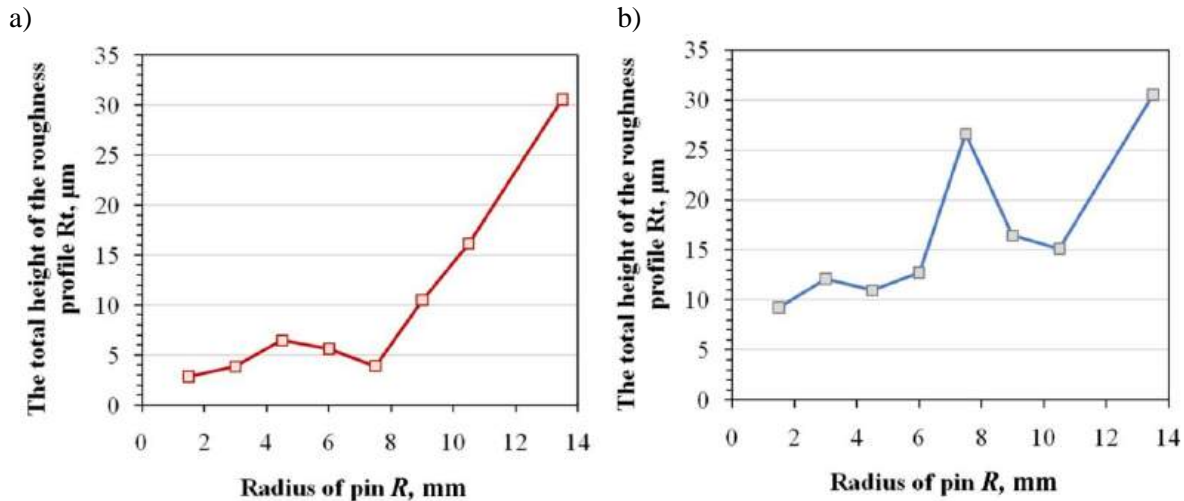
a)

b)

Fig. 6. Effect of the bending pin radius R on the Rt parameter of a) AW-1100 aluminium alloy and b) AISI 430 steel strips subjected to the BUT test.
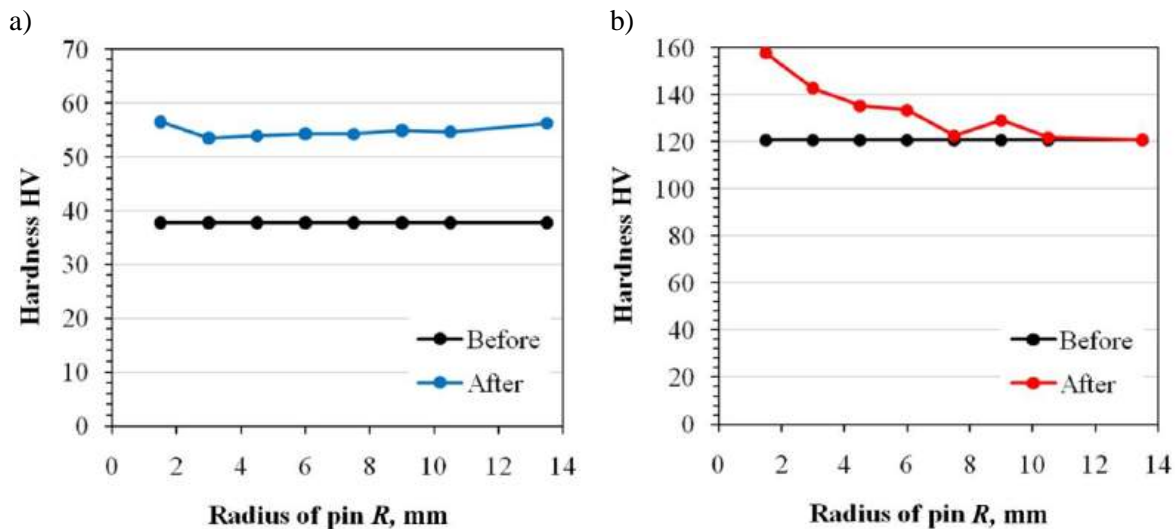
a)

b)

Fig. 7. Effect of the bending pin radius R on the hardness HV value of a) AW-1100 aluminium alloy and b) AISI 430 steel strips subjected to the BUT test.

In addition to the aspects discussed above, two important friction mechanisms most likely occurred at the contact interface of the solid surfaces (strip/pin) during the BUT test: frictional adhesion and interaction between the asperities of the hard tool and the relatively soft workpiece. Current literature explains that the first mechanism is caused by microwelding (Fig. 8a), that is, due to interatomic forces at the contact interface (Folle et al., 2022). The second is caused by a mechanical interaction of both asperities of the materials in contact (Fig. 8). In the first case, the material with the lower hardness (strip) is usually pulled out, and this debris ends up functioning as interface material, causing abrasive wear and, consequently, scratches on the surfaces of the formed parts. In the second case, there is closer contact between the solids, such that the asperities end up penetrating each other, also producing scratches on the soft surface (strip) caused by the harder one (pin).
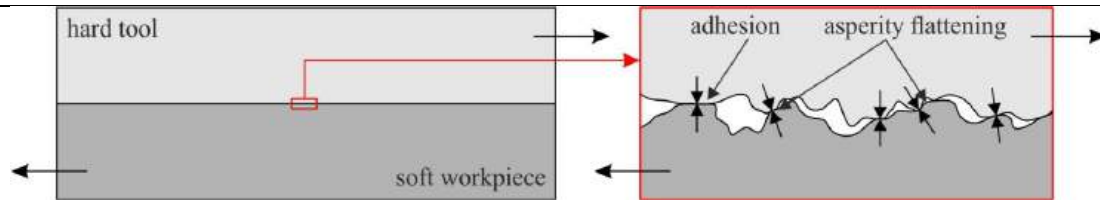
Fig. 8. Schematic illustration of the friction mechanisms presents in the stamping of metal sheets: frictional adhesion and asperity flattening.

In this case, it is also very likely that the material torn off the strip surface has increased the effect of abrasive wear at the contact interface (Devenport et al., 2023). Wear products can be suspended in the lubricant as a so-called third body and interact with the rubbing surfaces through a three-body abrasion mechanism (Chen & Li, 2022). In this way, this layer contains the lubricant and its tribological transformation products and wear products.

Another mechanism that may also have influenced the variation in the lubrication regime is the plastic deformation of the asperities of the softer material as its slides over the bending pin. The normal load exerted by the hard asperity of the tool increases on the soft asperity of the metal strip causing the latter to deform plastically when its yield limit is exceeded. As a result, it flattens, which increases the real contact area and, consequently, friction. However, when the flattening of asperities happens at the closed lubricant pockets (Wang et al., 2021), that is, the oil reserve that remains in the valleys of the metal strip, this improves the efficiency of the lubrication at the contact interface, attenuating the effect of friction and, as a result, the roughness parameters Ra and Rq also tend to be smaller, as observed in Fig. 4 for smaller radii. It is important to emphasise that Ra and Rq provide more stable results, that is, they are not as significantly affected by scratches, contamination and measurement noise as the Rt parameter. Generally, in the sheet with less roughness, the dominant mechanism is surface adhesion, while in the rougher sheet, the asperity flattening mechanism dominates the tribocontact, and the intensity of this mechanism increases with the increase in the surface roughness of the deformed sheet which has a much lower hardness than the tool material. Under specific conditions of contact pressure and properties of the rubbing bodies, the ploughing mechanism may occur. It is important to emphasise that these different friction mechanisms do not occur in isolation, but through a superposition of mechanisms that are difficult to quantify and control. In this regard, the tribological literature explains that the adhesion and plastic deformation mechanisms are strongly influenced by the increasing of the real contact area and work hardening of the surface asperities, respectively. This superposition occurs in undetectable proportions and varies over time and place, making it almost impossible to calculate the real CoF as well as wear (Bowden & Tabor, 1986). However, simulated friction tests provide very interesting results, which can be used, for example, as input data in computational numerical simulation of manufacturing processes.

The friction coefficients obtained in this work varied from 0.09 to 0.5 for the AW-1100 aluminium alloy and from 0.02 to 0.26 for AISI 430 steel sheets, depending on the pin radius. Luiz et al. (2022) tested the AISI 430 steel sheets in BUT conditions. The results of the CoF for different orientation of samples depending on the rolling direction and sliding speeds revealed that the CoF changes between 0.05 and 0.2, with the increase in sliding speed causing a decrease in the CoF. In another article, Luiz et al. (2023) determined the CoF of an AISI 430 sheet in the BUT test depending on the relative elongation. It was found that the CoF varied between 0.09 and 0.37, respectively, for relative elongation between 0.03 and 0.09. The results for a manganese drawing-quality uncoated steel sheet tested under lubricated conditions with a mineral seal oil revealed a coefficient of friction between 0.16 and 0.17 (Wenzloff et al., 1992), which is consistent with the average value of the CoF in this paper. The CoF of AW-1100 aluminium alloy sheets determined by Folle and Schaeffer (2016) using the BUT test varied between 0.12 and 0.27, depending on the equation used to estimate the CoF. The CoF determined by Azushima and Sakuramoto (2006) for AW-1100 aluminium alloy sheets varied between approximately 0.14 and 0.19 depending on the contact pressure during the BUT test. Thus, the results presented in this paper are consistent with the results of other authors, however, it should be noted that different countersample materials and different surface roughnesses of sheet and countersample were used in the reviewed sources.

4. Conclusions

Based on the experimental tests of friction for the AW-1100 and AISI 430 sheets in the BUT test, the following conclusions can be drawn:

- The values of the roughness parameters (Ra, Rq and Rt) tended to increase with increasing pin radius, this is because variations occurred in the lubrication regime at the contact interface between the strip and the pin.
- The total height of the roughness profile Rt parameter showed a more expressive increase, as it is significantly influenced by scratches, contamination and measurement noise due to its use of peak values.
- For both materials, the CoF increased with decreasing pin radius; however, this behaviour changed at a critical radius ($R = 4.5$ mm), after which the CoF increased with increasing pin radius.
- In general, the AW-1100 aluminium alloy strip presented a higher CoF ($\sim$1.5–9.6) than the AISI 430 steel strip, mainly due to its lower hardness and greater surface roughness.

The results can be used as input data in computational numerical simulations of deep drawing processes as well as in the design guidelines and failure prevention criteria based on the materials investigated, which can result in cost reduction, improvement in process performance and product quality. Commonly, in numerical simulations of sheet metal forming processes, a constant COF value is assumed for the entire contact surface. In reality, in sheet metal forming, the value of the coefficient of friction depends on the contact zone of the sheet metal with the tools and the pressures prevailing there. Moreover, the CoF value is not constant but evolves depending on the changes in contact pressures, sheet metal work hardening and surface topography. The results presented in this article do not exhaust the research topic of friction on the drawing die radius. It seems reasonable to check the lubricant viscosity, friction junctions and different roughness of the countersamples on the co-occurrence of different friction mechanisms at the contact interface.

Acknowledgements

References

ABNT VND. (2024, October 15). Available online: https://steelss.com/materials/Special-Steel/VND_45_6650.html

American Society for Testing and Materials (2021). *Standard test methods for tension testing of metallic materials* (ASTM Standard No. E8/E8M-22:2021). https://www.astm.org/e0008_e0008m-22.html

Andreasen, J. L., Olsson, D. D., Chodnikiewicz, K., & Bay, N. (2006). Bending under tension test with direct friction measurement. *Proceedings of the Institution of Mechanical Engineers, Part B: Journal of Engineering Manufacture*, *220*(1), 73-80. https://doi.org/10.1243/095440505X32913

Antonicelli, M., Piccininni, A., & Palumbo, G. (2024). Eco-friendly lubricants for improving performance and environmental impact in cold rolling. *Procedia CIRP*, *125*, 196-200. https://doi.org/10.1016/j.procir.2024.08.034

Arinbjarnar, Ú., & Nielsen, C. V. (2023). Effect of workpiece pre-straining on tribological performance of surface coatings in sheet metal forming. *Tribology International*, *180*, Article 108262. https://doi.org/10.1016/j.triboint.2023.108262

Ayllón, J., Miguel, V., Martinez, A., Rodríguez-Alcaraz, J. L., & Coello, J. (2017). Modelization of bending under tension tests with application to the SPIF processes. *Procedia Manufacturing*, *13*, 299-306. https://doi.org/10.1016/j.promfg.2017.09.076

Azushima, A., & Sakuramoto, M. (2006). Effects of plastic strain on surface roughness and coefficient of friction in tension-bending test. *CIRP Annals*, *55*(1), 303-306. https://doi.org/10.1016/S0007-8506(07)60422-3

Bowden, F. P., & Tabor, D. (1986). The friction and lubrication of solids. Oxford University Press.

Carcel, A. C., Palomares, D., Rodilla, E., & Puig, M. A. P. (2005). Evaluation of vegetable oils as pre-lube oils for stamping. *Materials and Design*, *26*, 587-593. https://doi.org/10.1016/j.matdes.2004.08.010

Ceron, E., Martins, P. A. F., & Bay, N. (2014). Thermal analysis of bending under tension test. *Procedia Engineering*, *81*, 1805-1810. https://doi.org/10.1016/j.proeng.2014.10.236

Chen, R., & Li, S. (2022). Novel three-body nano-abrasive wear mechanism. *Friction*, *10*, 677–687. https://doi.org/10.1007/s40544-020-0481-1

Coubrough, G. J., Alinger, M. J., & Van Tyne, C. J. (2002) Angle of contact between sheet and die during stretch-bend deformation as determined on the bending-under-tension friction test system. *Journal of Materials Processing Technology*, *130-131*, 69-75. http://dx.doi.org/10.1016/S0924-0136(02)00781-1

Devenport, T. M., Griffin, J. M., Rolfe, B. F., Pereira, M. P. (2023). Friction and wear in stages of galling for sheet metal forming applications. *Lubricants*, *11*, Article 288. https://doi.org/10.3390/lubricants11070288

Dilmec, M., & Arap, M. (2016). Effect of geometrical and process parameters on coefficient of friction in deep drawing process at the of lange and the radius regions. *International Journal of Advanced Manufacturing Technology*, *86*, 747-759. https://doi.org/10.1007/s00170-015-8225-5

Evin, E., Nemeth, S., & Vyrostek, M. (2014). Evaluation of friction coefficient of stamping. *Acta Mechanica Slovaca*, *18*(3-4), 20-27.

Folle, L. F., & Schaeffer, L. (2016). Evaluation of contact pressure in bending under tension test by a pressure sensitive film. *Journal of Surface Engineered Materials and Advanced Technology*, *6*, 201-214. http://dx.doi.org/10.4236/jsemat.2016.64018

Folle, L. F., Silva, B. C. S., Batalha, G. F., & Coelho, R. S. (2022). The role of friction on metal forming processes. In G. Pintaude, T. Cousseau, & A. Rudawska (Eds.), *Tribology of Machine Elements - Fundamentals and Applications* (pp. 1-20). IntechOpen. https://doi.org/10.5772/intechopen.101387

Gao, Y., Li, H., Zhao, D., Wang, M., & Fan, X. (2024). Advances in friction of aluminium alloy deep drawing. *Friction*, *12*, 396–427. https://doi.org/10.1007/s40544-023-0761-7

International Organization for Standardization (2021). *Geometrical product specifications (GPS) — Surface texture: ProfilePart 2: Terms, definitions and surface texture parameters* (ISO Standard No, 21920-2:2021). https://www.iso.org/standard/72226.html

Kim, Y. S., Jain, M. K. & Metzger, D. R. (2004). A finite element study of capstan friction test. *AIP Conference Proceedings*, *712*, 2264-2269. https://doi.org/10.1063/1.1766872

Kim, Y. S.; Jain, M. K.; & Metzger, D. R. (2012). Determination of pressure-dependent friction coefficient from drAW-bend test and its application to cup drawing. *International Journal of Machine Tools and Manufacture*, *56*, 69-78. https://doi.org/10.1016/j.ijmachtools.2011.12.011

Luiz, V. D., & Rodrigues, P. C. M. (2022). Failure analysis of AISI 430 stainless steel sheet under stretching and bending conditions. *International Journal of Advanced Manufacturing Technology*, *121*, 2759-2772. https://doi.org/10.1007/s00170-022-09451-2

Luiz, V. D., Santos, A. J., Câmara, M. A., & Rodrigues, P. C. M. (2023). Influence of different contact conditions on friction properties of AISI 430 steel sheet with deep drawing quality. *Coatings*, *13*(4), Article 771. https://doi.org/10.3390/coatings13040771

Nanayakkara, N. K. B. M. P., Kelly, G., & Hodgson, P. (2005). Application of bending under tension test to determine the effect of tool radius and the contact pressure on the coefficient of friction in sheet metal forming. *Materials Forum*, *29*, 114-118.

Parsa, M., & Ahkami, S. N. A. (2008). Bending of work hardening sheet metals subjected to tension. *International Journal of Material Forming*, *1*, 173–176. https://doi.org/10.1007/s12289-008-0019-y

Pereira, M. P., Duncan, J. L., Yan, W. & Rolfe, B. F. (2009). Contact pressure evolution at the die radius in sheet metal stamping. *Journal of Materials Processing Technology*, *209*, 3532-3541. http://dx.doi.org/10.1016/j.jmatprotec.2008.08.010

Pereira, R., Peixinho, N., & Costa, S. L. (2024). A review of sheet metal forming evaluation of advanced high-strength steels (AHSS). *Metals*, *14*, Article 394. https://doi.org/10.3390/met14040394

Roizard, X., Raharijaona, F., Von Stebut, J., & Belliard, P. (1999). Influence of sliding direction and sliding speed on the micro-hydrodynamic lubrication component of aluminium mill-finish sheets. *Tribology International*, *32*, 739-747. https://doi.org/10.1016/S0301-679X(00)00008-6

Semiatin, S.L. (Ed.). (2006). *Metalworking: Sheet Forming.* ASM International. https://doi.org/10.31399/asm.hb.v14b.9781627081863

Seo, H. Y., Jin, C. K., & Kang, C. G. (2018). Effect on blank holding force on blank deformation at direct and indirect hot deep drawings of boron steel sheets. *Metals*, *8*, Article 574. https://doi.org/10.3390/met8080574

Sulonen, M., Eskola, P., Kumpulainen, J., & Ranta-Eskola, A. A. (1981). Reliable method for measuring the friction coefficient in sheet metal forming. IDDRG Working Group Meetings, Paper WG, III/4, Tokyo.

Swift, H.W. (1948). Plastic bending under tension. *Engineering*, *166*, 333-359.

Trzepieciński, T., & Lemu, H. G. (2020). Effect of lubrication on friction in bending under tension test-experimental and numerical approach. *Metals*, *10*(4), Article 544. https://doi.org/10.3390/met10040544

Vega, M. R. O., Parise, K., Ramos, L. B., Boff, U., Mattedi, S., Schaeffer, L., & Malfatti, C. 23F. (2017). Protic ionic liquids used as metal-forming green lubricants for aluminum: Effect of anion chain length. *Materials Research*, *20*(3), 675-687. https://doi.org/10.1590/1980-5373-MR-2016-0626

Wang, W., Zhao, W., Liu, Y., Zhang, H., Hua, M., Dong, G., Tam, H.-Y., & Chin, K.S. (2021). A pocket-textured surface for improving the tribological properties of point contact under starved lubrication. *Materials*, *14*, Article 1789. https://doi.org/10.3390/ma14071789

Wenzloff, G. J., Hylton, T. A., & Matlock, D. K. (1992). Technical note: A new test procedure for the bending under tension friction test. *Journal of Materials Engineering and Performance*, *1*, 609–613. https://doi.org/10.1007/BF02649242

Więckowski, W., Adamus, J., & Dyner, M. (2020). Sheet metal forming using environmentally benign lubricant. *Archives of Civil and Mechanical Engineering*, *20*, Article 51. https://doi.org/10.1007/s43452-020-00053-x

Zhao, D., Zhao, K., Song, H., Ren, D., & Ying, C. Y. (2021). Influence of geometric attributes on friction coefficient in sheet metal stamping. *Mechanical Sciences*, *12*, 945-958. https://doi.org/10.5194/ms-12-945-2021

Wpływ Promienia Matrycy Ciągowej w Próbie Zginania z Rozciąganiem na Zachowanie Tarciowe Blach ze Stali AISI 430 i Stopu Aluminium AW-1100

Streszczenie

Tarcie jest niekorzystnym zjawiskiem w procesach kształtowania blach, ponieważ zwiększa wartość siły kształtowania, obniża jakość powierzchni wytłoczek i wpływa na zwiększone zużycie narzędzi kształtujących. W niniejszym artykule przedstawiono wyniki badań eksperymentalnych tarcia występującego na promieniu matrycy ciągowej. Materiałami testowymi były próbki w postaci taśm o grubości 0,8 mm wykonane ze stali AISI 430 oraz blachy ze stopu aluminium AW-1100. Do przeprowadzenia testów wykorzystano specjalny symulator testu tarcia zginania z rozciąganiem. Zastosowano przeciwpróbki (sworznie) o różnych promieniach w zakresie od 1,5 mm do 13,5 mm. Testy przeprowadzono w temperaturze pokojowej w warunkach smarowania olejem mineralnym. Testy tarcia uzupełniono o określenie twardości i pomiar parametrów chropowatości powierzchni próbek (Ra, Rq i Rt). Na podstawie wyników stwierdzono, że współczynnik tarcia zwiększał się wraz ze zmniejszaniem się promienia sworznia gnącego, jednak zachowanie to uległo zmianie po osiągnięciu krytycznego promienia (4,5 mm), po którym współczynnik tarcia zwiększał się wraz ze wzrostem promienia sworznia. Taśma ze stopu aluminium AW-1100 charakteryzowała się wyższym współczynnikiem tarcia niż taśma ze stali AISI 430.

Słowa kluczowe: stop aluminium AW-1100, stal AISI 430, współczynnik tarcia, test zginania z rozciąganiem, kształtowanie blach

Original Research

The Effect of Blankholder Pressure on the Amount of Springback in the U-Draw Bending Process

Romuald Fejkiel [ID]

Department of Mechanics and Machine Building, The University College of Applied Sciences in Krosno, ul. Wyspiańskiego 20, 38-400 Krosno, Poland

Correspondence: romuald.fejkiel@pans.krosno.pl

Abstract

Springback in sheet metal forming processes is a phenomenon that makes it difficult to obtain products with the desired geometry. This paper presents the results of research on the effect of the blankholder pressure on the elastic deformations of sheets during the forming of strip specimens (50 mm wide and 400 mm long) into U-shaped components. A special die was developed for the forming of sheet metals under variable blankholder pressure conditions in the range between 1 and 3 MPa. Three grades of sheets with significantly different properties were used as the research material: 6063 aluminium alloy, S235JR structural steel and X46Cr13 stainless steel. The research was conducted under dry friction conditions. The elastic deformations of the sheet metal in the U-draw bending process were of a different character in the punch radius and die radius areas. In the area of the punch edge, the springback coefficient decreased with increasing blankholder pressure. This relationship was observed for all the tested materials. In the area of the die edge, a decrease in the value of the bending angle was generally observed in relation to the bending angle in the loaded state.

Keywords: elastic properties, bending, sheet metal, sheet metal forming, springback

1. Introduction

A problem during sheet metal forming is the springback phenomenon. After the forming process is completed and the load is removed, residual stresses remain in the final product due to plastic deformation. Residual stresses cause an unintended change in the geometry of the formed component (El-Megharbel et al., 1990). Components formed from sheets are mainly used in the automotive industry. The growing use of high-strength steels and aluminium alloys for car bodies requires a multi-dimensional approach to the development of new forming technologies. One of the methods to reduce the negative impact of springback on the quality of components is to compensate for the shape of the tools (Nowosielski et al., 2013). The springback of the material depends on many factors, such as the mechanical properties of the sheet metal, material thickness, the shape of drawpiece, the forming method, bending radius, the sample orientation relative to the sheet metal rolling direction and the temperature (Lu et al., 2023; Slota et al., 2014).

Often, due to the complexity of the forming process, analytical estimation of the amount of springback is difficult. For this reason, many simple experimental tests have been developed to assess the tendency of sheets to springback. One way to investigate the springback of sheets is the technological processes of sheet forming: the L-bending process (Chen & Ko, 2006), the U-bending process (Wang et al., 2023), the U-draw bending process (Tong & Nguyen, 2018), the V-bending process (Khleif et al., 2020), draw beading (Ha et al., 2022) and the stretch bending (Slota et al., 2017). U-bending tests are the most common method to predict springback (Dessie & Lukacs, 2023). In addition to experimental studies, the finite element method (Hou et al., 2017) is commonly used to determine the elastic deformations of drawpieces. However, the accuracy of finite element method simulations depends on the approach to computational modelling, including the quality of the finite element mesh and the material model. Li et al. (2002) indicated that the direct model of work hardening affects the

accuracy of the springback simulation. Analytical methods (Zajkani & Hajbarati, 2017) expert systems using multilayer artificial neural networks (Bozdemir & Golcu, 2014), radial basis function networks (Han & Liao, 2014), genetic algorithms (Hu et al., 2011) and machine learning techniques (Wasif et al., 2023) are used to analyse the phenomenon of sheet metal springback.

The experimental analysis of the springback of sheets is focused on evaluation of the influence of material type, the bending method, the temperature and the strain rate on the amount of springback. Dessie and Lukacs (2023) used the U-bending test to study the effect of the die radius and punch radius on the springback phenomenon of DC01 steel sheets. They found that the coefficient of friction was the most influential parameter to have an impact on springback prediction. Choi and Huh (2014) investigated the effect of the punch speed on the amount of springback in dual-phase DP780 and SPCC sheets. A clear relationship was found between the material type and the springback phenomenon. For DP780 steel sheets, the amount of springback increased as the punch speed increased. For SPCC this relationship was reversed. Dou et al. (2020) used different methods (V-bend, U-bend, stretch bend and draw bend) to analyse the effect of forming speed on the springback of dual-phase steels. The amount of springback in the draw bend and U-bend samples increased as the forming speed increased. The opposite relationship was observed for the stretch-bend and V-bend tests. Sae-Eaw et al. (2013) investigated the effect of blankholder force and punch radius on the springback characteristics of ultra-high-strength steel sheets. The results revealed that increasing the blankholder force decreased the amount of springback. The amount of springback increased with increasing the punch radius value. Slota et al. (2013) investigated the effect of die radius on the springback behaviour of three grades of sheets (DC06, TRIP, H220PD) using the U-bending test. Greater die radius caused a smaller amount of springback in H220PD and DC06 steel sheets. A different relationship was observed for TRIP steel. Chen et al. (2023) explored the effects of punch motion curves on the springback of U-shaped AISI-1045 steel sheets. It was found that the punch movement strategy plays a key role in reducing the springback phenomenon. Rajesh et al. (2024) investigated the possibility of reducing the springback defect of EN AW-5052 aluminium alloy sheets using the Box-Behnken design of experiments approach. The results revealed that punch radius and sheet thickness had a major influence on the amount of springback.

This article presents the results of research on the effect of the blankholder pressure on the elastic deformation of sheets in the U-draw bending process. The aim of the research was to determine the effect of variable blankholder pressure on the springback of sheets with significantly different mechanical properties. There are limited studies on the U-draw bending test in the literature. This article tries to draw attention to the importance of blankholder pressure on springback behaviour. A special die was developed and built for the forming of components under conditions of variable blankholder pressure. Three grades of sheets with different elastic-plastic properties were selected for the research: EN AW-6063 aluminium alloy, S235JR structural steel and X46Cr13 stainless steel.

2. Material and methods

2.1. Materials

U-draw bending tests were carried out for three grades of 1-mm-thick sheets: EN AW-6063 aluminium alloy, S235JR structural steel and X46Cr13 stainless steel. The chemical composition of the EN AW-6063 alloy, according to the EN 571-1 standard, is (in wt.%): Mg – 0.10, Fe $\leq$ 0.35, Si – 0.20-0.60, Cu $\leq$ 0.10, Zn $\leq$ 0.10, Ti $\leq$ 0.10, Cr $\leq$ 0.10, others $\leq$ 0.05, Al (the remainder). The chemical composition of the S235JR steel, according to the EN 10025-2 standard, is (in wt.%): C – max. 0.2, Mn – max. 1.4, P – max. 0.04, S – max. 0.04, N – max. 0.012, Cu – max. 0.55, Fe (the remainder). The chemical composition of the X46Cr13 steel, in accordance with the EN 10088-2 standard, is (in wt.%): C – 0.43-0.5, Mn – max. 1, Si – max. 1, P – max. 0.04, S – max. 0.04, Fe (the remainder). The stress-strain curves of the tested sheets, determined using the Zwick/Roell Z100 uniaxial tensile testing machine, are presented in Fig. 1.

2.2. Experimental procedure

The U-draw bending tests were carried out using a stamping tool consisting of three main elements: a die, a punch and a blankholder. The appropriate pressure of the blankholder is ensured by M12×1.5×150 screws, which exert the load force on the springs, and these in turn press the blankholder against the die. The required position of the die and blankholder relative to each other is achieved

by two pins that are slidably fitted to the movable elements of the die. The base of the die was mounted in the lower holder of the uniaxial tensile testing machine Zwick-Roell Z100. The punch was mounted in the upper holder of this testing machine. A schematic drawing of the stamping tool is shown in Fig. 2. Although the stamping tool allows for forming sheet metals using draw beads, beads were not used in this work. As an alternative, stopper inserts were used.
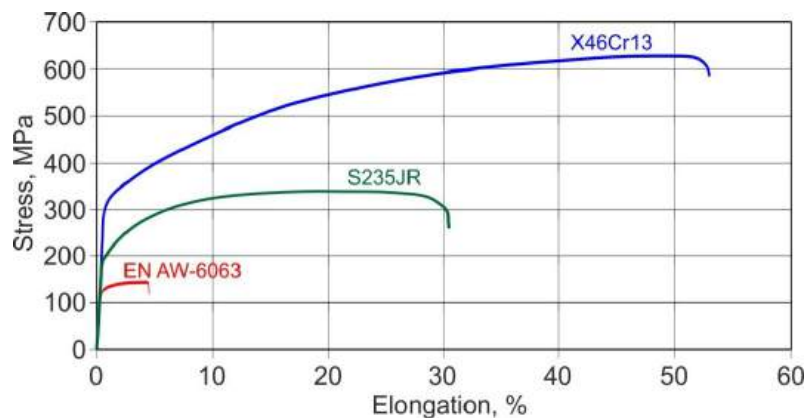

Fig. 1. Stress-strain curves for the test materials.
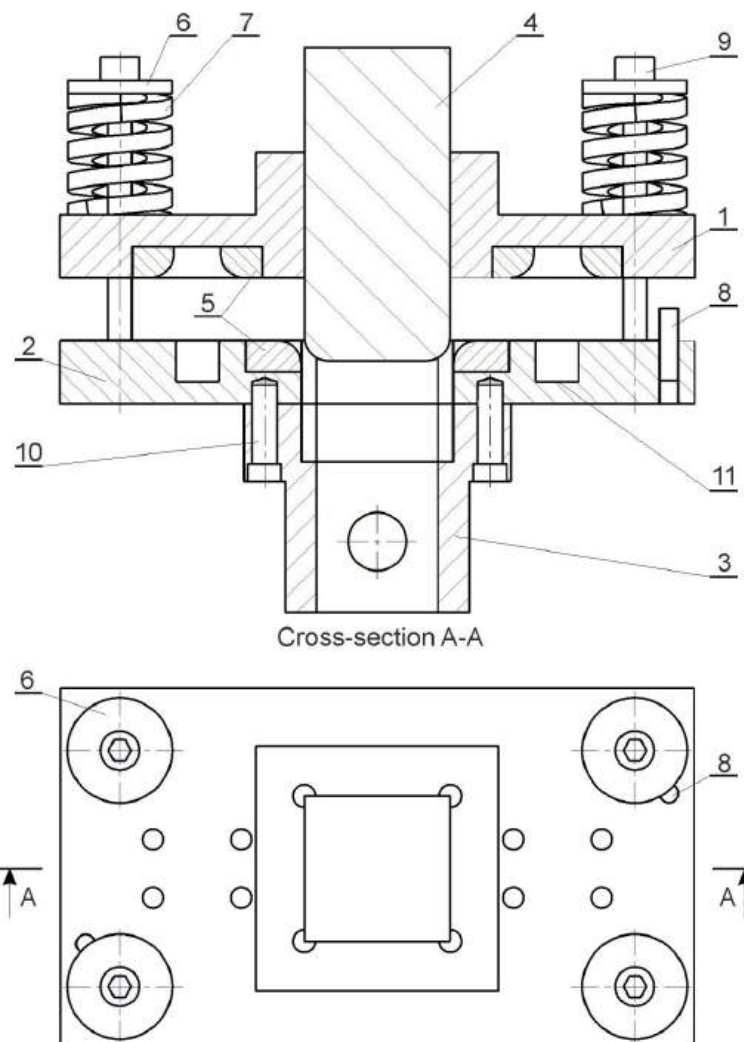
Fig. 1. Stamping die: 1 – blankholder; 2 – die; 3 – holder; 4 – punch; 5 – inserts; 6 – washer; 7 – spring; 8 – locating pin; 9, 10 – screws; 11 – draw bead socket.

The sheet metal was pressed using four springs. To accurately determine the blankholder force, it is necessary to know the spring coefficient k (spring constant). If the spring is compressed using a specific force F (in N), then the spring coefficient k is determined as the quotient of this force and the compression value Δx (in mm):

$$k = \frac{F}{\Delta x} \tag{1}$$

The springs used in the tests were R206-810 (Sodemann Industrifjedre A/S, Hinnerup, Danmark) with the parameters presented in Table 1.

Table 1. Geometric parameters of the R206-810 spring

Parameter	Value
Inner diameter	25 mm
Outer diameter	50 mm
Unloaded length	64 mm
Maximum loaded length	48 mm
Maximum travel	16 mm
Maximum load	10.344 kN

The spring constant was determined on a Zwick/Roell Z100 testing machine. Fig. 3 shows the graph of the applied force F as a function of the displacement x for the four springs used. Table 2 presents the experimental results and the average value calculated for the spring constant k.
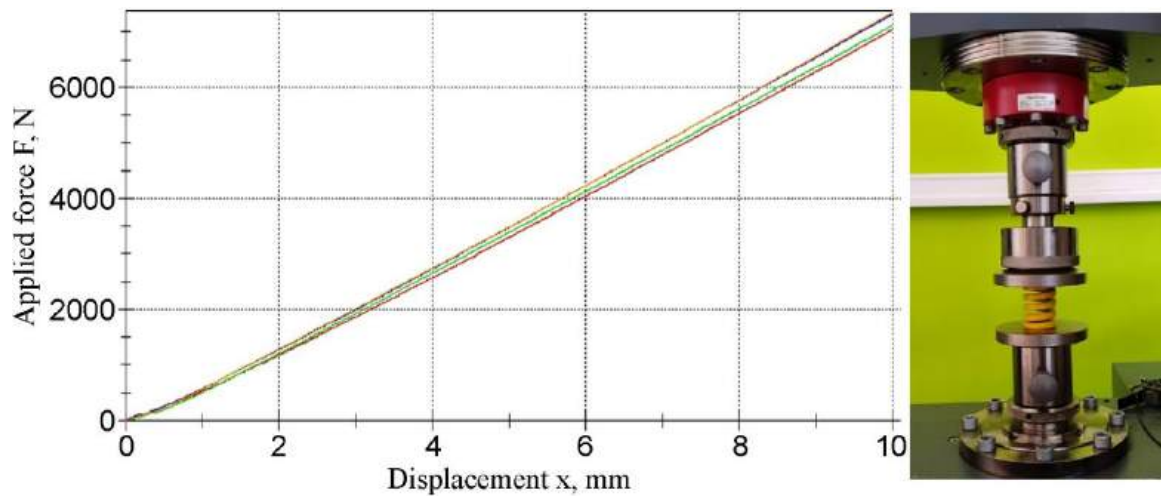

Fig. 3. Graph of the applied force as a function of the displacement of the R206-810 springs.

Table 2. Spring constant k for each spring.

Spring number	F_{max}, N	ΔL at F_{max}, mm	k, N/mm
1	7035.17	10.00	703.515
2	7111.93	10.00	711.188
3	7317.19	10.00	731.719
4	7350.74	10.00	735.072
		Average:	720.373

The determination of the amount of springback of the sheet metal strips (400 mm long and 50 mm wide) was carried out under contact pressures of 1, 2 and 3 MPa, which corresponds to spring deflections of 3.05, 6.1 and 9.15 mm, respectively. Contact pressures of this value occur in the blankholder zone during the sheet metal forming of steel and aluminium alloys (Erbel et al., 1986). When determining the required contact pressure, the spring height resulting from its shortening by the required amount was measured.

The tests were carried out under dry friction conditions. The stamping tool was mounted in the lower holder of the Zwick/Roell Z100 testing machine (Fig. 4). The blankholder was pressed by screwing in four M12×1.5 screws through the springs mounted in the blankholder sockets.

The U-draw bending process was performed at a constant punch movement speed of 10 mm/s. The forming depth was 50 mm (Fig. 5). The force measurement during U-draw bending was recorded using the measuring system of the testing machine. The cuboid-shaped punch had a square base of 70 × 70 mm and a radius of the working edge rounding r_s = 10 mm (Fig. 5). The dimensions of the square hole in the die were 74.5 × 74.5 mm and the radius of the die edge rounding r_m was 10 mm (Fig. 5). Considering that the sheet thickness was 1 mm and taking into account the clearance between the die and the punch, the bending angles at the die edge and the punch edge were α = 90.49° and β = 90.49°, respectively (Fig. 5). Three samples were tested for each setup. Based on the measured values of the

bending angles after unloading, the springback coefficients K_α and K_β were determined separately for angles α and β:

$$K_\alpha = \frac{\alpha_s}{\alpha_g} \quad (2)$$

$$K_\beta = \frac{\beta_s}{\beta_g} \quad (3)$$

where α_s is the springback bending angle at the die edge, β_s is the springback bending angle at the punch edge, α_g and β_g are the bending angles (under load) $\alpha_g = \beta_g = 90.49°$ (Fig. 5).

Fig. 4. The U-draw bending tool mounted on a testing machine.
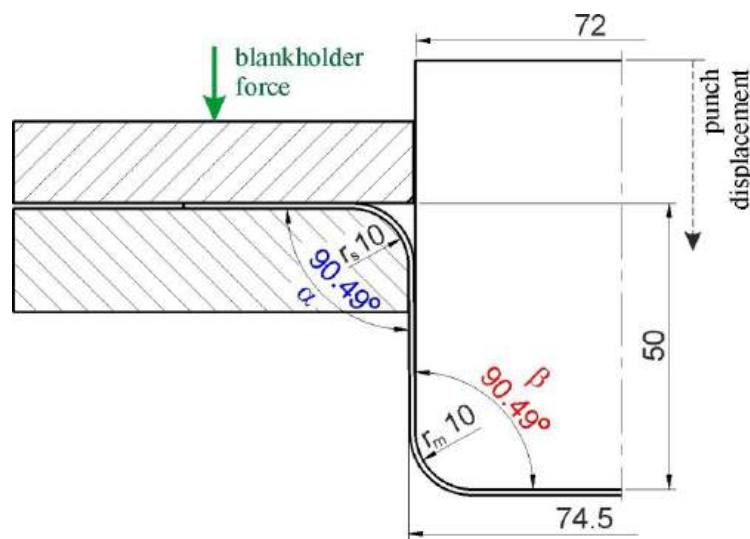

Fig. 5. Geometric parameters of U-draw bending process.

3. Results and discussion

3.1. X46Cr13 stainless steel

Figure 6a shows the average values of the springback coefficients for X46Cr13 stainless steel obtained for different contact pressures in the range of 1-3 MPa. On the punch edge, the average measured values of the bending angle increased in relation to the angle $\beta_g = 90.49°$. In the area of the die edge, the sheet bending angle decreased in relation to $\alpha_g = 90.49°$. Using this method, the springback coefficients for the punch edge are greater than 1, while in the die edge area it is the other way around. This is due to the compressive stresses prevailing on the inner side of the bended sheet metal and the

tensile stresses resulting from the use of the blankholder. With the increase in the contact pressure, the springback coefficient K_β on the punch edge increases. The increase in the tensile stresses in the sheet metal resulting from the increase of the contact pressures reduces the value of elastic deformations on the punch edge. Nevertheless, for the entire range of the analysed contact pressures, the springback coefficient K_β is greater than 1.12. This indicates high elastic properties of the tested X46Cr13 stainless steel.
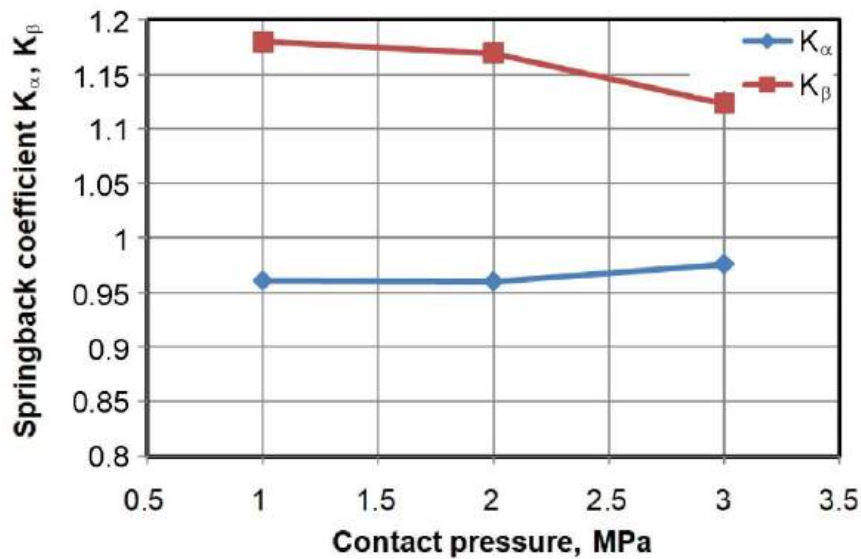

Fig. 6. Variation of die springback coefficients depending on contact pressure for the X46Cr13 stainless steel sheets.

3.2. S235JR structural steel

Fig. 7 shows the average values of the springback coefficients K_α and K_β for S234JR structural steel obtained for different contact pressures in the range of 1-3 MPa. Samples made of S235JT structural steel are characterised by a low value for the springback coefficient K_β in the area of the punch radius. Even at the lowest contact pressure, the springback coefficient value is below 1.1. For both analysed areas of the bent sample, it can be seen that the values of the springback coefficient show a tendency to decrease with increasing contact pressure. In the area of the punch radius, the values of the springback coefficient K_β were lower than the angles for the X46Cr13 stainless steel sheets by about 8.1%, 8.4% and 6.0% for contact pressures of 1 MPa, 2 MPa and 3 MPa, respectively. The value of the springback coefficient in the area of the die radius K_α is more stable for the entire range of analysed contact pressure values, compared to the results for the X46Cr13 stainless steel (Fig. 6).
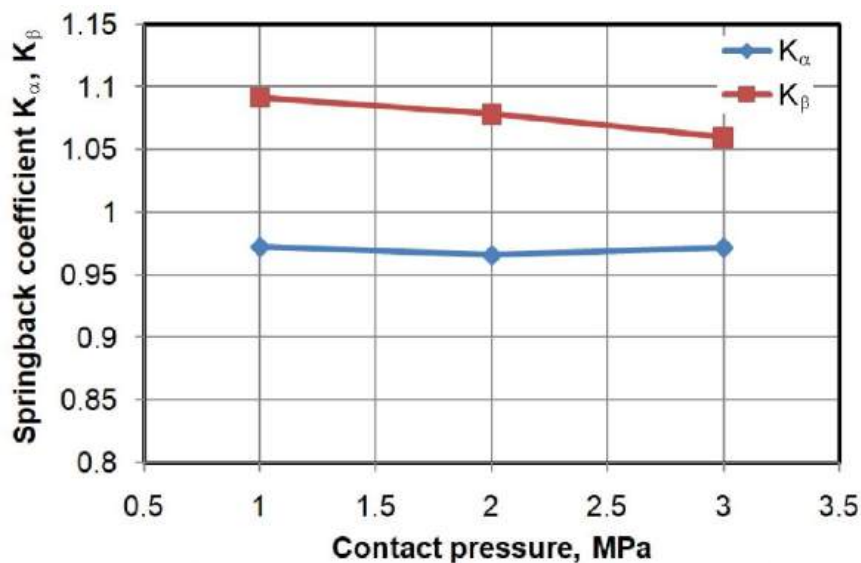

Fig. 7. Variation of the springback coefficients depending on contact pressure for the S235JR structural steel sheets.

For all applied contact pressures, the value of the punch force first increased linearly to a punch displacement of about 15-18 mm, and then stabilised at values of about 600 N (Fig. 8a), 800 N (Fig. 8b) and 1500 N (Fig. 8c) for contact pressures of 1 MPa, 2 MPa and 3 MPa, respectively. The initial almost linear range of changes in the punch force with the punch displacement can be associated with the gradual bending of the sheet metal on the punch and die radii, the value of which was $r_s = r_m = 10$ mm (Fig. 5). In this range of deformation, small sheet metal slip velocities occur where there is blankholder influence. At the same time, at the initial stage of U-draw bending, the bending area of the sheet metal increases as the radii of the punch and die gradually increase to the value $\alpha = \beta = 90.49°$. After completing this stage, the punch force value stabilises because the sheet metal moves on the rounded punch and die radii with a constant value of $\alpha = \beta = 90.49°$. At this stage, the contact surface of the sheet metal on the edges of the punch and die does not change. A similar character of punch force changes was observed for all tested materials.
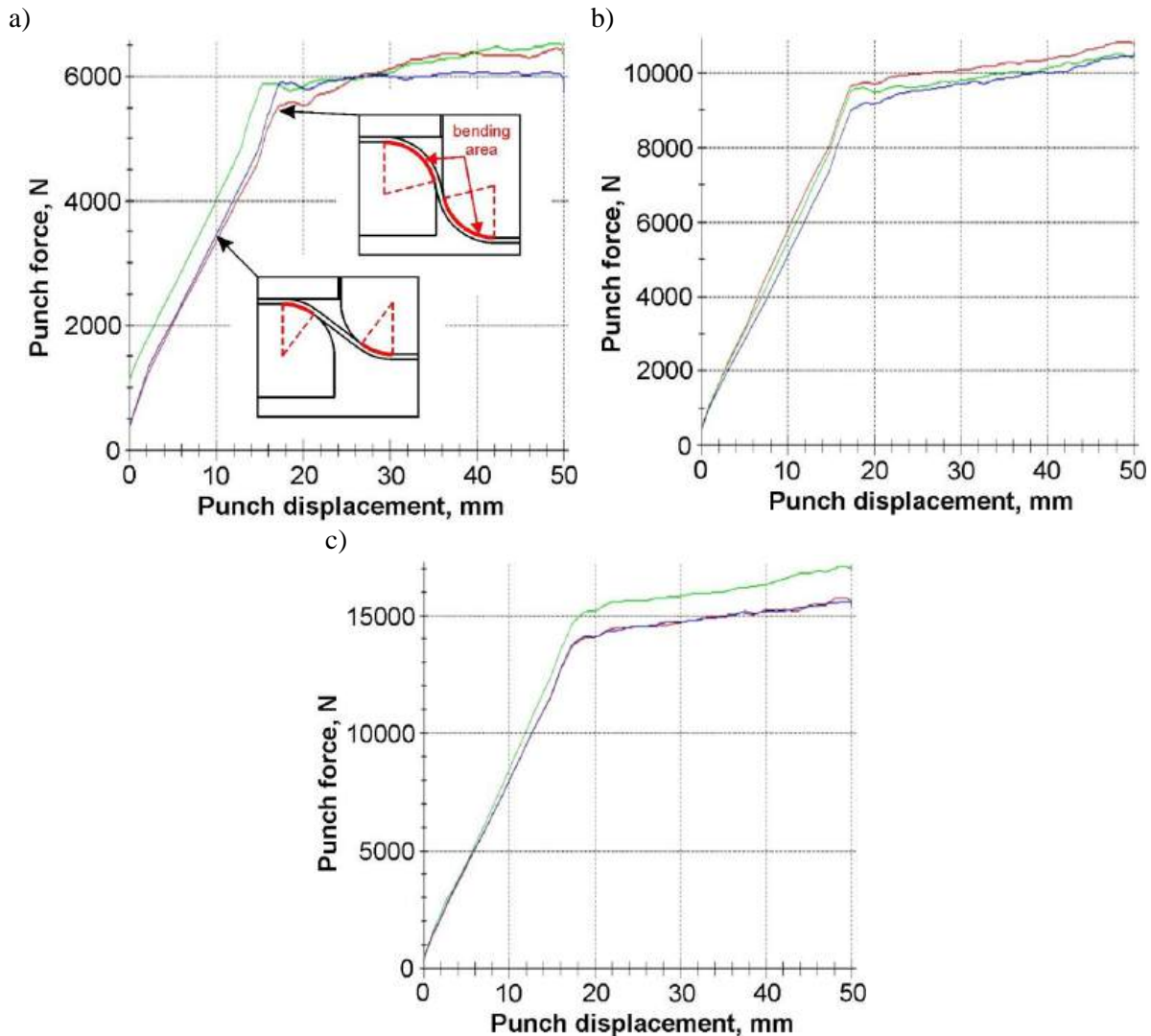

Fig. 8. Variation of the punch force during the forming of S235JR sheets under contact pressure conditions: a) 1 MPa, b) 2 MPa and c) 3 MPa.

3.3. EN AW-6063 aluminium alloy

Fig. 9 shows the average values of the springback coefficients K_α and K_β for the EN AW-6063 aluminium alloy sheets, obtained for different contact pressures in the range of 1-3 MPa. During the U-draw bending process with a pressure of 3 MPa, the sample ruptured (Fig. 10b). This means that the contact pressure of 3 MPa for this sheet was too high. Under such conditions, the friction forces between the flat surfaces of the blankholder and the die were too high and caused the sheet metal to stop moving. The EN AW-6063 aluminium alloy exhibits a low tendency to strain hardening and is characterised by low elongation (Fig. 1). With the increase in the blankholder pressure, the value of the

springback coefficient of this sheet decreases, but it was only measured at the edge of the punch. At the die edge, increasing the contact pressure caused an increase in the springback coefficient K_α (Fig. 9). The value of the maximum punch force for contact pressures of 1 MPa and 2 MPa stabilised at about 6000 and 10000 N, respectively. At the contact pressure of 3 MPa, the destructive force of the sample was about 13000 N (Fig. 10a). The most stressed region of the sheet metal was the transition of the punch radius into the flat part of the bent element. In this respect, the experimental results are consistent with theoretical and experimental studies of the deep drawing process, in which the most dangerous cross-section in terms of destruction is the side surface of the drawpiece (Gierzyńska, 1983).
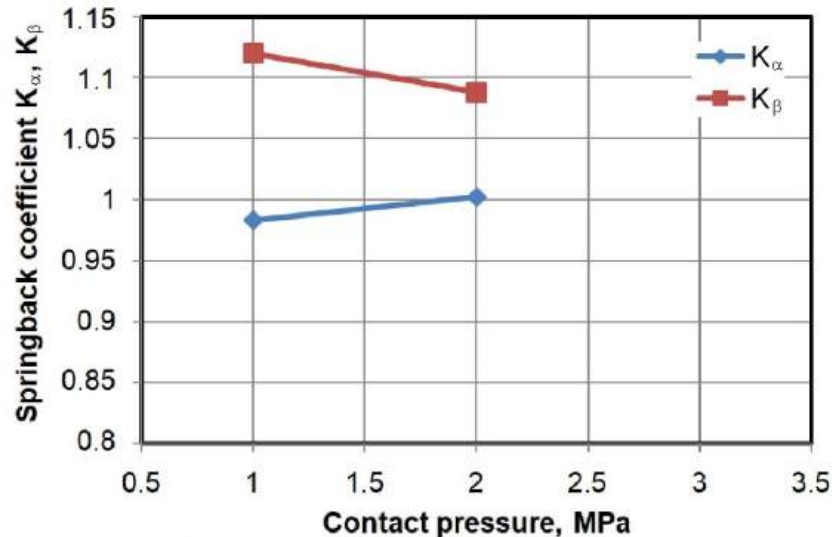

Fig. 9. Variation of the springback coefficients with contact pressure for the EN AW-6063 aluminium alloy sheets.
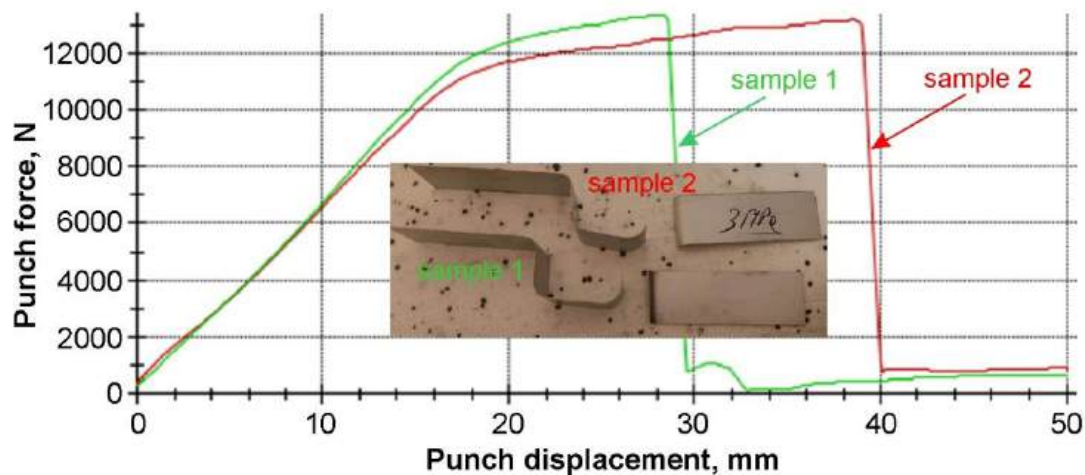

Fig. 10. Variation of the punch force during the forming of EN AW-6063 aluminium alloy sheets under a contact pressure of 3 MPa.

4. Conclusions

The springback investigations in the U-draw bending process presented in this article are aimed at comparing the behaviour of three grades of materials with different mechanical properties. A special die was built for this purpose, enabling the performance of tests with variable blankholder pressure. Moreover, due to its universal construction, the device can be mounted on a conventional uniaxial tensile testing machine. The common feature of the results obtained is that the springback phenomenon decreases with increasing blankholder pressure. Springback in the U-draw bending process has a different character in the punch radius and die radius areas. In the area of the die radius, an increase in the bending radius was observed after unloading the components. In the die radius area, the situation was the opposite – the bending angle in this area decreased in relation to the bending angle occurring in the loaded state.

The variations recorded for the punch force depending on its displacement during the U-draw bending of all grades of materials clearly indicates the occurrence of two specific stages of the bending

process. During the first stage, the angle of wrapping of the die edge and the punch edge gradually increases until the maximum value is obtained ($\alpha = \beta = 90.49°$). In this stage, the force increases approximately linearly. After the wrapping angles reach the value (90.49°). the punch force stabilises at a value dependent on the blankholder pressure. At the same time, the value of the maximum punch force depends on the material type (the mechanical properties of the sheet metal) and the blankholder pressure. The higher the blankholder pressure, the greater the maximum punch force. This is caused by the increased friction forces under the blankholder pressure, which must be overcome during U-draw bending. Moreover, increasing the bending angle intensifies the work hardening effect of the sheet metal and, consequently, the punch force increases.

References

Bozdemir, M., & Golcu, M. (2008). Artificial neural network analysis of springback in V bending. *Journal of Applied Sciences*, *8*(17), 3038-3043. https://doi.org/10.3923/jas.2008.3038.3043

Chen, F. K., & Ko, S. F. (2006). Deformation analysis of springback in L-bending of sheet metal. *Journal of Achievements in Materials and Manufacturing Engineering*, *18*(1-2), 339-342.

Chen, T. C., Chen, S. X., Wang, C. C., & Lee, T. E. (2023). Analysis of the punch motion curve for the springback of U-shaped sheet metal. *Advances in Mechanical Engineering*, *15*(3). https://doi.org/10.1177/16878132231161151

Choi, M., & Huh, H. (2014). Effect of punch speed on amount of springback in U-bending process of auto-body steel sheets. *Procedia Engineering*, *81*, 963-968. https://doi.org/10.1016/j.proeng.2014.10.125

Dessie, J. E., & Lukacs, Z. (2023). Determination of influential springback parameters in U-bending test. *Pollack Periodica*, *18*(2), 17-22. https://doi.org/10.1556/606.2023.00799

Dou, L., Li, X., Dong, H., Li, D., & Peng, X. (2020). Development of springback tester and the effect of forming speed on the springback of four sheet metal bending processes. *IOP Conference Series: Materials Science and Engineering*, *967*, Article 012065. https://doi.org/10.1088/1757-899X/967/1/012065

El-Megharbel, A., El-Domiaty, A., & Shaker, M. (1990). Springback and residual stresses after stretch bending of workhardening sheet metal. *Journal of Materials Processing Technology*, *24*, 191-200. https://doi.org/10.1016/0924-0136(90)90181-S

Erbel, S., Kuczyński, K, & Marciniak, Z. (1986). *Obróbka plastyczna*. Wydawnictwo Naukowe PWN.

Gierzyńska, M. (1983). *Tarcie, zużycie i smarowanie w obróbce plastycznej metali*. Wydawnictwa Naukowo-Techniczne.

Ha, T., Welo, T., Ringen, G., & Wang, J. (2022). A strategy for on-machine springback measurement in rotary draw bending using digital image-based laser tracking. *International Journal of Advanced Manufacturing Technology*, *119*, 705-718. https://doi.org/10.1007/s00170-021-08178-w

Han, L. F., & Liao, Z. L. (2014). The application of radial basis function neural network in springback prediction of sheet flanging. *Applied Mechanics and Materials*, *668-669*, 571-574. https://doi.org/10.4028/www.scientific.net/AMM.668-669.571

Hou, Y., Min, J., Lin, J., Liu, Z., Carsley, J. E., Stoughton, T. B. (2017). Springback prediction of sheet metals using improved material models. *Procedia Engineering*, *207*, 173-178. https://doi.org/10.1016/j.proeng.2017.10.757

Hu, J., Chung, K., Li, X. X., Park, T., Zhou, G. F., & Yao, R. (2011). An automatic spring-back compensation method in die design based on a genetic algorithm. *Metals and Materials International*, *17*, 527–533. https://doi.org/10.1007/s12540-011-0636-8

Khleif, A. A., Kasjkool, L. H., & Hassoon, O. H. (2020). Experimental investigation of hold time effect on springback in V-bending sheet metal forming process. *IOP Conference Series: Materials Science and Engineering*, *881*, 012071. https://doi.org/10.1088/1757-899X/881/1/012071

Li, X., Yang, Y., Wang, Y., Bao, J., Li, S. (2002). Effect of the material-hardening mode on the springback simulation accuracy of V-free bending. *Journal of Materials Processing Technology*, *123*(2), 209-211. http://dx.doi.org/10.1016/S0924-0136(02)00055-9

Lu, Z., Li, D., Cao, L., Cui, H., & Xu, J. (2023). Springback control in complex sheet-metal forming based on advanced high-strength steel. Coatings, 13, 930. https://doi.org/10.3390/coatings13050930

Nowosielski, M., Żaba, K., Kita, P., & Kwiatkowski, M. (2013). Compensation of springback effect in designing new pressing technologies. *Proceedings of the Metal2013 Conference* (pp. 1-5). http://dx.doi.org/10.13140/2.1.4897.6328

Rajesh, R., Bharath, K. A., Mohammed, N. P. K., & Subramanian, S. (2024). Springback defect minimization in u bending of AL5052 alloy sheet using Box Behnken design of experiments. *Academic Journal of Manufacturing Engineering*, *22*(1), 127-134.

Sae-Eaw, N., Thanadngarn, C., Sirivedin, K., Buakaew, V., & Neamsup, Y. (2013). The study of the springback effect in the UHSS by U-bending process. *Applied Science and Engineering Progress*, *6*(1), 19-25.

Slota, J., Gajdos, I., Spišák, E., & Šiser, M. (2017). Springback prediction of stretching process using finite element analysis for DP600 steel sheet. *Acta Mechanica et Automatica*, *11*(1), 5-8. https://doi.org/10.1515/ama-2017-0001

Slota J., Jurcisin M., Spišák E., & Sleziak T. (2014). An investigation of springback in sheet metal forming of high strength steels. *Applied Mechanics and Materials*, *693*, 370-375. https://doi.org/10.4028/www.scientific.net/AMM.693.370

Slota, J., Jurčišin M., Dvořák M. (2013). Experimental and numerical analysis of springback prediction in U-bendings of anisotropic sheet metals. *Zeszyty Naukowe Politechniki Rzeszowskiej - Mechanika*, *83*(3), 525-533. https://doi.org/10.7862/rm.2013.47

Tong, V. C., Nguyen, D. T. (2018). A study on spring-back in U-draw bending of DP350 high-strength steel sheets based on combined isotropic and kinematic hardening laws. *Advances in Mechanical Engineering*, *10*(9), https://doi.org/10.1177/1687814018797436

Wang, H., Huang, A., Xing, S., Zhang, C., & Luo, J. (2023). Finite element simulation and experimental study of U-bending forming of high-strength Mg-Gd-Y-Zn-Zr alloy. *Metals*, *13*, Article 1477. https://doi.org/10.3390/met13081477

Wasif, M., Rababah, M., Fatima, A., & Baig, S. U. R. (2023). Prediction of springback using the machine learning technique in high-tensile strength sheet metal during the V-bending process. *Jordan Journal of Mechanical and Industrial Engineering*, *17*(4), 481-488. https://doi.org/10.59038/jjmie/170403

Zajkani, A., & Hajbarati, H. (2017). An analytical modeling for springback prediction during U-bending process of advanced high-strength steels based on anisotropic nonlinear kinematic hardening model. *International Journal of Advanced Manufacturing Technology*, *90*, 349-359. https://doi.org/10.1007/s00170-016-9387-5

Wpływ Nacisku Dociskacza na Wartość Odkształceń Sprężystych w Procesie Gięcia Blach w Kształcie Litery U

Streszczenie

Sprężynowanie jest zjawiskiem, które utrudnia otrzymanie wyrobów o pożądanej geometrii w procesach kształtowania blach. W pracy przedstawiono wyniki badań wpływu nacisku dociskacza na odkształcenia sprężyste blach podczas ich kształtowania pasów blachy o szerokości 50 mm i długości 400 mm w wyroby w kształcie litery U. Opracowano specjalny tłocznik pozwalający na kształtowanie wyrobów w warunkach zmiennego nacisku dociskacza w zakresie 1-3 MPa. Jako materiał badawczy wykorzystano trzy gatunki blach o znacznie różniących się właściwościach: stop aluminium EN AW-6063, stal konstrukcyjna S235JR oraz stal nierdzewna X46Cr13. Badania przeprowadzono w warunkach tarcia suchego. Odkształcenia sprężyste blachy w procesie gięcia w kształcie litery U miały inny charakter w obszarach promienia stempla i promienia matrycy. W obszarze krawędzi stempla współczynnik sprężynowania zmniejszał się ze wzrostem nacisku dociskacza. Tę zależność zaobserwowano dla wszystkich badanych materiałów o różnych właściwościach mechanicznych. W strefie krawędzi matrycy generalnie zaobserwowano zmniejszenie kąta gięcia w stosunku do kąta gięcia w stanie obciążonym.

Słowa kluczowe: właściwości sprężyste, gięcie, blacha, kształtowanie blach, odkształcenia sprężyste

Original Research

Structural Effectiveness of Fixed Offshore Platforms with Respect to Uniform Corrosion

Abubakar O. Salihu [1] [ID], Kolawole Abejide [2,*] [ID], Olugbenga S. Abejide [1] [ID], Jibrin M. Kaura [1] [ID], Ibrahim Aliyu [1] [ID], Kehinde Adeshina [3] [ID], Olugbenga S. Abejide [4] [ID]

[1] Department of Civil Engineering, Ahmadu Bello University, Zaria, Nigeria; salihuao@ymail.com (A.O. Salihu), osabejide@abu.edu.ng (O.S. Abejide), jmkaura@abu.edu.ng (J.M. Kaura), ibrahimaliyu@abu.edu.ng (I. Aliyu)

[2] Department of Civil Engineering, University of KwaZulu-Natal, Durban, South Africa

[3] Department of Construction Management, Ulster University, 2-24 York Street, Belfast, BT15 1AP, Northern Ireland, United Kingdom; Adeshinaolayinka03@gmail.com

[4] Council for Scientific and Industrial Research, Brummeria, Pretoria. South Africa; sabejide@csir.co.za

* Correspondence: koladeabejide@gmail.com

Abstract

This study presents the structural effectiveness of fixed offshore platforms, addressing the challenges posed by complex loading conditions in marine environments. The structural performance of the fixed offshore platform was assessed using Finite Element Analysis performed in ABAQUS CAE software, with particular focus on the impact of intrinsic stress induced by corrosion and environmental loads such as; wind, waves, and operational activities. The reliability of the fixed offshore platform was also assessed using Monte Carlo's reliability method. The study utilized advanced design equations to evaluate the structural reliability and rate of corrosion of the fixed offshore platform in order to estimate the safety of the structure. Results indicated that there are high stress values in the beam and column connections and also in the columns due to the effect of depleting cross-sectional area with respect to time and also the intrinsic stresses as a result of the applied loadings. Hence, selecting a high-grade steel and a higher cross-sectional area for structural members with slow the rate of corrosion and also reduce the intrinsic stresses due to the loadings on the structure. This will not only improve the load-bearing capacity but also significantly reduced the risk of structural failure, aligning well with empirical data. Furthermore, the study highlighted the importance of considering the interaction between material properties, connection characteristics, and loading conditions in the design process. These findings contribute to the development of more robust and durable fixed offshore platforms, ensuring their safety and longevity in demanding operational environments.

Keywords: corrosion, finite element analysis, fixed-offshore platform, weld

1. Introduction

Fixed offshore platforms are vital structures in the energy sector, serving as essential hubs for extracting and processing oil and gas resources from beneath the ocean floor. The structural integrity of these platforms is of utmost importance, particularly given the severe and unpredictable marine environments in which they operate. The combination of harsh weather, corrosive saltwater, and dynamic loads presents significant challenges to the durability of these platforms. Steel beam and column joints, including welded connections, play a critical role in maintaining the platform's overall stability and load-bearing capacity, particularly when subjected to corrosion and fluctuating environmental forces (Abejide et al., 2022). Among the various structural elements, welded beam and column joints are integral to the platform's resilience, ensuring the transfer of loads between different components. These joints must withstand a combination of static and dynamic forces, including the weight of the platform, environmental loads from waves, wind, and ocean currents, as well as operational forces during drilling and production activities. The effects of corrosion further complicate this, as it reduces

the cross-sectional area of steel components, leading to reduced strength and increased vulnerability over time (He et al., 2023). As a result, ensuring the reliability of these joints is paramount for the long-term safety and operational efficiency of offshore platforms. Corrosion is particularly insidious in offshore environments, as the constant exposure to saltwater accelerates the deterioration of steel. In welded steel joints, corrosion can be even more problematic due to the presence of residual stresses from welding, which can act as initiation sites for cracks and corrosion pits. The presence of pitting corrosion, a localized form of corrosion, can drastically reduce the shear strength of welded joints, jeopardizing the platform's ability to withstand lateral forces and potentially leading to structural failure (Walter et al., 2024). Traditional design codes, such as SANS 10162 and AASHTO LRFD, offer general guidelines for designing welded joints and beams in offshore platforms, incorporating conservative safety factors to account for uncertainties. However, these codes may not fully account for the unique conditions encountered in marine environments, including corrosion degradation and complex load interactions. This highlights the growing need for more refined design methods that consider the specific challenges of offshore structures, especially under long-term exposure to corrosive conditions (Brijder et al., 2022). Recent advancements in computational modeling, such as Finite Element Analysis (FEA), have transformed the study of welded joints under complex loading and corrosion conditions. FEA allows for detailed simulations of stress distributions, deformation patterns, and potential failure modes in steel joints, considering the effects of corrosion on material properties and structural behavior. By integrating corrosion models into FEA, engineers can predict how corrosion-induced material loss affects the long-term reliability of the structure. This, in turn, provides insights into the development of mitigation strategies, such as optimized weld geometries, improved material selection, and protective coatings that enhance corrosion resistance (Zhou et al., 2024). Moreover, reliability analysis plays a crucial role in understanding the performance of offshore platforms over their service life. Reliability-based design approaches allow engineers to quantify the probability of failure and assess the long-term durability of welded joints subjected to corrosion. This is essential in ensuring that offshore platforms maintain a high level of safety and functionality despite the inevitable degradation of materials. Reliability modeling also helps in determining maintenance intervals and predicting when structural interventions may be needed, reducing the risk of catastrophic failures in service (Ghanadi et al., 2024).

This study seeks to address the critical issues of corrosion, shear strength, and reliability in welded steel beam and column joints in offshore platforms. By employing a combination of experimental investigations, numerical simulations, and reliability-based assessments, the research aims to develop practical design recommendations that improve the durability, safety, and cost-effectiveness of offshore structures. Understanding the behavior of welded joints under real-world conditions, including the impact of corrosion, is key to enhancing the resilience of offshore energy infrastructure for years to come.

2. Background of study

2.1. Welded column behavior in offshore environments

Welded steel columns are fundamental components in offshore platforms due to their capacity to bear axial and lateral forces. These columns in offshore structures endure complex loading conditions, including wave, wind, and seismic forces. A significant concern in such environments is the combination of these loads with the corrosive effects of seawater, which degrades the material over time, particularly at the welds. Weld quality is critical, as defects in welds substantially reduce the shear strength and overall stability of the columns (Wang et al., 2024a). The shear strength of a welded steel column can be estimated using classical shear strength theory. For thin-walled structures like I-section or tubular columns, which are common in offshore applications, the shear strength V is given by:

$$V = A_w \cdot \tau_{max} \tag{1}$$

where A_w is effective shear area of the web and τ_{max} is maximum shear stresses the material can withstand.

In welded connections, the properties of the weld metal and its geometry significantly influence τ_{max}. The welding process induces residual stresses and alters the microstructure at the heat-affected zone (HAZ), creating stress concentration points that reduce the effective shear strength (Rautiainen et al., 2023). Researches emphasize that corrosion-induced deterioration in the weld zone reduces the

ultimate shear capacity of welded joints in offshore platforms. Their study showed a decrease of up to 25% in shear strength within the first five years of seawater exposure (Wang et al., 2024b). Methods like applying corrosion-resistant coatings and performing post-weld heat treatments can improve the longevity and shear strength of these columns.

2.2. Shear strength optimization using welding techniques and codes

Optimizing the shear strength of welded columns involves careful material selection, advanced welding techniques, and strict adherence to design codes such as AWS D1.1: Structural Welding Code – Steel (American Welding Society, 2020) and ISO 19902 standard (International Organization for Standardization, 2020a). These codes specify the required weld size, material grade, and prequalification criteria for offshore applications, where extreme environmental conditions necessitate stronger and more reliable welded joints.

The AWS D1.1 structural welding code (American Welding Society, 2020) specifies that the design shear strength of a welded steel column V_n is calculated as:

$$V_n = 0.6 \cdot F_y \cdot A_w \tag{2}$$

where F_y is yield strength of the steel material, A_w is effective shear area.

For offshore platforms, this equation is adjusted to account for dynamic loading conditions like wave action and wind forces by introducing a dynamic load factor γ_d:

$$V_n = 0.6 \cdot F_y \cdot A_w \cdot \gamma_d \tag{3}$$

Welding techniques such as Submerged Arc Welding (SAW) and Friction Stir Welding (FSW) have been extensively researched for their ability to produce high-quality welds with minimal (Kollár, 2023). Friction Stir Welding, in particular, offers significant advantages by reducing common defects such as porosity and cracking, which adversely affect shear strength in the welded zone. The resulting joints exhibit higher fatigue resistance and lower stress concentrations, enhancing shear performance under cyclic loading conditions (Dutta et al., 2024). Research demonstrated that FSW increases the shear strength of welded offshore columns by 18% compared to traditional Gas Metal Arc Welding (GMAW). This improvement is attributed to the uniform microstructure and reduced residual stresses, leading to higher effective shear strength in both the weld zone and the surrounding material (Chen et al., 2024b).

2.3. Structural welding

Structural welding is a process by which the parts that are to be connected are heated and fused with supplementary molten metal at the joint. A relatively small depth of material will become molten, and upon cooling, the structural steel and weld metal will act as one continuous part where they are joined (Chen et al., 2024a).

Fillet welds are most common and used in all structures. Weld sizes are specified in 1/16 in. (1.5875 mm) increments. A fillet weld can be loaded in any direction in shear, compression, or tension. However, it always fails in shear (Şeker, 2021). In the simulations, E70XX welding electrodes were selected due to their compatibility with the base metal (S460 high strength structural steel). These electrodes have a tensile strength of 482 N/mm^2, which closely matches the base material's yield strength of 460 N/mm^2, ensuring minimal residual stresses and consistent mechanical properties in the welded zone. The chemical composition of the welding consumables was also chosen to align with that of the base steel, maintaining similar carbon equivalence and corrosion resistance. This ensures the mechanical and chemical homogeneity of the joint, which is critical for accurate finite element simulations and the reliability of offshore structures under corrosive conditions. The shear failure of the fillet weld occurs along a plane through the throat of the weld, as shown in the Fig. 1.
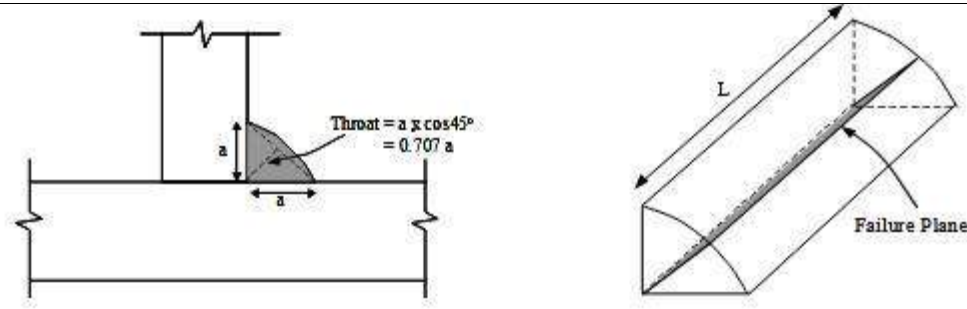
Fig. 1. Welded steel joint.

Table 1 shows the tensile strength of weld electrodes and their corresponding standard nomenclature.

Table 1. Tensile strength of weld electrodes (Pradhan et al., 2022)*.

Nomenclature of corresponding electrode	Tensile strength of weld electrode (ksi)	Tensile Strength (N/mm²)
E60XX	60	60 × 6.89476 = 413.69
E70XX	70	70 × 6.89476 = 482.63
E80XX	80	80 × 6.89476 = 551.58
E90XX	90	90 × 6.89476 = 620.53
E100XX	100	100 × 6.89476 = 689.48
E110XX	110	110 × 6.89476 = 758. 42
E120XX	120	120 × 6.89476 = 827.37

*Note: The strength of the electrode should match the strength of the base metal.

2.4. Monte Carlo reliability method

Monte Carlo simulations play a vital role in assessing the reliability of steel structures in offshore environments due to the inherent uncertainty in material properties, loadings, and environmental conditions. Offshore steel structures, such as platforms, are subjected to various corrosive forces that lead to the degradation of structural integrity over time, significantly affecting their reliability (Elqars et a., 2024). In the context of reliability analysis, Monte Carlo methods allow engineers to model these uncertainties by simulating numerous potential outcomes and quantifying the probability of failure (P_f) and the reliability index (β).

$$\beta = \frac{\mu_R - \mu_S}{\sqrt{\sigma_R^2 + \sigma_S^2}} \tag{4}$$

where μ_R and σ_R are the mean and standard deviation of the resistance, μ_S and σ_S are the mean and standard deviation of the loading

$$P_f = \int_{-\infty}^{0} f_g(g)\, dg \tag{5}$$

where $f_g(g)$ is the probability density function of the limit state function $g(x)$.
The limit state function for the fixed offshore platform is given by:

$$P_f = \int_{-\infty}^{0} f_g(g)\, dg \tag{6}$$

where A_0 is Initial cross-sectional area of the structural member; $\Delta A(t)$ is the cross-sectional area loss due to corrosion as a function of time t; f_y is the yield strength of the steel; $S_{wave}, S_{wind}, S_{current}$ are forces from waves, wind, and currents, respectively
Failure occurs when $g(x) \leq 0$, meaning that the applied loads exceed the structure's resistance.

3. Methodology

The offshore structure was subjected to high axial and lateral loads due to design loading and environmental conditions such as waves, wind, and current. In this analysis a fixed offshore platform is modeled, and loaded with respect to the design load as per AASHTO LRFD (American Association of State Highway and Transportation Officials, 2020) and ISO 19902:2020 (International Organization for Standardization, 2020a). The beam and column sections used are UB 254×102×25 and UB

356×137×33 respectively. These sections are fabricated using the hot-rolling process, which results in more uniform mechanical properties compared to cold-rolled or welded sections. Hot-rolled sections were selected for their superior performance in resisting dynamic loads and their higher reliability in corrosive environments. AWS D1.1/D1.1M (American Welding Society, 2020) is used to design the weld connection between the beam and column sections (American Institute of Steel Construction, 2024). The effect of uniform corrosion is also considered on the offshore structure over a design period of 50 years under service conditions. The intrinsic stress due to the applied loading and corrosion is then analyzed. The reliability of the structure during the course of its service life was also evaluated using Monte Carlo's reliability method.

3.1. Standard expression for corrosion rate

The fixed offshore platform is also being affected by uniform corrosion during its service life. This will lead to cross sectional area loss and more induced stress as the cross section available for carrying load is depleted (Soufnay et al., 2024). The formula for calculating corrosion rate (*CR*) is

$$CR = \frac{mm}{years} = 87.6 \ \frac{W}{DAT} \tag{7}$$

where *W* is weight loss in milligrams, *D* is density in g/mm^3, *A* is area in mm^2 and *T* is time of exposure in hours.

3.2. Steel cross sectional area loss

Cross-sectional area loss in steel structures, especially offshore platforms, is primarily caused by corrosion. Over time, exposure to harsh marine environments leads to the degradation of steel, reducing the effective cross-sectional area of critical structural components (Soufnay et al., 2024). This reduction increases the stress concentration on the remaining material, thereby weakening the structure and raising the probability of failure.

$$A(t) = A_0 \left(1 - \frac{CR \cdot t}{100}\right) \tag{8}$$

where A_0 is the initial cross-sectional area, *CR* is the corrosion rate (% loss per year) and *t* is the time in years

3.3. Load analysis

Several live load components are included in the AASHTO LRFD (American Association of State Highway and Transportation Officials, 2020) and ISO 19901-3:2020 (International Organization for Standardization, 2020b). Specifications, which were combined and scaled to provide design live loads. Included among the elements are: The AASHTO LRFD design specifications and ISO 1991-3:2020), which are a widely used design code for offshore structures in countries across the globe.

3.3.1. Offshore platform live load

The fixed platform live load consists of four components (International Organization for Standardization, 2020b):
- Personnel loads = 2 kN/m^2
- Equipment loads = 5 kN/m^2
- Storage loads = 7 kN/m^2
- Dynamic loads = 5 kN/m^2

Live load acting on the fixed platform = 2 + 5 + 7 + 5 = 19 kN/m^2

These four components; the personnel loads, equipment loads, storage loads, dynamic loads, are combined to create the model for live load

3.3.2. Offshore platform dead load

Dear load consists of three components (International Organization for Standardization, 2020b):
- Permanent equipment dead load = 5 kN/m^2
- Structural steel dead load = 10 kN/m^2
- Sacrificial anode (aluminum alloy) dead load: **5 kN/m²**

Total sum of dead load (estimated) = 5 + 10 + 5 = 20 kN/m^2

Taking into consideration: environmental loads, construction loads, and so on, the dead load will be approximated = 25 kN/m^2

The AASHTO LRFD Design Specification (3.4.1 – Load factors), for factored loading design load can be determined from the relationship (American Association of State Highway and Transportation Officials, 2020):

$$\text{Design load} = 1.25\mathbf{D} + 1.75\mathbf{L} \tag{9}$$

where **D** represents the dead load and **L** represents the live load.

The load factors of 1.2 and 1.6 are specific to the AASHTO LRFD code and may vary in other LRFD design codes. Therefore:

Design load = 1.25[25] + 1.75[19] = 31.25 + 33.25 = 64.50 kN/m^2

3.4. Offshore platform design according to AASHTO LRFD 2020

The offshore platform model was analyzed as a fixed platform, meaning its base was fully constrained to simulate real-world conditions where the foundation is anchored to the seabed. The boundary conditions applied include fixing all degrees of freedom (translations and rotations) at the base to replicate this support. Fig. 2 illustrates the boundary conditions applied to the platform model. These conditions were essential for accurately modeling the platform's response to environmental loads and the design load.
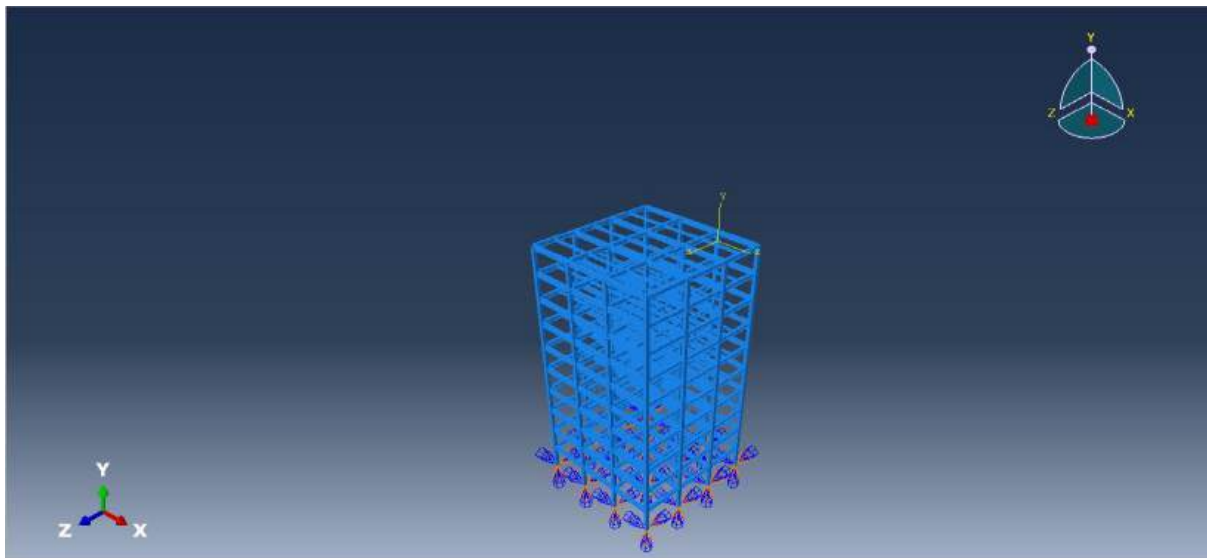

Fig. 2. Boundary condition of the fixed offshore platform (Encastre).

Table 2 gives the essential design parameters for the stochastic analysis used in the probabilistic determination of the safety criteria of the steel material.

Table 2. Parameters of stochastic model.

Material	Density	Young's modulus	Yield Stress	Poisson's ratio v	Strain
Steel	7850 kg/m^3	210 GPa	460 N/mm^2	0.3	0.0022

Fig. 3a illustrates the cross-sectional dimensions of the UB 254×102×25 beam, which was selected for the analysis of the fixed offshore platform. These dimensions provide the baseline reference for evaluating the structural performance of the beam under design and environmental loads. The beam's cross-section was integral to the FEA conducted in ABAQUS, where its geometric properties influenced stress distribution, deformation, and resistance to uniform corrosion.

Fig. 3b depicts the cross-sectional dimensions of the UB 356×137×33 column, used as a key structural element in the fixed offshore platform analysis. The column's geometry and size were critical in determining its load-bearing capacity, particularly under combined axial and lateral forces. This reference drawing serves as the foundation for incorporating the column into the FEA model, where its dimensions affected stress concentrations and reliability outcomes.
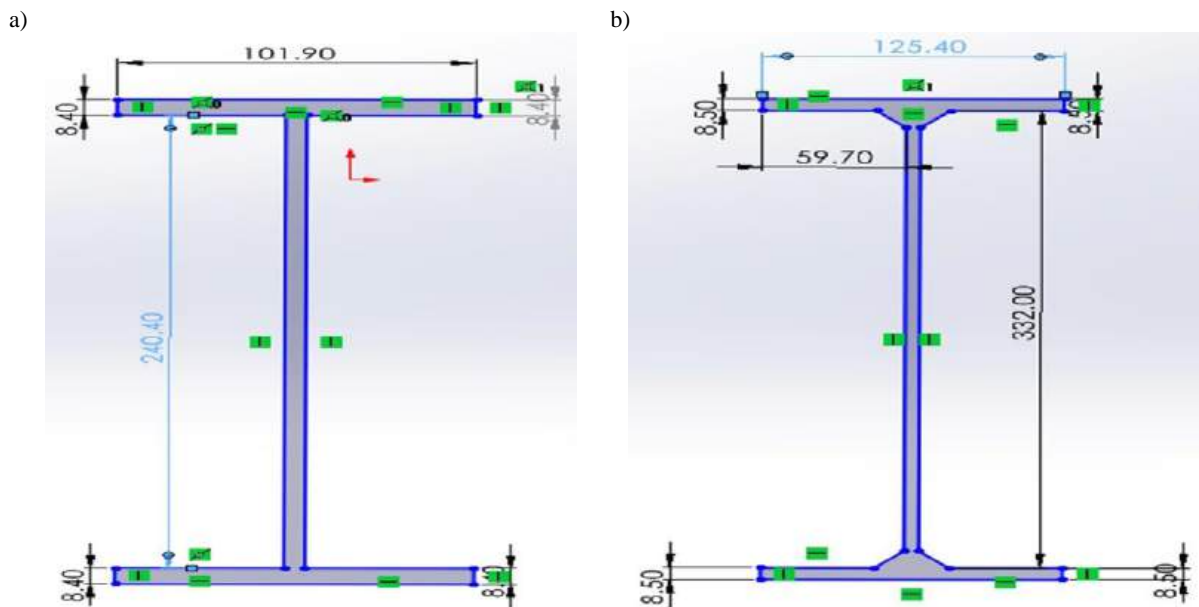
a)   b)

Fig. 3. a) steel beam cross section (UB 254×102×25) and b) steel column cross section (UB 356×137×33).

4. Results and discussion

4.1. Finite element analysis in Simulia ABAQUS CAE 2022

The fixed offshore platform was analyzed using Simulia ABAQUS CAE 2022 with respect to AASHTO-LRFD (American Association of State Highway and Transportation Officials, 2020) and AWS D1.1/D1.1M (American Welding Society, 2020). ABAQUS CAE does analysis based on finite element method and the analysis completed for this research is with respect to uniform corrosion in offshore and the effect on the integrity of the offshore structure. Over the course of 100 years at an interval of 10 years, the reduction in cross-sectional area with respect to uniform corrosion was examined in order to check the intrinsic stresses induced while in service. The reliability and the probability of failure of the fixed offshore structure was also evaluated using Monte Carlo's reliability method. The fixed offshore platform was subjected to design load of 64.50 kN/m². The FEA of the fixed platform following a non-linear stress pattern are also discussed below.

4.1.1. Von Mises stress distributions over fixed offshore platform in service condition

The fixed offshore platform subjected to uniform corrosion over a 100-year period exhibited increasing von Mises stresses due to cross-sectional area loss and material degradation. A non-linear finite element analysis revealed that after 10 years, maximum von Mises stresses were 7.846 N/m², as shown in Fig. 4. By 50 years, these values increased 8.000 N/m² as shown in Fig. 5. After 100 years, the stresses reached 8.311 N/m² as shown in Fig. 6. These findings confirm that uniform corrosion significantly affects the structural integrity of the platform over time, particularly at the columns and joints due to load transfer mechanisms. The von Mises stress criterion used here indicates the platform's susceptibility to yielding and potential failure. Importantly, despite the increase in stresses, the results remain within acceptable limits $\frac{f_y}{1.5}$ for S460 high strength structural steel. According to EN 10025-4:2023 (European Committee for Standardization, 2023), the yield strength of S460 grade steel is f_y = 460 N/mm² and its ultimate tensile strength ranges from 550 to 720 N/mm². The design stresses computed in this analysis do not exceed f_y when factoring in partial safety factors as per AASHTO LRFD (American Association of State Highway and Transportation Officials, 2020). The progressive stress accumulation highlights the detrimental impact of cross-sectional depletion, emphasizing the need for preventive measures to slow corrosion and maintain the platform's structural capacity.

The results underscore that while the platform's integrity remains intact within the design parameters, continued corrosion would necessitate reinforcement strategies and regular maintenance. This study demonstrates that addressing corrosion early could prolong the platform's lifespan and maintain its operational safety.
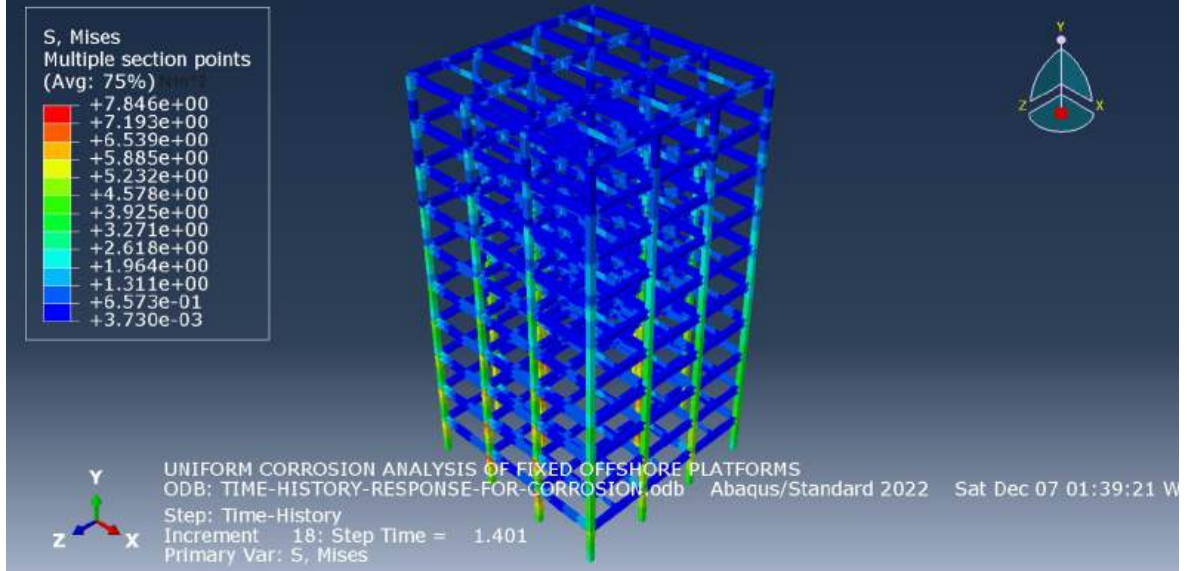
Fig. 4. Von Mises stress distribution (in N/m²) of the fixed offshore platform with respect to corrosion at 10 years.
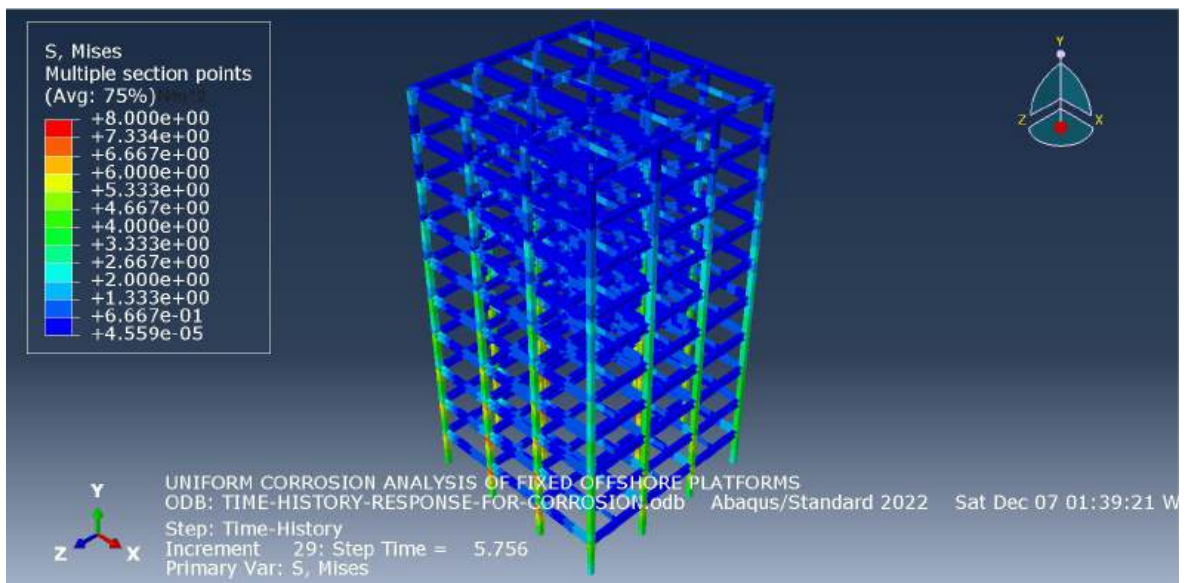

Fig. 5. Von Mises stress distribution (in N/m²) of the fixed offshore platform with respect to corrosion at 50 years.
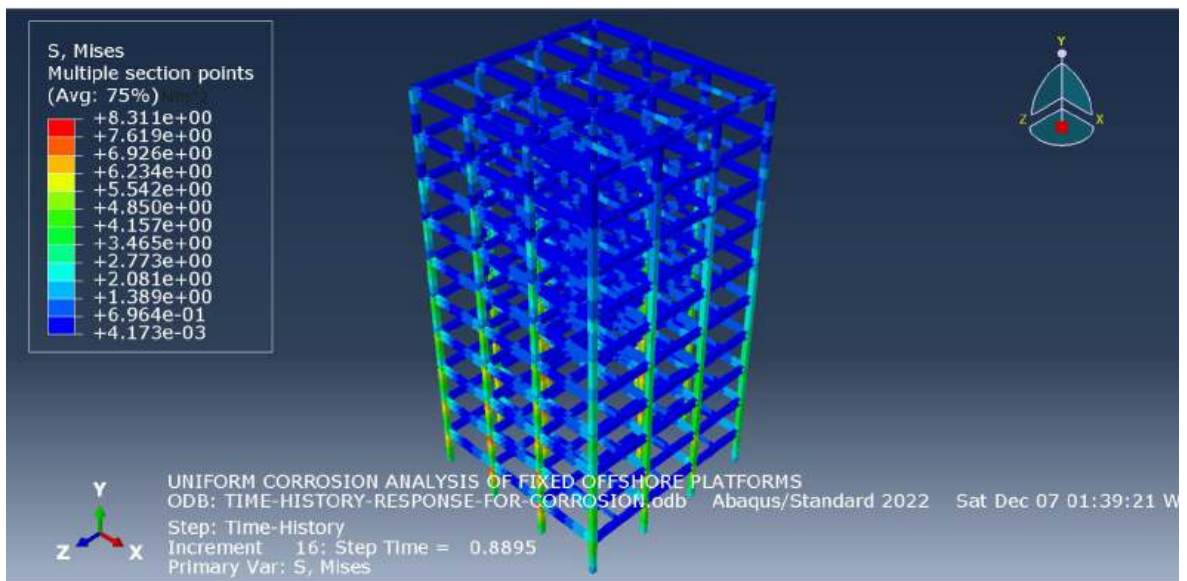

Fig. 6. Von Mises stress distribution (in N/m²) of the fixed offshore platform with respect to corrosion at 100 years.

4.1.2. Maximum principal stress distributions over fixed offshore platform in service condition

The fixed offshore platform under service conditions experienced increasing maximum principal stresses due to uniform corrosion and service loading. After 10 years, the maximum principal stress reached 1.665 N/m² as shown in Fig. 7, primarily concentrated at the columns and joints due to load transfer mechanisms. This trend intensified, with stress values rising to 1.940 N/m² as shown in Fig. 8 after 50 years and 2.253 N/m² as shown in Fig. 9 after 100 years. The progressive increase in maximum principal stresses highlights the critical impact of uniform corrosion on the platform's structural integrity. Although the stresses remain within the allowable limits $0.66\sqrt{f_{yk}}$, the rising trend indicates an elevated risk of localized failure over time, especially in areas subjected to high stress concentrations. These findings underscore the need for proactive maintenance strategies, including regular inspections and corrosion protection measures, to mitigate long-term degradation. The maximum principal stress distributions reveal that the platform's structural health degrades with time due to corrosion, emphasizing the importance of continuous monitoring to ensure safe operation over its service life.
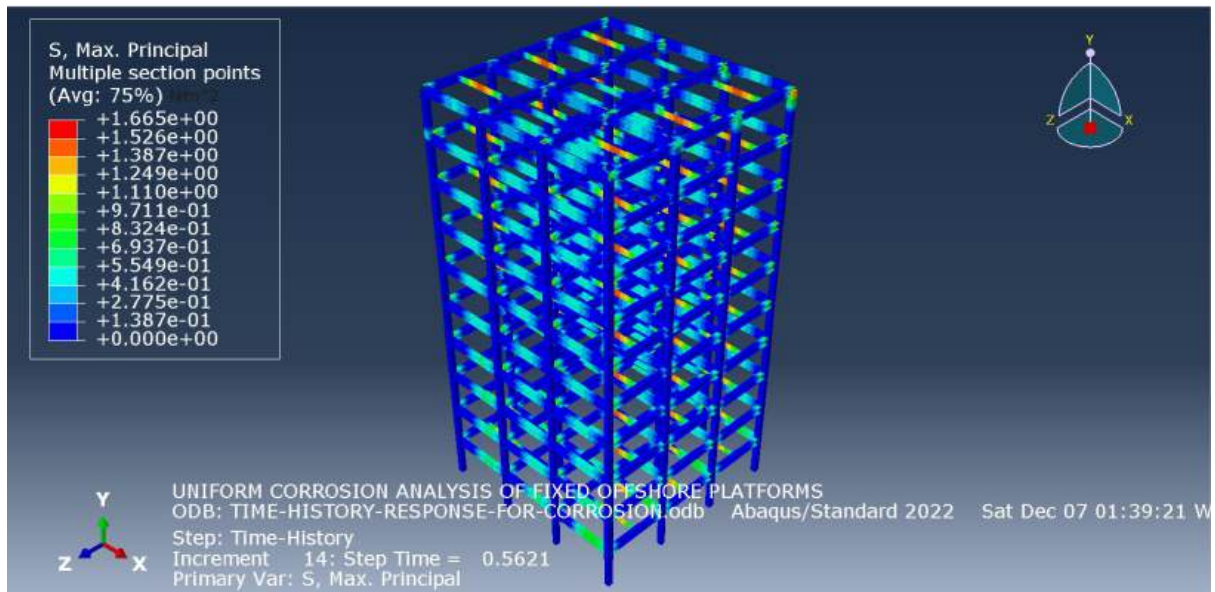

Fig. 7. Maximum principal stress distribution (in N/m²) of the fixed offshore platform with respect to corrosion at 10 years.
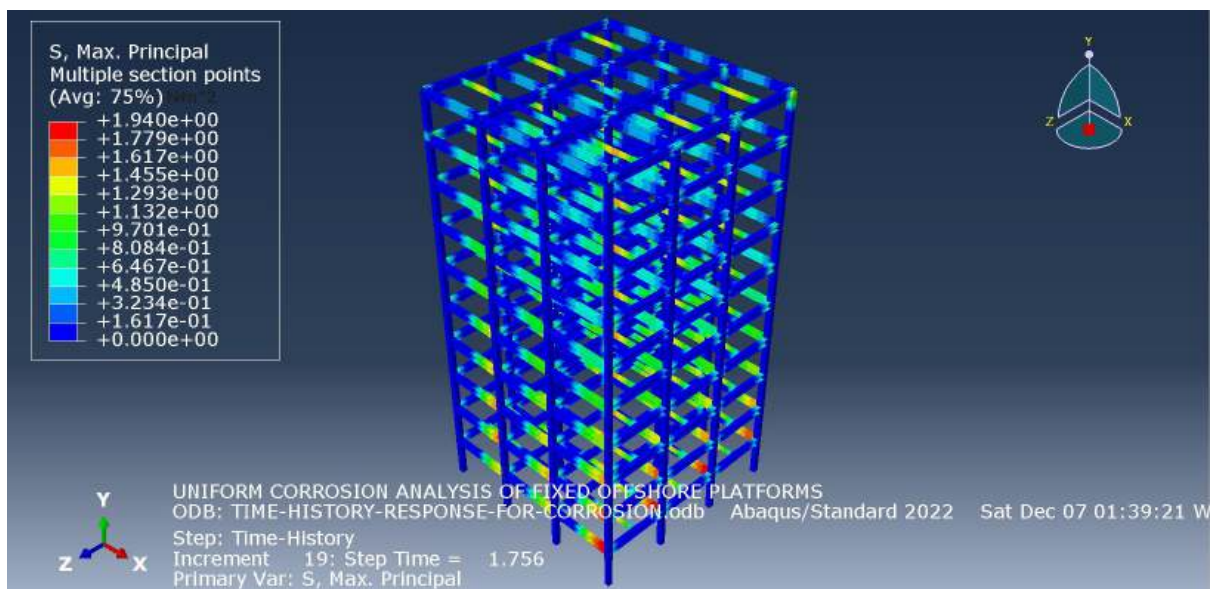

Fig. 8. Maximum principal stress distribution (in N/m²) of the fixed offshore platform with respect to corrosion at 50 years.
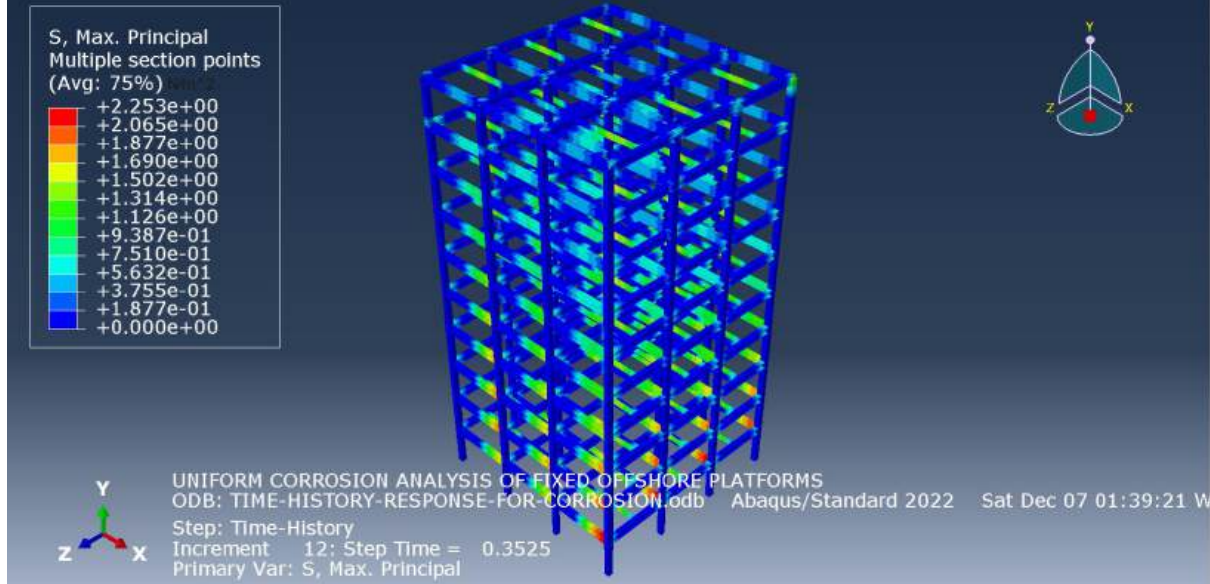
Fig. 9. Maximum principal stress distribution (in N/m²) of the fixed offshore platform with respect to corrosion at 100 years.

4.1.3. Tresca stress distributions over fixed offshore platform in service condition

The Tresca stress distribution in the fixed offshore platform subjected to uniform corrosion and design loading conditions reveals critical insights into its structural performance. At 10 years, the maximum Tresca stress reached 7.850 N/m² as shown in Fig. 10, with significant concentrations at the column bases and joints. By 50 years, the maximum stress increased to 8.000 N/m² as shown in Fig. 11, primarily due to cross-sectional area loss from corrosion, leading to higher stress concentrations around connections. After 100 years, the maximum Tresca stress reached 8.311 N/m² as shown in Fig. 12, indicating the potential for yielding and plastic deformation in highly stressed regions. The increasing shear stress over time highlights the platform's decreasing capacity to resist failure, particularly in areas subjected to load transfer. The progression of Tresca stress, driven by corrosion, suggests that beyond 50 years, the structure approaches critical stress levels, requiring maintenance or reinforcement to prevent yielding. The analysis confirms that while the platform remains within safe operating limits in the early years, the continuous rise in Tresca stress underlines the need for timely intervention to ensure long-term structural integrity.
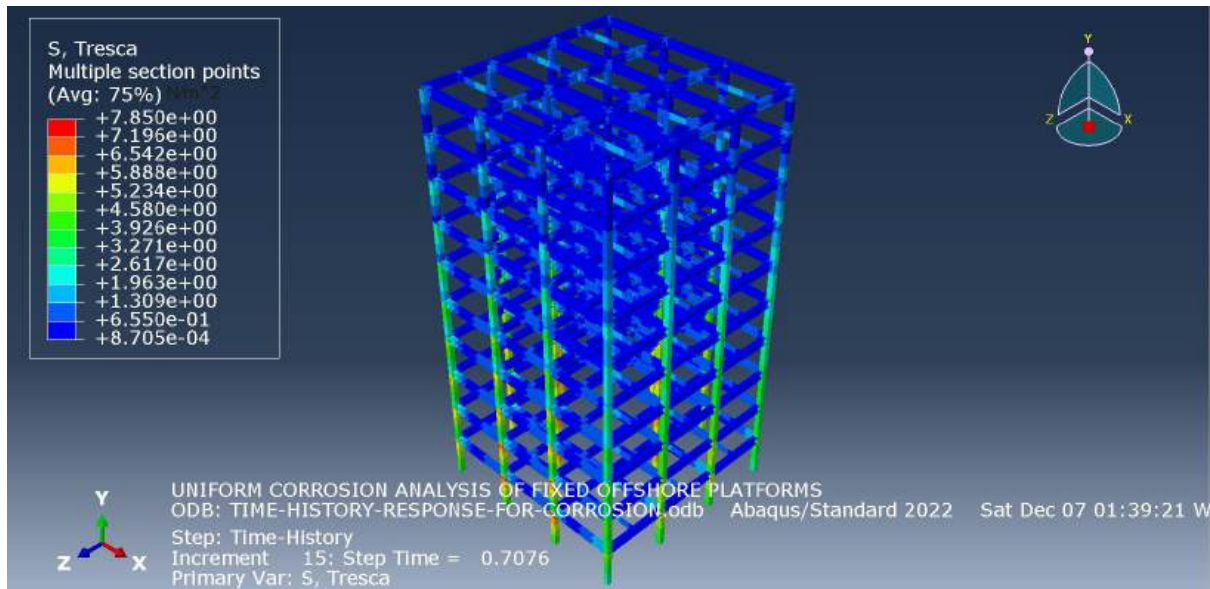

Fig. 10. Tresca stress distribution (in N/m²) of the fixed offshore platform with respect to corrosion at 10 years.
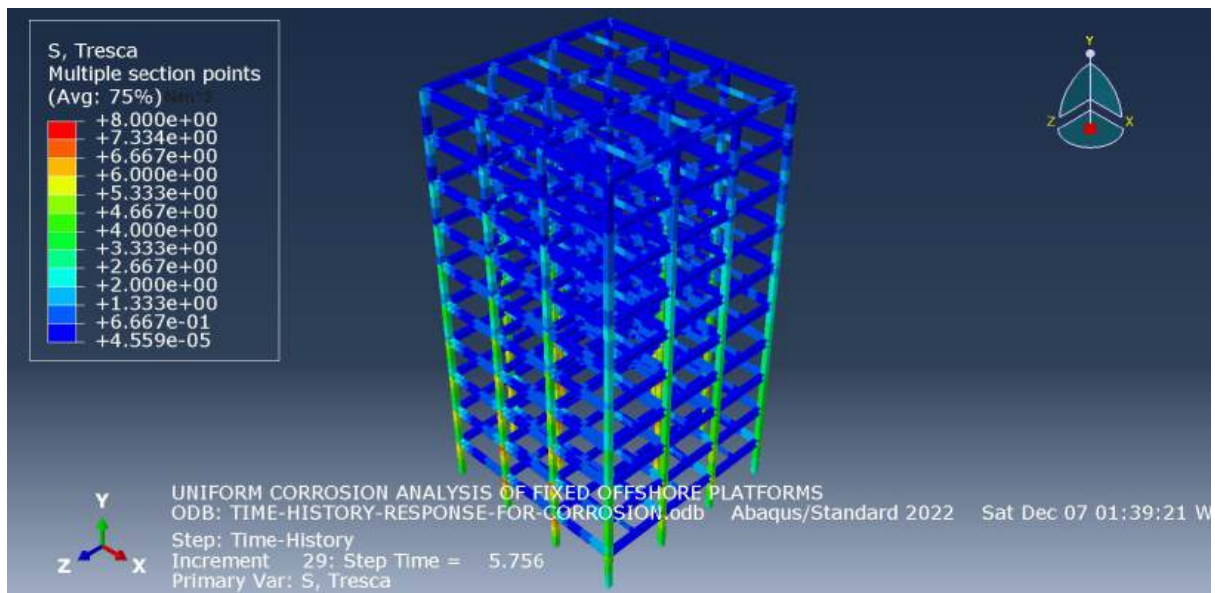
Fig. 11. Tresca stress distribution (in N/m^2) of the fixed offshore platform with respect to corrosion at 50 years.
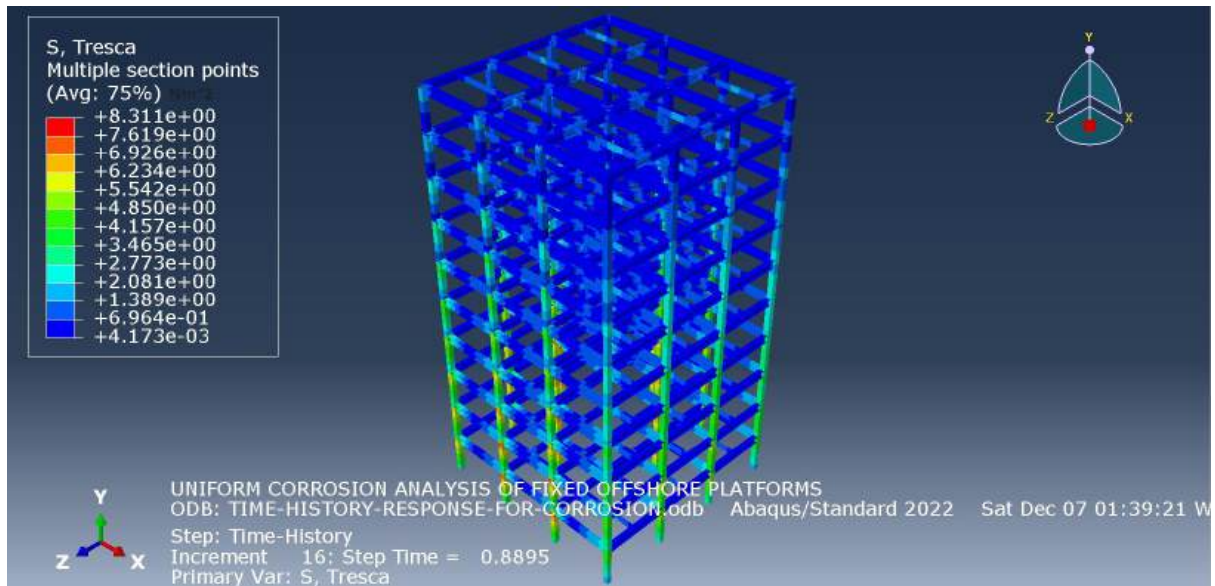

Fig. 12. Tresca stress distribution (in N/m^2) of the fixed offshore platform with respect to corrosion at 100 years.

Table 3 below captures the maximum stress distributions with respect to uniform corrosion over the course of the design period of the fixed offshore platform from the FEA in Simulia ABAQUS 2022 software.

Table 3. Maximum stress distributions in the fixed offshore platform during its service period.

Stress (N/m^2)	Period		
	10 Years	**50 Years**	**100 Years**
von Mises	7.846	8.000	8.311
maximum principal	1.665	1.940	2.253
Tresca	7.850	8.000	8.311

Fig. 13 shows a graphical representation of the FEA stress distribution over the fixed offshore platform. The values of the von Mises stress distribution and the Tresca stress distribution are closely similar hence the lines lap each other in the plot. Since von Mises stress is similar to the Tresca stress in the analysis of a fixed offshore platform, it implies that the material is experiencing uniform or nearly uniform stress conditions, particularly shear stress. This indicates that the principal stresses are distributed in a way that yields minimal differences between the distortion energy theory (von Mises) and maximum shear stress theory (Tresca). Such similarity suggests the structure is well-designed to handle the applied loading, with predictable material behavior and reduced complexity in evaluating

safety factors. This alignment highlights the platform's structural efficiency and durability under its operational conditions.
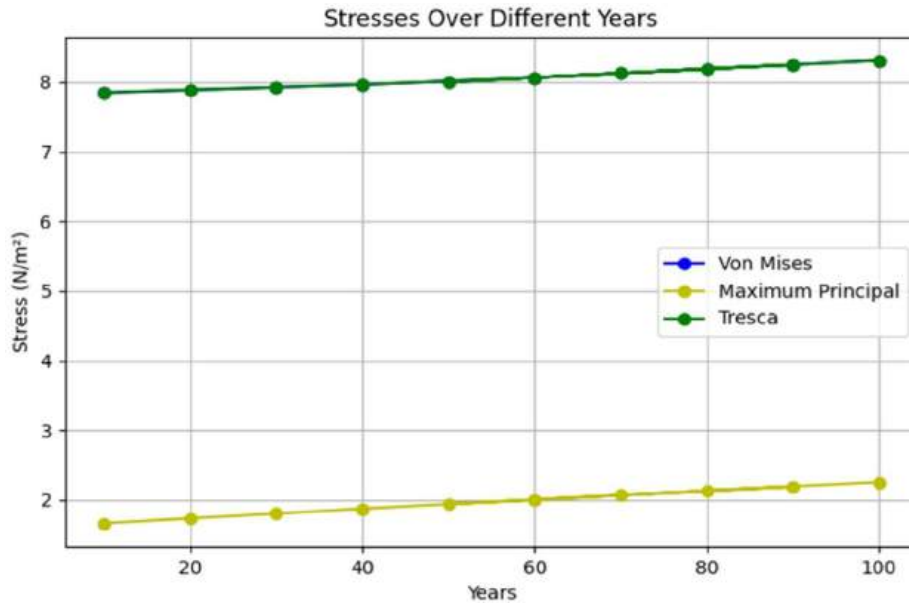

Fig. 13. Graphical representation of the stress distributions in the fixed offshore platform during its service life.

4.2. Monte Carlo's reliability analysis in PYTHON

This section discusses the findings of the reliability analysis using the Monte Carlo reliability analyses method conducted on the fixed offshore structure using an algorithm in PYTHON to examine and simulate the behavior of the fixed offshore platform on exposure to uniform corrosion during a design period of 100 years. Through an interval of 10 years, the reduction in cross- sectional area, the probability of failure, and the reliability of the structure was examined using the expression for the rate of corrosion and the limit state equation in order to check the structural effectiveness of the fixed offshore structure while in service, resisting the effect of moment, deflection and shear. Monte Carlo's reliability method coded in PYTHON is employed in the computation, making use of the tabulated data in Table 4 and the relevant limit state functions and the rate of corrosion expression.

Table 4. Parameters of the stochastic model for rolled steel beams on offshore platforms.

S/No	Design Variables	Unit	Distribution Type	COV	E(Xi)	S(Xi)
1	Steel strength (f_{yk})	N/mm²	Lognormal	0.15	350	52.5
2	Length (L)	mm	Normal	0.045	9000	450
3	Width (W)	mm	Normal	0.045	9000	450
4	Depth (d)	mm	Normal	0.15	30000	1500
5	Area of the structure	mm²	Normal	0.3	8.1×10^7	2.43×10^6
6	Imposed load Q_k	kN/m²	Lognormal	0.3	5.0×10^{-3}	1.5×10^{-3}
7	Wind load (W_k)	kN/m²	Lognormal	0.3	5.0×10^{-3}	1.5×10^{-3}
8	Wave load (W_v)	kN/m²	Lognormal	0.25	7.0×10^{-3}	2.1×10^{-3}
9	Current load (C_k)	kN/m²	Lognormal	0.25	3.0×10^{-3}	0.9×10^{-3}

The reliability levels were calculated using the deterministic and statistical parameters of Table 4. The *Coefficient of Variation* (COV) highlights the relative uncertainty of each parameter, identifying which variables are more prone to variability and impact reliability. The *Expected Value* (E(*Xi*)) represents the average performance or baseline value of each parameter, serving as the foundation for structural analysis. The *Standard Deviation* (S(*Xi*)) measures the dispersion of each parameter, indicating the range of possible deviations from the mean that influence design consistency and reliability. The rate of corrosion equation and the limit state equation *g(x)* was used based on Monte Carlo's reliability method in a PYTHON algorithm. The Fig. 14 depict the cross-sectional area loss of the fixed offshore structure with respect to time during its service period, the reliability of the fixed offshore structure with respect to time during its service period, and also the probability of failure of the fixed platform during its service period.

Based on the plot for the *Cross-Sectional Area Loss Over Time*, there is a steady linear increase in cross-sectional area loss for both the UB 254×102 beam (blue) and UB 356×137 column (green). As the years progress, corrosion causes the cross-sectional areas of both components to degrade, with the

column experiencing slightly higher losses due to its larger size. This reflects the expected cumulative material degradation from corrosion.
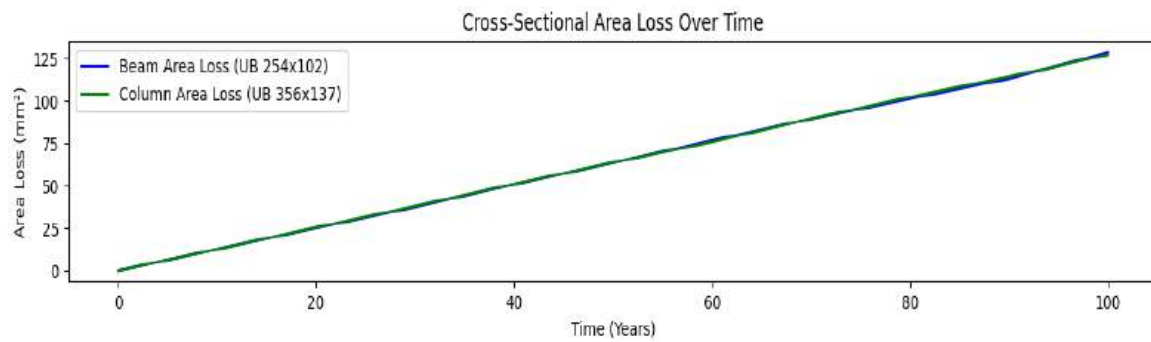

Fig. 14. A plot showing the relationship between corrosion in years and cross-sectional area loss of structural steel during its service life.

Based on the plot for the *Reliability Over Time* (Fig. 15), there is a progressive decrease in reliability over time for the UB 254×102 beam (blue) and the UB 356×137 column (green). The beam shows a more significant decline in reliability, suggesting it is more sensitive to cross-sectional area loss due to its size. This curve reflects the structural system's weakening due to material degradation, leading to lower reliability as time progresses. The cross-sectional area of is directly proportional to the reliability of the structure. Hence, a larger cross-sectional area implies a slower area loss.
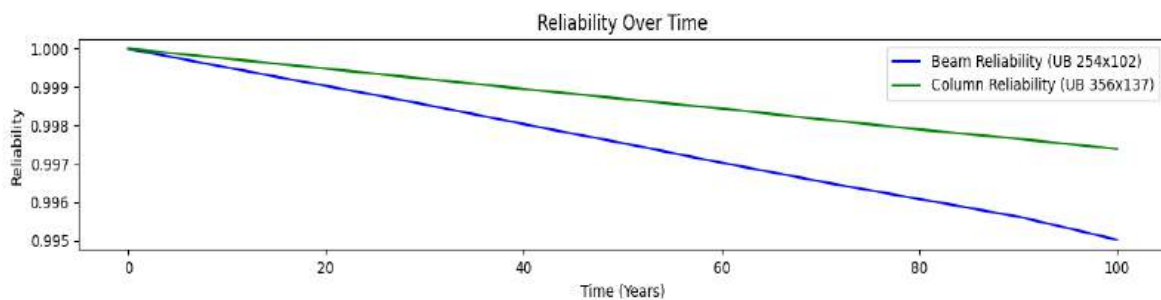

Fig. 15. A plot showing the relationship between reliability of the fixed offshore platform during its service life during its service life.

Based on the plot for *Probability of Failure Over Time* (Fig. 16) for the fixed offshore platform in service, there is an increasing probability of failure over time as the structure becomes more vulnerable due to corrosion. The UB 254×102 beam's probability of failure (red) grows more rapidly than the UB 356×137 column's (orange), indicating that the beam is more likely to fail sooner due to its smaller initial cross-sectional area. This implies that a smaller cross-sectional area is more susceptible to failure than a larger cross-sectional area as corrosion is simply the degradation and area loss of steel.

Corrosion has a progressive impact on the integrity of the structural steel in the fixed offshore structure making it vulnerable in terms of its reliability and it increases failure probability.
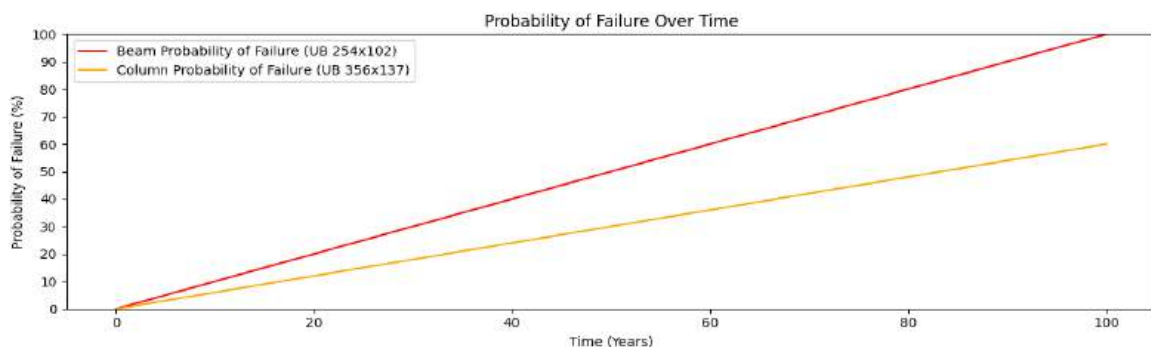

Fig. 16. A plot showing the relationship between probability of failure with respect to service life of the fixed offshore platform.

5. Conclusions and recommendations

5.1. Conclusions

This research has demonstrated a comprehensive assessment of the structural effectiveness of fixed offshore platforms subjected to uniform corrosion. Using Finite Element Analysis in ABAQUS CAE 2022 software and Monte Carlo reliability simulations in PYTHON 3.12 software, we evaluated the degradation of structural integrity under service conditions. The objectives of quantifying the impact of uniform corrosion, assessing intrinsic stress distributions, and predicting reliability over the platform's design life were successfully achieved. Results indicated progressive stress accumulation in critical structural elements, such as beams and column joints, attributed to cross-sectional area depletion. The von Mises, maximum principal, and Tresca stress distributions confirmed that even with acceptable limits for S460 high strength structural steel, continuous corrosion necessitates regular monitoring and maintenance. The reliability analysis further revealed declining reliability indices and increasing probabilities of failure over time, emphasizing the need for proactive structural interventions.

The study also validated that selecting high-grade steel and increasing cross-sectional areas can mitigate stress concentrations and reduce corrosion effects, ensuring extended service life. By aligning computational modeling with design standards such as AASHTO LRFD Bridge Design Specifications and AWS D1.1 Structural Weklding Code, this work contributes valuable insights for improving the durability and safety of offshore platforms in challenging marine environments.

5.2. Recommendations

The adoption of high-grade steel with superior corrosion resistance and fatigue properties is recommended to slow the degradation process and maintain structural effectiveness over time. Regular inspection and application of corrosion protection measures, such as coatings or cathodic protection, should be incorporated into the platform's lifecycle management.

References

Abejide, K., Akadang, O. L. B, & Abejide, O. S. (2022). Stochastic Evaluation of Structural Steel Plates Corrosion in Offshore Platforms. *Haya: The Saudi Journal of Life Sciences*, *7*(5), 163-175. https://doi.org/10.36348/sjls.2022.v07i05.004

American Association of State Highway and Transportation Officials. (2020). *LRFD Bridge Design Specifications* (9th Ed.). American Association of State Highway and Transportation Officials.

American Institute of Steel Construction. (2024). *AISC Student Steel Bridge Competition*. https://www.aisc.org/globalassets/aisc/university-programs/ssbc/rules/ssbc-2024-rules_final.pdf

American Welding Society. (2020). AWS D1.1/D1.1M*: Structural Welding Code – Steel (23rd Ed.). American Welding Society. https://pubs.aws.org/Download_PDFS/D1.1-D1.1M-2015-PV.pdf?srsltid=AfmBOoo13mUQ0-yYri65tN1UHx_4NOSb7RFxHbwmXRcrD55Y7rWgV8Ll

Brijder, R., Hagen, C. H., Cortés, A., Irizar, A., Thibbotuwa, U. C., Helsen, S., Vásquez, S., & Ompusunggu, A. P. (2022). Review of corrosion monitoring and prognostics in offshore wind turbine structures: Current status and feasible approaches. *Frontiers in Energy Research*, *10*, Article 991343. https://doi.org/10.3389/fenrg.2022.991343

Chen, B. Q., Liu, K., & Xu, S. (2024a). Recent advances in aluminum welding for marine structures. *Journal of Marine Science and Engineering*, *12*(9), Article 1539. https://doi.org/10.3390/jmse12091539

Chen, M. T., Gong, Z., Cao, H., Zhang, J., Ren, F., Ho, J. C. M., & Lai, M. (2024b). Residual mechanical properties of corroded ultra-high-strength steels and weld metals. *Thin-Walled Structures*, *205*, Article 112397. https://doi.org/10.1016/j.tws.2024.112397

Dutta, A., Pal, S. K., & Panda, S. K. (2024). Friction stir seam-and spot-welded aluminium honeycombs: Enhanced structural integrity eliminating adhesive bonding challenges. *Journal of Materials Processing Technology*, *330*, Article 118449. https://doi.org/10.1016/j.jmatprotec.2024.118449

Elqars, E., Bimoussa, A., Barhoumi, A., Laamari, Y., Byadi, S., Oubella, A., Riadi, Y., Essadki, A., Auhmani, A., & Itto, M. Y. A. (2024). Synthesis and characterization of bis-isoxazoline-thiosemicarbazone as a corrosion inhibitor for carbon steel: Experimental study, and molecular simulation. *Journal of Molecular Structure*, *1312*, Article 138476. https://doi.org/10.1016/j.molstruc.2024.138476

European Committee for Standardization. (2023). *Hot rolled products of structural steels - Part 4: Technical delivery conditions for thermomechanical rolled weldable fine grain structural steels* (EN Standard No 10025-4:2023).

Ghanadi, M., Hultgren, G., Narström, T., Clarin, M., & Barsoum, Z. (2024). Fatigue assessment of welded joints-size effect and probabilistic approach. *Journal of Constructional Steel Research*, *221*, Article 108884. https://doi.org/10.1016/j.jcsr.2024.108884

He, Z., He, C., Ma, G., Yang, W., & Kang, X. (2023). Performance assessment of partially corrosion-damaged RC segment incorporating the spatial variability of steel corrosion. *Construction and Building Materials*, *371*, Article 130789. https://doi.org/10.1016/j.conbuildmat.2023.130789

Kollár, D. (2023). Numerical modelling on the influence of repair welding during manufacturing on residual stresses and distortions of T-joints. *Results in Engineering*, *20*, Article 101535. https://doi.org/10.1016/j.rineng.2023.101535

International Organization for Standardization. (2020a). *Petroleum and natural gas industries – Fixed steel offshore structures* (ISO Standard No. 19902:2020). https://www.iso.org/standard/65688.html

International Organization for Standardization. (2020b). *Petroleum and natural gas industries – Specific requirements for offshore structures. Part 3: Topsides structure* (ISO Standard No. 19901-3:2020. https://www.iso.org/standard/65041.html

Pradhan, R., Joshi, A. P., Sunny, M. R., & Sarkar, A. (2022). Performance of predictive models to determine weld bead shape parameters for shielded gas metal arc welded T-joints. *Marine Structures*, *86*, Article 103290. https://doi.org/10.1016/j.marstruc.2022.103290

Rautiainen, M., Remes, H., Niemelä, A., & Romanoff, J. (2023). Fatigue strength assessment of complex welded structures with severe force concentrations along a weld seam. *International Journal of Fatigue*, *167*, Article 107321. https://doi.org/10.1016/j.ijfatigue.2022.107321

Saufnay, L., Jaspart, J. P., & Demonceau, J. F. (2024). Improvement of the prediction of the flexural buckling resistance of hot-rolled mild and high-strength steel members. *Engineering Structures*, *315*, Article 118460. https://doi.org/10.1016/j.engstruct.2024.118460

Şeker, Ö. (2021). *A practical finite element model of tsadwa type semi-rigid connections for push-over analysis of steel frames in SAP2000* [Master's thesis, Izmir Institute of Technology].

Walter, N. M. B., Lemos, G. V. B., Kieckow, G. S., Buzzatti, D. T., Buzzatti, J. T., Mattei, F., Reguly, A., Clarke, T., Paes, M. T. P., Dalpiaz, G., & Marinho, R. R. (2024). Investigating microstructure, mechanical properties, and pitting corrosion resistance of UNS S32760 super duplex stainless steel after linear friction welding. *Journal of Materials Research and Technology*, *31*, 1637-1643. https://doi.org/10.1016/j.jmrt.2024.06.191

Wang, H., Wang, J., Cao, J., Zhao, J., Qian, W., & Du, H. (2024a). Optimization design of main hinge joint structure based on weld failure analysis. *Engineering Failure Analysis*, *163*, Article 108447. https://doi.org/10.1016/j.engfailanal.2024.108447

Wang, L., Qian, X., & Feng, L. (2024b). Effect of welding residual stresses on the fatigue life assessment of welded connections. *International Journal of Fatigue*, *189*, Article 108570. https://doi.org/10.1016/j.ijfatigue.2024.108570

Zhou, H., Kinefuchi, M., Takashima, Y., & Shibanuma, K. (2024). Multiscale modelling strategy for predicting fatigue performance of welded joints. *International Journal of Mechanical Sciences*, *284*, Article 109751. https://doi.org/10.1016/j.ijmecsci.2024.109751

Efektywność Konstrukcyjna Stałych Platform Morskich w Kontekście Równomiernej Korozji

Streszczenie

W artykule przedstawiono skuteczność strukturalną stałych platform morskich, rozwiązując problemy związane ze złożonymi warunkami obciążenia w środowiskach morskich. Wydajność strukturalną stałej platformy morskiej oceniono przy użyciu analizy metodą elementów skończonych wykonanej w oprogramowaniu ABAQUS CAE, ze szczególnym uwzględnieniem wpływu naprężeń wewnętrznych wywołanych korozją oraz obciążeń środowiskowych, takich jak wiatr, fale i działania operacyjne. Niezawodność stałej platformy morskiej oceniono również przy użyciu metody niezawodności Monte Carlo. W badaniu wykorzystano zaawansowane równania projektowe do oceny niezawodności strukturalnej i szybkości korozji stałej platformy morskiej w celu oszacowania bezpieczeństwa konstrukcji. Wyniki wykazały, że w połączeniach belek i kolumn oraz w kolumnach występują wysokie wartości naprężeń ze względu na efekt zmniejszającego się pola

przekroju poprzecznego w stosunku do czasu, a także naprężeń wewnętrznych w wyniku zastosowanych obciążeń. Stąd wybór stali wysokiej jakości i większego pola przekroju poprzecznego dla elementów konstrukcyjnych spowalnia szybkość korozji, a także zmniejsza naprężenia wewnętrzne konstrukcji spowodowane obciążeniami. Nie tylko poprawia to nośność, ale także znacznie zmniejsza ryzyko awarii konstrukcyjnej, co dobrze wpisuje się w dane doświadczalne. Ponadto badanie podkreśliło znaczenie uwzględnienia interakcji między właściwościami materiału, cechami połączenia i warunkami obciążenia w procesie projektowania. Wyniki te przyczynią się do rozwoju bardziej wytrzymałych i trwałych stałych platform morskich, zapewniając ich bezpieczeństwo i długowieczność w wymagających środowiskach operacyjnych.

Słowa kluczowe: korozja, analiza elemntów skończonych, stałe platformy morskie, spoina

Original Research

Effect of Single-Point Incremental Forming Process Parameters on Roughness of the Outer Surface of Conical Drawpieces from CP Titanium Sheets

Marcin Szpunar [1],* [iD], Robert Ostrowski [2] [iD], Andrzej Dzierwa [3] [iD]

[1] MTU Aero Engines Polska, Tajęcina 108, 36-002 Jasionka, Poland

[2] Department of Materials Forming and Processing, Faculty of Mechanical Engineering and Aeronautics, Rzeszów University of Technology, al. Powstancow Warszawy 8, 35-959 Rzeszow, Poland; rostrows@prz.edu.pl

[3] Department of Manufacturing and Production Engineering, Faculty of Mechanical Engineering and Aeronautics, Rzeszów University of Technology, al. Powstancow Warszawy 8, 35-959 Rzeszow, Poland; adzierwa@prz.edu.pl

* Correspondence: marcin.szpunar@outlook.com

Abstract

With the widespread use of numerically controlled machine tools, single-point incremental forming (SPIF) process has enjoyed growing interest in the industry. This article presents the results of research on the influence of forming process parameters (step size, tool rotational speed, feed rate and forming strategy) on the roughness of the outer surface of conical drawpieces with a slope angle of $45°$ from commercially pure titanium sheets. The following variable process parameters were used: tool rotational speed varied from –600 to 600 rpm, feed rate varied from 500 to 2000 mm/min and step size varied from 0.1 to 0.5 mm. The SAE 75W85 synthetic gear oil was used as lubricant. Two basic roughness parameters were analyzed: the mean roughness Sa and the maximum height Sz. The influence of SPIF parameters on surface roughness was analysed using multi-layer artificial neural networks. It was found that reducing the feed rate with the climb strategy causes a decrease in the average roughness Sa. The opposite relationship was observed when forming according to the conventional strategy. At low tool feed rate (500 mm/min), reducing the step size caused an increase in the Sz parameter. At high tool feed rate (2000 mm/min), the effect of the step size is negligible.

Keywords: artificial neural networks, incremental sheet forming, sheet metal forming, SPIF, surface roughness

1. Introduction

Single-point incremental forming (SPIF) is a method of machining components made of sheet metal. The SPIF process involves the gradual forming of sheet metal using a pin tool moving along a programmed trajectory adapted to the shape of the drawpiece. The incremental forming processes are highly flexible, allowing different parts to be manufactured using the same tooling system, leading to significant material and energy savings. Additionally, the process offers lower costs and shorter lead times compared to conventional forming methods (Petek et al., 2007). Despite the many advantages of incremental forming, SPIFed components are sensitive to reduced surface roughness, geometric deviations and high springback (Najm & Paniti, 2023; Rosca et al., 2019). The deterioration of surface roughness is the result of frictional interaction between the tool surface and the sheet metal surface (Najm & Paniti, 2021a; Paniti et al., 2020). Additionally, on the opposite (outer) side of the drawpiece wall, an intensive change in surface topography occurs due to deformations of the sheet material. The effect is commonly called 'orange peel patterns' (Liao et al., 2020). The deterioration of the internal surface of the drawpieces is related to the small area of real contact of the forming tool with the sheet metal and severe friction conditions. Too much friction can lead to premature sheet metal fracture.

A common way to reduce friction is to use lubricants with properties adapted to the processing parameters (Milutinović, 2021).

The SPIF technique can be used to form practically all types of metallic materials that are formed using conventional sheet metal forming methods. Titanium sheets, due to their high mechanical strength and low weight, are used in the aviation industry and in luxury cars. The very good biocompatibility of titanium and its alloys makes these materials widely used as medical prostheses (Oleksik et al., 2010). Titanium exhibits good corrosion resistance due to its natural passivation in an atmosphere containing oxygen. The passive TiO_2 layer makes these materials resistant to seawater, weather conditions and chemicals. In the literature, SPIF applications can be found for forming hip prostheses (Sbayti et al., 2016), denture plates (Sbayti et al., 2018) and cranial implants (Cotigă et al., 2014).

The significant factors influencing the obtained surface roughness of the drawpieces include the step size (the smaller the step size, the lower the surface roughness), the tool diameter (the smaller the diameter, the lower the surface roughness) and the forming angle of the drawpiece (the larger the angle, the lower the surface roughness). The tool rotational speed value also has a significant effect on the resulted surface quality, but this is a more complex effect, which also depends on other process parameters. In terms of tool rotation, forming with a rotary tool is more advantageous than with stationary (non-rotating) tool (Hagan & Jeswiet, 2004). Friction in SPIF methods is difficult to analyse qualitatively and quantitatively due to the occurrence of severe mechanical interactions of the cooperating surfaces of tool and blank. This intensifies the adhesive wear phenomena, directly affecting the formability and surface quality of the components (Oleksik et al., 2008). Providing appropriate contact conditions is particularly important when forming titanium, aluminium and their alloy sheets (Najm & Paniti, 2020; 2021a). The improvement of sheet formability can be achieved by implementing the SPIF process at elevated temperature (Popp et al., 2024). Mainly, heating of the workpiece using a stream of hot air, resistance heating, a laser beam or ultrasound is used. Recent research also focuses on improving the geometric quality of parts manufactured by the SPIF techniques by optimising the forming process conditions, lubrication (Şen et al., 2022), numerical techniques such as the finite element method (Pepelnjak et al., 2022) and metamodeling (Sbayti et al., 2022).

The proper selection of SPIF parameters is a key issue for obtaining the required quality of drawpieces. There are many sources in the literature devoted to the influence of SPIF process parameters on the value of forming force, coefficient of friction, springback of the material, temperature in the contact zone and the maximum forming angle (Blaga et al., 2012). Due to many factors that simultaneously synergistically affect the course of SPIF and effects of the forming process, researchers often focus on the optimisation of a selected parameter, such as the surface roughness of the inner or outer surface of the drawpiece, the tool path and the geometric accuracy of the component shape (Najm & Paniti, 2021b). Methods for optimising forming parameters using machine learning and artificial neural networks are also used (Racz et al., 2019). Najm and Paniti (2023) used multilayer neural network for studying the effect of SPIF parameters on prediction of the wall diameter and pillow effect. The best performance of ANN was achieved by way of the Levenberg–Marquardt training algorithm. In another paper by Najm and Paniti (2021a) the ANNs were used to predict surface roughness parameters Sa and Rz, measured on the inner surface of the SPIFed frustum cones. The results showed that ANN gives a better result than support vector regression. Racz et al. (2019) used an adaptive network-based fuzzy inference system to extract the value of thrust force, which appears during incremental forming of DC04 steel drawpieces. The proposed method offering effective method for estimating the forces in SPIF. Oraon and Sharma (2021) applied ANN for predicting the average surface roughness Ra of SPIFed drawpieces from celamine brass Cu67Zn33. The overall efficiency of proposed ANN model was 94.7%. Choundary et al. (2025) predicted formability of material in SPIF of EN AW-7075-T6 aluminium alloy varying wall angle conical frustums by using single-output and double-output ANNs. It was concluded that the developed model allows to reduce the cost and time to select accurate SPIF parameters without performing expensive experiments. The application of artificial intelligence techniques in incremental sheet forming methods was presented by Nagargoje et al. (2023).

Most of the experimental studies of SPIF focus on the analysis of changes in the topography of the inner surface of the drawpieces. This surface is important from the technological point of view. However, the outer surface is often painted and further processed, which also requires meeting certain quality requirements. This article focuses on the analysis of the influence of SPIF process parameters (step size, tool rotational speed, feed rate and forming strategy) on the quality of the outer surface of conical drawpieces from commercially pure (CP) titanium sheets. The effect of tool rotation direction in relation to feed direction on surface roughness has not been the subject of many studies. This aspect

was also taken into account in our research. Due to the difficult to interpret relationship between input parameters and surface roughness, multilayer artificial neural networks were used.

2. Materials and methods

2.1. Workpiece

Incremental forming tests were conducted using 0.4-mm-thick CP titanium sheets grade 2 in annealed state. Chemical composition of the CP titanium sheet according to the requirements of the ASTM B348 (American Society for Testing and Materials, 2019) standard are presented in Table 1. The mechanical properties of the sheets were determined using a static uniaxial tensile test. The test specimens were cut along the rolling direction (RD). Three specimens were tested and on this basis the average values of selected mechanical parameters were determined. The average values of the basic mechanical parameters are presented in Table 2. The surface roughness parameters of the blanks were measured using a Bruker Contour GT 3D optical profilometer, in accordance with the ISO 25178 standard (International Organization for Standardization, 2019). The values of the basic surface roughness parameters were: $Sa = 0.458$ µm, $Sz = 4.63$ µm, $Sp = 2.17$ µm and $Sv = 2.46$ µm.

Table 1. Chemical composition (max., wt.%) of CP titanium sheet

Fe	C	O	N	H	Ti
0.3	0.1	0.25	0.03	0.015	balance

Table 2. Results of uniaxial tensile tests for CP titanium sheets

Yiels stress $R_{p0.2}$ MPa	Ultimate tensile strengths R_m, MPa	Elongation at fracture A, %
463.0	616.2	21.6

2.2. Experimental procedure

Experiment was carried out on 3-axis milling CNC machine Makino PS95. Inside machine working space, specially created device (Fig. 1) for incremental sheet forming was mounted. The device allows to fix up to Ø100 mm sheet blanks and such a titanium sheets were used in experiment. Ø8 mm hemispherical tool, made of sintered tungsten carbide was applied to punch. Conical drawpiece with a constant wall angle of 45° (Fig. 2) was selected as a specimen. Such a geometry allowed to achieve specimen height up to 28.3 mm while starting from cone diameter Ø60 mm. Siemens NX CAM module was used to generate spiral tool paths with constant step size. The tool path was generated based on the desired drawpiece geometry (Fig. 2). The conventional SPIF and climb SPIF (Fig. 3) were considered. To improve friction conditions between tool and sheet, SAE 75W85 synthetic gear oil was used. The SAE 75W-85 gear oil used in the tests provided adequate lubrication at the tool-sheet interface. This lubricant was selected based on preliminary tests and work by Krasowski (2021) on incremental forming of aluminium alloy sheets that are subject to galling.
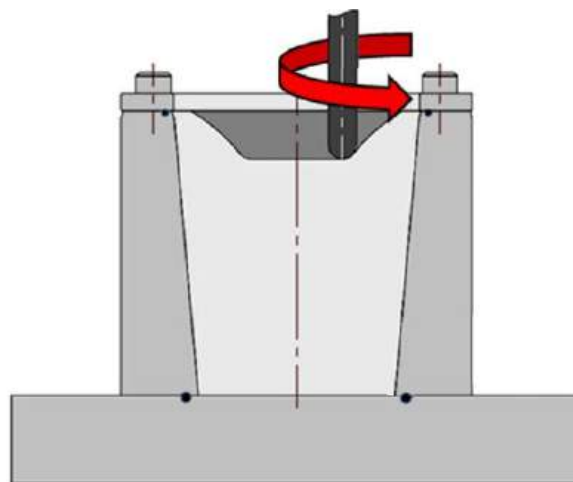

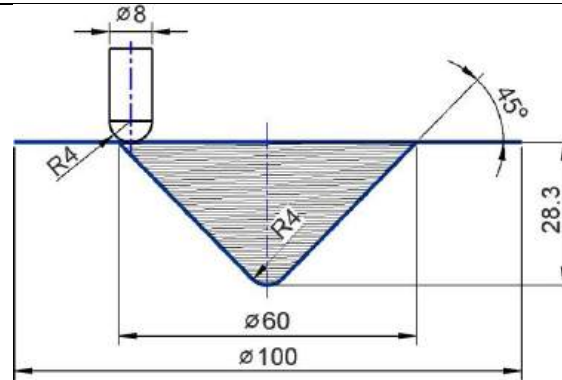**Fig. 1.** Test stand configured for the experiment.

Fig. 2. Geometry and dimensions (in mm) of the tool and the drawpiece.
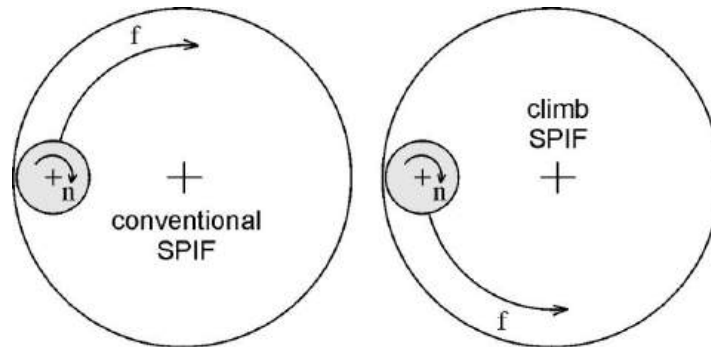

Fig. 3. The concept of conventional and climb SPIF.

Central composite design (CCD) was established to evaluate effect of forming parameters such as tool rotational speed, feed rate and step size on inner and outer drawpiece surface quality. The following variable process parameters were used: tool rotational speed varied from –600 to 600 rpm, feed rate varied from 500 to 2000 mm/min and step size varied from 0,1 to 0.5 mm. Placing some experimental runs outside the minimum and maximum factor ranges in CCD is a conscious strategy to obtain more accurate and useful results, which translates into a better understanding of the process being studied. Rotational speed values below zero means that the direction of the rotation has been switched to opposite (from left to right). Such a combination of input parameters with CCD plan results in 20 runs, where only drawpieces formed completely (without crack) were taken into account. Details of experiments are presented in paper (Szpunar et al., 2021). Only for some settings of SPIF parameters it was possible to form the drawpieces with the desired height h = 28.3 mm. This article focuses on modeling the surface roughness changes for successfully formed drawpieces with parameters shown in Table 3.

Surface topographies were measured in an area of 3.0 × 2.5 mm at a location at half the height of the drawpieces (Fig. 4) using a Talysurf CCI Lite profilometer. The average roughness Sa and the maximum height of profile Sz were selected as roughness parameters for the analysis of topography changes of the outer surface of the drawpieces. Due to the cyclic character of topography changes resulting from the movement of the tool along the spiral trajectory, these parameters are most often used and recommended for the analysis of topography of SPIFed components (Kurra et al., 2015).

Table 3. Experiment design according to central composite design.

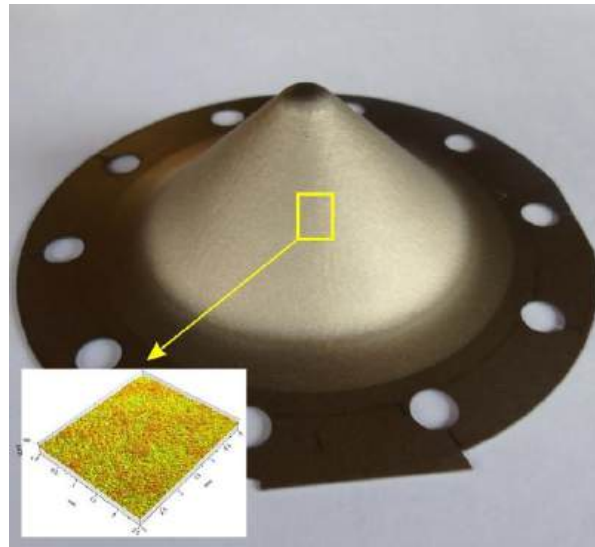| Test no.	Step size a_p, mm	Feed rate f, mm/min	Tool rotational speed n, rpm	Drawpiece height h, mm
1	0.3	1250	–200	28.3
2	0.1	2000	–600	28.3
3	0.3	1250	–790	28.3
4	0.5	500	600	28.3
5	0.3	1250	–400	28.3
6	0.1	500	600	28.3
7	0.1	500	–600	28.3
8	0.3	1250	790	28.3
9	0.5	2000	–600	28.3
10	0.5	2000	600	28.3
11	0.5	500	–600	28.3
12	0.3	1250	400	28.3

Fig. 4. Place of measurement of the surface topography of the drawpieces.

2.3. Artificial neural networks

To analyse the influence of SPIF parameters on the roughness of the outer surface of the draw-pieces, multilayer artificial neural networks (ANNs) were used, which are a module in the Statistica program. The input parameters were step size, tool rotational speed, feed rate and forming strategy. In the case of conventional strategy, the velocity value was negative (Szpunar et al., 2021). Neural networks with one output neuron were used. According to Garret et al. (1997), such an architecture is sufficient to model any complex task. Separate networks were built taking into account the average roughness Sa and maximum height of profile Sz at the output (Fig. 5).
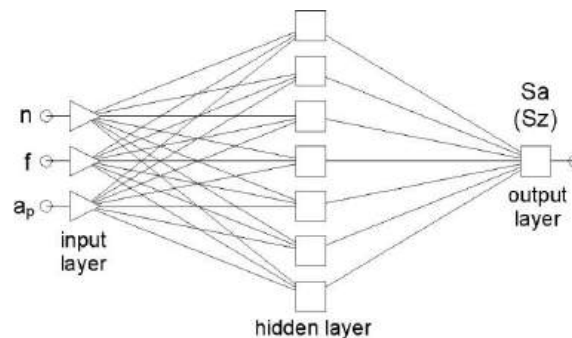

Fig. 5. Architecture of ANN used.

After entering the input data into Statistica and normalizing them to the interval <0, 1>, the program automatically performs the analysis for many ANN architectures with different numbers of neurons in the output layer and determines the ANN with the best quality. A validation set was separated from the training set and 20% of the data sets were randomly assigned to this set. The back propagation algorithm with momentum 0.3 and learning rate 0.1. was used to train the networks. This is the most commonly used and considered the most effective algorithm for training multilayer ANNs. The coefficient of determination R^2 between the experimental and predicted data was adopted as the network quality indicator (Najm & Paniti, 2021b):

$$R^2 = \frac{\sum_{i=1}^{n}(y_i^a - \bar{y})^2 - \sum_{i=1}^{n}\left(y_i^a - y_i^p\right)^2}{\sum_{i=1}^{n}(y_i^a - \bar{y})^2} \tag{1}$$

where n is number of measurement, y_i^p is the prediction value of specific surface roughness parameter, y_i^a is the actual value of specific surface roughness parameter and $\bar{y}$ is the average value of specific surface roughness parameter.

3. Results and discussion

The surface of the components formed with different machining parameters (Table 2) was characterised by a rough structure resulting from the formation of the 'orange peel' effect. This mechanism is created by the change in the orientation of the material grains caused by high subsurface stresses. The outer surface of the drawpiece, during the interaction of the tool with its inner surface, is subjected to local bending and tensile loads (Fang et al., 2014). The occurrence of such loads favours the occurrence of sheet metal surface defects in the form of voids and microcracks. The orange peel effect, presented in the photographs of the surfaces of selected incrementally formed drawpieces (Fig. 6), was first described by Hosford and Caddell (1983). During SPIF processing, the grains of the internal structure of the sheet material tend to thin out or change orientation. The outer surface of the drawpieces takes on a rough appearance due to the different orientations of the neighbouring grains on the surface (Hamilton & Jeswiet, 2010). Due to the character of the orange peel, the outer surfaces of the drawpieces can be divided into three groups: surfaces with a uniform surface of low roughness (Fig. 6a), surfaces with horizontal marks corresponding to the tool engagement on the inner surface of the drawpiece (Fig. 6b), and surfaces with high roughness with uneven valleys (Fig. 6c).
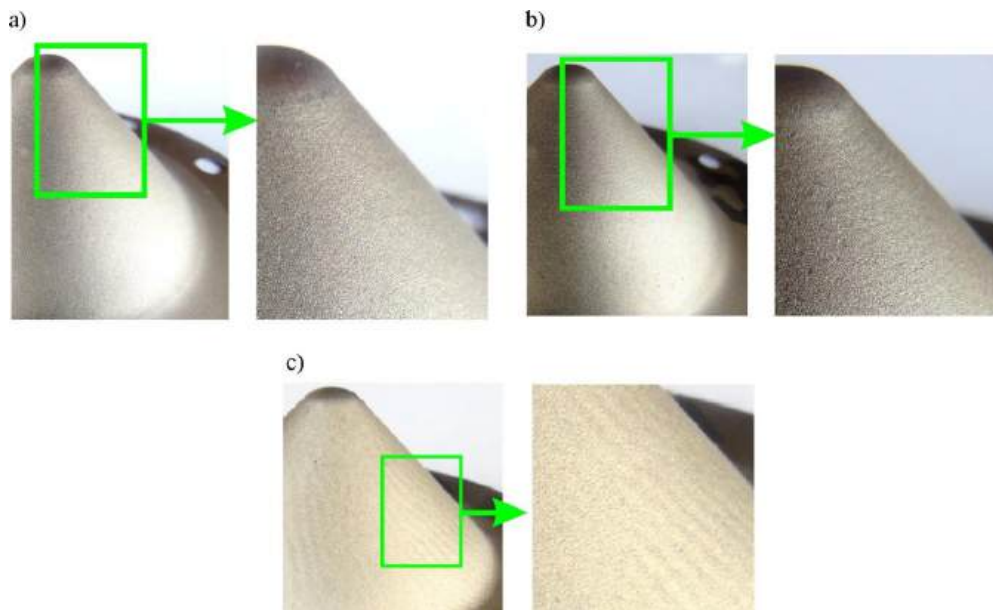

Fig. 6. Outer surface of the drawpieces formed at: a) n = 400 rpm, f = 1250 mm/min, a_p = 0.3 mm, climb strategy; b) n = 600 rpm, f = 2000 mm/min, a_p = 0.5 mm, conventional strategy; c) n = 600 rpm, f = 500 mm/min, a_p = 0.1 mm, conventional strategy.

Average roughness values and maximum height of profile are shown in Table 4. The average roughness values varied between 2.77 and 3.98 μm. The maximum height of profile varied in a much larger range between 74 and 239 μm. It should be mentioned that average roughness Sa and maximum height of profile Sz of as-received sheet metal were 0.458 μm and 4.63 μm, respectively. The outer surface topographies of the selected drawpieces are shown in Fig. 7. The outer surface of the drawpieces consists of evenly distributed dimples (Fig. 8). At high magnification (Fig. 8d) one can see dimples of various sizes, the character of which is similar to the surface of a ductile fracture.

Table 4. Selected surface roughness parameters measured on the outer surface of the cones.

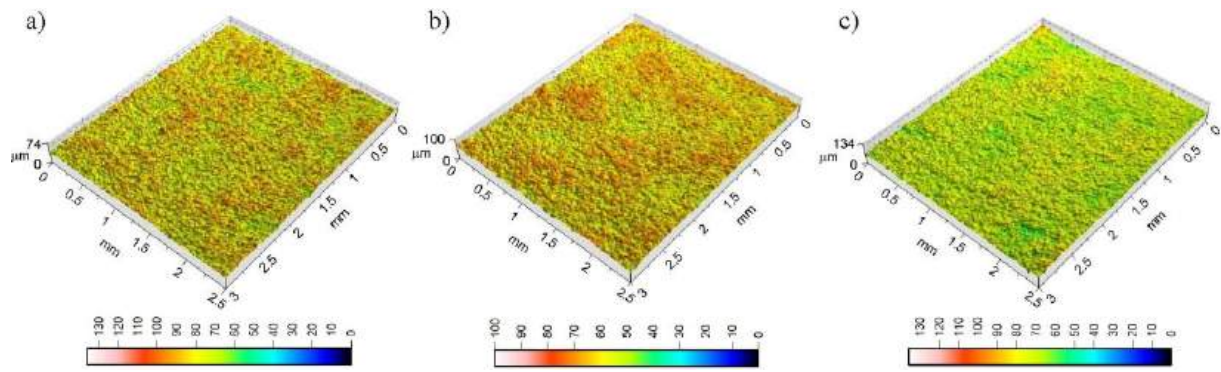| Test no.	Sa, μm	Sz, μm
1	2.77	74.3
2	3.98	136
3	3.4	108
4	3.7	168
5	3.21	239
6	3.42	100
7	3.45	142
8	3.55	195
9	3.38	149
10	2.83	74
11	3.38	103
12	2.95	74.8

Fig. 7. Topography of the outside surface of the drawpieces formed at a) a_p = 0.5 mm, f = 1250 mm/min, n = –200 rpm; b) a_p = 0.1 mm, f = 500 mm/min, n = 600 rpm and c) a_p = 0.1 mm, f = 2000 mm/min, n = –600 rpm.

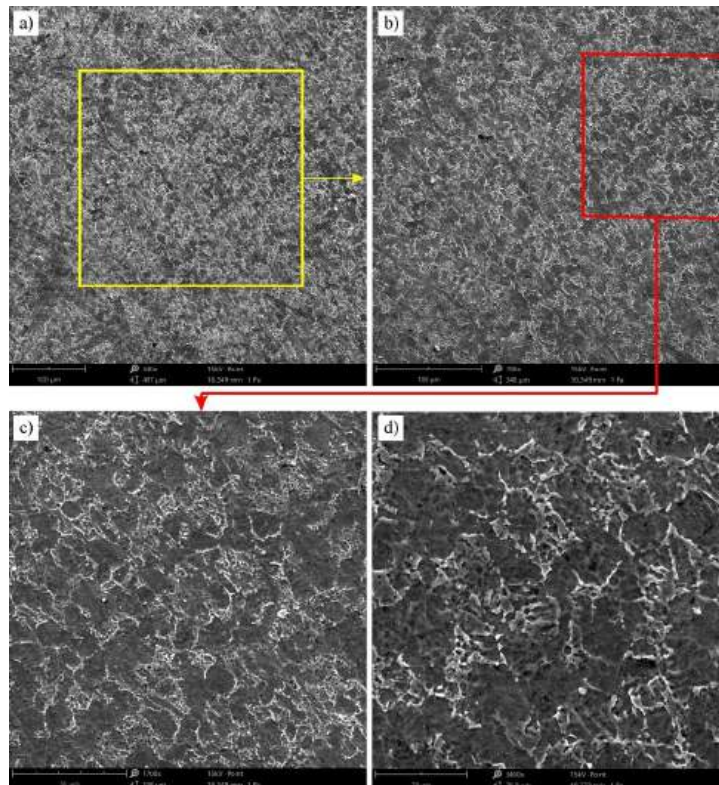**Fig. 8.** SEM micrographs of the outer surface of the drawpiece formed with n = 790 rpm, f = 1250 mm/min ap = 0.3 mm, conventional strategy, at magnifications: a) 540×, b) 790×, c) 1700× and d) 3400×.

After data analysis, the Statistica program proposed the best network architecture, separately for the Sa parameter and separately for the Sz parameter. In both cases, it was a network with 7 neurons in the hidden layer: ANN 3:3-7-1:1. The regression statistics of the obtained networks are presented in Table 5. The coefficients of determination R^2 for both networks exceed 0.92 (0.98 for analysed Sa parameter), so it can be assumed that the neural networks satisfactorily reproduce the experimental data. It should be noted that the amount of training data was not large, and yet the ANNs adapted to the training data in an acceptable way.

Table 5. Regression statistics of ANNs.

Output variable	Sa	Sz
data mean	3.307	131.41
standard deviation of data	0.3806442	55.98477
error mean	0.0001329	0.001395
standard deviation of errors	0.07404	28.94689
absolute terror mean	0.03912	20.51552
standard deviation ratio	0.1945242	0.5170494
Coefficient oif determination R^2	0.9809132	0.922311

Analyzing the response surfaces for average roughness as output variable (Fig. 9), it can be seen that the average roughness of the outer surface of drawpieces is sensitive to the change of tool rotational speed (Figs. 9a and 9b) in relation to the direction of feed rate (forming strategy). In conventional strategy, the values of the Sa parameter are definitely higher than during forming with the climb strategy. Increasing the feed rate with the climb strategy causes an increase in the Sa parameter (Fig. 9a). The opposite relationship occurs when forming according to the conventional strategy (Fig. 9a). It can be stated that the step size, when we consider this parameter together with the tool rotational speed (Fig. 9b), has a small effect on the average roughness. The effect of the step size in interaction with the feed rate is more significant (Fig. 9c). At low feed rate (500 mm/min), increasing the step size causes an increase in the Sa parameter. At high feed rate (2000 mm/min), increasing the step size reduces the average roughness. The rotational speed determines the frictional interaction of the tools with the sheet metal surface. A small feed rate causes faster local heating of the surface asperities, which on the one hand facilitates the forming of the sheet metal, but at the same time at an elevated temperature the tool has a more intensive impact on the deterioration of the surface quality (Fig. 9c).
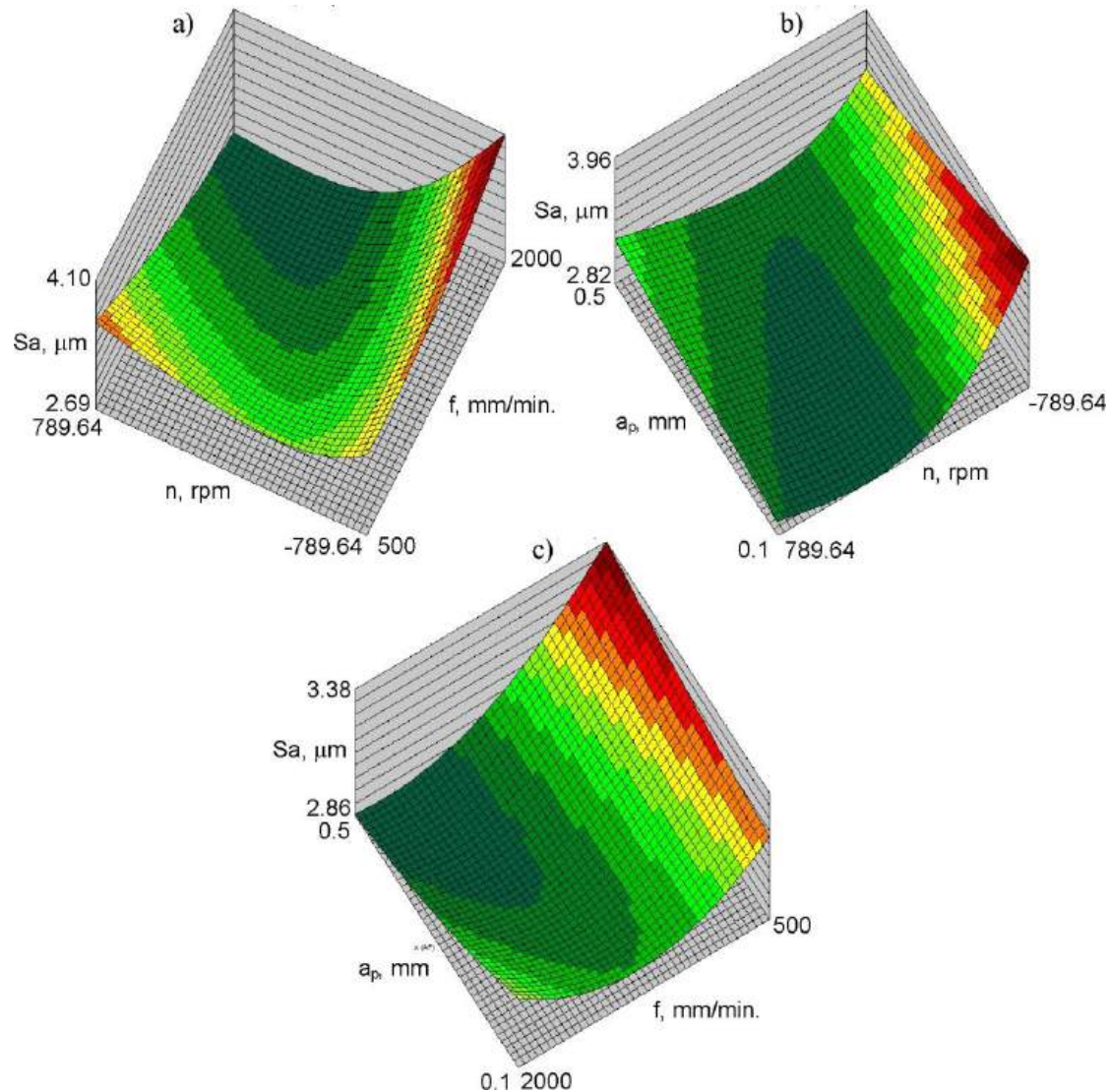

Fig. 9. Response surfaces of ANN showing the effect of a) tool rotational speed and feed rate, b) step size and tool rotational speed, and (c) step size and feed rate on the value of Sa parameter.

Figure 10 shows the response surfaces for maximum height of profile Sz. At a small tool feed rate (500 rpm), increasing the step size causes a decrease in the Sz parameter. At a large tool feed rate (2000 rpm), the effect of the step size is negligible. The effect of feed rate in combination with step size (Fig. 10c) is rather clear, increasing the feed rate increases the maximum height of profile of outer surface. The effect of tool rotational speed and step size (Fig. 10a), and feed rate and tool rotational speed (Fig. 10b) is more complex. Regardless of the rotational speed, decreasing the step size causes an increase in the Sz parameter (Fig. 10a).
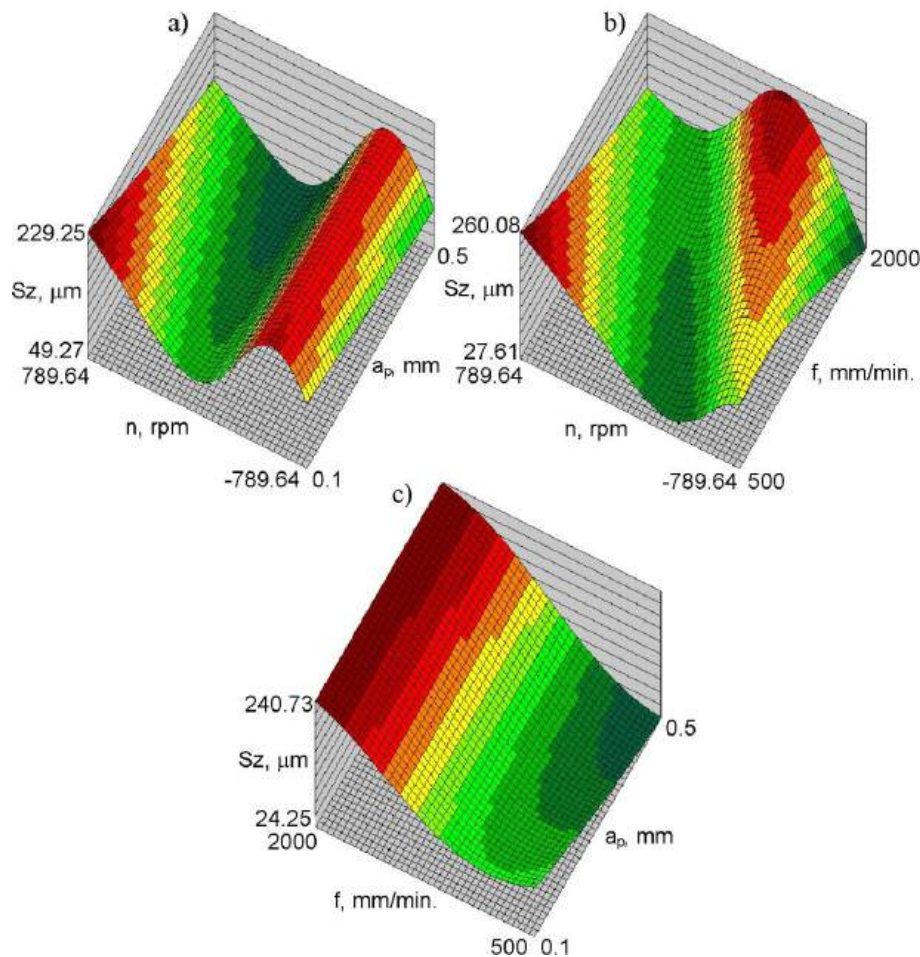
Fig. 10. Response surfaces of ANN showing the effect of a) tool rotational speed and step size, b) feed rate and tool rotational speed, and (c) step size and feed rate on the value of Sz parameter.

4. Conclusions

The article presents the results of experimental studies of changes in basic surface roughness parameters during the forming of conical drawpieces from commercially pure thin titanium sheets and their analysis using multilayer artificial neural network models. The conducted analyses allow for the following main conclusions to be drawn:

- The change in the topography of the outer surface of the drawpieces, depending on the forming parameters, can have a different character: uniform topography with low roughness, topography with horizontal marks corresponding to the tool engagement on the inner surface of the drawpiece and topography with high roughness with uneven valleys.
- Orange peel effect leads to plastic deformation of surface asperities, causing the formation of a grid with small dimples on the sheet metal surface, which roughly correspond to the view of ductile fracture.
- Based on the response surfaces of ANN, it can be stated that in the conventional strategy the average roughness Sa values are higher than during machining with the climb strategy. Reducing the feed rate with the climb strategy causes a decrease in the Sa parameter. The opposite relationship occurs when forming according to the conventional strategy.
- At a small tool feed rate (500 mm/min), reducing the step size causes an increase in the Sz parameter. At a large tool feed rate (2000 mm/min), the effect of the step size on the Sz parameter is negligible.

In future studies, it is planned to analyse the type of lubricant on the surface roughness of the inner and outer surfaces of the drawpieces. In addition, a problem that does not find wide research interest in the literature is the effect of the tool surface roughness on the resulting surface roughness of the drawpiece formed by the SPIF technique. Increasing the amount of training data will affect the better quality of the neural network models.

References

American Society for Testing and Materials. (2019). *Standard specification for titanium and titanium alloy bars and billets* (ASTM Standard No. B348-13). https://www.astm.org/standards/b348

Blaga, A., Bologa, O., Oleksik, V., & Pirvu, B. (2012). Experimental researches regarding the influence of geometric parameters on the principal strains and thickness reduction in single point incremental forming. *UPB Scientific Bulletin, Series D: Mechanical Engineering*, *74*(2), 111-120.

Choudhary, S., Chounchary, N., Kumari, S., Kumari, A., & Mulay, A. (2025). Application of artificial neural network in predicting the performance of SPIF for aerospace grade AA7075-T6. *Journal of Alloys and Compounds*, *1010*, Article 177146. https://doi.org/10.1016/j.jallcom.2024.177146

Cotigă, C., Bologa, O., Racz, S. G., & Breaz, R. E. (2014). Researches regarding the usage of titanium alloys in cranial implants. *Applied Mechanics and Materials*, *657*, 173–177. https://doi.org/10.4028/www.scientific.net/AMM.657.173

Fang, Y., Lu, B., Chen, J., Xu, D. K., & Ou, H. (2014). Analytical and experimental investigations on deformation mechanism and fracture behavior in single point incremental forming. *Journal of Materials Processing Technology*, *214*(8), 1503–1515. https://doi.org/10.1016/j.jmatprotec.2014.02.019

Garret, J. H., Gunarathan, D. J, & Ivezic, N. (1997). Introduction. In N. Kartam, I. Flood, J. H. Garrett (Eds.), *Artificial neural networks for civil engineers: Fundamentals and applications* (pp. 1-18). American Society of Civil Engineers.

Hagan, E., & Jeswiet, J. (2004). Analysis of surface roughness for parts formed by computer numerical controlled incremental forming. *Proceedings of the Institution of Mechanical Engineers, Part B: Journal of Engineering Manufacture*, *218*(10), 1307-1312. https://doi.org/10.1243/0954405042323559

Hamilton, K., & Jeswiet, J. (2010). Single point incremental forming at high feed rates and rotational speeds: Surface and structural consequences. *CIRP Annals*, *59*(1), 311–314. https://doi.org/10.1016/j.cirp.2010.03.016

Hosford, W., & Caddell, R. (1983). *Metal forming*. Prentice Hall.

International Organization for Standardization. (2019). *Geometrical product specifications (GPS) — Surface texture: Areal* (ISO Standard No. ISO 25178-600:2019). https://www.iso.org/standard/67651.html

Krasowski, B. (2021). *Analiza procesu kształtowania przyrostowego usztywnień w cienkościennych konstrukcjach nośnych wykonanych ze stopów aluminium EN AW-2024-T3 oraz EN AW-7075-T6* [Doctoral dissertation, Rzeszów University of Technology].

Kurra, S., Rahman, N. H., Regalla, S. P., & Gupta, A. K. (2015). Modeling and optimization of surface roughness in single point incremental forming process. *Journal of Materials Research and Technology*, *4*(3), 304–313. https://doi.org/10.1016/j.jmrt.2015.01.003

Liao, J., Liu, J., Zhang, L., & Xue, X. (2020). Influence of heating mode on orange peel patterns in warm incremental forming of magnesium alloy. *Procedia Manufacturing*, *50*, 5-10. https://doi.org/10.1016/j.promfg.2020.08.002

Milutinović, M., Lendjel, R., Baloš, S., Zlatanović, D. L., Sevšek, L, Pepelnjak, T. (2021). Characterisation of geometrical and physical properties of a stainless steel denture framework manufactured by single-point incremental forming. *Journal of Materials Research and Technology*, *10*, 605-623. https://doi.org/10.1016/j.jmrt.2020.12.014

Nagargoje, A., Kankar, P. K., Jain, P. K., & Tandon, P. (2023). Application of artificial intelligence techniques in incremental forming: A state-of-the-art review. *Journal of Intelligent Manufacturing*, *34*, 985–1002. https://doi.org/10.1007/s10845-021-01868-y

Najm, S. M., & Paniti, I. (2020). Study on effecting parameters of flat and hemispherical end tools in SPIF of aluminium foils. *Technical Gazette*, *27*(6), 1844-1849. https://doi.org/10.17559/TV-20190513181910

Najm, S. M., & Paniti, I. (2021a). Predict the effects of forming tool characteristics on surface roughness of aluminum foil components formed by SPIF using ANN and SVR. *International Journal of Precision Engineering and Manufacturing, 22*(1), 13-26. https://doi.org/10.1007/s12541-020-00434-5

Najm, S. M., & Paniti, I. (2021b). Artificial neural network for modeling and investigating the effects of forming tool characteristics on the accuracy and formability of thin aluminum alloy blanks when using SPIF. *International Journal of Advanced Manufacturing Technology*, *114*, 2591–2615. https://doi.org/10.1007/s00170-021-06712-4

Najm, S. M., & Paniti, I . (2023). Investigation and machine learning-based prediction of parametric effects of single point incremental forming on pillow effect and wall profile of AlMn1Mg1 aluminum alloy sheets. *Journal of Intelligent Manufacturing*, *34*(1), 331-367. https://doi.org/10.1007/s10845-022-02026-8

Oleksik, V., Bologa O., Breaz, R., & Racz, G. (2008). Comparison between the numerical simulations of incremental sheet forming and conventional stretch forming process. *International Journal of Material Forming*, *1*, 1187-1190. https://doi.org/10.1007/s12289-008-0153-6

Oleksik, V., Pascu, A., Deac, C., Fleacă, R., Bologa, O., & Racz, G. (2010). Experimental study on the surface quality of the medical implants obtained by single point incremental forming. *International Journal of Material Forming*, *3*, 935-938. https://doi.org/10.1007/s12289-010-0922-x

Oraon, M., & Sharma, V. (2021) Application of artificial neural network: A case of single point incremental forming (SPIF) of Cu67Zn33 alloy. *Management and Production Engineering Review*, *12*(1), 17-23. https://doi.org/10.24425/mper.2021.136868

Paniti, I., Viharos, Z. J., Harangozó, D., & Najm, S. M. (2020). Experimental and numerical investigation of single point incremental forming of aluminium alloy foils. *Acta Imeko*, *9*(1), 25-31. https://doi.org/10.21014/acta_imeko.v9i1.750

Pepelnjak, T., Sevšek, L., Lužanin, O., & Milutinović M. (2022). Finite element simplifications and simulation reliability in single point incremental forming. *Materials*, *15*(10), Article 3707. https://doi.org/10.3390/ma15103707

Petek, A., Gantar, G.; Pepelnjak, T., & Kuzman K. (2007). Economical and ecological aspects of single point incremental forming versus deep drawing technology. *Key Engineering Materials*, *344*, 931-938. https://doi.org/10.4028/www.scientific.net/KEM.344.931

Popp, G. P., Racz, S. G., Breaz, R. E., Oleksik, V. Ș., Popp, M. O., Morar, D. E., Chicea, A. L., Popp, I. O. (2024). State of the art in incremental forming: process variants, tooling, industrial applications for complex part manufacturing and sustainability of the process. *Materials*, *17*(23), Article 5811. https://doi.org/10.3390/ma17235811

Racz, S. G., Breaz, R. E., Bologa, O., Tera, M., & Oleksik V. S. (2019). Using an adaptive network-based fuzzy inference system to estimate the vertical force in single point incremental forming. International *Journal of Computers Communications & Control*, *14*(1), 63-77.

Rosca, N., Oleksik, V., Pascu, A., Oleksik, M., & Avrigean E. (2019). Optical study for springback prediction, thickness reduction and forces variations on single point incremental forming. *Materials Today: Proceedings*, *12*, 213-218. https://doi.org/10.1016/j.matpr.2019.03.116

Şen, N., Şirin, Ş., Kıvak, T., Civek, T., & Seçgin, Ö. (2022). A new lubrication approach in the SPIF process: Evaluation of the applicability and tribological performance of MQL. *Tribology International*, *171*, Article 107546. https://doi.org/10.1016/j.triboint.2022.107546

Sbayti, M., Bahloul, R., & Belhadjsalah, H. (2018). Numerical modeling of hot incremental forming process for biomedical application. In M. Haddar, F. Chaari, A. Benamara, M. Chouchane, C. Karra, N. Aifaoui (Eds.), *Design and modeling of mechanical systems—III* (pp. 881-891). Springer International Publishing. https://doi.org/10.1007/978-3-319-66697-6_86

Sbayti, M., Ghiotti, A., Bahloul, R., Belhadjsalah, H., & Bruschi, S. (2016). Finite element analysis of hot single point incremental forming of hip prostheses. *MATEC Web of Conferences*, *80*, Article 14006. https://doi.org/10.1051/matecconf/20168014006

Sbayti, M., Ghiotti, A., Bahloul, R., BelhadjSalah, H., & Bruschi, S. (2022). effective strategies of metamodeling and optimization of hot incremental sheet forming process of Ti6Al4 vartificial hip joint component. *Journal of Computational Science*, *60*, Article 101595. https://doi.org/10.1016/j.jocs.2022.101595

Szpunar, M., Ostrowski, R., Trzepieciński, T., & Kaščák, Ľ. (2021). Central composite design optimisation in single point incremental forming of truncated cones from commercially pure titanium Grade 2 sheet metals. *Materials*, *14*(13), Article 3634. https://doi.org/10.3390/ma14133634

Wpływ Parametrów Procesu Kształtowania Punktowego na Chropowatość Powierzchni Zewnętrznej Wytłoczek Stożkowych Wykonanych z Blach Tytanowych

Streszczenie

Wraz z upowszechnieniem obrabiarek sterowanych numerycznie, proces punktowego formowania przyrostowego cieszy się rosnącym zainteresowaniem w przemyśle. W artykule przedstawiono wyniki badań wpływu parametrów procesu formowania (krok narzędzia, prędkość obrotowa narzędzia, prędkość posuwu i strategia formowania) na chropowatość powierzchni zewnętrznej wytłoczek stożkowych kształtowanych z blach tytanowych o czystości technicznej. Przeanalizowano dwa podstawowe parametry chropowatości, średnią arytmetyczną wysokość powierzchni Sa i maksymalną wysokość powierzchni Sz. Wpływ parametrów procesu kształtowania przyrostowego na chropowatość powierzchni analizowano przy użyciu wielowarstwowych sztucznych sieci neuronowych. Stwierdzono, że zmniejszenie prędkości posuwu przy przeciwbieżnej strategii obróbki powoduje zmniejszenie średniej chropowatości Sa. Odwrotną zależność zaobserwowano podczas formowania według strategii współbieżnej. Przy małej prędkości posuwu narzędzia (500 mm/min) zmniejszenie wartości kroku narzędzia spowodowało wzrost parametru Sz. Przy dużej prędkości posuwu narzędzia (2000 mm/min) wpływ wartości kroku narzędzia jest pomijalny.

Słowa kluczowe: sztuczne sieci neuronowe, przyrostowe kształtowanie blach, kształtowanie blach, SPIF, chropowatość powierzchni